

https://dspace.org/

Developing of a parametrically resonw1t vibrating screen, modelling, simulation and dynamic testing

Mohanlal, Mishal

2023-07

University of the Witwatersrand, Johannesburg

https://hdl.handle.net/10539/40117

Mohanlal, Mishal. (2023). Developing of a parametrically resonw1t vibrating screen, modelling, simulation and dynamic testing. [Master's thesis, University of the Witwatersrand, Johannesburg]. WIReDSpace. https://hdl.handle.net/10539/40117

Downloaded from a DSpace repository. https://dspace.org/



DEVELOPING OF A PARAMETRICAL RESONANT VIBRATING SCREEN, MODELLING, SIMULATION AND DYNAMIC TESTING

Mishal Mohanlal

(Student number: 0602191Y)

School of Civil Engineering

University of the Witwatersrand

Johannesburg, South Africa.

Supervisor: Dr Kuinian Li

A dissertation submitted to the Faculty of Engineering and the Built Environment, University of the Witwatersrand, Johannesburg, in fulfilment of the requirements for the degree of Master in Science in Engineering

Date:17/03/20

DECLARATION

I declare that this dissertation is my own unaided work. It is being submitted to the Degree of Master of Science in Engineering to the University of the Witwatersrand, Johannesburg. It has not been submitted before for any degree or examination to any other University.

Signature:  Date: 17/03/2023

ABSTRACT

A novel coupled spring pendulum vibrating screen is proposed with the goal of developing efficient screening using parametric resonance. A simple spring pendulum is initially studied to provide the basis of the dissertation. The theoretical model of the proposed vibrating screen is developed using Lagrangian mechanics which includes damping and generalized forces. Two derivations of the vibrating screen are proposed, the first being a 4DOF (degree of freedom) system and the second being a 3DOF system. The 3DOF system is found to present better numerical stability and is thus utilized for the study. It is shown that the 3DOF system is comparable to the simple spring pendulum for the case where initial conditions are applied to similar coordinates. The proposed vibrating screen presents motion which is not indicative of traditional vibrating screens. It is found that a system where attributes are sized for parametric resonance requires far smaller excitation forces to achieve higher accelerations and displacements compared to traditional vibrating screens. The proposed vibrating screen is an unfeasible design due to the large displacements; high foundation loads and limitations on mechanical components. Discrete element method (DEM) simulations of the proposed vibrating screen are performed to study the efficiency with varying inclinations of the mesh deck. The results are compared to a linear motion vibrating screen. The proposed screen requires far less energy compared to traditional vibrating screens and achieves higher efficiencies with larger deck inclinations. The derived differential equations are verified by experimental testing using free vibrations. The numerical simulations and experimental tests present a good correlation. Signal processing is implemented to compare the natural frequencies from the experimental testing and numerical simulations, the results present a good correlation.

ACKNOWLEDGEMENTS

I would like to express my gratitude to my supervisor, Dr Kuinian Li who has presented a great deal of guidance and interest in the topic of vibrating screens. His background in mechanical engineering and interest in dynamics allowed for this research to occur.

The experimental testing is made possible from the generosity provided by ADMO Engineering who fabricated the test rig and provided a location where testing could be performed. I am grateful to Dawie Swanepoel and Michael Jooste from ADMO Engineering who played a key role in the fabrication of the test rig.

I would like to thank Zeyn Boston from Fank Gallo Springworks CC for donating the springs which have been used for the experimental study. The donated springs are used in the design of small Enduron vibrating screens thus making them more applicable to the study.

Dr Robert Warmbeir and Dr Keegan Anderson for the introduction to Lagrangian mechanics and reviewing the derivation of both the 4DOF and 3DOF system which I developed.

Thank you to Jozua Joubert and Cronje Visser from TANDM, who assisted with guidance on the experimental setup and provided measurement equipment. Unfortunately, the accelerometers and data loggers were never used due to the fear of damaging the accelerometers due to high accelerations.

A special thank you to Lungile Mdlazi who has always provided guidance on any engineering endeavour I follow. Thank you for providing the 6-axis IMU which allowed the experimental testing to be successfully implemented.

Lastly, I would like to thank my wife Mohini Mohanlal for her endless support during my studies, thank you for your patience, support, and love even through your pregnancy. To my son Taksh, I will always remember your smiles when your mum would say “you need to teach daddy about parametric resonance”.

TABLE OF CONTENTS

CHAPTER 1: INTRODUCTION AND LITERATURE REVIEW 1
1.2 RESEARCH BACKGROUND/CONTEXT 1
1.3. PROBLEM STATEMENT/MOTIVATION 3
1.4. RESEARCH QUESTIONS 4
1.5. RESEARCH OBJECTIVES 4
1.6. LITERATURE REVIEW 4
1.6.1. RESONANCE IN MECHANICAL/STRUCTURAL SYSTEMS 4
1.6.1.1. *DAMPING SYSTEMS* 5
1.6.1.2. *RESONANCE IN VIBRATING SCREENS* 5
1.6.1.3. *MOTION/TRACE OF VIBRATING SCREENS* 6
1.6.2. PARAMETRIC RESONANCE 8
1.6.3. INFLUENCE OF MOTION/TRACE ON THE SCREENING PROCESS 10
1.7. CONCLUSION 10
1.8. RESEARCH METHODS 11
CHAPTER 2: THEORETICAL STUDY OF A SIMPLIFIED 2DOF SYSTEM 14
2.1. SD18/36 LINEAR MOTION VIBRATING SCREEN 14
2.2. DERIVATION OF THE 2DOF SIMPLIFIED MODEL 14
2.3. 2DOF SYSTEM SIMULATED USING INITIAL CONDITIONS 17
2.4. 2DOF MODEL WITH EXCITATION AND DAMPING 23
2.5. CONCLUSION 36
CHAPTER 3: DERIVATION OF THE 4DOF SYSTEM 37
3.1. DERIVATION OF THE 4DOF SYSTEM 37
3.2. SIMULATION OF THE 4DOF SYSTEM 39
CHAPTER 4: 3-DOF SYSTEM 45
4.1. DERIVATION OF THE 3DOF SYSTEM 45
4.2. COMPARISON OF THE 3DOF AND 2DOF SYSTEM CONSIDERING INITIAL CONDITIONS FOR THE SPRING/S 50
4.3. INITIAL CONDITIONS FOR THE "x" AND "y" COORDINATES 50
4.3. INITIAL CONDITIONS FOR THE θ COORDINATE 53
4.4. PARAMETRIC RESONANCE AND INITIAL CONDITIONS FOR THE θ COORDINATE 65
4.5. DAMPING OF THE 3DOF SYSTEM 76
4.4.1. DAMPING WITH INITIAL CONDITIONS FOR θ 77
4.4.2. DAMPING AND INITIAL CONDITIONS FOR THE θ COORIDNATE (PARAMETRIC RESONANCE) 79
4.5. DERIVATION OF THE GENERALISED FORCES 86

4.6. PARAMETRIC EXCITATION OF THE 3DOF MODEL WITHOUT DAMPING ... 88
4.6.1. PARAMETRIC EXCITATION IN THE X COORDINATE ... 89
4.6.2. PARAMETRIC EXCITATION IN THE X AND Y COORDINATE ... 95
4.6.3. PARAMETRIC EXCITATION IN THE θ COORDINATE ... 99
4.6.4. PARAMETRIC EXCITATION WITH DAMPING ON THE θ COORDINATE ... 109
4.7. SUMMARY OF THE SIMULATIONS ... 116
4.8. SIZING A VIBRATING SCREEN ... 117
4.8.1. EXCITATION ON THE x AND θ COORDIANTE ... 117
4.8.1.1. CASE XN ... 118
4.7.1.2. CASE θN ... 118
CHAPTER 5: DEM STUDY ... 126
5.1. MATERIAL PROPERTIES ... 126
5.3. MODELLING OF MOTION IN LIGGGHTS AND TIMESTEP DETERMINATION ... 131
5.8. DEM ANALYSIS ... 135
5.8.1. MATERIAL DISTRIBUTION OVER THE DECK OF THE SCREEN ... 135
5.8.2. UNDERSIZE AND OVERSIZE MATERIAL FLOW ... 136
5.8.3. EFFICIENCY COMPARISON ... 138
5.9. DEM USING REVISED CAD GEOMETRY ... 141
5.10. DEM CONCLUSION ... 144
CHAPTER 6: EXPERIMENTAL STUDY ... 145
6.1. EXPERIMENTAL SETUP ... 145
6.3. EXPERIMENTAL TEST CASES ... 148
6.3.1. TESTS CASE A ... 148
6.3.2. TEST CASE B ... 149
6.3.3. TEST CASE C ... 150
6.4. EXPERIMENTAL RESULTS ... 151
6.4.1. EXPERIMENTAL RESULTS FOR CASE A ... 151
6.4.2. EXPERIMENTAL RESULTS FOR TESTCASE B ... 157
6.4.1. EXPERIMENTAL RESULTS FOR TEST CASE C ... 164
6.5. PARAMETRICALLY RESONANT TEST CASE ... 179
6.6. EXPERIMENTAL TESTING CONCLUSION ... 180
CHAPTER 7: FEASIBILITY OF THE PARAMTERICALLY RESONANT VIBRATING SCREEN ... 181
7.1. MECHANICAL FEASIBILITY ... 181
7.2. STRUCTURAL DESIGN ... 182
7.3. RESEARCH QUESTIONS AND OBJECTIVES ... 184

CHAPTER 8: CONCLUSION 185
CHAPTER 9: FURTHER RESEARCH 187
REFERENCES 188
APPENDIX A – MATLAB CODES 192
APPENDIX B – TIME DERIVATIVES OF $(\boldsymbol{r}+\boldsymbol{b})$ 198
APPENDIX C – RESULTS FOR THE 3DOF PARAMETRICALLY SIZED MODEL 200
APPENDIX B – RESULTS FOR THE 3DOF PARAMETRICALLY SIZED MODEL WITH EXCITATION 205
APPENDIX D – MATHEMATICA CODES 208
APPENDIX E – RESULTS FOR THE $\boldsymbol{XN}$ CASE 210
APPENDIX F – RESULTS FOR THE $\boldsymbol{\theta N}$ CASE 231
APPENDIX G – LIGGGHTS INSTALLTION 252
APPENDIX H – AUTOMATION OF LIGGGHTS INPUT SCRIPT FOR MOTION 253
APPENDIX I – LIGGGHTS INPUT SCRIPT 256
APPENDIX J – LM15 MATERIAL DISTRIBUTION ON THE DECK 260
APPENDIX K – SPRING DATA SHEET 262
APPENDIX L – DYTRAN 4401A2 6 AXIS ACCELEROMETER DRAWING 263
APPENDIX M – EXPERIMENTAL RESULTS 264

LIST OF FIGURES

Figure 1: Anatomy of a vibrating screen 1
Figure 2: Types of strokes. circular, elliptical, and linear motion 2
Figure 3: Relative screening rate Vs amplitude (Sullivan, n.d.) 2
Figure 4: Screening characteristics (He & Lui, 2009) 2
Figure 5: Evolution of vibrating screening (Makinde, et al., 2015) 3
Figure 6: SDOF with a tuned mass damper (Chopra, 2012) 5
Figure 7: Simplified model of a swing trace vibrating screen (Jianzhang & Xin, 2012) 6
Figure 8:Trajectory of particles (Jianzhang & Xin, 2012) 7
Figure 9: Comparison between linear motion and swing motion vibrating screen (Jianzhang & Xin, 2012) 7
Figure 10: Composite vibrating screen (Zhanfu, et al., 2018) 7
Figure 11: Parametric resonant screen (Zahedi & Babitsky, -) 8
Figure 13: Average particle velocity Vs time (Dong, et al., 2013) 10
Figure 14: Proposed screen design 11
Figure 15: Simplified 2DOF system 15
Figure 16:Freebody diagram for applied loads on the 2DOF system 17
Figure 17: Angular and translational displacements for the 2DOF using attributes from Table 4 18
Figure 18: Motion trace of the 2DOF model using attributes presented in Table 4 19
Figure 19: translation and rotational displacement and acceleration using attributes presented in Table 4 21
Figure 20: Motion trace for attributes presented in Table 4 21
Figure 21: 2DOF spring pendulum motion traces due to varying initial conditions 22
Figure 22: Displacement and acceleration results for attributes presented in Table 6 24
Figure 23:Motion trace for attributes presented in Table 6 24
Figure 24: PSD of acceleration results using attributes presented in Table 6 26
Figure 25: Zoomed view of the pendulum frequency presented in Figure 24 26
Figure 26: PSD and radial acceleration using larger excitation force on the spring 27
Figure 27: Displacement and acceleration results for a parametrically resonant 2 DOF model 28
Figure 28: Motion trace for parametrically resonant 2 DOF model 28
Figure 29: Power spectral density for the parametrically resonant model 29
Figure 30: Displacement and acceleration results for the model attributes in Table 7 30
Figure 31:Resultant acceleration and displacement 31
Figure 32: Motion plot for the attributes presented in Table 7 32
Figure 33:Radial and rotational displacements using the simplified model for various damping 33
Figure 34: Displacement and acceleration results for an excited 2DOF with damping 34
Figure 35: Motion trace for the excited 2 DOF system with damping 35
Figure 36: PSD for the excited 2DOF system with damping 35
Figure 37: Motion trace for various damping ratios 36
Figure 38: 4DOF model for the proposed vibrating screen design 37
Figure 39: Displacement comparison between the 2DOF and 4DOF system 39
Figure 40: Displacements of the 4DOF using initial conditions presented by Table 4 40
Figure 41: Filtered displacement results for coordinate *b* 40
Figure 42: Components of #1 41
Figure 43: Plot of the holonomic constraint 42
Figure 44: Simulation results over a 0.5 second time frame 43
Figure 45: Displacement results considering the positive and negative roots of #1 44

Figure 46: 3-DOF model for the proposed vibrating screen 45
Figure 47: Vectors used for the calculation of α 49
Figure 48: Freebody diagram for the accelerations (3DOF) 49
Figure 49:Comparison of the simplified model and 3DOF model with initial conditions applied to the spring/s 50
Figure 50:Comparison between the 2DOF and 3DOF system with x and y initial conditions (3DOF) 51
Figure 51: Angular displacements results of the rigid bar considering x and y initial conditions 51
Figure 52: PSD of the 3DOF system using initial conditions for x and y 52
Figure 53:PSD for the alpha and beta components due to initial conditions applied to the x and y coordinates 52
Figure 54: Displacement results using different ode solvers 54
Figure 55: Displacement results for the 3DOF system using various solvers on Mathematica and attributes presented by Table 9 56
Figure 56: Angular displacement and accelerations of the rigid bar using initial conditions presented in Table 9 57
Figure 57:Displacement and acceleration results for the X and Y coordinate for initial conditions presented in Table 9 58
Figure 58: Normalised acceleration results for initial conditions presented by Table 9 59
Figure 59: Normalised displacement results for attributes presented in Table 9 59
Figure 60: Plotting numerical values of Term A and B from the differential equations using attributes presented in Table 9 61
Figure 61: Various components of equations 63 and 64 using attributes presented in Table 9 61
Figure 62: FFT results for each coordinate using attributes presented in Table 9 62
Figure 63: Resultant acceleration and stretch in springs for attributes presented in Table 9 63
Figure 64: PSD for the stretch in the springs and angular displacements of springs, attributes from Table 9 64
Figure 65: Comparison of different Matlab solvers using attributes from Table 5 and initial conditions for θ 65
Figure 66: Offset normalised displacements using attributes from Table 5 and initial conditions for θ 66
Figure 67: Normalised displacement results with markers for attributes from Table 5 and initial conditions for θ 67
Figure 68: Acceleration results for each coordinate using attributes from Table 5 (3DOF) 68
Figure 69: Acceleration results for each coordinate using attributes presented by Table 5 (3DOF) 69
Figure 70: Term A and B for a parametrically sized system using attributes presented by Table 5 (3DOF) 70
Figure 71: Various components of Term A and B for results presented by Figure 72 70
Figure 73: PSD for the parametric resonant 3DOF system 72
Figure 74: Resultant acceleration and stretch for each spring using attributes from Table 5 73
Figure 75: Angular displacement of each spring using attributes from Table 5 (3DOF) 74
Figure 76: Motion plots for the attributes presented in Table 5 (3DOF) 75
Figure 77: Displacement for each coordinate for initial conditions presented in Table 9 and damping 77
Figure 78: Normalised acceleration with attributes from Table 9 and damping 78
Figure 79:Damping with attributes and initial conditions presented by Tale 9 78

Figure 80: Displacement results for the 3DOF considering attributes and initial conditions from Table 5 with damping....79
Figure 81: Normalised displacement results for each coordinate....80
Figure 82: Acceleration results....81
Figure 83: Damped and undamped acceleration results....82
Figure 84: Motion plot for each spring for attributes assigned from Table 5 and initial conditions for θ....83
Figure 85: Stretch in spring A and B due to attributes presented in Table 5 and initial conditions on θ....83
Figure 86: Angular displacement of each spring due to attributes presented in Table 5 and initial conditions on θ....84
Figure 87:Motion plot for attributes presented in Table 5 with increasing damping ratio (θ initial conditions)....85
Figure 88:Motion plot for Spring A, attributes presented in Table 5 with increasing damping ratio (θ initial conditions)....85
Figure 89: Generalised forces for the 3DOF....86
Figure 90: Displacement results of the 3DOF system with conditions assigned as per Table 7....88
Figure 91:Displacement results from Matlab using attributes assigned from Table 10....89
Figure 92: Displacement results from Mathematica using attributes assigned from Table 10....90
Figure 93: Combined results of ODE45, ODE23s and Mathematica using attributes assigned from Table 10....91
Figure 94: Acceleration results using attributes presented in Table 10....92
Figure 95:Power spectral density for the X and Y coordinates using attributes assigned from Table 11....93
Figure 96: Motion plot for the attributes assigned as per Table 11....94
Figure 97:Matlab displacement plots using attributes in Table 11 with excitation in X and Y....95
Figure 98: Mathematica displacement plots using attributes in Table 11 with excitation in x and y coordiantes....96
Figure 99: ODE and Mathematica results using attributes from Table 11 and excitation in x and y coordinates....97
Figure 100: Acceleration results using attributes presented in Table 10 with acceleration in x and y coordinates....98
Figure 101: Resultant acceleration and the displacement of each spring using attributes presented in Table 10 with acceleration in x and y coordinates....98
Figure 102:Motion plot for the attributes assigned as per Table 11 with excitation in x and y coordinates....99
Figure 103: Matlab displacement results with θ excitation and attributes assigned from Table 10....100
Figure 104: Mathematica displacement results with θ excitation and attributes assigned from Table 11....101
Figure 105: ODE and Mathematica results for excitation in θ coordinate....102
Figure 106: Acceleration results for excitation in θ coordinate....103
Figure 107: Acceleration results on a single plot for excitation in θ coordinate....104
Figure 108: 0 to 4.5 seconds for excitation in θ coordinate....104
Figure 109: 4.5-15 seconds for excitation in θ coordinate....105
Figure 110: Term A and B for excitation in θ coordinate....106
Figure 111: Components of term A and B for excitation in θ coordinate....106
Figure 112: PSD results for the excitation in θ and attributes from Table 10....107

Figure 113:Acceleration results for the attributes in Table 11 and excitation in the θ coordinate....108
Figure 114: θ coordinate displacement and accelerations for the attributes in Table 11 and excitation in the θ coordinate....108
Figure 115: Motion plot of the springs due to excitation in θ and attributes in Table 10....109
Figure 116: Displacement results for each coordinate using attributes in Table 10 and damping....110
Figure 117: Acceleration results for each coordinate using attributes in Table 10 and damping....111
Figure 118: Normalised acceleration results for Displacement results for each coordinate using attributes in Table 10 and damping....111
Figure 119: Term A and B Displacement results for each coordinate using attributes in Table 10 and damping....112
Figure 120: Components of term A and B Displacement results for each coordinate using attributes in Table 10 and damping....113
Figure 121: FFT results for 3DOF simulation with attributes from Table 10 and damping....114
Figure 122:Resultant acceleration results for 3DOF simulation with attributes from Table 11 and damping....115
Figure 123: Angular displacement results using attributes in Table 10 and damping....115
Figure 124:Motion plots for the 3DOF system with damping and attributes from Table 10 116
Figure 125: θ displacement results for simulation XN....118
Figure 126: θ excitation with incrementing the excitation frequency....119
Figure 127: Normalised acceleration results for θ coordinate excitation at the spring natural frequency....119
Figure 128: Normalised acceleration results for excitation applied to θ coordinate at the pendulum frequency....120
Figure 129: Displacement results for excitation at pendulum and spring natural frequency 120
Figure 130: Acceleration results for excitation at pendulum and spring natural frequency....121
Figure 131: Excitation at 1.34Hz in the θ coordinate with incremented dynamic loads....122
Figure 132: Displacement and accelerations results for varying values of N at 1.34Hz excitation....122
Figure 133: Displacement and acceleration results for varying values of N at 1.34 Hz excitation....123
Figure 134:Motion plot for incremented excitation using 1.34Hz excitation....123
Figure 135: Acceleration results for the final 3DOF model....124
Figure 136: Displacement results for the final 3DOF model....125
Figure 137: Motion trace for the final 3DOF model....125
Figure 138: Workflow for the pre and post processing in LIGGGHTS....126
Figure 139: Plan view of the SD18/36....129
Figure 140: Work flow diagram for the development of geometry in. stl format....130
Figure 141: Mesh deck....130
Figure 142: Isometric view of the screen box....131
Figure 143: Side view of the vibrating screen....133
Figure 144: Top view of the screen box with material feed....133
Figure 145: Collection box and screen model....134
Figure 146: Material distribution over the deck of the SD vibrating screen....135
Figure 147: LM material distribution over the deck....136
Figure 148: Material movement on the deck of a horizontal deck vibrating screen....137
Figure 149: Undersize and oversize material flow profiles for the SD screens....137
Figure 150: Oversize and undersize material flow for the LM screens....138

Figure 151: Mass of undersize material of the small category 139
Figure 152:Mass of small material found in the oversize collection box 139
Figure 153: Large particles in the undersize catchment volume 140
Figure 154: LM0 and LM15 at time 2.2 seconds 140
Figure 155: Efficiency of the LM and SD screen 141
Figure 156: Revised screen box with 4 mesh deck surfaces 142
Figure 157: LMR0 and LM0 at 2.4 seconds 142
Figure 158: Time to reach 60kg of undersize material in the undersize catchment volume for LM, LMR and SD 143
Figure 159: Screen efficiency of the SD, LM and LMR screens 143
Figure 160: Experimental setup 146
Figure 161: Side view of the experimental setup 146
Figure 162: Dytran 6 axis accelerometer 147
Figure 163: Experimental setup to impose initial conditions on the springs 148
Figure 164: Angle finder results on each end of the rigid bar presenting a 0 inclination 149
Figure 165: Setup for initial conditions in the x coordinate 149
Figure 166: Experimental setup with initial conditions on the x coordinate 150
Figure 167: Experimental setup for the initial conditions imposed on the θ coordinate 151
Figure 168: AZ acceleration results for experimental setup with initial conditions on the springs 152
Figure 169: Zoomed view of the AZ acceleration results for recording 2 153
Figure 170: PSD for the initial conditions imposed on the springs, experimental setup 154
Figure 171: Basic finite element model of the experimental setup 154
Figure 172: Mode shape of 114.514Hz natural frequency 155
Figure 173: AZ and y coordinate acceleration results for recording 2 and numerical simulation (test case A) 156
Figure 174: PSD for the numerical solution which mimics the experimental spring initial conditions 157
Figure 175: AY acceleration results for the initial conditions on the x coordinate 158
Figure 176: AZ acceleration results for the initial conditions imposed on the x coordinate. 158
Figure 177: FFT for initial conditions on the x coordinate (experimental setup) 159
Figure 178: FFT for the AZ results sing initial conditions on the x coordinate 160
Figure 179: Numerical comparison to experimental conditions (initial conditions imposed on the x coordinate) 160
Figure 180: AZ and y coordinate acceleration results for recording 1 and numerical simulation (test case B) 161
Figure 181: FFT results for a numerical simulation using x initial coordinates, results are for the y coordinate 162
Figure 182: AY and x coordinate acceleration results for recording 1 and numerical simulation (test case B) 163
Figure 183: PSD results of the numerical simulation presenting the experimental setup for initial conditions on the x coordinate 164
Figure 184: AZ acceleration results for experimental testing with initial conditions imposed on the θ 165
Figure 185: PSD for AZ results, experimental setup using initial conditions on θ 166
Figure 186: Pendulum motion for experimental setup using initial conditions imposed on the θ coordinate 166
Figure 187: Pendulum motion for experimental setup using initial conditions imposed on the θ coordinate (filtered data) 167

Figure 188: PSD for the pendulum motion using initial conditions imposed on the θ coordinate....167
Figure 189: RX results for the experimental setup with initial conditions imposed on the θ coordinate....168
Figure 190: PSD for the RX experimental results with initial conditions imposed on the θ coordinate....169
Figure 191: Comparison of AZ, AY and RX results for recording 2....170
Figure 192: Numerical solution for each coordinate using initial conditions presented in Table 19....171
Figure 193: AZ and y coordinate acceleration results for recording 1 and numerical simulation (test case C)....172
Figure 194: Normalised AZ and y coordinate acceleration results for recording 1 and numerical simulation (test case C)....173
Figure 195: Normalised AZ and y coordinate acceleration results for recording 1 and numerical simulation (test case C, no lag)....174
Figure 196: FFT results for the y coordinate, experimental results with initial conditions imposed on the θ coordinate....175
Figure 197: Normalised AY and x coordinate acceleration results for recording 1 and numerical simulation (test case C, no lag)....176
Figure 198: PSD results for the x coordinate subjected to initial conditions on the θ coordinate from experimental testing....177
Figure 199: Normalised GX and θ coordinate acceleration results for recording 1 and numerical simulation (test case C, no lag)....178
Figure 200: PSD for the θ coordinate with initial conditions imposed on the θ coordinate (experimental testing and numerical simulation)....179
Figure 201: Specification of the SH mounts (ACTOM, 2023)....181
Figure 202: Foundation loads for the SD18/36 vibrating screen....182
Figure 203: Dynamic loading for the 3DOF vibrating screen....183
Figure 204: Layout of excel data for automation....253
Figure 205: LM15 screen material profile....261
Figure 206: Spring data sheet....262
Figure 207: Dytran 4401A2 drawing....263
Figure 208: AZ and y coordinate acceleration results for recording 1 and numerical simulation (test case A)....264
Figure 209: AZ and y coordinate acceleration results for recording 2 and numerical simulation (test case A)....265
Figure 210: AZ and y coordinate acceleration results for recording 3 and numerical simulation (test case A)....265
Figure 211: AZ and y coordinate acceleration results for recording 4 and numerical simulation (test case A)....266
Figure 212: AZ and y coordinate acceleration results for recording 5 and numerical simulation (test case A)....266
Figure 213: AZ and y coordinate acceleration results for recording 1 and numerical simulation (test case B)....267
Figure 214: AZ and y coordinate acceleration results for recording 2 and numerical simulation (test case B)....268
Figure 215: AZ and y coordinate acceleration results for recording 3 and numerical simulation (test case B)....268
Figure 216: AZ and y coordinate acceleration results for recording 4 and numerical simulation (test case B)....269

Figure 217: AZ and y coordinate acceleration results for recording 5 and numerical simulation (test case B) 269
Figure 218: AY and x coordinate acceleration results for recording 1 and numerical simulation (test case B) 270
Figure 219: AY and x coordinate acceleration results for recording 2 and numerical simulation (test case B) 271
Figure 220: AY and x coordinate acceleration results for recording 3 and numerical simulation (test case B) 271
Figure 221: AY and x coordinate acceleration results for recording 4 and numerical simulation (test case B) 272
Figure 222: AY and x coordinate acceleration results for recording 5 and numerical simulation (test case B) 272
Figure 223: Normalised AZ and y coordinate acceleration results for recording 1 and numerical simulation (test case C) 273
Figure 224: Normalised AZ and y coordinate acceleration results for recording 2 and numerical simulation (test case C) 273
Figure 225: Normalised AZ and y coordinate acceleration results for recording 3 and numerical simulation (test case C) 274
Figure 226: Normalised AZ and y coordinate acceleration results for recording 4 and numerical simulation (test case C) 274
Figure 227: Normalised AZ and y coordinate acceleration results for recording 5 and numerical simulation (test case C) 275
Figure 228:Normalised AY and x coordinate acceleration results for recording 1 and numerical simulation (test case C, no lag) 275
Figure 229: Normalised AY and x coordinate acceleration results for recording 2 and numerical simulation (test case C, no lag) 276
Figure 230:Normalised AY and x coordinate acceleration results for recording 3 and numerical simulation (test case C, no lag) 276
Figure 231: Normalised AY and x coordinate acceleration results for recording 4 and numerical simulation (test case C, no lag) 277
Figure 232:Normalised AY and x coordinate acceleration results for recording 5 and numerical simulation (test case C, no lag) 277
Figure 233: Normalised GX and θ coordinate acceleration results for recording 1 and numerical simulation (test case C, no lag) 278
Figure 234: Normalised GX and θ coordinate acceleration results for recording 2 and numerical simulation (test case C, no lag) 278
Figure 235: Normalised GX and θ coordinate acceleration results for recording 3 and numerical simulation (test case C, no lag) 279
Figure 236: Normalised GX and θ coordinate acceleration results for recording 4 and numerical simulation (test case C, no lag) 279
Figure 237: Normalised GX and θ coordinate acceleration results for recording 5 and numerical simulation (test case C, no lag) 280

LIST OF TABLES

Table 1: Comparison of the screening performance for translation movement, swing motion, and composite mode (Zhanfu, et al., 2018) 7
Table 2: Comparison between the different studies 12
Table 3: Attributes of the SD18/38vibrating screen 14
Table 4: Initial conditions for a non-parametric resonant 2DOF system 17
Table 5: Attributes and initial conditions to develop parametric resonance for the 2DOF system 20
Table 6: Attributes for a non-parametric resonant 2DOF system with excitation forces 23
Table 7: Attributes for a parametric pendulum excited at parametric resonance for the 2DOF system 30
Table 8: Damping cases for the 2DOF systems 33
Table 9: Initial conditions to θ component 53
Table 10: Attributes for parametric resonance for the 3DOF system 88
Table 11: Summary of simulation results 117
Table 12: Final parameter for the 3DOF vibrating screen 124
Table 13: Sieve analysis of a material sample 127
Table 14: Mechanical properties of the particles 128
Table 15: DEM analysis cases 132
Table 16: Mass of the experimental setup 145
Table 17: Parameters of the experimental setup 147
Table 18: Correlation between the coordinates for the 3DOF and experimental setup 148
Table 19: Measured angle (θ) for the experimental test 164

LIST OF MATLAB CODE

Matlab Code 1: State representation of the 2DOF system....192
Matlab Code 2: Implementation of the 2DOF state representation....192
Matlab Code 3: State representation of the 4DOF system....193
Matlab Code 4: General use of the FFT function from the signal processing toolbox....194
Matlab Code 5: Custom function for the implementation of Butterworth filters....194
Matlab Code 6:State representation of the 3DOF system including damping and generalised forces....195
Matlab Code 7: The calculation of the numerical values of α and β....195
Matlab Code 8: Stretch in the springs and the coordinates of A and B....196
Matlab Code 9: Resultant accelerations of spring A and B....196
Matlab Code 10: Double integration of acceleration results to calculate displacements....197
Matlab Code 11: Low pass Butterworth filter for removing high frequencies and trendlines....197
Matlab Code 12: A function which removes a specific part of a data set....197

LIST OF MATHEMATICA CODE

Mathematica Code 1: 3DOF system solved using various numerical solving methods....209

LIST OF EXCEL VBA CODE

Excel VBA 1: Code to develop a .txt. file with required arguments to perform DEM analysis....254

LIST OF LIGGGHTS INPUT SCRIPT

LIGGGHTS script 1: Typical script for a single iteration of screen movement....255
LIGGGHTS script 2: DEM simulation setup excluding the modelling of screen motion....258
LIGGGHTS script 3: SD motion....258
LIGGGHTS script 4: LM motion....259

LIST OF SYMBOLS

Symbol	Description	Units
AZ, AY	Vertical and horizontal acceleration for the experimental results	m/s^2
a_i	Coordinate at the tip of the spring, where the subscript represents the coordinate	m
a_t	Tangential acceleration of the rigid bar	m/s^2
a, b	Elongation of the spring/buffer	m
b_i	Coordinate at the tip of the spring, where the subscript represents the coordinate	m
C_i	Damping, where the subscript defined the coordinate of concern	-
F_i	Applied force where the subscript represents the coordinate in which the force is applied Alternatively, the inclination of the mesh deck	N
k	Spring stiffness	N/m
L	Length of the rigid bar	m
m	Mass	kg
m_{s1}	Mass of particles whose diameter is smaller than the aperture size among the undersize material	kg
m_{s2}	Total mass of the particles whose diameter is smaller than the aperture	kg
m_{c1}	Mass of particles whose diameter is larger than the aperture among the undersized material	kg
m_{C2}	Total mass of particles whose diameter is larger than the aperture	kg
RX	Rotational velocity for the experimental testing	degree/s
r	Unstretched length of spring/buffer	m
x	Radial coordinate and horizontal coordinate	rad, m
$\dot{x}$	Radial and horizontal velocity	rad/s, m/s
$\ddot{x}$	Radial and horizontal acceleration	rad/s^2, m/s^2
y	Vertical coordinate	m
$\dot{y}$	Vertical velocity	m/s
$\ddot{y}$	Vertical acceleration	m/s^2
ω_s	Excitation frequency applied to the spring/buffer	Hz
ω_p	Excitation frequency applied to the pendulum	Hz
ω_{sn}	Natural frequency of the spring/buffer	Hz
ω_{pn}	Natural frequency of the pendulum	Hz
α, β	Damping ratio	-
θ	Rotational coordinate (displacement)	rad
$\dot{\theta}$	Rotational velocity	rad/s
$\ddot{\theta}$	Rotational acceleration	rad/s^2
η	Screening efficiency	-
Q_i	Generalized force, where the subscript represents the coordinate of concern	N
δ_i	Virtual displacement where the subscript represents the coordinate of concern	degrees, m

NOMENCLATURE / LIST OF ACRONYMS

Abbreviation	Description
CHPC	Centre for high performance computing
CAD	Computer aided design
CFD	Computational fluid dynamics
DEM	Discrete element method
DOF	Degrees of freedom
FFT	Fast Fourier transform
FAT	Fatigue class
FEA	Finite element analysis
IP	Information protection
LM	Lagrangian motion, can be followed by a number indicating deck inclination
LIGGGHTS	LAMMPS improved for general granular and granular heat transfer simulations
Matlab	Matrix laboratory
NAN	Not a number
Ode	Ordinary differential equation
PSD	Power spectral density or particle size distribution (depending on context)
SD	Single deck, can be followed by a number indicating deck inclination
VSD	Variable speed drive
VBA	Visual basic for applications

CHAPTER 1: INTRODUCTION AND LITERATURE REVIEW

1.2 RESEARCH BACKGROUND/CONTEXT

Vibrating screens are machines that, when subjected to mechanical vibration, carry out the separation of material mixtures to granulations, or fractions. The number of fractions is dependent on the number of stories (mesh decks) on the vibrating screen (Zeljko & Aleksandar, 2016). Vibrating screens are implemented in both commercial and mining sectors to classify materials/products. Vibrating screens consist of the following (Figure 1):

- Mesh deck, which acts as a sieve.
- Excitor motors or motors that drive unbalanced masses at a specified speed and acceleration so that material can be moved over the deck of the screen.
- Rubber buffers or springs which provide flexibility so that the screen can be excited and the dynamic loads transferred to the support structure can be kept at a minimum. For larger screens, subframes are used to further reduce loads transferred into support structures.

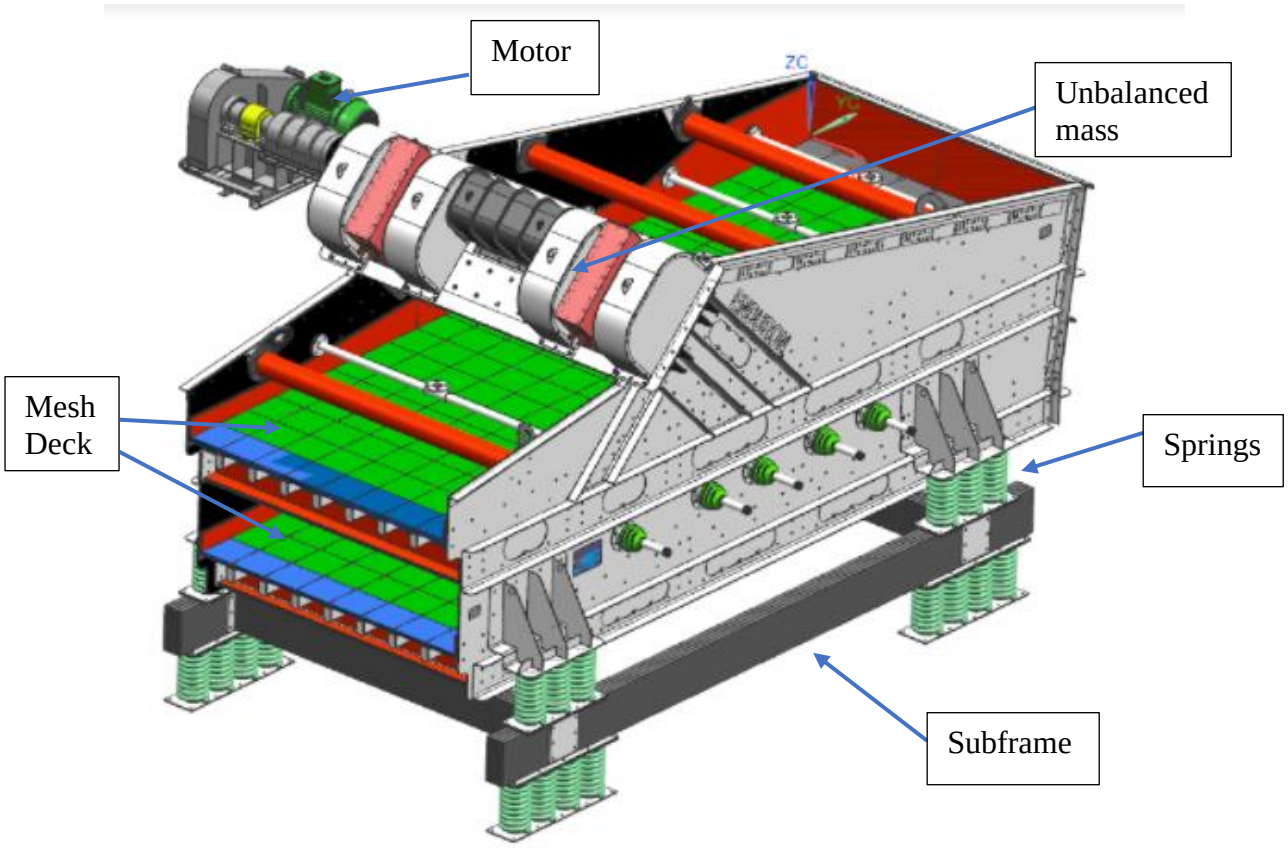

Figure 1: Anatomy of a vibrating screen

Vibrating screens have three common types of motion as presented in Figure 2. The motion of the screen has different benefits depending on the material that needs to be screened. Linear motion screens have the excitation force in line with the CG of the screen while the circular and oval/elliptical motion screens have the excitation force eccentric to the CG in a manner that induces the required motion.



Figure 2: Types of strokes. circular, elliptical, and linear motion

There are several studies which concern themselves with the movement of material on the screening deck and screening efficiency, these studies generally concern themselves with the Discrete Element Method (DEM) and are material specific.

Vibrating screen performance can be optimized for any application by changing amplitude (stroke) and frequency. Tests have shown that the screening rate is more responsive to changes in amplitude than frequency, refer to Figure 3 (Sullivan, n.d.). It has been found that the optimal vibration angle is 45° for nearly all kinds of particles (Ferenc, et al., 2019).

https://www.sssdynamics.com/wp-content/themes/va/pdf/screeningtheory.pdf
(Figure 4 in the above link)

Figure 3: Relative screening rate Vs amplitude (Sullivan, n.d.)

Material on the screen surface is moved by either throwing, rolling, or sliding motions. Material penetrates the screen within the first ¼ to ½ of the screen, which affects screening and lowers processing capacity. A decrease of fine-grained material causes the ratio of the particles close in size to, or larger than the mesh to increase. Thus, the screening efficiency declines dramatically. The material granularity simultaneously becomes uniform, and the energy imparted from the vibrations to the material suffers little loss. Hence the amplitude and velocity of material particles increase. This causes the material bed depth at the feed end to be thick while at the discharge end it is thin. This kind of motion leads to an asymmetrical penetration along the screen surface, which influences the screening efficiency and processing capability. The discussed characteristics are presented in Figure 4 (He & Lui, 2009).

https://www.sciencedirect.com/science/article/pii/S1674526409600958
(Figure 1 in the above link)

Figure 4: Screening characteristics (He & Lui, 2009)

1.3. PROBLEM STATEMENT/MOTIVATION

Makinde, Ramatsetse, & Mpofu presented a paper that discusses the trends in vibrating screening and the possibilities which the future may hold. Their market evolution is presented in Figure 5, which is divided into various phases:

- Phase I-II, where small minerals sieves have been used by mineral processing companies.
- Phase II-III, this phase is where the need to change over from small-scale laboratory sieving to industrial-scale applications. Only single deck screens were being designed and manufactured at this point
- Phase III-IV, design changes were driven by the problems experienced in the previous phase, these problems consisted of:
    - Wear of screen panels and other vibrating components
    - Noise levels
    - The requirement to achieve a finer minerals particle separation, which leads to the development of the multi-deck screens
- Phase IV-VIII, development of screening technologies in:
    - Movement analysis of both the screen and material
    - Structural adjustment
    - Novel design goals
    - Vibrating screens which use high frequency and low noise so that occupational health and safety requirements can be adhered to
    - Reconfigurable vibrating screens

(Makinde, et al., 2015)

https://www.sciencedirect.com/science/article/pii/S0301751615300417#f0010
(Figure 2 in above link)

Figure 5: Evolution of vibrating screening (Makinde, et al., 2015)

Based on the presented study it can be concluded that there is still a vast amount of research required in the field of vibrating screens which has been increasing with each phase. From the author's experience there are inefficiencies with regards to vibrating screens:

- Screening plants require recirculation of material to achieve good material grading/classification
- Vibrating screens need to overcome gravity and their support spring stiffness to function thus requiring large exciting forces to achieve the desired effects
- The efficiency of a vibrating screen is highly dependent on the deck loading thus overloading can make them inefficient
- The manner in which a screen is fed can dramatically affect efficiency

The research aims to investigate the following:

- A new type of vibrating screen that requires smaller excitation forces when compared to traditional vibrating screens
- The efficiency in screening due to compound movement of a vibrating screen
- The use of parametric resonance to induce vibrations in an efficient manner

1.4. RESEARCH QUESTIONS

The following research questions have been proposed:

- Can vibrating screens operate in a more efficient manner using parametric resonance?
- Are there more efficient ways of screening material other than linear, circular, and elliptical motion?
- Is it possible to use lower excitation frequencies or a combination of low and high excitation frequencies for screening material efficiently

1.5. RESEARCH OBJECTIVES

The following research objectives have been outlined:

- Development of a theoretical model of a vibrating screen which uses parametric resonance and can also develop a compound motion/trace
- Use DEM analysis to compare the theoretical model to a linear motion vibrating screen
- Check the accuracy of the theoretical model using an experimental setup

1.6. LITERATURE REVIEW

The below presents a review of literature that discusses various research regarding innovations in vibrating screens and/or aspects of dynamics.

1.6.1. RESONANCE IN MECHANICAL/STRUCTURAL SYSTEMS

Resonance in mechanical and structural systems is considered as an undesirable phenomenon as they cause significantly higher loads which in turn causes a lower fatigue life and affects human comfort levels. There are however several systems that use resonance successfully:

- Resonance hammer drilling, where resonance is used to increase the efficiency of drilling.
- Drive systems of vibratory conveyors
- Industrial robots
- Micro propulsion
- Microscale scavenging devices whereby vibrations are used to power sensors. (Wieslaw & Jakub, 2020)

A form of resonance that is not commonly discussed is parametric resonance. Parametric resonance differs from resonance because it is an instability phenomenon. The instability is rapidly caused by changing the system parameters, this leads to large variations in restoring forces and therefore instability (Laarhoven, 2009). The principle can be easiest explained through the use of a simple pendulum, where parametric resonance is achieved by shortening the length of the string by a small amount when the mass is at its lowest point with the maximum kinetic energy and increasing the length by the same amount at the top of the motion where the mass is instantaneously at rest, with the kinetic energy zero and the potential energy at a maximum (Hertbert, et al., 2000).

When designing vibrating screens finite element analysis is used to evaluate the likelihood of resonance and the stresses developed during operation. An overview of a vibrating screen design is presented by ZhaoTue-Min which was conducted at the 6th International Conference on Mining Science & Technology (Zhao, et al., 2009).

1.6.1.1. *DAMPING SYSTEMS*

A vibration absorber or tuned mass damper is a mechanical device used to decrease or eliminate unwanted vibration (Chopra, 2012). Such devices can be found in:

- Hair clippers
- Power transmission lines
- Aircrafts
- Automobiles
- Buildings and bridges
  (Chakraborty, et al., 2021)

In its simplest form, a tuned mass damper consists of a single spring and mass attached to SDOF as presented by Figure 6 (Chopra, 2012). The mathematical formulations regarding tuned mass dampers are covered in detail in various books specializing in dynamics.

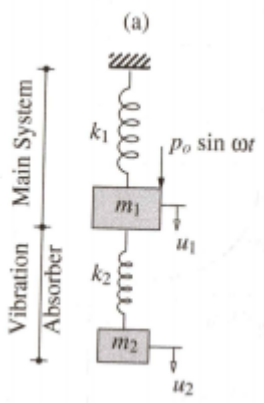

Figure 6: SDOF with a tuned mass damper (Chopra, 2012)

When vibrating screens present large dynamic loads, subframes are introduced (Figure 1), which act as a tuned mass damper. The resulting system transfers far smaller dynamic loads to the support structure.

1.6.1.2. *RESONANCE IN VIBRATING SCREENS*

There are a small group of companies which design vibrating screens which operate at resonance. Due to the information protection (IP) policies employed at these companies, there are not many research papers or any information available to the public. It is speculated that these screens have a linear motion with two decks that have opposite phases thus allowing for low transmissibility of dynamic loads to the supporting structure. Based on general research of company profiles it can be concluded that these types of screens may be inefficient when dealing with heavy-duty materials.

A study by Jiachen, Chuzhe, Ziqiu, & Kuanmin presents the use of a spring disk system for a vibrating screen so that a higher natural frequency of springs can be attained in an attempt to reduce the excitation force by excting the system at resonance. The natural frequency of the disk spring system was calculated to be 15.234Hz, which is in the region that vibrating screens operate. The following can be concluded from the work:

- Disc spring systems have excellent linearity in their stiffness.
- Small amplitudes (stroke) are achieved by using a disc spring system, in the region of 1.5-3mm (using different operating speeds).

(Jiachen, et al., 2020)

The above study concerns itself with the reduction in excitation force for the vibrating system, however, there is no comparison performed with regards to the conventional helical springs and rubber buffers. The study is also performed on a small model where it is uncertain whether the mass and configuration are comparable to commercially available vibrating screens. There is no study performed to assess the transmissibility of dynamic loads to the support structure, thus it is uncertain whether the solution can be successfully implemented. Based on the results presented it is proved that the use of resonance will reduce the excitation forces however it is uncertain if a disc spring system can provide efficient screening capability.

Electromagnetic screens have been studied by Lui Weisheng who presented a mathematical model which is in a state of near resonance (Liu & Jinli, 2011). The study does not present a full theoretical or experimental study; thus, it is difficult to make any conclusion from the work.

1.6.1.3. *MOTION/TRACE OF VIBRATING SCREENS*

As discussed previously vibrating screens have either a linear, elliptical, or circular motion. The motion follows the same path everywhere and thus has a constant transport velocity and throwing index. A vibrating screen with a variable elliptical motion trace has been proposed by He and Lui to develop a constant bed depth. Different points on the vibrating screen trace different elliptical paths, which is shown to increase the screening capacity and efficiency. The exciting force deviates from the centre of gravity, to change the motion pattern. The vibration is a combination of translation of the centre of gravity and the screen pitching about the centre of gravity. It was concluded that the ideal screening motion was achieved and that the design was able to effectively improve screening efficiency (He & Lui, 2009).

Jianzhang & Xin studied a new type of vibrating screen which follows a swing trace. A basic representation of the vibrating screen is presented in Figure 7, the different parts of the screen follow different swing traces which results in motions of varying amplitude and direction. The motion leads to material being sieved and distributed while penetrating along the screen length, thus segmenting both screening efficiency and processing capability. A mathematical model for the screen and particle motion is studied (Jianzhang & Xin, 2012).

https://www.sciencedirect.com/science/article/pii/S1674200113000783
(Figure 2 in the above link)

Figure 7: Simplified model of a swing trace vibrating screen (Jianzhang & Xin, 2012)

The trajectory of the particles is presented in Figure 8, the bounce height of particles at the feed and discharge end is larger than the middle part which presents the swing trace. This effectively avoids particles accumulation at the feed end and increases the probability of particles contacting the screen surface.

https://www.sciencedirect.com/science/article/pii/S1674200113000783
(Figure 4 in the above link)

Figure 8:Trajectory of particles (Jianzhang & Xin, 2012)

The following has been concluded by Jianzhang & Xin:

- The swing motion has greater efficiency compared to a linear motion screen, as presented by Figure 9.
- Due to the high exciting force, the swing motion prevents blinding.
- The efficiency and capacity of the screen are increased.
  (Jianzhang & Xin, 2012)

https://www.sciencedirect.com/science/article/pii/S1674200113000783
(Figure 7 and 8 in the above link)

Figure 9: Comparison between linear motion and swing motion vibrating screen (Jianzhang & Xin, 2012)

Composite vibrating screens have been studied by Zhanfu, Xin, Bi, Xiaole, & Jingxiu, where the mode of vibration is both translation and swing. The resulting screen is presented in Figure 10. The screen has been mathematically modelled using a 2DOF system. The exciter consists of two vibrating motors which rotate synchronously, it can generate a sinusoidal force which leads to the translational movement. Two forces F_{w1} and F_{w2} are applied using electromagnetic vibration exciters which act on opposite ends of the screen. The two forces have an equal magnitude with opposite phase which create the swinging motion of the screen.

https://www.hindawi.com/journals/sv/2018/1293273/
(Figure 1 in the above link)

Figure 10: Composite vibrating screen (Zhanfu, et al., 2018)

Table 1 presents data from the experimental tests performed on the different motions of a vibrating screen. The composite motion has the best screening efficiency, furthermore, the capacity has also increased.

Table 1: Comparison of the screening performance for translation movement, swing motion, and composite mode (Zhanfu, et al., 2018)

https://www.hindawi.com/journals/sv/2018/1293273/tab8/

1.6.2. PARAMETRIC RESONANCE

Parametric resonance is a widespread phenomenon that may be threatening or beneficial according to the system where it takes place since large oscillations can be generated by rather small parametric excitations (Zahedi & Babitsky, -).

An example of a parametric resonant screen is presented in Figure 11, the screen consists of the following:

1. Vibrating motor
2. The base
3. Beams fastening the sieve.
4. Side springs
5. Sieve plate

Figure 11 (b) presents the dynamic model of a parametric vibrating screen, an initially stretched system of two equal masses connected by an elastic string. The end masses, which can move horizontally, are also connected with a rigid frame by side springs. The longitudinal oscillations are excited by harmonic external forces acting synchronically on the left and right masses in the opposite horizontal directions. Under certain conditions, this motion results in transverse oscillations of the string (Zahedi & Babitsky, -).

https://www.sciencedirect.com/science/article/pii/S0022460X16302334
(Figure 2 in the above link)

Figure 11: Parametric resonant screen (Zahedi & Babitsky, -)

A mathematical model for the parametric resonant vibrating screen has been presented by (Leonid I & Victor I, 2013). The mathematical model presented compares well with conventional vibrating screen designs and is characterized by higher values of amplitude. The model presented in the paper is deemed insufficient, mainly due to the material not been included in the dynamic equations, noting that none of the previous studies account for material loads. The authors believe that the effects of material are too complex for an analytical study, thus further research is required through experimental procedures.

Abolfazl studied parametric resonance of vibrating screens using autoresonant control. The control system developed provides the possibility of self-tunning and self-adaptation which allow the screen to maintain a parametric resonant mode. The following was concluded:

- The proposed control strategy was verified by simulations.
- The system was able to perform with a wide deviation of material loads.
- An increase in productivity and efficiency can be achieved.
  (Zahedi & Babitsky, -)

A prototype parametric resonance screen was tested in a laboratory by Lukasz and Stachowicz. The study showed that parametric resonance can occur when $\omega_p = 2\omega/k$ (for k = 1,2, 3…).

The study by Lukasz and Stachowicz consisted of equipping a screen with sensors to measure the vibration rate of the sieve, the sieve tension, and the rotational speed of the electric motors. It was found that the measurements do not correlate well with the presented literature, it is however expected that modelling the screen as a beam opposed to a string can improve the theoretical model since this will allow the possibility to consider the load of the sieve (Lukasz, et al., 2015).

The topic of parametric resonance is not studied in detail with regards to vibrating screens. The topic of fatigue life is not discussed in any of the researched papers. Based on the consideration that the screening deck is made using a hot rolled plate, the FAT category would be 160 based on documentation from the international institute of welding (Hobbacher, 2007). Based on the operation of the parametrically resonant screen it is clear the mesh deck oscillates, implying that the stresses on opposite surfaces will have different directions. It is known that plates do not perform well in bending due to their low second moment of inertia, thus it is expected that the stresses would be large. Furthermore, all the referenced studies pertaining to parametric resonant screens present a solid deck that will not allow for material to be screened, the system is representative of a pan feeder. It is expected that the introduction of a meshed deck would complicate and further reduce the fatigue life. Due to the lack of a holistic study, it cannot be confirmed whether the presented vibrating screens can be implemented successfully in industry, further research is required.

1.6.3. INFLUENCE OF MOTION/TRACE ON THE SCREENING PROCESS

Dong, Liu, Zhao, & Zhao simulated different screening motions using discrete element analysis (DEM). The vibration modes considered are linear, circular, and elliptical. The study was performed using the same vibration frequency, amplitude, screen deck inclination, and material properties. The following is concluded:

- Travel velocity for the linear motion screen is the fastest followed by the elliptical motion screen with the circular motion screen having the lowest travel velocity, as presented by Figure 12.
- The circular motion screen has the highest screening efficiency followed by the elliptical motion screen and the linear motion screen having the lowest efficiency.
- The motion has a significant influence on the distribution of the undersized material. The linear motion has more near-mesh size and small size particles toward the front sections of the deck. The circular and elliptical motion shows the reverse with more of these particles appearing in the last sections.

(Dong, et al., 2013)

https://www.sciencedirect.com/science/article/pii/S2095268613000220
(Figure 4 in the above link)

Figure 12: Average particle velocity Vs time (Dong, et al., 2013)

The above study concerns itself with the commonly used motions implemented on vibrating screens. When dealing with complex motion as previously discussed the literature is limited as these complex motions are not used in industry.

1.7. CONCLUSION

The following conclusions can be made with regards to the presented research:

- The current market demands require improvements/research in motion analysis, novel designs, and high-frequency vibrating screens.
- Resonance in screening has been studied, however the presented studies are not conclusive due to the lack of information or an oversimplification of the study.
- The compound trace/motion of a vibrating screen is far more effective compared to the traditional circular, elliptical and linear motions.
- Parametric resonance is an effective method to develop efficient screening solutions however there is no conclusive proof that the technology can be successfully implemented in industry.

With the higher demands from mining companies, greater efficiency is required from vibrating screens which can be developed through compound motion as this has been shown to produce greater efficiency. Based on the designs presented it is logical that vibrating screens that have both linear/circular/elliptical motion combined with sway would require greater energy to operate as there is a multitude of equipment needed to develop such motion.

Parametric resonant screens require a flexible mesh deck to experience parametric resonance. From the literature studied the experimental screens have solid decks like that of vibrating pan feeders. The aspect of fatigue analysis has not been discussed. Further research into the traditional parametric resonance screen can be performed through experimental procedures which would require one to acquire/manufacture such a vibrating screen.

1.8. RESEARCH METHODS

The research seeks to study a parametrically resonant vibrating screen. For the purposes of this study a parametrically resonant vibrating screen will be defined as a system where the spring natural frequency will be double the pendulum natural frequency. Parametric excitation will be defined by excitation forces which are applied at the natural frequency of spring and/or pendulum.

Figure 13 presents an inverted vibrating screen such that a coupled spring pendulum is developed. The image presents the view along the length of the screening deck. The proposed screen consists of the following:

- The screen box is the structure of the screen which houses the mesh deck and accommodates the feed and discharge (which are not shown in Figure 13 as they are not of concern now)
- Various excitation forces ($F1$, $F2$ and $F3$) will be studied in different combinations to understand how the system works
- For simplicity, the mesh deck is not shown, however, the mesh deck may be sloped to promote material flow

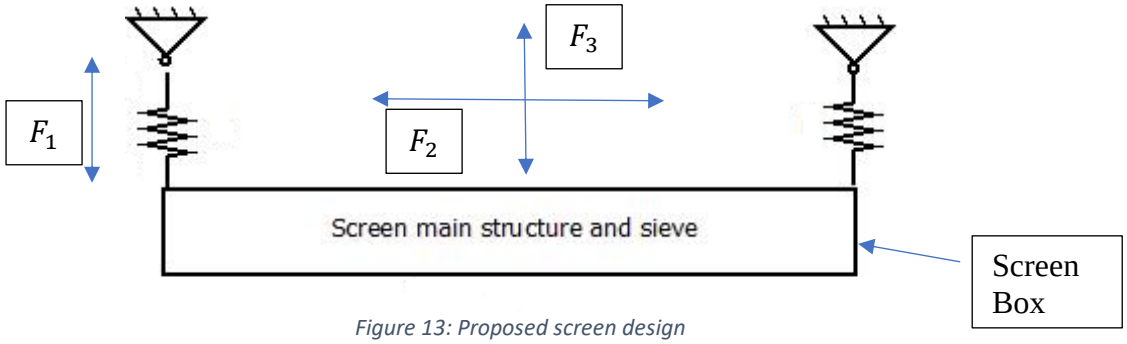

Figure 13: Proposed screen design

The system presented in Figure 13 is expected to present chaos, since it is indicative of an elastic pendulum which has been widely used in the study of chaos. To gain insight into the system a simplified model will be studied, this model will consist of a single elastic pendulum. The single elastic pendulum will be used to study the systems response to initial conditions, harmonic excitation, and damping. Parameters for the elastic pendulum will be chosen such that parametric resonance will exist. Thereafter a theoretical mode of Figure 13 will be developed and studied in a similar manner so that parameters for screening can be developed.

Table 2 presents a comparison between the different types of vibrating screens presented in the literature review and proposed study. The proposed study will induce a pendulum motion coupled with radial motion due to the elongation/contraction in the springs, if each spring experiences different displacements a compound motion will be developed. This compound motion will allow for varying accelerations and displacements along the length of the screen.

The presented studies on parametric resonance concern themselves with the vibration of the mesh deck which differs to the traditional vibrating screens where the motion is induced over the whole screen box. The proposed study intends to use parametric resonance in a manner similar to the traditional vibrating screens whereby the whole screen box is subjected to vibrations.

Table 2: Comparison between the different studies

Study	Traditional Motion	Novel Motion	Excitation	Resonance Type
(Jiachen, et al., 2020)	Linear	None	The motor driving eccentric mass	Traditional resonance
(He & Lui, 2009)	Elliptical	Variable elliptical	Excitor Motor	None
(Jianzhang & Xin, 2012)	None	Swing	Motor driving camshafts on feed and discharge end	None
(Zhanfu, et al., 2018)	Linear	Swing	Excitor motor and electromagnetic vibration exciters	None
(Leonid I & Victor I, 2013), (Zahedi & Babitsky, -) and (Lukasz, et al., 2015)	None	Bending of deck	Excitor motors	Parametric resonance
Proposed Study	None	Pendulum and radial motion	Excitor Motors	Parametric resonance

It is speculated that the proposed screen design will require far less energy to function when compared to conventional vibrating screens. The development of parametric resonance will also alleviate the requirements for large excitation forces.

The formulation of a mathematical model for the system can be developed using the Euler Lagrange equation presented by equation 1.

$$\frac{d}{dt}\left(\frac{\partial l}{\partial \dot{x}}\right) - \frac{\partial l}{\partial x} = 0 \qquad 1$$

It is expected that the theoretical model will consist of 4 nonlinear differential equations (it will be shown later that the theoretical model can be developed using 3 differential equations) which need to be solved simultaneously. Equation 2 presents the formulation for a simple pendulum, the equation is considered nonlinear due to $sin\theta$ being a transcendental function of θ. The simplification whereby $sin\,\theta = \theta$ is performed to make the differential equation linear. The simplifications are only valid for small angles.

$$\ddot{\theta} + \frac{g}{l}\sin\theta = 0 \qquad 2$$

Due to the expected large displacements of the model the above-mentioned simplification cannot be made. Thus, the resulting series of nonlinear differential equations will need to be solved without any simplification. Not all nonlinear differential equations can be solved from first principles thus numerical techniques will need to be implemented.

There are a variety of tools available to solve differential equations by numerical methods. The most commonly used tool is Matlab, which is commercial software that can only be accessed through a user license. Octave GNU is an open-source programming language that is mostly compatible with Matlab, using similar structure and functions (Eaton, 1998-2021), allowing Octave code to be compiled in Matlab and vice versa. The ode45 solver is one of many solvers available on Matlab/Octave which can be used to develop numerical solutions to differential equations. All ode solvers require the *n* degree of freedom system to be expressed concisely as a first-order system in *2n* unknowns for a vector $z = [x,v]$, where v is the time derivative of x (Howard, et al., 2003). Matlab has a variety of ode solvers to cater to different requirements arising from differential equations, thus it will be implemented in this study. The MathWorks help centre provides guidance on the different ode solvers and how to determine which solver should be implemented for a particular problem (MathWorks, 2021).

The solutions will be exclusively developed using numerical methods; thus, it is important to validate the results. Validation will be performed by comparing the results attained through the various numerical methods. The results should have a clear trend and similarity thus one can perform validation.

The damping for the springs will be determined by equation 3 which is referred to as proportional damping ($\boldsymbol{M}$ and $\boldsymbol{K}$ refer to the mass and stiffness matrix). It is difficult to develop a true reflection of damping since there is no existing test data. Thus, it is feasible to take the constants τ and φ far less than 1. Suitable numerical values for τ and φ will be chosen based on studying the model. Damping will be discussed further during its application.

$$\boldsymbol{C} = \boldsymbol{\tau M} + \varphi \boldsymbol{K} \qquad 3$$

The forcing functions are variable since one can develop a large variety of excitation forces at varying frequencies, this can be developed using a multitude of commercially available equipment. The determination of the required forcing functions will be done through trial and error. Since this is theoretical study there will be no focus on the mechanical setup.

The time history solutions developed using the ode solvers, will be used as an input for DEM analysis which will be performed using LIGGGHTS. Geometry for the mesh deck and screen box will be developed on Siemens NX (CAD and FEA package with licenses available at Weir Minerals) and/or SolidWorks (student license). A similar DEM simulation will be performed for an equivalent linear motion vibrating screen, so that a comparison can be made. Since the study is not material specific, the physical parameters of the particles will be modelled based on data available from research, such as the one performed by Dong, Liu, Zhao, & Zhao. The efficiency of the vibrating screen will be calculated using 4, where:

- η , is defined as the screening efficiency
- m_{s1}, is the mass of particles whose diameter is smaller than the aperture size among the undersized material
- m_{s2}, is the total mass of the particles whose diameter is smaller than the aperture
- m_{c1}, is the mass of particles whose diameter is larger than the aperture among the undersized material
- m_{c2}, the total mass of particles whose diameter is larger than the aperture

$$\eta = \left(\frac{m_{s1}}{m_{s2}} - \frac{m_{c1}}{m_{c2}}\right) \times 100 \qquad 4$$

CHAPTER 2: THEORETICAL STUDY OF A SIMPLIFIED 2DOF SYSTEM

The following chapter presents the theoretical model of a 2DOF spring pendulum. The system is to be studied using initial conditions, excitation and damping. The spring pendulum is well-studied with numerous papers available discussing the system; thus, this system will be studied briefly. The goal of this section is not to size attributes which would provide adequate screening criteria, but to understand the system thus allowing one further insight when studying a system with further complexity.

2.1. SD18/36 LINEAR MOTION VIBRATING SCREEN

For calibration purposes the proposed vibrating screen design will be compared to the SD18/36 linear motion vibrating screen which is designed by Weir Minerals. Table 3 summarises some of the key attributes of the SD18/36 vibrating screen. An important observation is the large forces required to develop the relatively small displacements.

Table 3: Attributes of the SD18/38vibrating screen

Attribute	Numerical Value	Units
Mass of SD18/36 vibrating screen	3755	kg
Operating speed	16.67	Hz
Horizontal acceleration	3.4	g
Vertical acceleration	3.4	g
Resulting acceleration	4.7	g
Horizontal screen displacement	2.98	mm
Vertical screen displacement	3.02	mm
Resultant screen displacement	4.24	mm
Horizontal excitation force	118.455	kN
Vertical excitation force	118.455	kN
Resultant excitation force	167.52	kN

2.2. DERIVATION OF THE 2DOF SIMPLIFIED MODEL

To gain an understanding into how the proposed screen design will function a simplified 2DOF model will be developed as presented by Figure 14. The purpose of the simplified model is to:

- Gain insight and understanding into how the system functions, this will assist in the understanding of the full-scale model which will be a 3DOF system.
- It is common industry practice to use simplified 1 or 2DOF models for the following:
    - Trial simulations to size motors and springs/buffers
    - Develop structural loading
    - Ensuring that the correct stroke can be achieved and check the sensitivity of the stroke to material loading

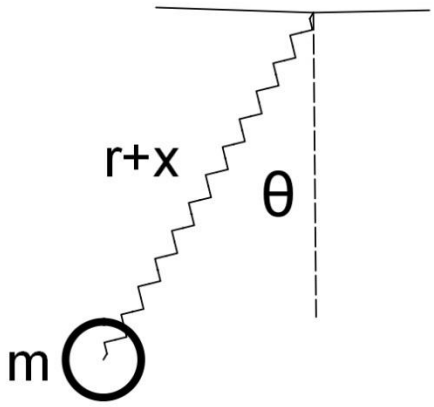

Figure 14: Simplified 2DOF system

Figure 14 presents a 2DOF model of an elastic pendulum. The model has 2 coordinates, x which is the radial component (noting that r is the natural length of the spring) and θ which is the rotational component. The derivation of the Euler-Lagrange equations is performed as follows:

- The kinetic energy is represented by equation 5

$$T = \frac{1}{2}m\dot{x}^2 + \frac{1}{2}m(r+x)^2\dot{\theta}^2 \quad (5)$$

- The potential energy is represented by equation 6

$$U = \frac{1}{2}kx^2 - \frac{1}{2}mg(r+x)^2 cos\theta \quad (6)$$

- Damping is represented by equation 7

$$D = \frac{1}{2}c_1\dot{x}^2 + \frac{1}{2}c_2\dot{\theta}^2 \quad (7)$$

- The expanded Euler-Lagrange equation is presented by 8, where $Q_{x,\theta}$ presents the generalised forces.

$$\frac{d}{dt}\left(\frac{\partial T}{\partial \dot{q}}\right) - \frac{\partial T}{\partial q} - \frac{d}{dt}\left(\frac{\partial U}{\partial \dot{q}}\right) + \frac{\partial U}{\partial q} + \frac{\partial D}{\partial \dot{q}} = Q_{x,\theta} \quad (8)$$

- The derivatives and partial derivatives for equation 8 are presented below. The time derivative of the $\frac{\partial T}{\partial \dot{\theta}}$ terms require the use of the chain rule as there are two time-dependent functions present.

$$\frac{\partial T}{\partial \dot{x}} = m\dot{x}\,; \frac{d}{dt}\left(\frac{\partial T}{\partial \dot{x}}\right) = m\ddot{x};\ \frac{\partial T}{\partial x} = m\dot{\theta}^2(r+x) \tag{9}$$

$$\frac{\partial U}{\partial \dot{x}} = 0;\ \frac{d}{dt}\left(\frac{\partial U}{\partial \dot{x}}\right) =\ 0;\ \frac{\partial U}{\partial x} = kx - mgcos\theta \tag{10}$$

$$\frac{\partial U}{\partial \dot{\theta}} = 0;\ \frac{d}{dt}\left(\frac{\partial U}{\partial \dot{\theta}}\right) = 0 \tag{11}$$

$$\frac{\partial T}{\partial \dot{\theta}} = m(r+x)^2;\ \frac{d}{dt}\left(\frac{\partial T}{\partial \dot{\theta}}\right) = m(r+x)^2\ddot{\theta}\ + 2m(r+x)\dot{x}\dot{\theta} \tag{12}$$

$$\frac{\partial D}{\partial \dot{\theta}} = c_p\dot{\theta};\ \frac{\partial D}{\partial \dot{x}} = c_s\dot{x} \tag{13}$$

- The free body diagram for the applied forces is presented by Figure 15. The virtual work associated with the radial component is presented by equation 14, with the generalised force presented by equation 15. When considering the rotational component (16) the δ_θ component does not represent a virtual displacement, a virtual displacement can be achieved by multiplying the virtual angle by the total length of the spring.

$$(\delta_{x1} + \delta_{x2})Q_x = F_h(t)[sin\theta\hat{\imath} + cos\theta\hat{\jmath}] \cdot \delta_{x1}\hat{\imath} + F_v(t)\delta_{x2}\hat{\imath} \tag{14}$$

$$Q_x =\ F_v(t) + F_h(t)sin\theta \tag{15}$$

$$\delta_\theta Q_\theta = F_h(t)[sin\theta\hat{\imath} + cos\theta\hat{\jmath}] \cdot x\delta_\theta\hat{\imath} \tag{16}$$

$$Q_\theta = (x+r)F_h(t)cos\theta \tag{17}$$

- The resulting differential equations are presented by 18 and 19. The differential equations are nonlinear due to the time dependent trigonometric functions.

$$m\ddot{x} - m\dot{\theta}^2(r+x) + kx - mgcos\theta =\ F_v(t) + F_h(t)sin\theta \tag{18}$$

$$2m\dot{x}\dot{\theta}(r+x) + m(r+x)^2\ddot{\theta} + mg(r+x)sin\theta = (x+r)F_h(t)cos\theta \tag{19}$$

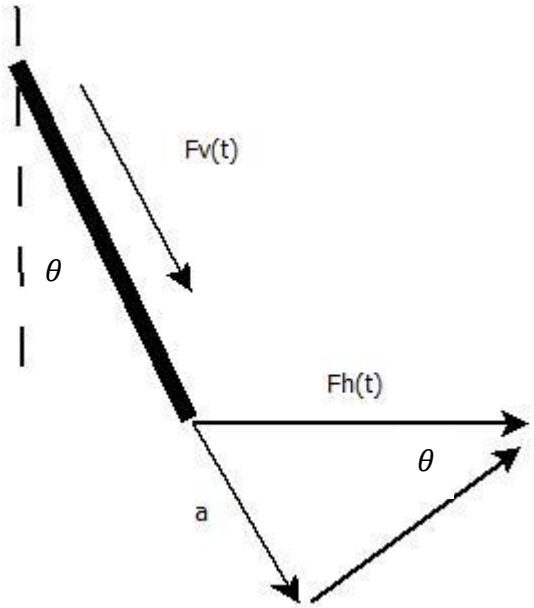

Figure 15:Freebody diagram for applied loads on the 2DOF system

2.3. 2DOF SYSTEM SIMULATED USING INITIAL CONDITIONS

The solution to the above-mentioned equations can be developed using the ode45 function in Matlab. Matlab requires the user to represent differential equations in state vector form as shown by 20 . Where $\ddot{x}$ and $\ddot{\theta}$ are made the subject of the formula using equations 18 and 19 respectively. The state vector form of the equations is presented by Matlab Code 1 with the general implementation presented by Matlab Code 2.

$$[S] = \begin{bmatrix} S1 \\ S2 \\ S3 \\ S4 \end{bmatrix} = \begin{bmatrix} x \\ \dot{x} \\ \theta \\ \dot{\theta} \end{bmatrix}; [\dot{S}] = \begin{bmatrix} S2 \\ \ddot{x} \\ S4 \\ \ddot{\theta} \end{bmatrix} \quad 20$$

Table 4 presents values used for simulating the 2DOF system, the mass is the same as that of the SD18/36 while the spring stiffness and length are representative of what is used on TRIO vibrating screens. The spring attributes are chosen since it is thought that the large length coupled with low stiffness will make an interesting simulation case. Damping and all forcing functions are 0. The system parameters are sized such that the parametric resonance will not occur.

Table 4: Initial conditions for a non-parametric resonant 2DOF system

Attribute	Numerical Value	Units
Mass	3755	kg
Spring Stiffness	266*2	N/mm
r	0.5	m
x(0)	0.1	m
θ(0)	5	degrees

The rotational and translation displacements are presented by Figure 16 with the motion trace being presented by Figure 17. As expected, the maximum angular and translational displacement are the same as the initial conditions, this is indicative of a system which has no damping. By inspecting displacement results the radial component has a higher frequency compared to the angular component.

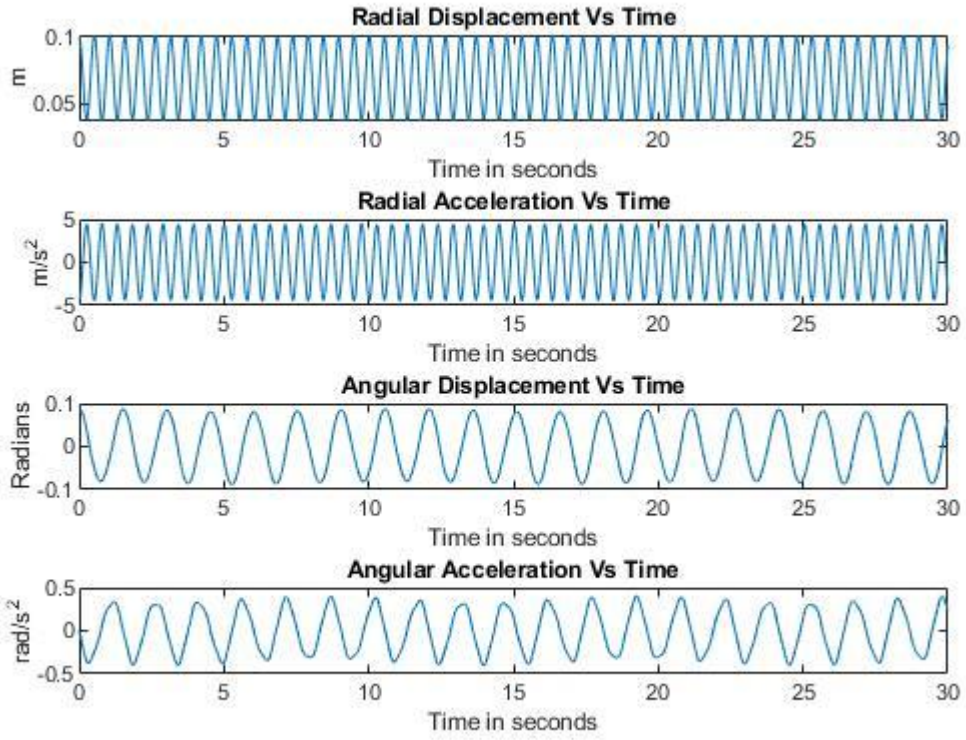

Figure 16: Angular and translational displacements for the 2DOF using attributes from Table 4

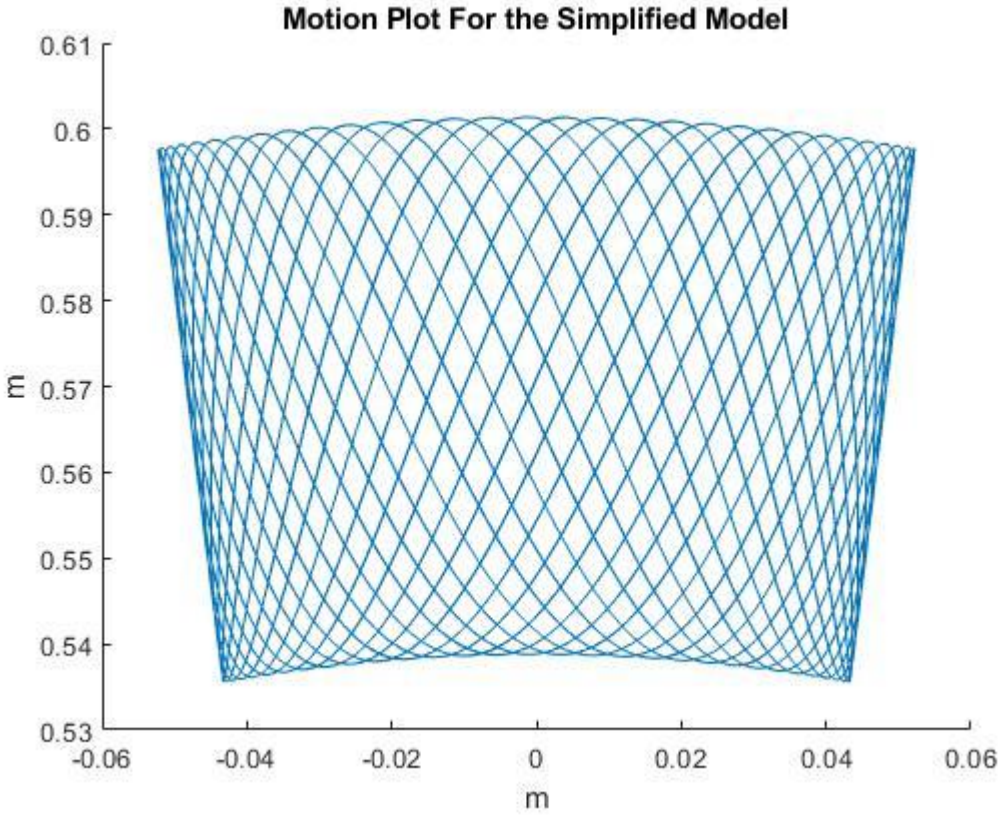

Figure 17: Motion trace of the 2DOF model using attributes presented in Table 4

The pendulum natural frequency can be represented by equation 21 and spring natural frequency is presented by equation 22, the resulting units for the equations are in rad/s. The natural frequency of the pendulum is independent from the mass of the system thus material loading will not have an influence on the pendulum natural frequency. The same is not true for the spring, thus mass fluctuations may have a negative effect on the development of parametric resonance.

$$\omega_{pn} = \sqrt{\frac{g}{r}} \qquad 21$$

$$\omega_{sn} = \sqrt{\frac{k}{m}} \qquad 22$$

$$\frac{\omega_{sn}}{\omega_{pn}} = 2 \qquad 23$$

The requirement for parametric resonance to exist is presented by equation 23. By using the information presented in Table 4 coupled with the presented equations, the length and quantity of springs can be adjusted so that parametric resonance can be achieved. The resulting attributes are presented in Table 5.

By inspection of equation 21 as the natural length of spring increases, the natural frequency of the pendulum gets smaller. Considering a spring of length 0.01 meters produces a natural frequency of 4.98Hz which is well below the operating speed of a SD18/36 vibrating screen. This would require the springs to be excited at 9.96Hz to develop parametric resonance. The presented system would be completely unfeasible since it would imply that the spring is only 10mm long. By inspection of data sheets regarding rubber buffers developed by ACTOM and conversations with representatives it was found that the radial dynamic stiffness of their SH mounts develop a dynamic stiffness of 135N/mm. Doubling up on the stiffness provides a stiffness of 270N/mm (ARNOT, 2022). The stiffness is close to the requirement presented by Table 5. The dimensions of such a buffer do not match the length requirements used on this study, however such buffer dimensions and attributes may be engineered to order.

Table 5: Attributes and initial conditions to develop parametric resonance for the 2DOF system

Attribute	**Numerical Value**	**Units**
Mass	3755	kg
Spring Stiffness	266x4	N/mm
r	0.138	m
x(0)	0.1	m
θ(0)	5	degrees
ω_s	2.68	Hz
ω_p	1.34	Hz

Figure 18 presents the translational and angular displacement for a system which is setup to develop parametric resonance. The displacements are far higher when compared to the displacements achieved in Figure 16. The results presented by Figure 18 correlate well with literature presented by (de Sousa, et al., 2018) and (Chen, et al., 2022). The spring and pendulum transfer energy to each other on limited time intervals. When the pendulum transfers energy to the spring, the spring is compressed or stretched, when the spring transfers energy to the pendulum the pendulum is observed to the have large rotations. The presented behaviour is that of autoparametric resonance.

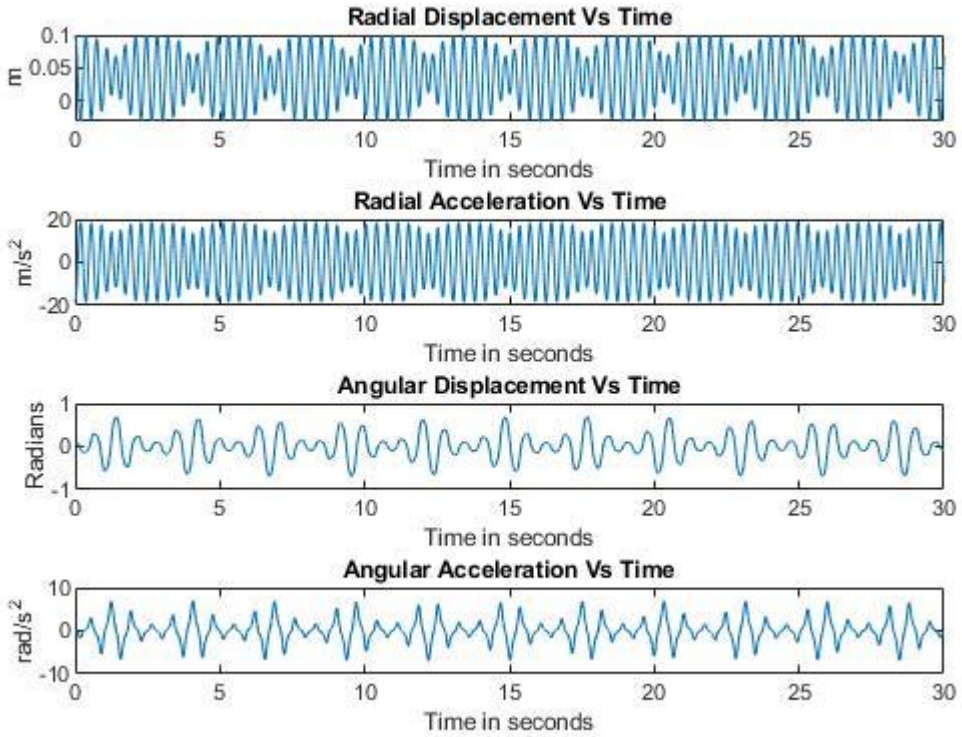

Figure 18: translation and rotational displacement and acceleration using attributes presented in Table 4

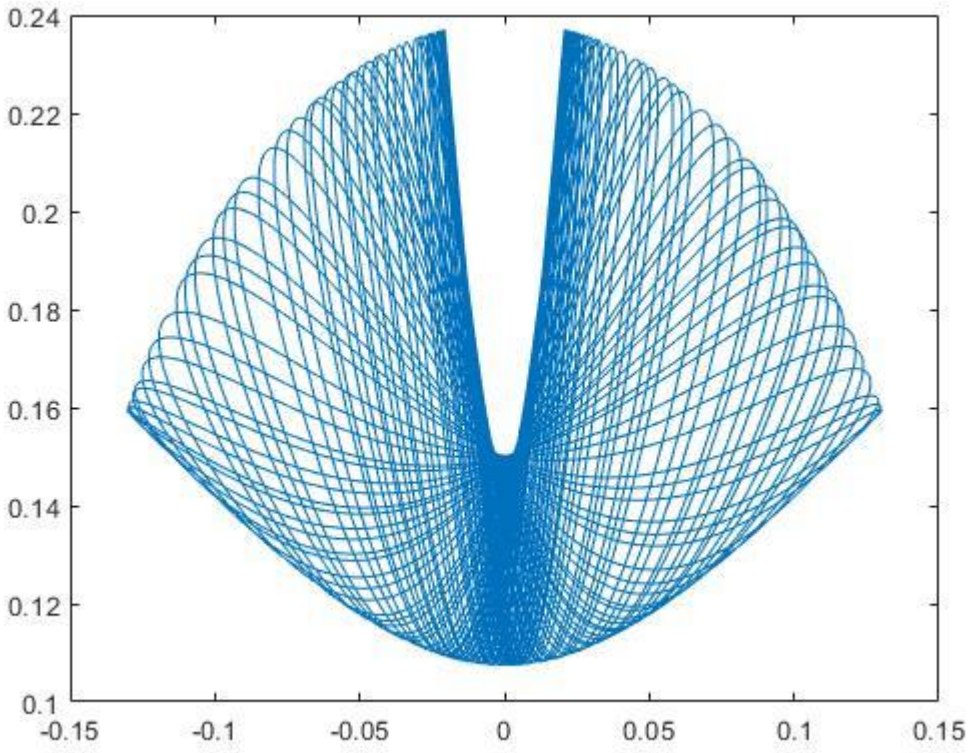

Figure 19: Motion trace for attributes presented in Table 4

It is well known that the elastic pendulum is a chaotic system which is highly dependent on the initial conditions. This is evident from Figure 20 which presents the trace of an elastic pendulum for changes in the initial conditions using the parameters presented by Table 5. The initial translational displacement and rotational displacement are incremented by $\frac{n}{1000}$ (meters) and n (radians) respectfully, where $n = 1,2,3 \ldots 10$. Changes in the initial conditions produce vastly different solutions.

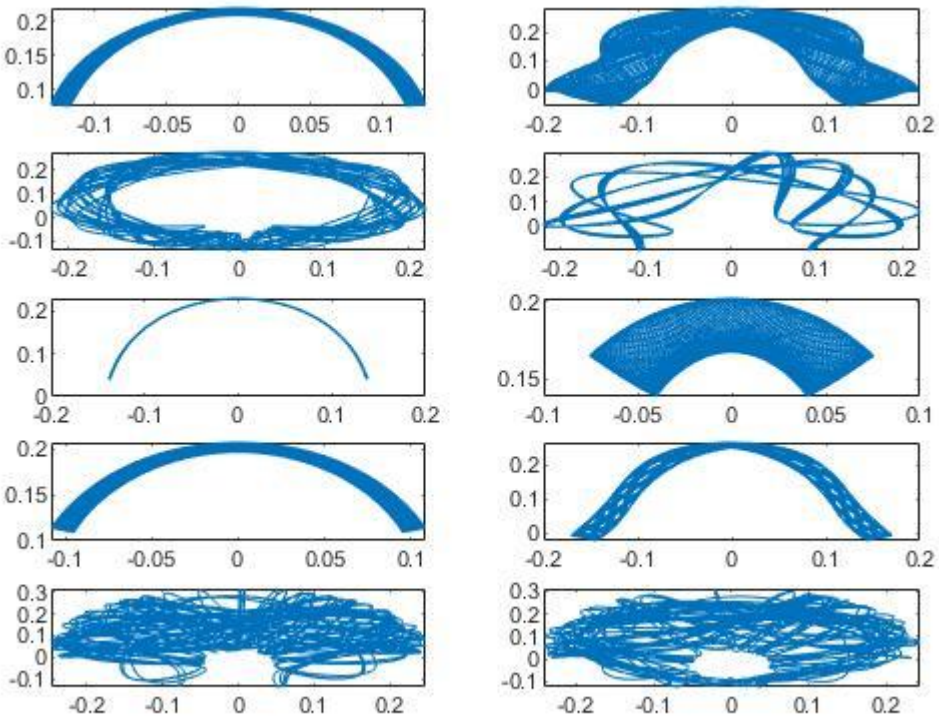

Figure 20: 2DOF spring pendulum motion traces due to varying initial conditions

2.4. 2DOF MODEL WITH EXCITATION AND DAMPING

In this section the simplified 2DOF model will be simulated with the applied forces and damping. The goal of this section is to determine how the generalised forces and damping affect the system.

Table 6: Attributes for a non-parametric resonant 2DOF system with excitation forces

Attribute	**Numerical Value**	**Units**
Mass	3755	kg
Spring Stiffness	266*2	N/mm
r	0.5	m
ω_s	16.67	Hz
ω_p	8.335	Hz
ω_{sn}	1.89	Hz
ω_{pn}	0.7	Hz
α	0	-
β	0	-
Fh(t)	$3000\sin(\omega_p t)$	N
Fv(t)	$3000\sin(\omega_s t)$	N

The first test case which is simulated is presented by Table 6, the parameters are chosen such that the system will not develop parametric resonance, however the excitation forces obey equation 23. The resulting displacements and accelerations are presented in Figure 21 with the motion being presented by Figure 22. The radial displacements and accelerations produce repetitive results where there is no energy transferred to the elastic pendulum and vice versa. The angular displacements and accelerations are small, it is thought that the high excitation frequency prevents the system from experiencing large displacements in a particular direction thus limiting the displacements. The radial accelerations are the same as that of gravity, implying that the applied forces are far too small to produce a large effect on the system.

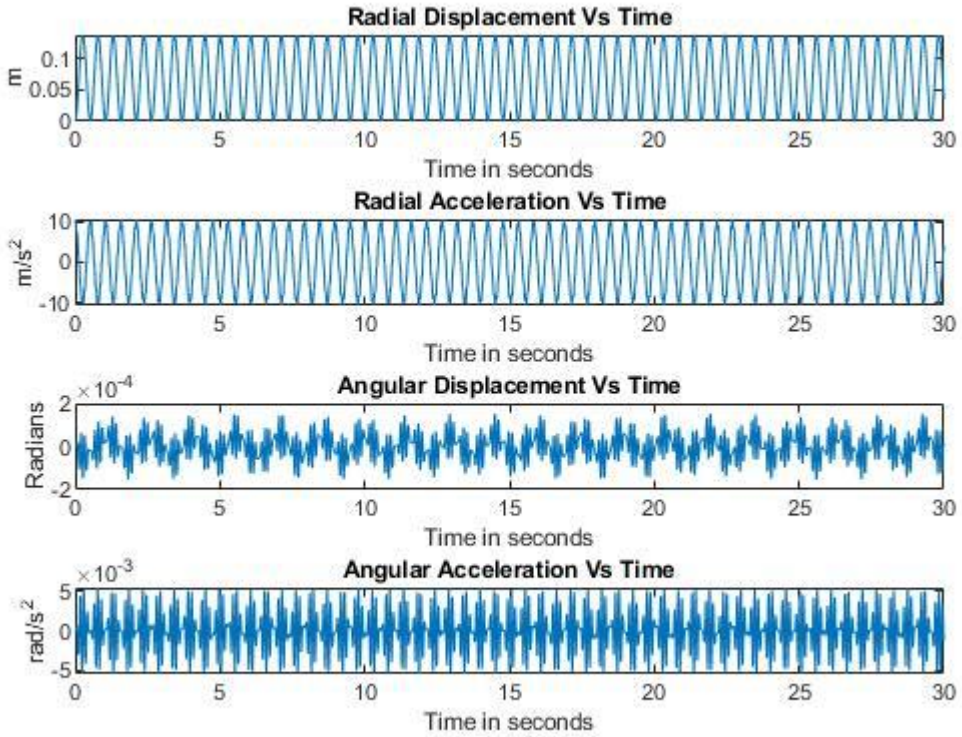

Figure 21: Displacement and acceleration results for attributes presented in Table 6

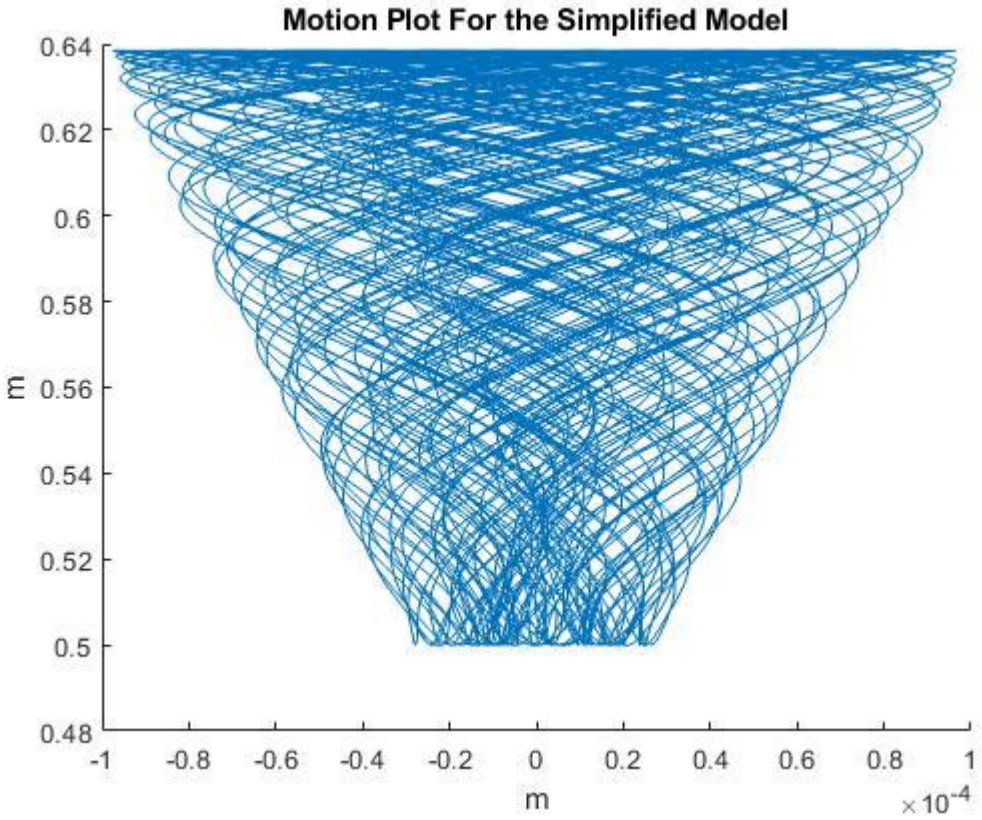

Figure 22:Motion trace for attributes presented in Table 6

Figure 23 presents the PSD for the spring and elastic pendulum. The following can be noted by studying Figure 23:

- The natural frequency of the spring system correlates well with the calculated values presented in Table 6. There is a large amount of energy presented for the natural frequency while the excitation frequency presents a small amount of energy which is only visible by zooming into the results. The natural frequency of the system dominates and ultimately governs the way the system reacts. If the excitation force applied to the spring is changed to $30000\sin(\omega_s t)$, the resulting PSD and radial acceleration results are presented by Figure 25. The larger excitation force subsequently develops larger energy in the system thus a pronounced peak is developed for the excitation frequency. The system still oscillates at its natural frequency and the excitation frequency simultaneously.
- The natural frequency of the pendulum is present (Figure 24) however its energy is extremely small when compared to that of spring. This implies the natural frequency of the pendulum is not dominant when assigned the presented excitation force. The forcing frequency of the pendulum (8.335Hz) is dominant and thus presents a large amount of energy.
- There are two additional frequencies presented for the elastic pendulum which are defined by $w_p - w_{sn}$ and $w_p + w_{sn}$. The results indicate that the pendulum excitation is the carrier frequency in the system. The sidebands presented have been studied at length with regards to system monitoring of gearboxes as presented by (Timothee, et al., 2013). With regards to gearboxes an increase in energy for the sideband frequencies generally presents geometrical changes in the system which may indicate failures. The phenomenon is also associated with nonlinear behaviour (Nader, 2016). For the case of the spring pendulum, the algorithm used for the FFT (and subsequently PSD) will present sideband frequencies when there exists a trace of two frequencies overlaying each other. This behaviour is not easily presented by Figure 21 however when reviewing Figure 18 all the coordinates trace two frequencies. This type of behaviour is typically not presented in mechanical systems since there generally exists only one dominant frequency in a system (Joubert, 2023). For the case of commercial vibrating screens, there would exist two frequencies only when geared exciters are used since there will be a motor frequency and a frequency for the excitation, however the motor frequency is not dominant and is well balanced thus presents little contribution to the global system since there is no direct excitation from the motor itself.

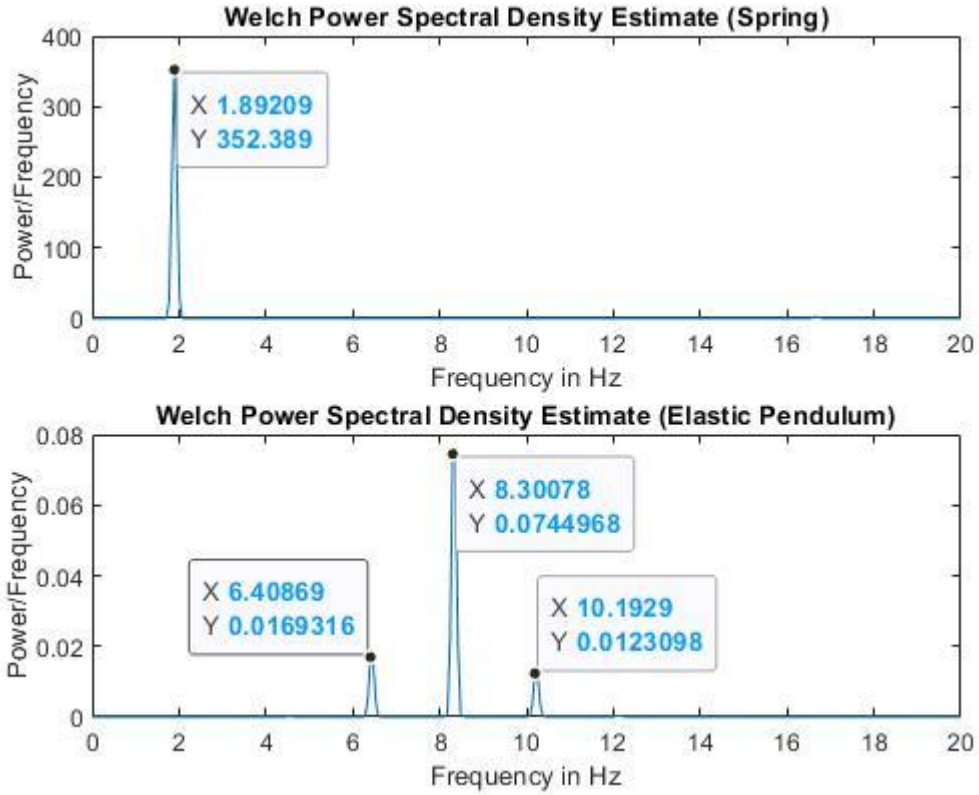

Figure 23: PSD of acceleration results using attributes presented in Table 6

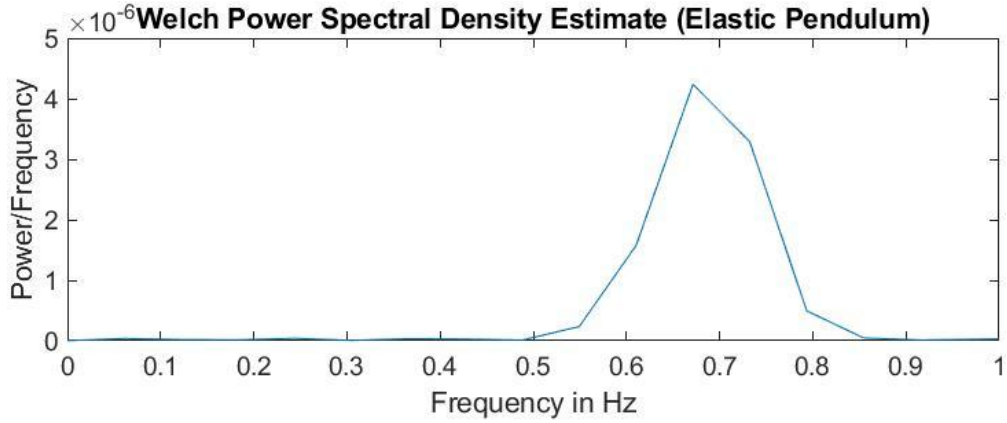

Figure 24: Zoomed view of the pendulum frequency presented in Figure 23

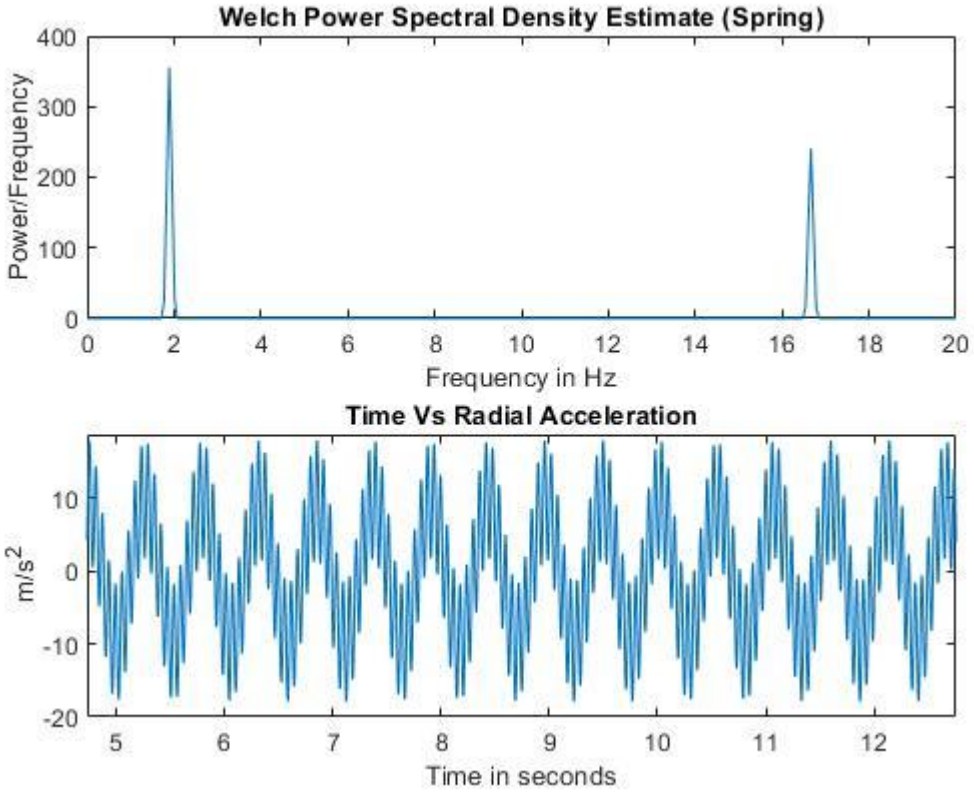

Figure 25: PSD and radial acceleration using larger excitation force on the spring

Another simulation is performed where the attributes presented in Table 7 are assigned with excitation frequencies applied as per Table 6, thus developing system parameters which are parametrically resonant however the applied forces are not at the natural frequencies of the system. Figure 26 presents the displacement and acceleration results attained from the simulation. The resulting motion trace (Figure 27) reflects the displacement results, the time interval presented by "A" consists of very small angular displacements with predominantly vertical displacements which are presented by the densely populated region of Figure 27. Time interval "B" presents a combination of radial and rotational motion which is presented by the sparsely populated regions of Figure 27 (both horizontal and vertical motion).

The results present autoparameteric resonance, a similar system has been studied by (de Sousa, et al., 2018) where the system is defined by low energy and small angles, it is however unclear what the criteria are for small angles. It was furthermore concluded that when the spring moves and pendulum remains still, the total energy of the system is defined by the spring, the system is analogous when considering movement of the pendulum.

The ratio $\frac{\omega_s}{\omega_{sn}}$, provides a numerical value of 6.22 which is close to 6. It is expected that there should exist weak parametric resonance since the ratio is approximately a multiple of 2.

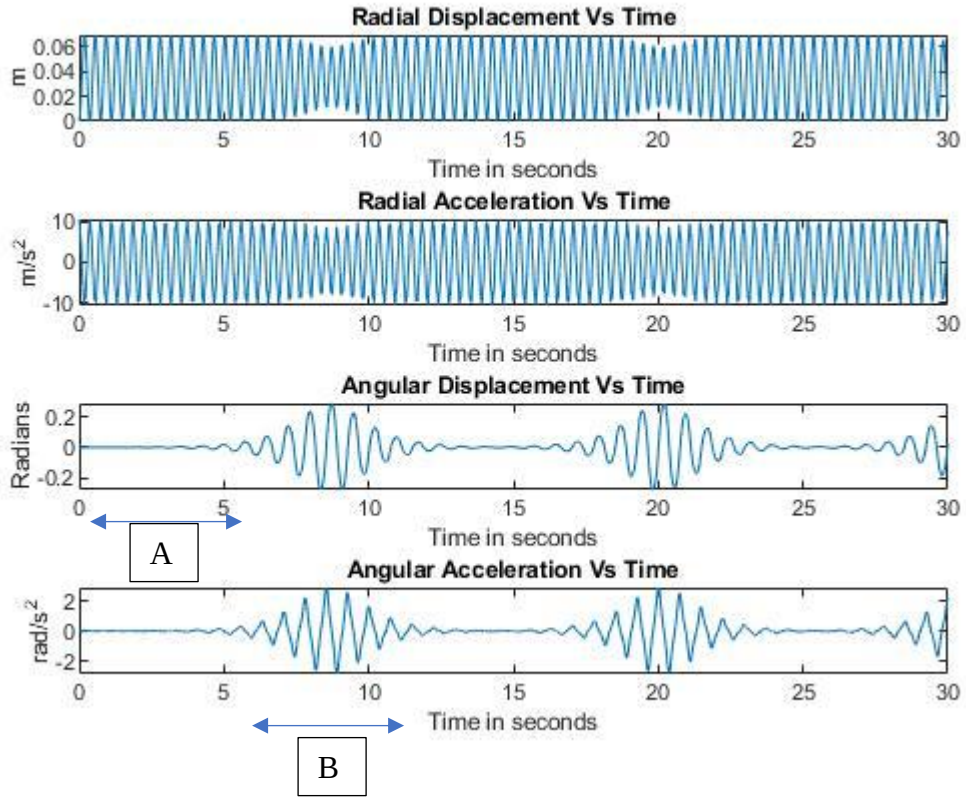

Figure 26: Displacement and acceleration results for a parametrically resonant 2 DOF model

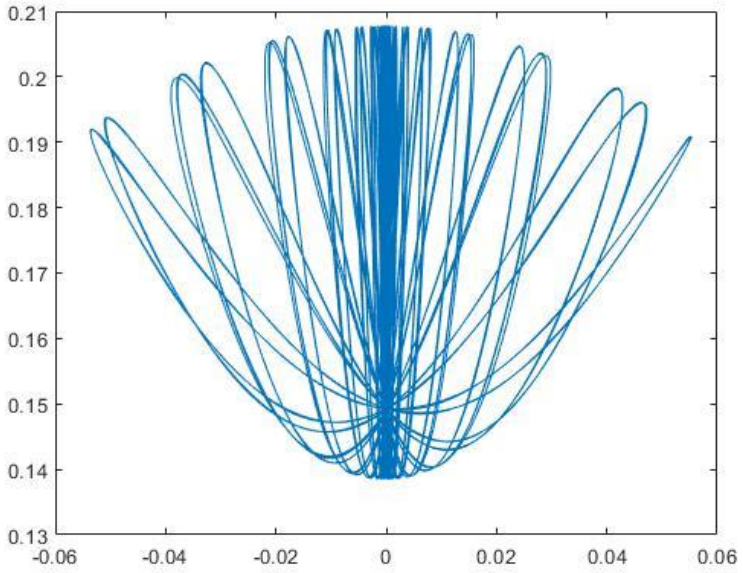

Figure 27: Motion trace for parametrically resonant 2 DOF model

Figure 28 presents the PSD for the model simulated above. The following conclusion can be made by studying Figure 28:

- The exciting frequency on the pendulum and spring are small, the results are not noticeable, however zooming in on the results presents the frequencies at which excitation occurs. The natural frequencies of the spring and pendulum are dominant since these frequencies produce pronounced peaks, thus the resulting motion is at the natural frequencies of the spring and pendulum.
- As with Figure 23 the natural frequency of the spring and pendulum correlate well with the calculated results presented in Table 6.
- The natural frequency of the pendulum has sideband frequencies, the sideband frequencies are produced about the spring natural frequency. This implies that the spring excitation is the carrier frequency for the system. It is evident that when the spring transfers energy to the pendulum, it continues to move however when the pendulum transfers energy to the spring the pendulum ceases to move.

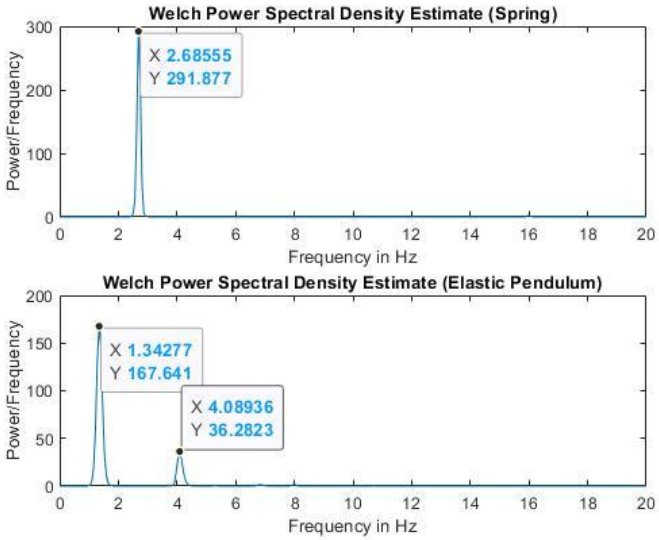

Figure 28: Power spectral density for the parametrically resonant model

Table 7 presents attributes such that the pendulum is parametrically proportioned, and the excitation forces correlate to the natural frequencies of the spring and elastic pendulum.

Table 7: Attributes for a parametric pendulum excited at parametric resonance for the 2DOF system

Attribute	Numerical Value	Units
Mass	3755	kg
Spring Stiffness	266x4	N/mm
r	0.138	m
ω_s	2.68	Hz
ω_p	1.34	Hz
ω_{sn}	2.68	Hz
ω_{pn}	1.34	Hz
α	0	-
β	0	-
Fh(t)	$3000\sin(\omega_p t)$	N
Fv(t)	$3000\sin(\omega_s t)$	N

The displacement and acceleration results are presented in Figure 29 with the motion plot presented by Figure 31. The radial displacements and accelerations have both increased with the acceleration results almost doubling. The rotational displacements and accelerations have dramatically increased with the maximum rotational displacement being in the order of ±57 degrees. The motion plot presents a system which does not favour the vertical component as presented by Figure 27. Throughout the entire time interval both the spring and pendulum are in constant motion and energy is exchanged regularly.

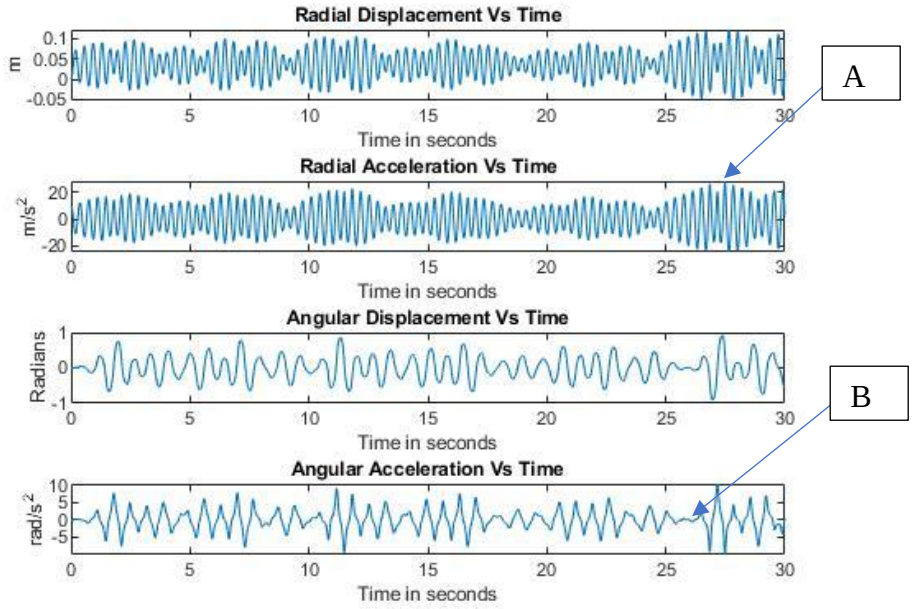

Figure 29: Displacement and acceleration results for the model attributes in Table 7

Figure 30 presents the resultant acceleration and displacement results for the above simulation. The resulting motion is far more complex compared to traditional linear motion vibrating screens which is expected to produce purely sinusoidal displacements and accelerations. The highest resultant acceleration is ±30m/s^2, which is less compared to the SD18/36 however the excitation force is applied to the 2DOF system is far smaller. It is suspected that there cannot be a direct comparison between the proposed parametrically excited system and a linear motion vibrating screen because of autoparamteric behaviour.

There are small decreases in radial acceleration as presented by "A" where energy is transferred to the pendulum, during these periods of energy transfer, the effects are far more pronounced on the pendulum, this can be attributed to the high energy present in the spring. The pendulum does transfer energy to the spring however the effects are less pronounced, the most evident time period for this is presented by "B".

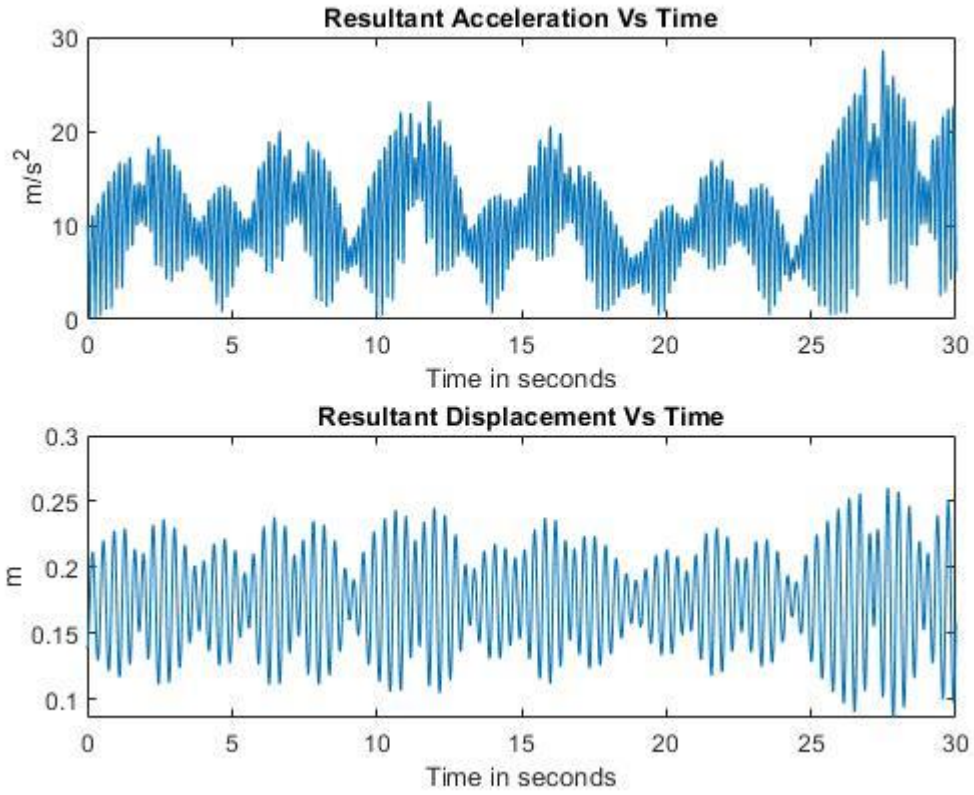

Figure 30:Resultant acceleration and displacement

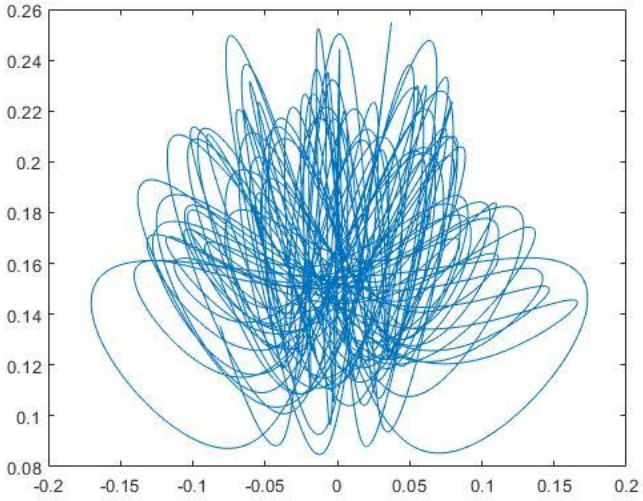

Figure 31: Motion plot for the attributes presented in Table 7

From the above simulations the following can be concluded:

- A model which is not setup for parametric resonance with excitation forces adhering to 23 does not develop any form of resonance or amplification in the results. This is an obvious conclusion since even though the excitation frequencies are parametrically chosen the frequencies do not tie up with the maximum kinetic and potential energies of the spring pendulum arrangement.
- When a model is setup in manner whereby the physical parameters develop a parametrically resonant system with excitation adhering to 23 however the excitation is not at resonant frequencies, the following is noted:
    - Parametric excitation of the elastic pendulum occurs however the times at which they occur are sparsely spaced within a given time interval.
    - No parametric excitation is found to exist in the spring, however there is a reduction in displacements and accelerations when the spring transfers energy to the pendulum motion.
- When the model is setup as discussed in the previous point, with excitation frequencies set to the natural frequencies of the spring and pendulum respectfully the following can be noted:
    - Parametric resonance is found to exist in both the spring and pendulum
    - Large accelerations and displacements can be achieved

As discussed in the literature review, damping is a complex system where damping ratios can be calculated experimentally. Liping considered proportional damping whereby τ and φ were taken as 0.01 (Liping, et al., 2018). For the design of Weir Minerals vibrating screens, a viscous damping factor of 0.1 used for the buffer/springs in accordance with equation 24 (Heyns, 2006). Damping has been chosen in this manner as it allows transient behaviour to diminish quickly since the steady state results are required. In both the above-mentioned cases the effects of damping are assumed and there is no experimental testing performed to verify the numerical values used.

$$C_h = 0.2\sqrt{km} \qquad 24$$

The damping for the spring (C_s) and pendulum (C_p) will be taken as 25 and 26 respectfully. Equation 26 has been chosen based on the worked presented by (John, 2005).

$$C_s = \tau M + \varphi K \quad 25$$

$$C_p = \mu r^2 \quad 26$$

Table 8: Damping cases for the 2DOF systems

Case	τ/ϕ/μ
1	0.001
2	0.005
3	0.01

Table 8 presents three cases considered for damping. The simulation with damping will be performed using the attributes presented in Table 5. The resulting radial and rotational displacements are presented by Figure 32. The effects of damping eventually cancel out the effects of parametric resonance, lower damping allows for greater parametric resonance during the early stages of the simulation.

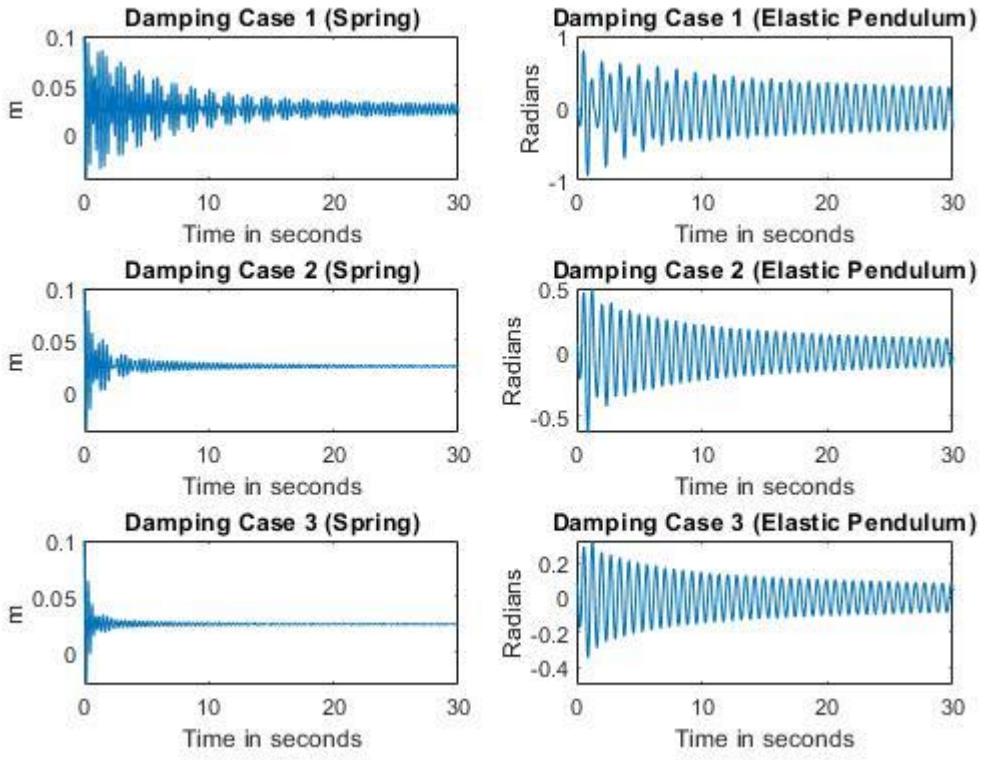

Figure 32:Radial and rotational displacements using the simplified model for various damping

The topic of damping is discussed by (Anton, et al., 2009) where a similar model was studied, it was found that the inclusion of damping leads to phase shifts and a decreasing amplitude for parametric resonance. Damping case 1 presents a small amount of damping which leads to a

small phase shift thus allowing parametric resonance to still exist. The phase shifts would be difficult to assess through means such as signal processing as they are estimations. The damped natural frequency can be used to calculate an excitation frequency which is indicative of the phase shift. The equation for the damped natural frequency is presented by 27. Equation 27 can be used to develop a frequency of excitation so that parametric resonance can exist.

$$\omega_d = \omega_n \sqrt{1 - \frac{c}{2\sqrt{km}}} \qquad 27$$

By taking τ and φ as 0.01 and using equation 27 the damped natural frequency of the spring can be calculated as 2.67Hz. The difference between the damped natural frequency and undamped natural frequency of the spring is 0.01Hz. The damped natural frequency of the pendulum is insignificantly different from the undamped natural frequency by an order of 1×10^{-9}. From the literature review it is evident that parametric resonance will exist when equation 23 is approximately equal to 2. It is thus evident that when damping is small, there will be little difference between the undamped and damped natural frequency of the system.

Figure 33 presents the displacement and acceleration results for each coordinate using the conditions presented in Table 7 with damping assigned as 0.01. The inclusion of damping provides enough resistance to prevent the system from experiencing parametric resonance. There exists parametric behaviour early on ($t \leq 5$ seconds), thereafter damping prevents the existence of parametric resonance.

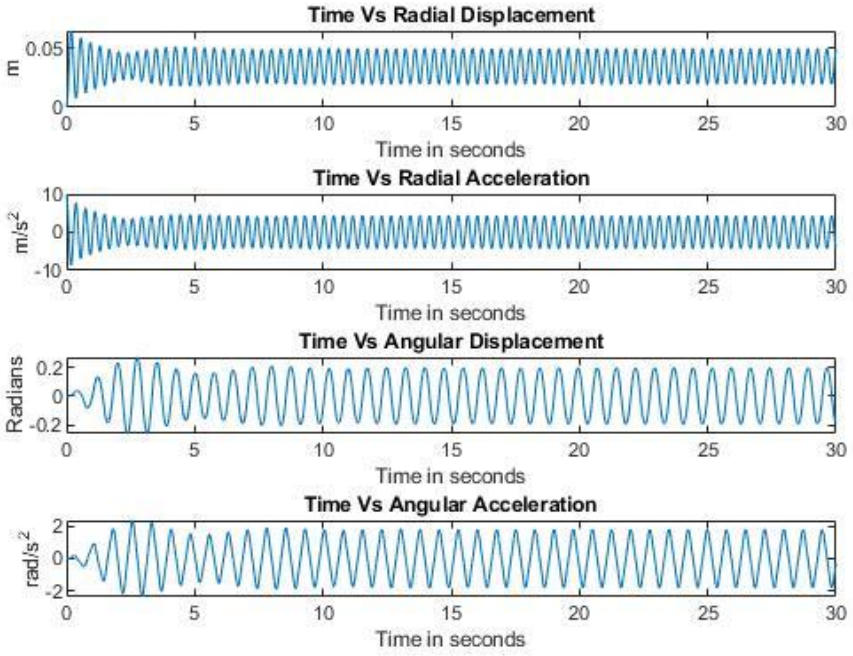

Figure 33: Displacement and acceleration results for an excited 2DOF with damping

The motion trace is presented by Figure 34. The results present a case where there exists a small amount of radial displacements, which is not very noticeable. The motion resembles that of a traditional pendulum. Figure 35 presents the PSD, where both the pendulum and spring natural frequency are the same as their analytical values, thus verifying the previous discussion regarding damped natural frequencies.

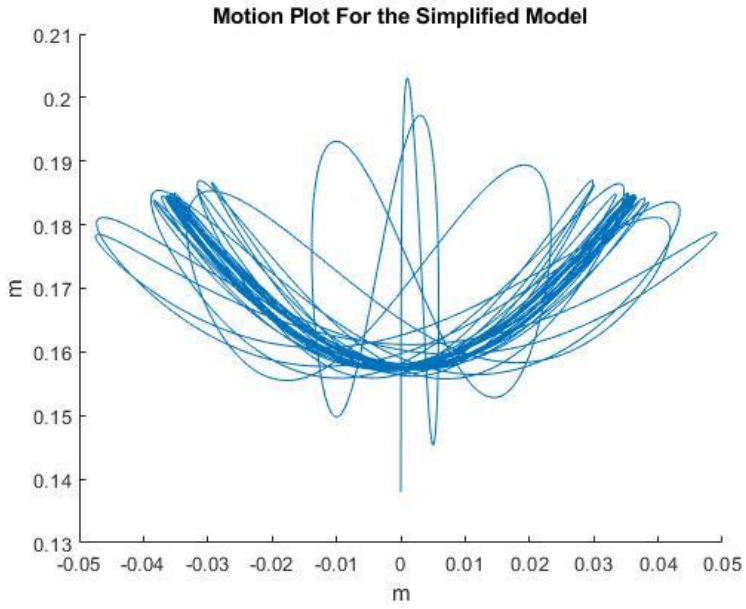

Figure 34: Motion trace for the excited 2 DOF system with damping

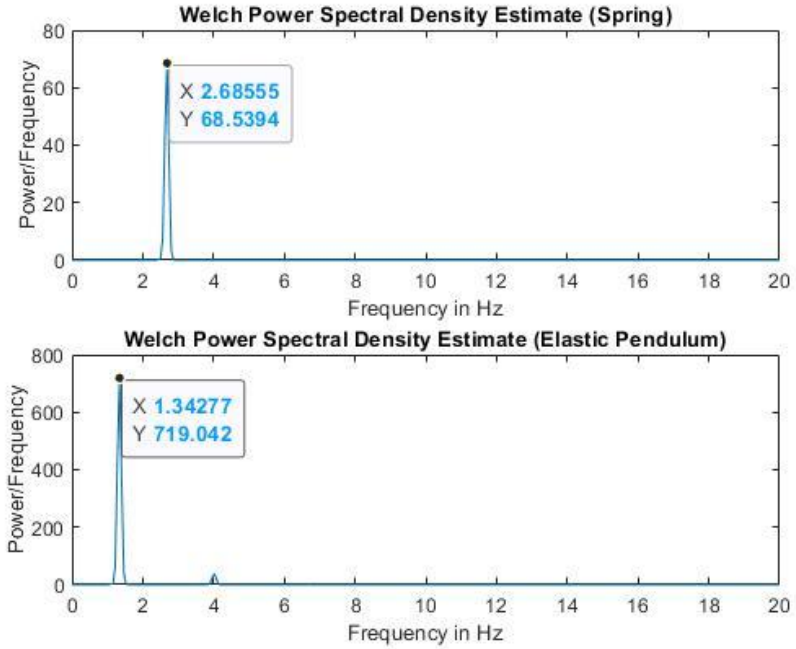

Figure 35: PSD for the excited 2DOF system with damping

The effects of damping on the motion trace will also be studied, this will be performed by incrementing the damping ratio for the system by increments of 0.01 until 0.04, thus creating 4 iterations. Each iteration will use the damped natural frequency as the excitation frequency. The results of the simulation are presented in Figure 36. The effect of damping ratio on the spring has a greater than the effect on the pendulum, thus with an increasing damping ratio it is found that the system presents results which tend to displace less radially. Each simulation presents a different motion trace thus implying that the effects of damping will have a dramatic effect of the motion of the proposed vibrating screen. The results do not correspond to (Liping, et al., 2018) statement that damping has little effect on a system which is excited.

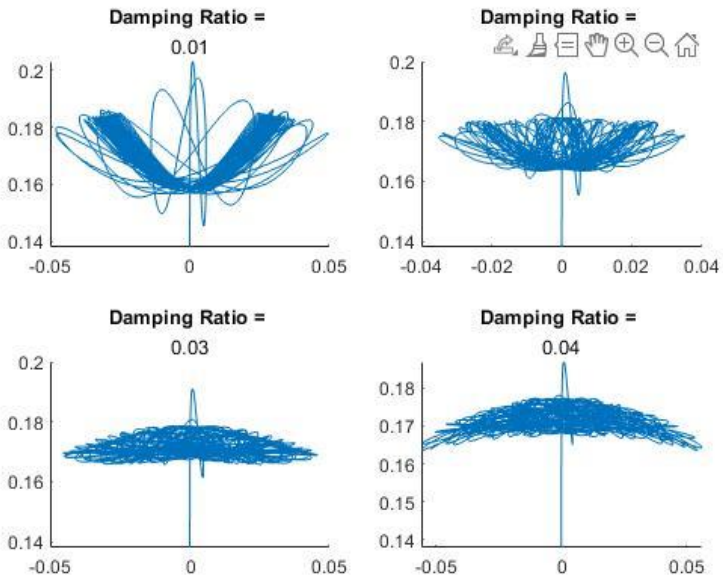

Figure 36: Motion trace for various damping ratios

2.5. CONCLUSION

A pendulum which is parametrically sized and excited presents continuous motion in both coordinates with energy transfer between both coordinates. When damping is included in the system energy transfer between coordinates still occurs however there are time points where the pendulum motion/acceleration is close to 0 thus developing a situation where the motion is only of the spring moving/accelerating vertically.

The system is not studied from a perspective of achieving adequate accelerations for screening since this chapter is developed to gain insight into the simple elastic pendulum. Based on the simulations there is no direct manner to compare a parametrically excited model to a traditional linear motion vibrating screen, this it attributed to the way autoparametric resonance affects the system. Displacements and accelerations are not purely repetitive functions as one expects from traditional vibrating screen.

The displacements results are far higher when compared to the SD18/36 vibrating screen. As per Figure 3 screen efficiency is impacted far more severely to amplitude compared to frequency. The numerical values presented for amplitude (Figure 3) are far smaller compared to what is experienced by the 2DOF system. This develops a case where large amplitudes can be studied with regards to screening efficiency, this however would be coupled with compound motion which present a unique type of vibrating screen.

CHAPTER 3: DERIVATION OF THE 4DOF SYSTEM

This chapter will deal with the derivation of a 4DOF system which represents the proposed vibrating screen. The 4DOF system is the most logical coordinate system to represent the system. The derivation considers two independent elastic pendulums which are coupled through a holonomic constraint. The system will be shown to be an unfeasible approach and thus will not be studied in detail. The derivation of the 4DOF system is considered novel since the author has found no other references which match the system.

3.1. DERIVATION OF THE 4DOF SYSTEM

Figure 37 illustrates a 4DOF system with the most logical coordinate system consisting of:

- a and b which represents the elongation/contraction of the spring with r being the natural length of the spring
- θ_1 and θ_2, which represents the rotational component of each spring

The two springs are connected by means of a rigid bar, it is assumed that the mass of the system distributes such that the masses are m_1 and m_2 at the ends of the springs.

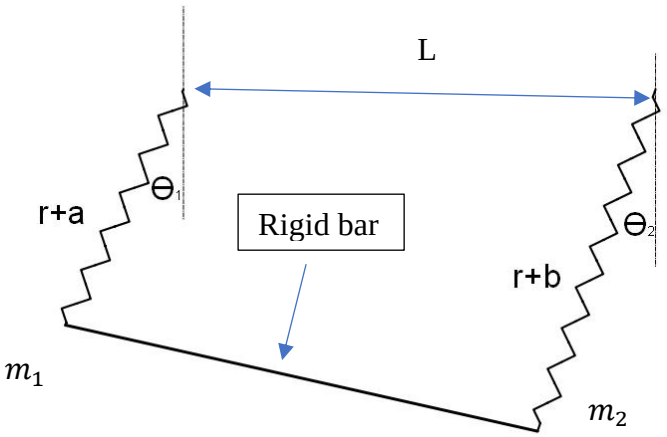

Figure 37: 4DOF model for the proposed vibrating screen design

The Euler-Lagrange formulation of each spring mass system can be derived as done previously; the resulting 4 differential equations are presented below.

$$m_2\ddot{b} = m_2\dot{\theta}_2^2(r+b) - kb + gm_2\cos\theta_2 \quad (28)$$

$$m_1\ddot{a} = m_1\dot{\theta}_1^2(r+a) - ka + gm_1\cos\theta_1 \quad (29)$$

$$m_1\ddot{\theta}_1(r+a)^2 = -2m_1\theta_1\dot{a}(r+a) - gm_1\sin\theta_1\,(r+a) \quad (30)$$

$$m_2\ddot{\theta}_2(r+b)^2 = -2m_2\theta_2\dot{b}(r+b) - gm_2\sin\theta_2\,(r+b) \quad (31)$$

The above equations independently model the behaviour of each spring mass system without providing any coupling of the system. The system can be coupled by means of using a holonomic constraint as presented by equation 32. The holonomic constraint implies that the distance between each mass subtracted by the length of the rigid bar will be 0.

$$[(r+a)\,sin\,\theta_1 + L - (r+b)\,sin\,\theta_2]^2 + [(r+a)\,cos\,\theta_1 - (r+b)\,cos\,\theta_2]^2 - L^2 = 0 \qquad 32$$

The holonomic constraint can be introduced into the above 4 differential equations by means of making any one of the coordinates the subject of the formula. Making either θ_1 or θ_2 the subject of the formula develops unfeasible solutions. The $(r+a)$ and $(r+b)$ terms are commonly used, making either of the terms the subject of the formula presents a logical approach. Equation 33 presents the case where $(r+b)$ is made the subject of the formula, the $\#1$ term presents two possible outcomes thus the resulting equation which represents $(r+b)$ has two roots.

$$(r+b) = \frac{2(a+r)\,cos\,\theta_1\,cos\,\theta_2 + 2L\,sin\,\theta_2 + 2(a+r)\,sin\,\theta_1\,sin\,\theta_2 + \#1}{2(sin\,\theta_2^2 + cos\,\theta_2^2)} \qquad 33$$

Where #1 is presented by equation 34.

$$\#1 = \pm\sqrt{2}\sqrt{-(a+r)^2 + L^2 + (a+r)^2\,cos(2\theta_1 - 2\theta_2) - L^2\,cos(2\theta_2) - 2(a+r)L\,sin\,\theta_1 - 2(a+r)L\,sin(\theta_1 - 2\theta_2)} \qquad 34$$

The right-hand side of equation 33 can be substituted into equation 31, this develops an equation which does not present any b terms. There is however a $\dot{b}$ term present in equation 31, this term can be removed by substituting the time derivative of equation 33 into equation 31. The time derivative of equation 33 can be found in APPENDIX B – TIME DERIVATIVES OF $(\boldsymbol{r+b})$. By performing the required substitutions, the $(r+b)$ and $\dot{b}$ can be completely removed from the set of differential equations, thus equation 31 can be replaced with equation 35.

$$m_2\ddot{\theta}_2\left(\frac{R_1 + R_2 \pm \#1}{2}\right) = \left[-2m_2\theta_2\frac{\dot{R}_3}{\sqrt[4]{R_3}} - gm_2\,sin\,\theta_2\right] \qquad 35$$

The resulting code which represents the 4DOF system is presented by Matlab Code 3, with the state representation of the variables presented by equation 36.

$$[S] = \begin{bmatrix} s_1 \\ s_2 \\ s_3 \\ s_4 \\ s_5 \\ s_6 \\ s_7 \\ s_6 \end{bmatrix} = \begin{bmatrix} \theta_1 \\ \dot{\theta}_1 \\ \theta_2 \\ \dot{\theta}_2 \\ a \\ \dot{a} \\ b \\ \dot{b} \end{bmatrix}; [\dot{S}] = \begin{bmatrix} s_2 \\ \ddot{\theta}_1 \\ s_4 \\ \ddot{\theta}_2 \\ s_6 \\ \ddot{a} \\ s_6 \\ \ddot{b} \end{bmatrix} \qquad 36$$

3.2. SIMULATION OF THE 4DOF SYSTEM

If one considers the attributes and initial conditions presented by Table 4 (neglecting the initial conditions imposed on the θ coordinate), the following can be noted:

- $m_1 = m_2 = 1877.5kg$
- $\theta = \theta_1 = \theta_2 = 0$
- $x(0) = a(0) = b(0) = 0.1\text{m}$
- L will be taken as 2m. The value of L in this case is irrelevant

Using the above-mentioned data, a simulation of the 4DOF system can be performed. The displacement results for a, b and the equivalent 2DOF system are presented by Figure 38. As expected, the results for a and b are identical, these results also correspond to the results from the 2DOF system.

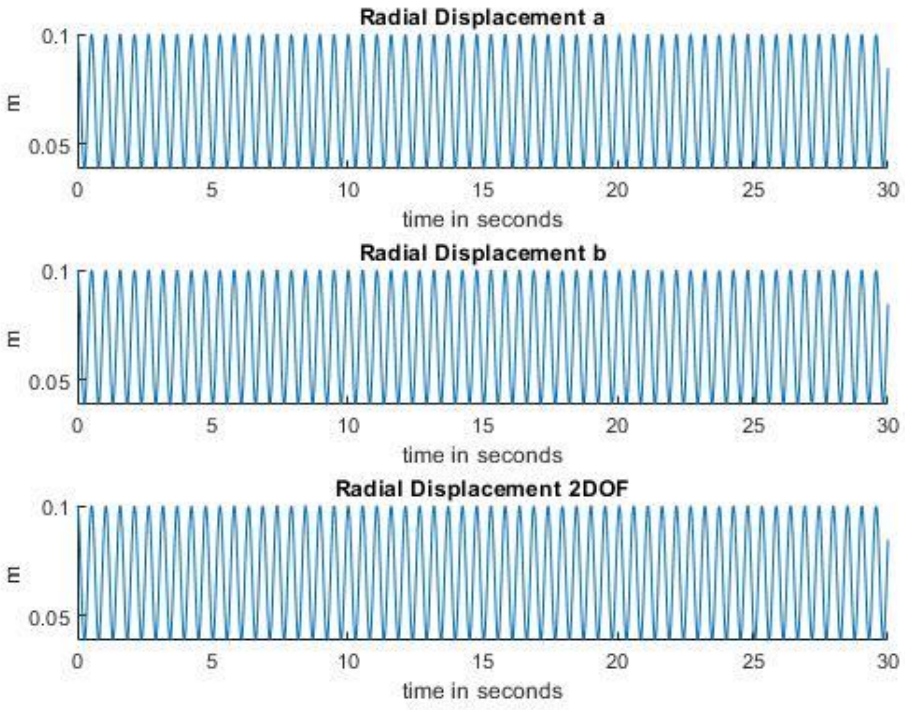

Figure 38: Displacement comparison between the 2DOF and 4DOF system

If one considers all the initial conditions presented by Table 4, thus implying that $\theta = \theta_1 = \theta_2 = 5^o$, another simulation can be performed where the displacement results for the 4DOF system are presented by Figure 39. It should be noted that the negative root is considered for equation 34. It is expected that all coordinates of the system move in sync with each other, this is however not the case. The displacements of coordinate b experiences linear drift, while θ_1 and θ_2 experience different displacements.

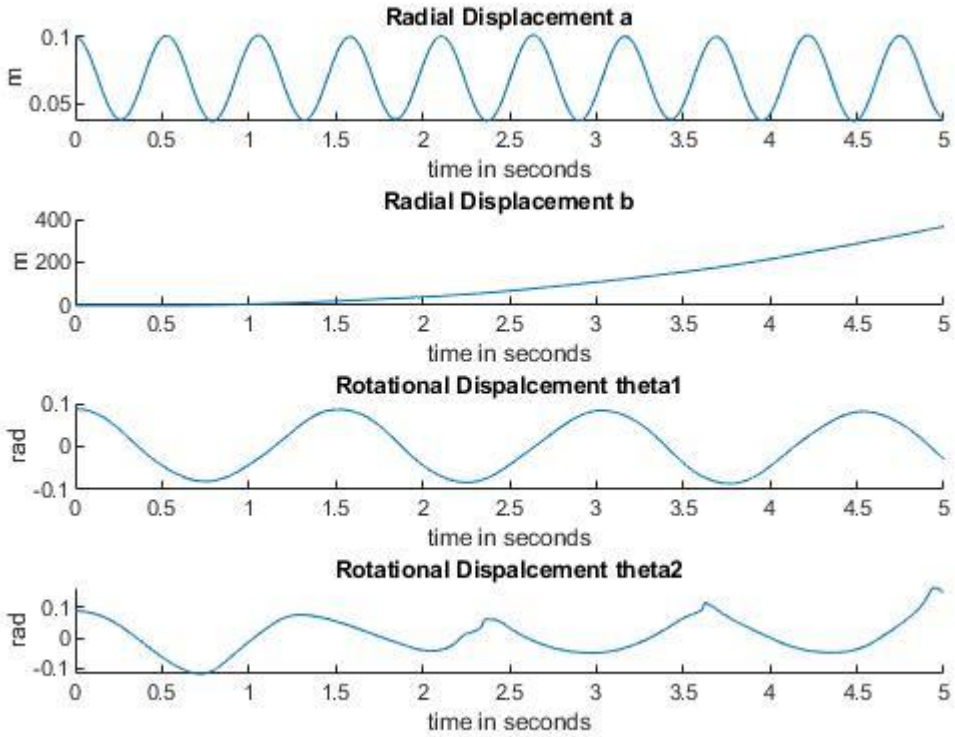

Figure 39: Displacements of the 4DOF using initial conditions presented by Table 4

If a Butterworth filter is implemented as per Matlab Code 5 the drift in displacement results for coordinate b can be rectified. The results are presented by Figure 40, the results are still not as expected since the displacements of coordinate b should mirror that of coordinate a and so should the periods which are clearly not identical. It should be noted that the numerical values for coordinate b may not be accurate due to the order of the Butterworth filter, thus the large displacements being produced. The results do present enough information for one to make the above-mentioned conclusions.

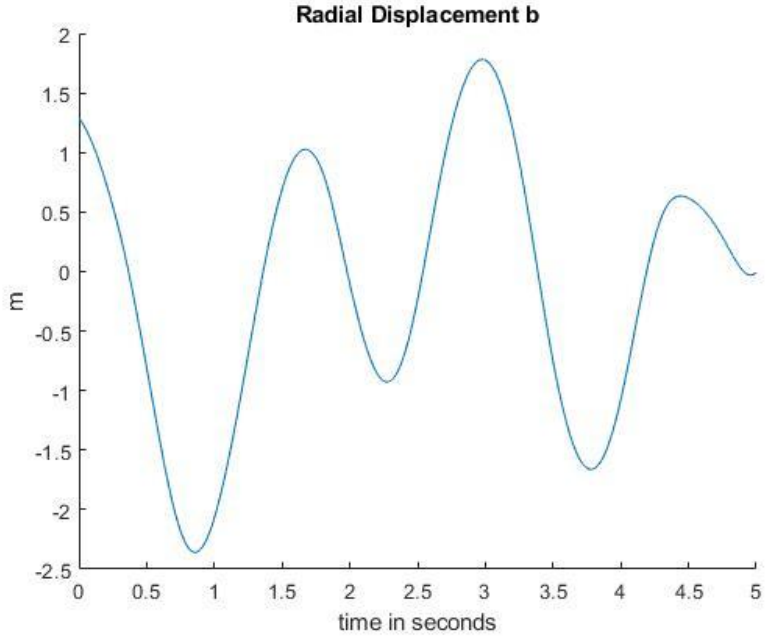

Figure 40: Filtered displacement results for coordinate b

It can be noted that the above plots do not include the imaginary components of the results, imaginary components exist for the θ_2 and b coordinates. Figure 41 presents the sum of terms $(1), (2), (3), (4)$ & (5), whose expression can be found in APPENDIX B – TIME DERIVATIVES OF $(\boldsymbol{r} + \boldsymbol{b})$. The results yield negative values over certain time intervals. If one considers equation 34 there will exist imaginary numbers since the square root will be taken of a negative number.

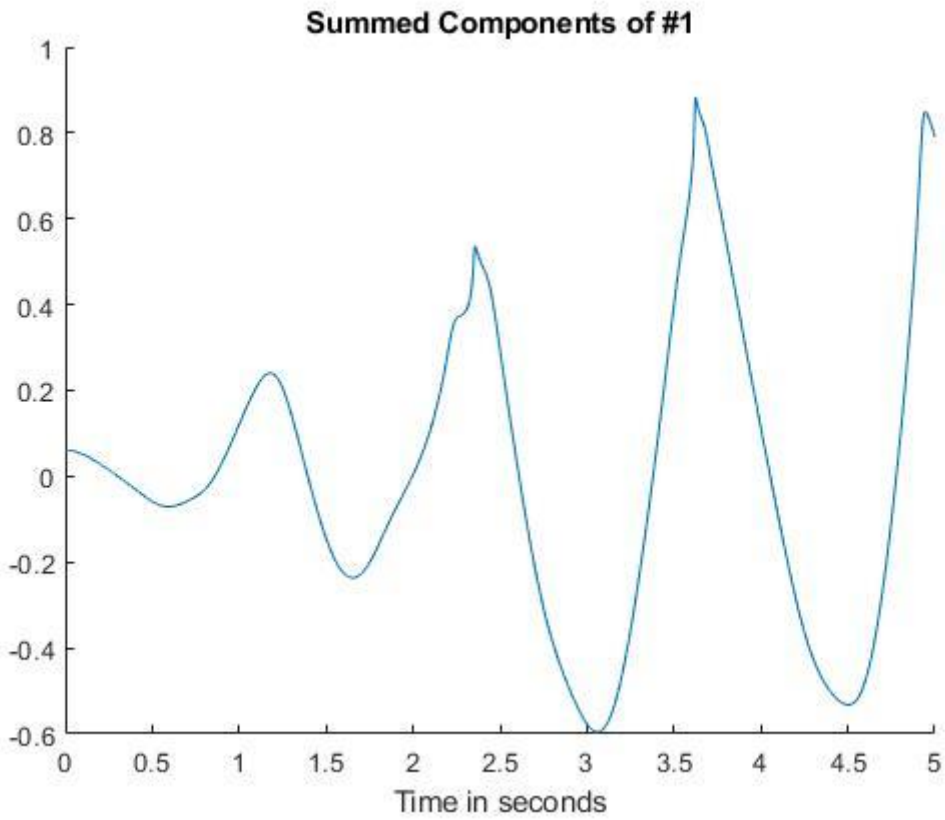

Figure 41: Components of #1

Figure 42 presents the plot of the holonomic constraint (equation 32), the results should produce a 0 value throughout the simulation, however this is clearly not the case. The results present an increasing distance, implying that the holonomic constraint is not obeyed.

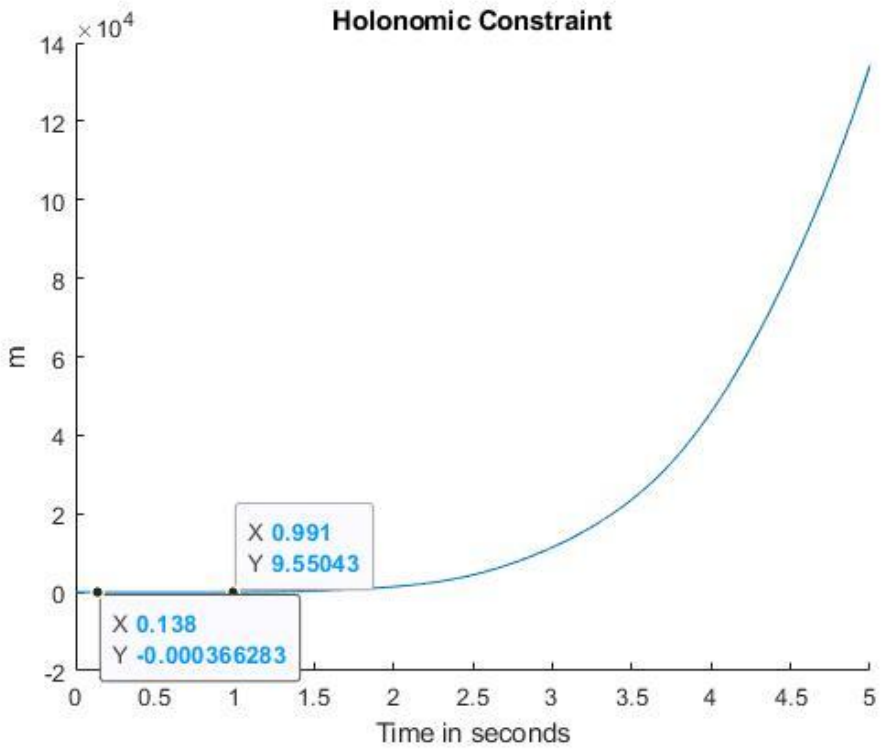

Figure 42: Plot of the holonomic constraint

If a smaller simulation time is considered, of 0.5 seconds, the above-mentioned results can be replotted as presented by Figure 43, noting that x and θ pertain to results from the equivalent 2DOF system. When reviewing the simulation over a shorter time frame the results present far better correlation. the following can be noted by studying Figure 43:

- The displacement results for coordinates a and b correlate well up to roughly 0.3 seconds, thereafter the results begin deviating
- The results for θ_1 and θ_2 also present good correlation however they begin to deviate at roughly 0.35 seconds, thus having a slightly longer period of correlation compared to the radial component.
- The components of #1 present negative values at roughly 0.3 seconds which correlates to the time point where the holonomic constraint begins to present non zero results. This also pertains to the rough point in time where the coordinates begin to deviate from each other.
- The 2DOF and 4DOF system correlate well until imaginary numbers are generated for the 4DOF system.

The negative values presented by the sum of $(1), (2), (3), (4)$ & (5) are problematic, since they correlate to deviations in the expected results. The imaginary numbers developed by equation 34 may require one to process the results differently in order to develop consistency with the 2DOF system.

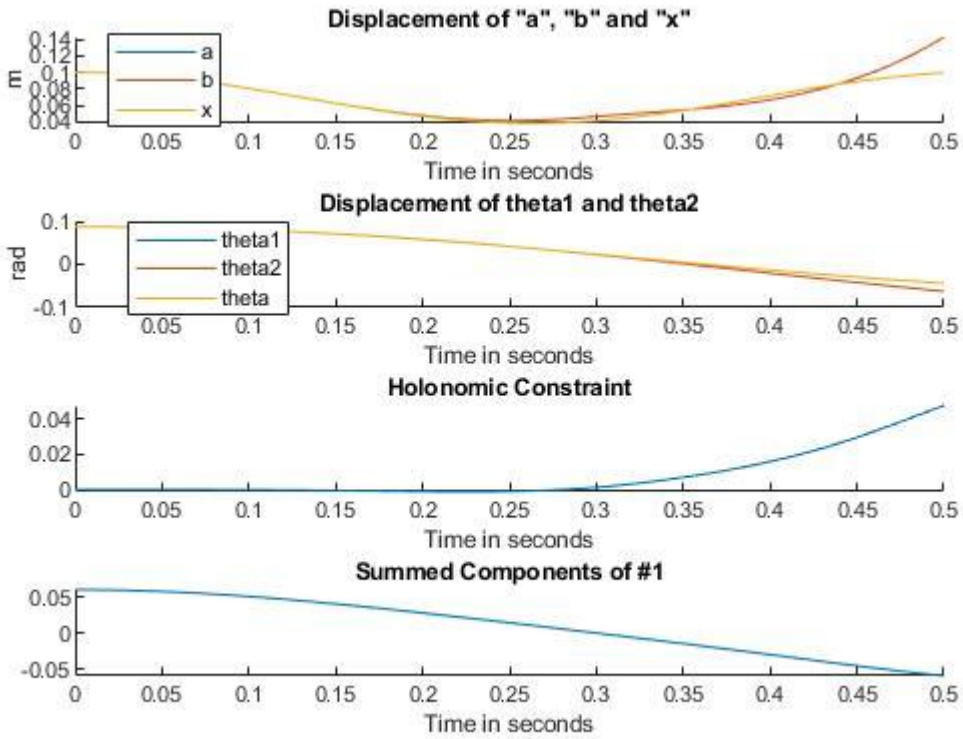

Figure 43: Simulation results over a 0.5 second time frame

The above simulations consider the negative root for equation 34, Figure 44 presents the displacement results for each coordinate considering the negative and positive roots. Coordinate a and θ_1 presents results which overlap each other for both the negative and positive roots, this is not the case for coordinate b and θ_2. The results are similar while there exist no imaginary numbers (less the 0.3 seconds), this is a clear indication that equation 34 does not have a huge impact on the outcome (for this specific case) since regardless of the sign convention the results are similar. When imaginary numbers are developed the results for b and θ_2 begin deviating, thus indicating that equation 34 is playing a larger role in the results.

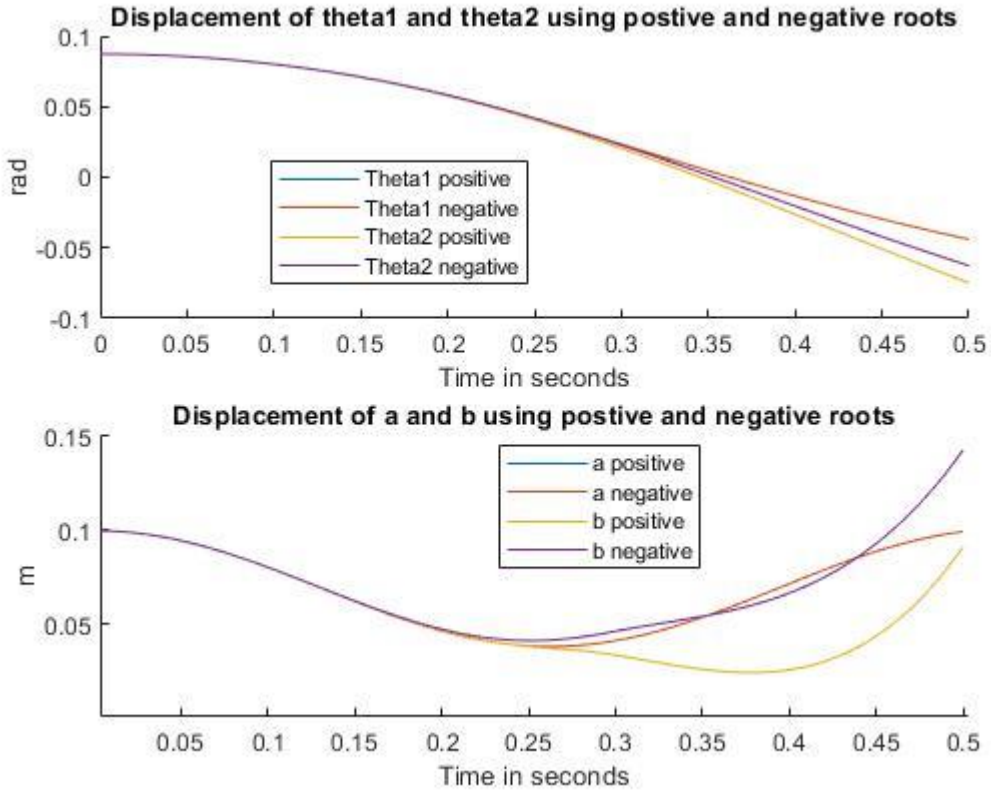

Figure 44: Displacement results considering the positive and negative roots of #1

Through discussions with an applied mathematician, it was concluded that holonomic constraints can become complex when trying to solve a system numerically, it was concluded that an alternate derivation should be developed (Anderson, 2021). It was also noted by Anderson that a specific solver for the derivation would possibly need to be developed due to the complexity of the problem.

CHAPTER 4: 3-DOF SYSTEM

This chapter will deal with the derivation and study of a 3DOF system which represents the proposed vibrating screen. The derivation and model of the 3DOF system is novel since the author has found no similar work. The model will be studied using established attributes presented in the study of the 2DOF model, following a similar layout however presenting more detail. The 2DOF and 3DOF models will be compared where possible. The goal of this chapter is to develop criteria for screening.

As performed previously signal processing techniques will be implemented to gain a deeper understanding of the system. PSD and FFT will be used for signal processing, the choice of method will be dependent on the readability of the results. Processing signals taken from sensors should be done using PSD since PSD's are normalised to the frequency bin width preventing the duration of the data set from changing the amplitude of results, the FFT cannot do this. This allows one to compare PSD's between environments, test instrumentation, settings and duration (Hanly, -). For the case of this study the PSD and FFT create identical results when reviewing excitation and natural frequencies however the energies of the frequencies may change the visualisation of the results thus making one more understandable compared to the other.

4.1. DERIVATION OF THE 3DOF SYSTEM

The 4DOF system presented by Figure 37 can be simplified as presented by Figure 45 which is a 3DOF system consisting of x, y and θ coordinates. The variables α and β present the angle of the springs with respect to the vertical, these variables will not form part of the Euler-Lagrange formulation, however they will be discussed later. The cartesian coordinates are used to represent the centre of the rigid bar. When the system is at rest the x coordinate will have a numerical value of 0 implying that the origin of the cartesian coordinates is placed at the centre of the rigid bar (for the horizontal case). A third coordinate, θ is used to represent the angle of the rigid bar with respect to the horizontal plane. The mass of the system will be denoted by m. The chosen set of coordinates allows one to represent the proposed vibrating screen without the use of any holonomic constraints.

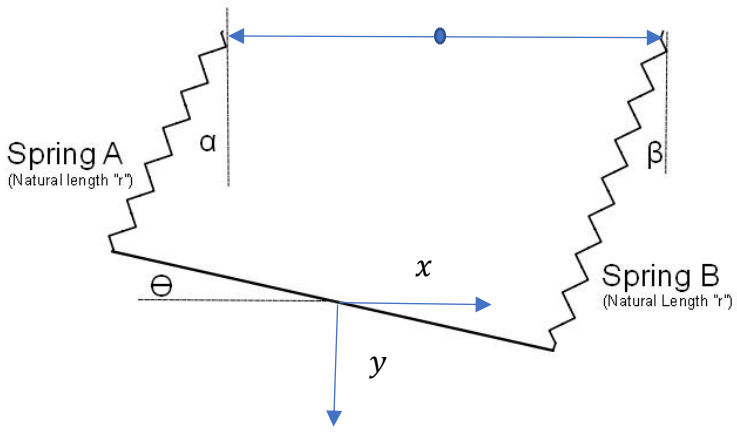

Figure 45: 3-DOF model for the proposed vibrating screen

The coordinates of A and B can be represented by:

$$(x - \frac{L}{2}cos\,\theta, y - \frac{L}{2}sin\,\theta) \quad 37$$

$$(x + \frac{L}{2}cos\,\theta, y + \frac{L}{2}sin\,\theta) \quad 38$$

The potential energy of the system can be represented by:

$$U = 0.5k\left[\sqrt{\left(x - \frac{L}{2}cos\,\theta + \frac{L}{2}\right)^2 + \left(y - \frac{L}{2}sin\,\theta\right)^2} - r\right]^2 + 0.5k\left[\sqrt{\left(x + \frac{L}{2}cos\,\theta - \frac{L}{2}\right)^2 + \left(y + \frac{L}{2}sin\,\theta\right)^2} - r\right]^2 - mgy \quad 39$$

The kinetic energy of the system can be represented by:

$$T = 0.5m\left[\left(\dot{x} + \frac{L}{2}\dot{\theta}\,sin\,\theta\right)^2 + \left(\dot{y} - \frac{L}{2}\dot{\theta}\,cos\,\theta\right)^2\right] + 0.5m\left[\left(\dot{x} - \frac{L}{2}\dot{\theta}\,sin\,\theta\right)^2 + \left(\dot{y} + \frac{L}{2}\dot{\theta}\,cos\,\theta\right)^2\right] \quad 40$$

By expanding and simplifying the kinetic and potential energy they can be represented in a manner such that derivatives can easily be taken this is represented by equations 41 and 42:

$$U = \frac{KL^2}{4} + kr^2 + kx^2 - gmy + ky^2 - \frac{kL^2\,cos\,\theta}{2} + \frac{kL^2\,cos\,\theta^2}{4} + \frac{kL^2\,sin\,\theta^2}{4} - kr\sqrt{A} - kr\sqrt{B} \quad 41$$

$$T = \frac{L^2 m\dot{\theta}^2}{4} + m\dot{x}^2 + m\dot{y}^2 \quad 42$$

The derivatives and time derivatives required by the Euler-Lagrange formulation are presented below:

$$\frac{\partial T}{\partial \dot{x}} = 2m\dot{x}, \frac{d}{dt}\left(\frac{\partial T}{\partial \dot{x}}\right) = 2m\ddot{x} \quad 43$$

$$\frac{\partial T}{\partial x} = 0, \frac{\partial U}{\partial \dot{x}} = 0, \frac{d}{dt}\left(\frac{\partial U}{\partial \dot{x}}\right) = 0 \quad 44$$

$$\frac{\partial U}{\partial \dot{x}} = 2kx - kr\left(\frac{L + 2x - L\,cos\,\theta}{2\sqrt{A}}\right) - kr\left(\frac{-L + 2x + L\,cos\,\theta}{2\sqrt{B}}\right) \quad 45$$

$$\frac{\partial T}{\partial \dot{y}} = 2m\dot{y}, \frac{d}{dt}\left(\frac{\partial T}{\partial \dot{y}}\right) = 2m\ddot{y} \quad 46$$

$$\frac{\partial T}{\partial y} = 0, \frac{\partial U}{\partial \dot{y}} = 0, \frac{d}{dt}\left(\frac{\partial U}{\partial \dot{y}}\right) = 0 \quad (47)$$

$$\frac{\partial U}{\partial \dot{y}} = -gm + 2ky - kr\left(\frac{2y - L\sin\theta}{2\sqrt{A}}\right) - kr\left(\frac{2y + L\sin\theta}{2\sqrt{B}}\right) \quad (48)$$

$$\frac{\partial T}{\partial \dot{\theta}} = \frac{1}{2}L^2 m, \frac{d}{dt}\left(\frac{\partial T}{\partial \dot{\theta}}\right) = \frac{1}{2}m\ddot{\theta}L^2 \quad (49)$$

$$\frac{\partial U}{\partial \dot{\theta}} = 0, \frac{d}{dt}\left(\frac{\partial U}{\partial \dot{\theta}}\right) = 0 \quad (50)$$

$$\frac{\partial U}{\partial \dot{\theta}} \quad (51)$$

$$= 0.5kL^2\sin\theta + \frac{KL^2}{4}(-2\cos\theta\sin\theta)$$
$$+ \frac{KL^2}{4}(2\sin\theta\cos\theta)$$
$$- kr\left[\frac{0.5kL^2 + Lx\sin\theta + 0.25L^2(-2\cos\theta\sin\theta) - Ly\cos\theta + 0.25L^2(2\sin\theta\cos\theta)}{2\sqrt{A}}\right]$$
$$- kr\left[\frac{0.5kL^2 - Lx\sin\theta + 0.25L^2(2\cos\theta\sin\theta) + Ly\cos\theta + 0.25L^2(2\sin\theta\cos\theta)}{2\sqrt{B}}\right]$$

Where A and B are represented by:

$$A = \frac{L^2}{4} + Lx + x^2 + y^2 - \frac{L^2\cos\theta}{2} - Lx\cos\theta + \frac{L^2\cos\theta^2}{4} - Ly\sin\theta + \frac{L^2\sin\theta^2}{4} \quad (52)$$

$$B = \frac{L^2}{4} - Lx + x^2 + y^2 - \frac{L^2\cos\theta}{2} + Lx\cos\theta + \frac{L^2\cos\theta^2}{4} + Ly\sin\theta + \frac{L^2\sin\theta^2}{4} \quad (53)$$

When taking the derivative of $\sqrt{A}$ and $\sqrt{B}$ the chain rule needs to be implemented with the standard form of the solution being presented by *55* while *54* presents the function which is differentiated.

$$f(x) = \sqrt{g(x) + c} \quad (54)$$

$$f'(x) = \frac{g'(x)}{\sqrt{g(x)+c}} \quad (55)$$

The differential equations for the three coordinates with acceleration being the subject of the formula is be represented by equations *56*, *57* and *58*:

$$\ddot{x} = \frac{-\left[2kx - kr\left(\frac{L + 2x - L\cos\theta}{2\sqrt{A}}\right) - kr\left(\frac{-L + 2x + L\cos\theta}{2\sqrt{B}}\right)\right]}{m} \quad (56)$$

$$\ddot{y} = \frac{-\left[-gm + 2ky - kr\left(\frac{2y - L\sin\theta}{2\sqrt{A}}\right) - kr\left(\frac{2y + L\sin\theta}{2\sqrt{B}}\right)\right]}{m} \quad 57$$

$$\ddot{\theta} \quad 58$$
$$= -4\left\{0.5kL^2\sin\theta + \frac{KL^2}{4}(-2\cos\theta\sin\theta)\right.$$
$$+ \frac{KL^2}{4}(2\sin\theta\cos\theta)$$
$$- kr\left[\frac{0.5kL^2 + Lx\sin\theta + 0.25L^2(-2\cos\theta\sin\theta) - Ly\cos\theta + 0.25L^2(2\sin\theta\cos\theta)}{2\sqrt{A}}\right]$$
$$\left. - kr\left[\frac{0.5kL^2 - Lx\sin\theta + 0.25L^2(2\cos\theta\sin\theta) + Ly\cos\theta + 0.25L^2(2\sin\theta\cos\theta)}{2\sqrt{B}}\right]\right\}$$
$$\div mL^2$$

The differential equations can be presented in state form as per *59*, thus allowing one to implement the ode solvers in Matlab.

$$[S] = \begin{bmatrix} S1 \\ S2 \\ S3 \\ S4 \\ S5 \\ S6 \end{bmatrix} = \begin{bmatrix} x \\ \dot{x} \\ y \\ \dot{y} \\ \theta \\ \dot{\theta} \end{bmatrix}; [\dot{S}] = \begin{bmatrix} S2 \\ \ddot{x} \\ S4 \\ \ddot{y} \\ S6 \\ \ddot{\theta} \end{bmatrix} \quad 59$$

When solving in Matlab the solution will present the displacements and velocities of each coordinate, the resulting acceleration can be calculated by substituting the displacements and velocities into equations 56, 57 and 58. The Matlab function developed for the state representation of the 3DOF is presented by Matlab Code 6. It should be noted that the code also includes damping and the generalised forces which will be discussed later.

The angle of spring A (α) can be calculate using the following procedure (Figure 46):

- Vector $\bar{A}$ can be defined from the base of spring to its displaced location. Another vector defined by $\bar{U}$ can be chosen such that it reflects the horizontal direction towards the negative x direction. Refer to Figure 46 for illustration.
- The angle with respect to the vertical can then be calculated using equation 60

$$\cos\alpha = \frac{\pi}{2} - \frac{\bar{A}\cdot\bar{U}}{\|A\|\|U\|} \quad 60$$

A similar procedure to the one presented above can be adopted for the calculation of β. The code for the above-mentioned procedure is presented by Matlab Code 7.

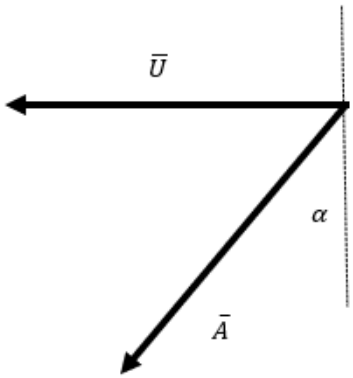

Figure 46: Vectors used for the calculation of α

$$\Delta A = \sqrt{(a_x + 0.5L)^2 + a_y^2} - r \tag{61}$$

The resulting Matlab code to implement the above-mentioned system is presented by Matlab Code 8. It should be noted that the result will develop positive values for elongation and negative values for contraction.

The acceleration of the θ coordinate is calculated in rad/s^2, this can easily be converted to a tangential acceleration with equivalent units to the x and y coordinates (Figure 47). The equation which presents the tangential component is given by 62. The x and y accelerations are global (experienced by both springs) while the tangential accelerations for the θ coordinate would oppose each other for spring A and B thus creating different accelerations at each spring. The function developed to calculate the resultant acceleration for each spring is presented by Matlab Code 9, which implements the following:

- Tangential acceleration is calculated
- The tangential acceleration is then calculated into its corresponding x and y components
- The components of the tangential acceleration are added to the global x and y accelerations
- Resultant acceleration for each spring can be calculated by using $\ddot{A}\ or\ \ddot{B} = \sqrt{\ddot{x}_{A/B}^2 + \ddot{y}_{A/B}^2}$

$$a_t = \frac{\ddot{\theta}^2 L}{2} \tag{62}$$

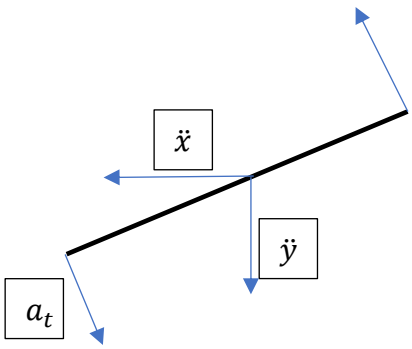

Figure 47: Freebody diagram for the accelerations (3DOF)

4.2. COMPARISON OF THE 3DOF AND 2DOF SYSTEM CONSIDERING INITIAL CONDITIONS FOR THE SPRING/S

It is expected that the 3DOF and the 2DOF system will develop the exact same results when considering initial conditions applied only to the springs (y coordinate for 3DOF and x coordinate for 2DOF). The results are expected to produce a system where there exist results only for the y coordinate. The attributes presented by Table 4 will be considered with $\theta(0) = 0$, instead of 5°, thus developing motion only in the y coordiante. To replicate the results for the 3DOF model the spring stiffness presented in the Table 4 is to be halved since there are two springs in the system, further to this the initial conditions for the y coordinate will be assigned a value of 0.6m, which comprises of 0.5m which is the natural length of the spring and 0.1m which takes into account the initial conditions of the spring. Based on the derivation of the 3DOF, the y coordinate does not contain the initial length of the spring thus the initial conditions need to also account for the unstretched spring length.

The results for the 3DOF and 2DOF system are presented by Figure 48, the results can be considered identical. It can be concluded that the 2DOF model and 3DOF model develop the same solution when assigned initial conditions to the spring/s.

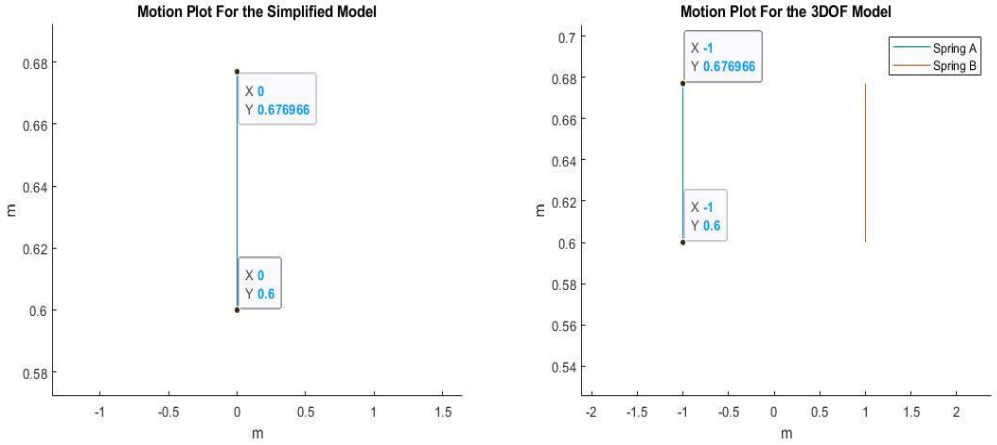

Figure 48:Comparison of the simplified model and 3DOF model with initial conditions applied to the spring/s

4.3. INITIAL CONDITIONS FOR THE "x" AND "y" COORDINATES

By inspection of the differential equations presented by 56, 57 and 58 it is expected that any initial conditions provided to x and y coordinate will have no effect on the θ component, thus that rigid bar will remain horizontal throughout the simulation. To replicate the initial conditions presented by Table 4 the x coordinate can be assigned a numerical value of 0.052293m which develops an angle (α and β) of 5o. The derived equations for the 3DOF system require the spring stiffness presented in Table 4 to be halved as done previously.

Figure 49 presents a comparison of results between the 2DOF and 3DOF system. There exists a small difference in results which can be considered negligible. Figure 50 presents the angular displacement results for the θ coordinate, there exists small amounts of motion, in the order of $\times 10^{-15}$. The motion can be considered small and can approximated to 0. The displacements

in the θ cordiante can be attributed to errors in the numerical solution, this will be discussed further in later sections.

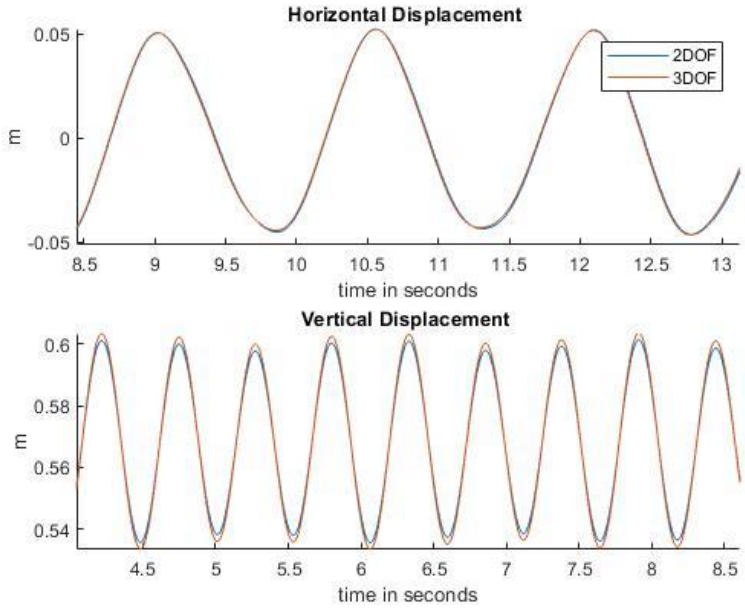

Figure 49:Comparison between the 2DOF and 3DOF system with x and y initial conditions (3DOF)

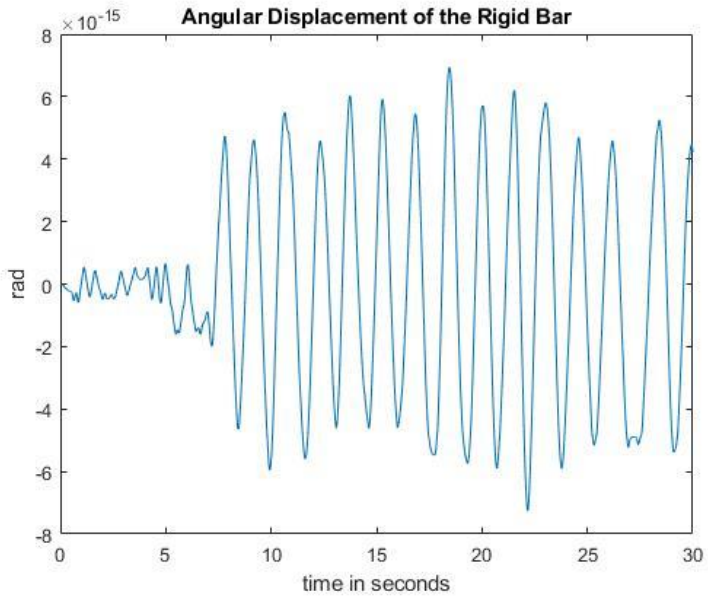

Figure 50: Angular displacements results of the rigid bar considering x and y initial conditions

Figure 51 presents the PSD results, the natural frequency of the x coordinate is 0.68Hz while the result using the analytical solution is 0.7Hz. The natural frequency of the spring system is 1.855Hz while the analytical solution is 1.89Hz. In both cases there is a small error arising.

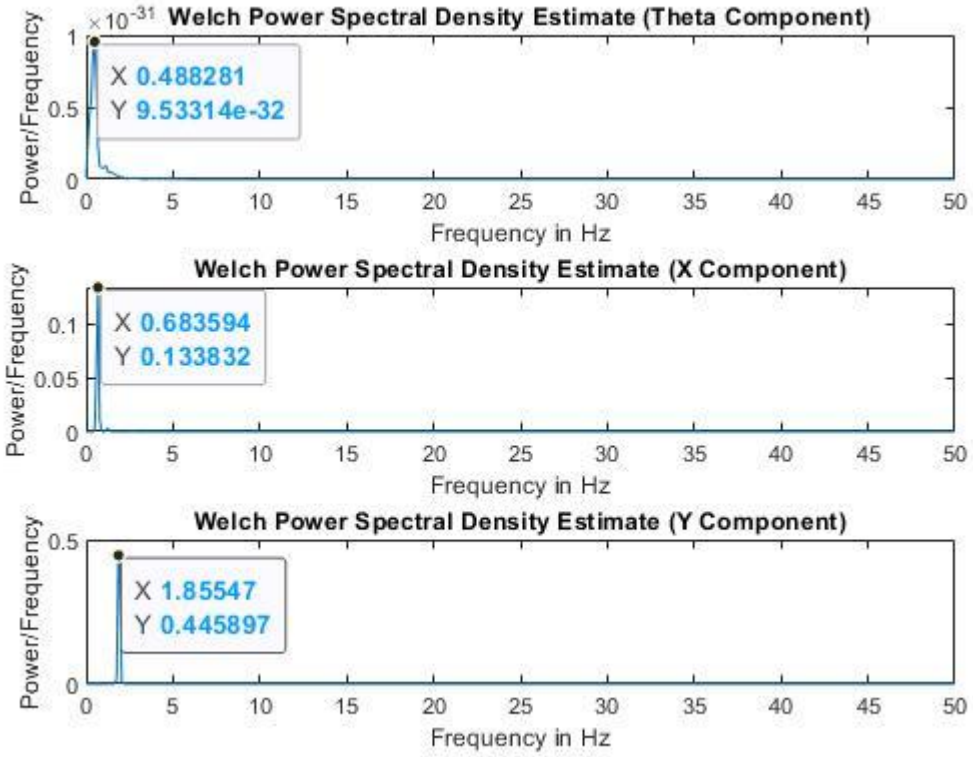

Figure 51: PSD of the 3DOF system using initial conditions for x and y

Figure 52 presents the PSD for the α and β components, the frequencies match to the x coordinate, since this coordinate is representative of the pendulum motion. This substantiates the derived methodology for the calculation of α and β.

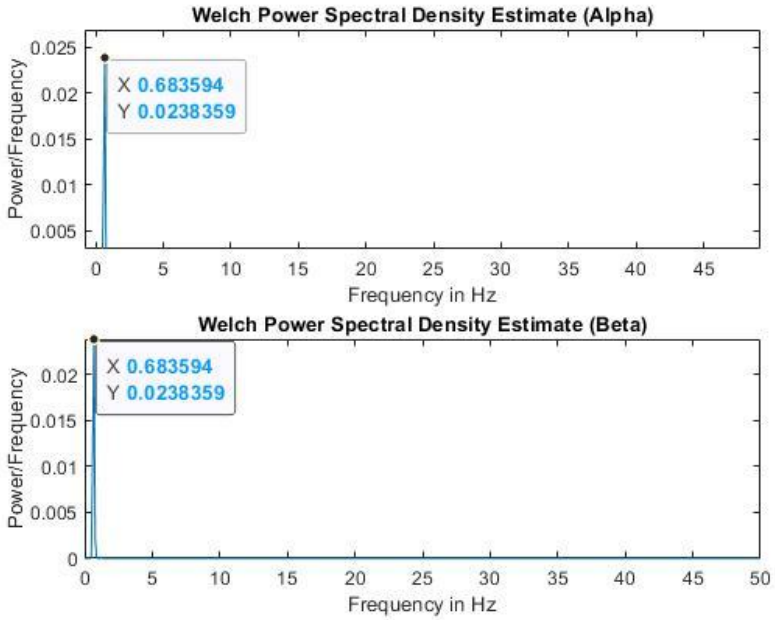

Figure 52:PSD for the alpha and beta components due to initial conditions applied to the x and y coordinates

Based on the presented results the 2DOF and 3DOF system compare well when considering initial conditions applied to the x and y (3DOF) coordinate. It can thus be concluded that the set of differential equations are comparable, thus substantiating the derivation of the 3DOF for initial conditions applied to the x and y coordinates.

4.3. INITIAL CONDITIONS FOR THE θ COORDINATE

The θ coordinate incorporates the major difference when comparing the 2DOF and 3DOF model, this coordinate allows the rigid bar to rotate about the horizontal. Table 9 presents the initial conditions used to simulate motion of the θ coordinate.

Table 9: Initial conditions to θ component

Attribute	**Numerical Value**	**Units**
Mass	3755	kg
Spring Stiffness (total)	266x2	N/mm
$x(0)$	0	m
$y(0)$, (Natural length of spring)	0.5	m
$\theta(0)$	2	degrees
L	1	m

The previous simulations for the 2DOF and 3DOF model present consistent results regardless which ode solver is implemented on Matlab. Numerical methods in Matlab consist of Runge-Kutta algorithms which are implemented on the ode45, ode23 and ode23s solvers. Multi-step algorithms are implemented on the ode113 and ode15s, these solvers can use the results from previous steps (Loren, 2015). The ode23s and ode15s solvers are better equipped to handle stiff differential equations while the other mentioned solvers work well with nonstiff differential equations (MathWorks, 2022).

Figure 53 presents the displacement results for each of the three coordinates using different ode solvers available on Matlab. It is evident that the solvers present consistency until roughly 15 seconds, thereafter the results begin to deviate. Furthermore, using smaller values of θ present higher consistency between the various solvers. The results for the θ coordinate present drift which would require the use of structure preserving methods to mitigate if one is to avoid this behaviour in the numerical solver. (Anderson, 2021). Drift can also be experienced in measurements from sensors, and can be attributed to electronic aging of components or reference standards in the sensor (Irish, 2005). During discussions with a Megatronics engineer it was concluded that signal processing techniques can also be implemented to mitigate the drift in results (Mdlazi, 2021). Butterworth filters will be used where required to correct drift in results. Matlab Code 5 presents a function which can be implemented to correct drift in results.

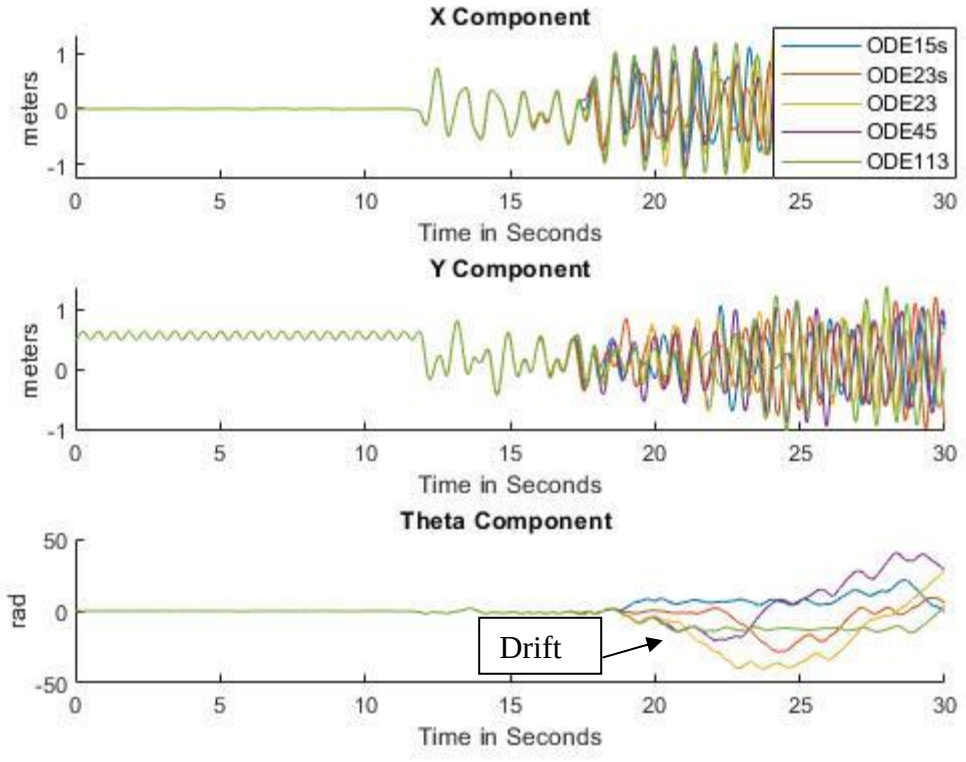

Figure 53: Displacement results using different ode solvers

The deviation of results with respect to the different solvers is suspected to be attributed to the differential equations being stiff. In literature the term stiff has been used with different meanings. The simplest and most straightforward definition is that initial value problems are stiff if they are (exceedingly) difficult to solve by ordinary explicit step-by-step methods, whereas certain implicit methods perform quite well (Spijker, 1995). An example of a stiff initial value differential equation can be described by one that has various solutions that vary on drastically different time scales (MathWorks, 1994-2021), this is evident by the introduction of the θ component. It should be noted that Mike Hosea a developer at Matlab stated that, "Some methods can integrate farther than others before failing, but all numerical initial value solvers will stray from the correct mathematical solution curve eventually" (MathWorks, n.d.).

By reviewing literature presented by (Shampine, et al., 2003) it is found that the inconsistent results may also be developed by the presence of inhomogeneous terms in the derivatives. The inhomogeneous terms can be defined as terms which are not derivatives or functions in the variable used in the derivative.

If the inconsistencies in results are due to the differential equations being stiff, the inconsistencies should not arise during simulations where there are no initial values. If the inconsistencies continue to exist without initial values, it will then present strong evidence that the inconsistencies are developed because of the inhomogeneous terms. This will be reviewed again when studying the 3DOF being subjected to harmonic excitation.

Mathematica is a technical computing language which presents similar functionality as Matlab using a slightly different coding philosophy. Mathematica Code 1 can be used to solve the 3DOF system using the initial conditions presented in Table 9. The code presents the same set of equations presented by Matlab Code 6. The code uses three different numerical methods to

develop the solution, it should be noted that the third method "Mathematica Optimised" allows Mathematica to decide on an appropriate solver/s, the solving methodology can also change midway through a simulation.

The results for the above-mentioned analysis are presented by Figure 54. The "Mathematica optimised" and Adams method have produced the same results, however the Explicit Euler method deviates. Drift has also been found in the results pertaining to the θ coordinate. There also exists a perturbation in the results pertaining to the y coordinate (label A), this is the point in time where the x and θ coordinate begin to present significant displacements. The results for the Adams method and "Mathematica optimised" present the same solution with the perturbation occurring at the same time point. When considering other solving schemes on Mathematica, poor results are produced with errors pertaining to stiff equations being presented.

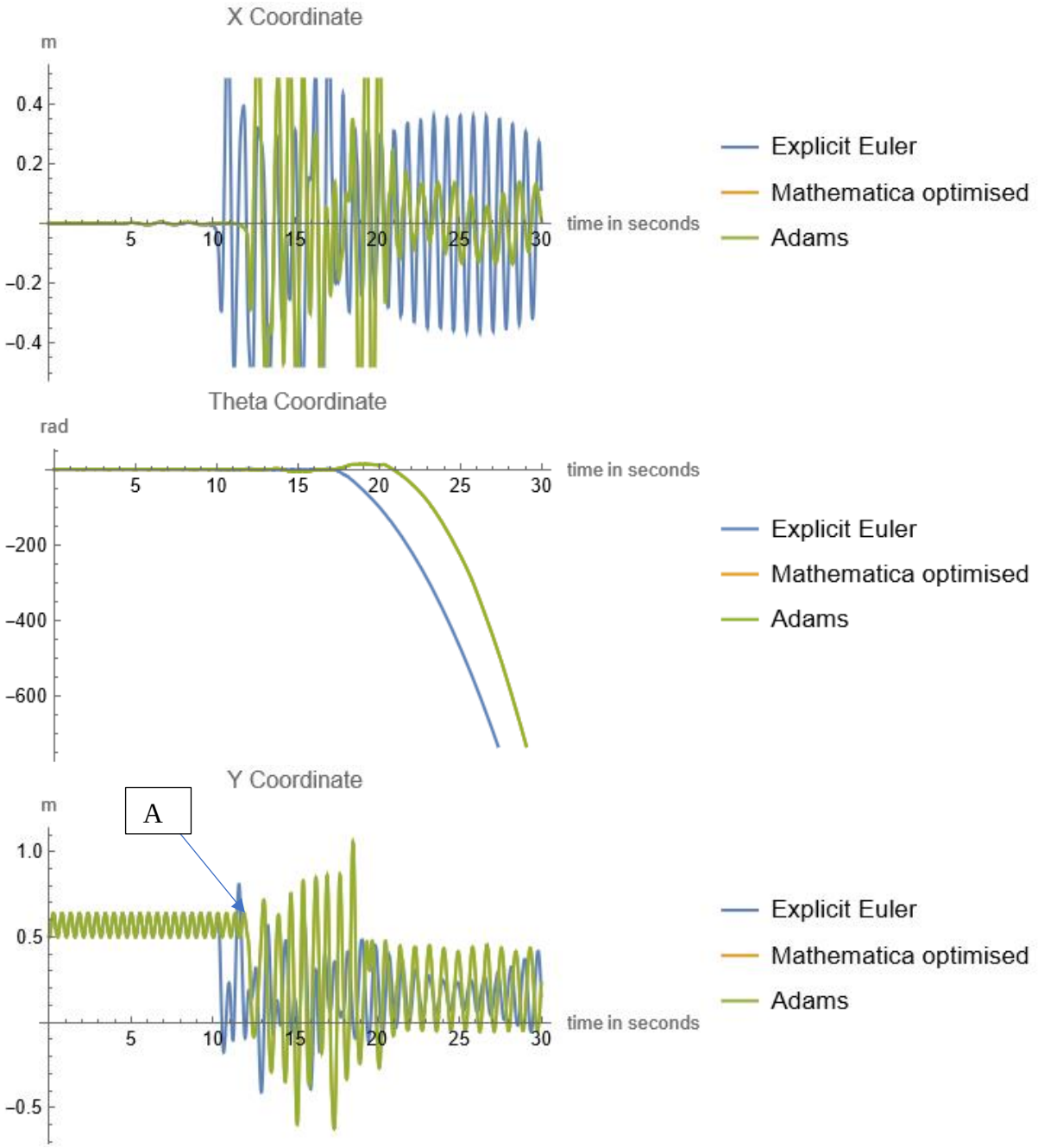

Figure 54: Displacement results for the 3DOF system using various solvers on Mathematica and attributes presented by Table 9

Mathematica also struggles to develop accurate results for the differential equations. If one considers a time interval of 10 seconds, this provides accurate data for one to study the system. The system will be studied using a smaller time interval on Matlab.

Figure 55 presents the angular displacements and accelerations for the θ coordinate. The motion of the rigid bar is sinusoidal, with small changes in results, however the acceleration results are interesting as they present varying amplitudes. The acceleration results present a repetitive shape which consists of a large peak and two smaller peaks on either side of the larger peak. The large peak can be defined by "A" while the smaller peaks can be defined by "B".

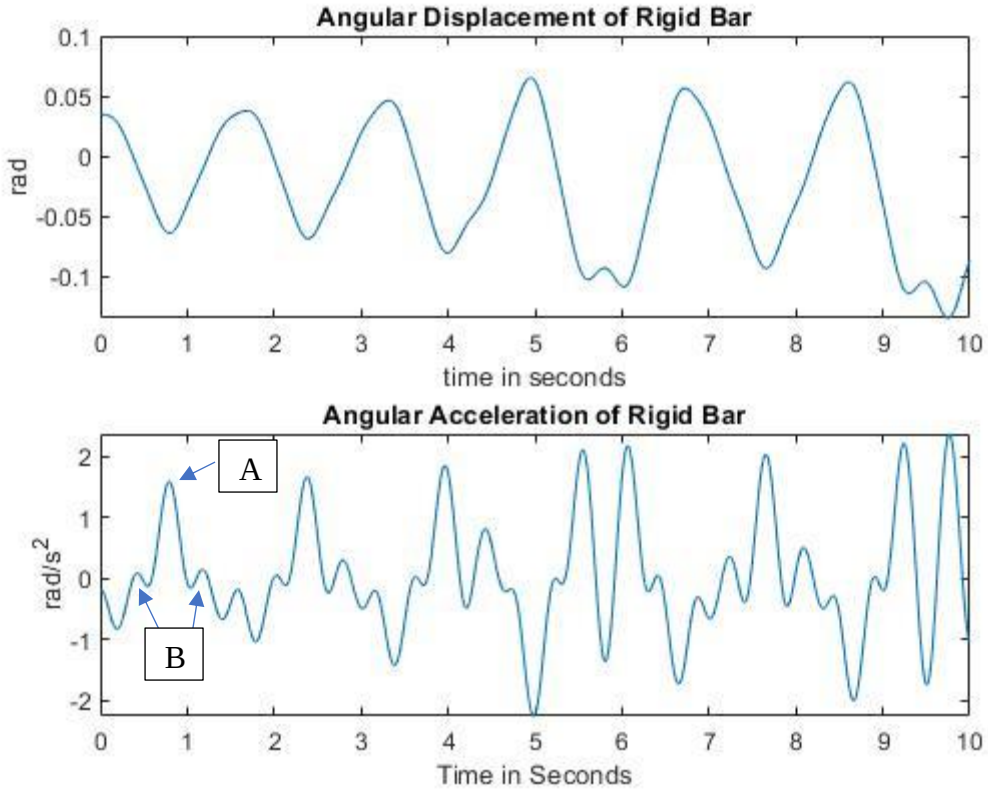

Figure 55: Angular displacement and accelerations of the rigid bar using initial conditions presented in Table 9

Figure 56 presents the displacement and accelerations results for the x and y coordinates. The displacement and acceleration for the y coordinate presents undisturbed sinusoidal results, implying that the results are undisturbed by the motion of the other coordinates. The displacements for the x coordinate are also sinusoidal however the peaks are continuously increasing, the increase can be attributed to the influence that the θ coordinate has on the x coordinate, thus implying that there exists energy transfer between the coordinates.

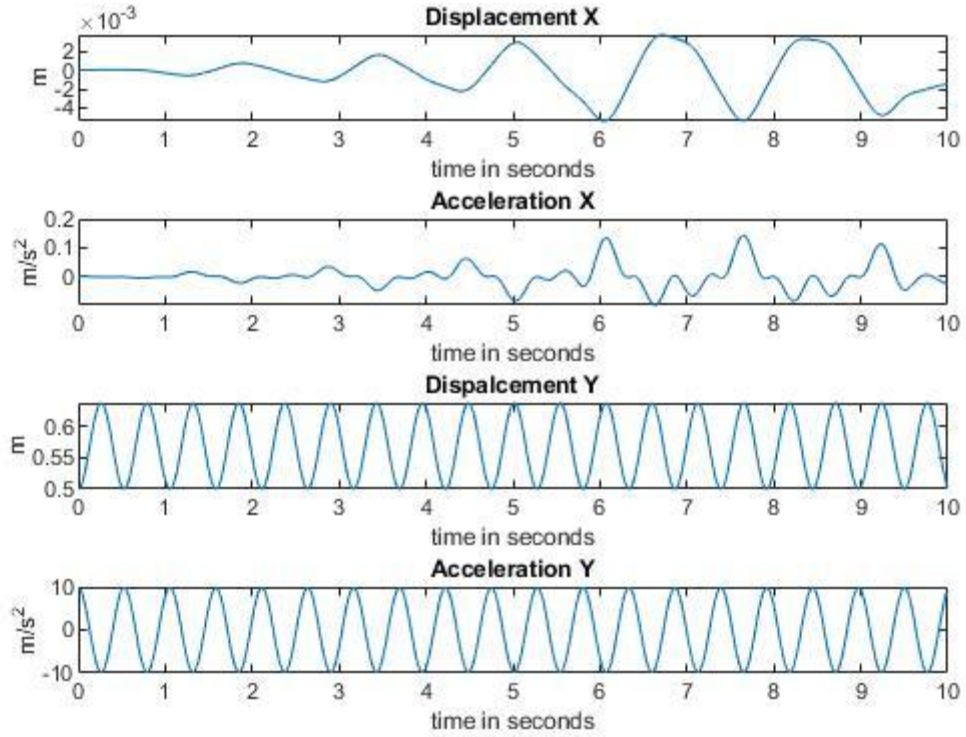

Figure 56:Displacement and acceleration results for the X and Y coordinate for initial conditions presented in Table 9

To further understand the system, the acceleration and displacement results will be normalised and plotted as presented by Figure 57 and Figure 58. The x coordinate at certain time intervals roughly traces the θ coordinate, furthermore the x coordinate is initially out of phase with the θ coordinate. When large displacements are experienced the x and θ coordinate are in phase. Unfortunately, only a small-time interval of results can be accurately simulated, however it is suspected that the x and θ coordinate will continuously move in and out of phase with each other. Based on the results there is a transfer of energy from the θ coordinate to the x coordinate.

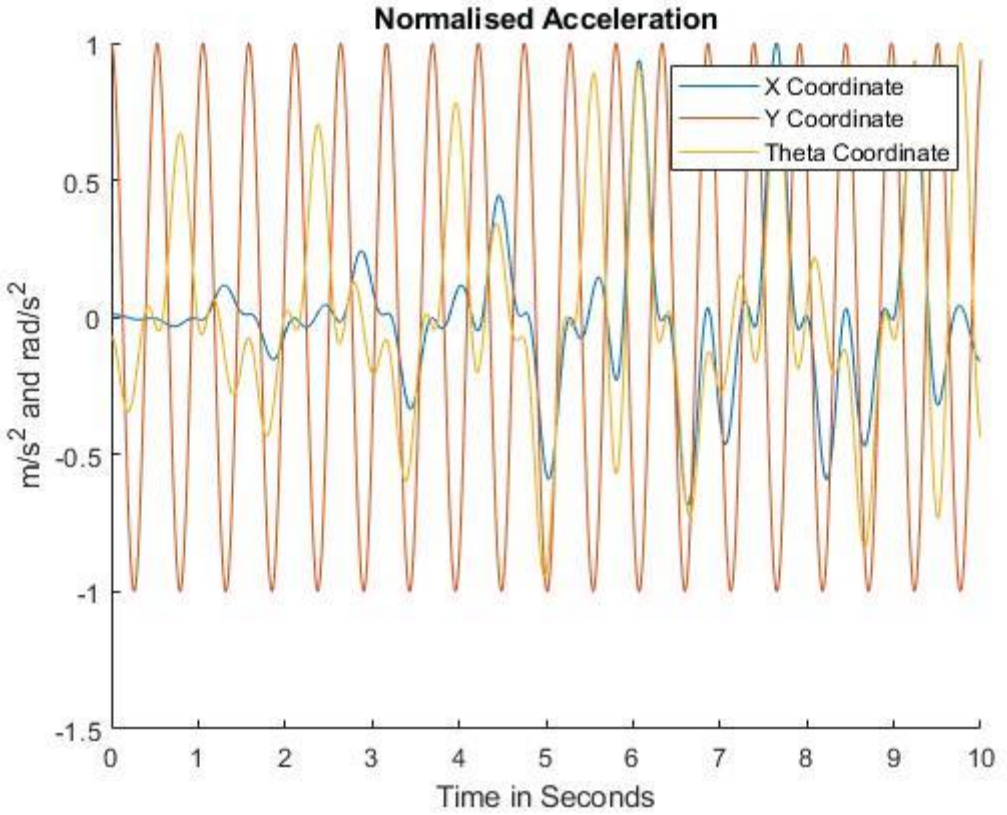

Figure 57: Normalised acceleration results for initial conditions presented by Table 9

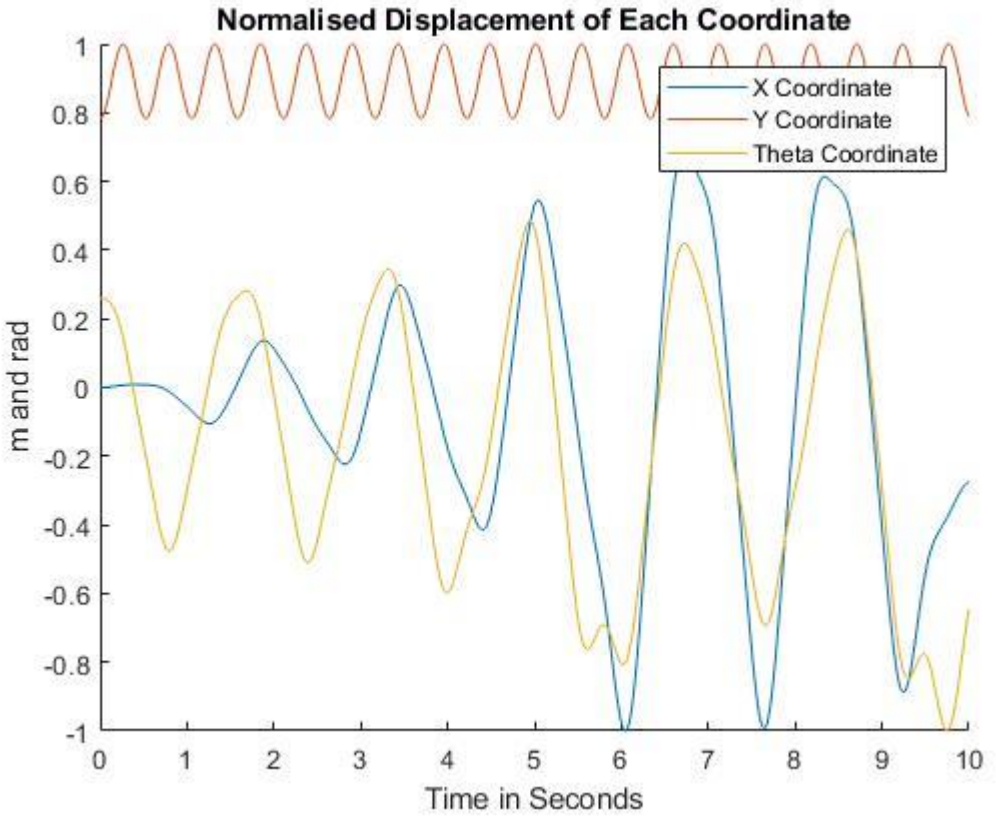

Figure 58: Normalised displacement results for attributes presented in Table 9

Figure 59 presents the numerical values for *63* and *64*, which are taken from the set of differential equations describing the x and y coordinate accelerations respectfully.

$$Term\ A = \left(\frac{L\cos\theta}{2\sqrt{A}}\right) \quad 63$$

$$Term\ B = \left(\frac{L\sin\theta}{2\sqrt{B}}\right) \quad 64$$

It is clear that "Term A" has a higher influence on the system when compared to "Term B" (based on the larger numerical values) implying that the x coordinate is far more aggressively affected by the θ coordinate compared to the y coordinate which is established earlier.

It is also clear that "Term A" and "Term B" present different frequencies through inspection of the results. The $\sqrt{A}$ and $\sqrt{B}$ terms present small values (Figure 60), which for the given case are always less than 0.8. Thus, if one considers $\frac{1}{\sqrt{A\ or\ B}}$, the solution will always develop numerical values greater than 1, since $\sqrt{A}$ and $\sqrt{B}$ produce numerical values less than 1. The $\cos\theta$ term develops larger values when compared to the $\sin\theta$ term, this is substantiated by the fact that there are small angular displacements being experienced for θ, implying that $\cos\theta \approx 1$ for all values of θ. This can clearly be seen if one reviews Figure 60. Coupling the effects of all above-mentioned terms allows one to understand how the coordinates interact with each other and further substantiates the energy transfer from θ to x.

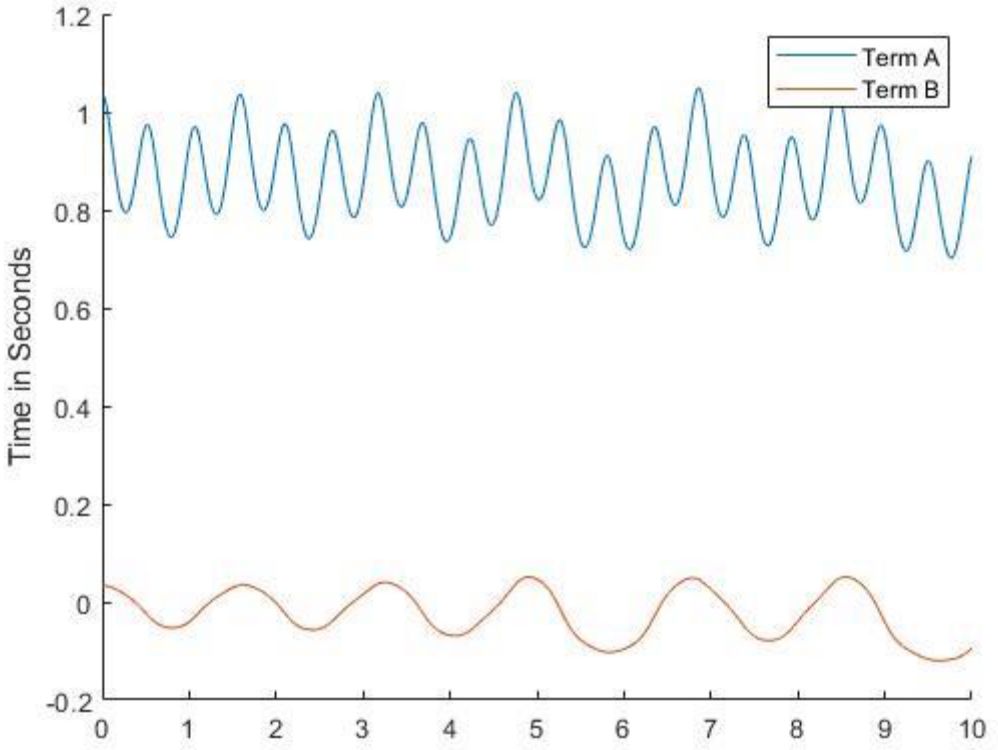

Figure 59: Plotting numerical values of Term A and B from the differential equations using attributes presented in Table 9

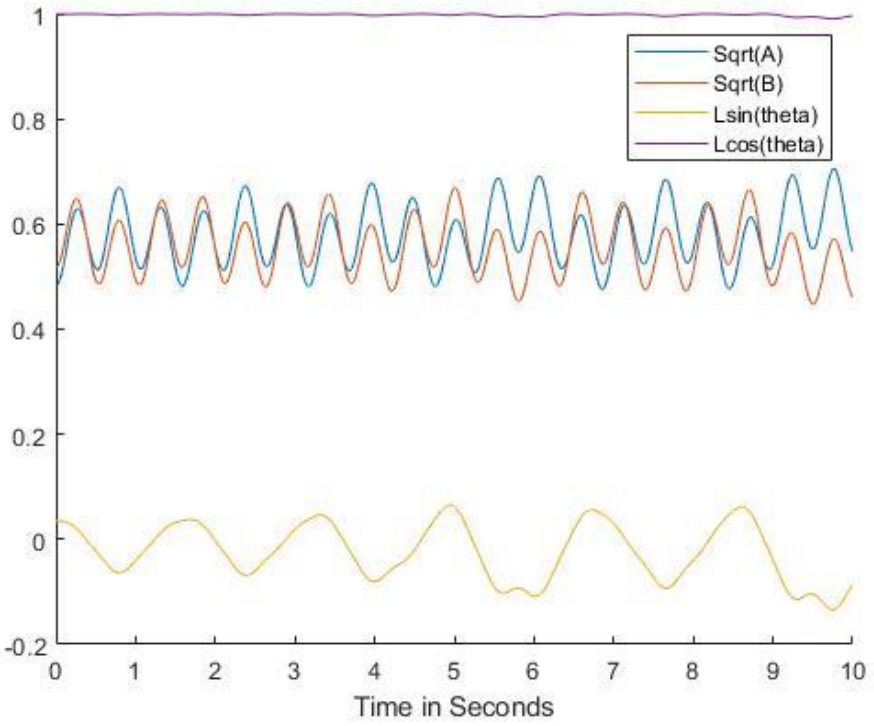

Figure 60: Various components of equations 63 and 64 using attributes presented in Table 9

Figure 61 presents the FFT results for each coordinate. The following can be noted:

- The y coordinate presents the natural frequency of only the spring arrangement. It is thought that the high stiffness of the spring arrangement may prevent the other coordinates from interacting with the y coordinate. The single frequency presented by the y coordinate is also substantiated by the acceleration results which present a system not interacting with any other coordinates.
- The x coordinate presents the pendulum frequency; the analytical value is 0.7Hz however the FFT has produced a value of 0.6Hz. The spring frequency can also be found however the energy is small. There exist sideband frequencies for the spring frequency which are 0.6Hz away from the spring frequency resulting in 1.3Hz and 2.5Hz respectfully. This indicates that the spring frequency is the carrier frequency when considering the x coordinate.
- The θ coordinate presents the same results as the x coordinate, with the exception that the spring frequency is more pronounced, thus indicating that there is more energy contributed from the spring compared to the x coordinate.

The FFT supports the initial discussions regarding the transfer of energy from θ to x. Since there are shared frequencies between the x and θ coordinate it is clear that there exists interaction between the systems as presented by the acceleration and displacement results. It should also be noted that the θ coordinate presents the spring frequency thus implying that the coordinate is affected by the spring also, this makes sense since the displacement of the springs would directly affect the behaviour of the θ coordinate. This can be seen if one reviews the results presented by Figure 62, the initial conditions for the θ coordinate present opposing results for the elongation/contraction of the springs as presented at $t = 0$.

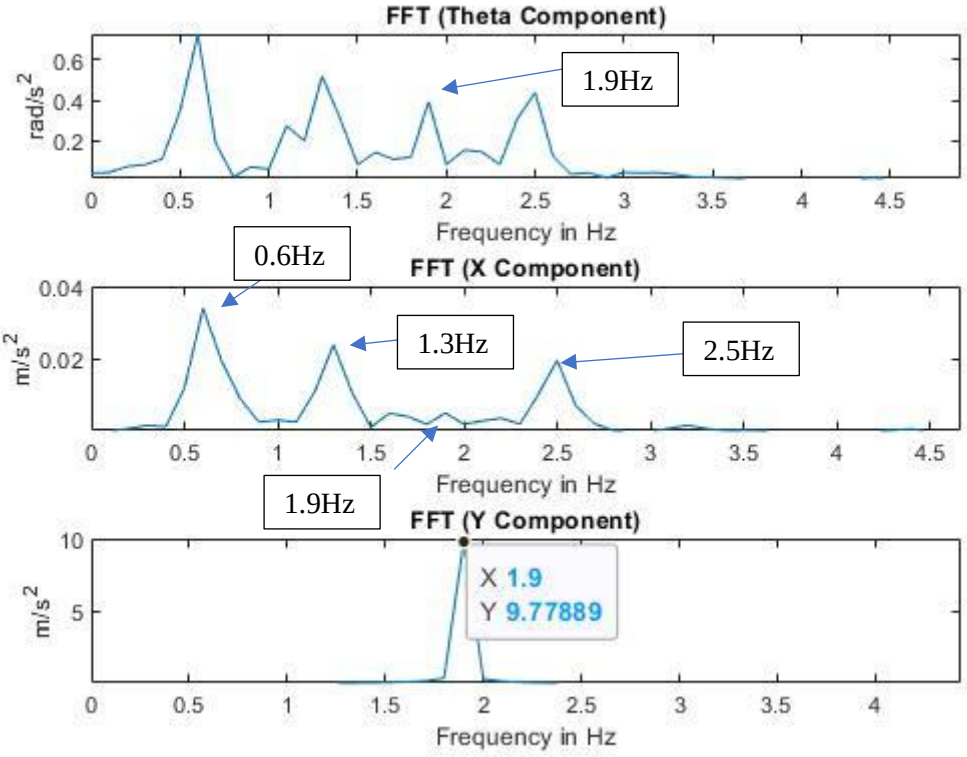

Figure 61: FFT results for each coordinate using attributes presented in Table 9

Figure 62 presents the resultant acceleration in each spring and the elongation/contraction experienced in each spring. The resultant acceleration is in the region of 10m/s^2, with each spring experiencing a slightly different acceleration. The elongation/contraction in the spring presents results which imply that for the most part the springs have elongated with only a small amount of contraction occurring. Both springs have different elongation/contraction and thus the results imply a system where the rigid bar has non zero values of θ which is expected from the results previously discussed.

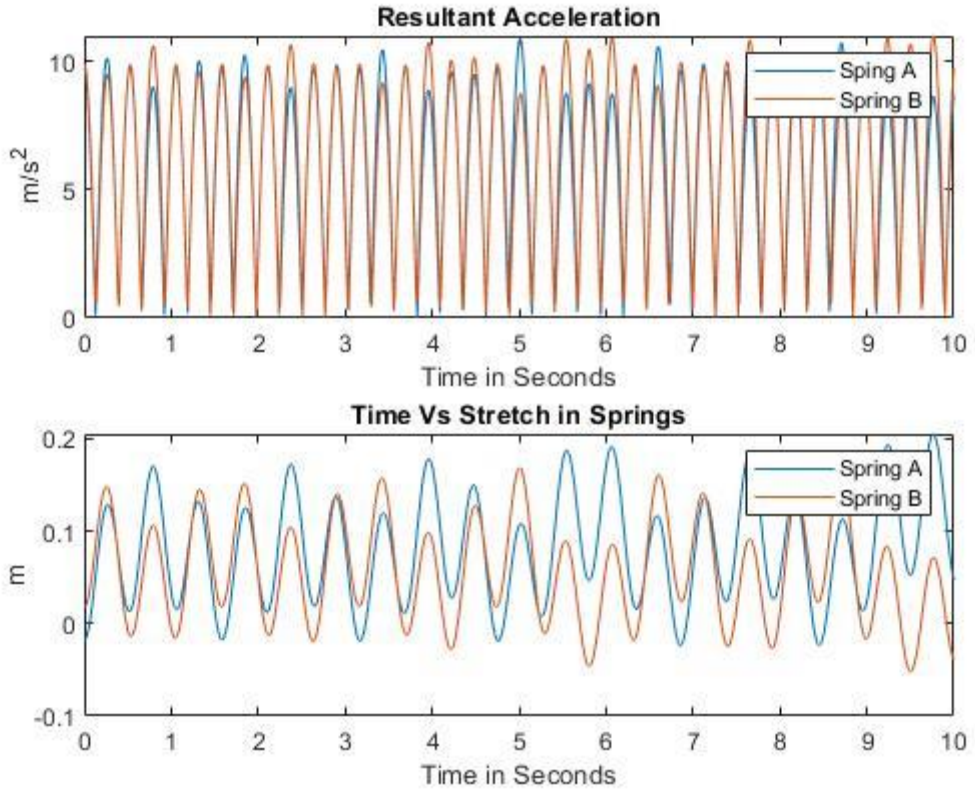

Figure 62: Resultant acceleration and stretch in springs for attributes presented in Table 9

Figure 63 presents the PSD for the elongation/contraction in the springs. The first frequency is 0.58Hz which is representative of the pendulum motion and the second frequency is 1.855Hz which is representative of the spring arrangement. The existence of the two frequencies is logical since both these motions ultimately affect how the springs elongation/contraction. The angular motion develops centripetal forces which elongate the spring and the gravity component also allows the spring to oscillate.

The angular displacements of α and β present different values throughout the simulation. At the start of the simulation the values of α and β oppose each other, which is expected since the initial conditions present a case where the one spring will be pulled towards the centre of the rigid bar while the other spring will be pulled away from the rigid bar. The angular displacements also present large displacements when they are in phase with each other.

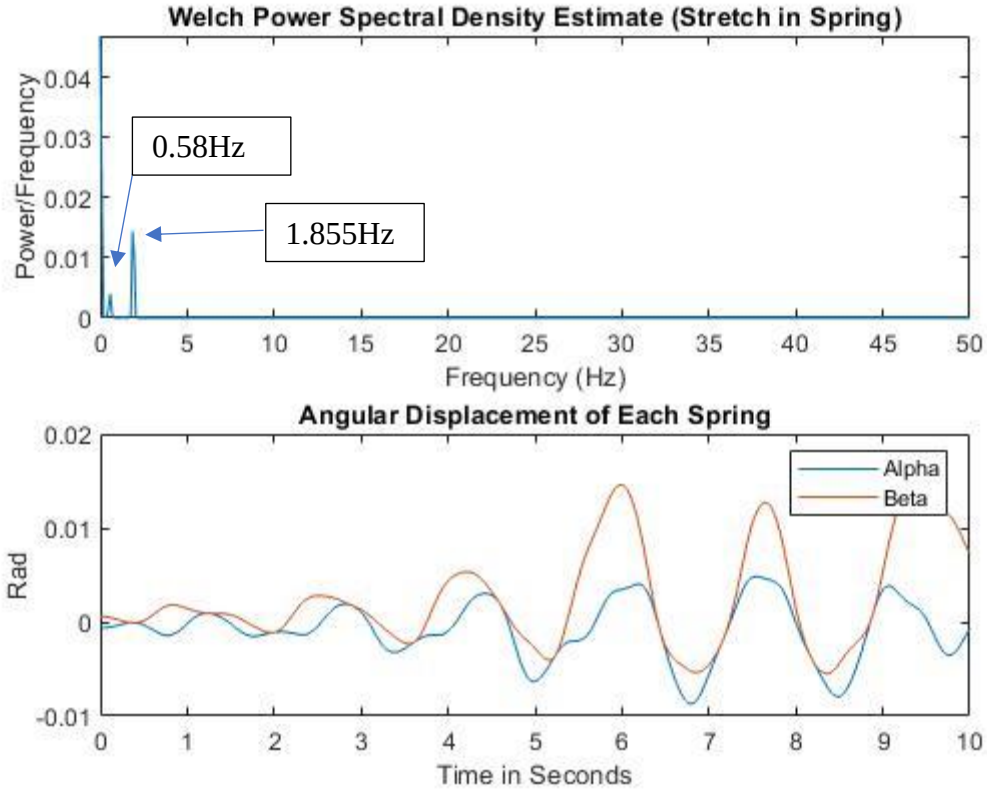

Figure 63: PSD for the stretch in the springs and angular displacements of springs, attributes from Table 9

4.4. PARAMETRIC RESONANCE AND INITIAL CONDITIONS FOR THE θ COORDINATE

The 3DOF system will be studied using the attributes presented in Table 5, with only initial conditions assigned to the θ coordinate, the numerical value will be 2 degrees. Furthermore L will be set to a numerical value of 2 meters. Figure 64 presents the displacement results for each coordinate, all solvers have produced the same results.

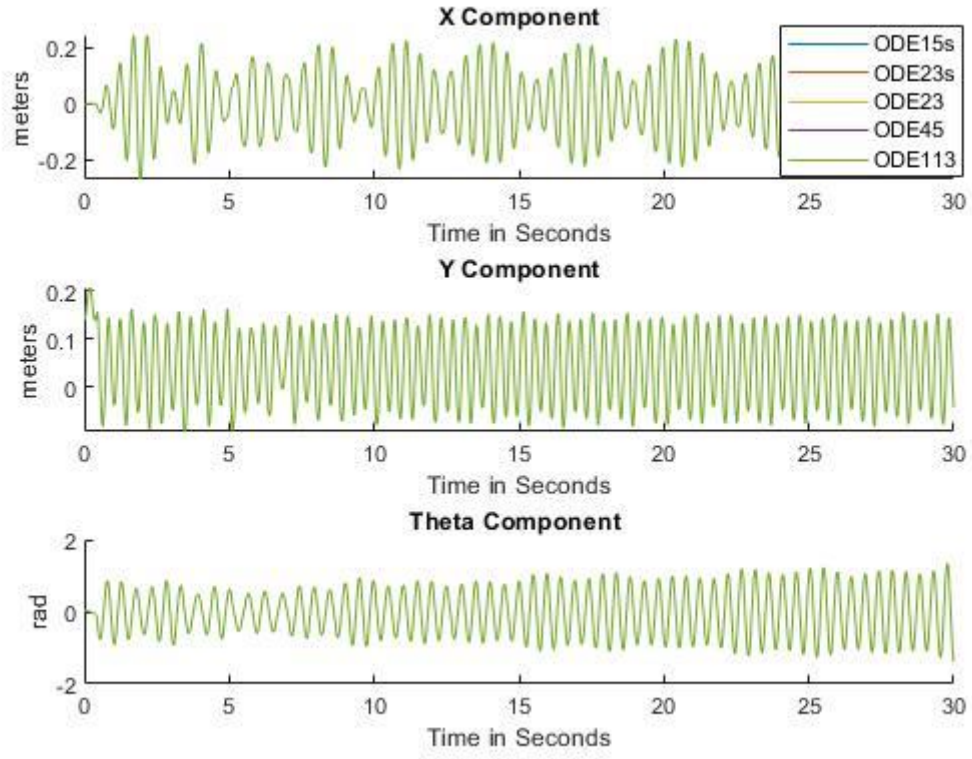

Figure 64: Comparison of different Matlab solvers using attributes from Table 5 and initial conditions for θ

The results presented by Figure 64 clearly present autoparametric behaviour, to understand the system in further detail the displacement results will be normalised and thereafter plotted on the same axis. The normalised displacement results for the x coordinate will be left as is, while the normalised results for the y and θ will be offset by 2 meters and 4 radians respectfully. The resulting plot is presented by Figure 65 and Figure 66, both plots present the same information however Figure 66 presents various markers at time points of interest. The following observations can be concluded:

- The energy transfer to the x coordinate occurs over longer time intervals compared to the other coordinates, with the θ coordinate having the second longest time intervals.
- The y coordinate presents very small periods where energy is transferred to the coordinate. The energy transfer to the coordinate exists over a single period, while the coordinate transfers energy for 2 periods thereafter (there does exist deviations from the 2 periods at various locations).
- At time point A, the x and y coordinates are in phase with each other with the θ coordinate being slightly out of phase. The x coordinate transfers energy to the y coordinate.

- At time point B, the y and θ coordinate are in phase with each other with the x coordinate being slightly out of phase with the other coordinates. The x and y coordinates transfer energy to the θ coordinate.
- At time point C, the x and y coordinates are in phase with each other, the θ coordinate being slightly out of phase from the other coordinates. There is clear energy transfer to both the x and y coordinates. The x coordinate is at its peak energy for the period during which energy transfer occurs and this would explain the θ coordinate being out of phase as this is indicative of the decrease in energy which exists after the peak experienced in the x coordinate. The θ coordinate is responsible for energy transfer to the other coordinates.
- Time point D, presents a similar case to C, however the time point is just after the peak in the x coordinate. The y and θ coordinates are now in phase with each other with energy transfer from y to θ. It should be noted that the same behaviour is found just after the time point presented by C.

The process of energy transfer is complex with each coordinate presenting complex interactions of energy transfer between each other. The clear trend is the energy transfer between the x and θ which is the most evident when reviewing the results. When all the coordinates are in phase energy is transferred to the θ coordinate. The points in time where peak energy exists for the y coordinate never coincide with peaks from the θ coordinate however they do coincide with peaks from the x coordinate.

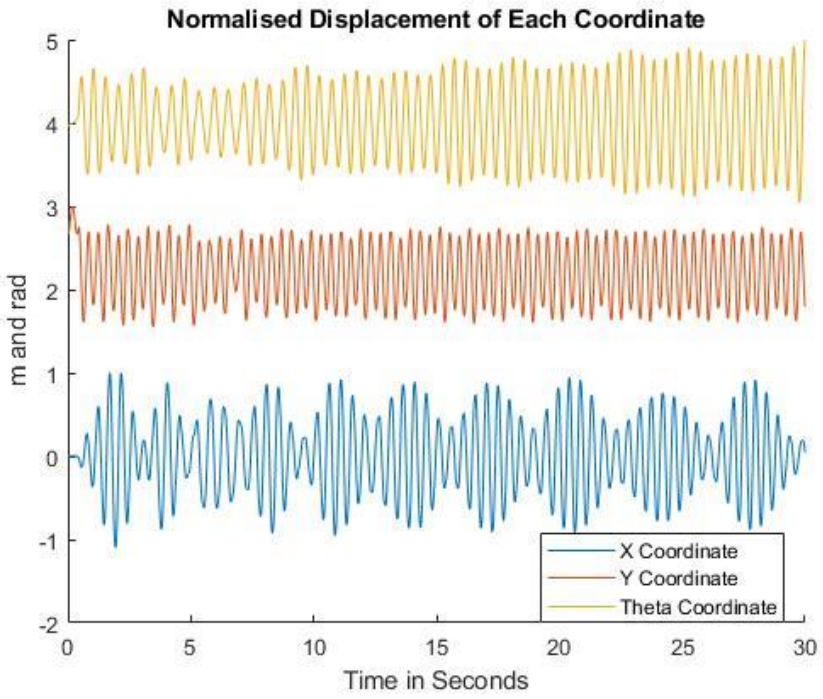

Figure 65: Offset normalised displacements using attributes from Table 5 and initial conditions for θ

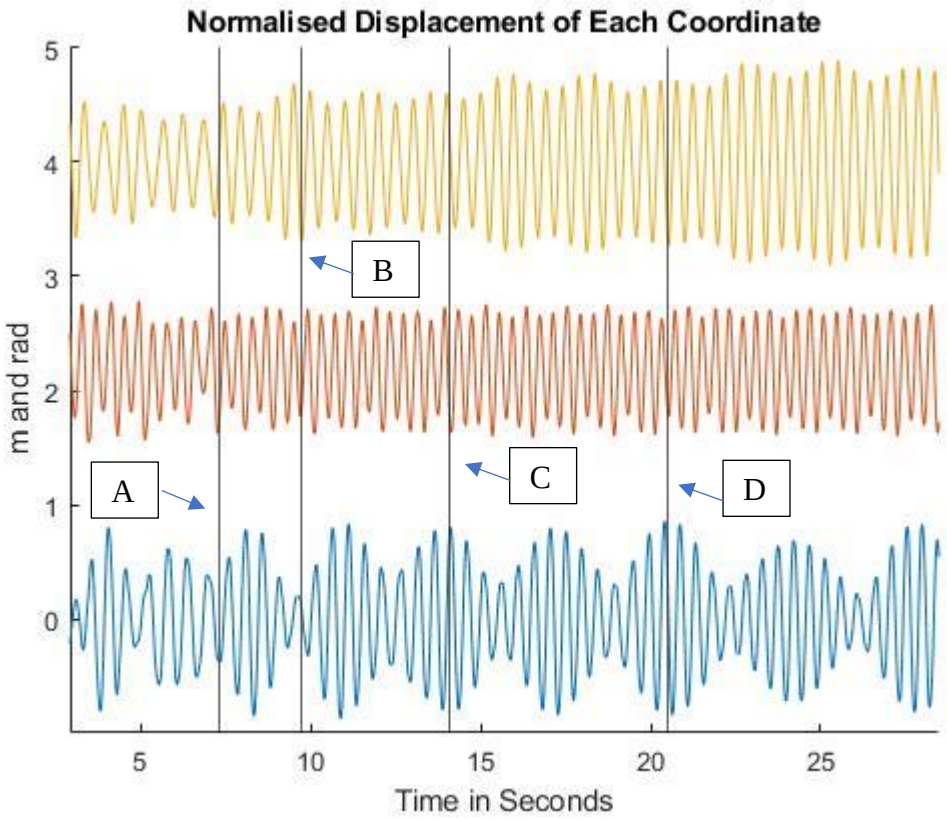

Figure 66: Normalised displacement results with markers for attributes from Table 5 and initial conditions for θ

Figure 67 presents the acceleration results for each coordinate. The most striking aspect of the results is the sudden perturbations which occur for each coordinate. These perturbations do present themselves in the displacement results, however the effects are far less pronounced and consist of a slight change in the gradient of the curve. From 0 to roughly 0.4 seconds the acceleration results for the x and θ coordinate present extremely small values while the y coordinate presents sinusoidal results (the system moving vertically up and down). The acceleration results for the θ coordinate present similarities when compared to the results attained by Figure 55, the similarities consist of the general profile of the acceleration results, which consist of a peak with smaller peaks existing on each side of the peak. The parametrically sized setup presents sharper peaks which indicate far more sporadic accelerations compared to the case which does not experience parametric resonance.

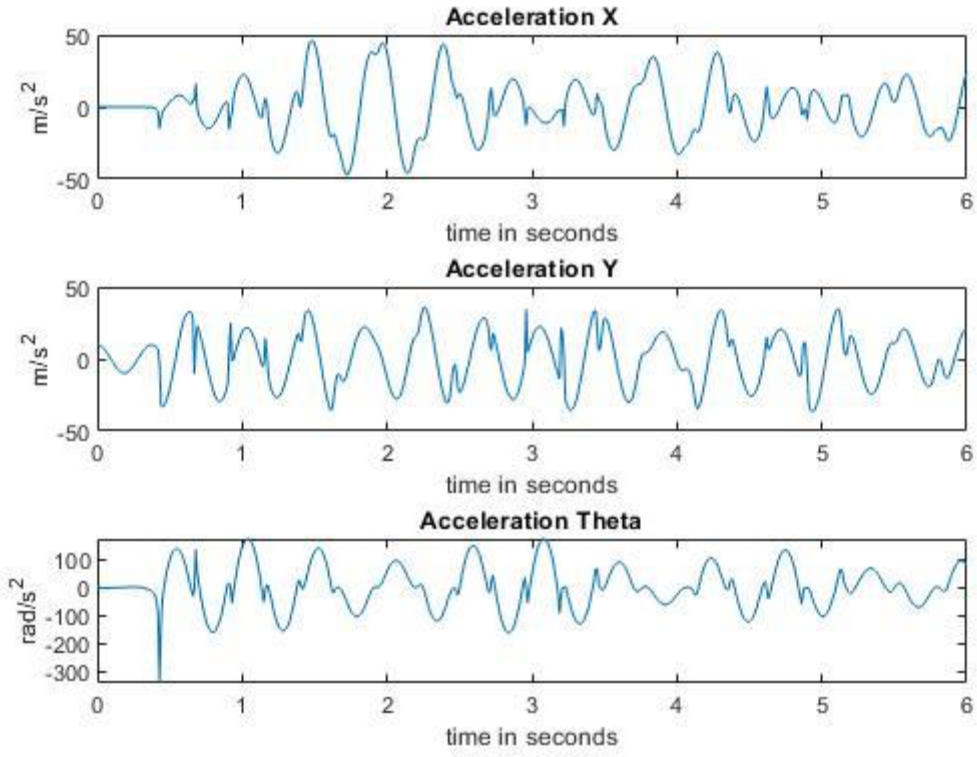

Figure 67: Acceleration results for each coordinate using attributes from Table 5 (3DOF)

To study the acceleration results in further detail the results will be plot on a single axis allowing one to understand how they interact with each other, this plot is presented by Figure 68. Each coordinate experiences abrupt perturbations at the same point in time. The θ coordinate is the only coordinate which presents undisturbed peaks. The acceleration results also present the coordinates moving in and out of phase with each other as discussed with displacement results, the results are however far more difficult to interpret due to the perturbations.

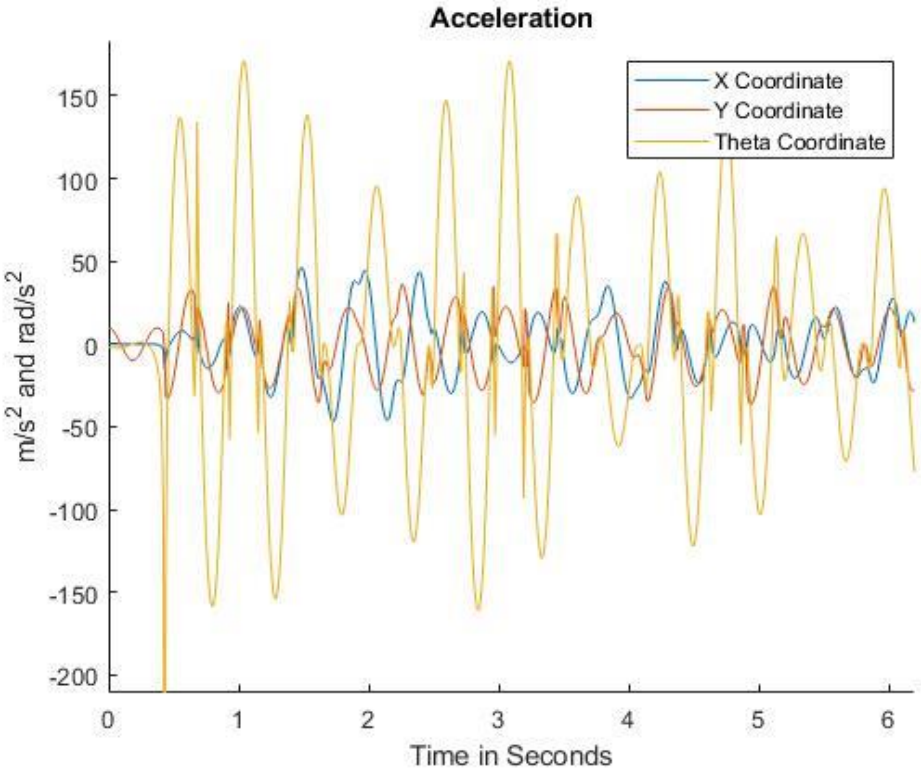

Figure 68: Acceleration results for each coordinate using attributes presented by Table 5 (3DOF)

Following the previous procedure, "Term A" and "B" have been plotted and presented by Figure 69 with the various components making up the terms being presented by Figure 70. "Term A" presents large numerical values which were not presented in the previous simulation. The large numerical values can be attributed to the model being setup for parametric resonance. The x coordinate is far more aggressively affected by θ compared to the y coordinate, which correlates well with the energy transfer to the x coordinate being more pronounced compared to the other coordinates. $\sqrt{A}$ and $\sqrt{B}$ present values which are similar and range between 0 and 1. Based on the angular displacement results the numerical values for θ are large enough such that $\sin\theta$ can now develop values which are far greater than 0. It can thus be concluded that the θ coordinate has a greater influence on the y coordinate when the system is parametrically setup.

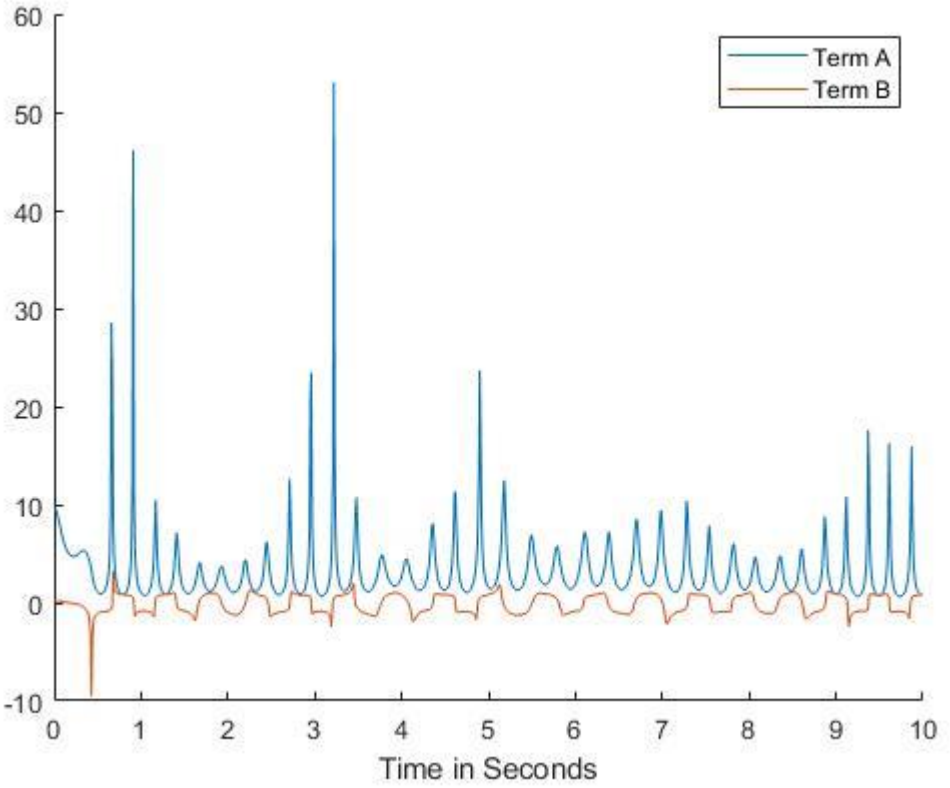

Figure 69: Term A and B for a parametrically sized system using attributes presented by Table 5 (3DOF)

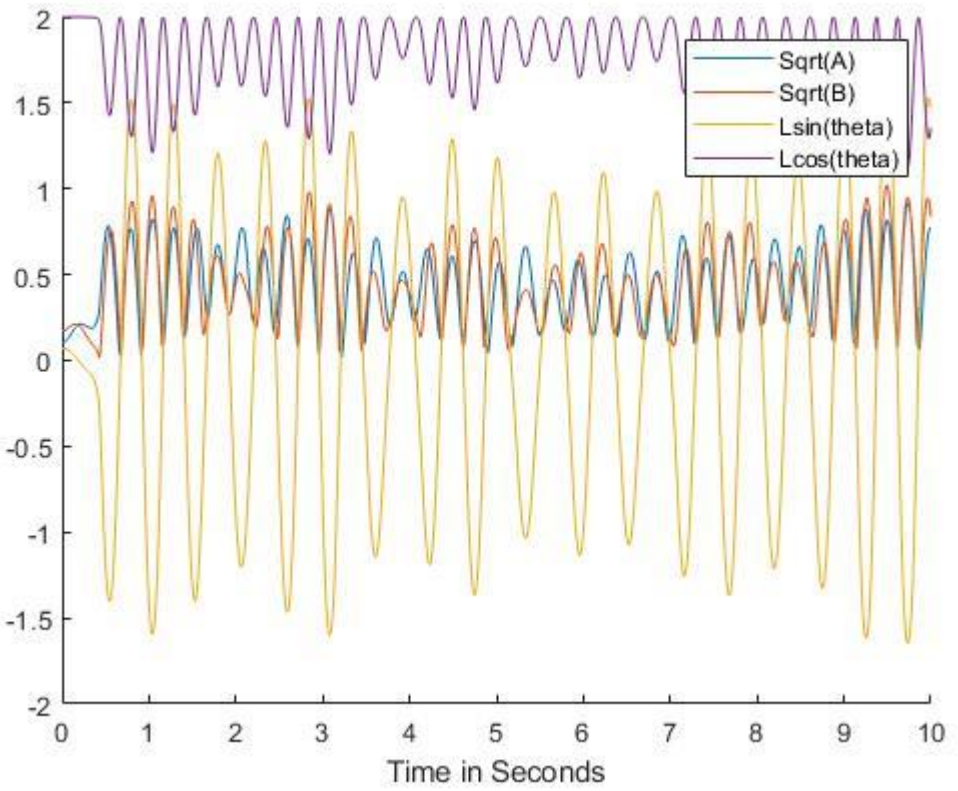

Figure 70: Various components of Term A and B for results presented by Figure 71

APPENDIX C – RESULTS FOR THE 3DOF PARAMETRICALLY SIZED MODEL presents the above figures which have been zoomed and with data points being labelled. The following observations can be made:

- At 0.43 seconds there exists a peak for "Term B", this peak has no effect on the y coordinate, however it does present a peak for the x and θ coordinates. This may imply that the y coordinate has transferred energy to the other coordinates. This time point is indicative of when the other coordinates begin to experience significant motion and acceleration.
- The peaks for "Term A" and "Term "B" do not exist at the exact same time interval. Each peak for "Term A" and "Term B" corresponds to a peak in the displacement and acceleration results and another peak at approximately the average time of peaks at "Term A" and "Term B" (this refers to peaks which are close to each other).
- The smaller peaks presented by "Term A" correspond to points in time where there is high energy transfer to the x coordinate, as presented by location "A" in Figure 64.
- The abrupt changes in the accelerations (also identified by the peaks of "Term A" and "Term B") generally occur at points in time which are close to or at the peak velocities.
- $\sqrt{A}$ and $\sqrt{B}$ present behaviour where the numerical values move in and out of phase with each other. When the values are in phase it corresponds to times where there is large energy transfer to the x coordinate. When out of phase it is also representative of time periods where energy is reducing in the x coordinate.

Figure 72 presents the PSD results for the simulation. The x and θ coordinate present the same frequency which is indicative of the pendulum motion (2.05Hz), this frequency is off from the analytical value of 1.34Hz. The y coordinate presents a 2.53Hz frequency which is representative of the spring natural frequency, this frequency is close to the analytical value of 2.68Hz. The x and θ coordinate present side band frequencies which are 0.29Hz away from their natural frequency. The side band frequencies for the x coordinates do not present the same energy as expected from literature. The sideband frequencies may be occurring due to the perturbations of variable amplitudes which are found in the acceleration results (Alsalaet, 2020)

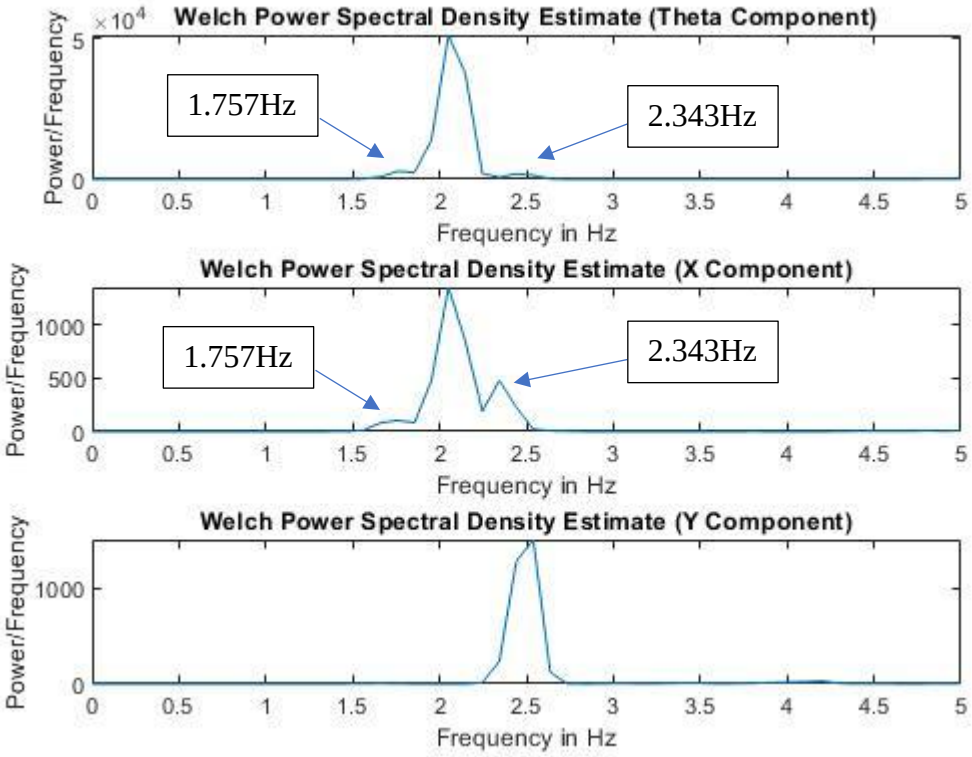

Figure 72: PSD for the parametric resonant 3DOF system

Figure 73 presents the resultant accelerations and the elongation/contraction for each spring. It is clear from the results that parametric resonance is experienced, this however it not as apparent when reviewing the displacement results for the y coordinate. As per the previous results it is clear the springs are predominantly elongated with each spring have opposing initial conditions which are indicative of the initial conditions. The resultant accelerations are large, in the order of $+150 m/s^2$ which is far higher when compared to the acceleration results presented by the SD18/36.

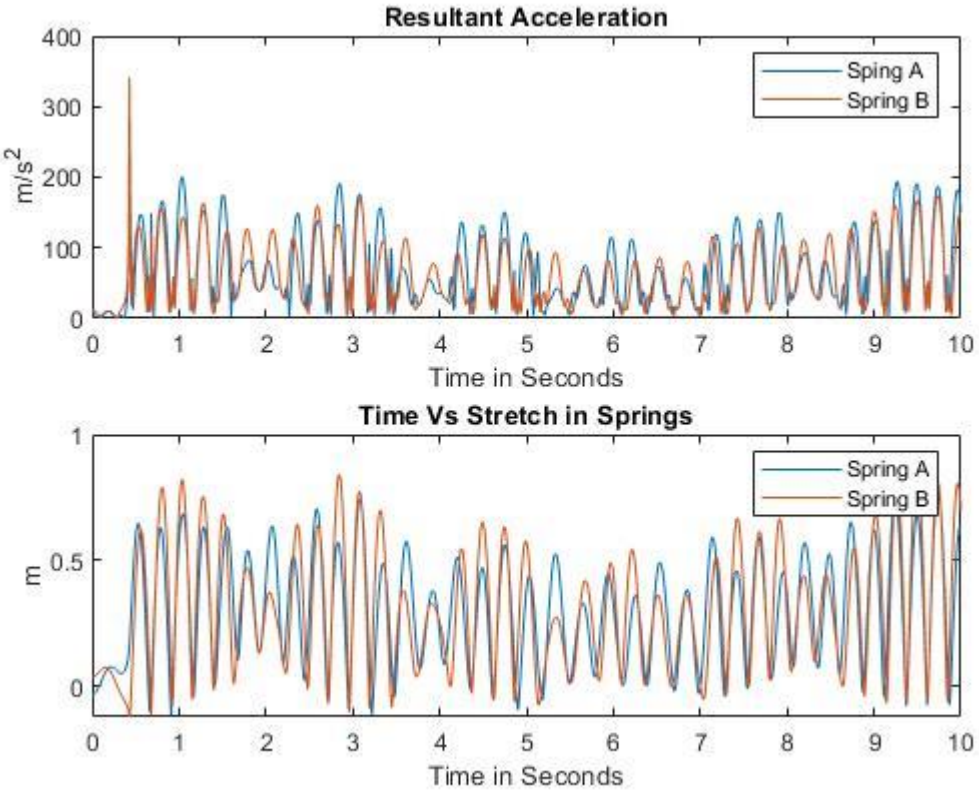

Figure 73: Resultant acceleration and stretch for each spring using attributes from Table 5

Figure 74 presents the angular displacement for each spring and the θ coordinate. The shape of the motion presents similar results as the acceleration results, where there exists a large peak and two smaller peaks on either side. The peak displacements occur at roughly the same time points as the abrupt changes found in the acceleration results. The peaks either occur in close succession at the same point in time. The results allow us to understand the motion of the system in greater detail:

- The peak values for the θ coordinate tie up with the smaller peaks (adjacent to the prominent peaks). It is thus clear that for peaks in the θ coordinate, the angular displacements for each spring oppose each other.
- When the θ coordinate has a 0 displacement the angular displacement for each spring is in the same direction and presents a peak value. This implies that the rigid bar is horizontal and there exists displacement in the x coordinate thus allows each spring to present the same angular displacement and direction.

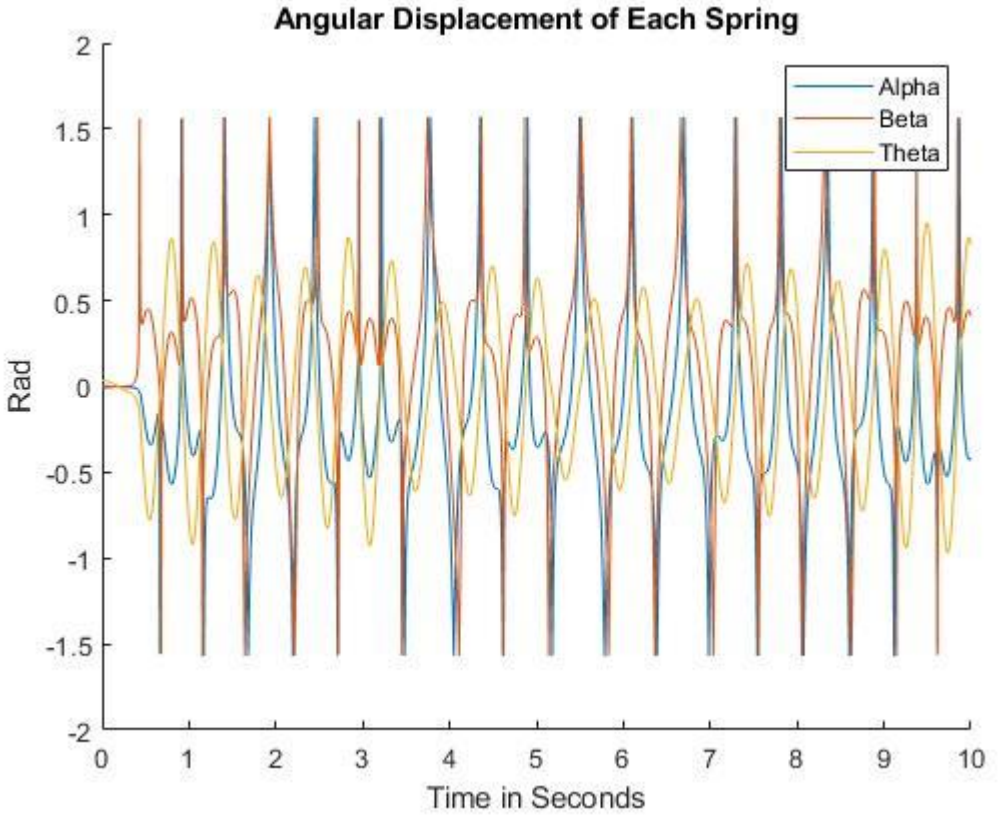

Figure 74: Angular displacement of each spring using attributes from Table 5 (3DOF)

Figure 75 presents the motion plots for the centre of the rigid bar and spring A and B. Each spring traces a different motion, this is as expected as per the results which have been previously discussed. The motion at the centre of the rigid bar is not impacted by the θ coordinate and thus only presents the x and y coordinates which are the translational displacements.

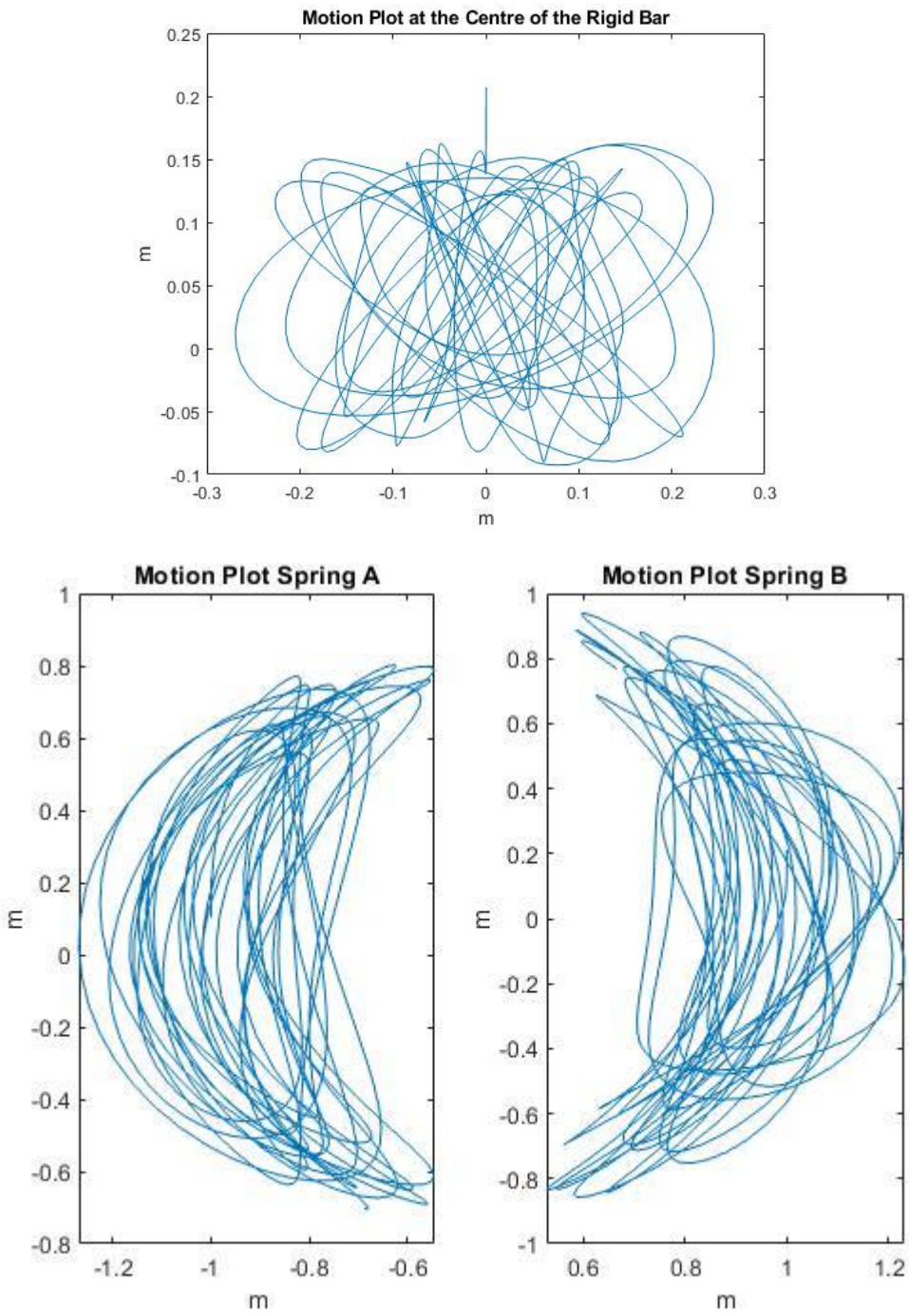

Figure 75: Motion plots for the attributes presented in Table 5 (3DOF)

4.5. DAMPING OF THE 3DOF SYSTEM

The inclusion of damping is realistic and occurs throughout nature. As mentioned previously the effects of damping need to be assumed since realistic values of damping can only be developed through testing.

As performed previously for the 2DOF system, proportional damping will be assumed for the springs while equation 26 will be implemented for the rotation of the rigid bar. If we let the right-hand side of equations 56, 57 and 58 equal $\mathcal{A}$, $\mathcal{B}$ and $\mathcal{C}$ respectfully, the resulting equations can be rewritten to include damping as presented below. The x coordinate represents the pendulum motion thus it will be assigned damping as per equation 26, and the y coordinate will be assigned as per equation 25 as this represents the springs. The damping for the θ coordinate is thought to be complex since it may be influenced by both the x and y coordinates. It has been shown that the x coordinate is very sensitive to the θ coordinate, thus it is expected that the pendulum damping will have a larger influence on θ compared to the springs. The damping for the θ coordinate will be assigned the same as that of the pendulum motion.

$$\ddot{x} = \mathcal{A} - \frac{C_p \dot{x}}{m} \tag{65}$$

$$\ddot{y} = \mathcal{B} - \frac{C_p \dot{y}}{m} \tag{66}$$

$$\ddot{\theta} = \mathcal{C} - \frac{C_s \dot{\theta}}{m} \tag{67}$$

The effect of numerical stability with the inclusion of damping is a topic that has been studied in detail, more specifically with regards to the equation of motion (68). Equation 68 is used to perform for linear and nonlinear transient dynamic analysis on FEA software. The numerical stability with damping has been studied a great deal with Newmark's method with well-defined criteria for stability, this is discussed by (Eleni, et al., 2017). There are also various developments in new direct integration methods and their associated stability. It is thus expected that the inclusion of damping will develop better accuracy with regards to the simulations.

$$M\ddot{u} + C\dot{u} + Ku = F(t) \tag{68}$$

4.4.1. DAMPING WITH INITIAL CONDITIONS FOR θ

The simulation will be performed using the initial conditions presented in Table 9 with all damping coefficients assigned a value of 0.01. Figure 76 presents the displacement results for each coordinate, the results present consistency across the different ODE solvers. The consistency substantiates that the inclusion that damping assists with numerical stability.

Furthermore, it can be noted that the damping assigned to the spring acts far more aggressively when compared to the rigid bar and pendulum motion. When assigning more aggressive damping all the coordinates present a similar plot to that of the y coordinate. The x coordinate presents what is expected from parametric resonance even though the system has not been sized for such. Based on the previous discussions it is known that the θ coordinate has a great influence on the x coordinate thus explaining the motion of the x coordinate. It can thus be explained that the θ and x coordinate continually move in and out of phase with each other thus developing the presented results of the x coordinate. There is an extremely small amount of energy being transferred to the x coordinate which is evident through the small displacements.

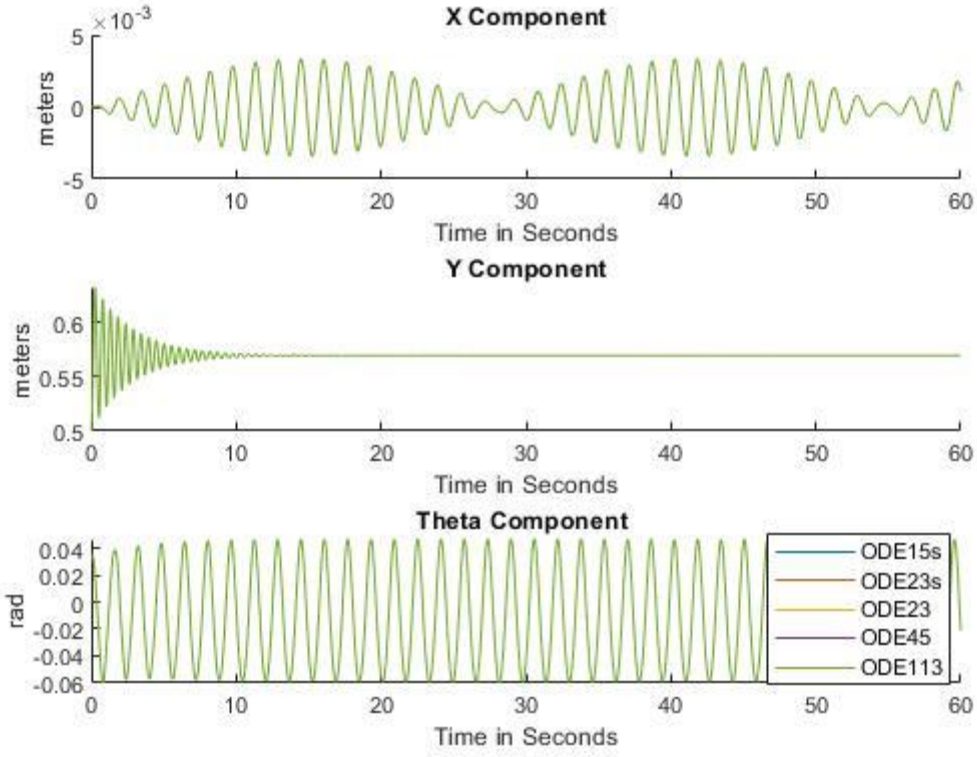

Figure 76: Displacement for each coordinate for initial conditions presented in Table 9 and damping

Figure 77 presents the normalised accelerations, the accelerations are not always in phase with each other when considering the x and θ coordinate, noting that for this case a 180-degree phase shift exists. When the coordinates are out of phase (not 180-degreephase shift) the energy transfer is small and thus damping reduces the displacements and accelerations of the x coordinate, however when they are in phase energy in added to the x coordinate.

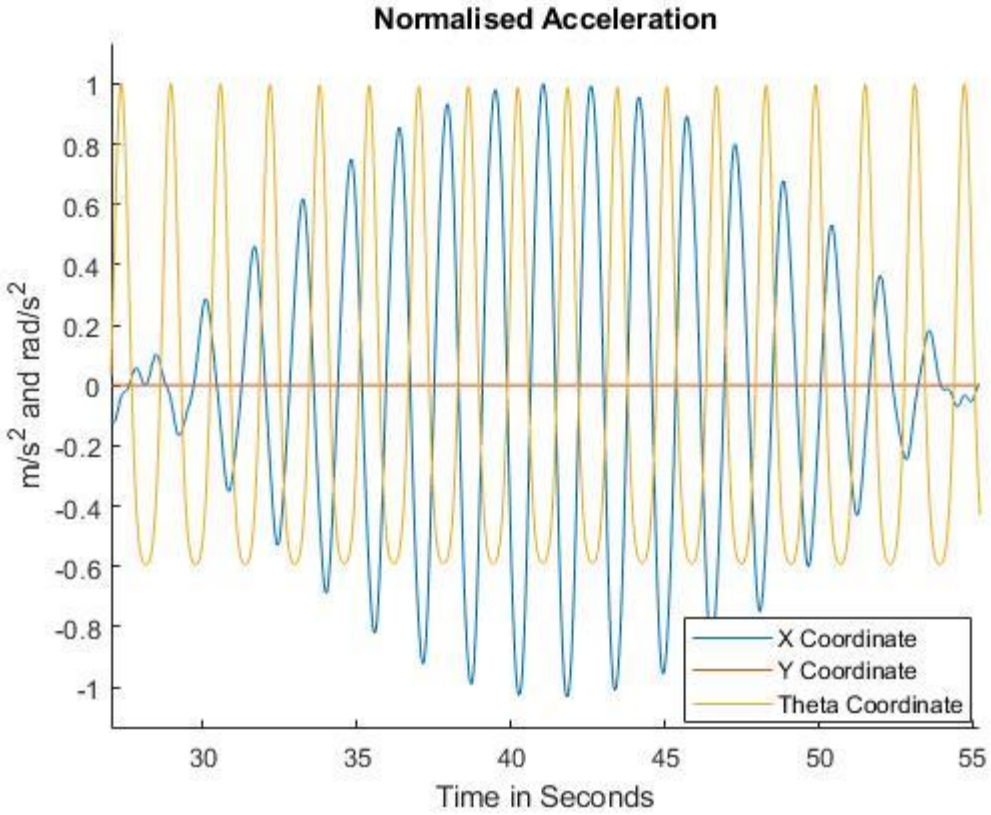

Figure 77: Normalised acceleration with attributes from Table 9 and damping

To further study the system with the inclusion of damping the attributes presented in Table 9 will be assigned, however damping will be varied in increments of 0.01 up to 0.04. Figure 78 presents the motion at the centre of the rigid bar. The effects of damping affect the spring far more compared to the pendulum and the angular motion of the rigid bar.

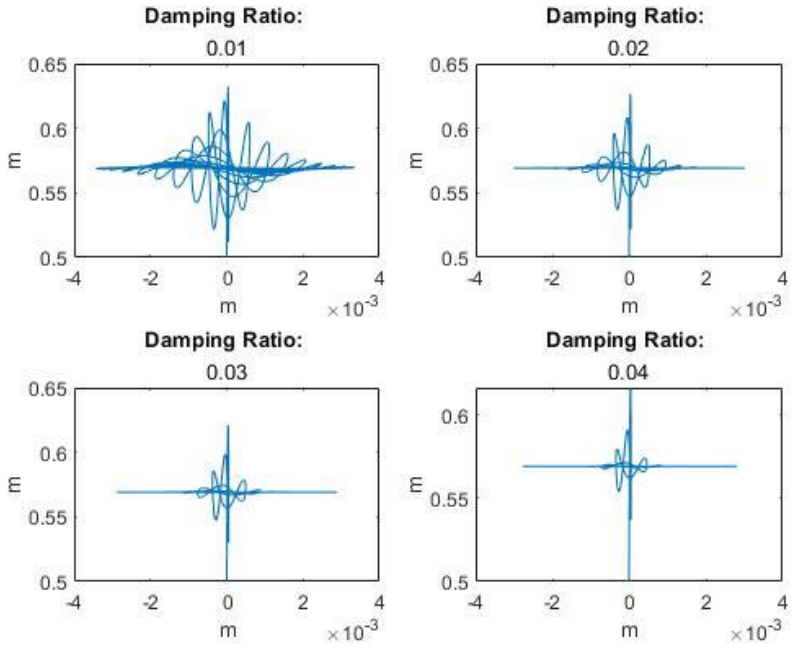

Figure 78:Damping with attributes and initial conditions presented by Tale 9

4.4.2. DAMPING AND INITIAL CONDITIONS FOR THE θ COORIDNATE (PARAMETRIC RESONANCE)

This case will be simulated using the initial conditions and attributes presented by Table 5 however initial conditions will only be applied to the θ coordinate. The θ coordinate will be assigned initial conditions of 2 degrees.

The results using various solvers on Matlab are presented by Figure 79, consistency between all the solvers is good. The damped and undamped case for the parametrically sizes setup present consistency with regard to the results.

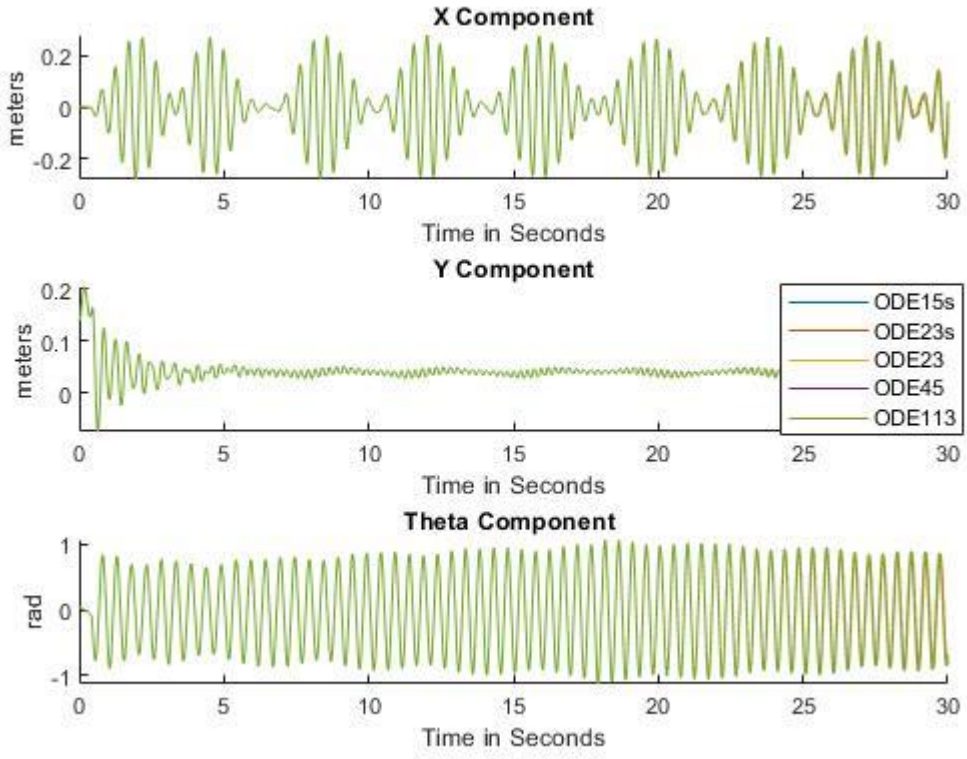

Figure 79: Displacement results for the 3DOF considering attributes and initial conditions from Table 5 with damping

Figure 80 presents the normalised displacements as performed previously. The effect of damping has the greatest effect on the y coordinate, which results in dramatically smaller numerical values for the motion compared to the undamped case. The x and θ coordinate present very similar results to the undamped case. The results are as expected since it is clear from previous simulations that the springs are far more aggressively affected by damping compared to the other coordinates. By reviewing the presented data, the θ coordinate transfers energy to the x coordinate and vice versa, however it is difficult to understand the energy transfer to and from the y coordinate (this will be studied later).

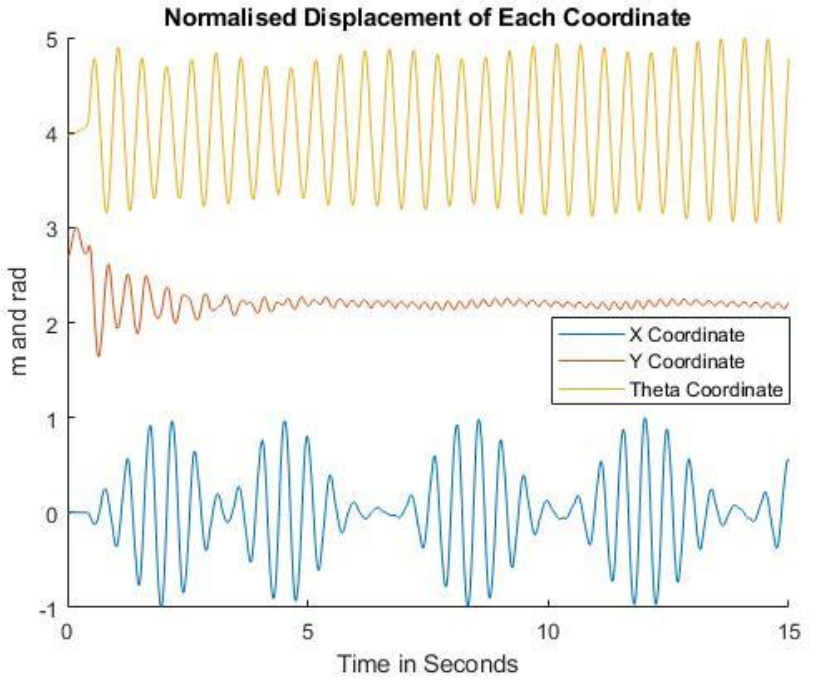

Figure 80: Normalised displacement results for each coordinate

Figure 81 presents the accelerations results for each coordinate. The results for the x and θ tie up well with the undamped case, this statement relates to the general profile of the results not the numerical values. The biggest difference can be found with regards to the y coordinate, where the peak values (where energy is transferred to the y coordinate) present sharper peaks which do not gradually build up as presented by the undamped case.

The acceleration results present a clearer image of how the coordinates transfer energy to each other. The x coordinate transfers energy to both the y and the θ coordinate, the energy transfer also works in reverse whereby the x coordinate receives energy from both the y and θ coordinate. This clearly differs from the undamped case, where the energy transfer is far more complex and varies drastically along a time interval.

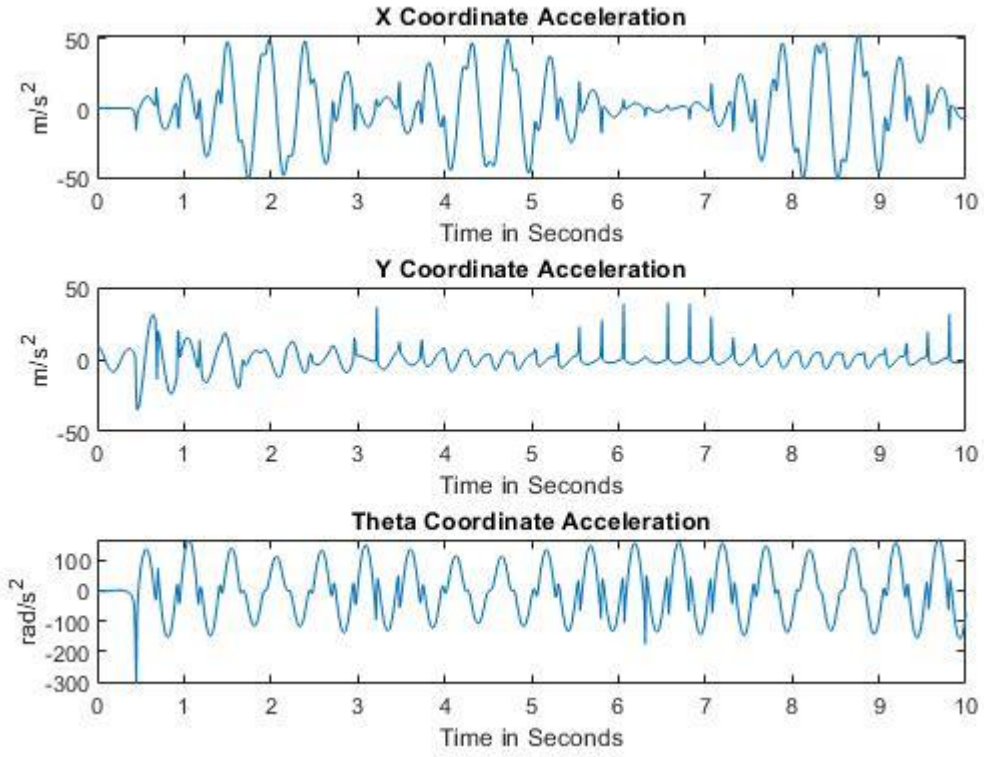

Figure 81: Acceleration results

To understand the results further the acceleration results for the damped and undamped case are plotted on a single axis as presented by Figure 82. From 0 to roughly 3 seconds the results for the x and θ coordinate present good correlation between the damped and undamped case. During periods of time where the x coordinate or the θ receive energy the results present better similarity to the undamped case. The damped and undamped acceleration results present small phase shift, this is most evident by inspecting the θ coordinate.

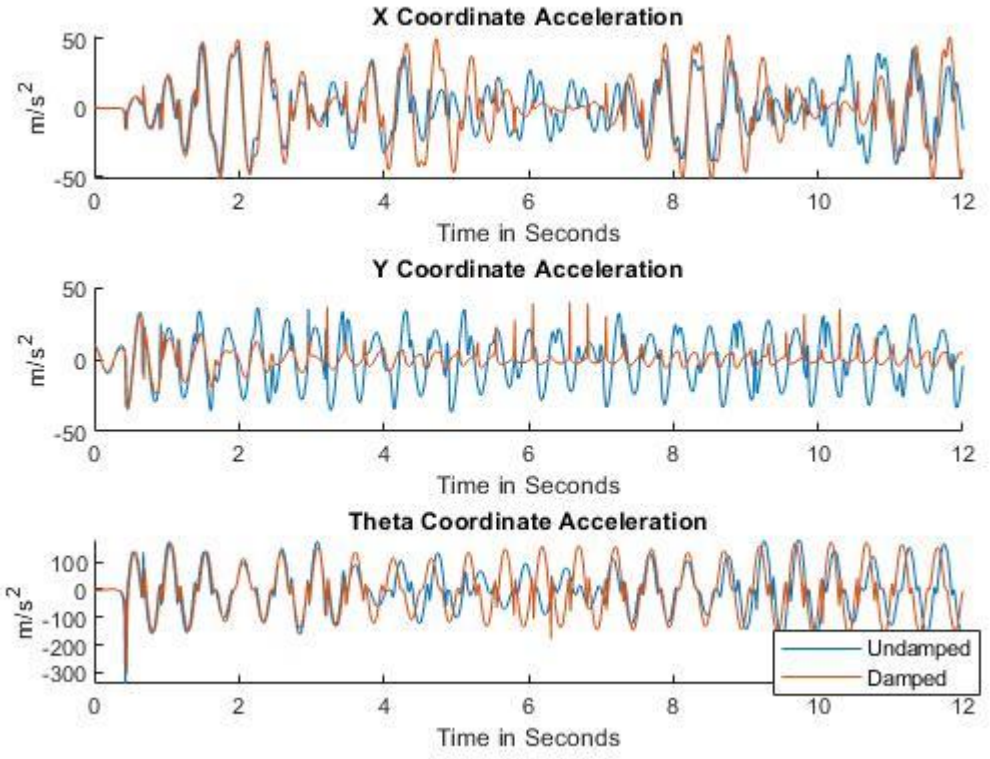

Figure 82: Damped and undamped acceleration results

The motion plot for each spring is presented by Figure 83. The results present a system where each spring is tracing a crescent shape. The elongation/contraction in each spring is presented by Figure 86, it is evident that each spring presents different elongations while the contraction of the springs presents similar results. The results present a similar trend compared to the undamped case. Figure 85 presents the displacements of α, β and θ, the results correlate well with the undamped case and present similar behaviour and displacements.

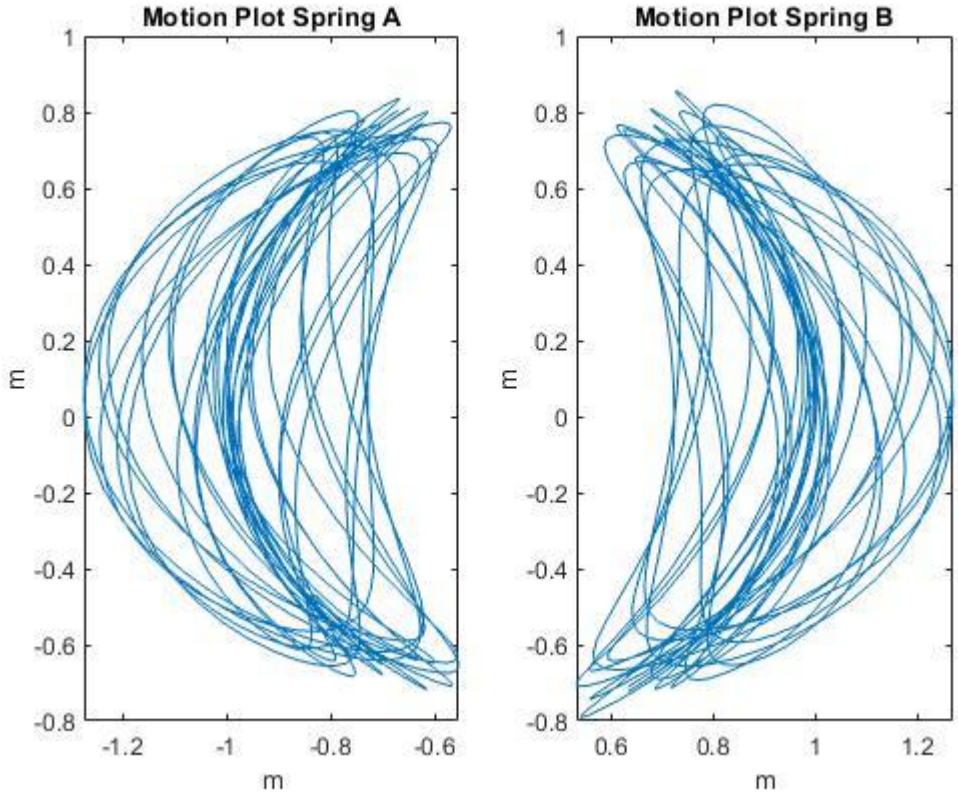

Figure 83: Motion plot for each spring for attributes assigned from Table 5 and initial conditions for ϑ

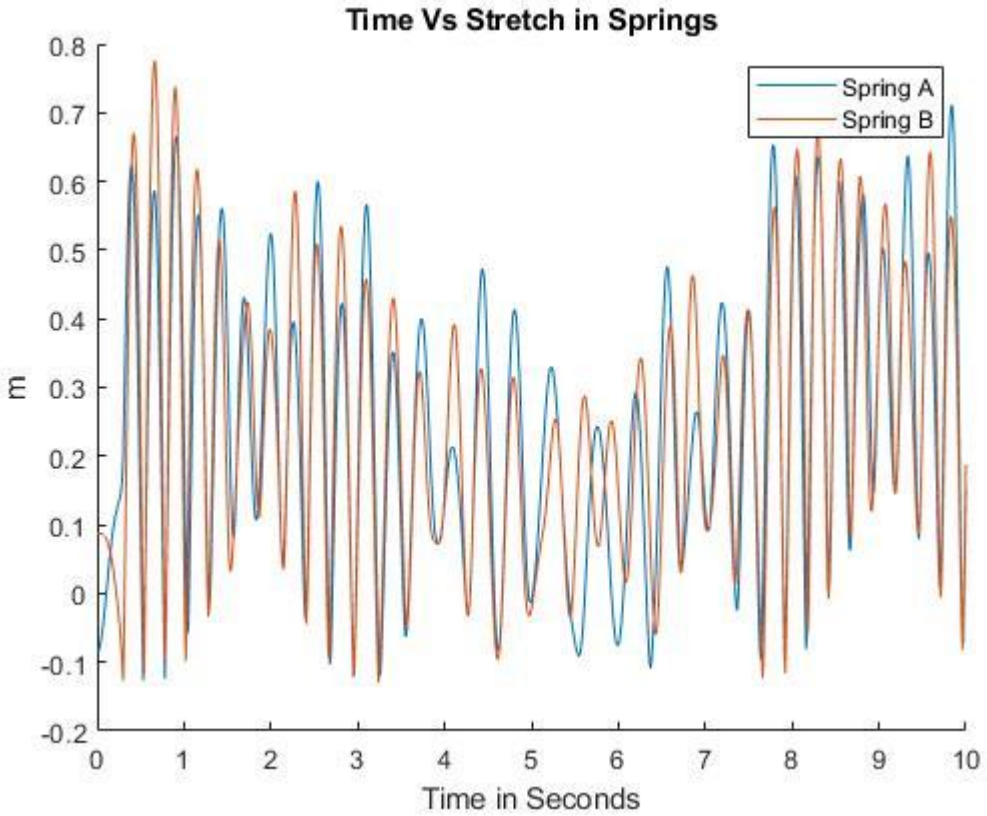

Figure 84: Stretch in spring A and B due to attributes presented in Table 5 and initial conditions on θ

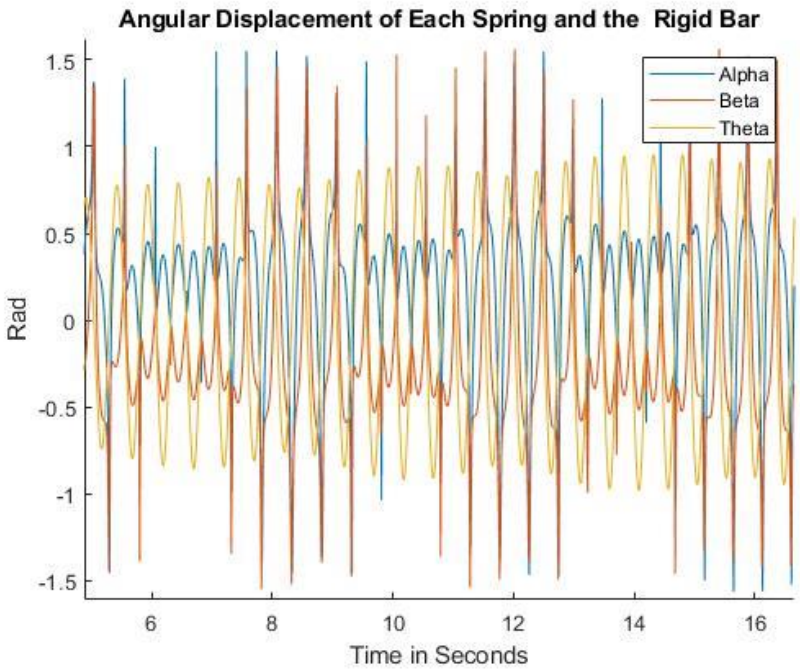

Figure 85: Angular displacement of each spring due to attributes presented in Table 5 and initial conditions on θ

Figure 86 presents the motion plot with a varying damping ratio, the motion plot is presented at the centre of the rigid bar. As per the previous discussions damping affects the spring far more aggressively, however it mainly affects the transient behaviour which initially exists. Figure 87 presents the motion plot for Spring A, allowing one to view the effects of damping on the x and θ coordinate in greater detail. On close inspection the increase in damping has a small effect of the displacement in the x and θ coordinate, this is however small and the increase in damping can be considered negligible.

The study of damping has been discussed in further details regarding the 2DOF system. Due to the lack of experimental data of the proposed 3DOF system the damping study will not be further considered and the values will be assumed.

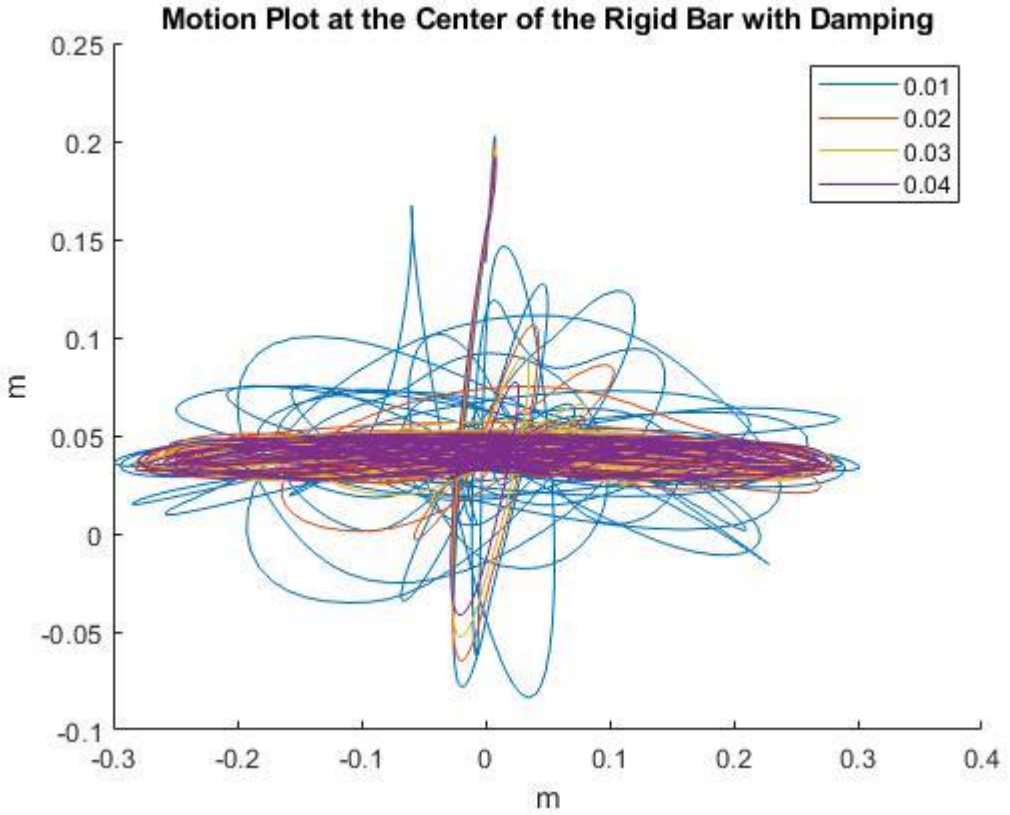

Figure 86:Motion plot for attributes presented in Table 5 with increasing damping ratio (θ initial conditions)

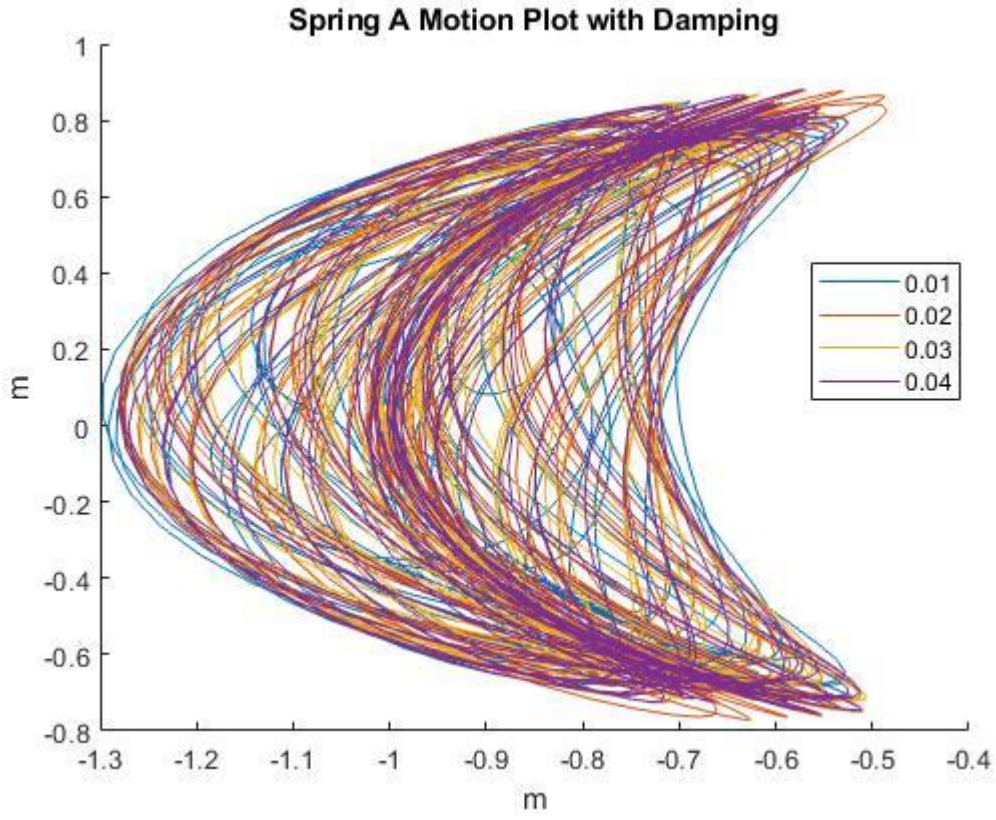

Figure 87:Motion plot for Spring A, attributes presented in Table 5 with increasing damping ratio (θ initial conditions)

4.5. DERIVATION OF THE GENERALISED FORCES

The generalised forces for the x and y coordinate can be presented as per equations 69 and 70. The forces are assumed to act at the CG of the system which is at the midpoint of the rigid bar. It is assumed that the generalised forces applied to the x and y coordinates do not affect each other, implying that the forces are independent. Due to the location at which the forces act they also do not influence the θ coordinate.

$$Q_x = F_h(t) \tag{69}$$

$$Q_y = F_y(t) \tag{70}$$

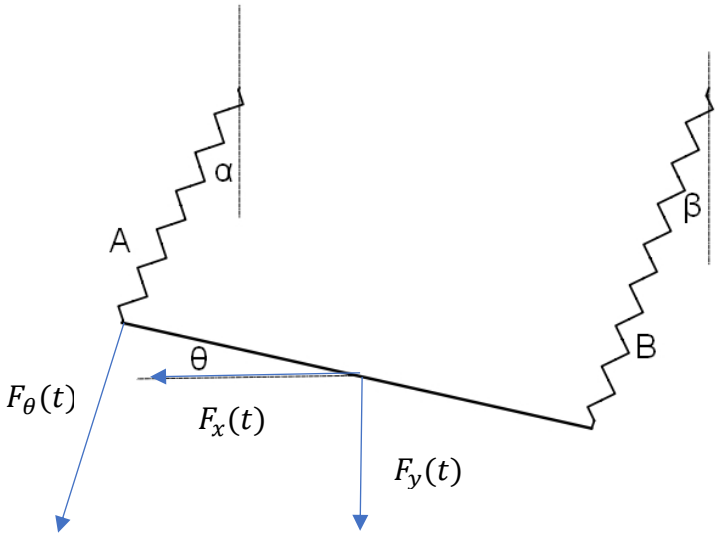

Figure 88: Generalised forces for the 3DOF

The generalised force for the θ coordinate is derived in a similar manner as to the derivation of the generalised force for the θ coordinate in the 2DOF system. The derivation is as follows:

- It is assumed that the force always acts perpendicular to the rigid beam. The resulting equation with the virtual displacements is presented by 71

$$\delta_\theta Q_\theta = F_t(t) \cdot \frac{L}{2} \delta_\theta \tag{71}$$

- The resulting generalised force is then represented by 72. The $\frac{L}{2}$ term is developed through the requirement for the virtual displacement using the assumption that the system rotates about the centroid.

$$Q_\theta = F_\theta(t) \cdot \frac{L}{2} \tag{72}$$

The θ coordinate has an influence on both the x and y coordinates which results in 73 and 74.

$$Q_x = F_h(t) + F_\theta(t)\, sin\, \theta \tag{73}$$

$$Q_y = F_y(t) + F_\theta(t)\, cos\, \theta \tag{74}$$

The resulting differential equations can now be presented by equations 75, 76 and 77 which now includes the generalised forces.

$$\ddot{x} = \mathcal{A} - \frac{C_1\dot{x}}{m} + F_h(t) + F_\theta(t)\,sin\,\theta \quad (75)$$

$$\ddot{y} = \mathcal{B} - \frac{C_2\dot{y}}{m} + F_y(t) + F_\theta(t)\,cos\,\theta \quad (76)$$

$$\ddot{\theta} = \mathcal{C} - \frac{C_3\dot{\theta}}{m} + F_\theta(t) \cdot \frac{L}{2} \quad (77)$$

The expectation is that excitation will be applied to the x and y coordinates at the natural frequency of the pendulum and spring respectfully, thus developing parametric resonance in the system. Based on the information presented in Figure 4 it is expected that a higher frequency would be required in order to promote screening thus the θ will be studied with an excitation frequency at 16.67Hz.

From previous simulations it is evident that errors are introduced into the numerical simulations, these errors are further introduced when applying generalised forces. A simulation was performed assigning the attributes presented in Table 7 with the following amendments:

- All numerical values for generalised forces are 10000N
- All damping coefficients are assigned as 0.01.
- The excitation of the θ is assigned as 2.66Hz.

The displacement results for the above-mentioned simulation are presented in Figure 89, it can clearly be seen that each ode solver presents different results. Since we are no longer applying initial conditions and still achieving errors, the source of the errors can be supported by the presence of inhomogeneous terms. Upon further investigation by the Matworks team it was found that the various ode solvers deviate from each other due to the accumulative errors which can be attributed to a chaotic system.

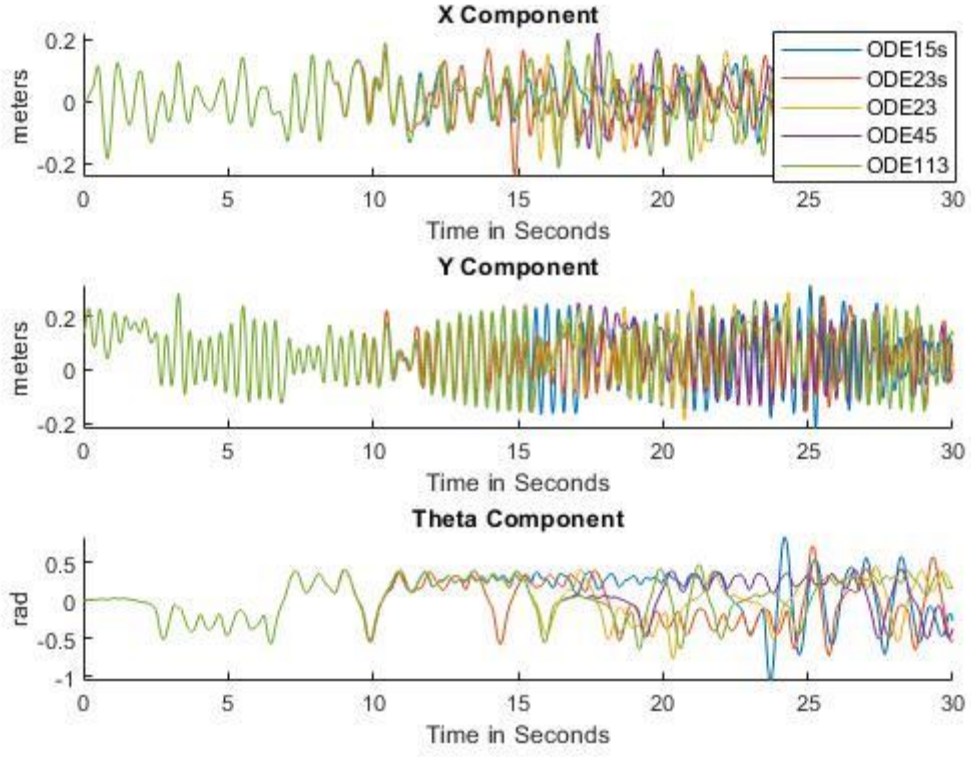

Figure 89: Displacement results of the 3DOF system with conditions assigned as per Table 7

4.6. PARAMETRIC EXCITATION OF THE 3DOF MODEL WITHOUT DAMPING

This section will study the 3DOF system with excitation applied to every coordinate individually, this will assist in the greater understanding of the system and how it reacts to parametric excitation. Table 10 presents the physical attributes for the 3DOF system, these attributes will be applied in conjunction with excitation forces in the various coordinates.

Table 10: Attributes for parametric resonance for the 3DOF system

Attribute	**Numerical Value**	**Units**
Mass	3755	kg
Spring Stiffness (per spring)	266x2	N/mm
r	0.138	m
Ws	2.68	Hz
Wp	1.34	Hz

4.6.1. PARAMETRIC EXCITATION IN THE X COORDINATE

The first simulation will consider an excitation force of $1000\sin(\omega_p t)$, where ω_p is assigned as per Table 10. As discussed previously the differential equations for the system are setup in a manner which requires the natural length of the spring to be assigned as the initial conditions, thus developing a system which theoretically starts at rest. Due to the simulations being transient in nature, coupled with the absence of damping the system is expected to experience displacements in the y coordinate even though there is no excitation in this coordinate. This movement will inherently promote parametric excitation of the system.

Figure 90 presents the results developed on Matlab for the above-mentioned simulation. At roughly 20 seconds the different solvers begin to deviate from each other.

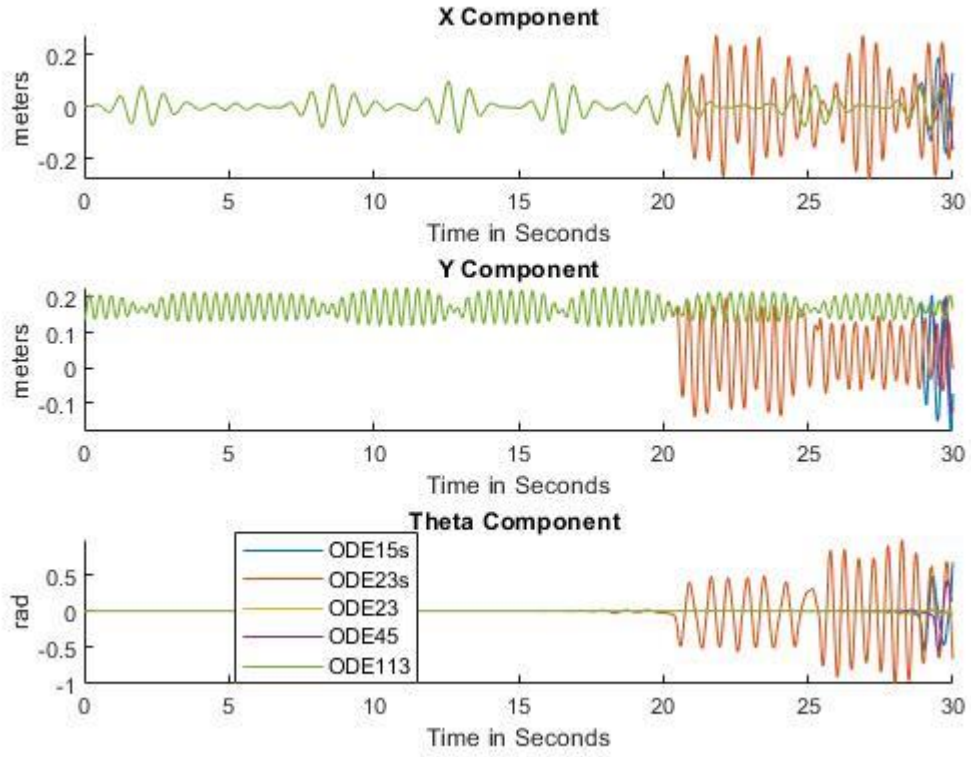

Figure 90:Displacement results from Matlab using attributes assigned from Table 10

The results attained from the above-mentioned simulation using Mathematica are presented in Figure 91. The Explicit Runge Kutta method was also explored however has not been included in the simulations as the results are poor. The Adams and "Mathematica optimised" solutions present good correlation while the Explicit Euler method does not correlate well. There exists good correlation with results up to roughly 8 seconds.

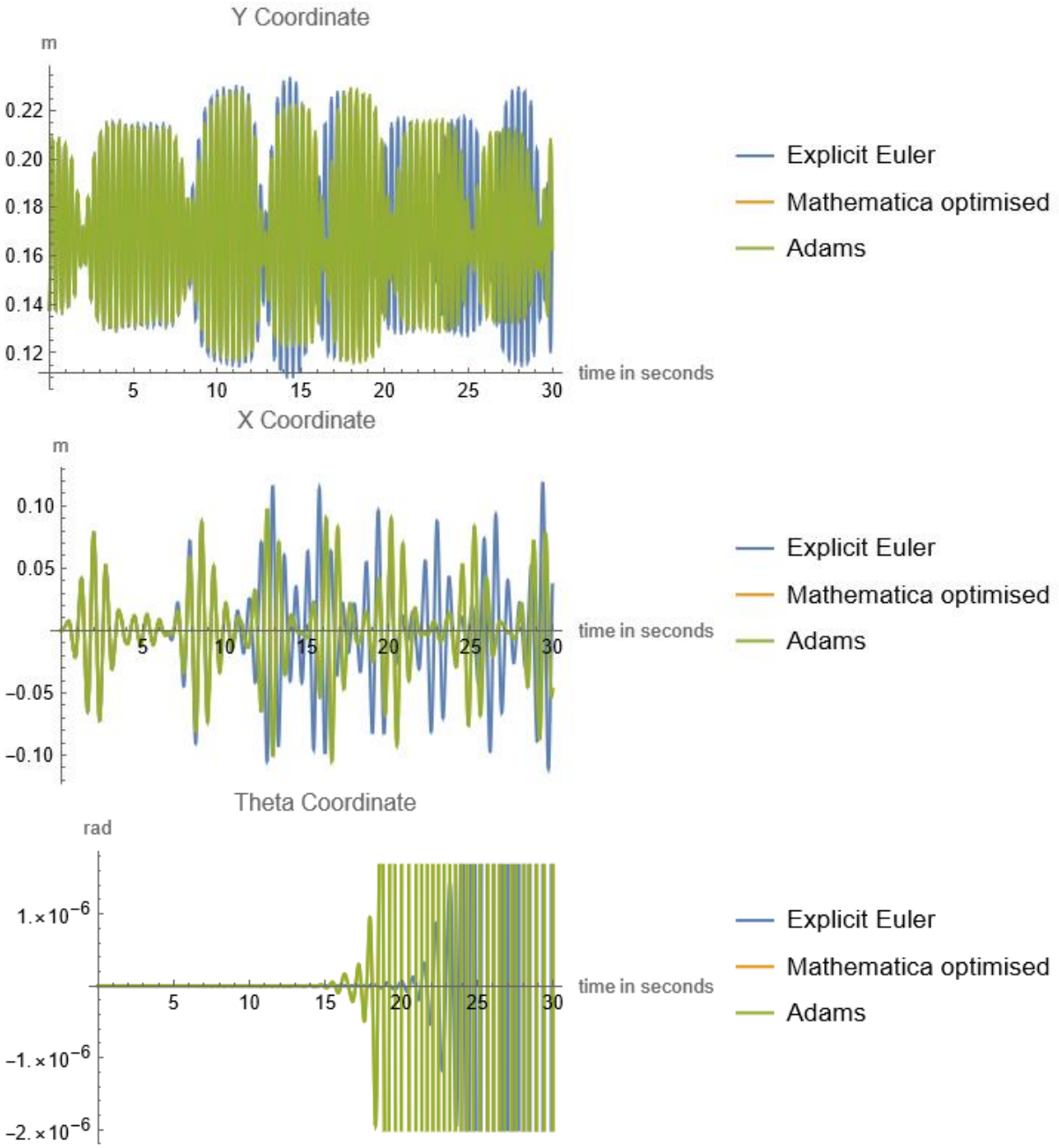

Figure 91: Displacement results from Mathematica using attributes assigned from Table 10

Figure 92 presents the ode45, ode23s and the Mathematica results on a single plot. Label "A" presents a time period where the x coordinate results have a phase shift, since the ode45 and ode23s solvers sill overlap each other, it can be concluded that the phase shift occurs with the Mathematica solution. During the same point in time the y coordinate (label "B") presents different solutions for Matlab and Mathematica, these errors may be a contributing factor to the presented phase shift. The θ coordinate presents small errors for the time period between 0 and ±18seconds which is unnoticeable due to the graph presenting large errors post18 seconds.

The region presented by "C" presents the only θ coordinate values for the Mathematica solution. Mathematica is unable to export very small numbers to excel correctly, the numbers are saved as "*^-13" as opposed to "*10^-13", which is then taken as "NAN" by Matlab thus producing no data points. After roughly 25 seconds the errors are now in a significant region which allows for an accurate export, thus leading to the conclusion that the Mathematica results

also begin to deviate from the actual solution, however this occurs at a slower rate compared to Matlab.

The results presented by Figure 92 share the same pattern with the results presented by Figure 26. The results presented in Figure 26 consist of two excitation forces with the results in this section only considering excitation for only the pendulum motion.

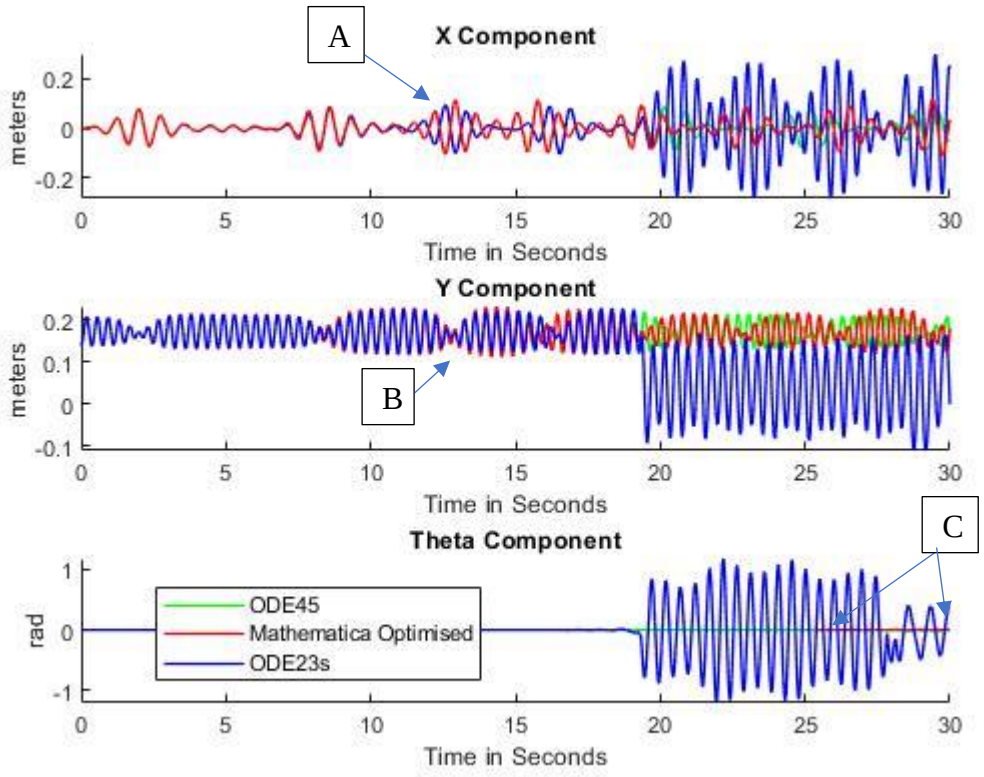

Figure 92: Combined results of ODE45, ODE23s and Mathematica using attributes assigned from Table 10

By studying the results, parametric resonance has occurred. Parametric resonance can be developed for this case since the y coordinate naturally oscillates, from its resting position thus enabling parametric resonance.

Figure 93 presents the acceleration results for each coordinate. The results present a case where the x and y coordinate transfer energy to each other on different time intervals. The θ coordinate beings to present errors at roughly 6 seconds. The x coordinate acceleration results present trace a very similar pattern as presented previously for the θ coordinate, peak acceleration values are generally followed by a much smaller peak on either side.

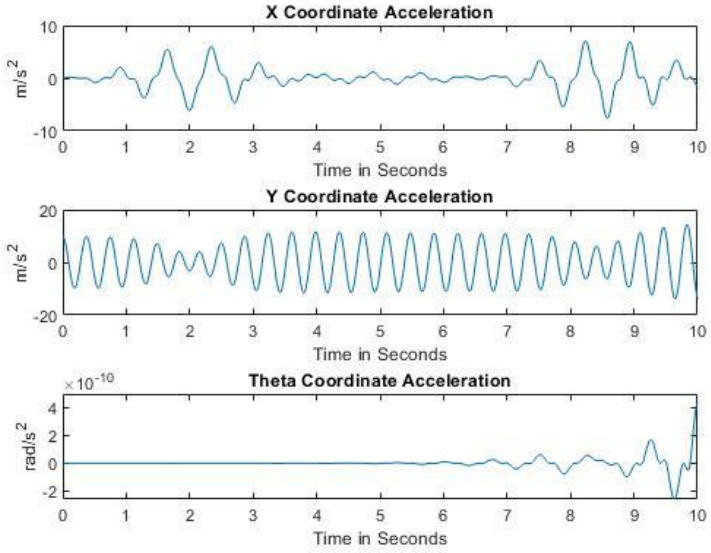

Figure 93: Acceleration results using attributes presented in Table 10

Figure 94 presents the PSD for the x and y coordinates. The x coordinate has two frequencies:

- 1.36Hz, which corresponds to the natural frequency of the pendulum movement
- 2.73Hz,which is the natural frequency of the spring arrangement
- 4.19Hz, this frequency can be considered to be the sideband frequency of the spring frequency (2.734Hz, y coordinate).

The y coordinate is the carrier frequency of the system due to the sideband frequencies developed in the x coordinate, noting that the natural frequency of the x coordinate is one of the sideband frequencies of the y coordinate. The sideband frequencies are 1.36Hz away from the carrier frequencies which is the pendulum frequency.

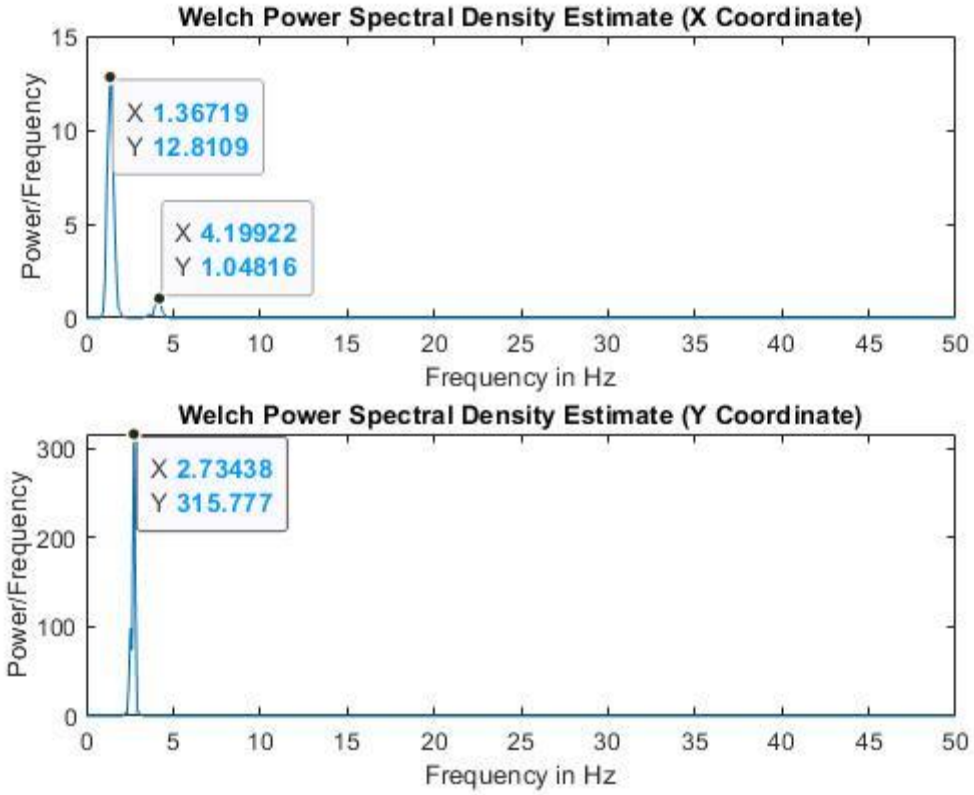

Figure 94:Power spectral density for the X and Y coordinates using attributes assigned from Table 11

The motion plot at the centre of the rigid bar is presented by Figure 95. The motion shape ties up well with the results presented in Figure 31, the numerical values do not correspond well, this however can be attributed to their existing no excitation in the y coordinate. The motion results for each spring have not been plotted as these results remain the same as that presented by Figure 95, since there is no motion in the θ coordinate to allow each end to experience different results.

The displacement results for each coordinate assist in explaining the motion trace. During periods of time where the x coordinate transfers energy to the y coordinate, the x coordinate experiences very small displacements and is indicative of the high-density region presented by A. During periods where the y coordinate transfers energy to the x coordinate, the y coordinate still experiences displacements at a far more significant level compared the scenario previously discussed, thus the displacements are indication of the region not covered by A.

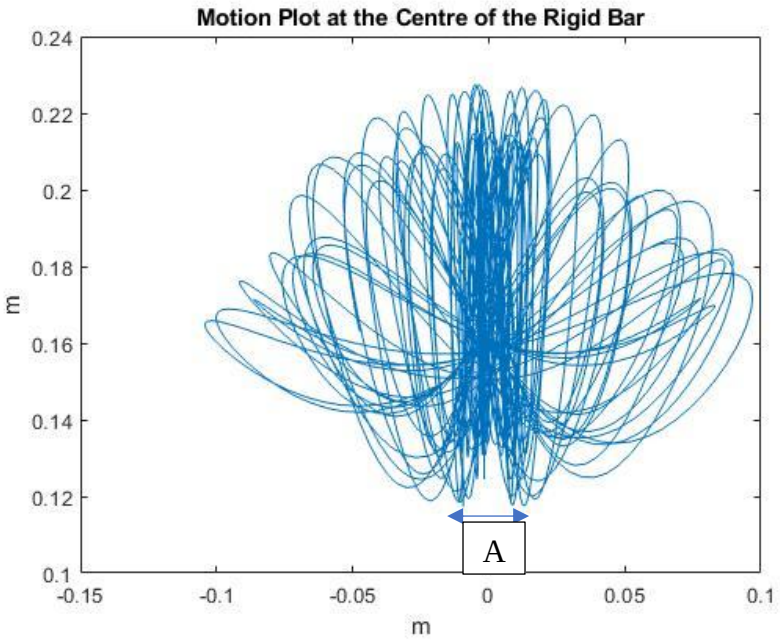

Figure 95: Motion plot for the attributes assigned as per Table 11

4.6.2. PARAMETRIC EXCITATION IN THE X AND Y COORDINATE

As discussed previously it would be fruitless to perform a simulation where there exists only excitation in the y coordinate, this is because parametric excitation will not be developed. The approach presented in 4.6.1 will be implemented however an additional excitation force will be applied to the y coordinate. The excitation force will be $1000\sin(\omega_s t)$, where ω_s is assigned as per Table 10. Figure 96 presents the Matlab displacement plots for the above-mentioned scenario. As per previous simulations it is evident that the solutions diverge, this occurs at roughly 20 seconds.

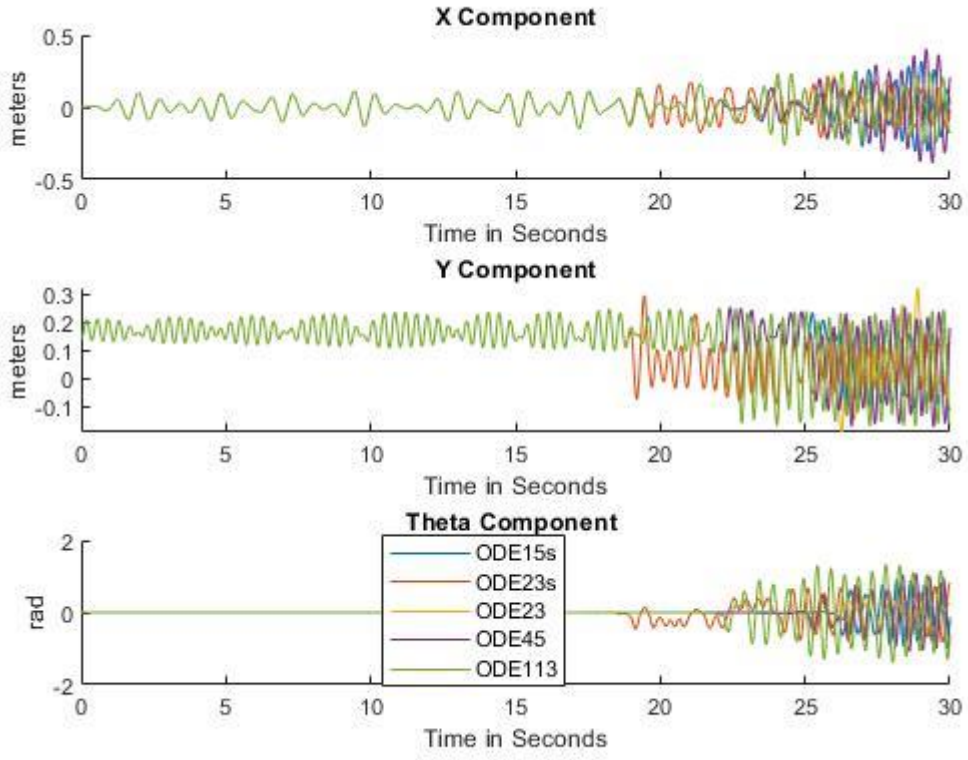

Figure 96:Matlab displacement plots using attributes in Table 11 with excitation in X and Y

Figure 97 presents the results from the Mathematica simulation, the results present consistency up to ±10 seconds where small differences can be noted, at ±23 seconds the results present large errors and the results do not conform to the expected shape any longer. The deviation can be attributed to the θ coordinate experiencing displacements which should not exist. The displacements for the θ coordinate are produced due to error accumulation, as similarly discussed previously. The Mathematica solvers are however able to produce consistent results for a slightly longer time period when compared to Matlab.

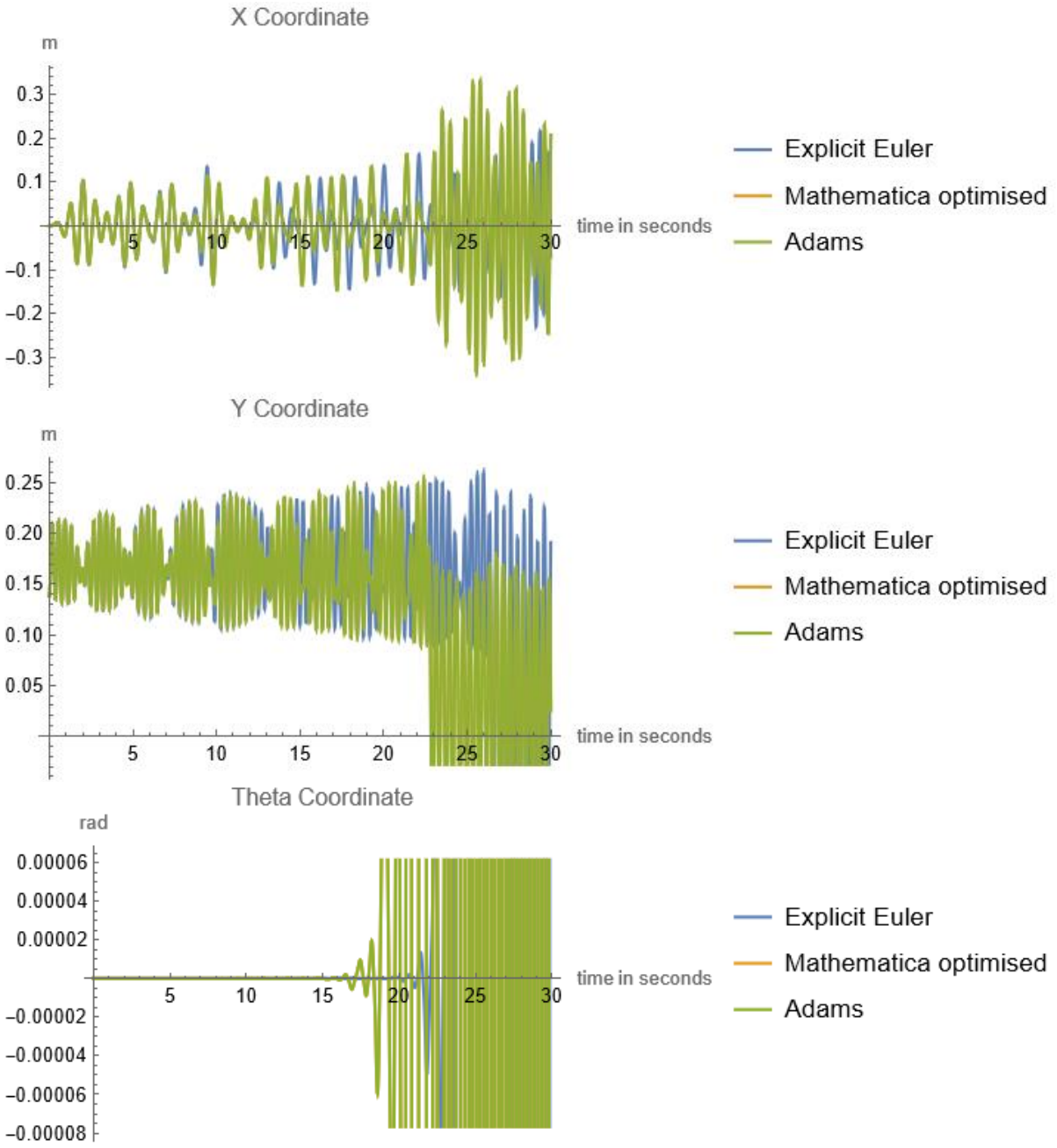

Figure 97: Mathematica displacement plots using attributes in Table 11 with excitation in x and y coordiantes

Figure 98 presents the results for Matlab and Mathematica on a single plot. The first deviance in results can be found at roughly 10 seconds which is marked by label "A". Label "B" (±22 seconds) presents the point in time where the numerical values for the θ coordinate become significant enough such that the values can be exported correctly for the Mathematica solution. Just after 25 seconds the error accumulation is large enough such that significant θ coordiante displacements can be found for the Mathematica solutions. There exists consistency in results till roughly 13 seconds.

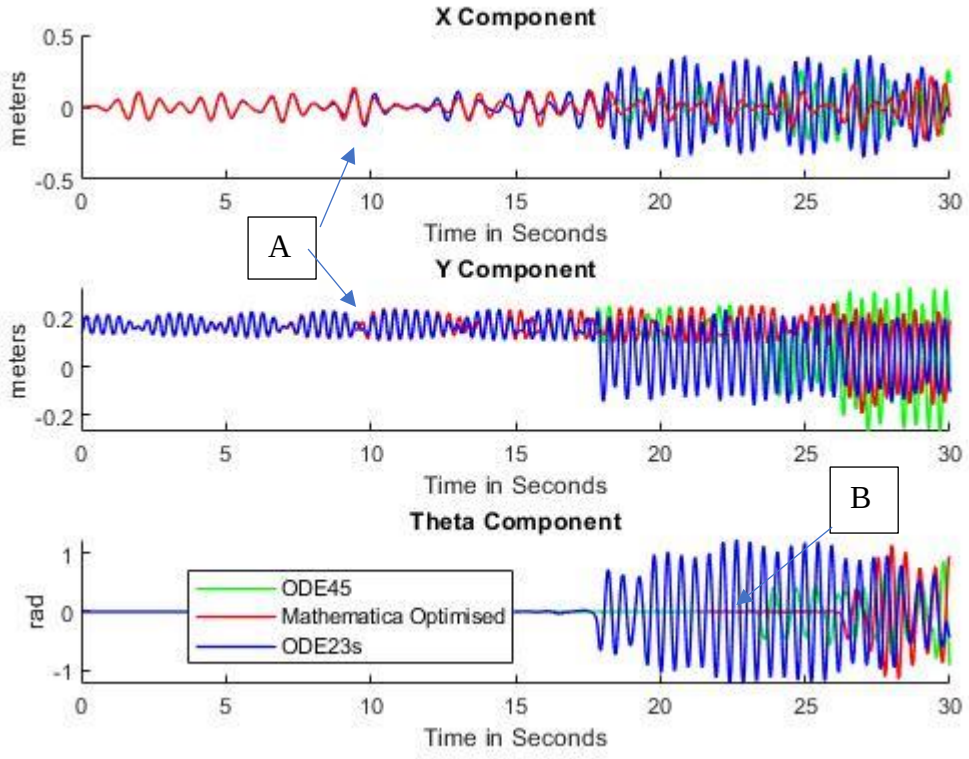

Figure 98: ODE and Mathematica results using attributes from Table 11 and excitation in x and y coordinates

Figure 99 presents the acceleration results for the simulation up to 15 seconds The accelerations for the θ coordinate is in the region of $4 \times 10^{-7} rad/s^2$ as the time approaches 15 seconds. This error is small however the error accumulation occurs rapidly. Figure 100 presents the resultant acceleration for each spring and the angular displacement for each spring. Resultant displacement presents a trend where the numerical values tend to increase with time. The angular displacement of each spring presents the same results, which implies that the rigid bar is horizontal during the simulation. This behaviour is expected since there is no rotational component of the rigid bar to allow each of the springs to react differently.

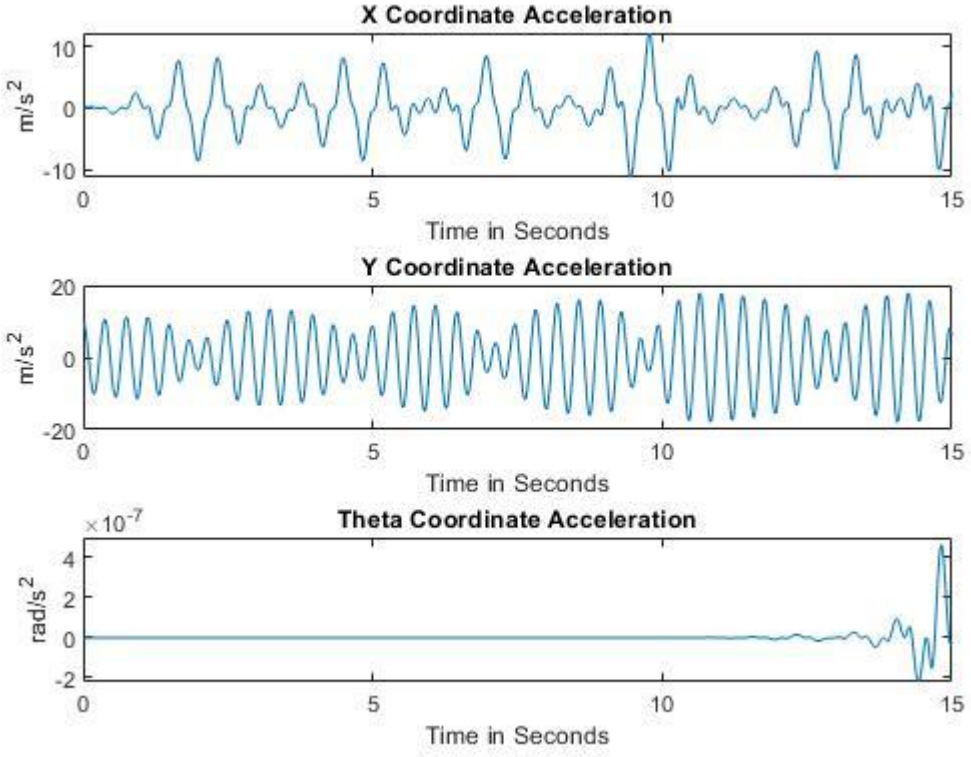

Figure 99: Acceleration results using attributes presented in Table 10 with acceleration in x and y coordinates

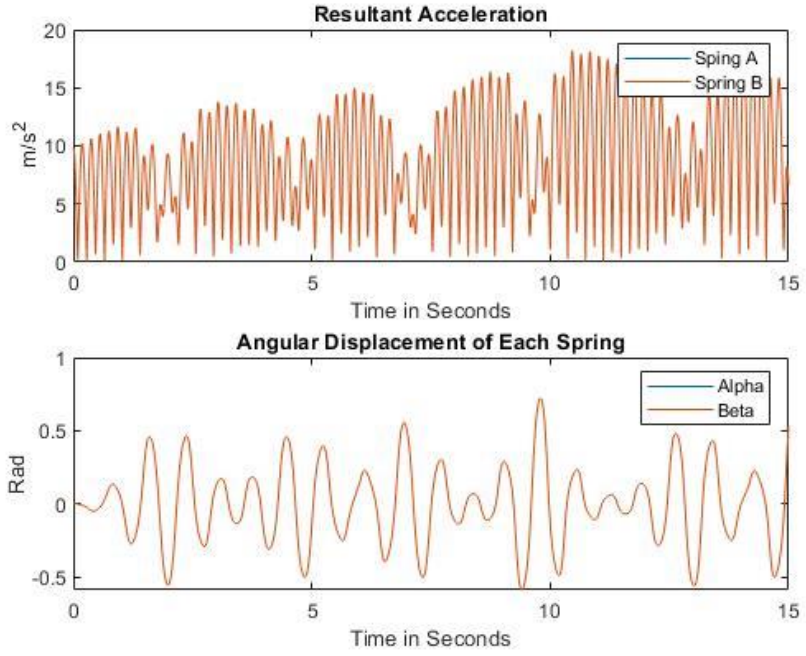

Figure 100: Resultant acceleration and the displacement of each spring using attributes presented in Table 10 with acceleration in x and y coordinates

The PSD for the simulation is similar to the one presented by Figure 94, with more energy being presented at the excitation frequencies which is expected with the additional excitation being provided. The motion plot at the centre of the rigid bar is presented by Figure 101, the motion presented by A is up to ±20 seconds while the motion presented by B is post ±20 seconds where there exists errors in the solution. The motions presented by A ties up well with what is presented by Figure 31.

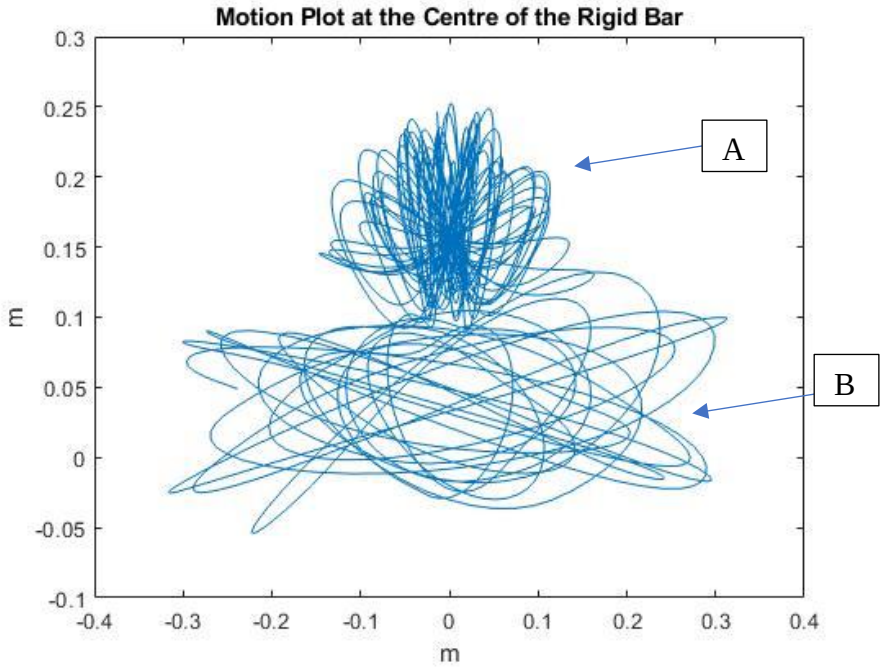

Figure 101:Motion plot for the attributes assigned as per Table 11 with excitation in x and y coordinates

4.6.3. PARAMETRIC EXCITATION IN THE θ COORDINATE

By inspecting Figure 3 any frequency above 16.67Hz will have little effect on the efficiency however lower frequencies have a greater impact on efficiency. The frequencies of the spring and pendulum are small compared to the 16.67Hz of SD18/36 thus, in order to promote screening it would be beneficial to introduce a 16.67Hz frequency to the θ coordinate.

An excitation force of $1000\sin(104.687t)$ will be applied to the θ coordinate. No other excitation forces will be considered, this will allow one to study the effects on the x and y coordinate due to excitation in the θ coordinate.

Figure 102 presents the displacement results attained from Matlab, it is evident that the results are consistent up to roughly 20 seconds. The x coordinate initially presents almost no movement and only begins motion at roughly 7.2 seconds. During the period when the x coordinate experiences motion, there is energy transfer from the y coordinate since there is a clear decrease in the displacements for the y coordinate (the location is denoted by label "A").

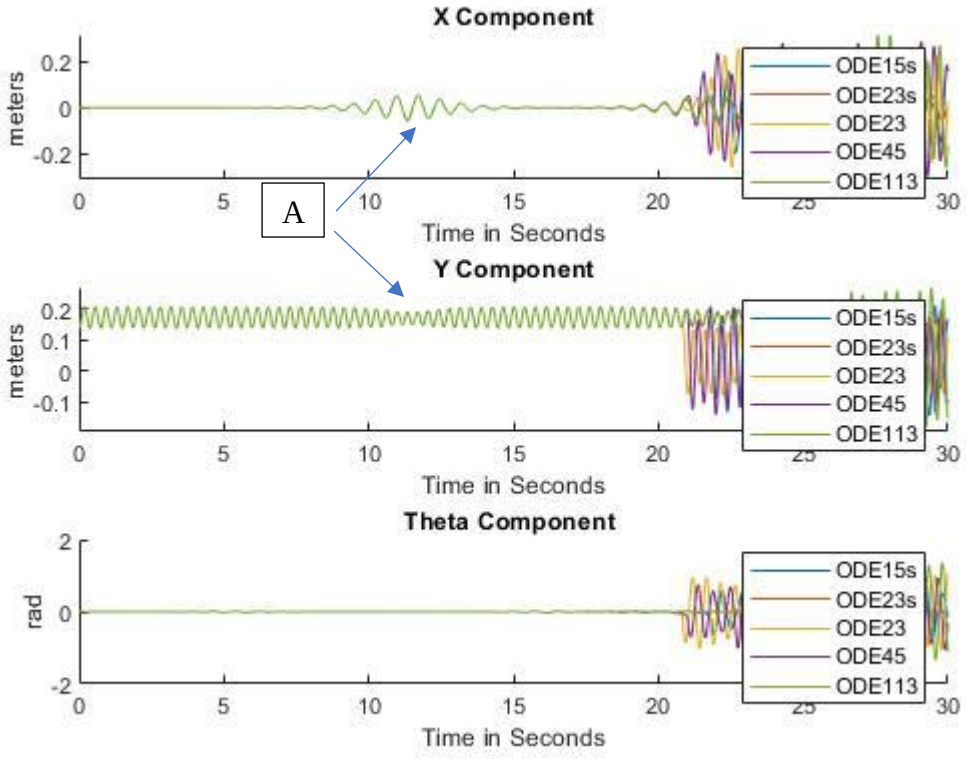

Figure 102: Matlab displacement results with θ excitation and attributes assigned from Table 10

Figure 103 presents the displacement results for the Mathematica simulation. Once again, the Mathematica optimised solution and Adam's method have produced the same solution. The Explicit Euler method presents small deviations from the "Mathematica optimised" and Adam's method for the x coordinate, this occurs between 10-15 seconds. For the same time period the θ coordinate displacements present larger errors where a phase shift in the results can be seen.

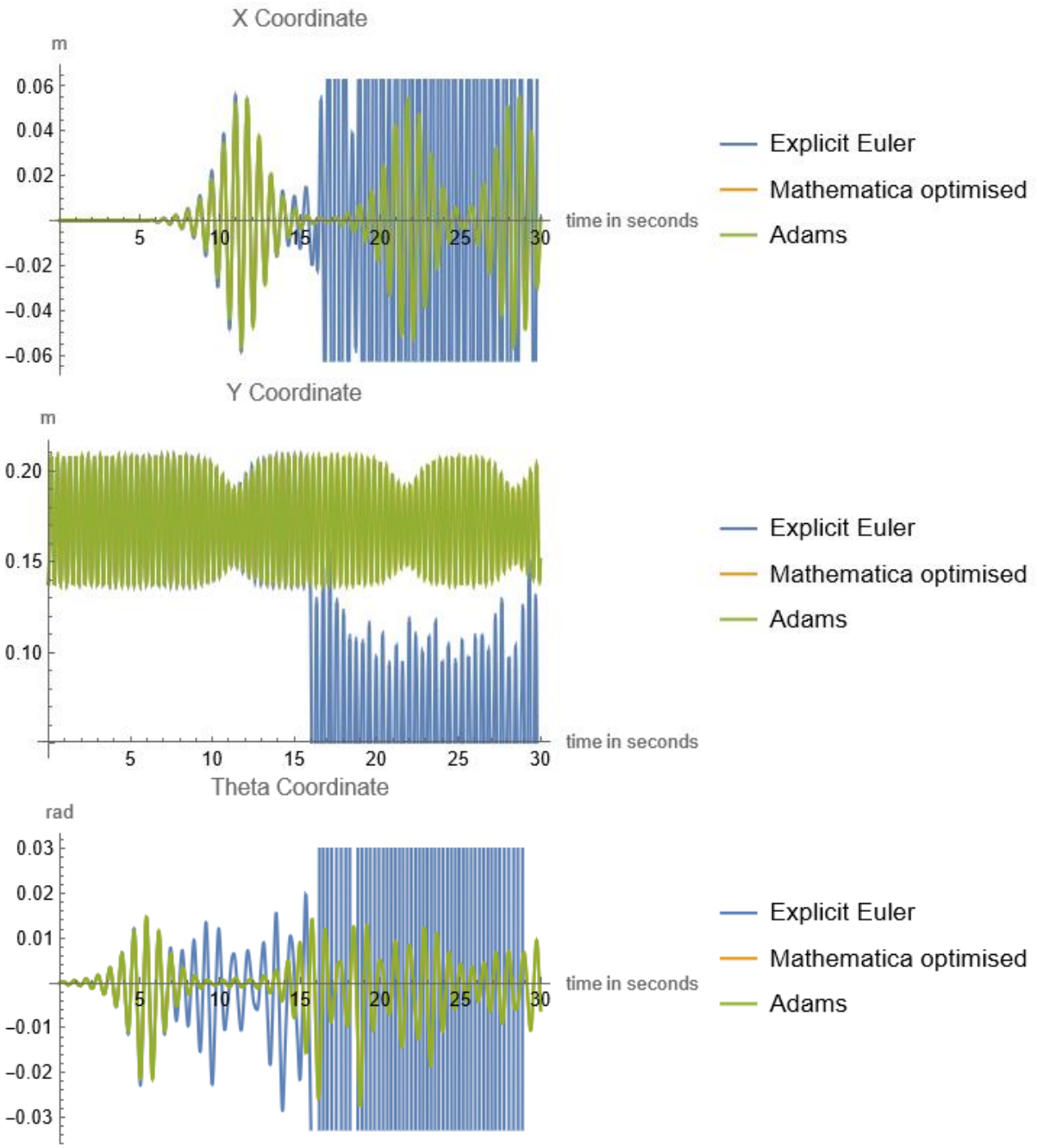

Figure 103: Mathematica displacement results with θ excitation and attributes assigned from Table 11

Figure 104 presents the Matlab (ode45 and ode23s) and Mathematica results on a single plot. The results are as expected, there is good correlation until the solvers begin to deviate. The results do not present phase shifts as seen previously.

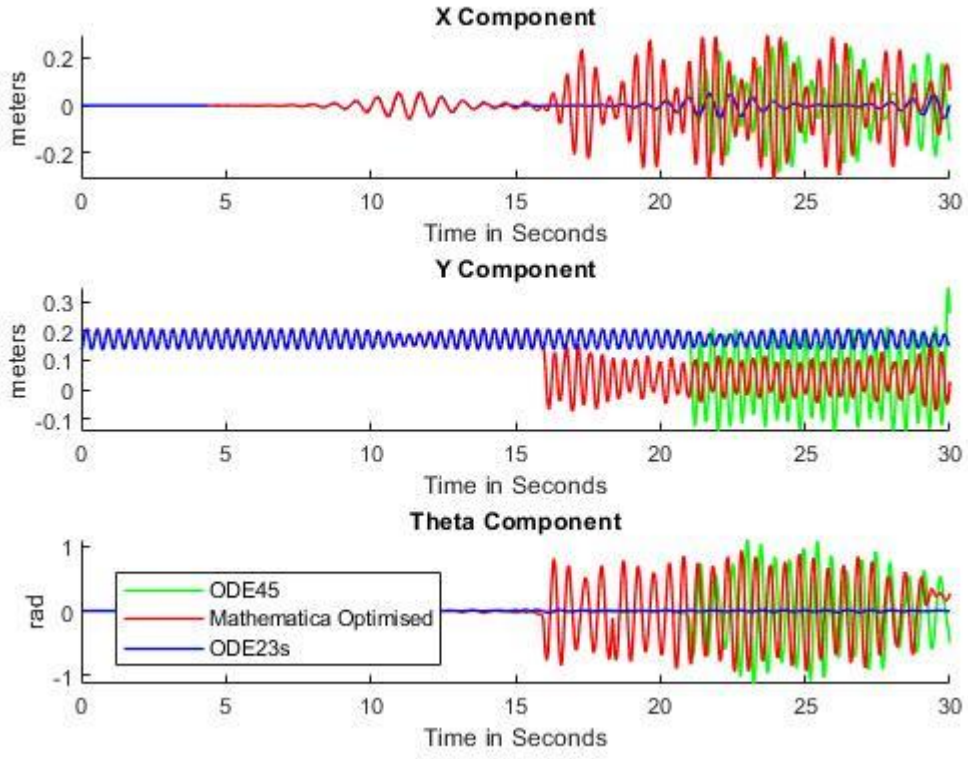

Figure 104: ODE and Mathematica results for excitation in θ coordinate

Figure 105 presents the acceleration results for each coordinate, the x coordinate transfers energy to the y coordinate. Furthermore, the θ coordinate is receiving energy, however from the presented data it is difficult to tell how this occurring. The high frequency excitation of 16.67Hz is present in the θ coordinate, this however is not translated to the other coordinates.

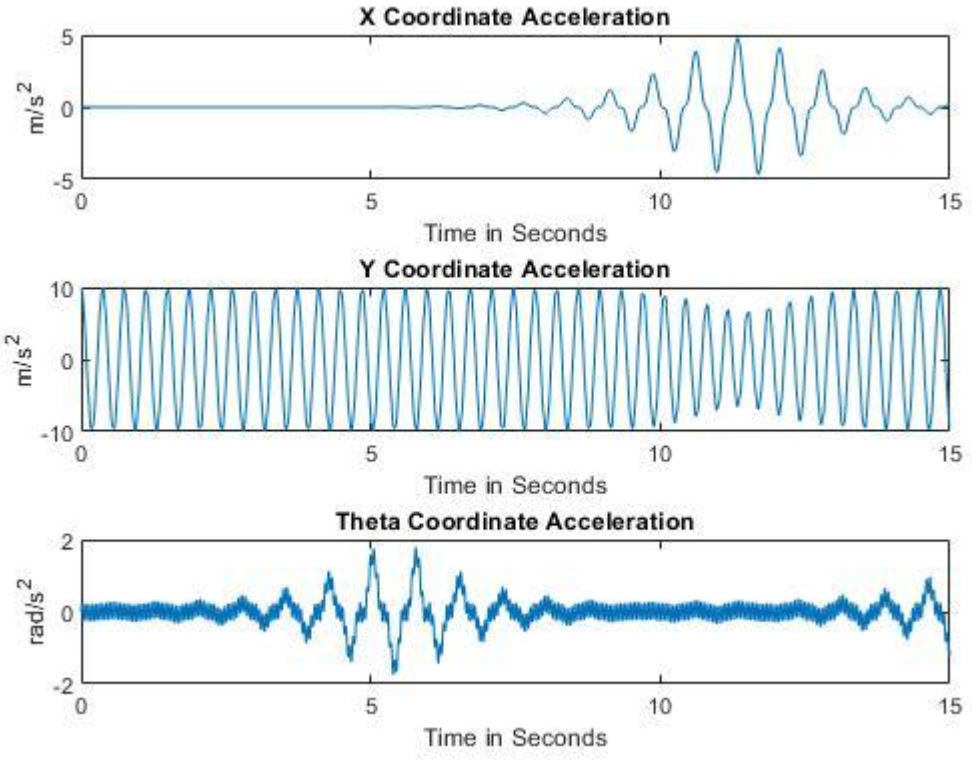

Figure 105: Acceleration results for excitation in θ coordinate

Figure 106 presents the acceleration plots for each coordinate on a single plot, while Figure 107 presents the normalised results from 0 to 4.5 seconds and Figure 108 presents the results from 4.5-15 seconds. There exists energy transfer from the y coordinate to the x coordinate. From 0-4.5 seconds the x coordinate experiences the excitation frequency, this does continue to roughly 6 seconds however it is not visible in Figure 108. The x coordinate continuously increases in acceleration until a point in time where it becomes in phase with the y coordinate. Thereafter the x coordinate no longer experiences the excitation frequency and gains energy from the y coordinate. The region defined by A presents subtle changes in the accelerations for the y coordinate which is transferring energy to the θ coordinate, the energy transfer to the θ coordinate is most evident when inspecting Figure 107.

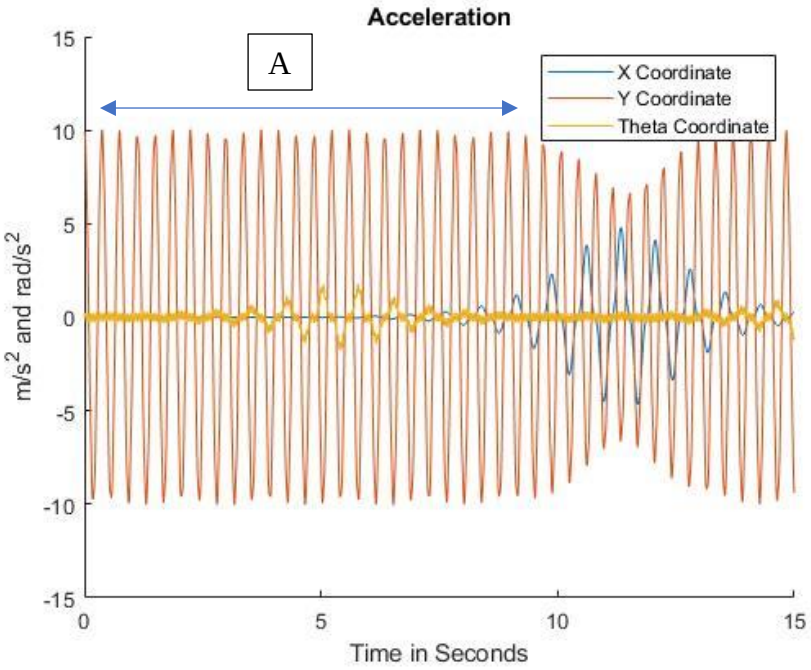

Figure 106: Acceleration results on a single plot for excitation in θ coordinate

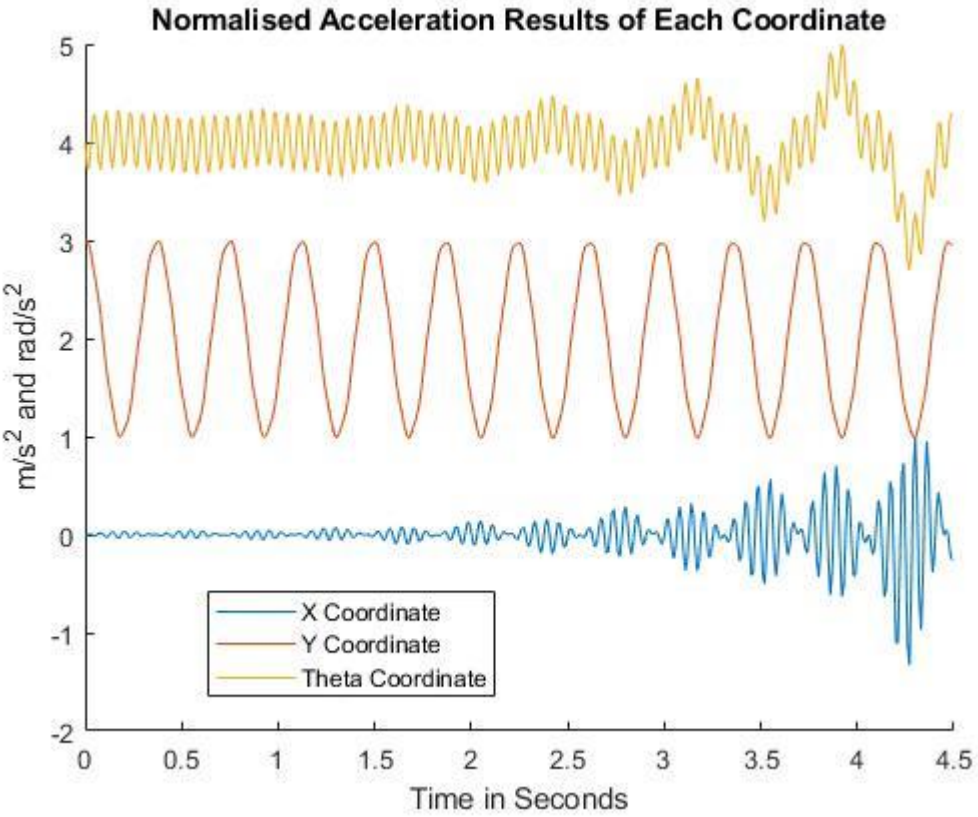

Figure 107: 0 to 4.5 seconds for excitation in θ coordinate

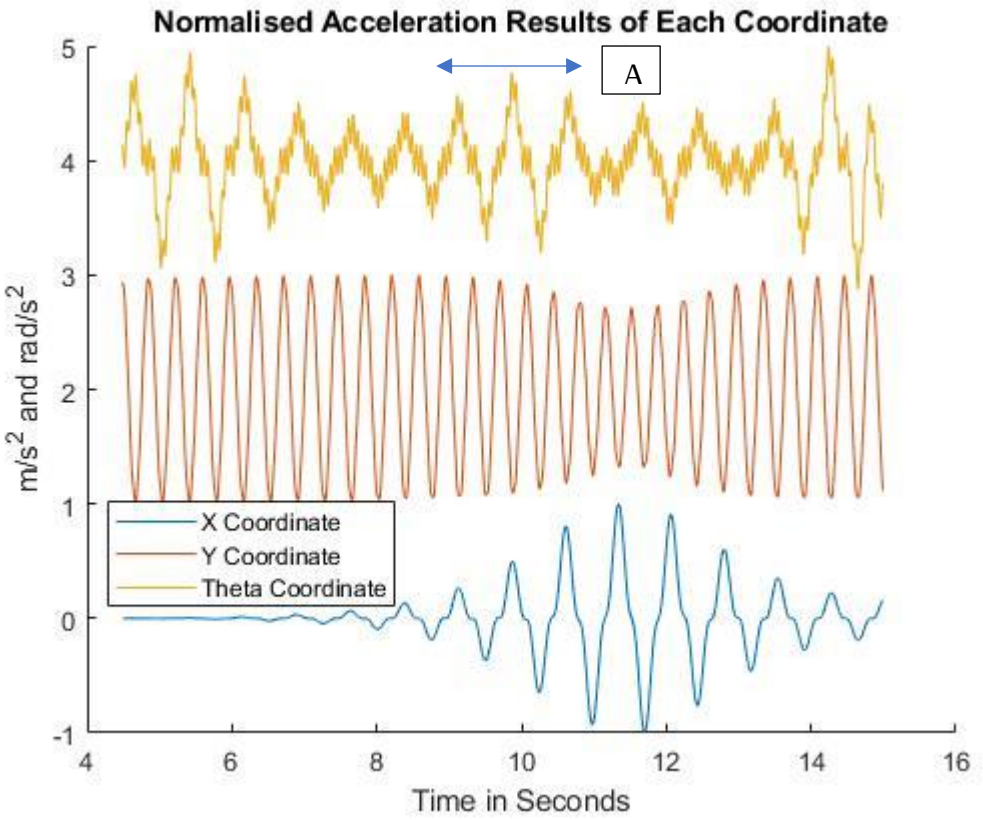

Figure 108: 4.5-15 seconds for excitation in θ coordinate

Using the same methodology as presented previously Term A and B can be plot with various other quantities of the differential equations, this is presented by Figure 109 and Figure 110. The results are as expected, the small displacements of the θ coordinate cause Term A to develop numerical values close to 0, this allows Term A to develop far larger numerical values. During the period where energy is transferred to the θ coordinate larger numerical values are experienced which subsequently allows the $L\sin\theta$ term to develop larger numerical values, this is evident in both Figure 109 and Figure 110.

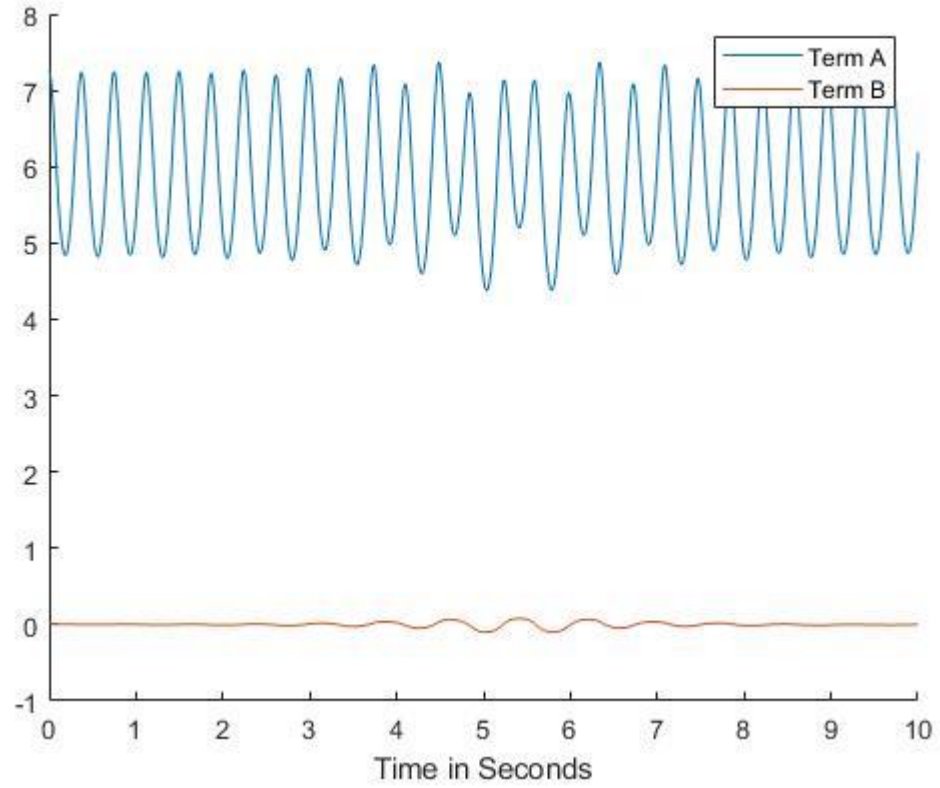

Figure 109: Term A and B for excitation in θ coordinate

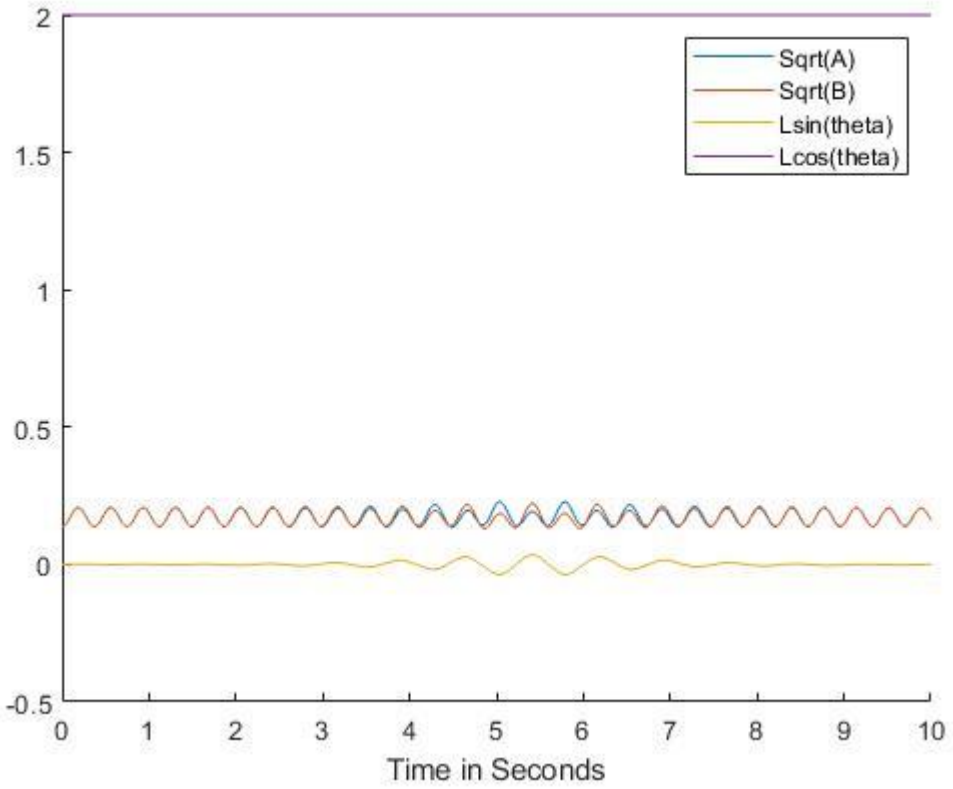

Figure 110: Components of term A and B for excitation in θ coordinate

Figure 111 presents the PSD results for the system, the following can be noted:

- The excitation frequency is only found in the θ coordinate which is where the excitation force is being applied. The excitation frequency exists in the x coordinate for limited time intervals, however this frequency is not presented in the PSD. This can be attributed to the small energy presented at the excitation frequency for the x coordinate and the limited time interval over which it occurs. The pendulum frequency (1.36Hz) presents the highest energy indicating its influence on the system, this is presented by region A (Figure 108).
- There is a 4.1Hz frequency which exists for the θ and x coordinate, this frequency is 2.73Hz (spring frequency) away from the pendulum frequency.
- When considering the y coordinate the spring frequency is presented as expected. The frequencies presented in the x and θ coordinate (1.36 and 4.1Hz) can be seen as sideband frequencies for the y coordinate. The 1.36Hz and 4.1Hz frequencies are symmetrical about spring frequency by 1.36Hz which is equivalent to the pendulum frequency. The system indicates that the spring is the carrier frequency.

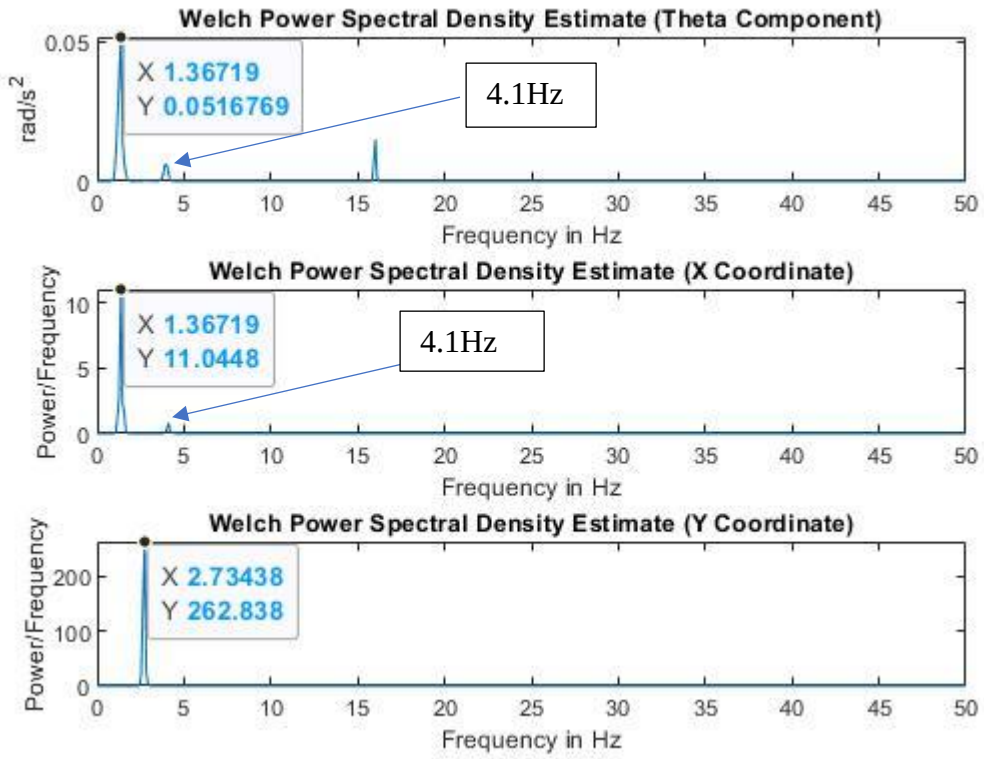

Figure 111: PSD results for the excitation in θ and attributes from Table 10

The resultant accelerations and angular displacement for each spring are presented by Figure 112. The resultant accelerations are in the region of 10m/s^2 with spring A experiencing slightly higher displacements when compared to spring B, this is more pronounced when energy is transferred to the θ coordinate. When there exists energy transfer from the y coordinate to the x coordinate energy is also transferred to the rotational component of each spring. The angular displacement for each spring appears the same when inspecting Figure 112, however when inspecting the numerical values there are small differences, these however are insignificant. This presents a case where the rotation of the rigid bar has little effect on the rotational displacements of the springs.

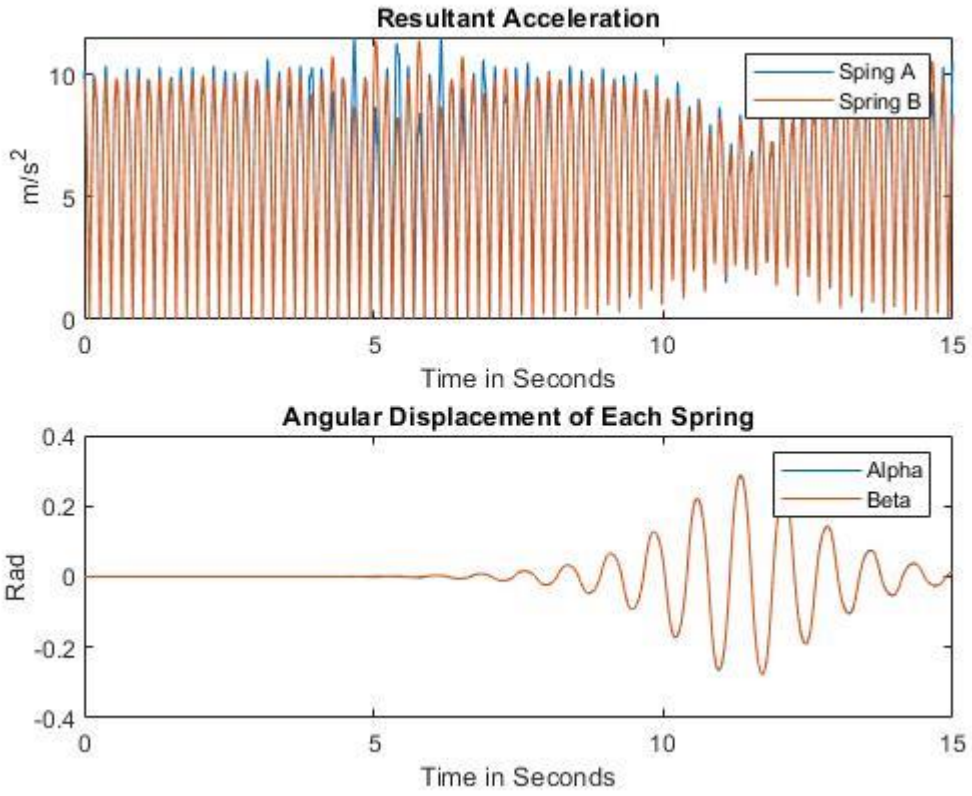

Figure 112:Acceleration results for the attributes in Table 11 and excitation in the θ coordinate

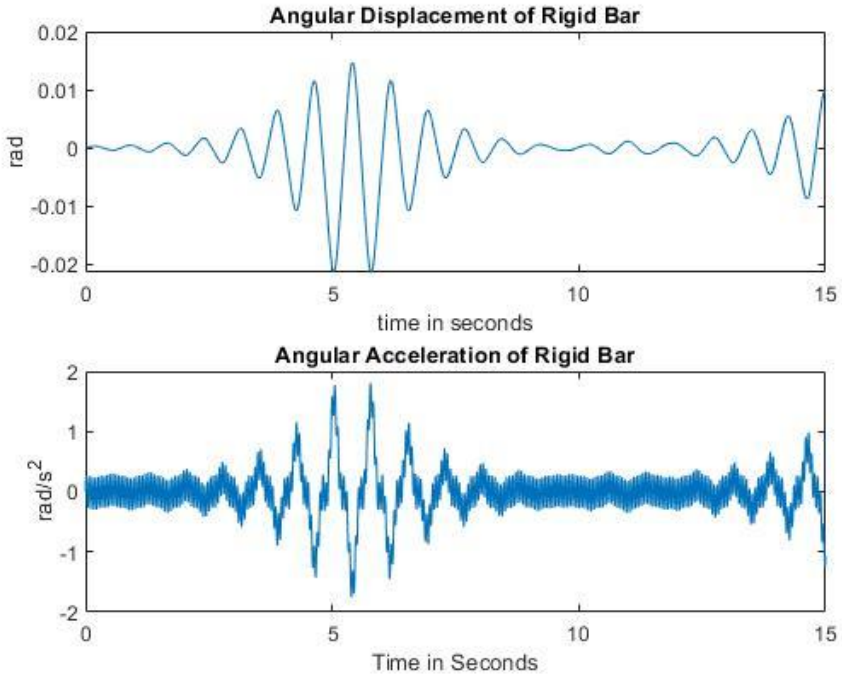

Figure 113: θ coordinate displacement and accelerations for the attributes in Table 11 and excitation in the θ coordinate

The motion of each spring is presented by Figure 114. The motion is divided into two parts, a time period less than 7 seconds and another time period which is above 10 seconds. The time period from 0 to 7 seconds presents motion in the y coordinate this is also supported by the y coordinate displacements presented previously, furthermore deviations from the pure vertical motion can be attributed to the displacements occurring in the θ coordinate. The motion for the time interval greater than 7 seconds presents results where there exist displacements in the x coordinate.

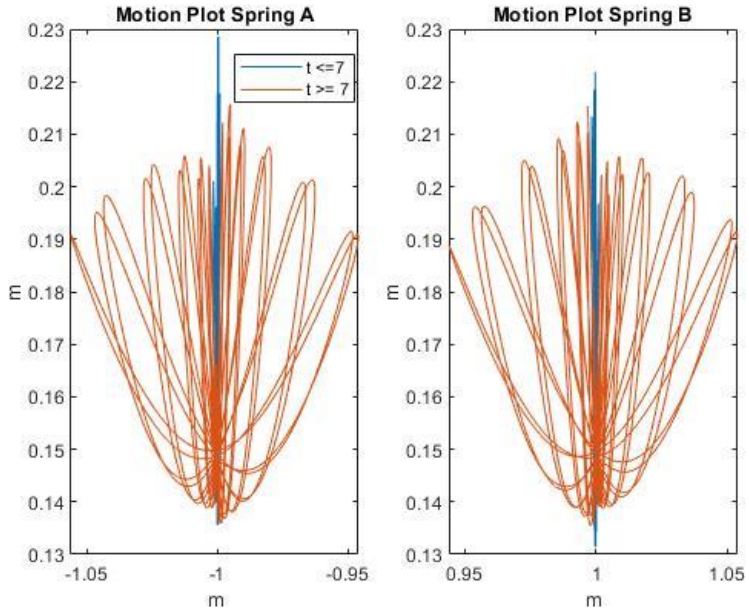

Figure 114: Motion plot of the springs due to excitation in θ and attributes in Table 10

4.6.4. PARAMETRIC EXCITATION WITH DAMPING ON THE θ COORDINATE

The above studies present good correlation with regards to the 3DOF and 2DOF (simplified model) when considering initial conditions applied to both the x and y coordinates. The major difference is that the 3DOF system has the θ coordinate, which due to error accumulation begins to produces inaccurate results. Thus, it is fruitless to continue studying excitation and damping when considering the x and y components individually. This section will study the system as done in the previous chapter however damping will be introduced into the system. The damping will be assigned as 0.01 for each coordinate with the same attributes and conditions assigned above.

The displacement results for each coordinate using the different Matlab solvers is presented by Figure 115. All the solvers present consistent results, thus there is no need to make any comparison to Mathematica. The displacement results reveal very little information regarding the system.

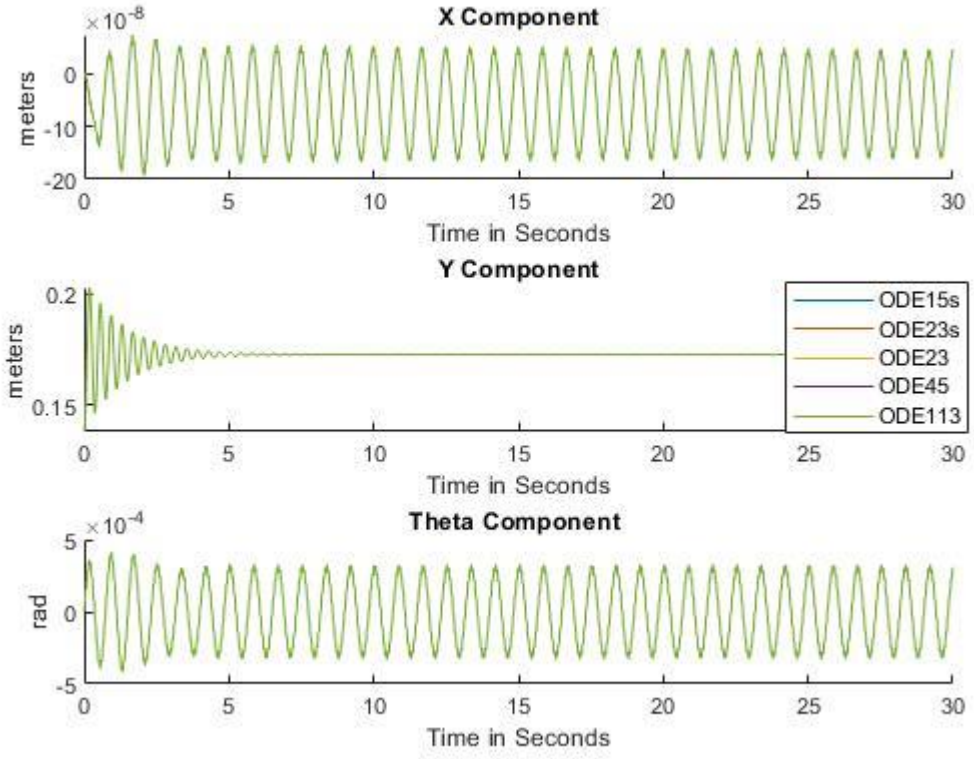

Figure 115: Displacement results for each coordinate using attributes in Table 10 and damping

Figure 116 presents the acceleration results for each coordinate, the results reveal far more information compared to the displacements. It is clear each coordinate experiences the effects of the excitation frequency. It is furthermore clear that there is energy transfer between the x and θ coordinate. By reviewing the normalised acceleration results (Figure 117) which are offset (as performed previously), it is clear that the y coordinate does not present any energy transfer.

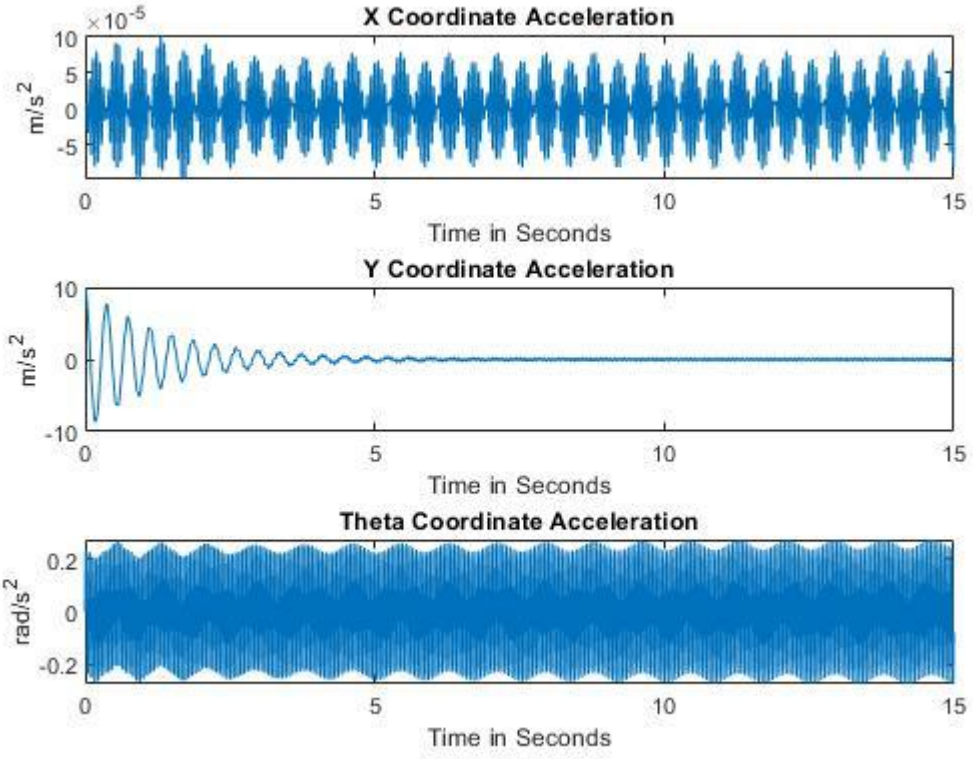

Figure 116: Acceleration results for each coordinate using attributes in Table 10 and damping

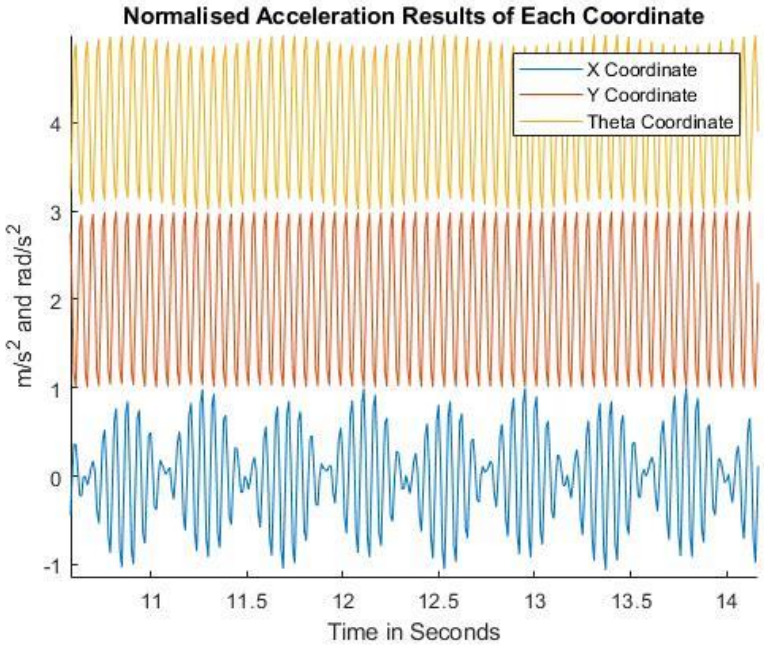

Figure 117: Normalised acceleration results for Displacement results for each coordinate using attributes in Table 10 and damping

Figure 118 presents Term A and B and Figure 119 presents additional attributes of the system. The displacements of the θ coordinate is extremely small which is reflected in the $L\sin\theta$ and $L\cos\theta$ terms, these terms remain at 0 and 1 respectfully since the angular displacement of the rigid bar is extremely small. The $\sqrt{A}$ and $\sqrt{B}$ terms present almost identical results; the deviance can only be found by zooming into the results. Term B remains at 0 due to the small effect the θ coordinate has on the y coordinate, while Term A presents sinusoidal behaviour initial which eventually gets smaller due to the effects of damping.

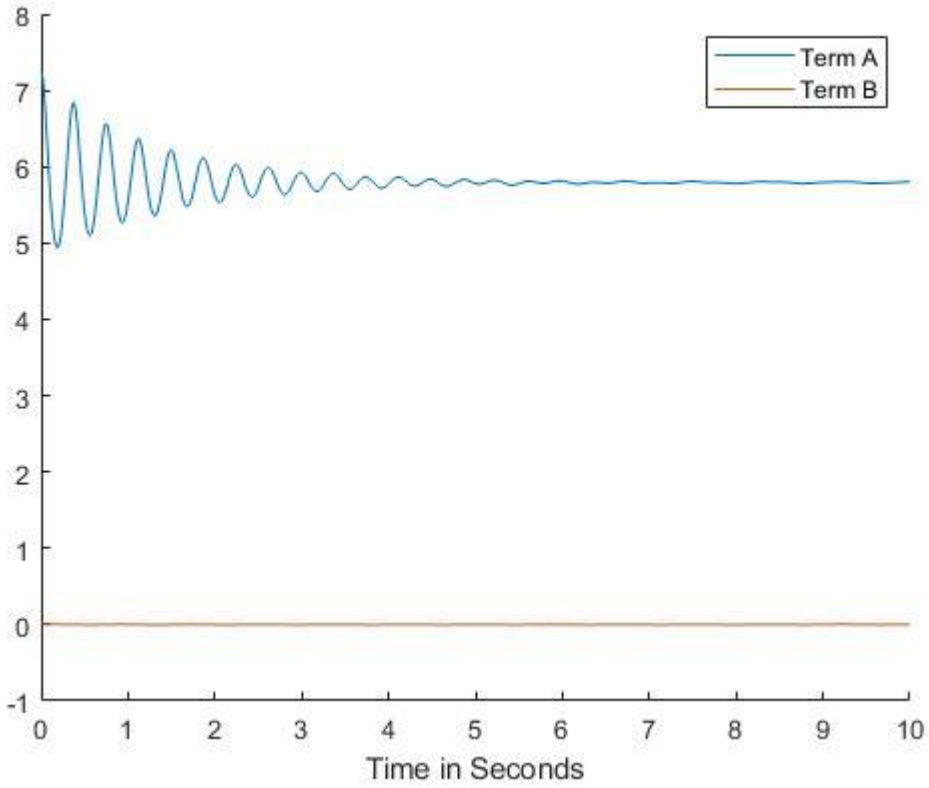

Figure 118: Term A and B Displacement results for each coordinate using attributes in Table 10 and damping

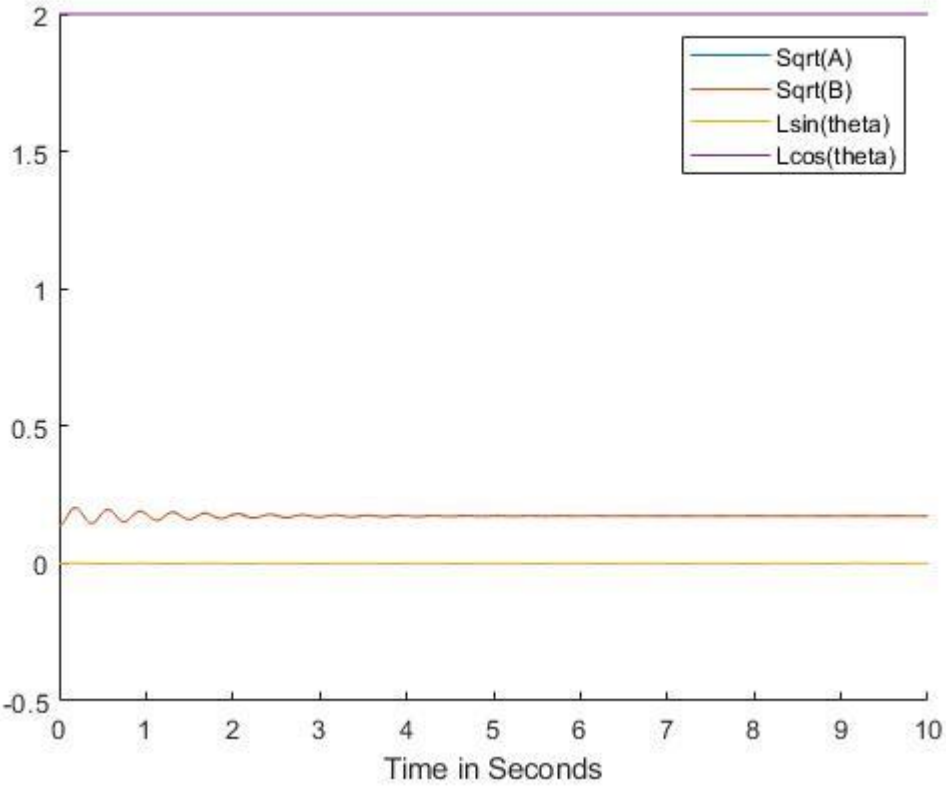

Figure 119: Components of term A and B Displacement results for each coordinate using attributes in Table 10 and damping

The FFT results are presented by Figure 120. The results differ to the undamped case presented by Figure 111. The following can be noted:

- The excitation frequency is found in the y and θ coordinates, this was not the case for the undamped simulation.
- There are sideband frequencies to the excitation frequency which is found in the x coordinate indicating that the coordinate.. The side band frequencies are developed though modulation of the excitation frequency with the modulation being the same as the pendulum natural frequency.
- The x coordinate presents an extremely small amount of energy for its natural frequency. The natural frequency is found to be 1.17Hz which is off from the analytical value of 1.34Hz. The difference in frequency cannot be attributed to the damped natural frequency of the system since it has been shown that there is a small difference between the damped and undamped frequency.
- The spring natural frequency has more energy compared to that of the excitation. This can be attributed to the effects of parametric resonance.
- The results present a system which would still experience parametric resonance due to the natural frequencies of the spring and pendulum being present.

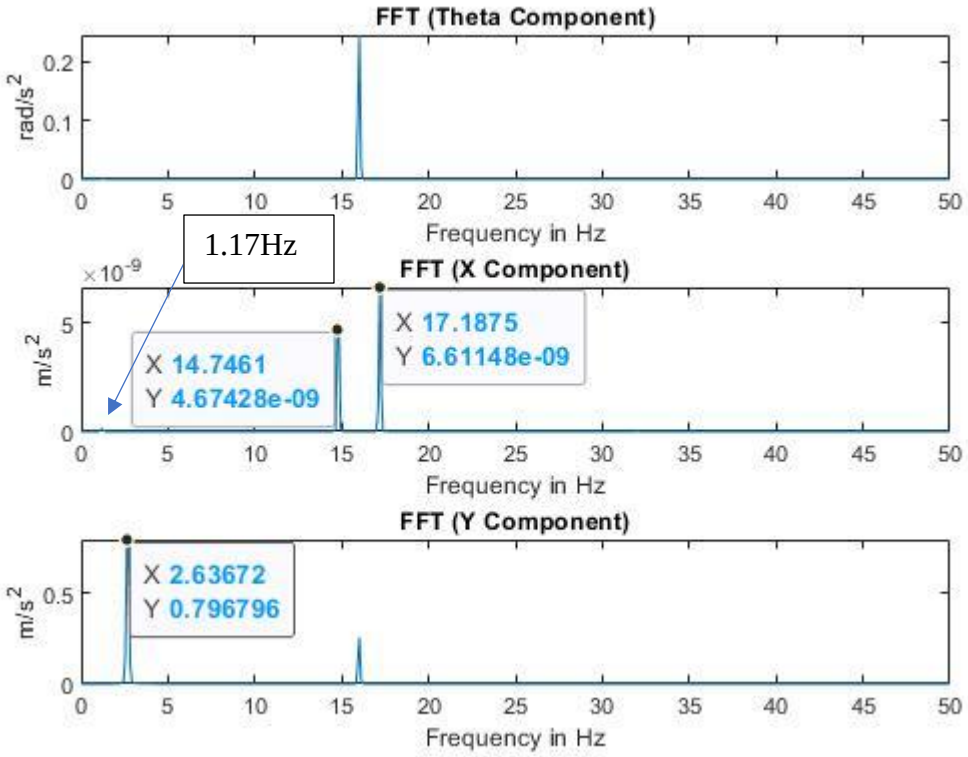

Figure 120: FFT results for 3DOF simulation with attributes from Table 10 and damping

The resultant acceleration results are presented by Figure 121, The effect of damping has reduced the resultant acceleration results dramatically. The elongation/contraction in each spring presents similar magnitudes during the simulation. By reviewing the motion plots presented by Figure 123 the rotational displacement is so small that motion trace for spring A and B presents motion which is always in the same direction. The motion experienced for each spring is however different but in the same direction.

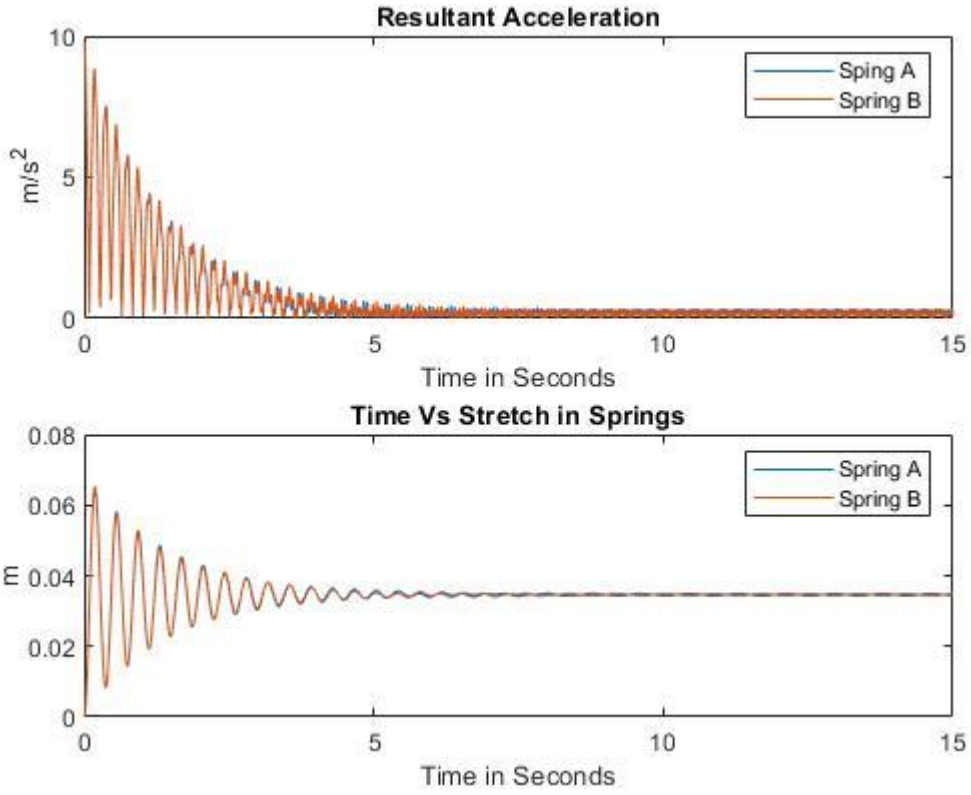

Figure 121:Resultant acceleration results for 3DOF simulation with attributes from Table 11 and damping

The angular displacements of α, β and θ are presented by Figure 122, each spring presents extremely small displacements which can be approximated to 0. This behaviour can be seen in the motion plot presented by Figure 123, where the angular displacements of the θ coordinate present displacements which are in the order of ±30mm which further indicates the small values of θ

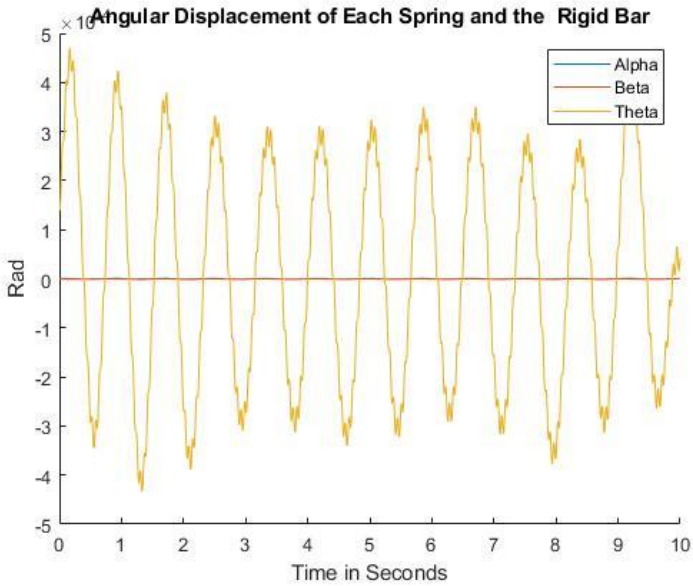

Figure 122: Angular displacement results using attributes in Table 10 and damping

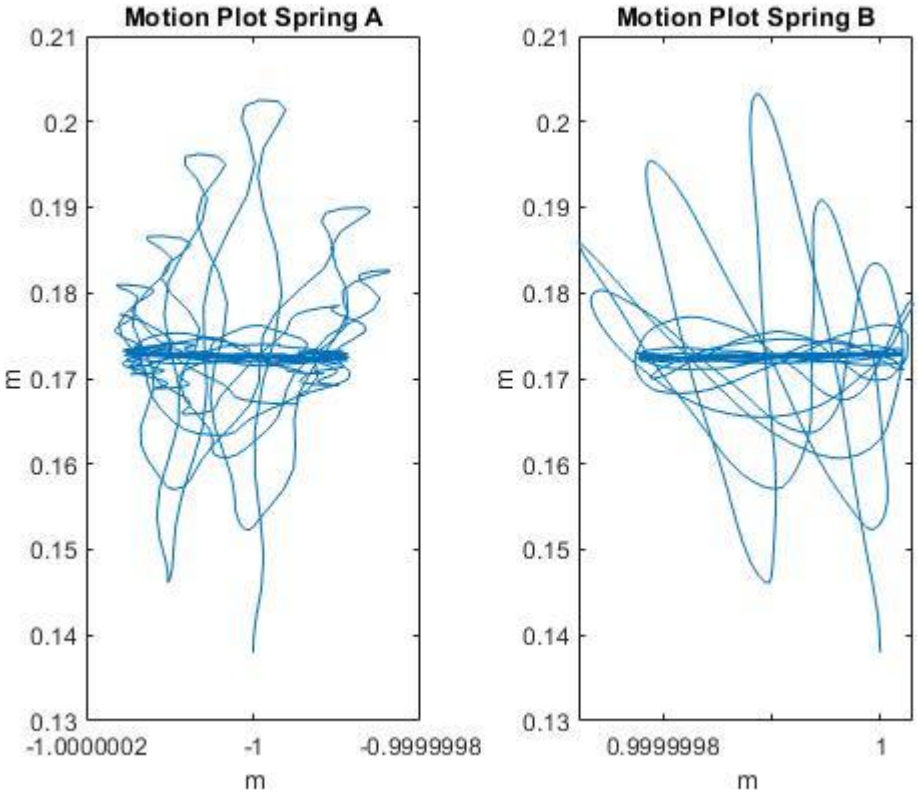

Figure 123:Motion plots for the 3DOF system with damping and attributes from Table 10

4.7. SUMMARY OF THE SIMULATIONS

Table 11 presents a summary of the simulation results studied thus far in the chapter with regards to initial conditions applied to the θ coordinate and excitation applied to the coordinates. For the non-parametrically sized setup the most common energy transfer is from the x coordinate to the θ coordinate. This occurs since the results indicate that the coordinates share the same natural frequency. This case also presents consistency with literature regarding the inclusion of damping assisting with numerical stability, however there are only two simulation cases which have been performed thus no conclusive evidence can substantiate the conclusion.

The parametrically resonant system presents only one case that achieves numerical stability, this case pertains to high frequency excitation (16.67Hz) with damping. All the other cases present numerical instability. The cases where their exists excitation on the x and y coordinates present energy transfer between the x and y coordinates only. This is a logical solution since there is no energy which can be added to the θ coordinate due to it being horizontal throughout the simulation. This would not occur in reality since there always exists deviations in fabrication, loads and load paths which would inherently cause the θ coordinate to displace thus introducing itself into the system.

Table 11: Summary of simulation results

Setup	Excitation frequency			Damping	Intial Conditions	Numerical Stability	Energy Transfer
	x	y	θ		θ		
Non parametric resonant attributes	0	0	0	No	2	Unstable	$\theta \leftrightarrow x$
	0	0	0	Yes	2	Stable	$\theta \leftrightarrow x$
Parametric resonant attributes	0	0	0	No	2	Stable	$\theta \leftrightarrow x$
	0	0	0	Yes	2	Unstable	$x \leftrightarrow y \; and \; \theta$
	1.34	0	0	No	0	Unstable	$x \leftrightarrow y$
	1.34	2.68	0	No	0	Unstable	$x \leftrightarrow y$
	0	0	16.67	No	0	Unstable	$x \rightarrow y \; and \; y \rightarrow \theta$
	0	0	16.67	Yes	0	Stable	$\theta \leftrightarrow x$

4.8. SIZING A VIBRATING SCREEN

This section discusses and develops adequate attributes to size a screen which can produce parameters adequate for screening purposes.

The system attributes presented by Table 10 will be adopted since the parameters have already been sized for parametric resonance and in addition the system has been studied in detail. The forcing functions applied to the system will be studied in greater detail with a focus on the displacement and acceleration results as these parameters are critical for efficient screening. From the previous simulations it is known that the y coordinate is greatly affected by damping and thus requires large excitation to develop adequate accelerations and displacements. This section will focus on the application of excitation forces on the x and θ coordinates to develop criteria for screening.

4.8.1. EXCITATION ON THE x AND θ COORDIANTE

In order to develop parameters for screening the following will be followed:

- Simulations will be performed by keeping the excitation on the θ coordinate at 0 and the x coordinate will be incremented by $1000\,\mathrm{N}\sin(\omega_p t)$ where N will have values from 1 to 10. This case will be known as XN and ω_p will be assigned as the pendulum frequency.
- From the previous simulations it is known that an excitation frequency of 16.6Hz applied to the θ coordinate will develop small displacements, thus it would be feasible to run a simulation where the excitation frequency is incremented. The excitation force will be assigned as $1000\sin(N\omega_\theta t)$, where N will represent increments of the excitation frequency. Ten simulations will be performed, each having an increment of 0.3Hz which then results at 3Hz when N = 10.
- Damping will be assigned as 0.01.

The above-mentioned methodology will assist in developing data which will allow one to adequately size parameters for the vibrating screen. It will allow one to gain insight into however the behaviour changes with regards to changes in the excitation force.

From previous simulations it is known that the system develops inaccuracies. The θ coordinate can be used to assess inaccuracies, thus the displacement results for the θ coordinate will be plot for each simulation case using various Matlab solvers as done previously. This will allow one to determine when and where the errors have been produced.

4.8.1.1. CASE XN

The displacement results for the θ coordinate is presented by Figure 124. The simulation results do not present any labels, headings, and values for each axis as these clutters the graph making it unreadable. The first plot starts with N = 1 with each plot below increasing in value. The θ values are expected to be approximately 0. The first 3 plots present θ displacements which are in the order of $\times 10^{-11}$, which can be considered insignificant. The errors become significant from N = 6 onwards.

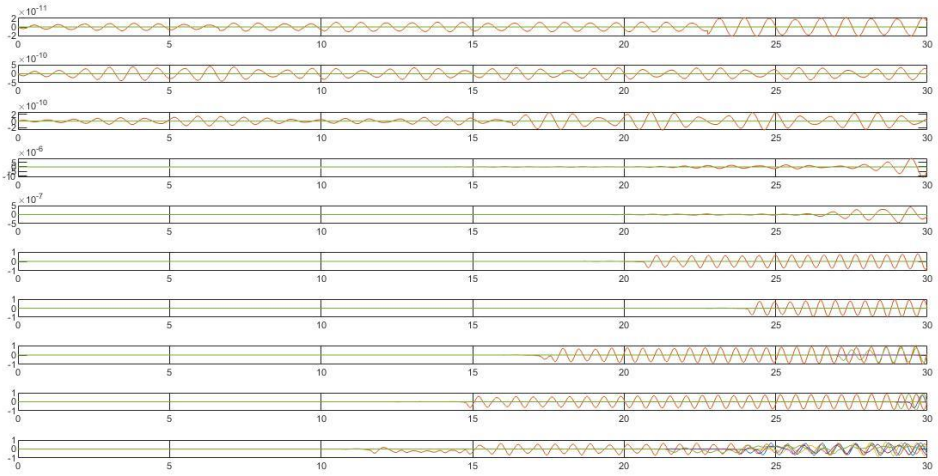

Figure 124: θ displacement results for simulation XN

The results for each simulation can be found in APPENDIX E – RESULTS FOR THE $\boldsymbol{XN}$ CASE, the time interval is 10 seconds, this was chosen as this allows for accurate results for each analysis. XN7 onwards presents the highest resultant acceleration results, these results are well below that experienced by the SD18/36 vibrating screen.

4.7.1.2. CASE θN

The results for each simulation can be found in APPENDIX . At N = 3 and 4 (0.9Hz and 1.2Hz) there exist large accelerations for all the coordinates. The excitation frequencies are close to that of the pendulum and it is clear that parametric resonance is taking place. This behaviour is also found for N = 9 (2.7Hz) which is close to the natural frequency of the spring, however it is far less pronounced. All the other results do not look promising as they produce extremely small numerical values.

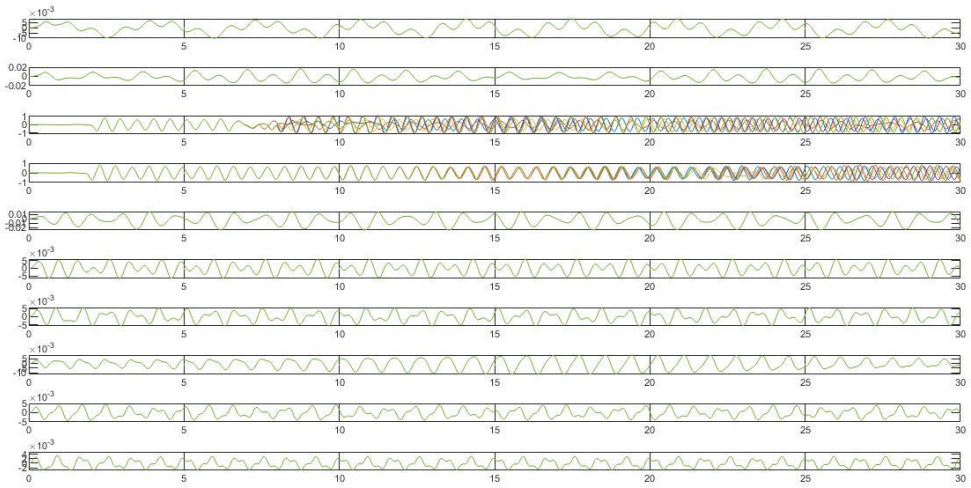

Figure 125: θ excitation with incrementing the excitation frequency

Figure 126 presents the normalised acceleration results as done previously for the case where excitation on the θ coordinate is applied at the natural frequency of the spring, while Figure 127 presents the results for excitation applied to the θ coordinate at the natural frequency of the pendulum. The results for excitation at the spring natural frequency only present autoparametric behaviour between the x and θ coordinate. This behaviour is such due to the x and θ coordinate sharing the same frequency thus enabling this behaviour. For the case where the excitation frequency is set to the natural frequency of the pendulum, far more complex energy transfer has occurred. The y coordinate transfers energy to both the x and θ coordinate, this also occurs in reverse.

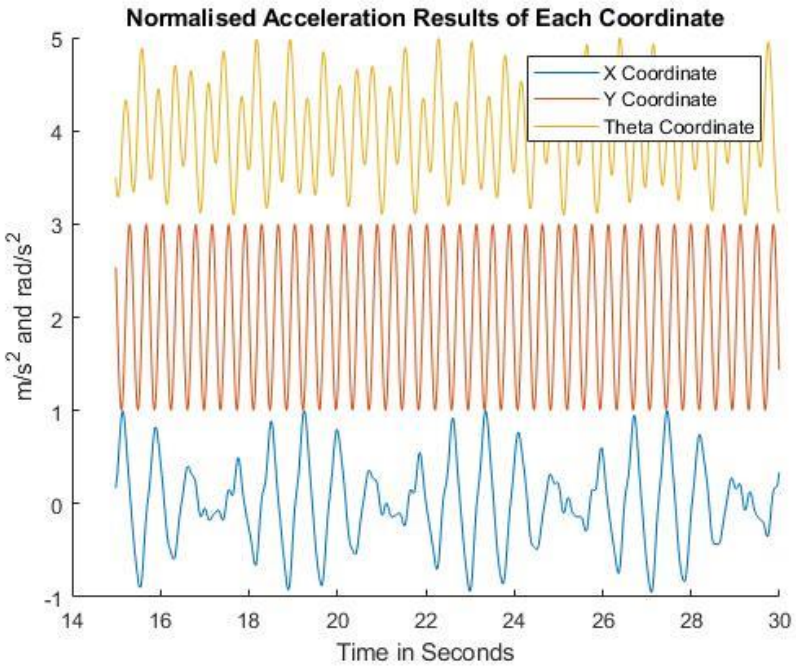

Figure 126: Normalised acceleration results for θ coordinate excitation at the spring natural frequency

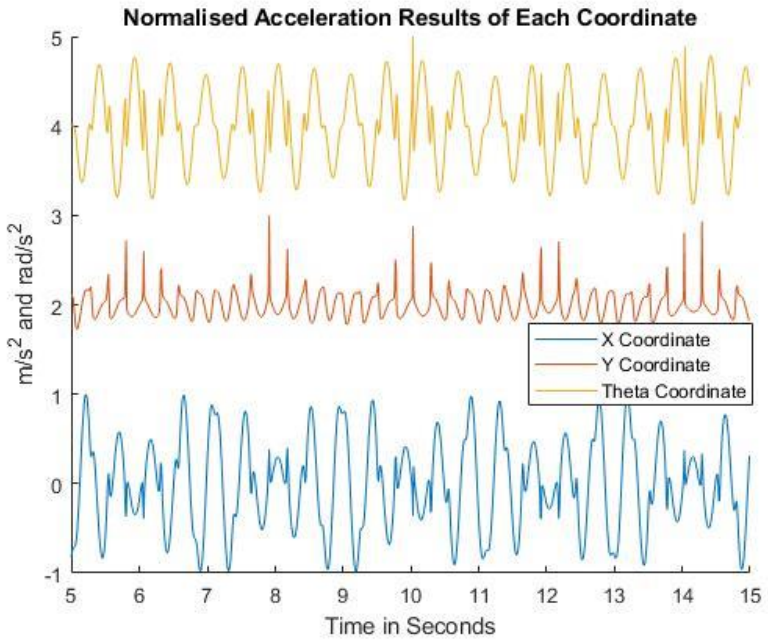

Figure 127: Normalised acceleration results for excitation applied to θ coordinate at the pendulum frequency

To understand the two excitation frequencies in further detail the acceleration and displacement results are plotted as presented by Figure 128 and Figure 129. The displacements and accelerations for the excitation at the natural frequency of the spring produce dramatically lower results compared to the case where excitation is assigned at the natural frequency of the pendulum. The y coordinate displacements and accelerations for both cases are large enough such that both cases can be seen on a single plot, this however is not the case for the x and θ coordiante. The 2.68Hz excitation does not present the perturbation for the y coordinate as developed for the 1.34Hz excitation.

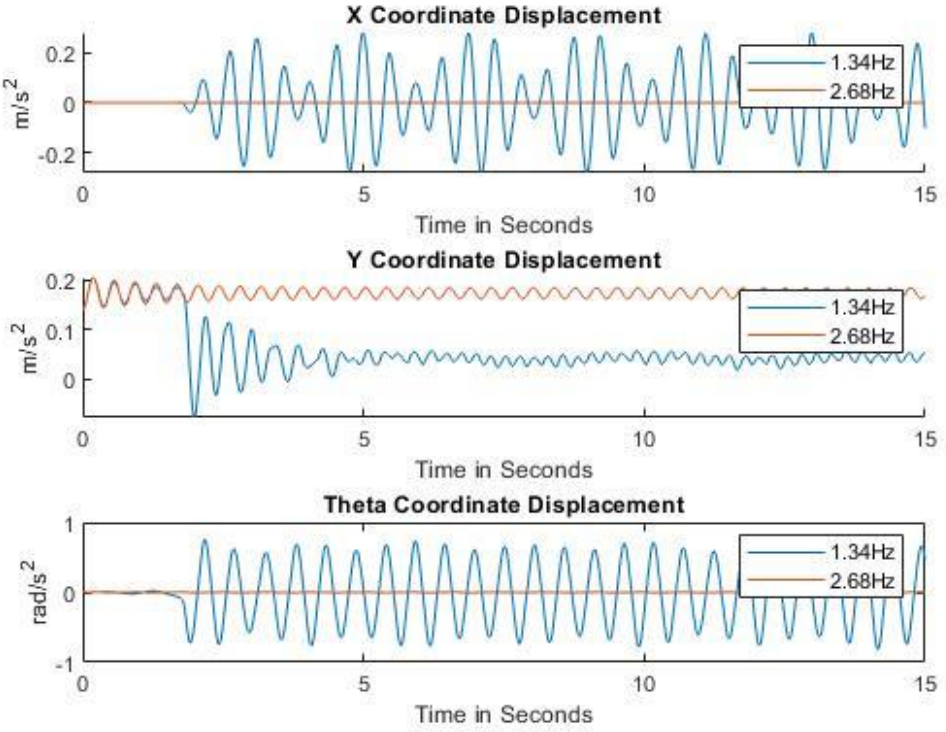

Figure 128: Displacement results for excitation at pendulum and spring natural frequency

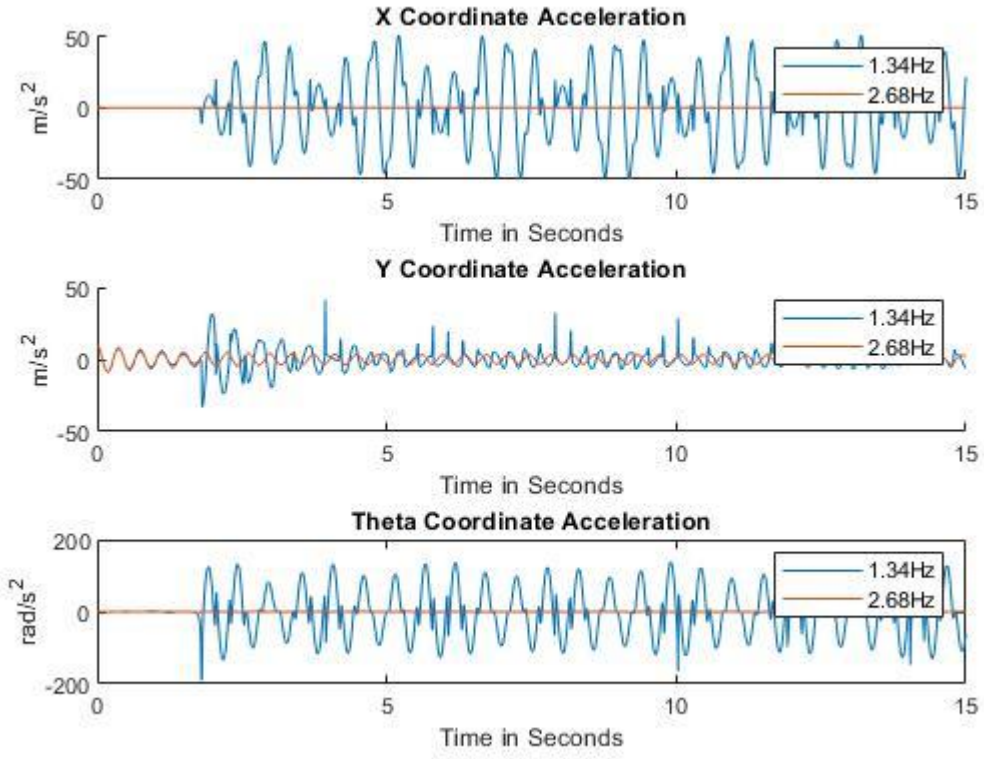

Figure 129: Acceleration results for excitation at pendulum and spring natural frequency

Based on the above simulations it can be concluded that for excitation frequencies close to that of the pendulum natural frequency, high accelerations and displacements can be achieved in all coordinates.

Another set of simulations will be performed where the excitation force on the θ coordinate will be varied while the excitation frequency will be set to develop parametric resonance (1.34Hz). Figure 130 presents the θ coordinate displacements for an incremented excitation of $N \times 100\sin(\omega_\theta t)$ where N is incremented from 1 to 10. For values of N less than 6 the displacements are small and generally consistent regardless of the magnitude of the excitation force. For values of N greater than 6 (including 6) the displacements dramatically increase to values ranging from ±0.65 to ±0.85rad. In all instances parametric resonance exists.

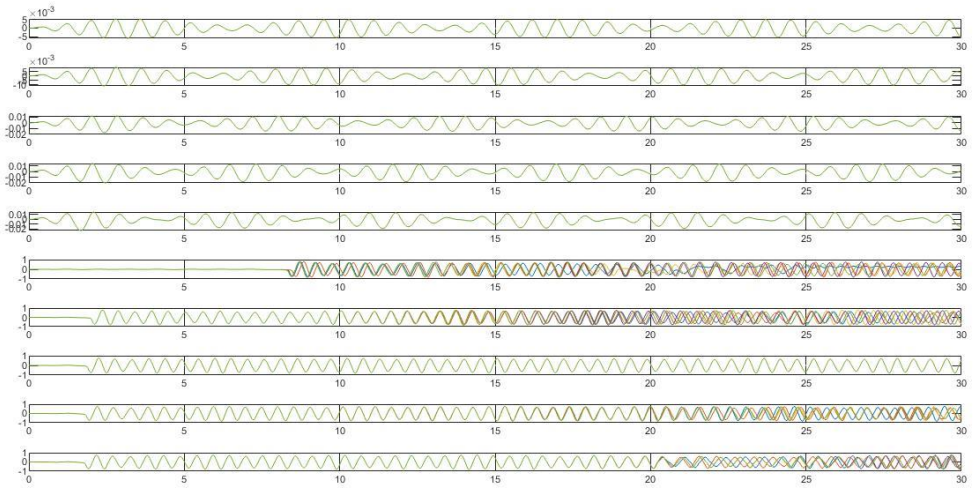

Figure 130: Excitation at 1.34Hz in the θ coordinate with incremented dynamic loads

Values of *N* equal to 7 onwards present good consistency with regards to the various solvers, the shortest time period with accurate results is just below 10 seconds. The displacement and acceleration results for N = 8,9 and 10 are presented by Figure 131 and Figure 132. The peaks present very similar results thus implying that the increase in the excitation force presents a minimal effect on the system. For the N = 8 case, there is a significant phase shift compared to the other results. The N = 9 and 10 case also presents phase shifts however they are less pronounced compared to the N = 8 case.

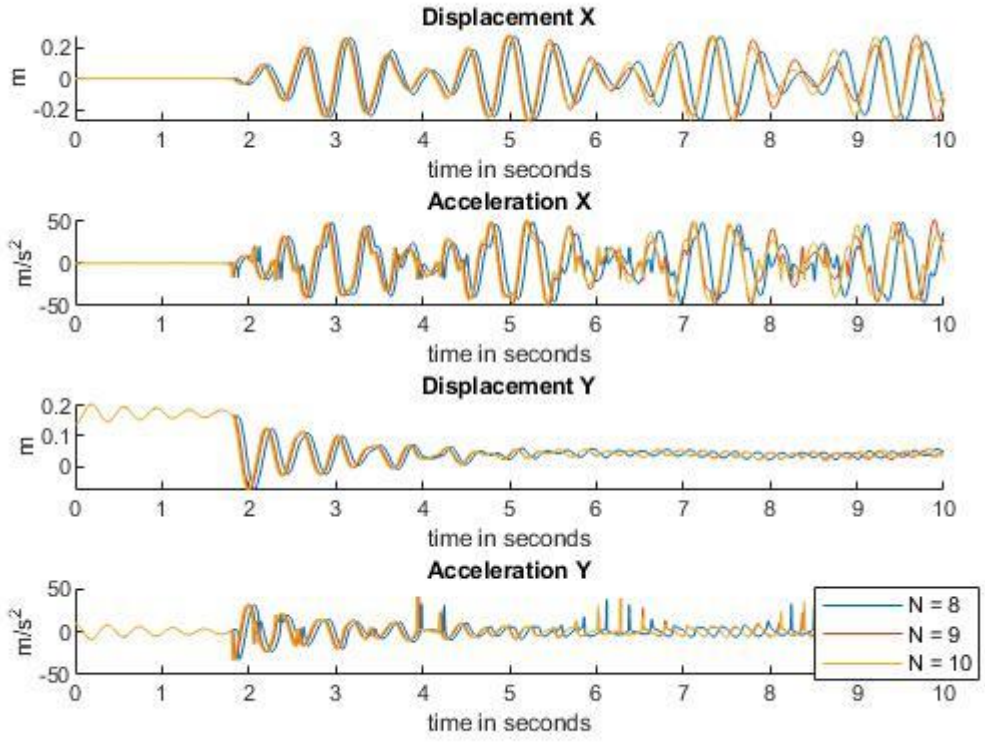

Figure 131: Displacement and accelerations results for varying values of N at 1.34Hz excitation

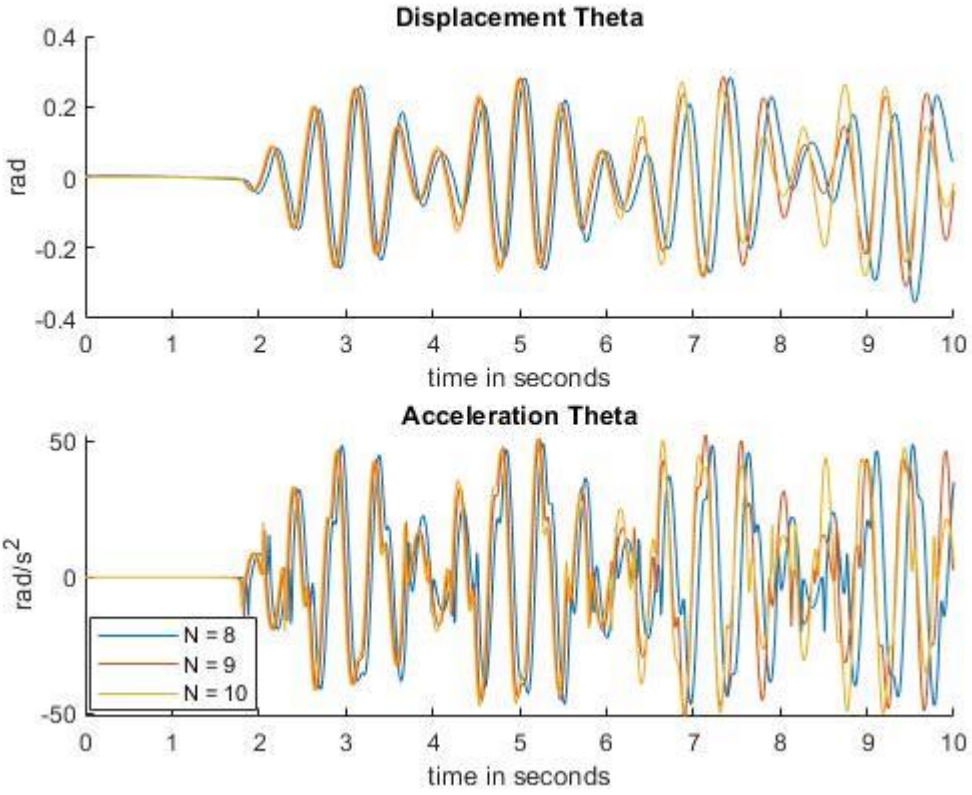

Figure 132: Displacement and acceleration results for varying values of N at 1.34 Hz excitation

Figure 133 presents the motion plot for various values of N. The motion is very similar regardless of the difference in the excitation force being applied. The motion consists of a seesaw movement coupled with movement in the x coordinate.

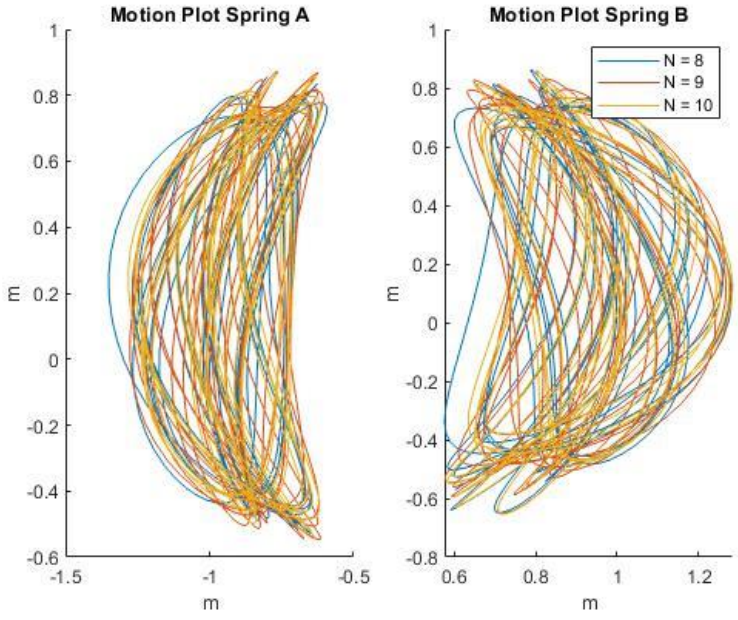

Figure 133:Motion plot for incremented excitation using 1.34Hz excitation

Table 12: Final parameter for the 3DOF vibrating screen

Attribute	Numerical Value	Units
Mass	3755	kg
Spring Stiffness per support	266x2	N/mm
r	0.138	m
Fx	0	N
F_y	0	N
F_θ	1000	N
ω_x	0	Hz
ω_y	0	Hz
ω_θ	1.34	Hz
Damping (all)	0.01	-

Table 12 presents the attributes for the 3DOF model which will be used for the DEM simulations. The acceleration, displacement and motion trace are presented by Figure 134, Figure 135 and Figure 136 respectfully. A detailed representation of the results is presented in APPENDIX B – RESULTS FOR THE 3DOF PARAMETRICALLY SIZED MODEL WITH EXCITATION, with data points being marked with areas of interest. The results can be interpreted in the same manner as done previously.

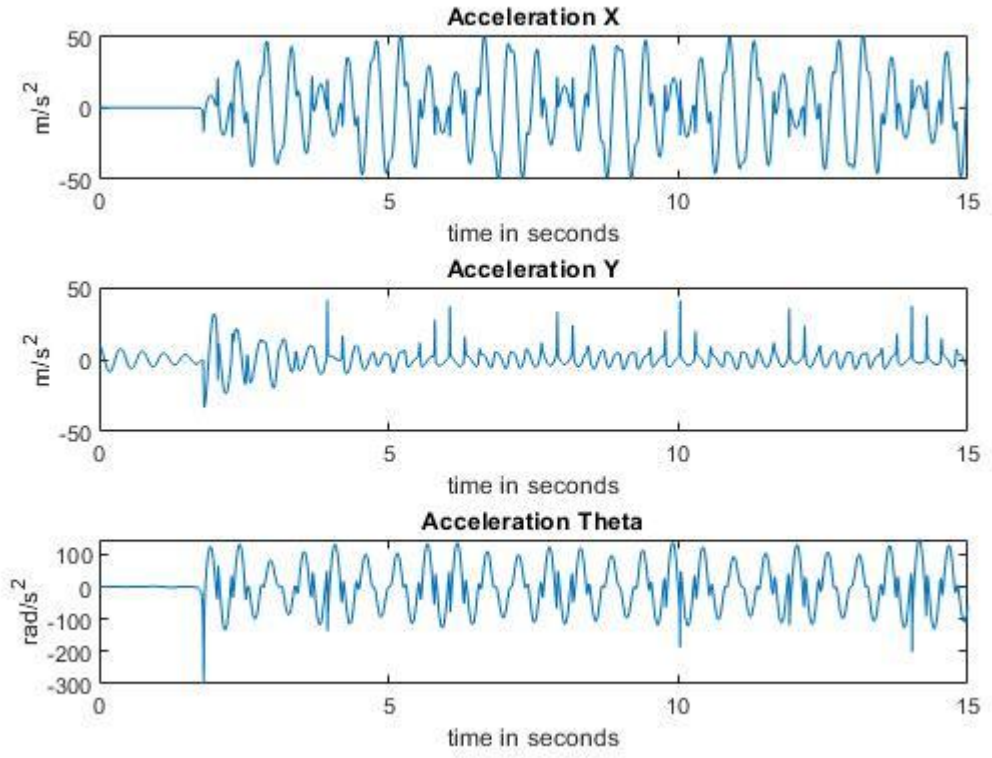

Figure 134: Acceleration results for the final 3DOF model

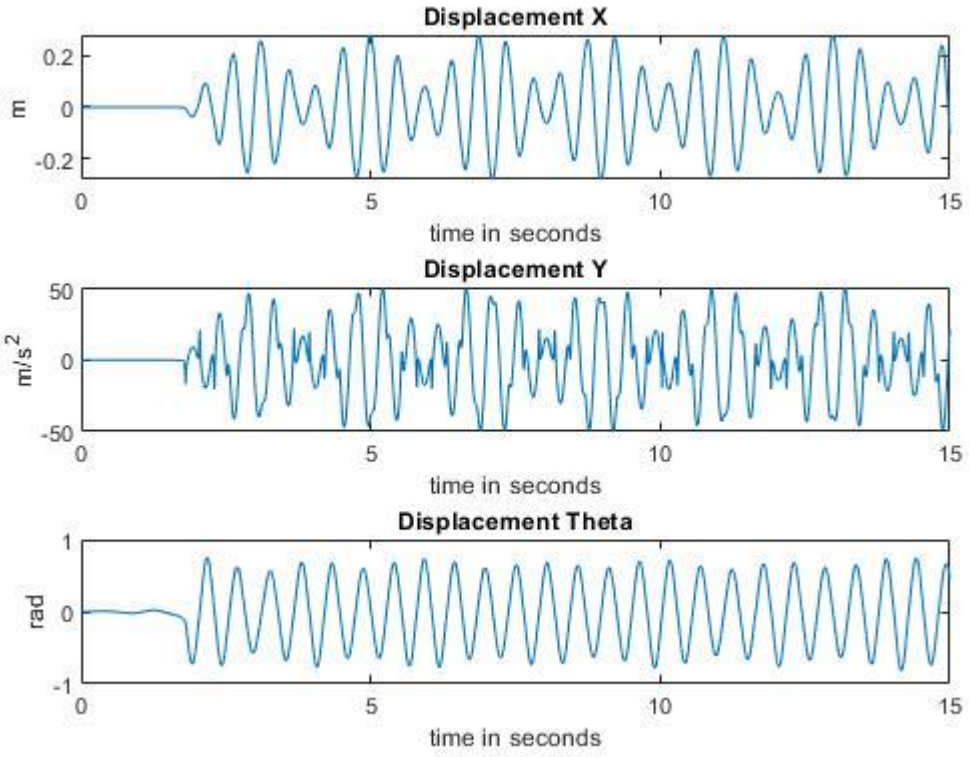

Figure 135: Displacement results for the final 3DOF model

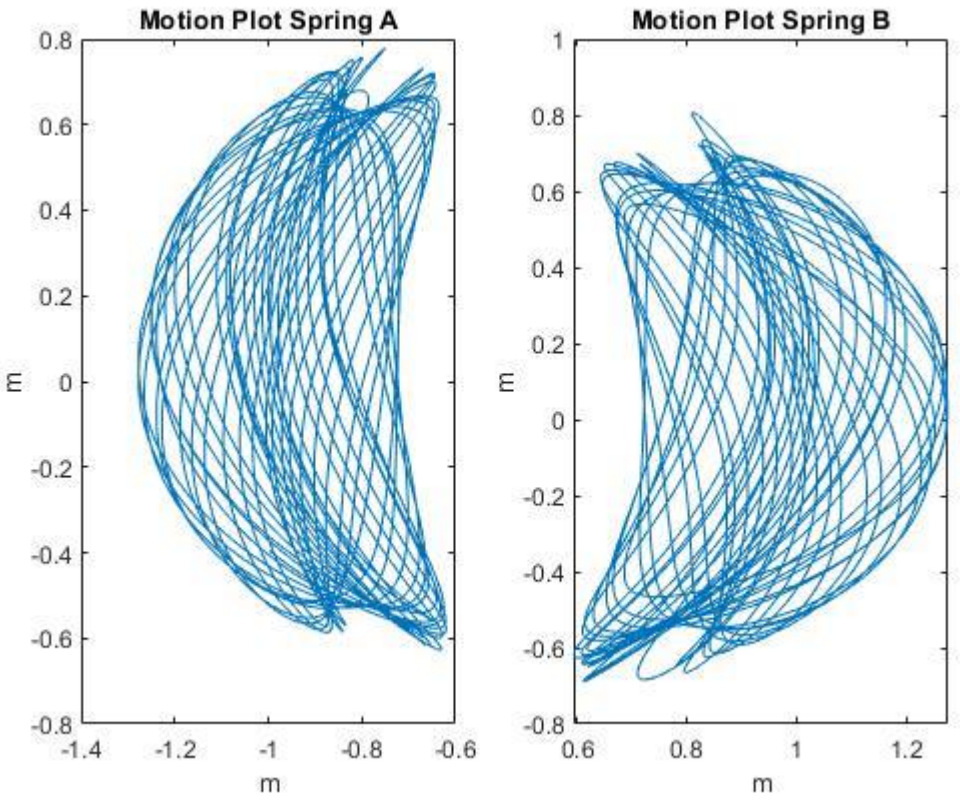

Figure 136: Motion trace for the final 3DOF model

CHAPTER 5: DEM STUDY

This chapter will deal with the DEM study of the 3DOF system using the results attained from assigning parameters presented by Table 12. The DEM study will be performed using LIGGGHTS, which is an opensource particle simulation software. The procedure for installing LIGGGHTS can be found in APPENDIX G – LIGGGHTS INSTALLTION.

LIGGGHTS does not have a pre and post processing interface, thus one needs to use a text file to communicate with the software. An output can be saved in VTK format which can then be viewed on Paraview which is an opensource data visualisation tool. Furthermore, CSV files can be created to store data, for this study CSV files will be used to store masses of different types of material in various catchment volumes. The general workflow for a LIGGGHTS simulation is presented by Figure 137.

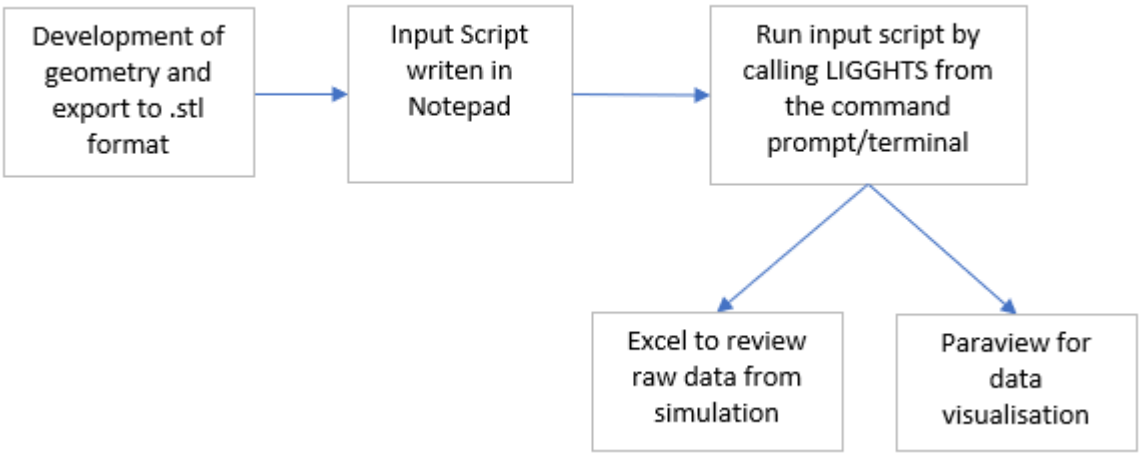

Figure 137: Workflow for the pre and post processing in LIGGGHTS

5.1. MATERIAL PROPERTIES

Zhanfu, Jianzhang and Dong present studies with regards to vibrating screens where DEM simulations have been performed. Each researcher presents different material properties for their simulations. Both Jianzhang and Zhanfu use extremely small particles 0.5-1mm and 0.7-0.9mm respectfully. There is no explicit mention of the materials which are being considered, however based on the particle size it is speculated that the materials are either sand or commercial products such as seeds and grains, both studies also present small screens. Dong presents a large particle range of 2-15mm with an aperture size of 10mm, however the screen is also small, being only 275x150mm.

Material properties and aperture size of the mesh deck can vary based on the study at hand, it is thus impractical to use other studies as a comparison which is initially envisioned. For the case of this study, Table 13 will be used, the data presented is of an actual sieve analysis which has been obtained from process engineers at Weir Minerals.

Table 13: Sieve analysis of a material sample

Feed Analysis		% Particles
Size (mm)	% Passing	
76.2	100	0
63.5	97	3
50.8	91	6
38.1	81	10
25.4	65	16
19.06	56	9
12.7	40	16
9.56	30	10
6.7	20	10
4.78	15	5
0	0	15

Table 13 presents the particle distribution as a percentage. The percentages do not represent a specific particle size, they present a particle size range, however for the presented study the percentages will represent the corresponding particle size. For simplicity all particles smaller than and equal to 9.53mm will be defined by the term "small" while all particles larger than and equal to 12.7mm will be defined by the term "large". The 4.78mm particle will be assigned 20% instead of 5%, the 20% percent includes the 5% from the 4.78 particle size and the reminder presents the particles from 0 to 4.78mm.

Table 14 presents the mechanical properties for the particles. There are numerous sources of research which discuss the topic of calibration for DEM analysis. DEM calibration essentially discusses numerical parameters which can be assigned so that realistic simulations can be developed for a specific scenario. There are papers which also discuss input parameters for DEM simulations and various methodologies and test procedures for how these parameters can be calculated. Many of these papers discuss very specific types of materials and scenarios. In industry DEM calibration often requires significant time and budget in order to study the material so that adequate parameters can be assigned in the simulation environment. Elskamp presents a strategy to calculate various parameters required for DEM analysis, the work presents a consolidation from various other studies (Elskamp, et al., 2017). Due to the study being theoretical in nature coupled with the lack of material samples (Table 13) to perform testing, the mechanical properties will be assumed based on best practice as per conversations with a material handling expert, the resulting properties are presented by Table 14. With regards to Table 14 the following can be noted:

- The coefficient of restitution is defined as the ratio of the difference in velocities before and after collision (Teffo & Naude, 2013). The coefficient of restitution is calibrated at the particle level to get the first approximation. To determine the coefficient of restitution, a particle at the end of a pendulum is dropped so that it can bounce of a wall or another particle which is at rest. By recording the velocities and heights which the particles travel the coefficient of restitution can be calculated (Elskamp, et al., 2017).
- Rolling friction can be estimated in two different ways:
  - The normalized average contact eccentricity of particles

- Energy dissipation associated with relative rotation between particles in contact (Lunlum, et al., 2017)

Table 14: Mechanical properties of the particles

Property	Numerical Value	Units
Density	2800	Kg/m^3
Young's modulus	2.7	GPa
Poisson's Ratio	0.25	-
Coefficient of restitution	0.3	-
Rolling coefficient	0.6	-
Friction Coefficient (particles)	0.5	-
Friction Coefficient (boundary and particles)	0.3	-

5.2. SCREEN AND MESH DECK MODEL

It was initially envisioned that the feed and discharge of the 3DOF will be in line (parallel) with the x coordinate thus requiring material to flow along the x axis from the feed to the discharge. Due to the large motion experienced by the 3DOF model there are several difficulties which arise:

- The location of material being fed on the deck will vary greatly since there is large displacements occurring in the x coordinate. This will reduce the available screening area as material will have less distance to cover in certain circumstances. It is general screening practice to have the feed as far back as possible (first set of blocks on the feed end Figure 138, marked "feed end")
- The discharge of the screen will not have a fixed location in the x axis thus making the chute work complex, furthermore it may not be feasible/possible to design chutes which will cater for such movement
- The high accelerations and large displacements may cause material to be thrown off the vibrating screen. The feed location will vary over the length of the screen, this requires a large area of the screen be open to facilitate feed, this ultimately means that there is a larger area for material to also escape.

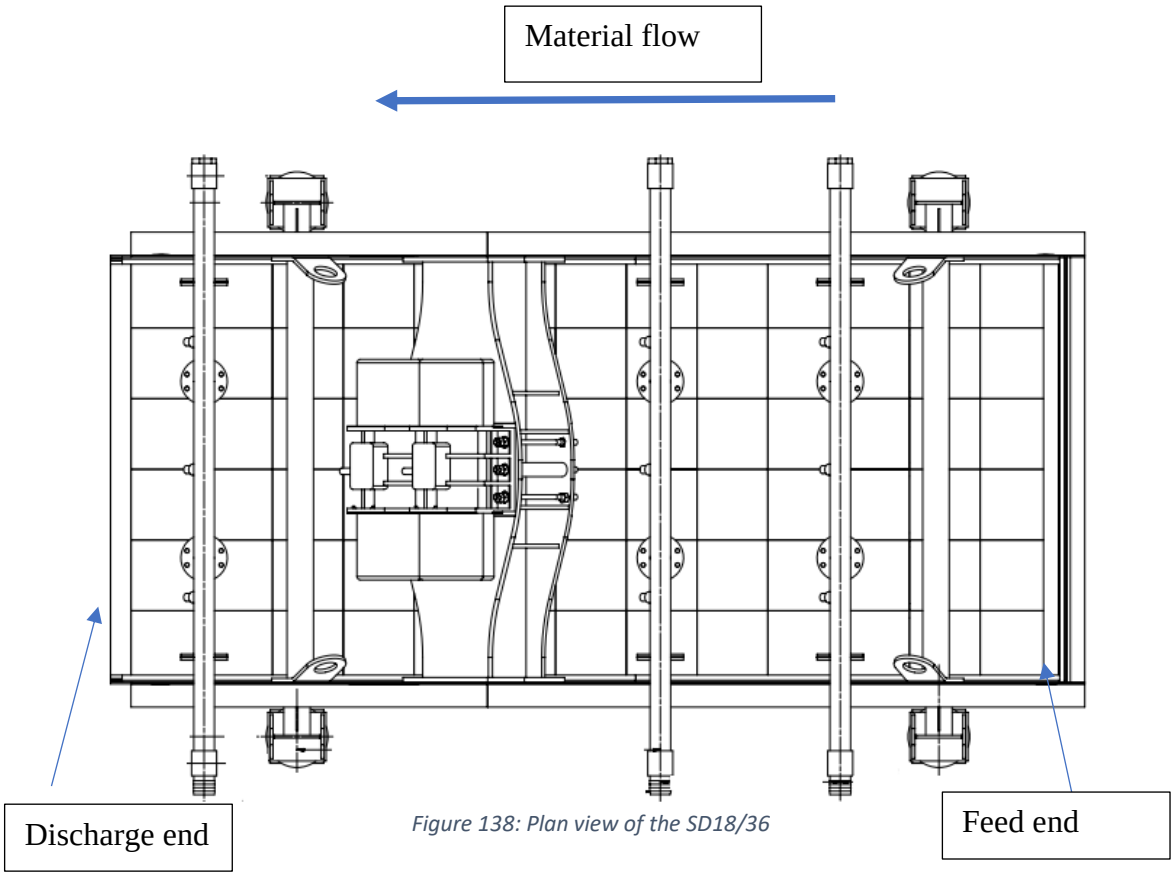

Figure 138: Plan view of the SD18/36

In order to mitigate the issues presented above the 3DOF system will be fed along the *z* axis, thus material will be thrown along the width of the screen as opposed to been thrown along the length of the screen. The feed can be localised over a smaller area as it is speculated that the rocking motion will cause the material to stratify over the width of the deck. Uneven material distribution over the width of the deck is common in screening, this behaviour is known to reduce the efficiency of the vibrating screen. The cause of the issue is generally attributed to poor feeding of the vibrating screen.

With the proposed feed along the *z* axis, a horizontal deck will not promote material to move from the feed end to the discharge end, thus is it speculated that the horizontal deck will develop poor screening. To facilitate movement along the screen deck, the deck will be inclined.

The screen deck model has been developed on a CAD package by Siemens called NX. CAD software generally does not allow for good quality exports of stl files (the file format used by LIGGGHTS) when developing complex geometry, thus conversion of the files is done on Gmsh. Gmsh is an opensource 3D finite element mesh generator that also has a built in CAD engine and post-processor (Christophe, et al., 2022). Figure 139 presents the workflow used to develop stl files which are fit for use on LIGGGHTS.

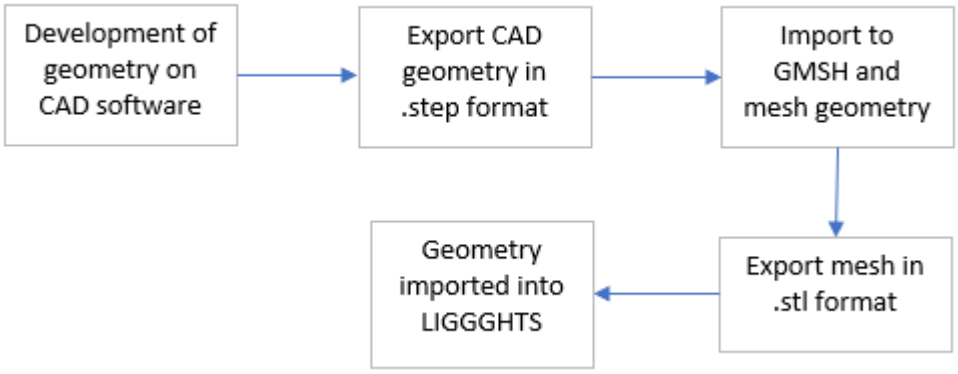

Figure 139: Work flow diagram for the development of geometry in. stl format

Figure 140 presents a portion of a mesh deck with critical dimensions. In reality mesh decks have much smaller dimensions between the apertures since the deck is made from wire. The 12.5mm between apertures has been assigned as this value allows for the development of a good quality stl mesh resulting in no geometry errors.

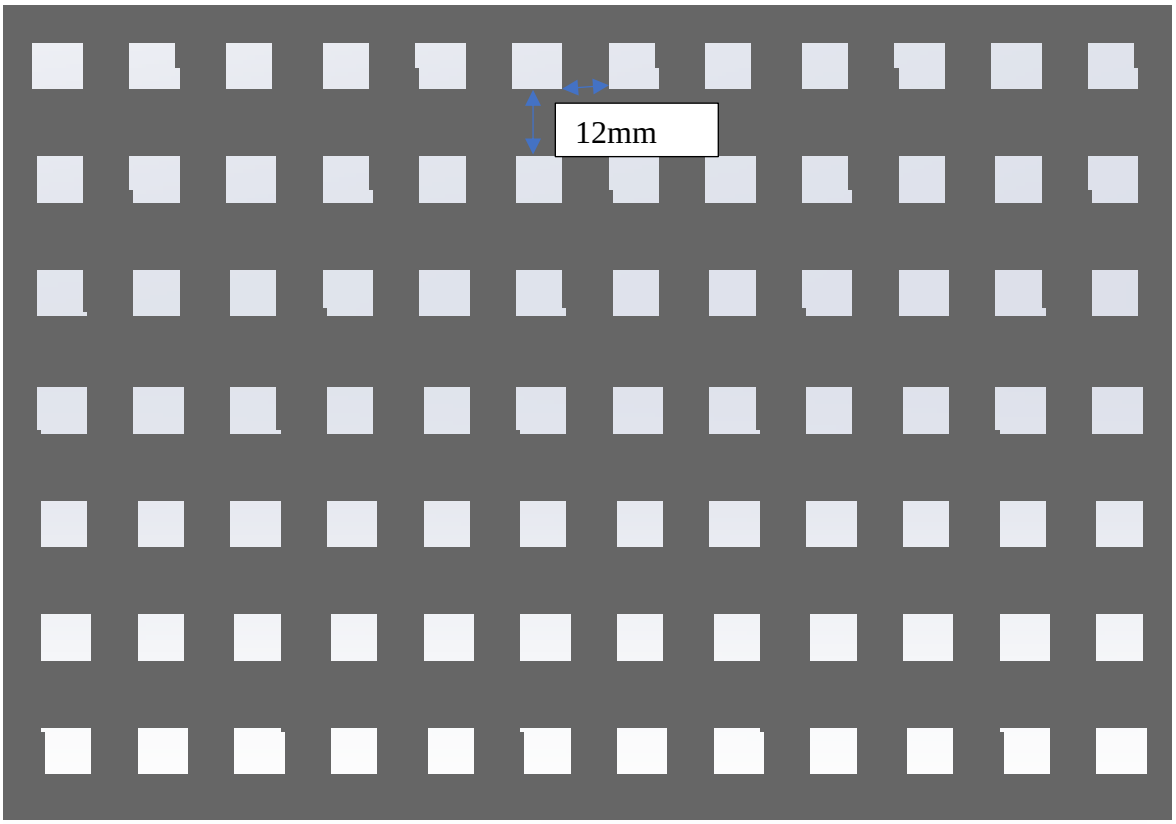

Figure 140: Mesh deck

Figure 141 presents an isometric view of the CAD geometry used for the SD0 and LM0 screen box. The dimensions have been chosen based on the dimensions of the SD18/36 vibrating screen, the length and width has been rounded off to 2 meters. Vibrating screens are not closed at the top, Figure 141 presents a screen where the top is closed, this has been performed as it is speculated that the 3DOF model will throw material out of the screen. The closed top thus allows material to be kept within the enclosed volume of the screen box. There are circumstances where rubber hoods are provided for vibrating screens, this is generally provided

to mitigate dust and is generally used on aggregate crushing and screening plants. The open space (250x2000mm) will be used to feed the screen box.

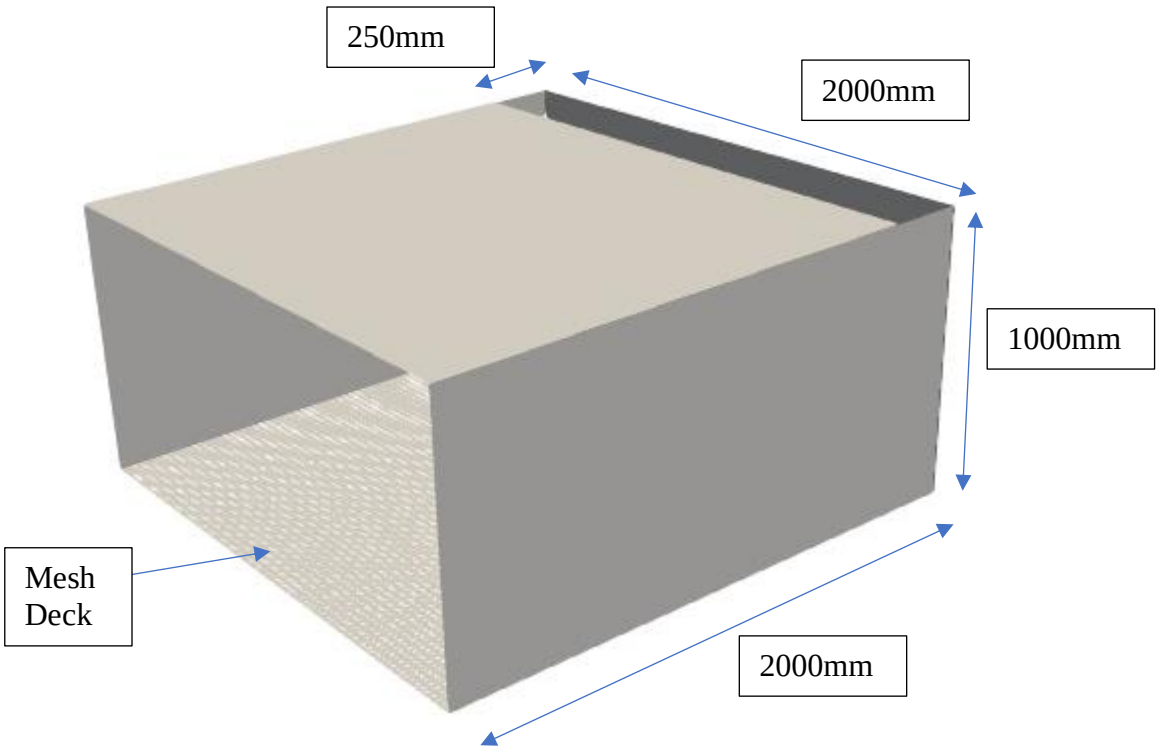

Figure 141: Isometric view of the screen box

5.3. MODELLING OF MOTION IN LIGGGHTS AND TIMESTEP DETERMINATION

The motion of the SD18/36 vibrating screen can easily be achieved on LIGGGHTS using the "wiggle" command which allows one to define an amplitude vector in cartesian coordinates with a period of oscillation (DCS, 2016). This is easy to implement since all the required information is easily available as per Table 3.

The motion of the 3DOF system is far more complex and requires both rotation and translation simultaneously. The displacement and acceleration results developed on Matlab are required in the LIGGGHTS input file for the motion to be achieved, since there is no way to directly apply the derived differential equations in LIGGGHTS. The motion can be achieved by means of using two "move/mesh" commands with the "linear" and "rotate/variable" styles for a specified time step. This procedure requires a huge amount of typing in order to incorporate all the commands into the input file. To facilitate the process an Excel spreadsheet is developed where the Matlab simulation results would be stored, the spreadsheet has an excel VBA which then develops a text file with all the required commands to replicate the motion. The code and explanation for the excel VBA is presented in APPENDIX H – AUTOMATION OF LIGGGHTS INPUT SCRIPT. The data in the text file is simply copied and pasted at the end of the LIGGGHTS input script. It should be noted that the data for the x coordinate is placed in the z coordinate, this is done to develop motion laterally as opposed to in line with the material flow, noting that the feed and discharge for the CAD models exist along the x axis.

It is standard practice to start with the Rayleigh timestep which is defined by equation 78. This equates to a timestep of 0.0024 seconds. Usually, the chosen timestep is taken as 20% of the Rayleigh timestep (Shenouda & Hoff, 2020), this equates to the time step of 0.0004 seconds. Based on trial simulations and the required setup, a timestep of 0.0001 seconds is chosen for simplicity.

$$Rayleigh\ timestep = \frac{\pi R\sqrt{\frac{P}{G}}}{0.1631\upsilon + 0.8766} \quad 78$$

The results from Matlab use a time step of 0.001seconds while the LIGGGHTS simulation uses a time step of 0.0001seconds, thus for every 0.001 seconds in Matlab there exists 10 steps in LIGGGHTS. This implies that the data developed in Matlab stays constant over the 10 steps performed in LIGGGHTS.

Each increment requires 10 input statements in LIGGGHTS to develop the required motion and to save the required data. The setup develops 8000 lines of input script for a single second of analysis. A smaller Matlab timesteps would develop far more data in the input files making the file handling processes cumbersome, thus the difference in the Matlab and LIGGGHTS time step. It should be noted that the resulting input script is approximately 27Mb in size, resulting in Notepad responding very slowly.

5.4. DEM ANALYSIS CASES

Table 15 presents the DEM analysis cases which will be simulated, "SD" refers to the SD18/36 vibrating screen while "LM" refers to the" Lagrangian Model" (3DOF), the number refers to the inclination of the mesh deck (δ, refer to Figure 142).

Table 15: DEM analysis cases

DEM Case	Sub Case	Deck Inclination
1	SD0	0
	LM0	
2	SD5	5
	LM5	
3	SD10	10
	LM10	
4	SD15	15
	LM15	

Figure 142 presents the side view of the vibrating screen box, with the feed and discharge ends being denoted. δ, refers to the inclination of the mesh deck as presented by Table 15. With an increase in the value of δ, the length and area of the mesh deck will also increase, this also allows for more apertures which ultimately results in a larger screening area.

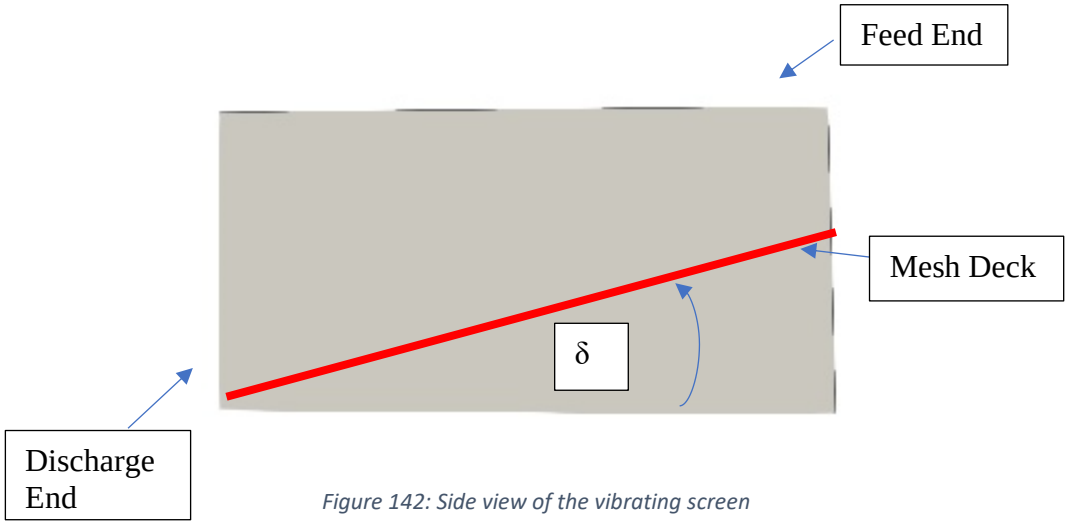

Figure 142: Side view of the vibrating screen

Figure 143 presents the top view of the screen box with material feed. As discussed previously it is general screening practice to have a distribution chute which will distribute the feed over the width of the vibrating screen. For the purposes of the study the feed will be 150x1000mm and placed in the centre of the feed opening.

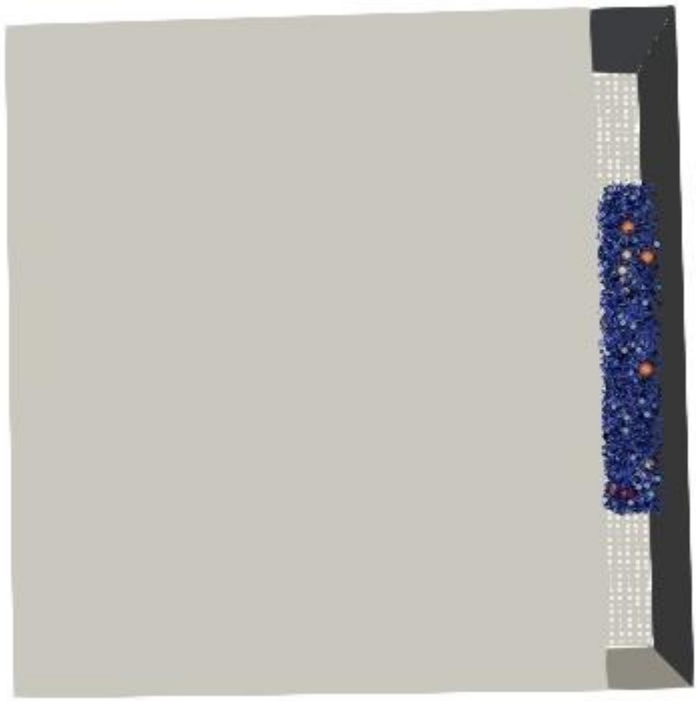

Figure 143: Top view of the screen box with material feed

Catchment volumes are required in order to collect the oversize and undersize material, the geometry used for the catchment volumes are presented by Figure 144 with some of its associated dimensions. The catchment volume is completely closed so that no material will be able to leave the system resulting in a system where material will never exit the bounding.

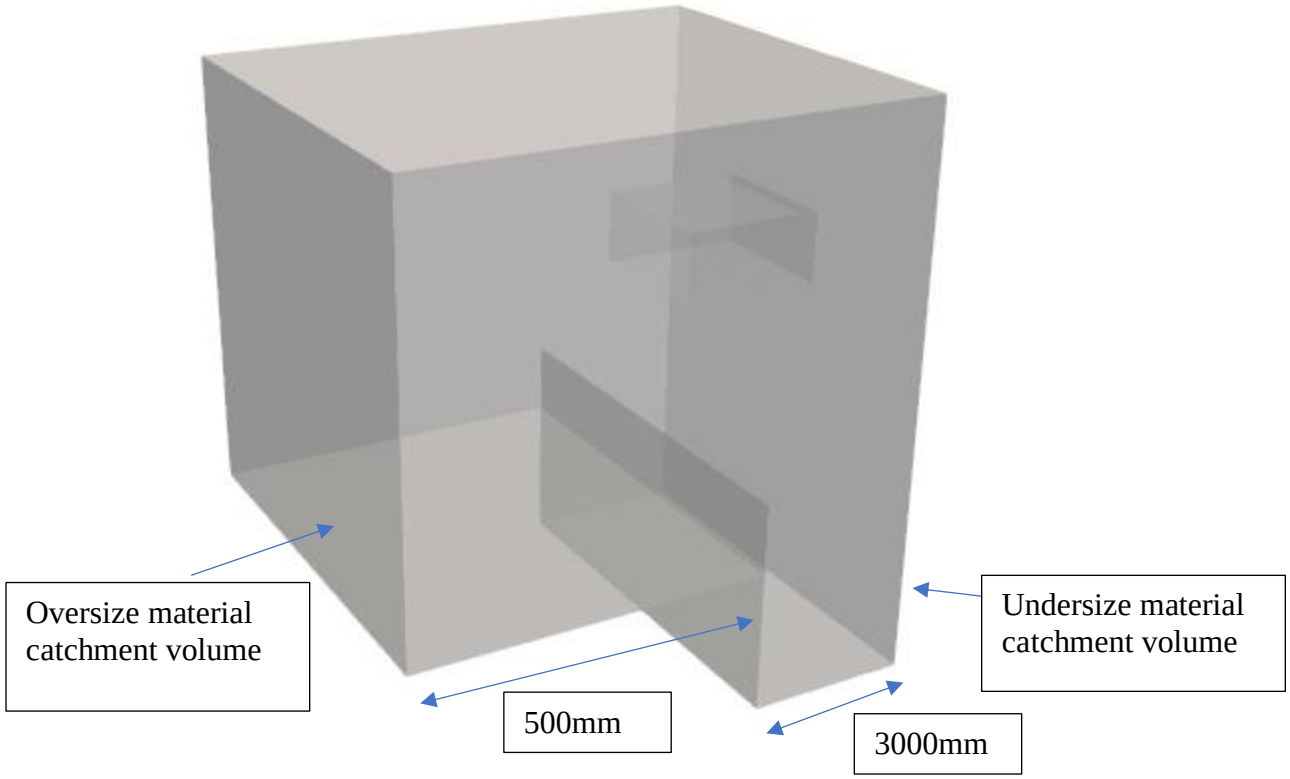

Figure 144: Collection box and screen model

The author initially explored the use of the CHPC (Centre for high performance computing) where a cluster could be used to perform the required DEM analysis. The CHPC has been used for CFD simulations by companies in industry and various research institutions. Currently the CHPC uses CentOS 7 as their operating system which is a Linux distribution (Wikipedia, 2022). During discussions with a support engineer at CHPC it was discovered that an installation of LIGGGHTS does exists, however it was unmaintained. Furthermore, it was mentioned that the installation of LIGGGHTS on CentOS was complicated and the CHPC currently does not have any support for the software. A further complication is that the build of LIGGGHTS does not support VTK output thus making it impossible to develop any visualisation. The use of .VTK files is important as it allows one to visually assess the simulation to ensure that the model is behaving as expected and to interpret and understand results. Based on the above-mentioned issues it was decided that the simulation would be performed on the authors spare laptop. The DEM simulations will be performed on a laptop with the following specifications:

- i7-2677M CPU @ 1.8GHz×4
- HDGraphics 3000(SNB GT2)
- Memory 3.4GiB
- 120GB disk capacity (solid state hard drive)

During trial simulations it was found that the analysis time was roughly 4-5 days to attain ±20 seconds of results. For this reason, simulations will be run until 60kg of small particles are recorded in the undersize catchment volume. The resulting LIGGGHTS input script is presented in APPENDIX I – LIGGGHTS INPUT SCRIPT.

5.8. DEM ANALYSIS

This section will discuss the results for the DEM simulations presented by Table 15. The links below present animations of the following setups:

- LM10
- SD0
- LMR10

The animations can be used to review the behaviour of the vibrating screens. It should be noted that the SD0 video does present an error where at the end of the vide material is being chaotically spread over the entire catchment volume. This is a visualisation error which can be ignored.

https://www.youtube.com/watch?v=R-UuykSWL60
https://www.youtube.com/watch?v=uLtYWe712JE
https://www.youtube.com/watch?v=yVJU1Dj9_60

5.8.1. MATERIAL DISTRIBUTION OVER THE DECK OF THE SCREEN

Figure 145 presents the material distribution over the deck of the SD vibrating screen at 8 seconds, the SD0 is presented in the top left-hand corner with an increase in deck inclination occurring in the clockwise direction (this convention will hold for all images). Material has not distributed evenly over the width of the deck. The SD0 has attained the best distribution of material over the width of the deck, which is attributed to the slow movement of material along the length of the deck due to deck being horizontal. Every arrangement has a deep layer of material at the feed end which reduces as it gets closer to the discharge, this has been discussed as per the explanation of Figure 4.

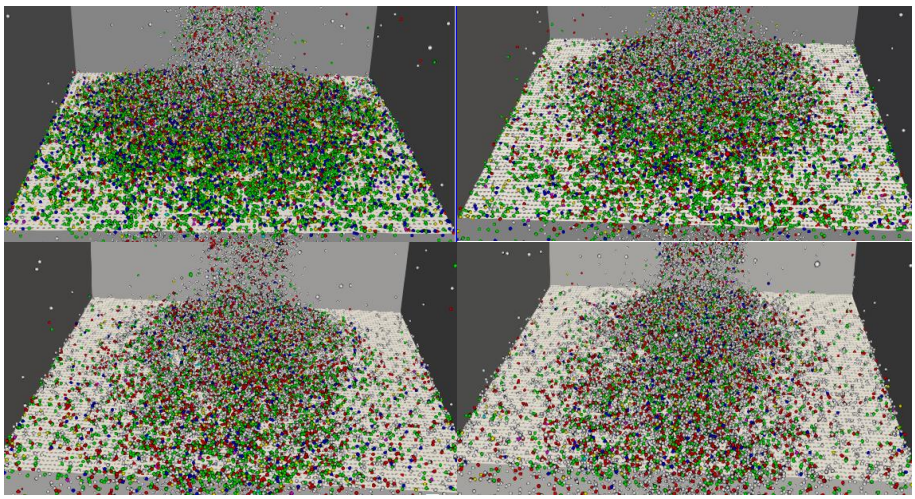

Figure 145: Material distribution over the deck of the SD vibrating screen

Figure 146 presents the material distribution over the deck of the LM screens. As the deck inclination increases there exists more movement of material along the length of the screen deck. The motion of the LM screen also causes the material to be thrown all over the enclosed volume of the screen box.

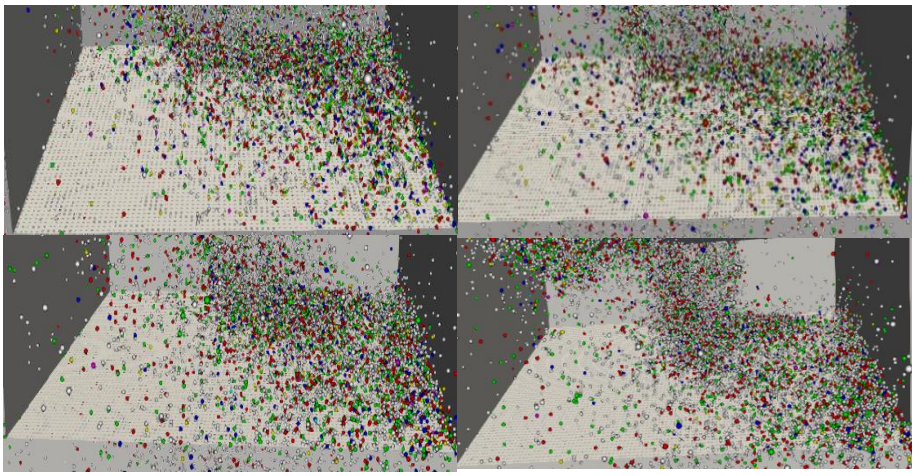

Figure 146: LM material distribution over the deck

It is expected that the SD screens would not allow material to flow evenly along the width of the deck, given the assigned material feed location. The material distribution over the width of the LM screen decks is constantly changing due to motion of the screen. Images of the various time points for the LM15 screen setup are presented in APPENDIX J – LM15 MATERIAL DISTRIBUTION ON THE DECK. By inspection of the images, the material presents far more chaotic behaviour compared to the SD vibrating screens which present the same pattern regardless of the time interval being inspected. The material movement of the LM screen consists of material being pushed against the side plates, roof, and mesh deck of the screen box. Based on this observation the current screen box layout is inefficient as the material is in contact with all faces of the screen box yet only one face provides the ability to screen material.

5.8.2. UNDERSIZE AND OVERSIZE MATERIAL FLOW

Figure 148 presents the undersize and oversize material flow profiles for the SD screens. The undersize material profile presents a similar trend for all deck inclinations, where the flow rate of material reduces along the length of the screens with the highest flow rate occurring at or near the feed end. As the deck inclination increases the flow rate of the undersize material slows down. It is well known that the material movement on a horizontal deck linear motion screen is representative of Figure 147. With a change in the inclination of the deck, material would be forced to move along the deck due to gravity, once coupled with the excitation force this would develop faster material flow. Material would also be thrown further ultimately resulting in less interaction with the mesh deck, this is representative of the smaller flow rates for the undersize material. It is also expected that less undersize material will be screened.

The above-mentioned discussion would also imply that a higher flow rate is expected at the discharge end with an increase in deck inclination, this is clearly visible by inspecting the discharge at the oversize presented by Figure 148. The higher material velocity associated with an increase in deck inclination also presents material been thrown further away from the discharge.



Figure 147: Material movement on the deck of a horizontal deck vibrating screen



Figure 148: Undersize and oversize material flow profiles for the SD screens

Figure 149 presents the undersize and oversize material flow for the LM screens. Each variation of the LM screen presents a large density of small material being screened very close to the feed end. Unlike the SD screens the material flow does not gradually reduce along the length of the deck (towards the discharge), the material flow abruptly reduces. It is thus clear that the small material is mainly screened very close to the feed, as the material moves along the deck it spends most of its time being pushed against the side plates and rolling along the width of the screen deck. When rolling over the width the material travels at a high velocity thus it is uncertain as to how much contact is made with the mesh deck.



Figure 149: Oversize and undersize material flow for the LM screens

5.8.3. EFFICIENCY COMPARISON

Figure 150 presents the masses of the small material found in the undersize catchment volume with respect to time. As expected, the first ±1second of the simulation presents 0 material for all the cases, this is representative of the material still falling from the particle factory. The LM screens are able to screen the undersize material far quicker compared the SD screens. The SD5 and the LM0 have screened material at a similar rate since the results are almost identical throughout the simulation. The following can be noted by studying Figure 150:

- The LM15 has screened material slowest when compared to the other LM screen variations. This can be attributed to the material flowing far too quickly along the deck of the screen thus preventing adequate screening. This would also imply that there would be a large quantity of small material in the oversize collection box, this is supported by reviewing Figure 151
- The SD0 screen has screened material the slowest when compared to all other variations of the SD screen, this can be attributed to points which have been raised previously
- The SD15, LM15 and SD10 have the three largest amounts of small material being captured in the oversize catchment volume and have taken the longest to achieve the 60kg of small material in the undersize collection volume, thus implying a low screening rate. If these screens were to be implemented in a crushing/screening plant

the material would need to be recirculated several times in order to develop good quality screened products.

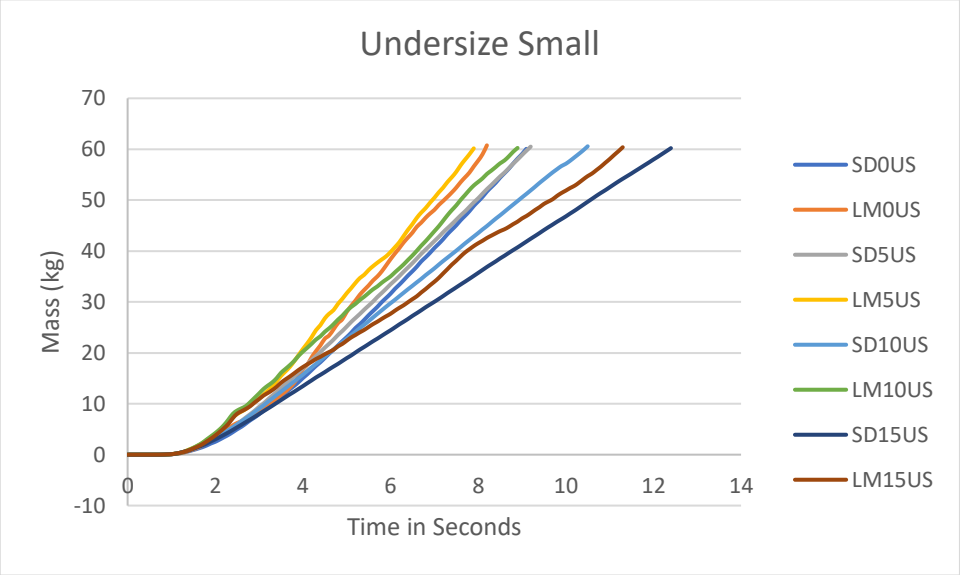

Figure 150: Mass of undersize material of the small category

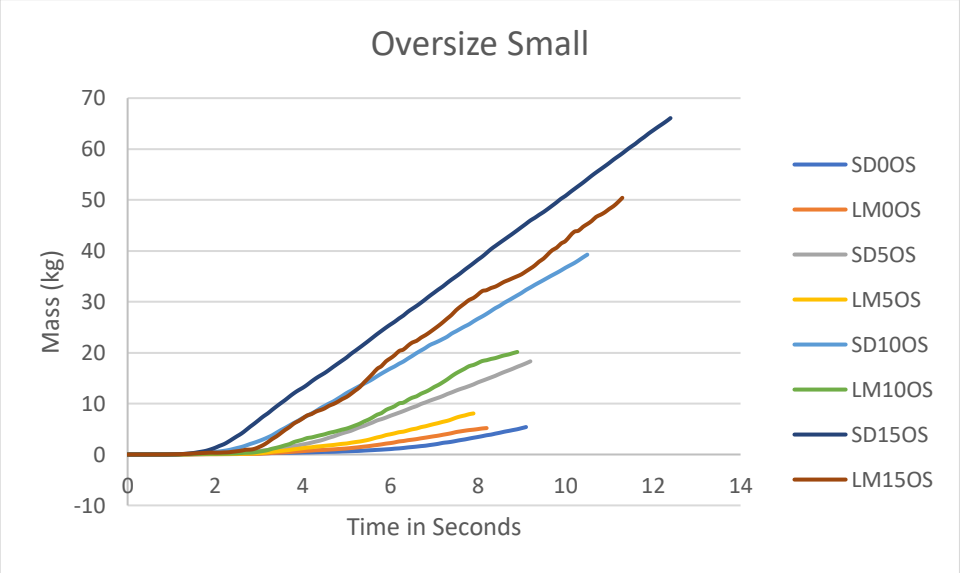

Figure 151:Mass of small material found in the oversize collection box

Figure 152 presents the large material found in the undersize catchment volume. All the SD variations presents small amounts of large material in the undersize catchment volume, the numerical values being less 0.3kg. Based on Figure 145 the material flow on the SD screens is far more controlled with material not been thrown large distances, thus there is a low probability of material been thrown out of the feed opening. The small amounts of large material found in the undersize catchment volume can be attributed to material passing through the mesh and/or material falling on the topside of the roof.

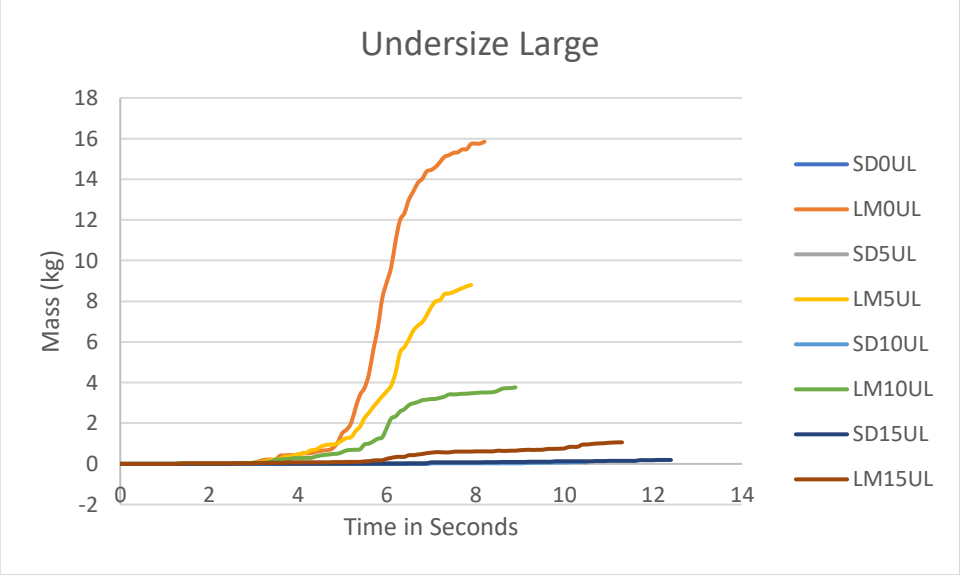

Figure 152: Large particles in the undersize catchment volume

Figure 153 presents the LM0 (left) and LM15 (right) screen at time 2.2 seconds. The material presented by region A is being thrown out of the feed opening, this occurs since there is no driving force for the material towards the discharge, resulting a large mass of material accumulating directly below the feed opening. This can be further substantiated by the reviewing Figure 146 which presents a large amount material build up in line with the feed opening. This ultimately causes material to be thrown out of the screen resulting in significant quantities of large material mass being found in the undersize catchment volume. The LM screens which present an inclined deck promote material flow towards the discharge thus accumulating less mass in line with the feed opening. Furthermore, the motion in the *z* component due to the inclination coupled with the screen motion allows mass to be thrown forward as well as sideways allowing material to be in a region where it is not in line with the feed opening.

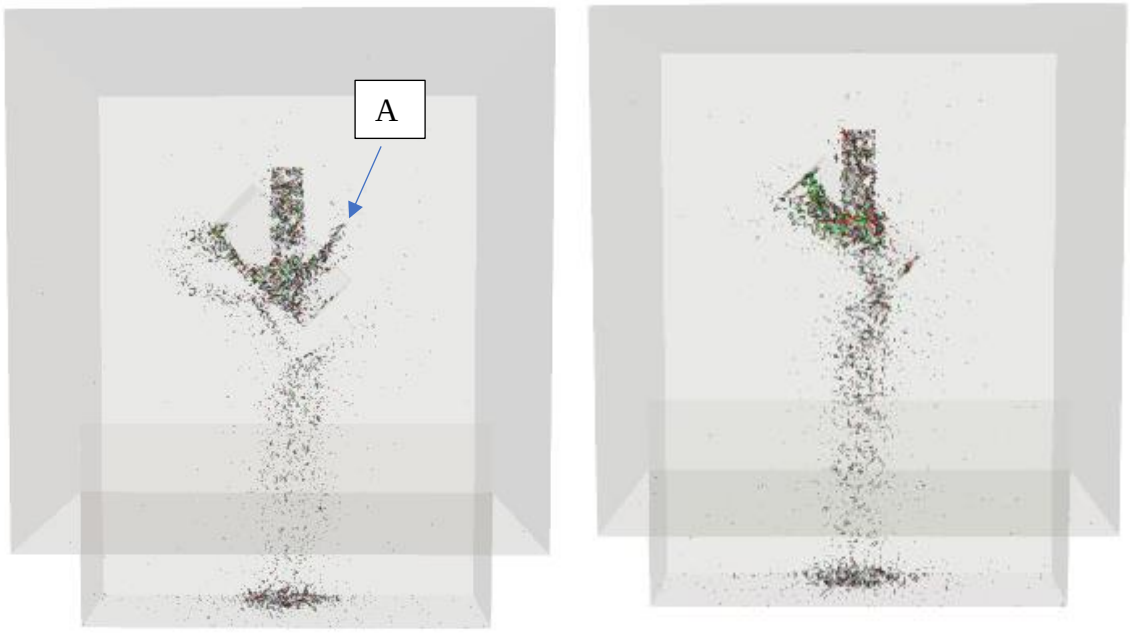

Figure 153: LM0 and LM15 at time 2.2 seconds

Figure 154 presents the efficiency of the undersize material using equation 4. The SD screens present a linear trend downwards as the deck inclination increases. SD0 screen presents the highest efficiency at 91%. The LM screens present an increasing efficiency with 10 degrees being the peak efficiency (68%). The LM10 and LM15 present higher efficiency when compared to the equivalent SD screens.

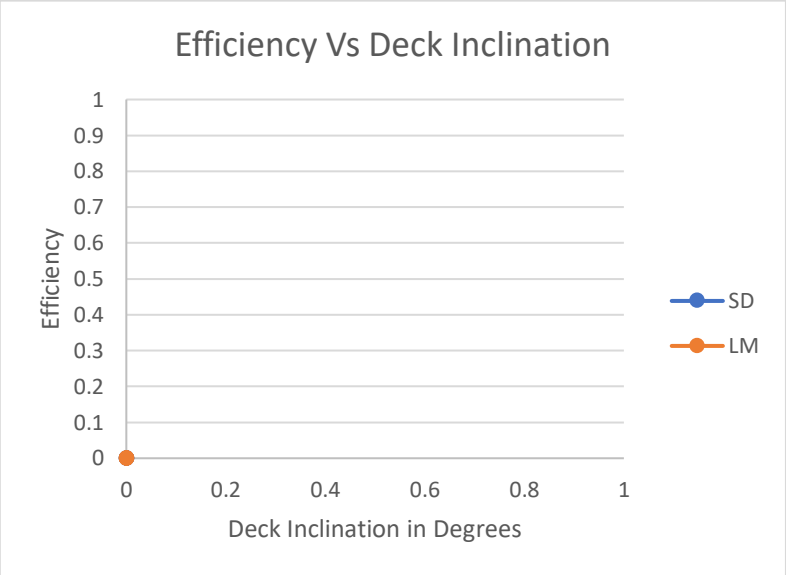

Figure 154: Efficiency of the LM and SD screen

Based on the results the SD0 screen has the highest efficiency thus it is the best performing arrangement. The LM screens except for the LM15 can screen undersize material far quicker compared to the SD screens which would ultimately lead to higher tonnages of material.

5.9. DEM USING REVISED CAD GEOMETRY

The LM screens present poor screening capabilities when compared to a linear motion screen with a horizontal deck. Linear motion screens do not throw material large distances thus material stays relatively close to the deck allowing, the screen to utilise the deck area far more efficiently when compared to the LM screens. The LM screens present a very poor utilisation of the screen box since there are 4 possible surfaces which can be used for screening while only 1 is utilised.

Using the same screen box dimensions as presented by Figure 141, and providing additional apertures on the side plates and roof of the screen box, a large surface area can be developed for material to be screened. The apertures are as defined by Figure 140. A solid plate will be provided presented by “A”, this is expected to prevent material from escaping the feed area. the resulting screen box is presented by Figure 155.

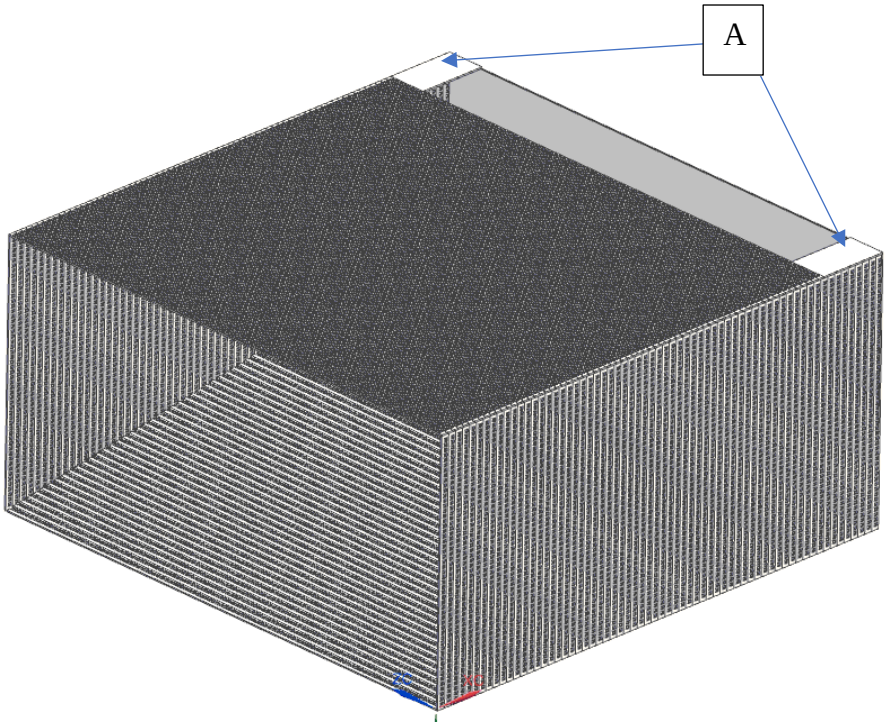

Figure 155: Revised screen box with 4 mesh deck surfaces

The resulting screen box will be defined as LMRXX, where "XX" represents the inclination of the screen deck. The material movement within the screen box has remained the same as for the previous simulations (LM). Figure 156 presents the LMR0 (left) and LM0 (right) at 2.2 seconds, there is a small amount of material which is escaping the screen box for the LM0, as presented by "A". The material is contained when considering the extra plate being introduced for the LMR0 variation of the screen box.

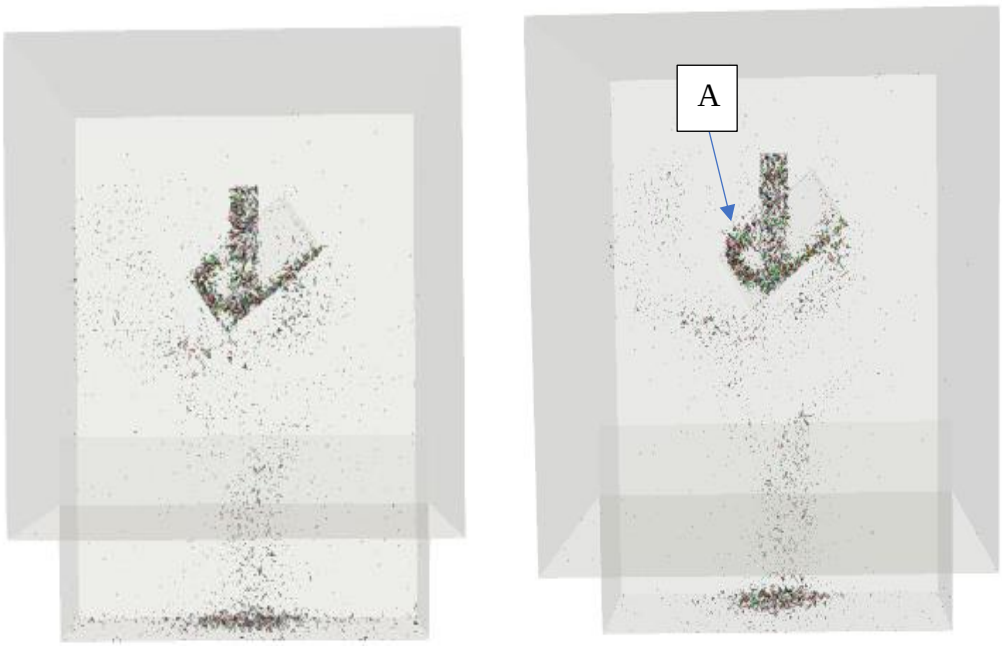

Figure 156: LMR0 and LM0 at 2.4 seconds

Figure 157 presents the time taken for each variation of SD, LM and LMR to reach 60kg of undersize material in the undersize catchment volume. It is clear the inclusion of the additional mesh area has increased the rate of screening however this is marginal. With larger inclinations

the rate of screening increases far more when compared to lower deck inclinations. The SD screens have the slowest rate of screening this however has been presented previously.

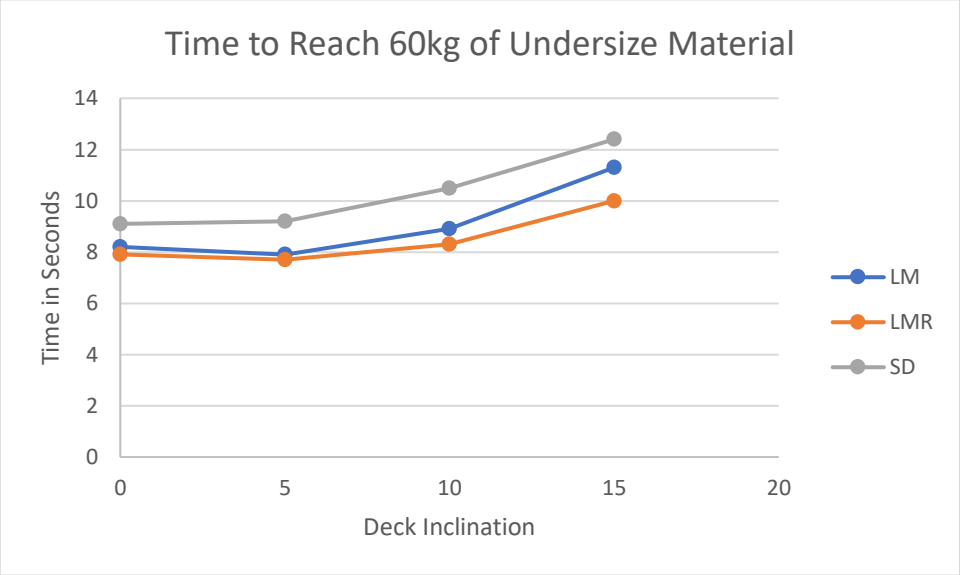

Figure 157: Time to reach 60kg of undersize material in the undersize catchment volume for LM, LMR and SD

Figure 158 presents the efficiency of the vibrating screens on a single plot. The efficiency of the LMR screen is higher than that of the LM screens, with the LM10 and LMR10 performing the best out of all the parametrically excited screens. At a 0-deck inclination the LM and LMR perform very similar, this it attributed to the fact that the material is contained close to the feed opening thus there is poor utilisation of the additional mesh areas. Higher deck inclinations have shown to develop higher rates of screening as per Figure 157 however this also comes at a loss since the LMR15 presents a decrease in efficiency. The 10-degree variation of the LM and LMR screen have produced the highest efficiencies.

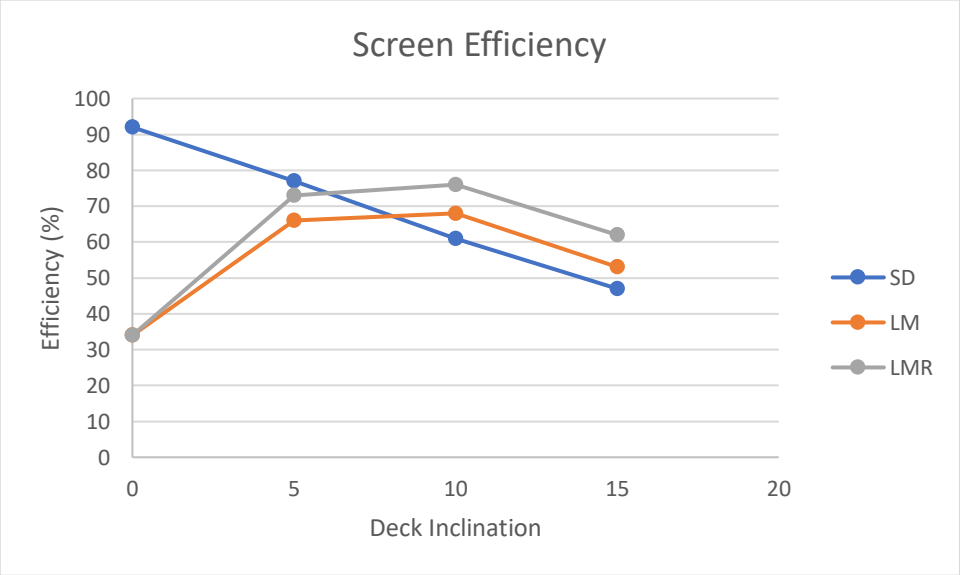

Figure 158: Screen efficiency of the SD, LM and LMR screens

5.10. DEM CONCLUSION

The DEM results present the SD0 as the most efficient vibrating screen, however it should be noted that from a process perspective the SD18/36 vibrating screen is chosen to cater to the PSD and material properties used in this study. This gave the SD0 variation an advantage against all the other vibrating screen variations. The LM10 and LMR10 present highest efficiencies with regards to the LM variations, these screens produced efficiencies of 68 and 76% percent respectfully which can be considered high when reviewing the cited literature and considering that the screen and materials have not been sized for compatibility.

The study by Jianzhang presents a linear motion vibrating screen which developed an efficiency between 30-50% and 30-53% for the cases which were studied (Jianzhang & Xin, 2012). Parameters of the vibrating screen and/or material are not sized from a process perspective thus developing the lower efficiencies compared to the current study. Furthermore, the swing trace studied by Jianzhang presented higher efficiencies in the region of 35-55% which is higher compared to the linear motion presented in the same study however these values are far lower compared to the efficiencies developed using the LM and LMR variation for 5, 10 and 15 degrees. The study by Zanfu presents high efficiencies indicating that the material and vibrating screen present better coherence.

The LMR variation presents a purely theoretical system which would be difficult to replicate in reality. The entire screen box is used for screening, this would develop safety concerns and furthermore immense complexities around the required chute work. The LMR variation does however present the conclusion that the layout of the screen box is inefficient for the presented motion. A larger area for screening presented almost a 10% increase in efficiency. It is thought that utilising the volume of the screen box for screening purposes may produce even higher efficiencies.

CHAPTER 6: EXPERIMENTAL STUDY

This chapter presents an experimental setup and testing which is used to check the accuracy of the 3DOF system with regards to initial conditions. The goal of this chapter to develop an experimental system which represents a the Lagrangian model so that the legitimacy of the equations can studied.

6.1. EXPERIMENTAL SETUP

Figure 159 presents a fabricated representation of the 3DOF system, consisting of the following:

- A, presents the rigid beam which is fabricated using an IPE140 hot rolled section
- B, consists of the springs, the data sheet for the can be found in APPENDIX K – SPRING DATA SHEET
- Figure 160 presents the side view of the experimental setup, with label C presenting the pinned joints between the support structure and the rigid bar. The pinned joints have been fabricated as lugs on the IPE140 section, end plate for the springs and the support structure. Adjacent lugs are connected by means of a loose bolt thus allowing the system to move with ease.

Table 16 presents the mass of the individual items of the experimental setup and the total mass.

Table 16: Mass of the experimental setup

-	**kg**
Item	**Mass**
IPE140 beam	19.3
Total spring mass	3.89
Dytran 4401A2	0.45
Total	23.64



Figure 159: Experimental setup

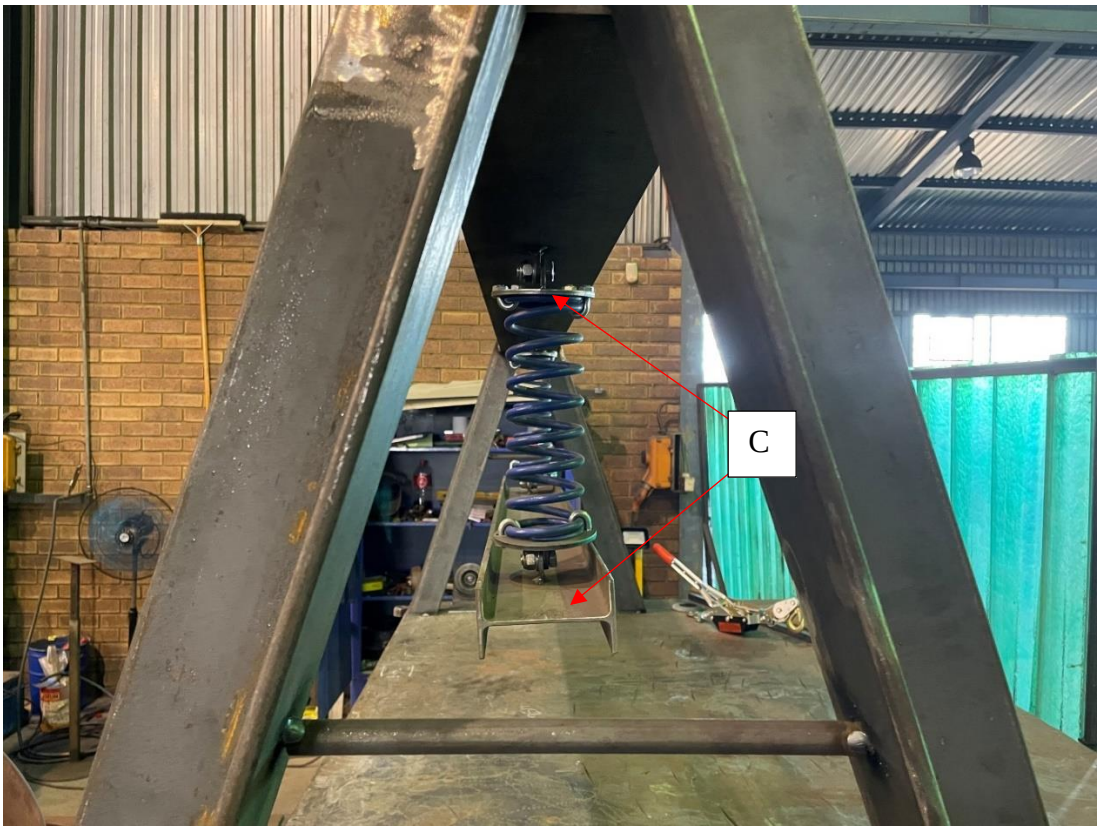

Figure 160: Side view of the experimental setup

A single 6 axis accelerometer will be used to record the results, the accelerometer will be placed at the centre of the rigid bar. This allows one to replicate the coordinates used by the differential equations. The translational directions can measure the acceleration for the x and y coordinates while the gyroscope can measure the rotational velocity which is representative of the θ coordinate.

The results will be recorded using the Dytran 4401A2 vibration recorder which is presented by Figure 161. The dimensional details regarding the mounting bracket can be found in APPENDIX L – DYTRAN 4401A2 6 AXIS ACCELEROMETER DRAWING. The Dytran 4401A2 has a built-in data logger which saves data directly to a micro-USB card, thus alleviating the need for any wires or bulky data loggers.



Figure 161: Dytran 6 axis accelerometer

Table 17 presents the parameters for the experimental setup with the translational axis of the accelerometer being presented in Figure 159. The rotational component will exist about the x axis with positive being represented in a clockwise direction. The axis setup for the accelerometer does not correlate with the derivation of the 3DOF system.

Table 17: Parameters of the experimental setup

Attribute	Numerical Value	Units
Spring stiffness (per spring)	27594	N/m
Distance between springs (L)	1.1	m
Mass	23.64	kg

It is possible to set up the accelerometer such that the axis correlates to the coordinates of the 3DOF system, this however would require the accelerometer to be attached to the flange of IPE140 beam. The accelerometer would be offset from the centre of the beam. Based on discussions with TANDM it was suggested by their test and measurement experts that the centre of the beam be used even though the axis will not correlate with the theoretical model, this would allow for the best possible experimental setup. Table 18 presents the equivalent coordinates/axis so that the numerical simulations and experimental setup can be compared.

Table 18: Correlation between the coordinates for the 3DOF and experimental setup

Coordinates/axis	
3DOF	**Experimental Setup**
x	Y
y	Z
θ	about X

6.3. EXPERIMENTAL TEST CASES

There will be 3 experimental test cases which will be considered. Each experimental test case will impose initial conditions on a coordinate, thus producing 3 cases.

6.3.1. TESTS CASE A

This experimental test will impose initial conditions on the springs. A rachet is used to strap around the beam and then tensioned so that the centre of the lugs is displaced 410mm. Once this criterion has been achieved the rachet has a quick release allowing the system to be released from its initial conditions.



Figure 162: Experimental setup to impose initial conditions on the springs

Based on Figure 162 the strap cannot be wrapped around the centre of the beam due to the location of the accelerometer; the strap is thus located adjacent to the beam. It is thought that this would develop an angular displacement in the beam (θ coordinate) thus altering the

requirement of initial conditions to be only imposed on the springs. Due to the proximity of the strap to the centre of the beam it was found that the angular displacement is negligible, this is confirmed using an angle finder as per Figure 163. Noting that Figure 169 presents a 0 inclination when placed on the right- and left-hand side of the experimental setup. The proposed experiment will be performed 5 times.



Figure 163: Angle finder results on each end of the rigid bar presenting a 0 inclination

6.3.2. TEST CASE B

Case B will consider initial conditions for the x coordinate, with the setup being presented by Figure 164. The centre of the rigid beam and the beam on the support structure are marked and a nut hanging from a string is placed at 160mm away from the centre line. The string is attached to the support structure by means of a clip.



Figure 164: Setup for initial conditions in the x coordinate

The centre line of the rigid beam is moved in line with the string as presented by Figure 165, once this is achieved the system is released. By imposing the above-mentioned initial conditions there will exist another set of initial conditions for the y coordinate which is measured as 311mm (from centres of the spring lugs). This experiment will be performed 5 times.

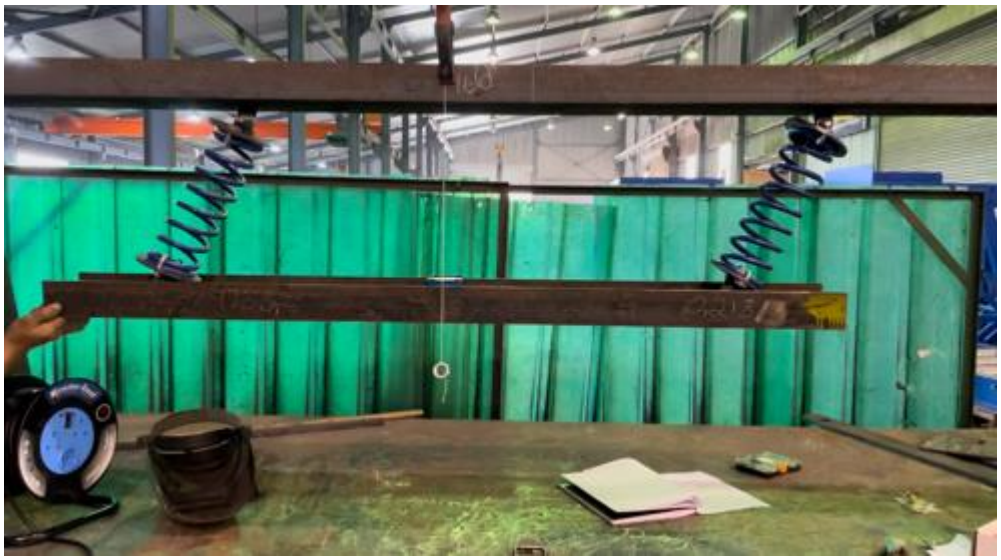

Figure 165: Experimental setup with initial conditions on the x coordinate

6.3.3. TEST CASE C

This test case will consider initial conditions imposed on the θ coordinate as presented by Figure 166. The setup is similar to the one used for imposing initial conditions on the y coordinate, however the rachet is placed on onside of the beam thus allowing the beam to rotate when the rachet is tightened. The rachet will be tightened until the beam is rotated to roughly 4 degrees, which will be measured using an angle finder. Due to the difficulty in replicating the 4-degree rotation, the target angle will be ±4 degrees with the measured angle being recorded for numerical simulation purposes.



Figure 166: Experimental setup for the initial conditions imposed on the θ coordinate

6.4. EXPERIMENTAL RESULTS

This chapter deals with the results attained from the experimental testing and the comparison with the derived 3DOF system.

6.4.1. EXPERIMENTAL RESULTS FOR CASE A

A video of a dummy test run with initial conditions imposed on the x coordinate can be found in the link below.

https://www.youtube.com/watch?v=NLs21bnc5E8

The results for the AZ acceleration are presented by Figure 167, recording 2,3 and 4 present correlation with similar accelerations results have been achieved, however recording 1 and 5 present far lower accelerations. The deviance may be due to experimental errors. The accelerations present values which are over 200m/s^2 (20.38g) for certain time points, these accelerations are well over the tolerance of the Dytran 4401A2 accelerometer which is rated at 16g. Exposure to such accelerations may cause damage to the accelerometer and thus the testing will not be repeated to review the deviances experienced. The accelerometer is setup up so that once recording is activated, the accelerometer will only begin recording once it experiences motion. Recording 3 has partially recorded the time between when the recording button is pressed and the initial conditions have bene released. Figure 168 presents a zoomed view of the AZ results from recording 2. It is evident that there exist two frequencies, a high

frequency which resembles noise and a lower frequency which is thought to be the frequency of the springs.

If one reviews the video of the experiment, there exists motion about GY and AX. This motion cannot be restrained and is expected, the effects of the motion would influence the AX results, however it is thought that there would not be a significant influence.

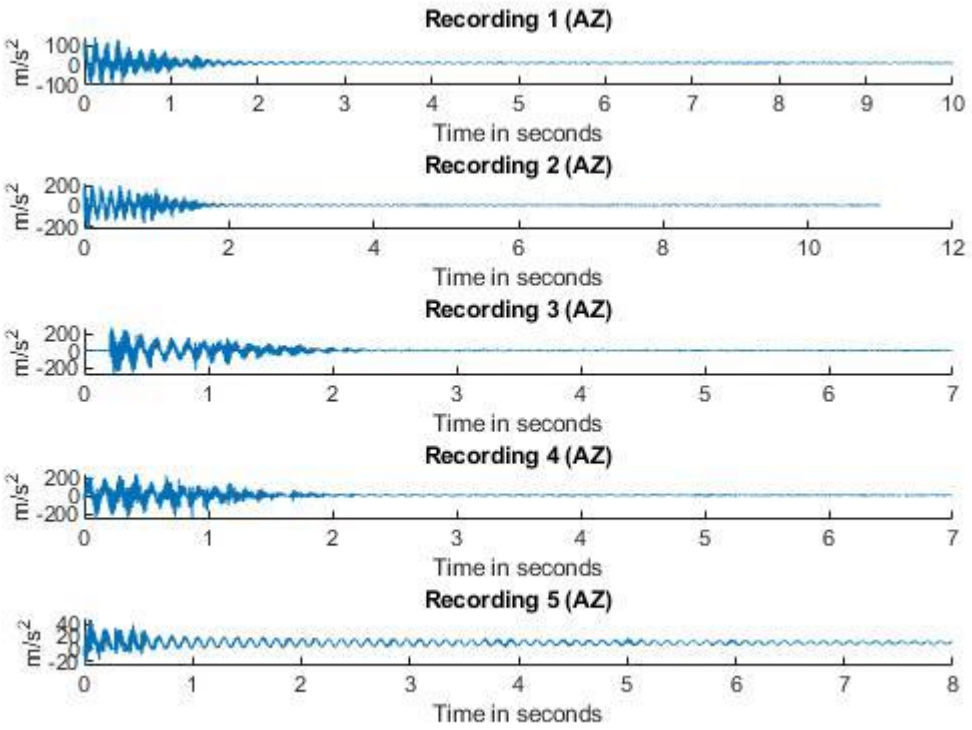

Figure 167: AZ acceleration results for experimental setup with initial conditions on the springs

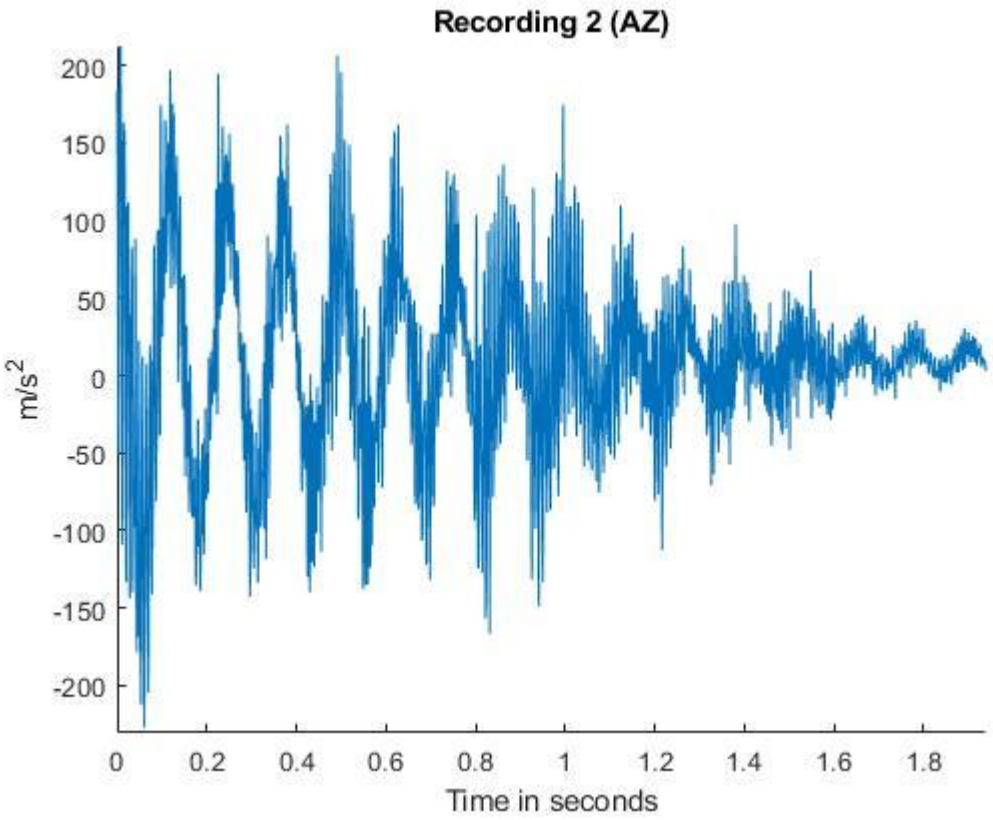

Figure 168: Zoomed view of the AZ acceleration results for recording 2

Figure 169 presents the PSD for the AZ acceleration results, the results from all three recordings overlay each other exactly. If one considers equation 22, the natural frequency of the spring system can be calculated as 7.68Hz which is close to the 7.83Hz presented by the PSD, thus presenting good correlation.

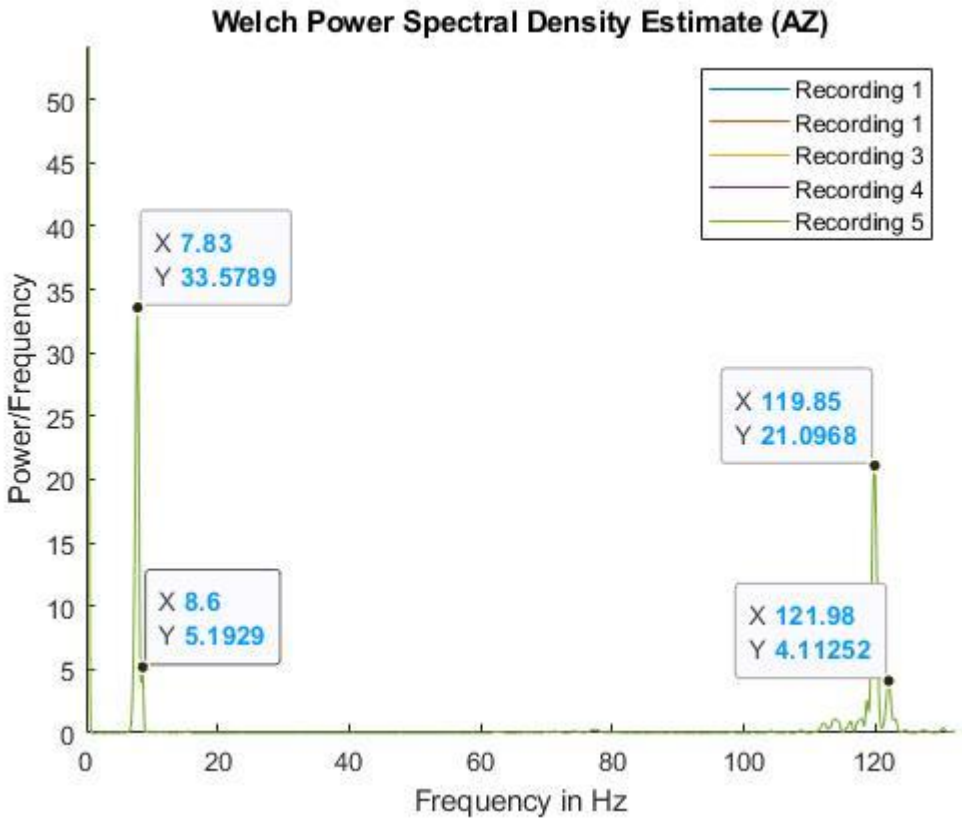

Figure 169: PSD for the initial conditions imposed on the springs, experimental setup

The 119.85Hz frequency which is initially thought to be noise can be explained using a finite element model as presented by Figure 170, the model consists of the following:

- The IPE140 section has been modelled using shell elements, the lugs have not been considered in the analysis
- The location where the springs connect to the IPE140 section are restrained in translation and a rotational restraint is applied about the x axis. The restraints can be considered a simplification, since:
  - Stiffness contribution of the lugs is not accounted for
  - Contact between the lugs is not considered
  - Spring stiffness is neglected since the horizontal stiffness of the springs is unknown and applying only axial stiffness to the model presents errors due to the lack of restraint
- The Dytran 4401A2 accelerometer is modelled as non-structural mass

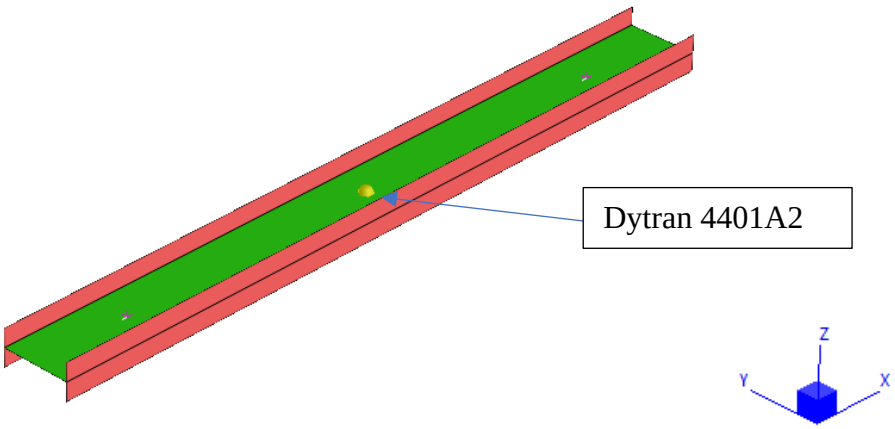

Figure 170: Basic finite element model of the experimental setup

A Natural frequency analysis of the above-mentioned finite element model presents a frequency of 114.514Hz (mode shape presented by Figure 171) which is close to the 119.85Hz frequency presented by the PSD. There exists a deviance of 5.33Hz which may be attributed to the finite element model not being a true representation of the system. The 119.85Hz frequency can thus be explained as a natural frequency of the IPE140 beam. This frequency is found in all the measured results including the experimental testing which follows this chapter.

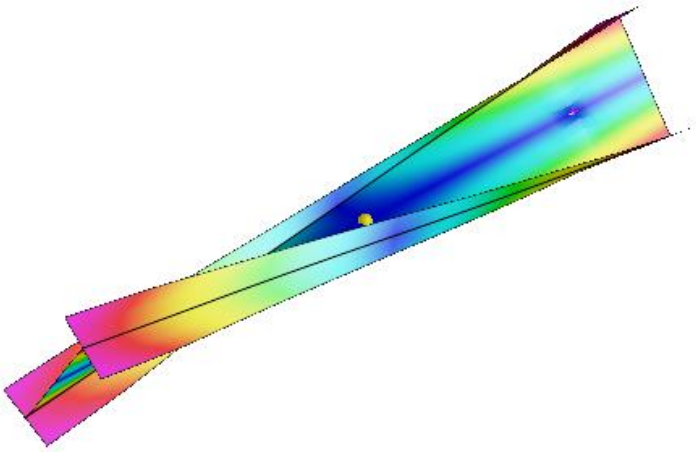

Figure 171: Mode shape of 114.514Hz natural frequency

The 119.85Hz frequency presents a noisy signal which will make it difficult to compare to the numerical simulations. A low pass Butterworth filter will be implemented to remove the 119.85Hz frequency and clean up the signal so that an appropriate comparison will be made. This will be implemented for all the test cases. The general Matlab code for implementing the Butterworth filter and removing trendlines is presented by Matlab Code 11. A cut off frequency of 60Hz is considered.

The parameters presented in Table 17 have been assigned as constants for the differential equations derived for the 3DOF system, with the initial conditions for the y coordinate being assigned a numerical value of 0.355 meters. An initial value of 0.41 meters is not considered since the initial conditions for this experiment are based on the spring length and not the total length of the system which includes the lugs.

Figure 172 presents the acceleration results for recording 2 and the equivalent simulation using the differential equations. Note that the titles for the figure have been left out for clarity purposes since the inclusion of the title causes the results to become unreadable. The results present an increase in proportional damping starting at 0.1% and incrementing by the same amount for each subsequent simulation.

The numerical simulations and experimental results in all cases present good correlation. At $t = 0$ the acceleration results for the numerical simulation and experimental test correlate almost exactly. When damping is assigned 0.1-0.3% there exists the best comparison between the results. As time increases there exists a phase shift in the results which may be attributed to the effect of damping. Furthermore, it is clear that the natural frequency of experimental tests (119.85Hz) affects the acceleration results to a large extent when comparing Figure 172 and Figure 167. The original recordings present accelerations in the order of 20g while the filtered results present acceleration results which are much lower.

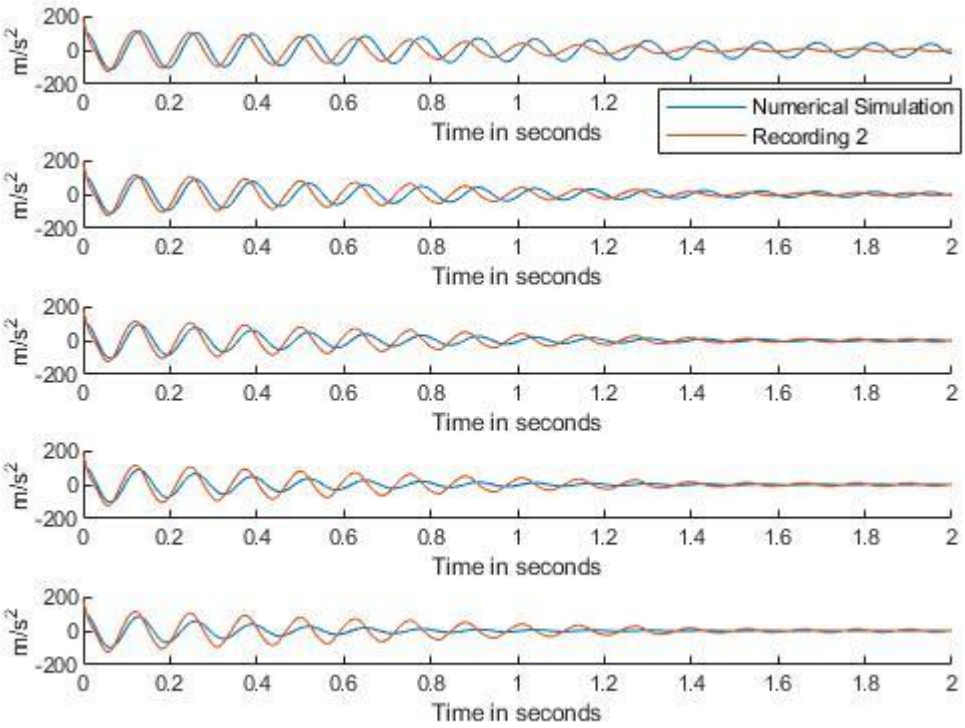

Figure 172: AZ and y coordinate acceleration results for recording 2 and numerical simulation (test case A)

A comparison for the all the other recordings can be found in APPENDIX M – EXPERIMENTAL RESULTS, the following can be noted:

- Recording 1 presents better correlation when damping is assigned between 0.3-0.5%. There exists very small phase shifts in these results. This may imply that with lower acceleration the assumption of proportional damping may present better correlation.
- Recording 3 correlates well with the numerical simulations, however the recording started prematurely thus causing results which present not acceleration early on. This causes a 180-degree phase shift when comparing results due to the additional time recorded
- The acceleration results for recording 3 and 4 present far smaller numerical values at $t = 0$ when compared to the numerical simulation and recording 1 and 2
- Recording 5 presents poor correlation with the numerical simulation, which may be attributed to experimental errors

Figure 173 presents the PSD for the numerical simulation presented above, the results tie up well with the analytical values and experimental values. Based on the presented results the differential equations are compatible with the experimental setup, however inaccuracies are caused due to differential equations assuming that the beam is rigid. The beam will never be rigid and thus there will be additional frequencies which may exist in the system which alters its behaviour.

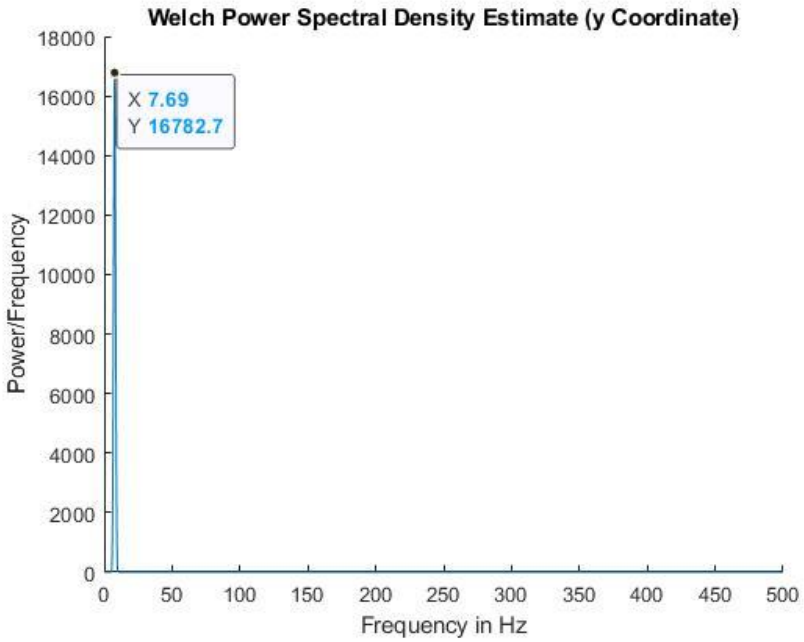

Figure 173: PSD for the numerical solution which mimics the experimental spring initial conditions

6.4.2. EXPERIMENTAL RESULTS FOR TESTCASE B

A video of the experimental test can be viewed by using the link below.

https://www.youtube.com/watch?v=0lyaDj9W8Yw

For this study only the results pertaining to AY and AZ are important since this is the axis which ties up to x and y coordinates. By reviewing the video footage, the other coordinates do not play a significant role the experiment, this is further justified by the random noise presented in the signals. The acceleration results for AY and AZ for each recording are presented by Figure 174 and Figure 175 respectfully. The AY acceleration results trace a sinusoidal curve as expected with a high frequency sinusoidal wave being traced close to or at the peaks. The AZ acceleration results present what appears to be two frequencies, a high frequency which would be the spring and a lower frequency which would be the pendulum motion.

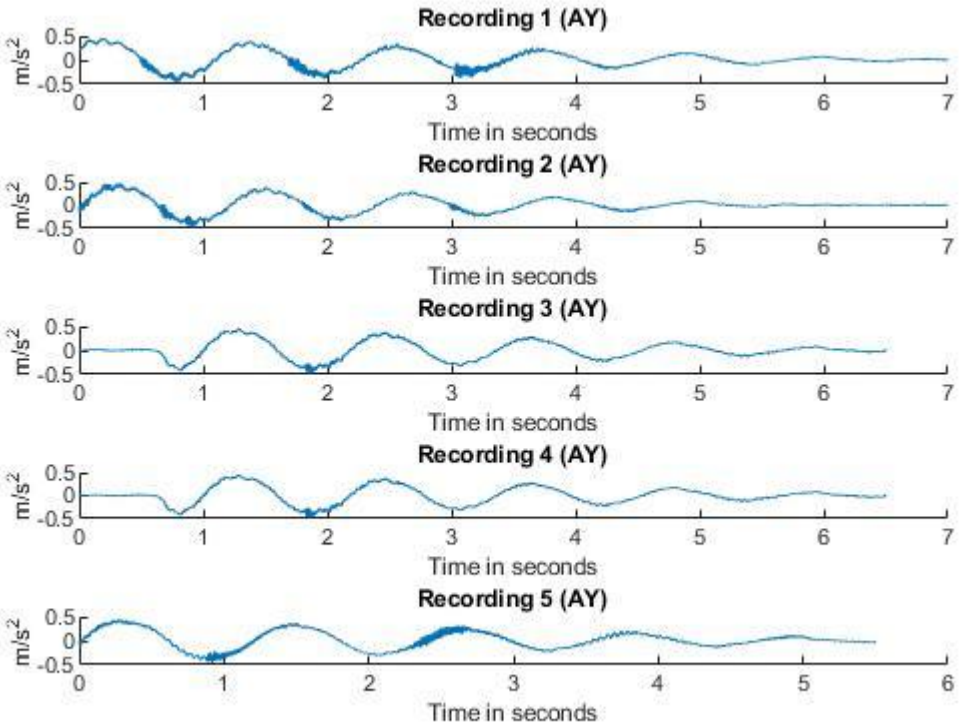

Figure 174: AY acceleration results for the initial conditions on the x coordinate

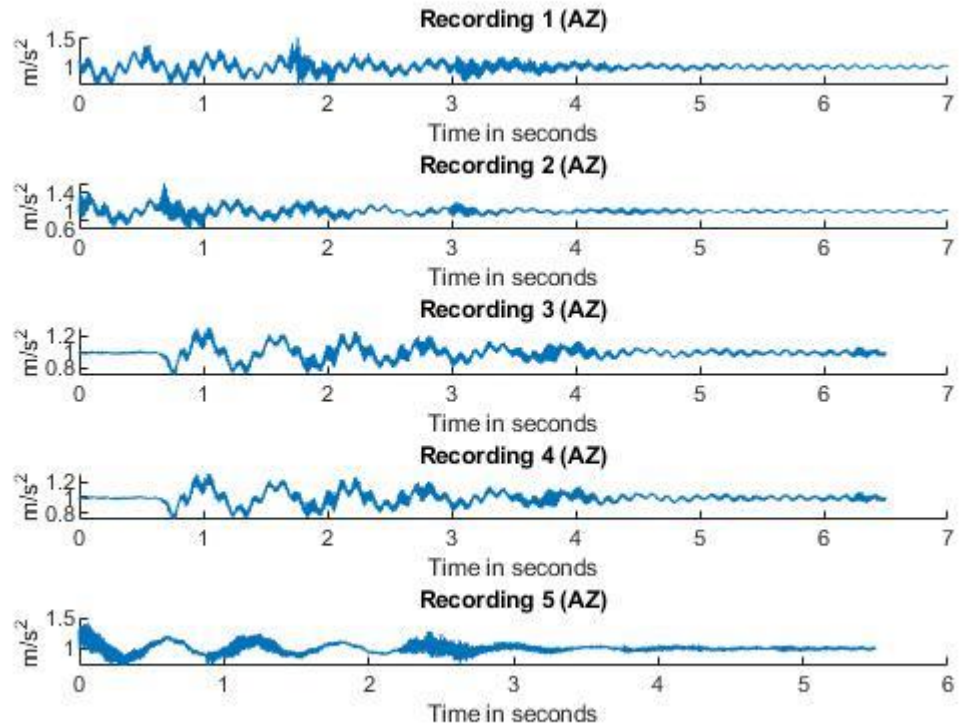

Figure 175: AZ acceleration results for the initial conditions imposed on the x coordinate

Figure 176 presents the FFT for the AY results, the natural frequency of 0.857Hz is representative of the pendulum motion. The measured distance between the centres of the lugs is 355mm, implementing equation 21 the analytical value for the natural frequency is 0.837Hz. If one only considers the natural length of the spring the natural frequency can be calculated as 0.91Hz. The analytical equation does not account for the rigid components in the experimental setup (the lugs) thus the natural frequencies calculated are not a true representation of the system. The correlation between results is however close and can thus can be deemed similar. The 7.57Hz frequency is representative of the spring system, which confirms that the higher frequency presented in the acceleration results pertains to the springs. The spring frequency presents a small amount of energy compared to the pendulum motion which is as expected since the springs can be considered relatively stiff and thus will not elongate/contact a great deal for the experimental testing.

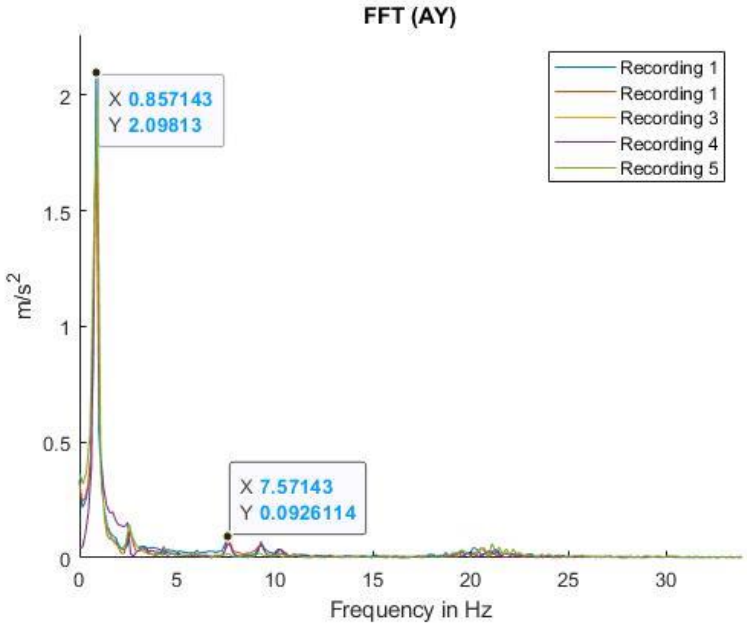

Figure 176: FFT for initial conditions on the x coordinate (experimental setup)

Figure 177 presents the FFT results for AZ, there are two frequencies as expected. When considering the results from the previous section, it is expected that the spring frequency should exist at 7.83Hz, however the results present a frequency at 8.42Hz. Furthermore, there is no explanation for the 1.69Hz frequency, this is however close to double that of the pendulum frequency.

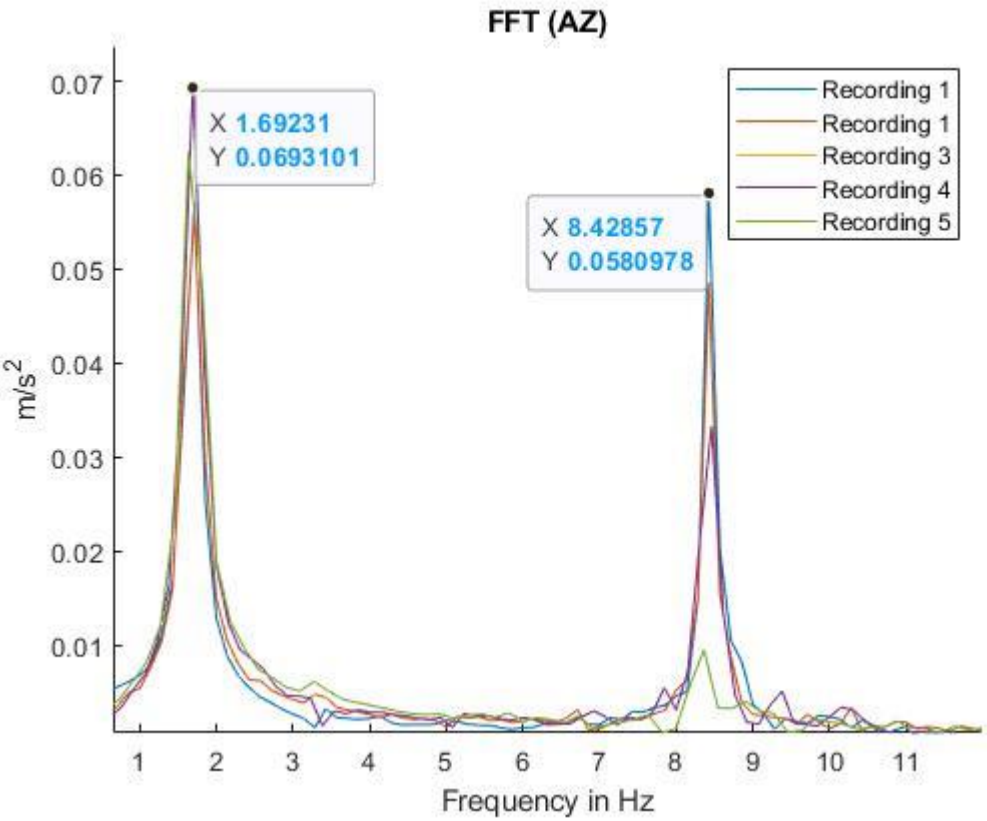

Figure 177: FFT for the AZ results sing initial conditions on the x coordinate

Implementing the above-mentioned initial conditions (including 0.1% damping) for the numerical simulation yields deviances in the Matlab results as presented by Figure 178. A similar result is achieved on Mathematica, however the simulation takes several minutes to produce results.

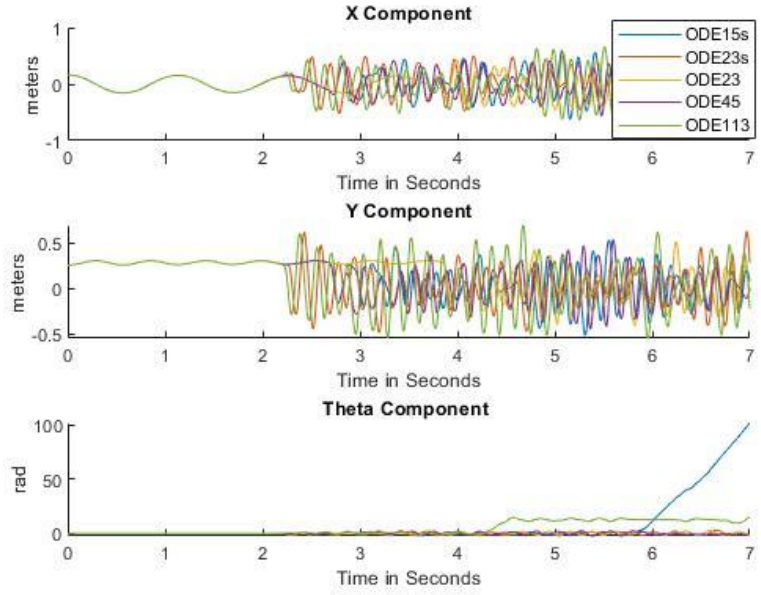

Figure 178: Numerical comparison to experimental conditions (initial conditions imposed on the x coordinate)

Using the procedure performed in the previous section, damping will be varied for the simulation case and compared to each recording, only the accurate range of the simulation results will be considered. The accurate rage is 0-2 seconds for all cases except the case where damping is assigned as 0.2%. Figure 179 presents the comparison of results between recording one and the numerical simulation, the results pertain to the y coordinate (AZ).

The results for both the numerical simulation and experimental testing present two frequencies, a high frequency, and a low frequency, this is substantiated by Figure 177. At $t = 0$ the acceleration for the numerical simulation and experimental tests do not correlate well, however the results begin to present correlation at later time periods. The high frequency which is representative of the springs, initially does not correlate well for all the test cases, the amplitude of the numerical simulation is far higher compared to the experimental results. For the case where damping is 0.2% the amplitudes present better correlation when $t \geq 1$. The deviance in the results can be attributed to damping. The lower frequency presents better correlation when damping is between 0.2-0.5%. The lower frequency is indicative of the pendulum motion, from the theoretical study it is known that the damping assigned for the pendulum acts far less aggressively. Thus, as damping increases its effects are far less pronounced compared to the springs. Based on the data the assumption for the pendulum damping is far more realistic compared to that applied to the springs. The numerical simulations and experimental tests are initially 180 degrees out of phase when considering the spring motion, they however move in phase at later time periods for all the presented cases.

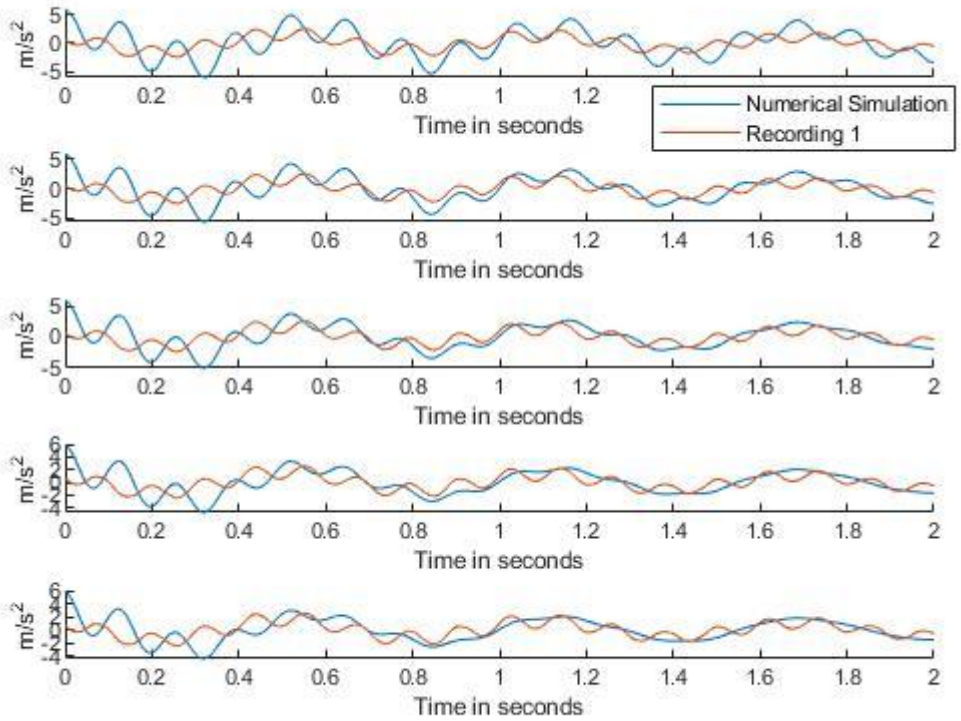

Figure 179: AZ and y coordinate acceleration results for recording 1 and numerical simulation (test case B)

APPENDIX M – EXPERIMENTAL RESULTS, presents the comparison of the numerical simulation with the reminding recordings, the following can be concluded:

- Recording 2 presents similar results to recording 1
- There exists a premature start with recording 3, however when the initial conditions are released there exists good correlation with the numerical solution
- Recording 5, presents good correlation with the numerical solution when damping is assigned as 0.4% and 0.5% (this is post 1 second). The results present smaller energy in the springs thus lower accelerations for the springs allowing better correlation.

Figure 180 presents the FFT results for the y coordinate. The results can be considered crude due to the short time span considered for the numerical simulation. The 2Hz frequency is equivalent to the 1.69Hz frequency presented in the AZ results. While the 8Hz frequency is equivalent to the 8.42Hz frequency found presented in the AZ results. The frequencies correlate well with the experimental testing.

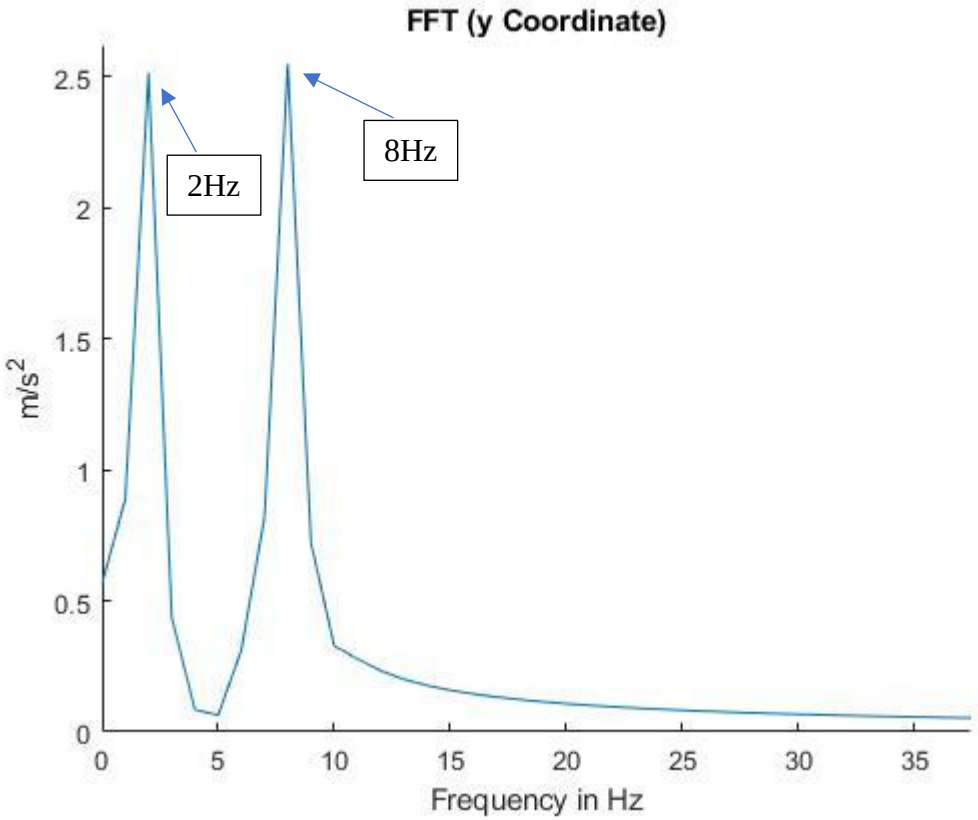

Figure 180: FFT results for a numerical simulation using x initial coordinates, results are for the y coordinate

Figure 181 presents the results for the x coordinate (AY) as performed above for the y coordinate, the results pertain to recording 1. The results trace a similar profile which consists of a low frequency sinusoidal function with a high frequency sinusoidal function at the peaks. The results present a phase shift which may be attributed to damping. The acceleration results at $t = 0$ correlate well between the numerical simulation and the experimental tests. If one neglects the phase shift which has occurred in the results, the numerical simulation values for the slower sinusoidal frequency tie up well with the results from the experimental setup. The deviance occurs with the high frequency sinusoidal frequency which occurs at the peaks of the lower frequency. The numerical simulation values for the high frequency sinusoidal frequency present larger more pronounced peaks when damping is assigned as 0.01%. As the damping

value gets higher the high frequency presents better consistency with the experimental data. From past simulations it is known that the damping from the springs acts far more aggressively compared to that of the pendulum motion, this explains why the lower frequency numerical simulation results are almost constant for all cases while the higher frequency is affect more while damping is increased. Based on the results one can conclude that the low frequency would be the pendulum motion while the high frequency is that of the spring system.

The results for all the other recordings can be found in the APPENDIX M – EXPERIMENTAL RESULTS. The other results do not present the consistency is at $t = 0$ as found with recording 1, however the other aspects of the results correlate well.

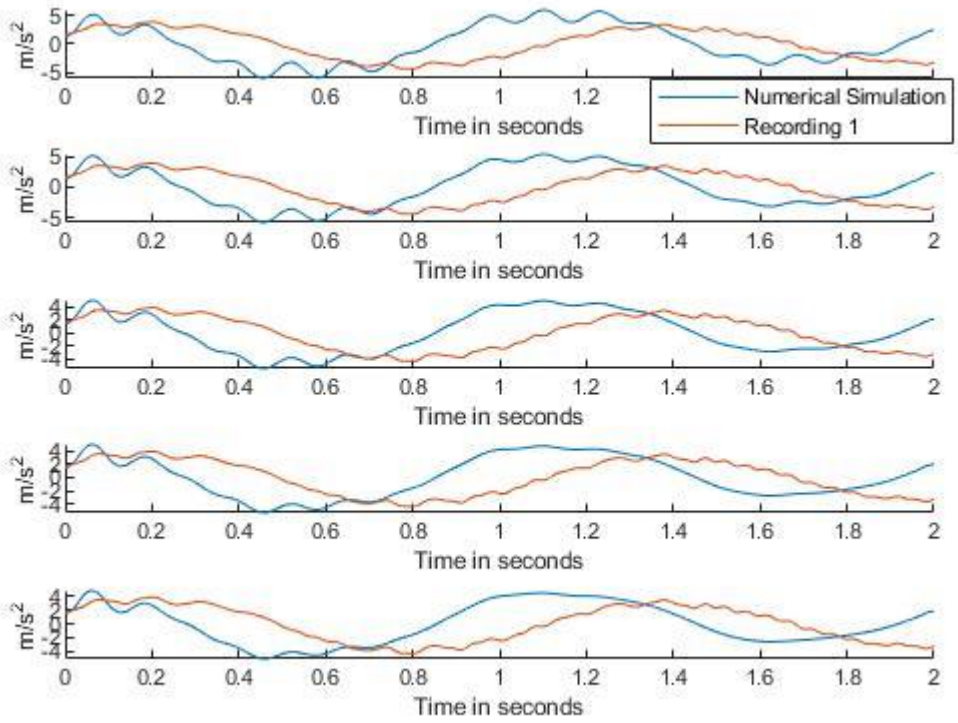

Figure 181: AY and x coordinate acceleration results for recording 1 and numerical simulation (test case B)

The PSD of the acceleration results is presented by Figure 184. Both the numerical simulation and experimental results produce the same frequencies. The natural frequencies for the pendulum and spring system correlate well with analytical values. There exists a frequency at 2.57Hz which has no known analytical solution however this frequency is presented for both the numerical and experimental results.

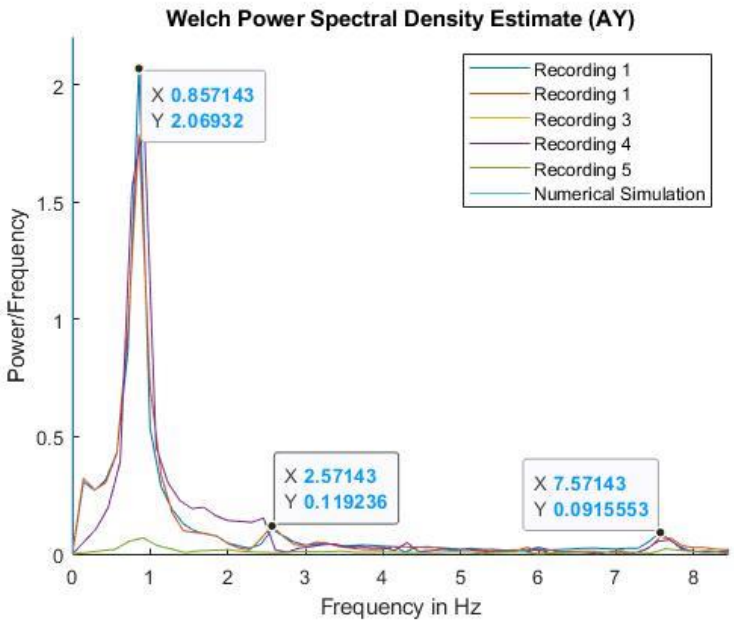

Figure 182: PSD results of the numerical simulation presenting the experimental setup for initial conditions on the x coordinate

The numerical simulations present good correlation with the experimental testing. There exists no analytical solution for the 8.42Hz (experimental test) frequency however this frequency can be found in both the experimental and numerical simulations. It is evident that this frequency does form part of the system. Since frequencies of the numerical solutions correlate well with the experimental testing it can be concluded that there does exist a direct correlation, even though the numerical values may differ.

6.4.1. EXPERIMENTAL RESULTS FOR TEST CASE C

The link below presents a recording of the experimental test for case C. The recording was made using the slow-motion option on the camera, however the upload could not keep the video in its slow motion form and thus the video appears to be sped up.

https://www.youtube.com/watch?v=-B4ls5CkOCY

Table 19 presents the initial conditions for the θ coordinate for each test case.

Table 19: Measured angle (θ) for the experimental test

Test Number	degrees
	θ
1	3.8
2	4
3	3.87
4	3.7
5	4.1

The AZ acceleration results are presented by Figure 183, the results for recording 1 and 2 follow a similar pattern as the results from test case A. Recording 3 presents similarities to recording 1 and 2, however it seems that there exists far less energy, thus producing accelerations which are not as high. Up to ±0.6 seconds, recording 5 presents the expected results however at a lower acceleration compared to recording 1 and 2, thereafter the results resemble that of recording 4. The results present what appears to be a single frequency, this result is consistent with what is presented for test case A.

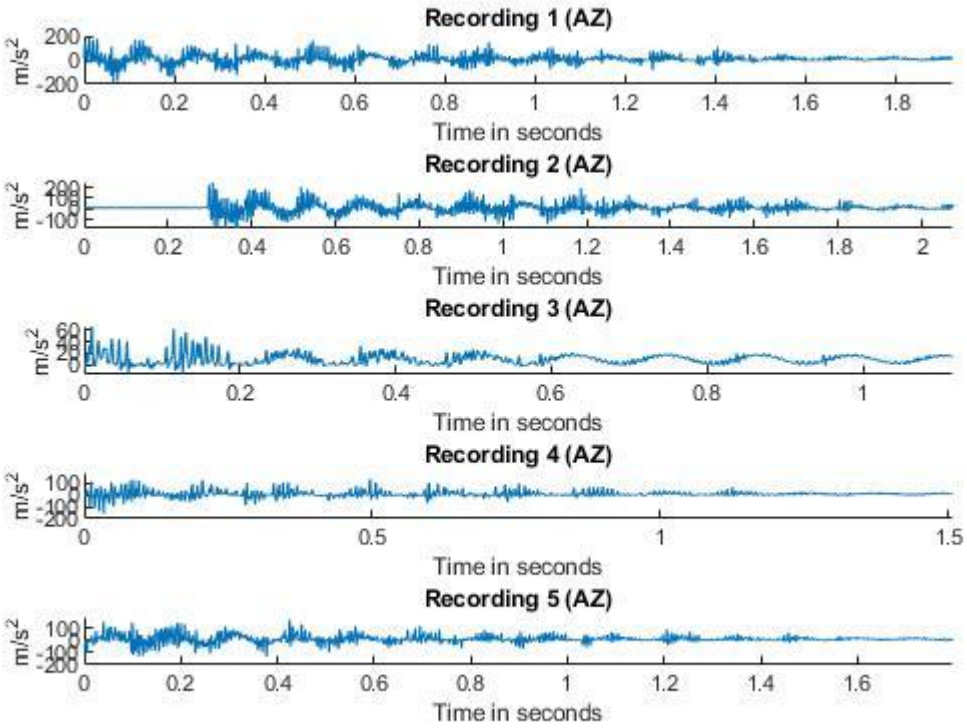

Figure 183: AZ acceleration results for experimental testing with initial conditions imposed on the θ

The PSD for the AZ results is presented by Figure 184, the results present a 7.84Hz frequency which is inline with the results developed when initial conditions have been imposed on the y coordinate (test case A). The results are as expected since the spring natural frequency is presented and close to the analytical value.

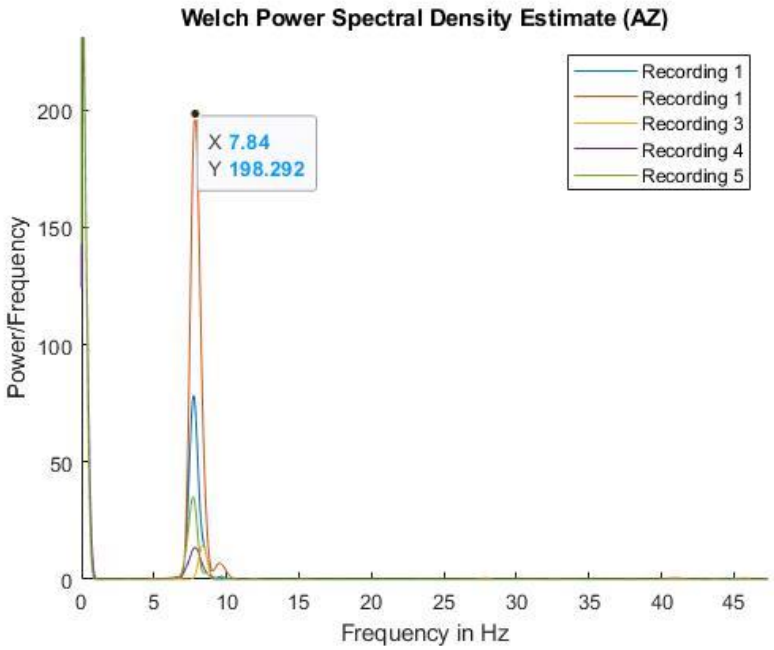

Figure 184: PSD for AZ results, experimental setup using initial conditions on θ

Figure 185 presents the AY acceleration results. The results present a large amount of noise which would be attributed to the 119.85Hz frequency. The presented results are far too noisy due to the 119.85Hz frequency, thus to study the data further it will be filtered as done when comparing the numerical and experimental testing.

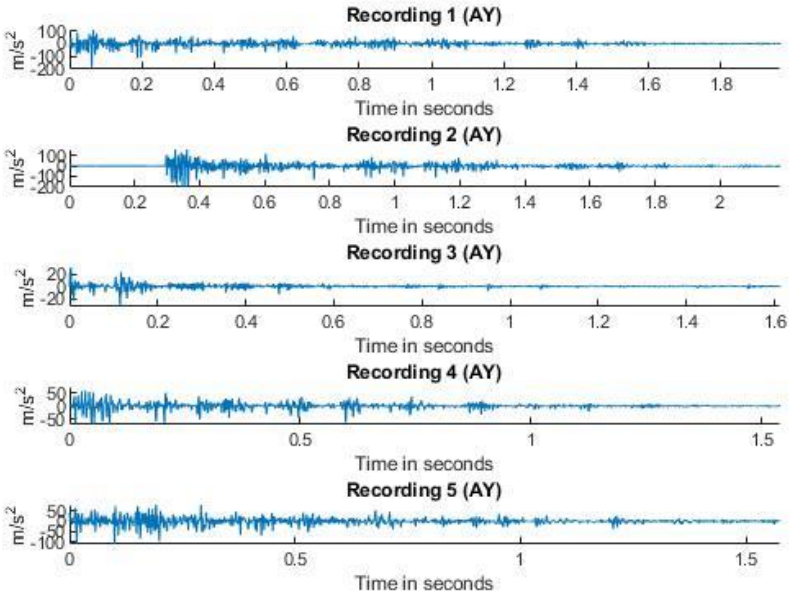

Figure 185: Pendulum motion for experimental setup using initial conditions imposed on the θ coordinate

Figure 186 presents the AY results, however the results have been filtered to remove any frequency higher than 60Hz. The results present a sinusoidal function as expected. The accelerations results have drastically reduced for each recording, the results from Figure 185 present far higher accelerations. It can be noted that the high accelerations are developed from the natural frequency of the beam.

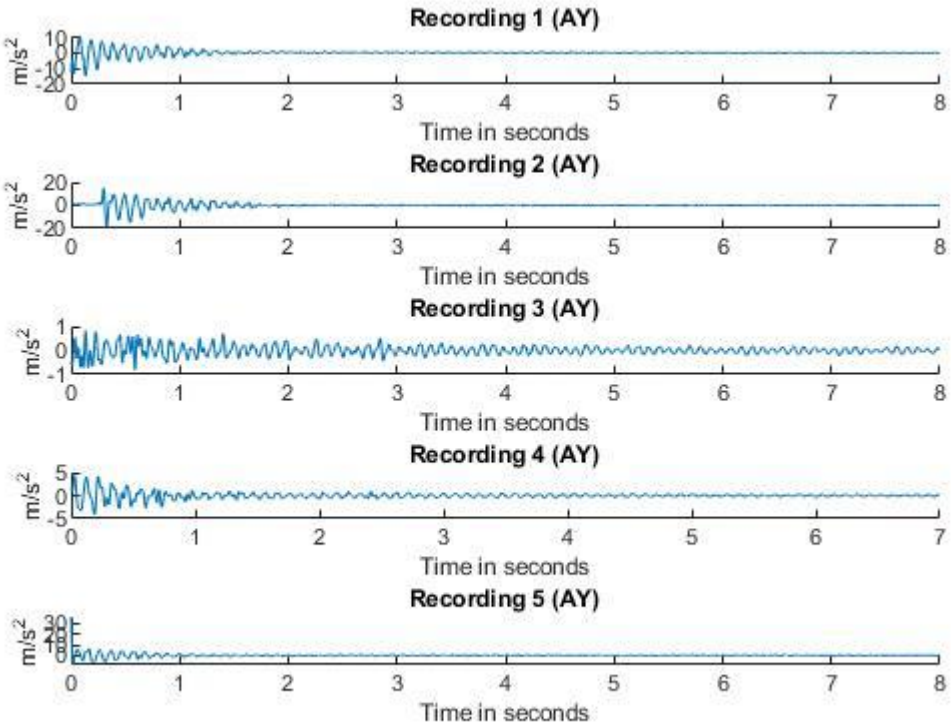

Figure 186: Pendulum motion for experimental setup using initial conditions imposed on the ϑ coordinate (filtered data)

Figure 187 presents the PSD for the *AY* results, there exists a 9.82Hz frequency for all the recordings except recording 3 which presents only a 10.46Hz frequency. The 10.46 Hz frequency also exists for recording 4 and 5, however they exist with an extremely small amount of energy. The presented frequencies do not correlate with any analytical values thus it is unclear where this frequency originates from. Recording 1 and 2 present far higher 9.82Hz frequencies thus the 10.46Hz frequency may not be clearly visible or may have not been excited.

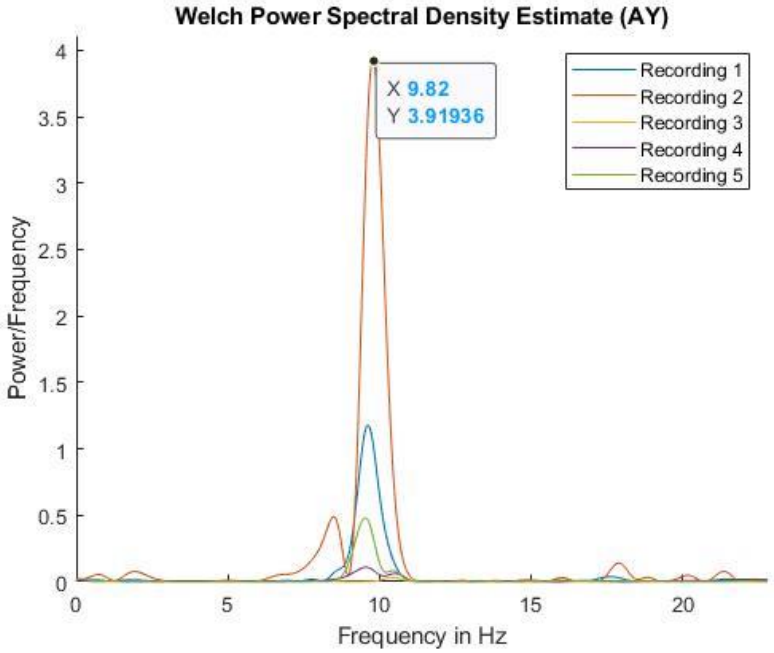

Figure 187: PSD for the pendulum motion using initial conditions imposed on the θ coordinate

Figure 188 presents the RX results all plotted on the same axis. It is expected that there is a variance between all the results since the initial conditions are all different, this is substantiated by the system being chaotic in nature. The results for recording 3 present very small rotational velocities when compared to the other recordings. Once the system has settled down the recordings present what appears to be random noise and excitation from the other directions.

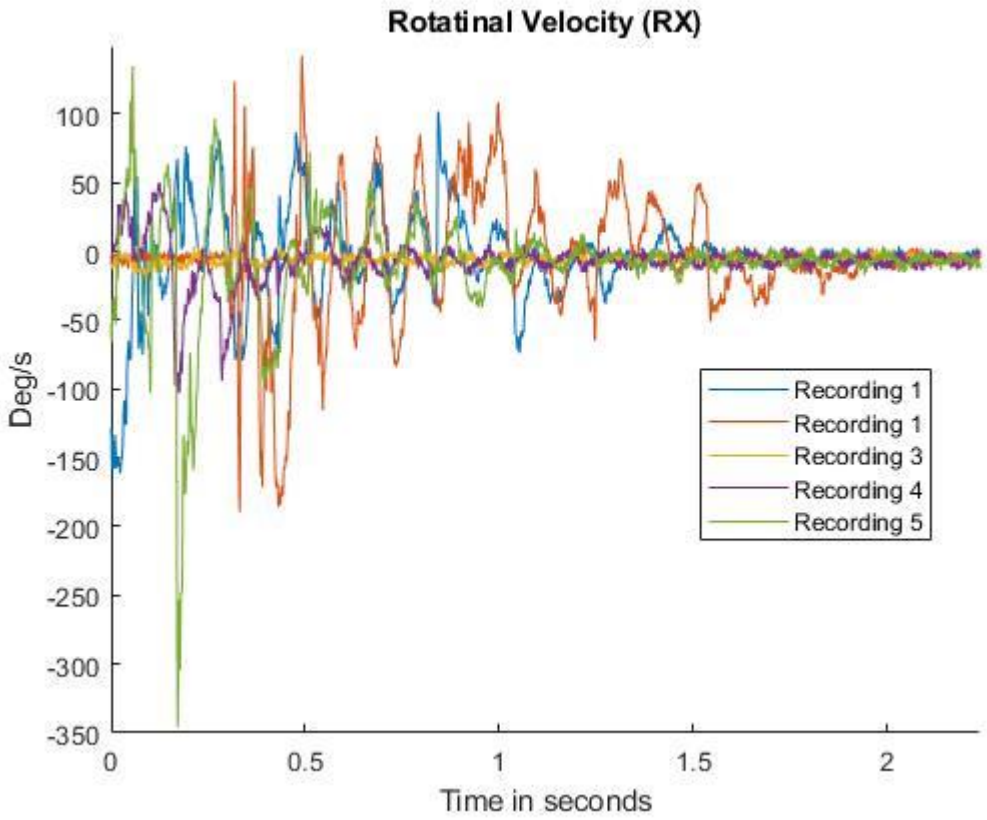

Figure 188: RX results for the experimental setup with initial conditions imposed on the θ coordinate

The PSD for the RX results is presented by Figure 189. There exists a frequency at 9.76Hz for all recordings, however recording 5 presents a frequency of 10.47Hz as presented by the results for AY, again recording 4 and 5 also present the 10.47Hz frequency however there is a small amount of energy present. The 9.76Hz frequency ties in very close with the results present by AY, based on the previous numerical simulations it is known that the x and θ coordinate are closely linked and thus it is expected that they will share the same frequencies. The numerical value of the frequency is unique, since it does not correlate with any of the analytical calculations. Recording 1 and 2 also present 0.71Hz and 2.71Hz frequency, the energy for these frequencies (recording 2) is high thus making these frequencies very pronounced, however for recording 1 they are less pronounced but still exist. The 0.71Hz is close to the pendulum frequency which is presented when imposing initial conditions on the x coordinate. The 2.71Hz frequency presents no resemblance to any of the known frequencies, this is also the case for the 6.39Hz frequency which is only found for recording 2.

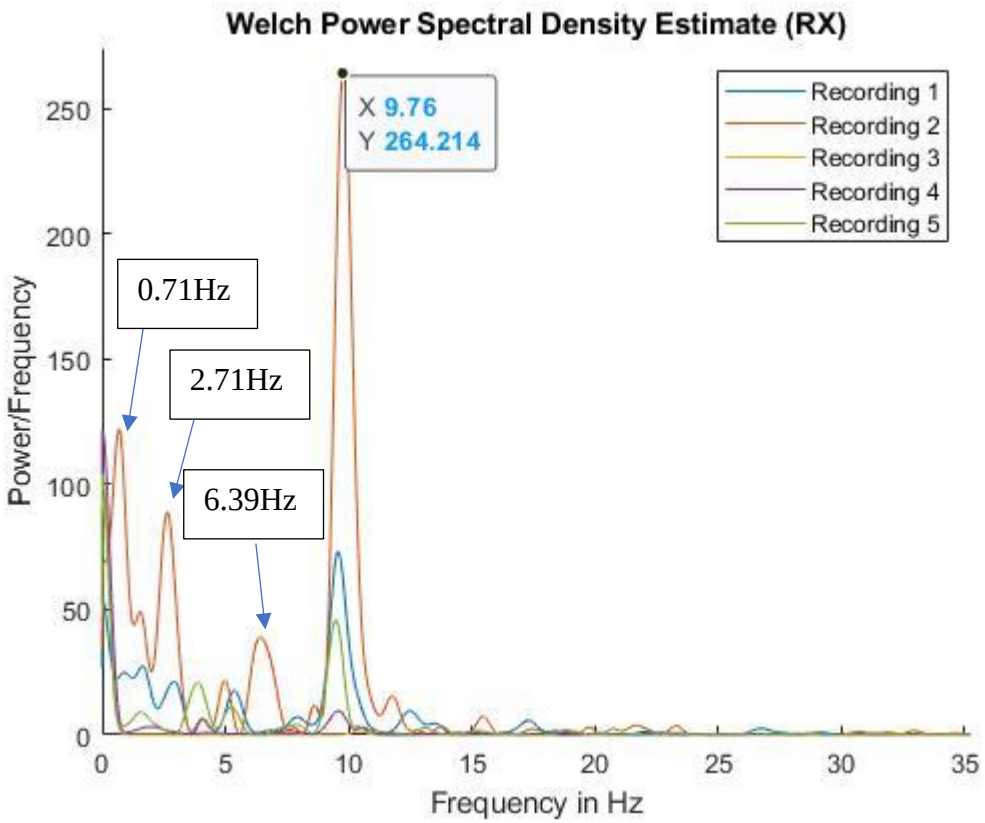

Figure 189: PSD for the RX experimental results with initial conditions imposed on the θ coordinate

Figure 190 presents the filtered and normalised results for AZ, AY and RX as done previously with numerical simulations. The AZ results presents undisturbed sinusoidal functions, which is similar to what has been observed with regard to previous numerical simulations with initial conditions assigned to the θ coordinate (for the case where the setup does not present parametric resonance). There is a clear connection between the AY and RX results, this is outlined when studying the 3DOF system. It is observed that when the peaks of AY and RX do not coincide, the AY results then present perturbations which is assumed to originate from the influence from the RX component. Furthermore the RX component also presents perturbations which line up with peaks in the AY component.

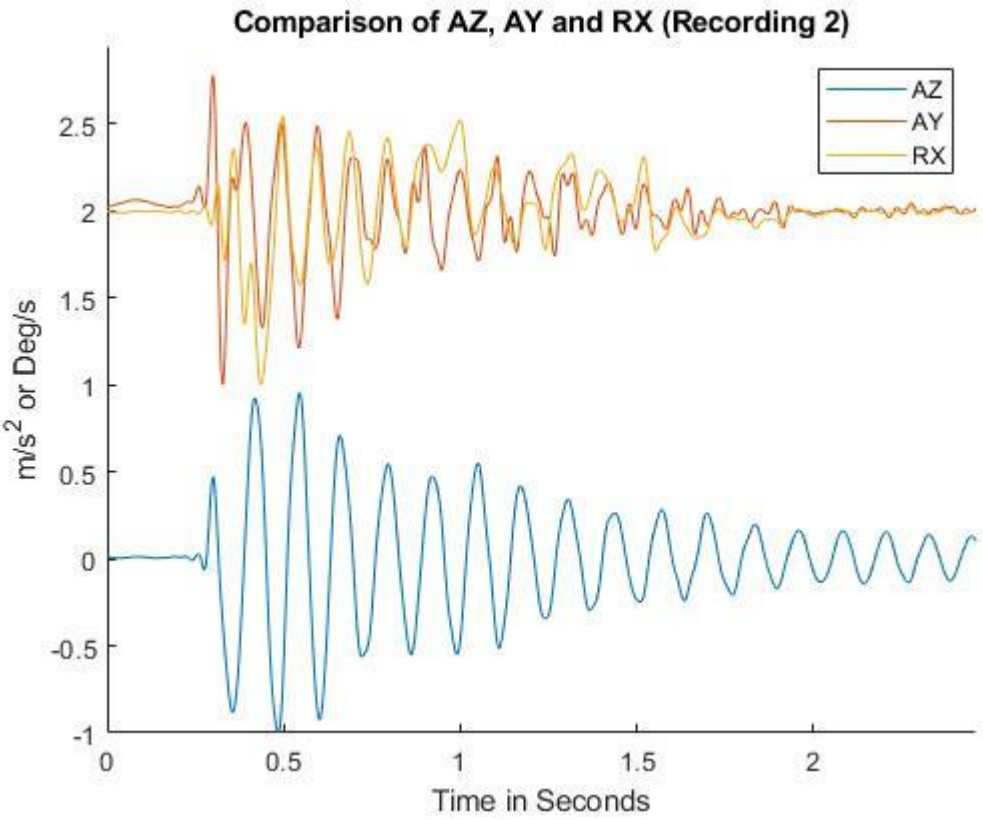

Figure 190: Comparison of AZ, AY and RX results for recording 2

The numerical simulations for the initial conditions imposed on the θ coordinate present poor convergence and thus only small-time intervals can be simulated. Figure 191 presents the results for all three coordinates using the initial conditions presented by Table 19, the results present good consistency thus implying that the change in initial conditions is small enough such that the solutions are relatively similar. Thus, for simplicity the experimental results will be compared to the case where the numerical solution is imposed a 4-degree initial condition.

Previously the numerical simulations implemented damping as defined in the theoretical study. However, for the case where initial conditions are imposed on the θ coordinate, it was found that better consistency is achieved when considering damping as defined by equation 3 for all the coordinates. The percentage of damping will for each case will be defined as previously done in this chapter.

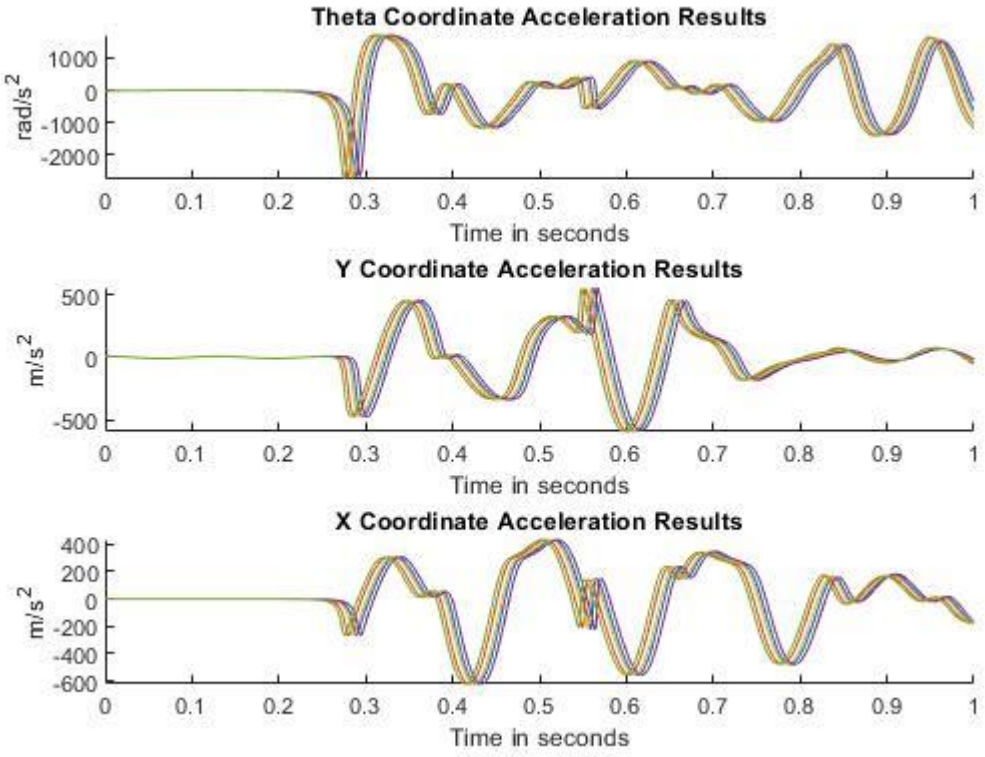

Figure 191: Numerical solution for each coordinate using initial conditions presented in Table 19

Figure 192 presents the comparison between the y coordinate and AZ results. The results present poor consistency with regards to the numerical values. When reviewing Figure 191 there exists large accelerations for all three coordinates. It is thought that the effect of damping would be a complex mechanism for this case. As previously stated, damping for the proposed system is unknown and thus needs to be assumed. To develop a comparison the results will be normalised thus allowing one to evaluate common patterns.

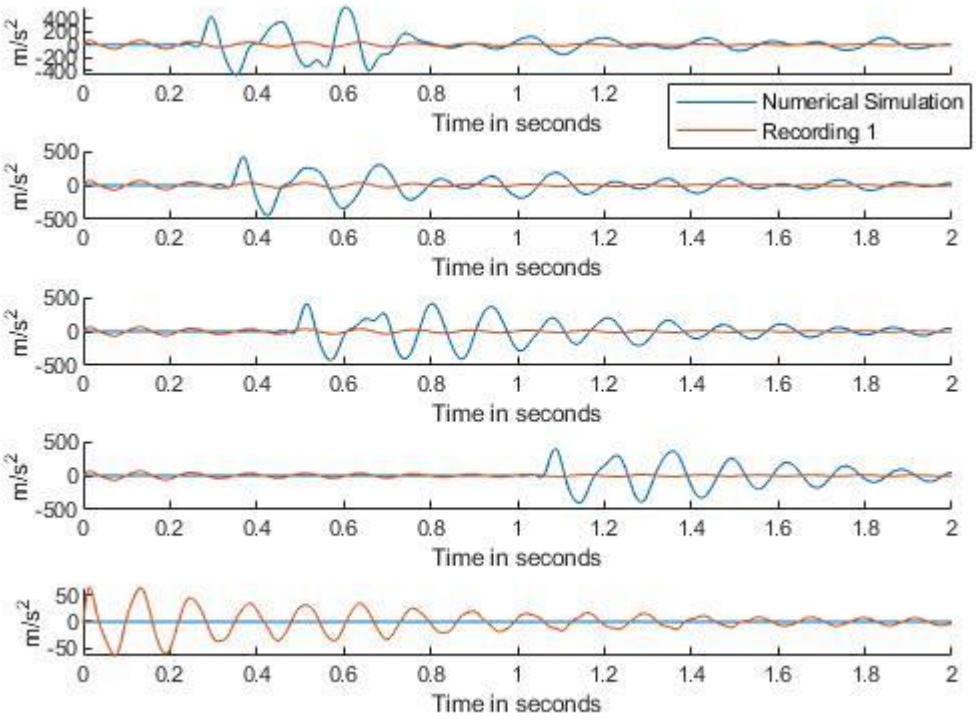

Figure 192: AZ and y coordinate acceleration results for recording 1 and numerical simulation (test case C)

Figure 193 presents the normalised results for the AZ and y coordinate accelerations. The experimental results present immediate accelerations while the numerical solution presents lag in the y coordinate accelerations. The lag increases with an increase in damping until there is 0.5% damping being assigned. Once damping is assigned a value of 0.5% the accelerations are immediate as seen with the experimental test. With damping values between 0.1-0.3% there exists perturbations in the numerical solution which occur early on (label A), these perturbations cease to exist with higher damping values. The case where damping is assigned a value of 0.5% presents good correlation with experimental results however at ±0.5 seconds the experimental tests decay far quicker compared to the numerical simulation.

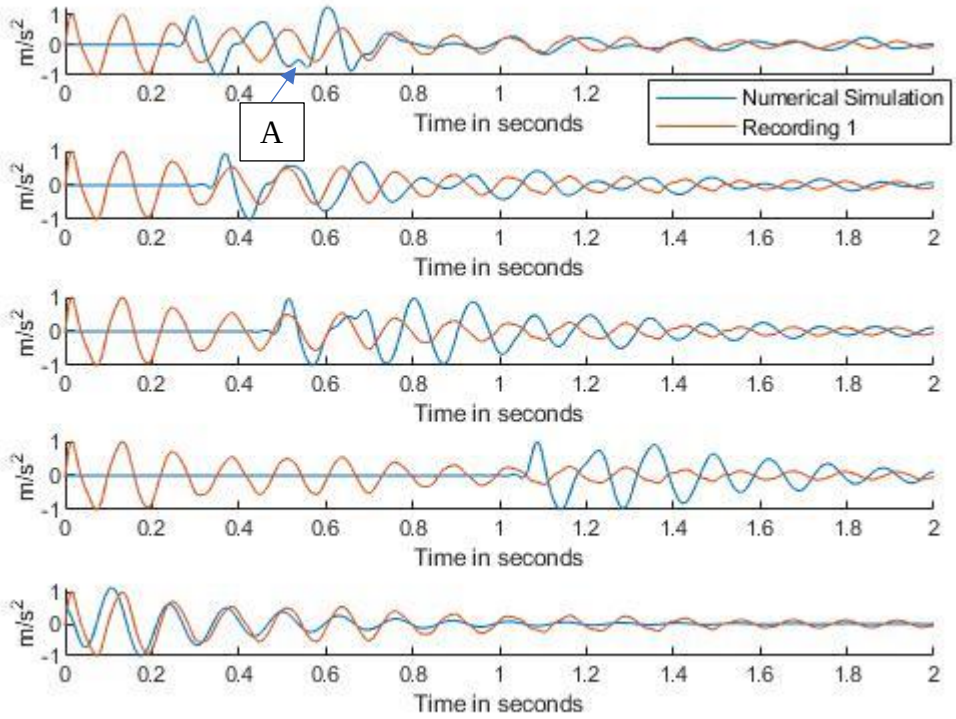

Figure 193: Normalised AZ and y coordinate acceleration results for recording 1 and numerical simulation (test case C)

Matlab Code 12 is implemented to remove the lag in the system, this allows one make a better comparison of results. Figure 194 presents the results which exclude the lag in the numerical simulation. Numerical simulations 1 to 4 present good correlation to the experimental tests from 0-0.08 seconds, the effect of damping has little effect on the system for these cases. There exists a phase shift after 0.08 seconds for all the presented cases, the case where damping is assigned 0.5% presenting the smallest phase shift. The numerical simulations and experimental results present similar patterns, in several circumstances the normalised values are similar, this would indicate that the results are factors of each other.

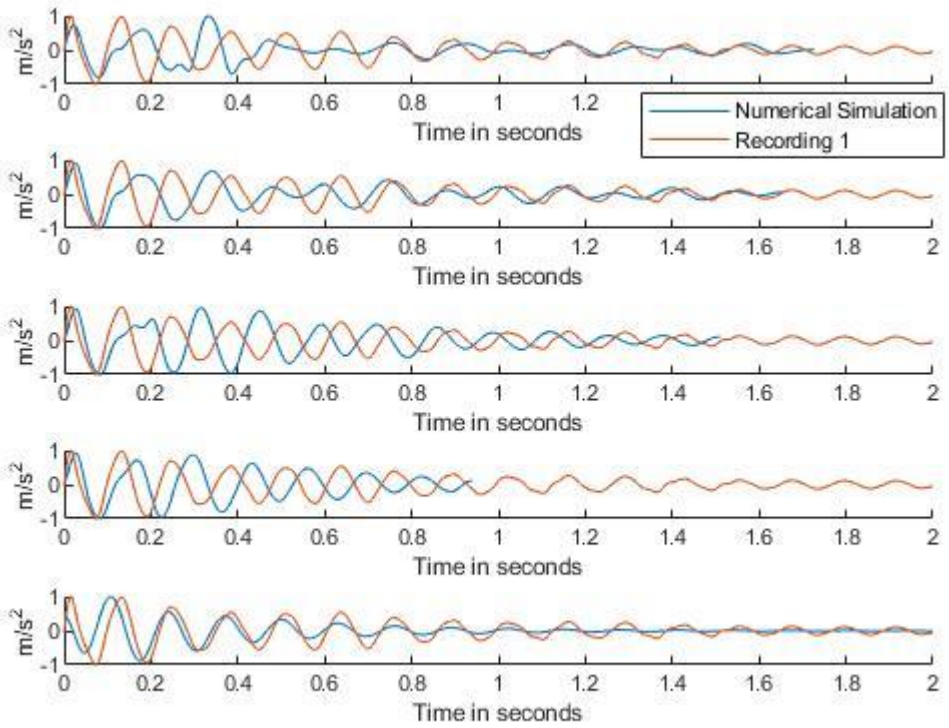

Figure 194: Normalised AZ and y coordinate acceleration results for recording 1 and numerical simulation (test case C, no lag)

The comparison with all other recordings can be found in APPENDIX M – EXPERIMENTAL RESULTS, the following can be noted:

- Recording 1 and 2 present very similar results which correlate with the numerical simulation in a similar manner
- All recordings expect for 5 present the same correlation between 0-0.08 seconds
- Recording 4 and 5 present a 180-degree phase shift with regards to the numerical simulation when damping is assigned as 0.5%
- There exists better consistency with regards to the experimental tests and numerical simulations for recording 4 and 5, where damping is assigned between 0.1-0.4%

Figure 195 presents the PSD results for the y coordinate, there exists a single frequency which is roughly 7Hz. This frequency correlates well with the processed AZ results, thus both results present the frequency of the spring system.

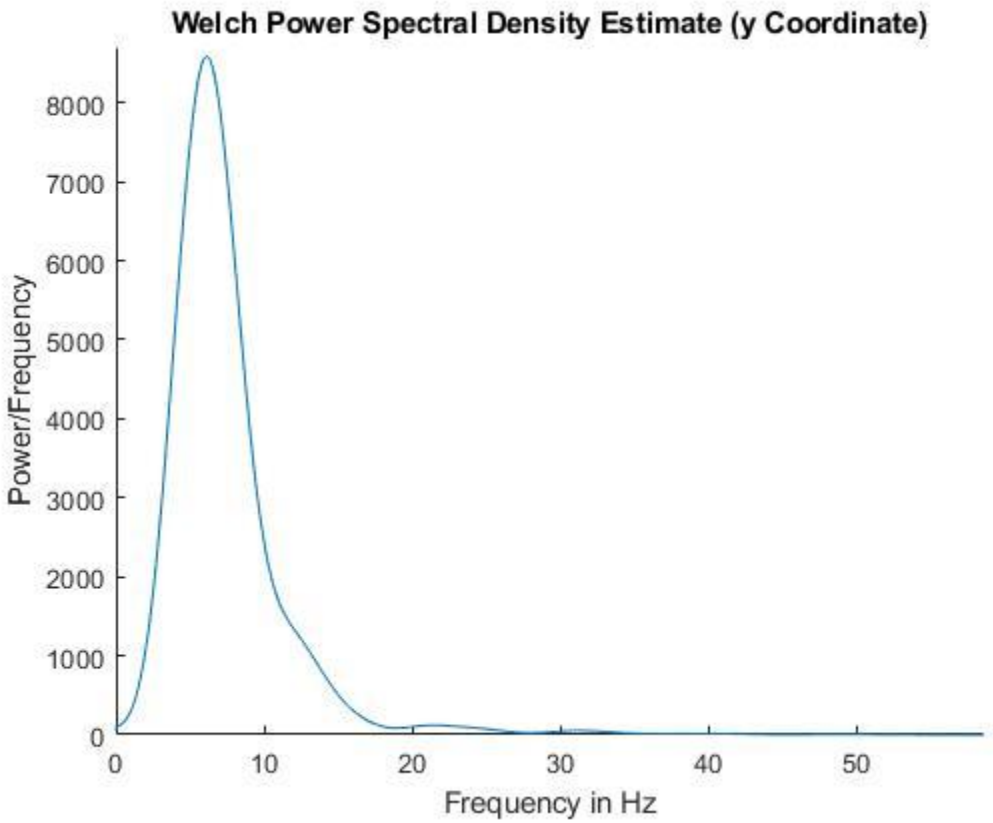

Figure 195: FFT results for the y coordinate, experimental results with initial conditions imposed on the θ coordinate

Figure 196 presents the comparison of the x coordinate results and AY. When damping is assigned a value of 0.5% the pendulum motion is overdamped. The numerical simulation and experimental testing present good correlation for all other damping cases. When damping is assigned 0.1%-0.2% there exists pronounced perturbations while 0.3% damping produces far less pronounced perturbations and 0.4% produces no perturbations. The perturbations can also be found for the experimental results; however they do not line up with the numerical simulations due to the results presenting a phase shifts. The perturbations do however follow a similar trend, they occur very close to or at peaks.

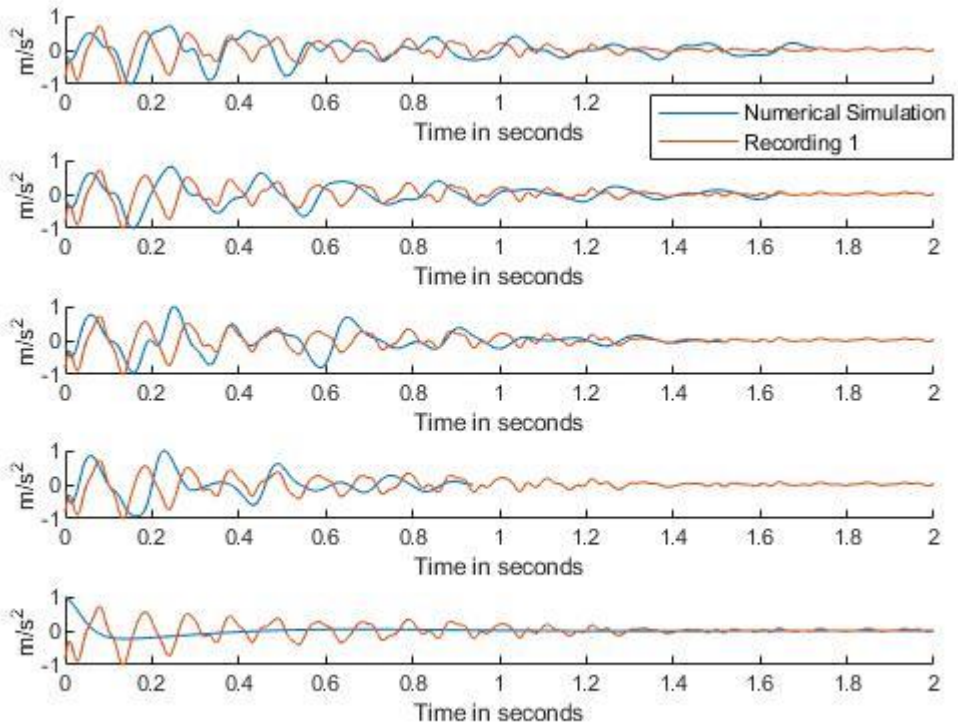

Figure 196: Normalised AY and x coordinate acceleration results for recording 1 and numerical simulation (test case C, no lag)

A comparison of all the other results can be found in APPENDIX M – EXPERIMENTAL RESULTS, the following can be noted:

- Recording a 1 and 2 present similar results
- The perturbations presented in recording 3 are far more pronounced compared to the other recordings. The results present very little correlation with regards to the numerical simulations
- Recording 4 presents larger perturbations compared to recordings 1 and 2, however the results still correlate well with the numerical simulations.
- The results for recording 5 present a peak at $t = 0$, with very small values thereafter. It is thought that is recording had experimental errors thus the deviance compared to the other recordings. The overall pattern of the results is however similar.

Figure 197 presents the PSD with the results being indicative of the spring frequency. This implies that the x coordinate is influenced by the y coordinate when imposed initial conditions on the θ coordinate. The results do not correspond well with Figure 187 which presents a 9.82Hz.

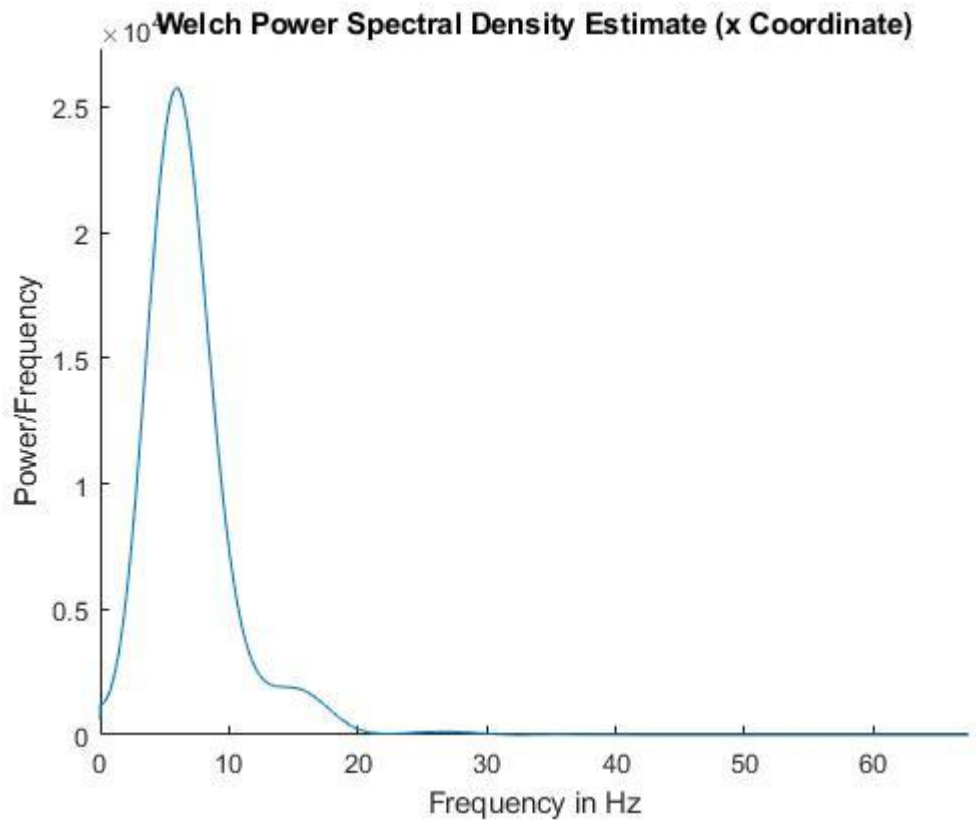

Figure 197: PSD results for the x coordinate subjected to initial conditions on the θ coordinate from experimental testing

Figure 198 presents the comparison between the numerical simulation and experimental testing for the θ coordinate and RX. For all damping cases excluding 0.5%, there exists a peak velocity at ±0.04 seconds, there does exist a peak for the experimental results however it is far smaller in magnitude. It is be hypothesized that damping may not be linearly proportional to the velocity, thus there exists a damping function which acts more aggressively at high velocities compared to lower ones. When damping is assigned values from 0.2-0.4% there exists far better correlation with the experimental results. There are several perturbations found the experimental results ($t \leq 0.2$), however there is one which is most noticeable in the numerical simulation, this is presented by label A.

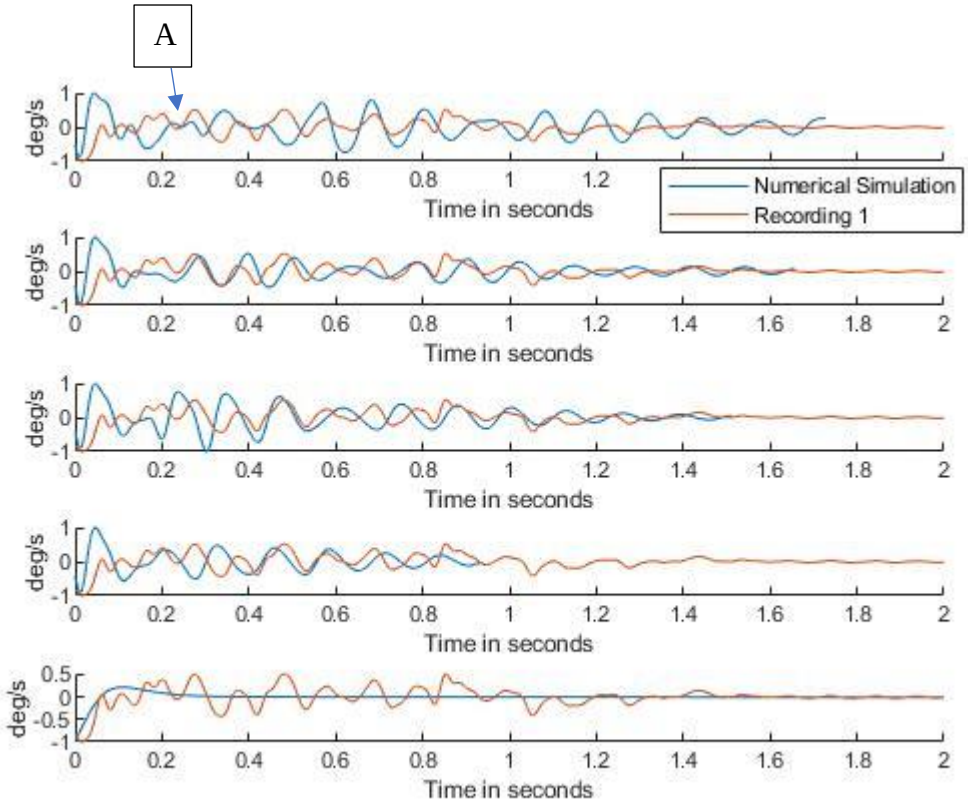

Figure 198: Normalised GX and θ coordinate acceleration results for recording 1 and numerical simulation (test case C, no lag)

Figure 199 presents the PSD results for the numerical and experimental testing on a single plot. The numerical simulation overlays with the experimental results at several locations:

- The 8Hz frequency which is assumed to be linked to the spring system corresponds to frequencies in the region of 7.6-7.95Hz represented by A. the experimental results present a small amount of energy compared to energy experienced in the numerical results. This conclusion is only valid when comparing energies within a specific recording and/or numerical simulation. The spring frequency is dominant in the numerical simulation however this is not the case for the numerical simulation
- The highest peaks for recordings 1 to 5 exist in a range of 9.44-10.44Hz. A similar peak exists for the numerical simulation at 9.5Hz. There is no analytical solution for this frequency however it is clear that it forms part of the 3DOF and not a natural frequency of the structural components
- There is a 3.87Hz frequency which is present for the numerical simulation and recording 5, this frequency does not reflect any analytical values

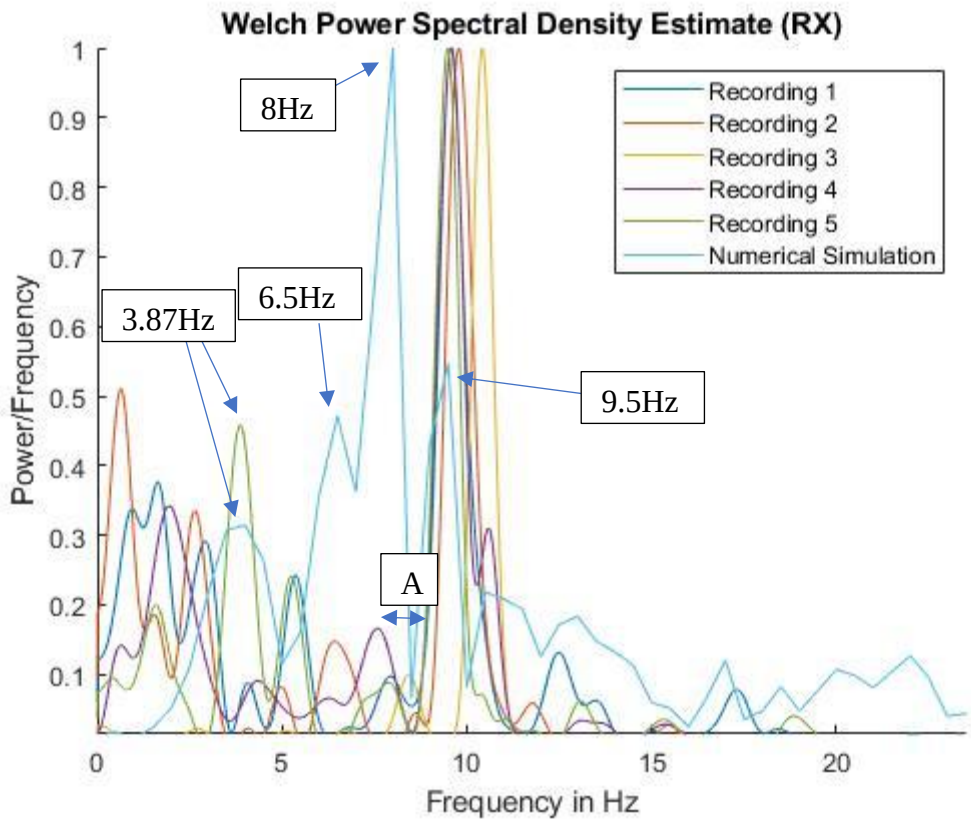

Figure 199: PSD for the θ coordinate with initial conditions imposed on the θ coordinate (experimental testing and numerical simulation)

6.5. PARAMETRICALLY RESONANT TEST CASE

The previous experiment deals with the experimental setup of a system which does not experience parametric resonance. Given the parameters of the current springs a parametrically resonant system can be developed if the mass of the system is changed to 484kg. This would imply that a total mass of 460.36kg would need to be added to the current system. This presents an unfeasible case since there exists limit area where mass can add. Furthermore, the addition of mass would change the location of the CG dramatically thus the system would not be inline with the derivation of the presented differential equations. Based on this the parametrically sized experimental setup cannot be developed with the current resources.

6.6. EXPERIMENTAL TESTING CONCLUSION

The inclusion of the lugs on the experimental setup is not considered in the 3DOF, it is thought that a simpler experimental setup using elastics would better replicate the 3DOF. Elastics will not require fabricated lugs to develop the pendulum system thus simplifying the system to what is mathematically modelled.

The numerical and experimental testing correlate well for the case where initial conditions are imposed on the x and y coordinates. When assigning initial conditions to the θ coordinate the numerical and experimental results present a similar trend, however numerical values do not correlate. The lack of numerical corelation is thought to be linked to damping. The numerical simulations assume a linear damping which is based on the stiffness and mass of the system. When imposing initial conditions on the θ coordinate, this introduces another coordinate where damping will exist, it is believed that damping for the θ coordinate may exist in a complex manner where it may not be linear. From the numerical simulations it has been shown that the θ coordinate can be influenced by both the x and y coordinate, thus there may also exist an influence on the effect of damping from other coordinates.

The PSD/FFT results for the test cases present good correlation. There exist several frequencies for which no analytical solutions exist, these frequencies are however common between both the numerical simulations and experimental testing. This would imply that the 3DOF system does mimic the behaviour of the experimental tests even though the numerical vales of the test may differ.

The 3DOF system neglects the stiffness contribution of the rigid bar which is an assumption used for the derivation. Based on the experimental tests the natural frequency of the rigid bar affects the system in a significant manner and thus would need to be considered in further studies of the system.

CHAPTER 7: FEASIBILITY OF THE PARAMTERICALLY RESONANT VIBRATING SCREEN

The previous chapters deal with the theoretical and experimental study, this chapter will ultimately answer the questions which have been proposed at the beginning of this study. During the research the author has outlined the following additional criteria which is deemed important when considering the proposed vibrating screen:

- Mechanical design:
  - Feasibility of mechanical items such as springs/buffers and motors which would form part of the proposed vibrating screen
  - The mechanical philosophy of how the system would be put together in reality and if this would be a realistic design
- Structural design (support structure):
  - Can an economical design of a support structure for the proposed vibrating be designed?
  - How do the loads compare with traditional vibrating screen designs?

7.1. MECHANICAL FEASIBILITY

This topic is initially presented in the study of the 2DOF system where it is shown that buffer stiffness used for the theoretical study do exist. These buffers do have limitations since they cannot experience large displacements. Figure 200 presents a load deflection graph for typical rubber buffers, the peak displacement is just over 10mm. Based on the numerical simulations, a parametrically resonant setup will experience far higher displacements thus causing failures in the presented buffers.

http://www.arnotavs.co.za/products/
(Refer to SH mounts pdf)

Figure 200: Specification of the SH mounts (ACTOM, 2023)

Based on the DEM analysis, linear motion screens present steady material flow where the discharge produces a constant stream of material. This allows one to use DEM analysis to develop suitable chutes to allow material to flow effectively. The proposed vibrating screen presents chaotic material movement, where material can easily escape the screen box and flow through the discharge at vastly varying rates. This would present complexities when designing the required chutes since there does not exist a definitive stream of material.

When considering large displacements as presented by 3DOF it would not be feasible to use a motor which drives unbalanced masses to develop excitation. This method requires a cardan shaft which has a pinned joint so that the motion of the vibrating screen is not transferred to the motor and motor base. The 3DOF system presents large displacements which may transfer translational displacements even with a pinned joint. Thus, the presented system would only be feasible if one uses exciter motors.

Springs and rubber buffers are prone to fatigue and it is common practice to replace springs and rubber buffers during a vibrating screens life. Failures on vibrating screens may occur during operation, this however does not pose any significant health and safety issues. The 3DOF system presents high accelerations and displacements, thus failures of springs/buffers may be a health and safety risk since there is a large amount of energy in the system.

7.2. STRUCTURAL DESIGN

Support structures which are designed to house vibrating equipment such as vibrating screens need to consider natural frequency analysis, harmonic response analysis and fatigue for their design. Natural frequency analysis allows one to calculate eigen values and vectors which are representative of natural frequencies and mode shapes. These can be used to understand the structures response to various frequencies and ultimately design a support structure such that the operating speed of the equipment and structure do not coincide.

The design of support structures for vibrating equipment is dependent on the dynamic loads which equipment induce. Lower dynamic loads make it easier to design a support structure while higher dynamic loads make it more challenging. Fatigue can be assessed through various design codes and human exposure time can be evaluated by means of ISO2631. Figure 201 presents the foundation loads for the SD18/36 vibrating screen, the input from the excitor motors (167kN, Table 3) is greatly reduced with the vertical dynamic loads being 1.74 and 1.19kN for the vertical component and 1.08kN for the horizontal component.

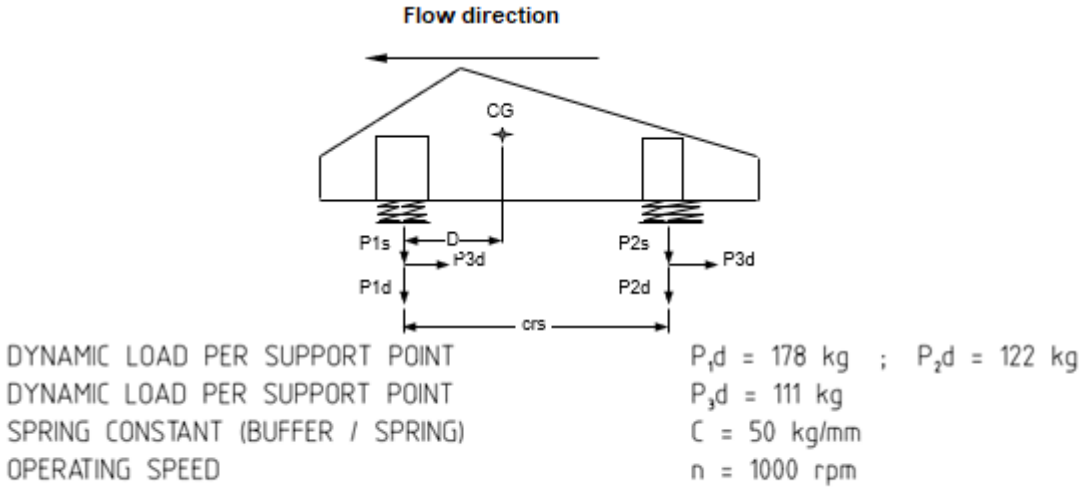

Figure 201: Foundation loads for the SD18/36 vibrating screen

If one considers the parametrically resonant screen in this study the dynamic loads can be calculated using the displacement results and the known stiffness of the springs. The foundation loads due to the pendulum motion will not be considered, only the loads induced due to the spring will be considered.

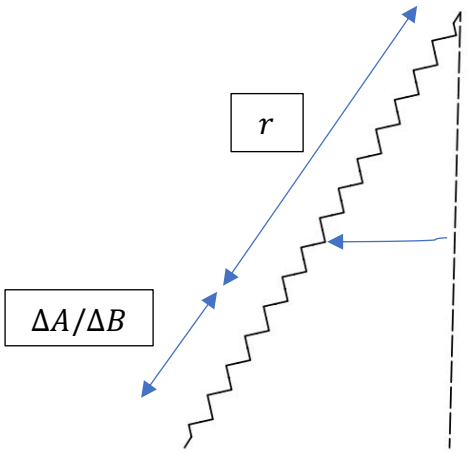

The resulting dynamic loads are presented by Figure 202.The resulting loads are far higher compared to those developed by the SD18/36 vibrating screen (Table 3). Based on the presented loads it is clear that a support structure for the 3DOF vibrating screen will be less economical compared to a traditional linear motion vibrating screens. Due to the complex nature of the loads, it would also be impossible to perform the analysis using harmonic response analysis since the loads do not present pure sinusoidal functions as they do for traditional vibrating screens. One would need to consider transient analysis where loads can be varied by means of graphs/equations.

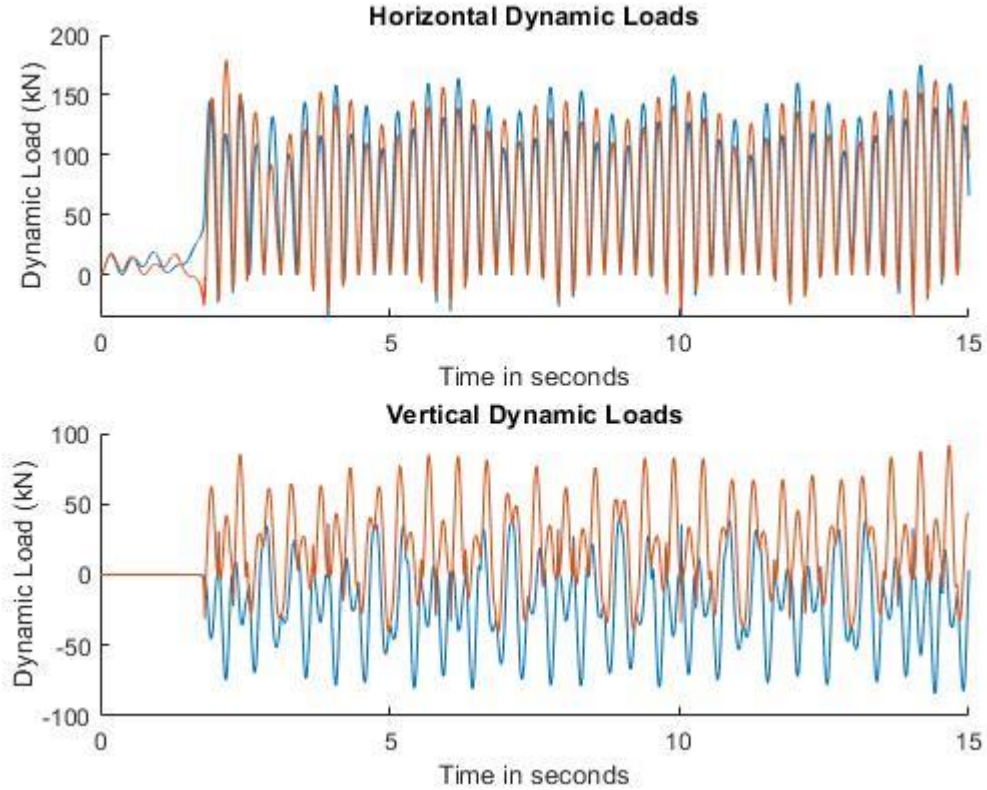

Figure 202: Dynamic loading for the 3DOF vibrating screen

7.3. RESEARCH QUESTIONS AND OBJECTIVES

The following research questions have been proposed earlier in the study:

- Can vibrating screens operate in a more efficient manner using parametric resonance?
    - Based on the 3DOF system there is little benefit to using parametric resonance in this form. The efficiency of the proposed screen is far lower compared to that of a horizontal deck linear motion vibrating screen. The 3DOF is capable of screening material at a higher rate thus developing higher tonnages, however the infrastructure required to facilitate such a vibrating screen would be uneconomical.
- Are there more efficient ways of screening material other than linear, circular, and elliptical motion?
    - From the literature review novel vibrating screen motion has produced higher efficiency
    - For the case of the 3DOF system there only exists higher efficiencies when dealing with a screen deck inclination of 10 degrees
    - Based on the data gathered in this study the complex motion trace does not present any benefit with regards to the efficiency
- Is it possible to use lower excitation frequencies or a combination of low and high excitation frequencies for screening material efficiently?
    - This is shown to be true for the case of the 10-degree deck inclination.
    - The results also present a case where low frequencies coupled with high accelerations do not obey the data presented by Figure 3. It can thus be concluded that low excitation forces can develop criteria for screening

CHAPTER 8: CONCLUSION

The 2DOF system is developed which represents a single spring pendulum. The system presents a simplified version of the 3DOF which is later studied, noting that the 2DOF presents one less coordinate. It is found that an elastic pendulum which is parametrically sized will transfer energy between each of the two coordinates. When the results are processed into the frequency domain an interesting phenomenon occurs where side band frequencies occur. This presents modulation which is commonly studied in electrical engineering and found when gearboxes experience failures. Simplistic 1DOF or 2DOF system are generally derived in industry to perform preliminary analysis of a vibrating screen to calculate foundation loads and ensure the chosen parameters meet the requirements. The 2DOF cannot be used as a simplified model for the 3DOF due to the complexities introduced by the θ coordinate.

A 4DOF system is also proposed which correlates well with the 2DOF when considering initial conditions applied to only the springs. When considering initial conditions applied to θ_1 and θ_2 the system presents very small-time intervals which are accurate when compared to the 2DOF. The system also develops imaginary numbers which are thought to require a different interpretation to the results which may present correlation to the 2DOF, this however is not studied. Based on the results from the numerical simulations it is concluded that a simpler system is to be derived which does not present a holonomic constraint.

A theoretical model of the proposed vibrating screen is developed using Lagrangian mechanics. When considering the initial conditions for the x and y coordinates the 3DOF system produces good correlation with regards to the simple spring pendulum (x and θ coordinates). This is expected since no rotation of the rigid bar would imply that the 2DOF and 3DOF are compatible. The results present a small amount of error accumulation for the rotation of the rigid bar (θ coordinate). For the numerical simulation time periods which have been studied the error accumulation presents little to no effect on the overall results.

When assigning initial conditions to the θ coordinate or excitation forces to any of the coordinates it was found that error accumulation occurred far more rapidly. The error accumulation has a large impact on the results thus developing significant inaccuracies in the results. There also exists a complex transfer of energy between the coordinates which is not always consistent and varies depending on the initial conditions and excitation forces, this is indicative of a chaotic system.

The error accumulation in the 3DOF system is found to be a result of the differential equations presenting a high degree of non-linearity. Error accumulation is found when using both Matlab and Mathematica, however Mathematica is found to produce larger time intervals with accurate results.

The use of parametric resonance with excitation at the natural frequency of the pendulum develops large accelerations and displacements, making it difficult to fit into generally accepted criteria for screening. Parameters for the 3DOF system develop accelerations which are 3 times higher compared to conventional vibrating screens with displacements which can also be considered large. The criteria developed a unique set of results to study the efficiency of a vibrating screen.

The DEM study presents promising results with the LM10 variation presenting 68% percent efficiency and the LMR10 presenting 76% percent efficiency. These values are low compared to the SD0 which developed 91% percent efficiency. The results are however in favour of the SD0 variation since the vibrating screen was chosen for the presented PSD and material properties. When considering the literature studied the efficiency of the LM and LMR vibrating screen can be considered high, this however neglects the differences in material properties.

The experimental testing presents good correlation to the numerical simulations. There does exist deviances in the results which are attributed to assumptions made for damping. When considering initial conditions on the x and y coordinates the assumptions for damping present good numerical correlation with the experimental testing. Initial conditions for the θ coordinate do not present numerical correlation between the experimental tests and numerical simulations. It is thought that the effect of damping is complex for the case where initial conditions are applied to the θ coordinate. Damping may not be a linear combination of the mass and stiffness. The results for initial coordinates assigned to the θ coordinate do present similarities between the numerical simulation and experimental tests. The processed signals present good correlation between numerical simulations and experimental tests, these results also correlate with analytical solutions. There also exists several frequencies for which there are no analytical solutions, these frequencies are however common between the numerical simulations and experimental tests. Based on the results it can be concluded that the derived equations correlate well with the experimental tests which ultimately imply that the equations mimic reality.

When considering the mechanical feasibility of the 3DOF system it is found that the system cannot be replicated in reality. The stiffness of the rubber buffers used in this study do exist however the rubber buffers do not meet the dimensional requirements. It is thought that the stiffness and dimensional quantities of the rubber buffers used in this study could be developed, however when one considers the accelerations and displacements of the system the rubber buffers will fail. Furthermore the foundation loads which would be transmitted into the support structure are tremendously larger compared to conventional vibrating screens.

The large displacements of the 3DOF will also present complexities from a material flow perspective. It is shown that feeding the 3DOF system is possible however the undersize and oversize material do not present uniform material flow as presented with the linear motion screen. This would require very complex chute work to capture material, the chute work and the vibrating screen will be subjected to large impact loads from material which would be a health and safety concern. Furthermore, the high accelerations may also cause material to fracture on impact.

It can be concluded that the presented parametrically excited vibrating screen would be an unfeasible venture due to the complexities mentioned. The system does present good efficiencies however it is not in line with the future screening goals presented by Makinde.

CHAPTER 9: FURTHER RESEARCH

The following can be considered for further research:

- The development of a custom numerical solver for the 3DOF system, such that the errors can be reduced. Such systems have been developed and studied by Kunian Li, where a high precision direct intergration scheme for nonlinear dynamic systems is proposed (Kuinian & Anthony, 2009)
- Studying a non-parametrically resonant 3DOF system and its application to screening. It is thought that this system would still present complex and novel motion, however the accelerations and displacements would be more in line with traditional vibrating
- The development of an experimental model for the above mentioned non parametrically resonant 3DOF system

REFERENCES

ACTOM, 2023. *Anti-Vibration And Rubber Products,* Johannesburg: ACTOM.

Alsalaet, J., 2020. *Towards better understanding of sideband creation.* [Online]
Available at: https://www.cbmconnect.com/towards-better-understanding-of-sidebands-generation/
[Accessed 21 07 2022].

Anderson, K., 2021. *Inhomogenous terms in an equation* [Interview] (12 06 2021).

Anton, B., Alexander, S. & Angelo, L., 2009. Dynamics of the pendulum with periodically varying length. *Physica D: Nonlinear Phenomena,* 238(16), pp. 1589-1597.

ARNOT, 2022. *Industrial Anti Vibration.* [Online]
Available at: chrome-extension://efaidnbmnnnibpcajpcglclefindmkaj/http://www.arnotavs.co.za/wp-content/uploads/2022/04/SH-Mounts-New.pdf
[Accessed 04 08 2022].

Bouchaib, R., Abdelkhalak & Hami, 2018. *Advanced numerical methods with Matlab. Resolution of nonlinear differential & partial differential equations.* Volume 7 ed. -: Wiley.

Brain, S. & Mark, R., -. *Proportional damping from experimental data,* California: Vibetech.

Chakraborty, S., Ghosh, A. & Ray-Chaudhuri, S., 2021. A Novel Tune Mass-Conical Spring System for Passive Vibration Control of a Variable Mass Structure. *Journal of Vibration and Control,* 28(13-14), pp. -.

Chen, D.-k.et al., 2022. A New Dynamic Solution Of Spring Pendulum Based On Time Finite Element Method. *Engineering Mechanics,* 39(4), pp. 209-218.

Chopra, A. K., 2012. *Dynamics of Structures.* Boston: Pearson.

Christophe, Geuzaine, J.-F. & Remacle, 2022. *Gmsh.* [Online]
Available at: https://gmsh.info/
[Accessed 26 03 2022].

David, B. & Michael, G., 2009. Eliminating constraint drift in the numerical simulation of constrained dynamical systems. *Computer methods in applied mechanics and engineering,* 198(37-40), pp. 3151-3160.

DCS, C., 2016. *fix move command.* [Online]
Available at: https://www.cfdem.com/media/DEM/docu/fix_move.html
[Accessed 24 03 2022].

de Sousa, M., Marcus, F., Caldas, I. & Viana, R., 2018. *Energy Distribution in Intrinsically Coupled Systems: The Spring Pendulum Paradigm,* Brazil: Department of Physics, Federal University of Parana.

Department, M. T. S., 2021. *ODE45 - Interval of intergration - Inconsistent Results CRM:0114064.* -: Weir Minerals email address.

Dong, H., Liu, C., Zhao, Y. & Zhao, L., 2013. Influence of vibration mode on the screening process. *International Journal of Mining Science and Technology,* 23(1), pp. 95-98.

Eaton, J. W., 1998-2021. *GNU Octave.* [Online]
Available at: https://www.gnu.org/software/octave/about
[Accessed 04 July 2021].

Eleni, C., Giuseppe, A. & Konstantinos, A., 2017. *The finite element method for the analysis of non-linear and dynamic systems: non-linear dynamics Part 1,* s.l.: s.n.

Elskamp, F., Kruggel-Emdan, Henig, M. & Teipel, U., 2017. A strategy to determine DEM parameters for spherical and on-spherical particles. *Granular Matter,* 19(3), pp. -.

Engineerdo, 2022. *Installation of LIGGGHTS.* [Online]
Available at: https://www.engineerdo.com/2020/06/25/installation-of-liggghts/
[Accessed 04 03 2022].

Ferenc, S., Bela, C., Attila, H. & Istvan, K., 2019. Optimal Oscillation Parameters of Vibrating Screens. *Journal of Mechanical Science and Technology*.
Hanly, S., -. *Why the Power Spectural Density (PSD) is the Gold Standard of Vibration Analysis.* [Online]
Available at: https://blog.endaq.com/why-the-power-spectral-density-psd-is-the-gold-standard-of-vibration-analysis#ComparisonToFFT
[Accessed 14 07 2022].
Hertbert, G., Poole, C. & Safko, J., 2000. *Classical Mechanics.* New York: Addison Wesely.
He, X. m. & Lui, C. s., 2009. Dynamics and screening characteristics of a vibrating screen with variable elliptical trace. *Science Direct, Mining Science and Technology,* 19(4), pp. 508-513.
Heyns, S., 2006. *Dynamic Analysis of Vibratory Screens,* Pretoria: Buisiness enterprises, University of Pretoria.
Hobbacher, 2007. *International institute of welding, IIW Document XII-2151-07/XV-1254-07,* Paris: International institute of welding.
Howard, W., Louis, t. & David, H., 2003. *Advanced Mathematics and Mechanics Applications using MATLAB.* 3 ed. Florida: Chapman & Hall/CRC.
Irish, J., 2005. *Ocean instrumentation, Course.* s.l.:s.n.
Jiachen, Z., Chuzhe, Z., Ziqiu, W. & Kuanmin, M., 2020. Study on the characteristics of disk spring system vibration screen. *Shock andVibration,* Volume 2020.
Jianzhang, X. & Xin, T., 2012. Characteristics and efficiency of a new vibrating screen with a swing trace. *Science Direct,* 11(5), pp. 601-606.
John, R., 2005. *Classical Mechanics.* United States: University Science Books.
Joubert, J., 2023. *General chat with regard to condition monitoring* [Interview] (7 Feburary 2023).
Kendall, A., Weimin, h. & David, S., 2009. *Numerical solutions of ordinary differential equations.* New Jersey: Wiley-Interscience.
Kopel, R. et al., 2019. No time for drifting: Comparing performance and applicability of signal detrending algorithms for real-time FMRI. *NeuroImage,* Volume 191, pp. 421-429.
Kuinian, L. & Anthony, D., 2009. A high precision direct intergration scheme for nonlinear dynamic systems. *Journal of computitional and nonlinear dynamics,* 4(4).
Laarhoven, V., 2009. *Stability analysis of parametric roll resonance,* Eindhoven: Eindhoven University of Technology.
Leonid I, S. & Victor I, S., 2013. Coupled mode parametric resonance in a vibrating screen model. *Mechanical Systems and Signal Processing,* 43(1-2), pp. 295-304.
Liping, P. et al., 2018. A more accurate dynamic model for a dual-side excitation large vibrating screen. *Journal of Vibroengineering,* 20(2), pp. 858-871.
Liu, W. & Jinli, Z., 2011. The Working Principle of Multi-Layer Electromagnetic Screens and the Dynamic Analysis. *Applied Mechanics and Materials,* Volume 50-51, pp. 229-233.
Loren, S., 2015. *Loren on the Art of Matlab.* [Online]
Available at: https://blogs.mathworks.com/loren/2015/09/23/ode-solver-selection-in-matlab/?doing_wp_cron=1655655016.9026920795440673828125
[Accessed 19 06 2022].
Lukasz, B., Stanislaw, N. & Feliks, S., 2015. Testing of the laboratory screen prototype operating under parametric resonance conditions. *Buletin Stiintific,* Volume 2015 No.XXIX, pp. 10-14.
Lunlum, Z., Xihua, C. & Yuanjie, X., 2017. *DEM investigation on characteristics of rolling resistance for modelling particle shape.* Wuhan, EPJ Web of Conferences (Powerders & Grains).

Makinde, Ramatsetse & Mpofu, 2015. Review of vibrating screen development trends: Linking the past and future in mining machinery industries. *Internation Jounral of Mineral Science,* Volume 145, pp. 17-22.
MathWorks, 1994-2021. *MathWorks Help Center.* [Online]
Available at: https://www.mathworks.com/help/matlab/
[Accessed 12 November 2021].
MathWorks, 2021. *Choose an ODE Solver.* [Online]
Available at: https://www.mathworks.com/help/matlab/math/choose-an-ode-solver.html
[Accessed 27 11 2021].
MathWorks, 2021. *MathWorks Help Center.* [Online]
Available at: https://www.mathworks.com/help/matlab/math/choose-an-ode-solver.html
[Accessed 09 12 2021].
MathWorks, 2021. *MatWorks Help Center.* [Online]
Available at: https://www.mathworks.com/help/signal/ref/filtfilt.html
[Accessed 07 12 2021].
MathWorks, 2022. *Choose an ODE Solver.* [Online]
Available at: https://www.mathworks.com/help/matlab/math/choose-an-ode-solver.html#bu13kwa
[Accessed 19 06 2022].
MathWorks, n.d. *Matlab Answers.* [Online]
Available at: https://www.mathworks.com/matlabcentral/answers/156178-ode45-failing-to-produce-a-sensible-solution
[Accessed 17 11 2021].
Mdlazi, L., 2021. *Processing of Linear Drift* [Interview] (27 Octotber 2021).
Nader, S., 2016. Vibration sideband modulations and harmonics seperation of a planetary helicopter gearbox with two configurations. *Hindawi, Advances in acoustic and vibration,* Volume 2016, p. 9.
Oli, 2021. *Oli Vibrating Motors.* [Online]
Available at: https://www.olivibra.com/products/mve-standard-range/
[Accessed 19 August 2021].
Shampine, L., Gladwell, L. & Thompson, S., 2003. *Solving ODE's with Matlab.* United Kingdom: Cambridge.
Shenouda, S. & Hoff, A., 2020. *Discrete Element Method Analysis for Metal Powders Used in Additive Manufacturing, and DEM Simulation Tutorial Using LIGGGHTS-Public,* United States: Lawrence Livermore National Laboratory.
Spijker, N., 1995. Stiffness in numerical initial-value problems. *Journal of Computer Science and Applied Mathematics,* 72(-), pp. 393-406.
Steen, K., 2009. *Non-linear modeling and analysis of solids and structures.* 1 ed. Cambridge: Cambridge University Press.
Sullivan, J., n.d. *Screening Theory and Practice.* s.l.:Triple/S Dynamics, Inc.
Teffo, V. & Naude, N., 2013. Determination of the coefficients of restitution and static rolling friction of Eskom-grade coal for discrete element modelling. *Journal of the Southern African Institute of Mining and Metallurgy,* 113 ISSN2225-6253(4).
Timothee, G., Nadine, M. & Corinne, M., 2013. *Identification of harmonics and sidebands in a finite set of spectral components.* Poland, HAL archives-ouvertes.
Wieslaw, F. & Jakub, W., 2020. Energy Accumulation in Mechanical Resonance and its use in Drive Systems of Impact Machines. *Archives of Civil and Mechanical Engineering.*
Wikipedia, 2022. *Wikipedia.* [Online]
Available at: https://en.wikipedia.org/wiki/CentOS
[Accessed 19 04 2022].

Zahedi, A. & Babitsky, V., -. *Modelling of autoresonant control of a parametically excited screen machine,* Manchester: School of Mechanical, Aerospace and Civil Engineering, University of Manchester.
Zeljko, V. & Aleksandar, P., 2016. Regulated Drive of Vibratory Screens with Unbalanced Motors. *INFOTEH-JAHORINA,* Volume 15, pp. 155-160.
Zhanfu, L. et al., 2018. Design and efficiency research of a new composite vibrating screen. *Shock and Vibration,* Volume 2018.
Zhao, Y.-m.et al., 2009. *Dynamic Design Theory and Application of Large Vibrating Screen.* China, International Conference on Mining Science & Technology, pp. 776-784.

APPENDIX A – MATLAB CODES

The function below presents the state representation of the simplified 2DOF system.

```
function xp = Statespace1(t,x,m,k,cv,ch,r,Fv,Fh,F,w,w2,w3)
xp = [x(2);
    (m*x(4)^2*(r+x(1))-
k*x(1)+m*9.81*cos(x(3))+F*sin(w3*t)+Fv*sin(w2*t)+Fh*sin(w*t)*sin(x(3))-
cv*x(2))/m;
    x(4);
    (-2*m*x(2)*x(4)*(r+x(1))-
m*9.81*(r+x(1))*sin(x(3))+(x(1))*Fh*sin(w*t)*cos(x(3))-
ch*x(4))/(m*(r+x(1))^2)];
End
```

Matlab Code 1: State representation of the 2DOF system

The ode45 solver is implemented as per the below code to solve the simplified 2DOF system.

```
SolverOptions = odeset('RelTol',1e-5,'AbsTol',1e-5);
m = 3755; %mass in kg
k = 266*1000; %stiffness in N/m
r = 0.5; %spring length in m
Fv = 2642*2; %N
Fh = 788;
F = 76993*2;
w = 3.088/2*6.28; % pendulum rotational rad/s
w2 = 3.088*6.28; % spring translational rad/s
w3 = 16.67*6.28;
cv = (m+k)*0.001;
ch = (r^2)*0.001;
inc = 0.001;
[t,y] = ode45(@Statespace1,[0:inc:10],[0 0
0],SolverOptions,m,k,cv,ch,r,Fv,Fh,F,w,w2,w3);
```

Matlab Code 2: Implementation of the 2DOF state representation

The below function presents the 4DOF of system in state representation.

```
function xp = Statespace6(t,x,r,L,k,m1,m2)

theta1 = x(1);
theta1_dot = x(2);
theta2 = x(3);
theta2_dot = x(4);
a = x(5);
a_dot = x(6);
A = (a+r);

%B
R1 = 2*A*cos(theta1)*cos(theta2);
R3 = 2*L*sin(theta2)+2*A*sin(theta1)*sin(theta2);

one = -A^2+L^2;
two = A^2*(cos(2*theta1)*cos(2*theta2)+sin(2*theta1)*sin(2*theta2));
three = -L^2*cos(2*theta2);
four = -2*A*L*sin(theta1);
five = -2*A*L*(sin(theta1)*cos(2*theta2)-cos(theta1)*sin(2*theta2));
R2 = -sqrt(2)*sqrt(one+two+three+four+five);
```

```
B = 0.5*(R1+R2+R3);


%b_dot

R1_dot = 2*(a_dot*cos(theta1)*cos(theta2)  -  A*theta1_dot*sin(theta1)*cos(theta2)
-  A*theta2_dot*cos(theta1)*sin(theta2));
R3_dot = 2*L*theta2_dot*cos(theta2) + 2*(a_dot*sin(theta1)*sin(theta2)  +
A*theta1_dot*cos(theta1)*sin(theta2)  +  A*sin(theta1)*theta2_dot*cos(theta2));

one_dot = -2*a_dot*A;
two_dot = 2*a_dot*A*cos(2*theta1)*cos(2*theta2)  +  -
A^2*2*theta1_dot*sin(2*theta1)*cos(2*theta2)  +  -
A^2*cos(2*theta1)*2*theta2_dot*sin(2*theta2)  +
2*a_dot*A*sin(2*theta1)*sin(2*theta2)  +
A^2*2*theta1_dot*cos(2*theta1)*sin(2*theta2)  +
A^2*sin(2*theta1)*2*theta2_dot*cos(2*theta2);
three_dot = L^2*2*theta2_dot*sin(2*theta2);
four_dot = -2*a_dot*L*sin(theta1)-2*A*L*theta1_dot*cos(theta1);
five_dot = -2*a_dot*L*sin(theta1)*cos(2*theta2)  -
2*A*L*theta1_dot*cos(theta1)*cos(2*theta2)  -
2*A*L*sin(theta1)*2*theta1_dot*sin(2*theta2)  +
2*a_dot*L*cos(theta1)*sin(2*theta2)  -  2*A*L*theta1_dot*sin(theta1)*sin(2*theta2)
+  2*A*L*cos(theta1)*2*theta2_dot*cos(2*theta2);

R2_dot = -sqrt(2)*(one_dot+two_dot+three_dot+four_dot+five_dot)/(2*sqrt(B));

b_dot = (R1_dot+R2_dot+R3_dot)/(4*sqrt(R1+R2+R3));


%differential equations

%theta1
theta1_dotdot = (-2*m1*theta1_dot*a_dot*A-9.81*m1*sin(theta1)*A)/(m1*A^2);
%theta2
theta2_dotdot = (-2*m2*theta2_dot*b_dot*B-9.81*m2*sin(theta2)*B)/(m2*B^2);
%a
a_dotdot = (m1*theta1_dot^2*A-k*a+9.81*m1*cos(theta1))/m1;
%b
b_dotdot = (m2*theta2_dot^2*B-k*(B-r)+9.81*m2*cos(theta2))/m2;

xp = [x(2);
      theta1_dotdot;
      x(4);
      theta2_dotdot;
      x(6);
      a_dotdot;
      x(8);%b_dot;
      b_dotdot;];
end
```

Matlab Code 3: State representation of the 4DOF system

The below code presents the use of the FFT function in Matlab.

```
% A custom function to perform FFT
% srate = sampling rate
% t = column vector of the time
% S = data
function [freq,amp] = FastFt(srate,t,S);
      Nyquist = 0.5*1/srate;
      npnts = size(t);
      npnts = npnts(1);
      X = fft(S);
      amp = (2*abs(X))/npnts;
      freq = linspace(0,Nyquist,floor(npnts/2+1));
      amp = amp(1:length(freq));
end
```

Matlab Code 4: General use of the FFT function from the signal processing toolbox

The below code presents the use of a Butterworth filter coupled with the "filtftit" function on Matlab. The function can be used for filtering data attained from numerical simulations. The "filtfilt" function performs zero-phase digital filtering by processing the input data in both the forward and reverse directions (MathWorks, 2021).

```
%A custom function to call the butter and filtftilt function
%srate = sampling rate
%order = order of the butterworth filter
%data = data to be filtered
%A = filtered data
function A = ButterF(srate,order,data)
    Fc = srate/2; %cut off frequency
    [b1 a1] = butter(order,Fc,'high');
    A = filtfilt(b1,a1,data);
end
```

Matlab Code 5: Custom function for the implementation of Butterworth filters

The below code presents the state representation of the 3DOF system including damping and generalised forces.

```
function xp = Statespace3dof2excited(t,X,r,L,k,m,c1,c2,c3,Fh,Fv,Ft,Wh,Wv,Wt)

x = X(1);
x_dot = X(2);
y = X(3);
y_dot = X(4);
theta = X(5);
theta_dot = X(6);


A = L^2/4+L*x+x^2+y^2-0.5*L^2*cos(theta)-L*x*cos(theta)+0.25*L^2*cos(theta)^2-
L*y*sin(theta)+0.25*L^2*sin(theta)^2;
B = L^2/4-L*x+x^2+y^2-
0.5*L^2*cos(theta)+L*x*cos(theta)+0.25*L^2*cos(theta)^2+L*y*sin(theta)+0.25*L^2*si
n(theta)^2;

%theta
one_line1 = 0.5*k*L^2*sin(theta) + 0.25*k*L^2*(-
2*cos(theta)*sin(theta))+0.25*k*L^2*(2*sin(theta)*cos(theta));
```

```
one_line2 = -k*r*(0.5*L^2*sin(theta) + L*x*sin(theta) + 0.25*L^2*(-
2*cos(theta)*sin(theta)) - L*y*cos(theta) +
0.25*L^2*(2*sin(theta)*cos(theta)))/(2*sqrt(A));
one_line3 = -k*r*(0.5*L^2*sin(theta) - L*x*sin(theta) +
0.25*L^2*(2*cos(theta)*sin(theta)) + L*y*cos(theta) +
0.25*L^2*(2*sin(theta)*cos(theta)))/(2*sqrt(B));
one = one_line1+one_line2+one_line3;
%theta_dotdot = -4*one/(L^4*m);
theta_dotdot = 4*(-one-c3*theta_dot+L/2*Ft*sin(Wt*t))/(m*L^2);
%X
two = 2*k*x-k*r*(L+2*x-L*cos(theta))/(2*sqrt(A))-k*r*(-
L+2*x+L*cos(theta))/(2*sqrt(B));
%x_dotdot = (-two)/(m);
x_dotdot = (-two-c1*x_dot)/m+Fh*sin(Wh*t)/m+Ft*sin(Wt*t)*sin(theta)/m;

%Y
three = -9.81*m+2*k*y-k*r*(2*y-L*sin(theta))/(2*sqrt(A))-
k*r*(2*y+L*sin(theta))/(2*sqrt(B));
%y_dotdot = (-three)/(m);
y_dotdot = (-three-c2*y_dot)/m+Fv*sin(Wv*t)/m+Ft*sin(Wt*t)*cos(theta)/m;

xp = [X(2)
      x_dotdot;
      X(4);
      y_dotdot;
      X(6);
      theta_dotdot;];
end
```

Matlab Code 6:State representation of the 3DOF system including damping and generalised forces

The below code can be used to calculate the numerical values of α and β, the variables ax, ay, bx and by present the location of the tip of spring A and B respectfully.

```
%Alpha, Beta and length
 ax = X-0.5*L*cos(theta);
 ay = Y-0.5*L*sin(theta);
 bx = X+0.5*L*cos(theta);
 by = Y+0.5*L*sin(theta);
 for i = 1:size(ax)
     A = [-0.5*L;0]-[ax(i);ay(i)];
     U = [-0.5*L;0]-[15;0];
     A_dot = dot(A,U);
     R = sqrt(dot(A,A))*sqrt(dot(U,U));
     alpha(i) = (acos(A_dot/R))-pi/2;

     B = [0.5*L;0]-[bx(i);by(i)];
     U = [0.5*L;0]-[15;0];
     B_dot = dot(B,U);
     R = sqrt(dot(B,B))*sqrt(dot(U,U));
     beta(i) = (acos(B_dot/R))-pi/2;
     Length(i) = sqrt((ax(i)-bx(i))^2+(ay(i)-by(i))^2);
 End
```

Matlab Code 7: The calculation of the numerical values of α and β

```
%Calculates the coordinates for each mass and the stretch of the spring
function [ax,ay,bx,by,stretch_a,stretch_b] = AandB(theta,X,Y,L,r);

 ax = X-0.5*L*cos(theta);
 ay = Y-0.5*L*sin(theta);
 stretch_a = sqrt((ax+0.5*L).^2+(ay).^2)-r;

 bx = X+0.5*L*cos(theta);
 by = Y+0.5*L*sin(theta);
 stretch_b = sqrt((bx-0.5*L).^2+(by).^2)-r;
end
```

Matlab Code 8: Stretch in the springs and the coordinates of A and B

```
%A function to calculate the resultant acceleration for springs A and B
%The resultant acceleration considers the directions of the X and
%Y components developed by rotation of the rigid bar
function [A B] = ResultantACC(t_dotdot,x_dotdot,y_dotdot,L,theta)

j =size(t_dotdot);
tangential_t = (t_dotdot.^2).*L*0.5;

%Spring A
ax = tangential_t.*sin(abs(theta));
ay = tangential_t.*cos(abs(theta));
for i = 1:j(1,1)
    if tangential_t(i) > 0
        ax(i) = ax(i);
        ay(i) = ay(i);
    end
    if tangential_t(i) < 0
        ax(i) = -ax(i);
        ay(i) = ay(i);
    end
end
A = sqrt((ax+x_dotdot).^2+(ay+y_dotdot).^2);
%Spring B
bx = tangential_t.*sin(abs(theta));
by = tangential_t.*cos(abs(theta));
for i = 1:j(1,1)
    if tangential_t(i) > 0
        bx(i) = -bx(i);
        by(i) = -by(i);
    end
    if tangential_t(i) < 0
        bx(i) = bx(i);
        by(i) = -by(i);
    end
end
B = sqrt((bx+x_dotdot).^2+(by+y_dotdot).^2);
end
```

Matlab Code 9: Resultant accelerations of spring A and B

```
function [dx dy dz ax_new ay_new az_new] = ACDisp(t,ax,ay,az,srate,order)

Fc = 1/(srate/2); %cut off frequency

[b1 a1] = butter(order,Fc,'high');
ax_new = filtfilt(b1,a1,ax);
vx = cumtrapz(t,ax_new); %velocity
vx_new = filtfilt(b1,a1,vx);
dx = cumtrapz(t,vx_new); %displacement
dx = filtfilt(b1,a1,dx);


ay_new = filtfilt(b1,a1,ay);
vy = cumtrapz(t,ay_new); %velocity
vy_new = filtfilt(b1,a1,vy);
dy = cumtrapz(t,vy_new); %displacement
dy = filtfilt(b1,a1,dy);

az_new = filtfilt(b1,a1,az);
vz = cumtrapz(t,az_new); %velocity
vz_new = filtfilt(b1,a1,vz);
dz = cumtrapz(t,vz_new); %displacement
dz = filtfilt(b1,a1,dz);

end
```

Matlab Code 10: Double integration of acceleration results to calculate displacements

```
Fc = 60/1200; %cut off frequency
[b1 a1] = butter(6,Fc,'low');
A = filtfilt(b1,a1,az1);
A = detrend(A);
```

Matlab Code 11: Low pass Butterworth filter for removing high frequencies and trendlines

```
% takes out specific time interval from a data set
 function [tt axx ayy azz] = cut(t,ax,ay,az,C1,C2,deltaT)

n=0;
s = size(t);
s = s(1,1);
for k = 1:size(t(:,1))
  if (t(k) >= C1) && (t(k) < C2)
    n = n+1;
    tt(n) = deltaT*(n-1);

    axx(n) = ax(k);
    ayy(n) = ay(k);
    azz(n) = az(k);
  end
  end
end
```

Matlab Code 12: A function which removes a specific part of a data set

APPENDIX B – TIME DERIVATIVES OF $(r + b)$

$$\#1 = \pm\sqrt{2}\sqrt{\underbrace{-(a+r)^2 + L^2}_{(1)} + \underbrace{(a+r)^2\cos(2\theta_1 - 2\theta_2)}_{(2)} \underbrace{- L^2\cos(2\theta_2)}_{(3)} \underbrace{- 2(a+r)L\sin\theta_1}_{(4)} \underbrace{- 2(a+r)L\sin(\theta_1 - 2\theta_2)}_{(5)}}$$

The below presents the time derivatives of the smaller functions which make up equation #1.

$$(\dot{1}) = -2\dot{a}(a+r)$$

$$\begin{aligned}(\dot{2}) = {} & 2\dot{a}(a+r)(\cos(2\theta_1)\cos(2\theta_2) - (a+r)^2\, 2\dot{\theta}_1 \sin(2\theta_1)\cos(2\theta_2) \\ & - (a+r)^2\cos(2\dot{\theta_2})\sin(2\theta_2) - 2\dot{a}\,(a \\ & + r)\sin(2\theta_1)\sin(2\theta_2) + (a+r)^2 2\dot{\theta}_1\cos(2\theta_1)\sin(2\dot{\theta}_2) \\ & + (a+r)^2\sin(2\theta_1)2\dot{\theta}_2\cos(2\theta_2)\end{aligned}$$

$$(\dot{3}) = 2L^2\dot{\theta}_2\sin(2\theta_2)$$

$$(\dot{4}) = -2\dot{a}L\sin\theta_1 - 2(a+r)L\dot{\theta}_1\cos\theta_1$$

$$\begin{aligned}(\dot{5}) = {} & -2\dot{a}L\sin\theta_1\cos(2\theta_2) - 2(a+r)L\dot{\theta}_1\cos\theta_1\cos(2\theta_2) \\ & - 2(a+r)L\sin(\theta_1)2\dot{\theta}_1\sin(2\theta_2) + 2\dot{a}\,L\cos\theta_1\sin(2\theta_2) \\ & - 2(a+r)L\dot{\theta}_1\sin\theta_1\sin(2\theta_2) + 2(a+r)L\cos(\theta_1)2\dot{\theta}_2\cos(2\theta_2)\end{aligned}$$

The smaller functions of the #1 term can be represented by ϵ, thus allowing for a neater representation

$$\epsilon = (1) + (2) + (3) + (4) + (5)$$

$$\#1 = \pm\sqrt{2}\sqrt{\epsilon}$$

The derivative of the #1 term can be represented as shown below in terms of ϵ.

$$\dot{\#1} = \frac{\pm\sqrt{2}\dot{\epsilon}}{2\sqrt{\epsilon}}$$

Using the above, the time derivative of $(r + b)$ can then be formulated.

$$R_1 = 2(a+r)\cos\theta_1\cos\theta_2$$

$$R_2 = 2L\sin\theta_2 + 2(a+r)\sin\theta_1\sin\theta_2$$

$$\dot{R}_1 = 2\dot{a}\cos\theta_1\cos\theta_2 - 2(a+r)\dot{\theta}_1\sin\theta_1\cos\theta_2 - 2(a+r)\dot{\theta}_2\cos\theta_1\sin\theta_2$$

$$\dot{R}_2 = 2L\dot{\theta}_2\cos\theta_2 + 2\left[\dot{a}\sin\theta_1\sin\theta_2 + (a+r)\dot{\theta}_1\cos\theta_1\sin\theta_2 + (a+r)\sin(\theta_1)\dot{\theta}_2\cos\theta_2\right]$$

$$(r+b) = \frac{R_1 + R_2 \pm \#1}{2}$$

$$R_3 = R1 + R2 \pm \#1$$

$$\dot{b} = \frac{\dot{R}_3}{4\sqrt{R_3}}$$

APPENDIX C – RESULTS FOR THE 3DOF PARAMETRICALLY SIZED MODEL

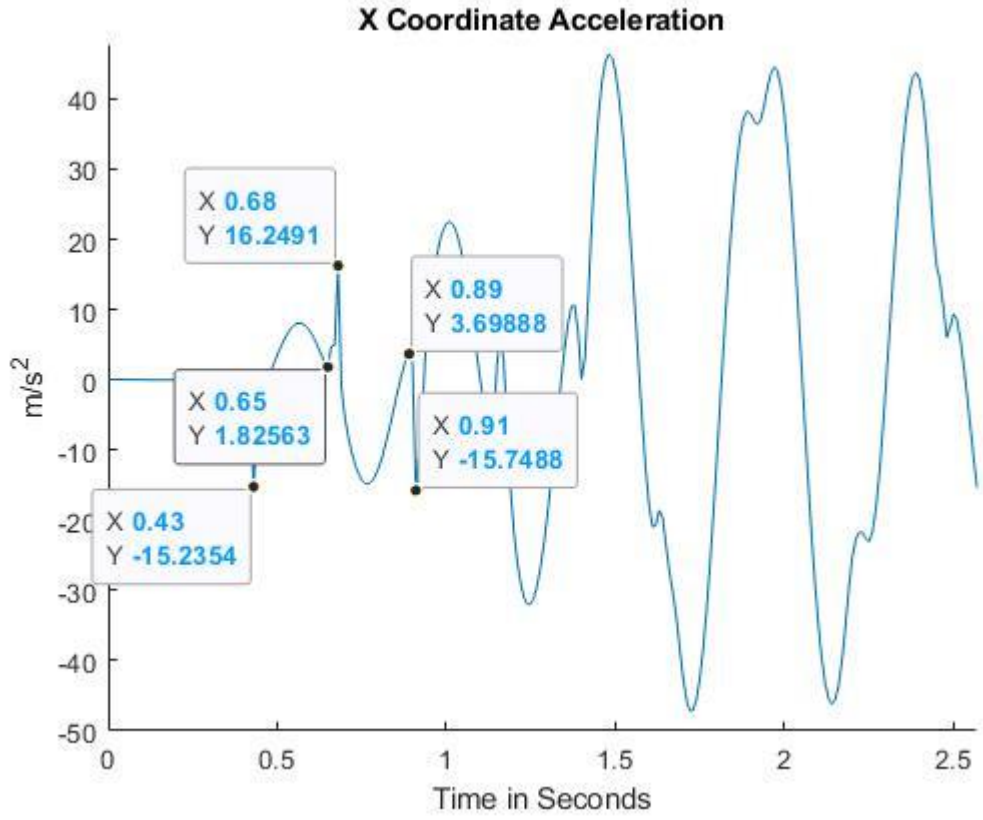

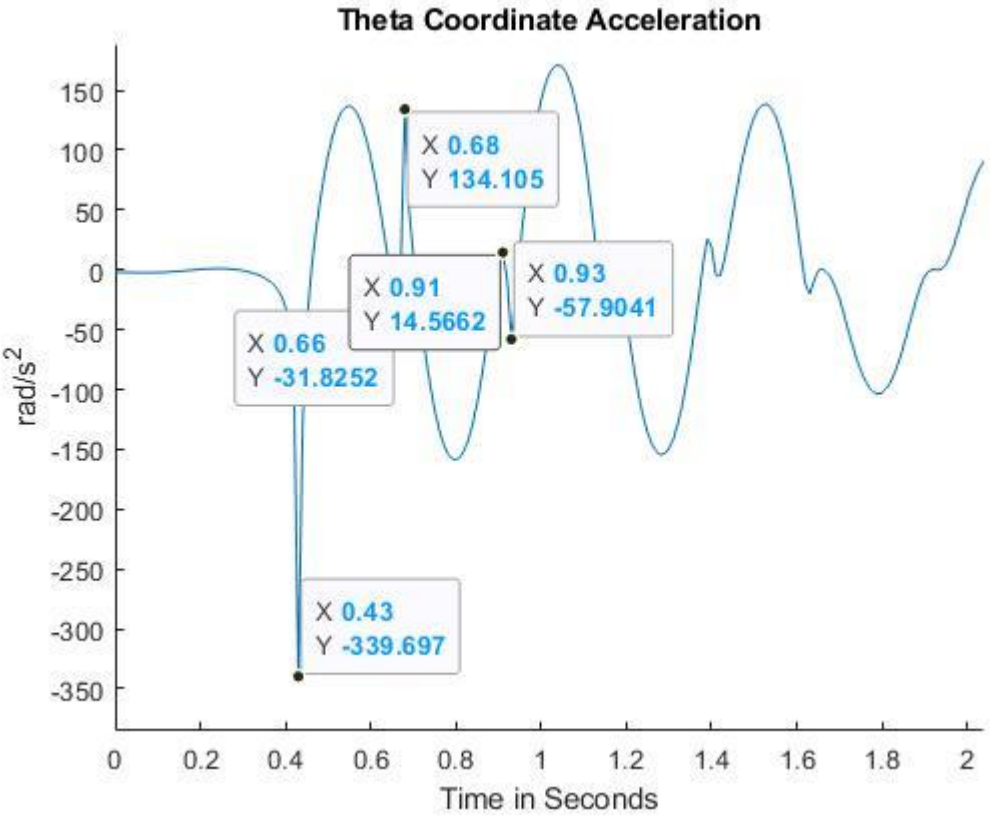

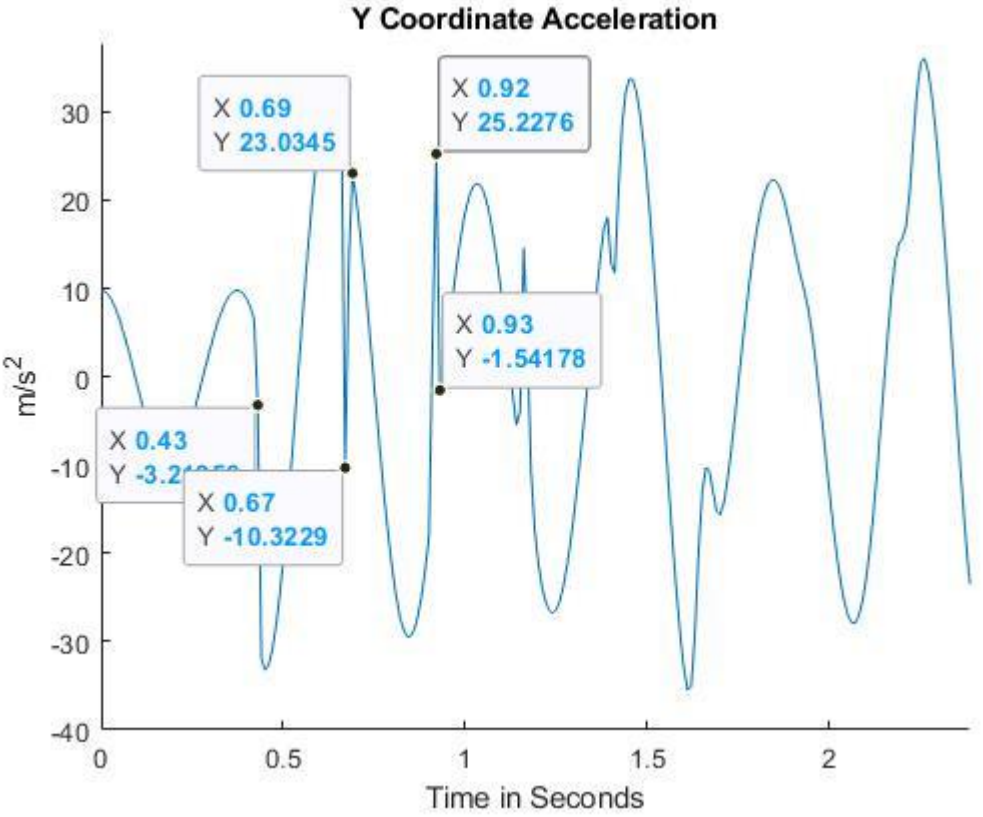
Y Coordinate Acceleration
X 0.69
Y 23.0345
X 0.92
Y 25.2276
X 0.93
Y -1.54178
X 0.43
X 0.67
Y -10.3229
m/s2
Time in Seconds

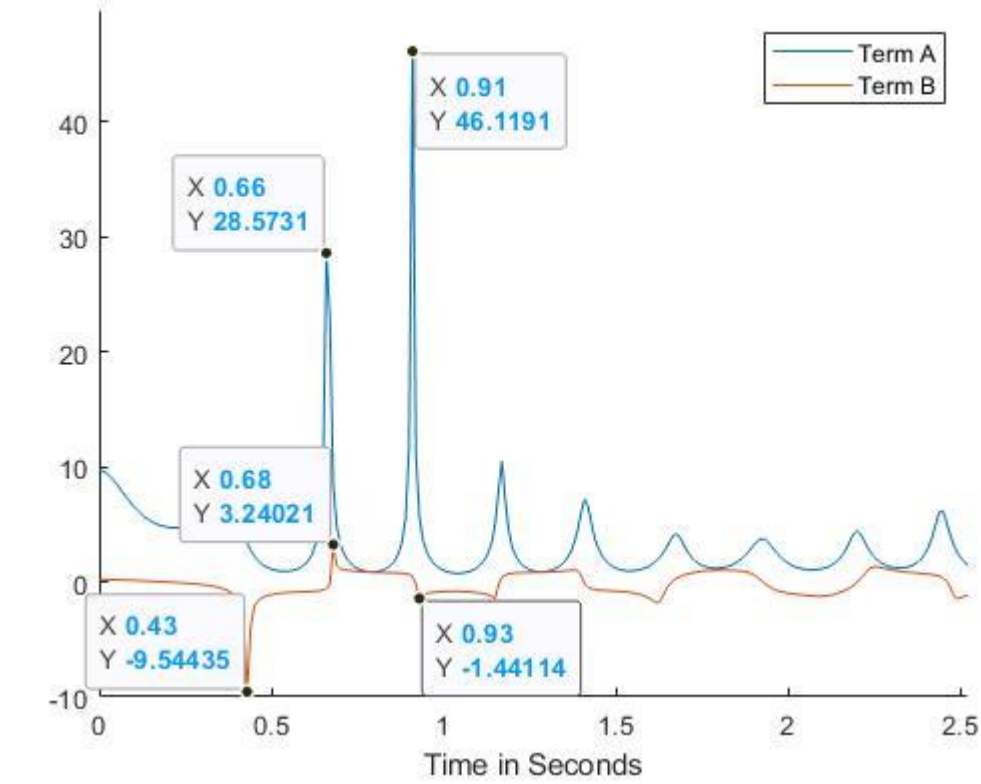
Term A
Term B
X 0.91
Y 46.1191
X 0.66
Y 28.5731
X 0.68
Y 3.24021
X 0.43
Y -9.54435
X 0.93
Y -1.44114
Time in Seconds

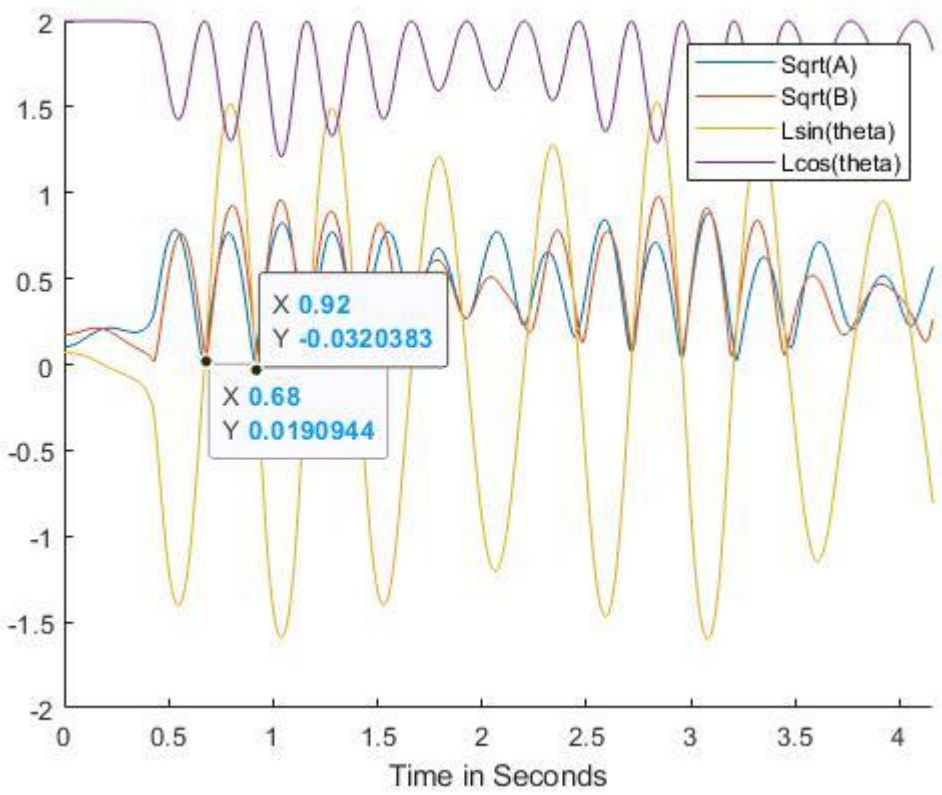
Sqrt(A)
Sqrt(B)
Lsin(theta)
Lcos(theta)
X 0.92
Y -0.0320383
X 0.68
Y 0.0190944
Time in Seconds

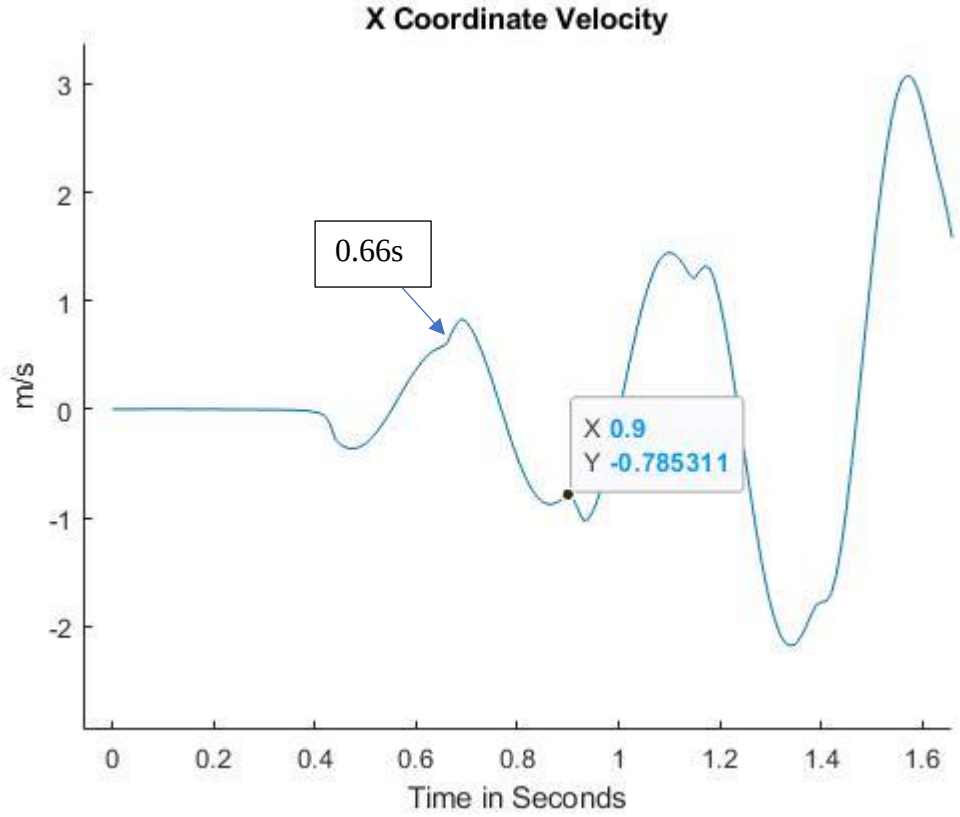
X Coordinate Velocity
0.66s
X 0.9
Y -0.785311
m/s
Time in Seconds

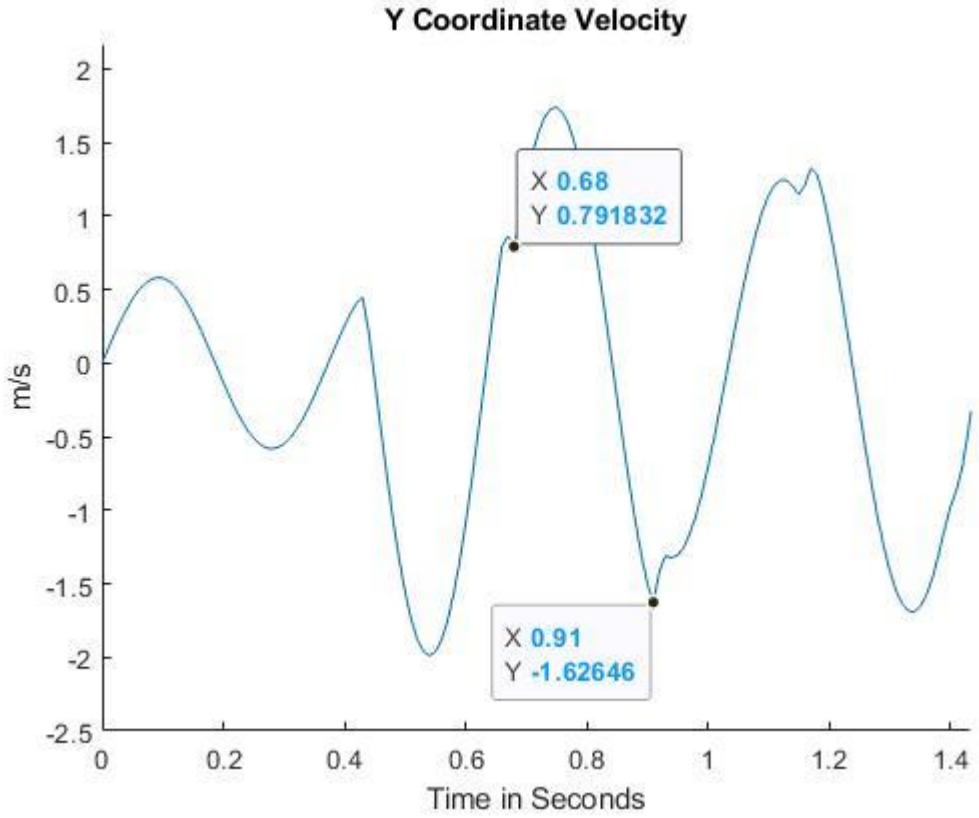
Y Coordinate Velocity
X 0.68
Y 0.791832
X 0.91
Y -1.62646
m/s
Time in Seconds

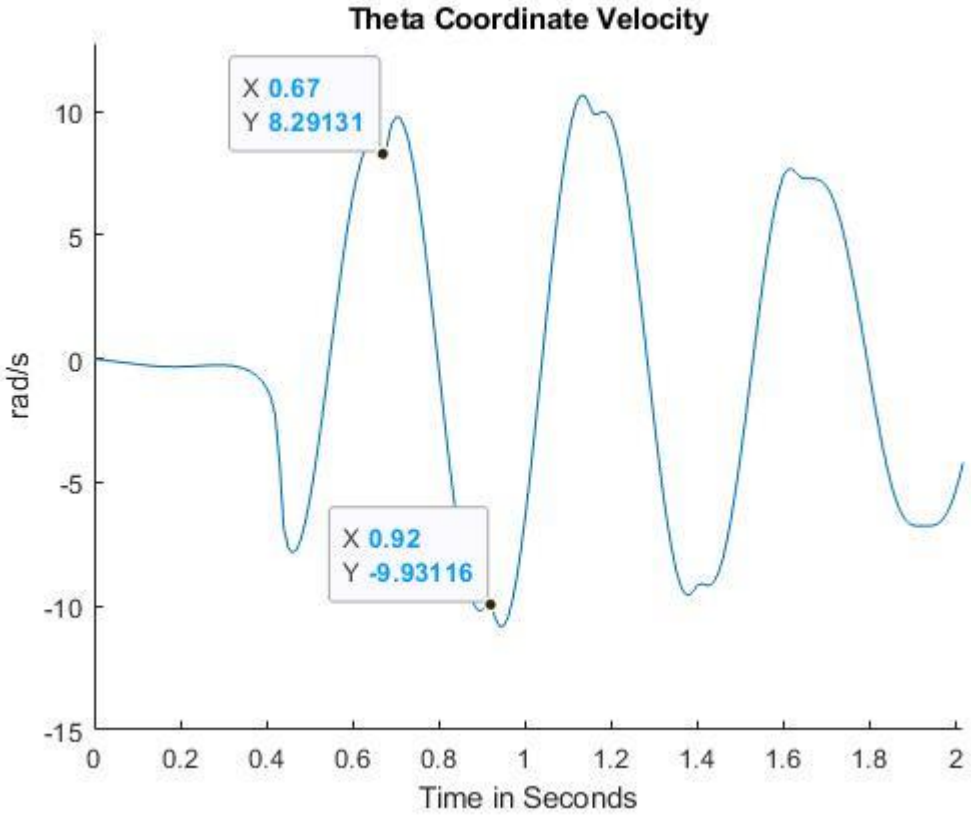
Theta Coordinate Velocity
X 0.67
Y 8.29131
X 0.92
Y -9.93116
rad/s
10
5
0
-5
-10
-15
0
0.2
0.4
0.6
0.8
1
1.2
1.4
1.6
1.8
2
Time in Seconds

APPENDIX B – RESULTS FOR THE 3DOF PARAMETRICALLY SIZED MODEL WITH EXCITATION

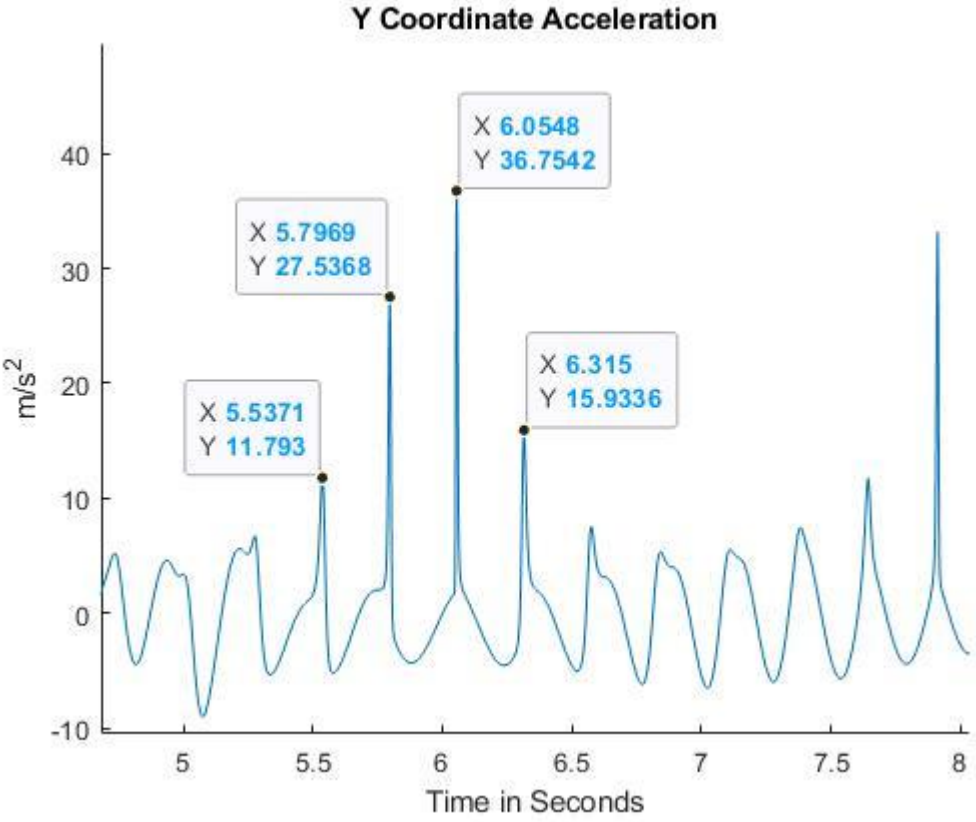

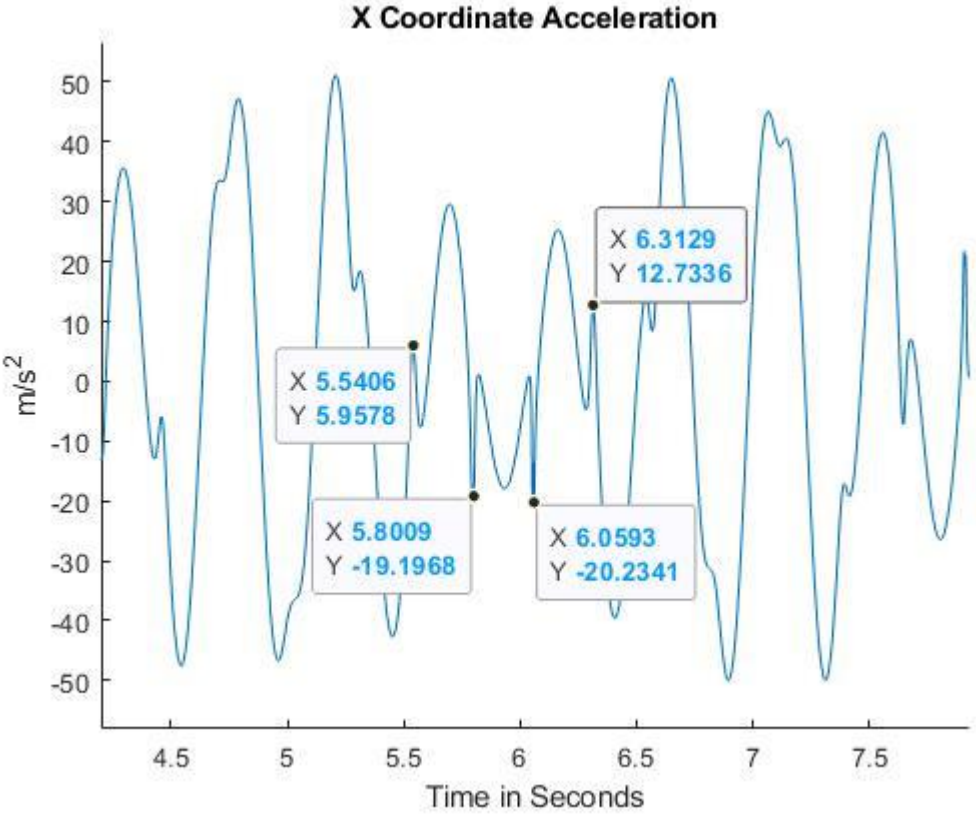

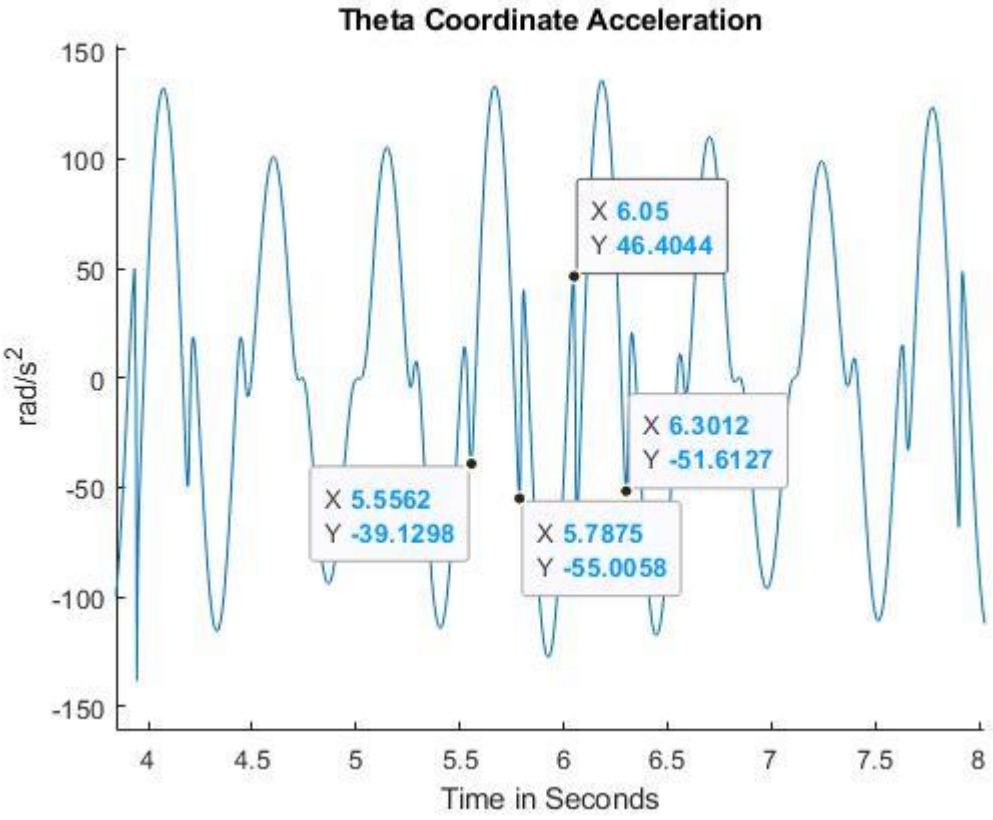
Theta Coordinate Acceleration
rad/s^2
Time in Seconds
X 6.05
Y 46.4044
X 6.3012
Y -51.6127
X 5.5562
Y -39.1298
X 5.7875
Y -55.0058

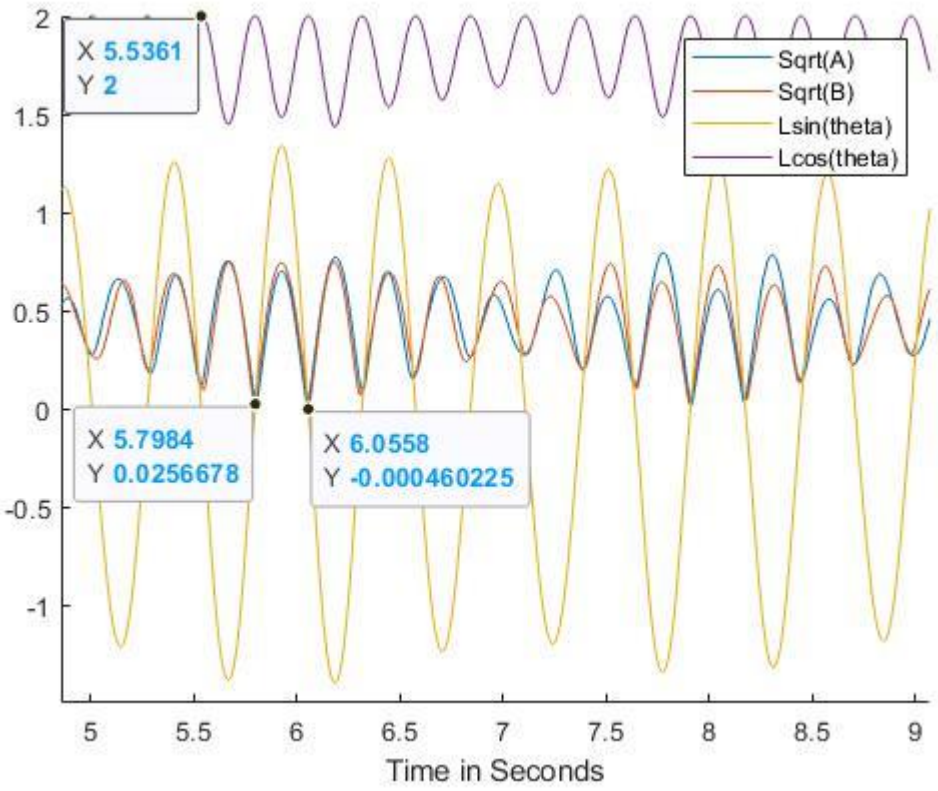
Sqrt(A)
Sqrt(B)
Lsin(theta)
Lcos(theta)
X 5.5361
Y 2
X 5.7984
Y 0.0256678
X 6.0558
Y -0.000460225
Time in Seconds

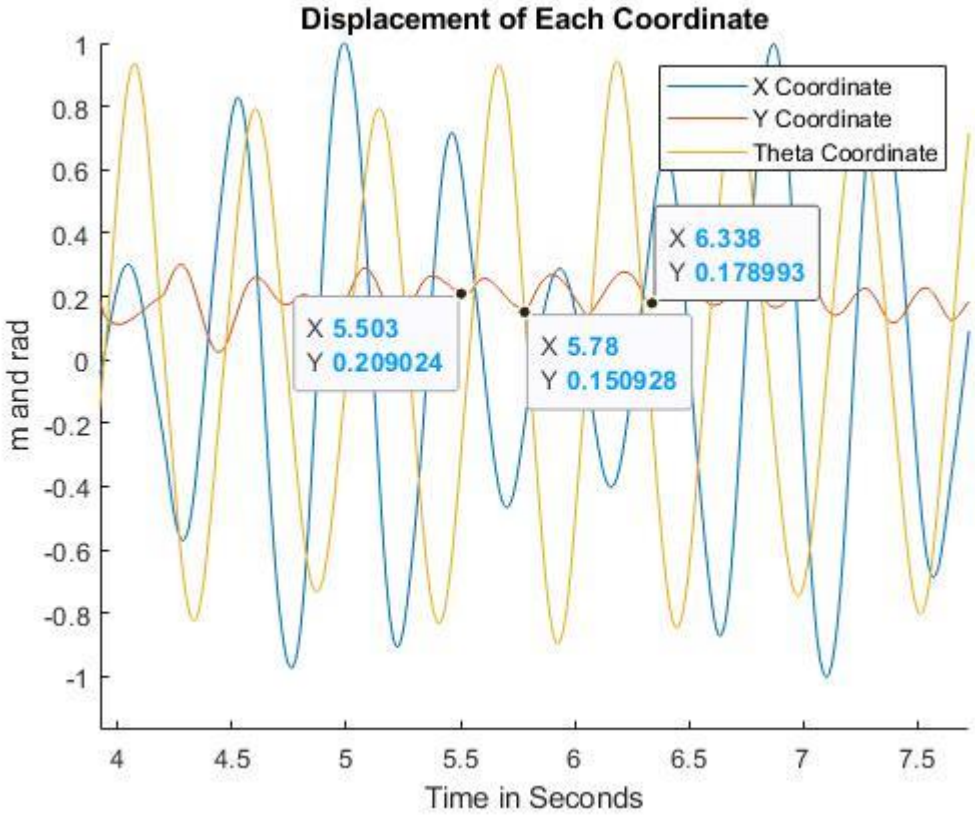
Displacement of Each Coordinate
X Coordinate
Y Coordinate
Theta Coordinate
X 6.338
Y 0.178993
X 5.503
Y 0.209024
X 5.78
Y 0.150928
m and rad
Time in Seconds

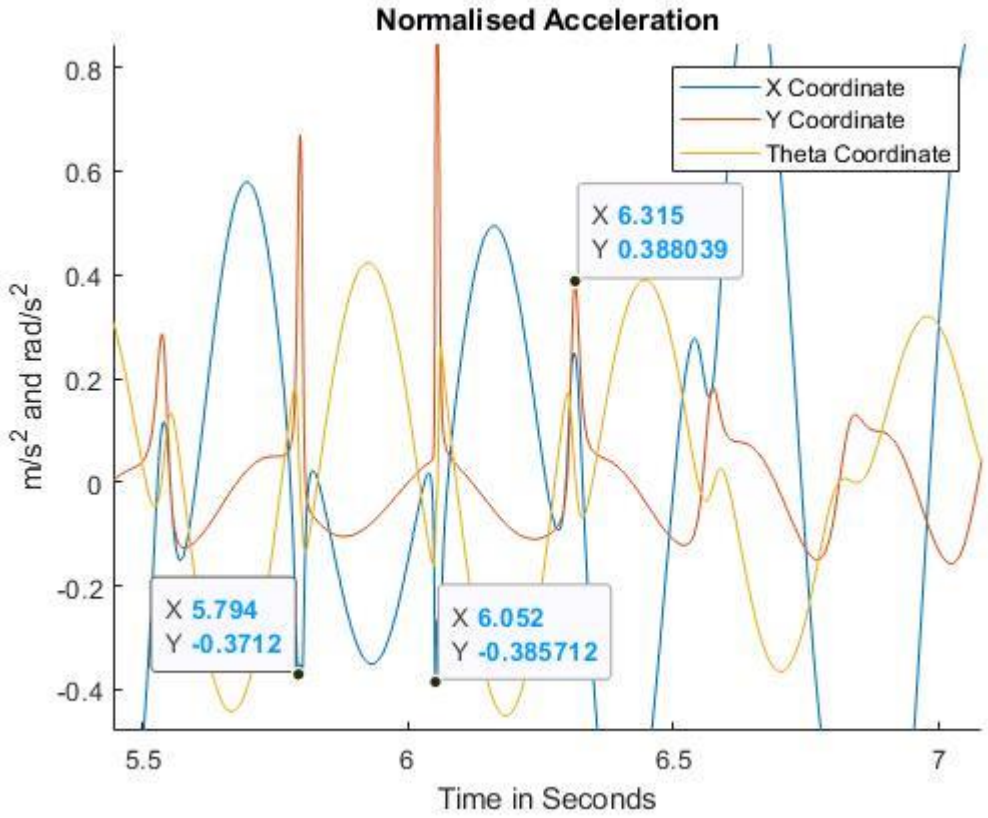
Normalised Acceleration
X Coordinate
Y Coordinate
Theta Coordinate
X 6.315
Y 0.388039
X 5.794
Y -0.3712
X 6.052
Y -0.385712
m/s2 and rad/s2
Time in Seconds

APPENDIX D – MATHEMATICA CODES

The code below presents the 3DOF system being solved using three different schemes on Mathematica. The code presents the general procedure of implementing differential equations and solving. The procedures for solving can be changed as required, this however is not presented.

```
k=266*1000;
m=3755;
r= 0.5;
L = 2;
IC = {x[0]==0.0522,y[0]==0.6,theta[0]==0.032,x'[0]==0,y'[0]==0,theta'[0]==0};

A = L^2/4+L*x[t]+x[t]^2+y[t]^2-0.5*L^2*Cos[theta[t]]-
L*x[t]*Cos[theta[t]]+0.25*L^2*Cos[theta[t]]^2-
L*y[t]*Sin[theta[t]]+0.25*L^2*Sin[theta[t]]^2;
B = L^2/4-L*x[t]+x[t]^2+y[t]^2-
0.5*L^2*Cos[theta[t]]+L*x[t]*Cos[theta[t]]+0.25*L^2*Cos[theta[t]]^2+L*y[t]*Sin[the
ta[t]]+0.25*L^2*Sin[theta[t]]^2;
oneA = 0.5*k*L^2*Sin[theta[t]]+0.25*k*L^2*(-
2*Cos[theta[t]]*Sin[theta[t]])+0.25*k*L^2*(2*Sin[theta[t]]*Cos[theta[t]]);
oneB = -k*r*(0.5*L^2*Sin[theta[t]]+L*x[t]*Sin[theta[t]]+0.25*L^2*(-
2*Cos[theta[t]]*Sin[theta[t]])-
L*y[t]*Cos[theta[t]]+0.25*L^2*(2*Sin[theta[t]]*Cos[theta[t]]))/(2*Sqrt[A]);
oneC = -k*r*(0.5*L^2*Sin[theta[t]]-
L*x[t]*Sin[theta[t]]+0.25*L^2*(2*Cos[theta[t]]*Sin[theta[t]])+L*y[t]*Cos[theta[t]]
+0.25*L^2*(2*Sin[theta[t]]*Cos[theta[t]]))/(2*Sqrt[B]);
ONE= oneA+oneB+oneC;
two = 2*k*x[t]-k*r*(L+2*x[t]-L*Cos[theta[t]])/(2*Sqrt[A])-k*r*(-
L+2*x[t]+L*Cos[theta[t]])/(2*Sqrt[B]);
three = -9.81*m+2*k*y[t]-k*r*(2*y[t]-L*Sin[theta[t]])/(2*Sqrt[A])-
k*r*(2*y[t]+L*Sin[theta[t]])/(2*Sqrt[B]);
S1 = NDSolve[{x''[t]==-two/(m),y''[t]==-three/(m),theta''[t]==-
ONE*4/(m*L^2),IC},{x,y,theta},{t,0,30},Method->{"TimeIntegration"-
>{"ExplicitRungeKutta","DifferenceOrder"->8}}];
S2 = NDSolve[{x''[t]==-two/(m),y''[t]==-three/(m),theta''[t]==-
ONE*4/(m*L^2),IC},{x,y,theta},{t,0,30},Method->{"TimeIntegration"-
>"ExplicitEuler"}];
S3 = NDSolve[{x''[t]==-two/(m),y''[t]==-three/(m),theta''[t]==-
ONE*4/(m*L^2),IC},{x,y,theta},{t,0,30}];
S4 =  NDSolve[{x''[t]==-two/(m),y''[t]==-three/(m),theta''[t]==-
ONE*4/(m*L^2),IC},{x,y,theta},{t,0,30},Method->{"Adams"}];

X1 = Evaluate[{x[t]} /.S2];
X2 = Evaluate[{x[t]} /.S2];
X3 = Evaluate[{x[t]} /.S3];
X4 = Evaluate[{x[t]}/.S4];
Plot[{X1,X2,X3,X4},{t,0,30},PlotLabel->Style["X Coordinate",FontSize->18],Axes-
>True,AxesLabel->{"time in seconds","m"},PlotLegends->{"Explicit Runge
Kutta","Explicit Euler","Mathematica optimised","Adams"}]


Y1 = Evaluate[{y[t]} /.S2];
Y2 = Evaluate[{y[t]} /.S2];
Y3 = Evaluate[{y[t]} /.S3];
Y4 = Evaluate[{y[t]}/.S4];
```

```
Plot[{Y1,Y2,Y3,Y4},{t,0,30},PlotLabel->Style["Y Coordinate",FontSize-
>18],AxesLabel->{"time in seconds","m"},PlotLegends->{"Explicit Runge
Kutta","Explicit Euler","Mathematica optimised","Adams"}]

t1 = Evaluate[{theta[t]} /.S2];
t2 = Evaluate[{theta[t]} /.S2];
t3 = Evaluate[{theta[t]} /.S3];
t4 = Evaluate[{theta[t]}/.S4];
Plot[{t1,t2,t3,t4},{t,0,30},PlotLabel->Style["Theta Coordinate",FontSize-
>18],AxesLabel->{"time in seconds","rad"},PlotLegends->{"Explicit Runge
Kutta","Explicit Euler","Mathematica optimised","Adams"}]
```

Mathematica Code 1: 3DOF system solved using various numerical solving methods

APPENDIX E – RESULTS FOR THE *XN* CASE

This section presents the acceleration, displacement, and resultant acceleration plots for the XN case.

N = 1

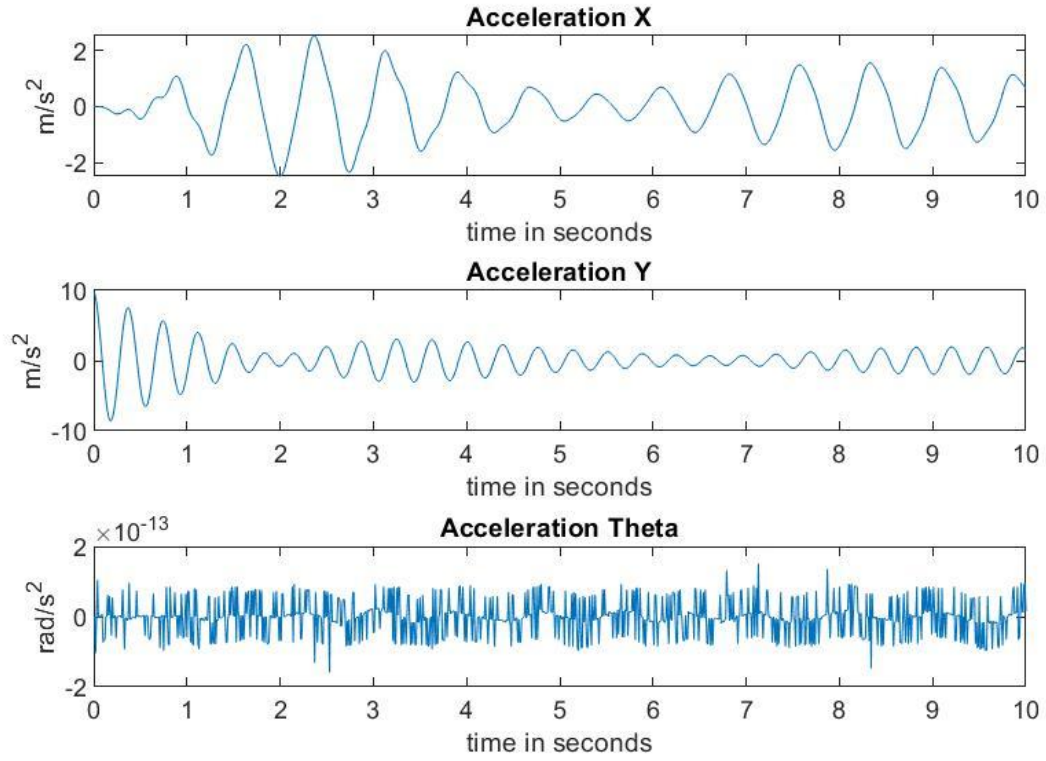
Acceleration X
m/s2
time in seconds
Acceleration Y
m/s2
time in seconds
Acceleration Theta
×10-13
rad/s2
time in seconds

N = 1

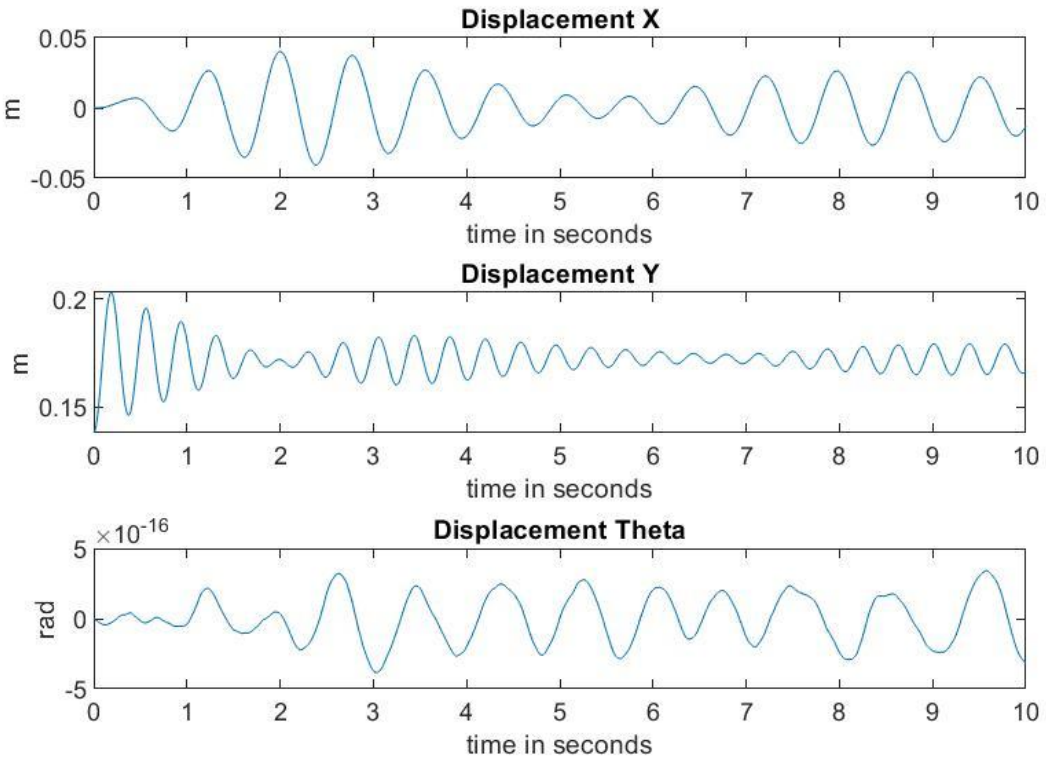
Displacement X
m
time in seconds
Displacement Y
m
time in seconds
Displacement Theta
×10-16
rad
time in seconds

N = 1

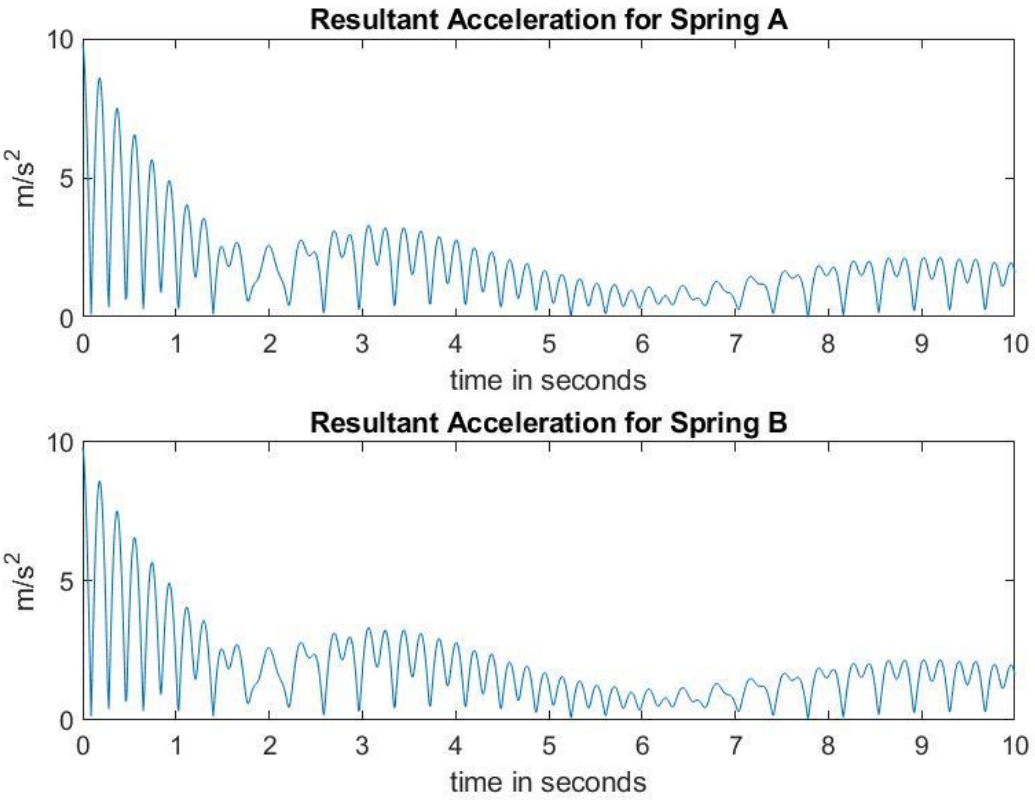
Resultant Acceleration for Spring A
m/s^2
time in seconds
Resultant Acceleration for Spring B
m/s^2
time in seconds

N = 2

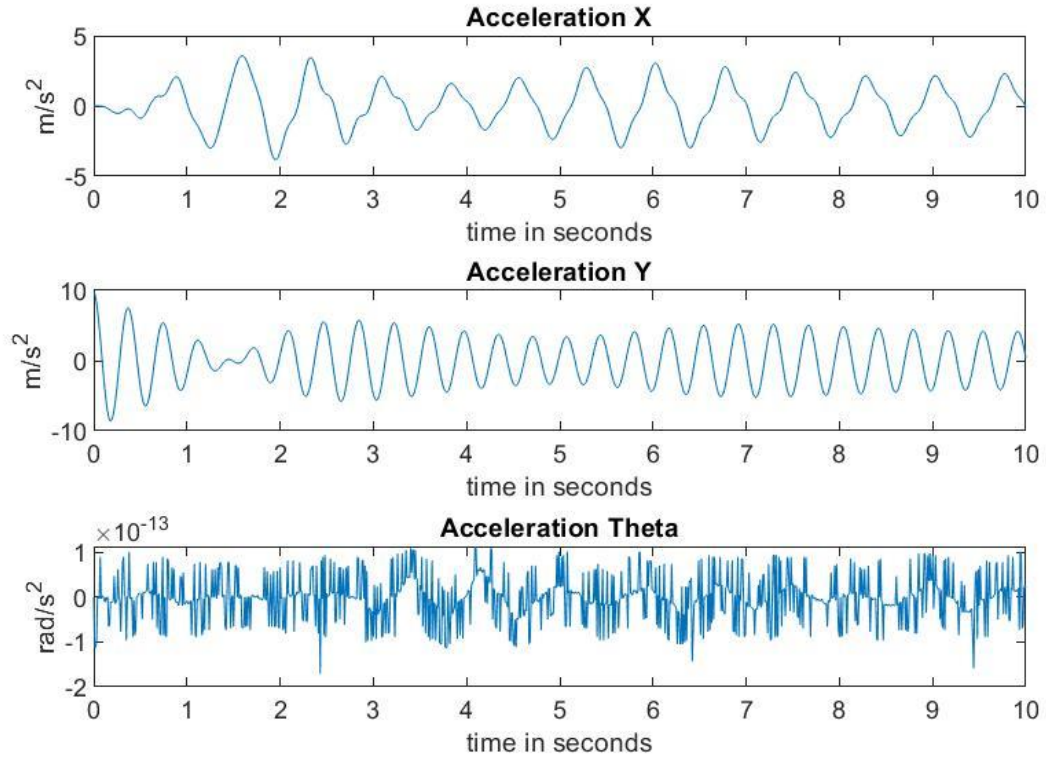
Acceleration X
m/s2
time in seconds
Acceleration Y
m/s2
time in seconds
Acceleration Theta
×10-13
rad/s2
time in seconds

N = 2

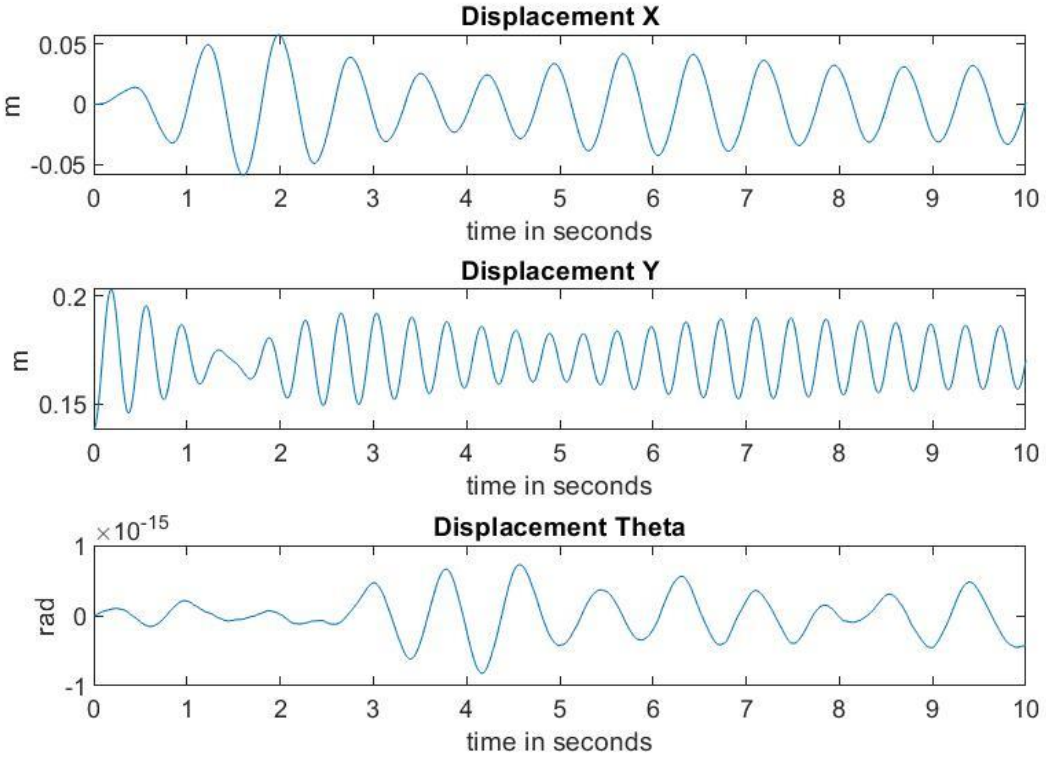
Displacement X
m
time in seconds
Displacement Y
m
time in seconds
Displacement Theta
×10-15
rad
time in seconds

N = 2

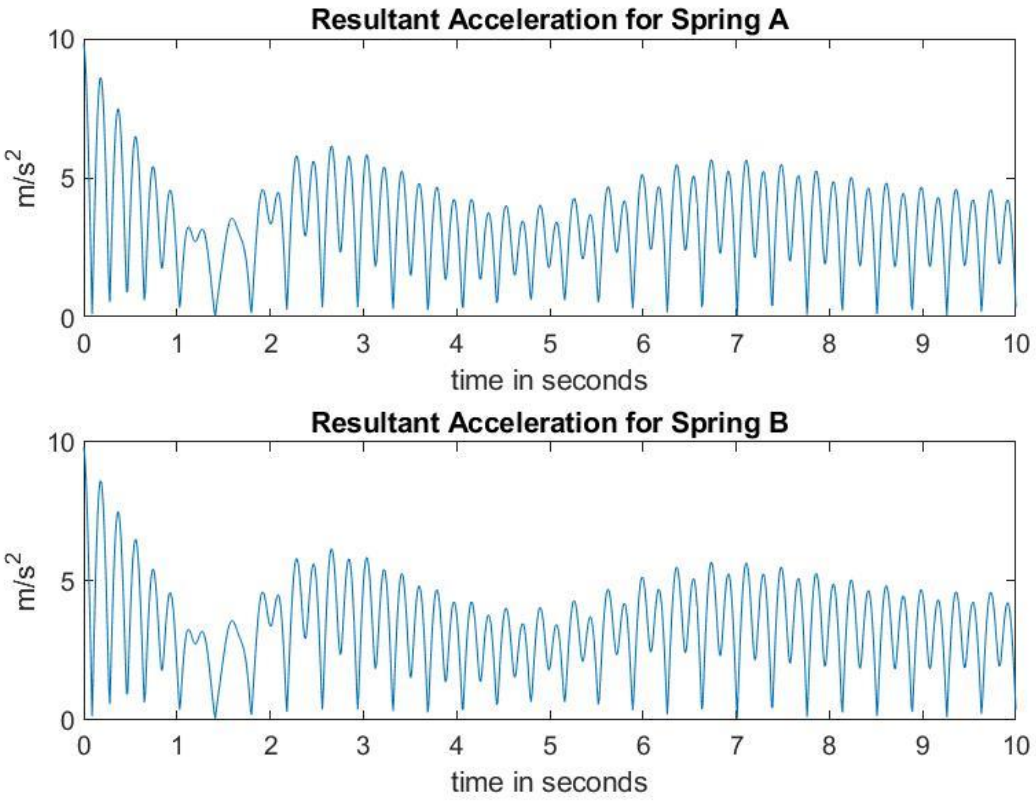
Resultant Acceleration for Spring A
m/s^2
time in seconds
Resultant Acceleration for Spring B
m/s^2
time in seconds

N = 3

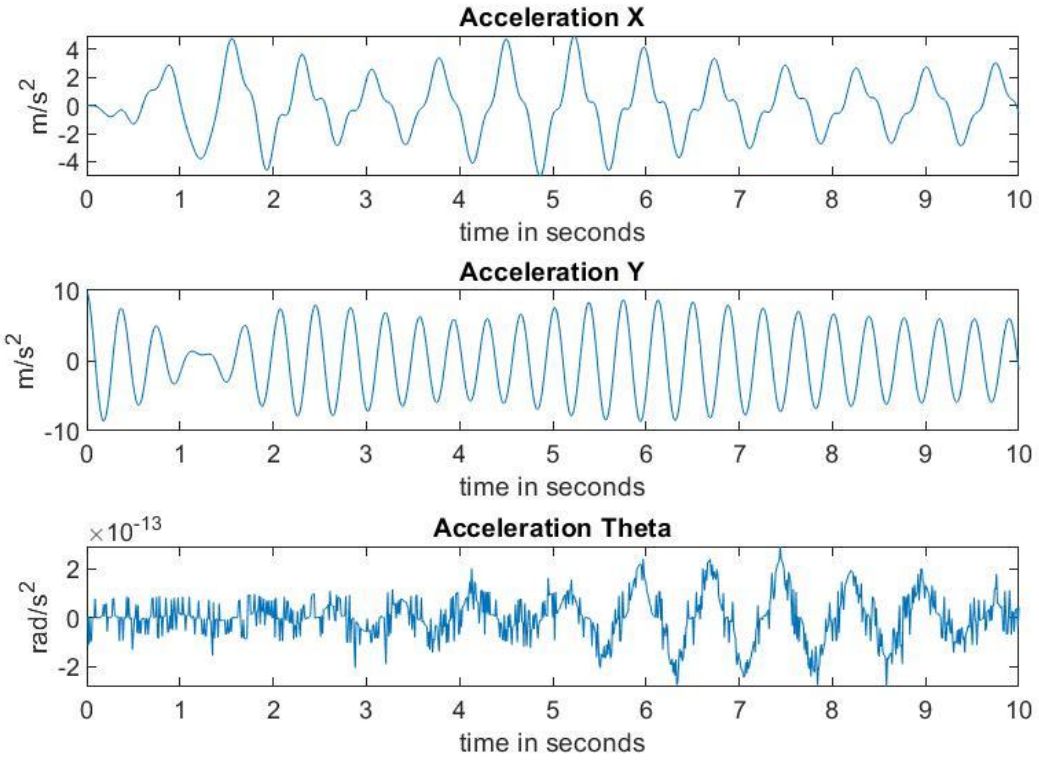
Acceleration X
m/s2
time in seconds
Acceleration Y
m/s2
time in seconds
Acceleration Theta
×10-13
rad/s2
time in seconds

N = 3

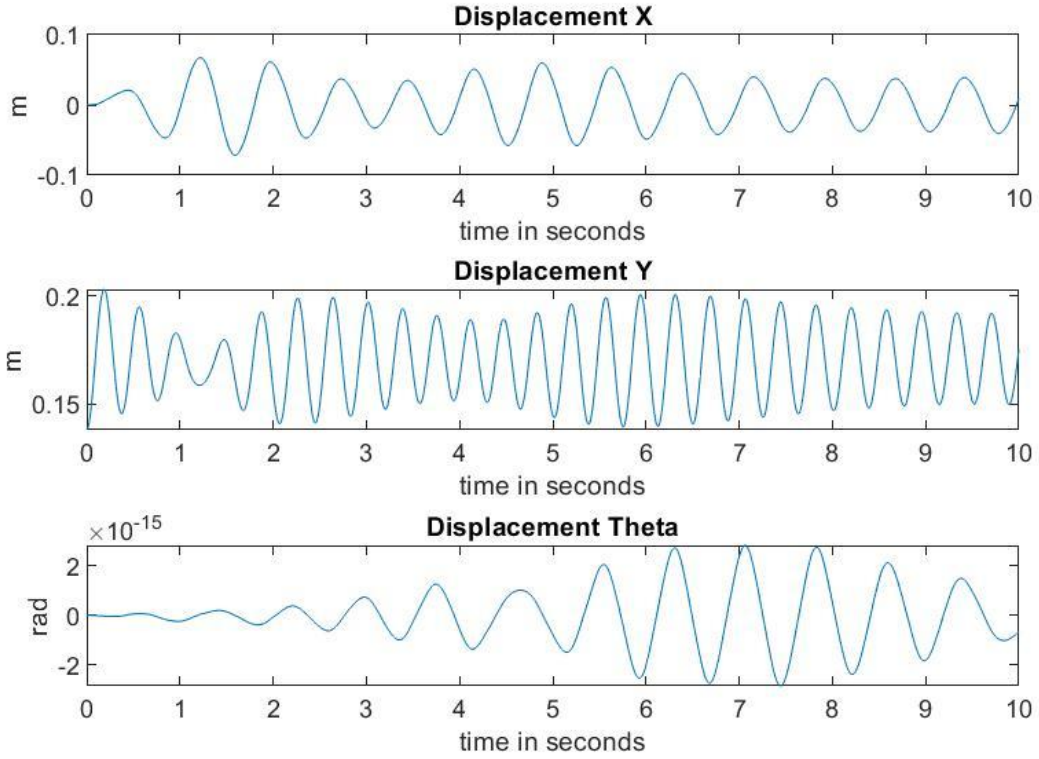
Displacement X
m
time in seconds
Displacement Y
m
time in seconds
Displacement Theta
×10-15
rad
time in seconds

N = 3

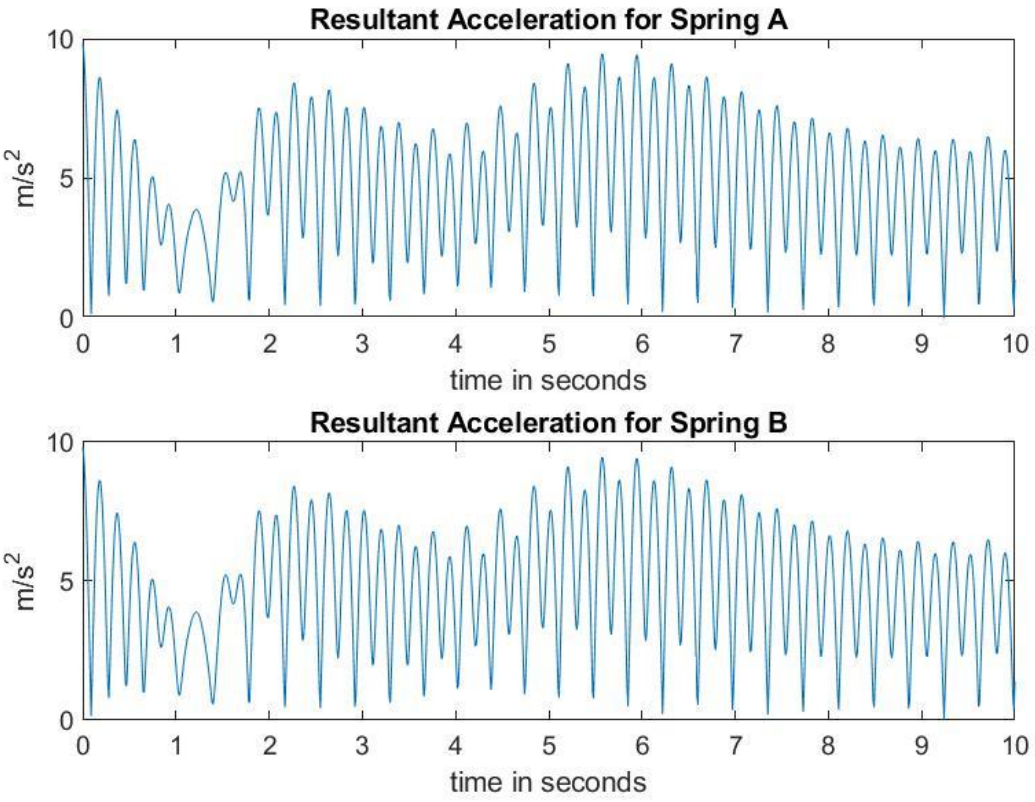
Resultant Acceleration for Spring A
m/s^2
time in seconds
Resultant Acceleration for Spring B
m/s^2
time in seconds

N = 4

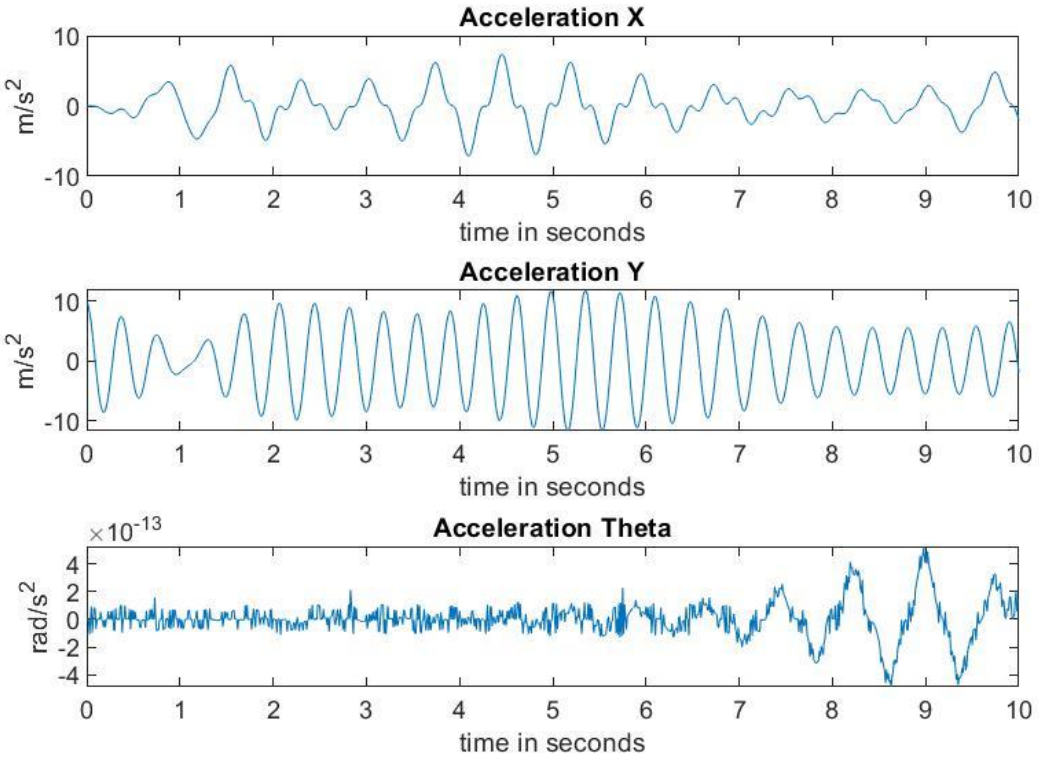
Acceleration X
m/s2
time in seconds
Acceleration Y
m/s2
time in seconds
Acceleration Theta
×10-13
rad/s2
time in seconds

N = 4

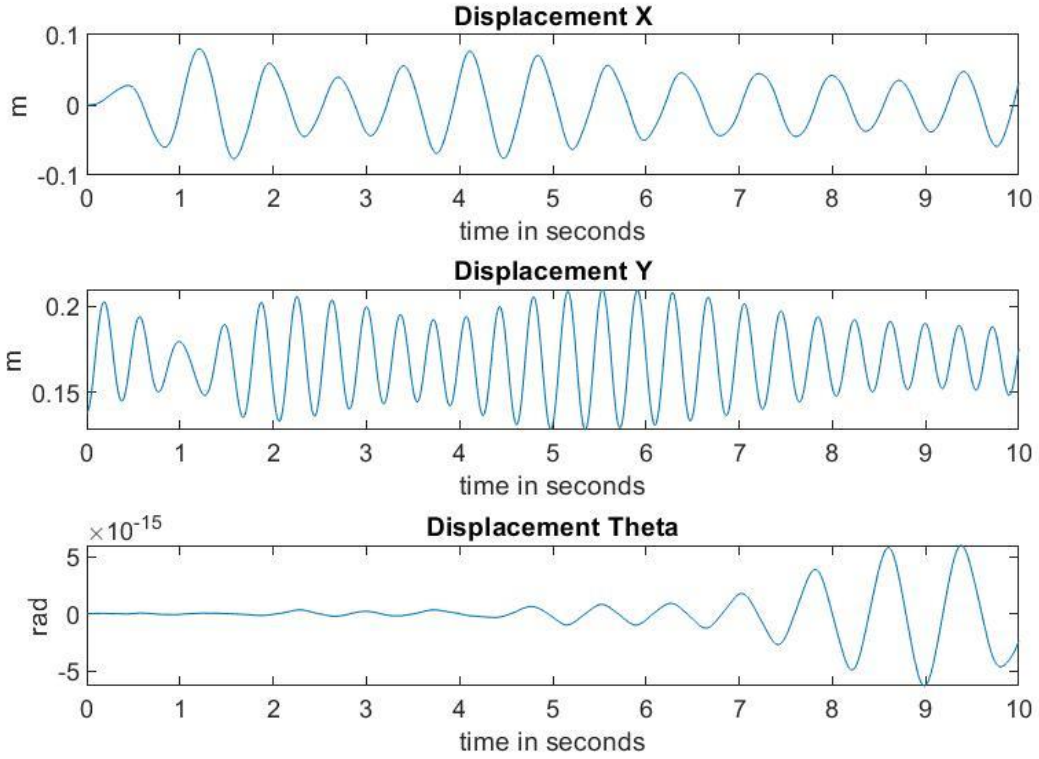
Displacement X
m
time in seconds
Displacement Y
m
time in seconds
Displacement Theta
×10-15
rad
time in seconds

N = 4

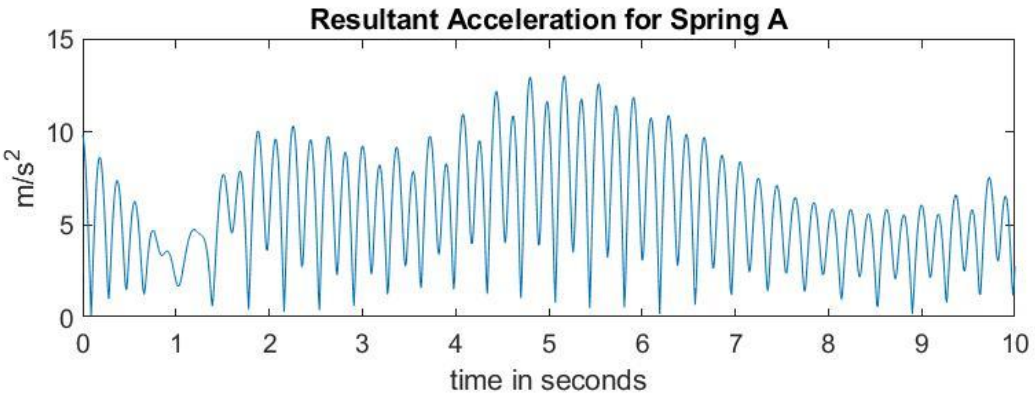
Resultant Acceleration for Spring A
m/s^2
time in seconds

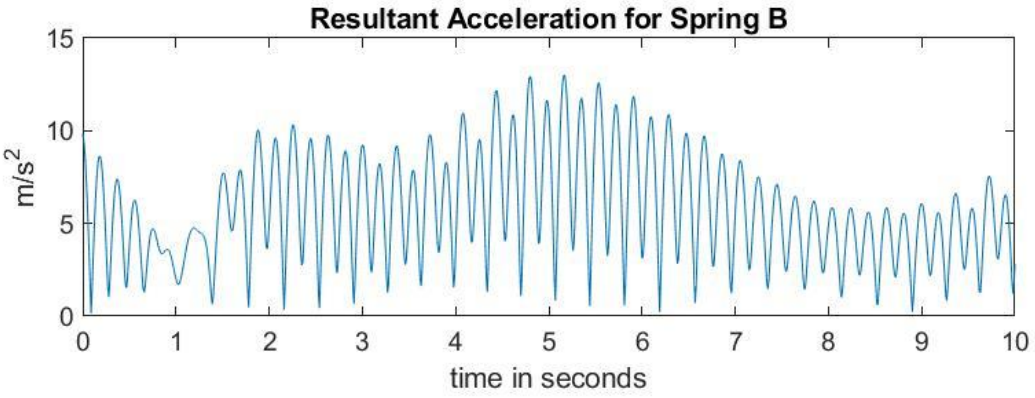
Resultant Acceleration for Spring B
m/s^2
time in seconds

N = 5

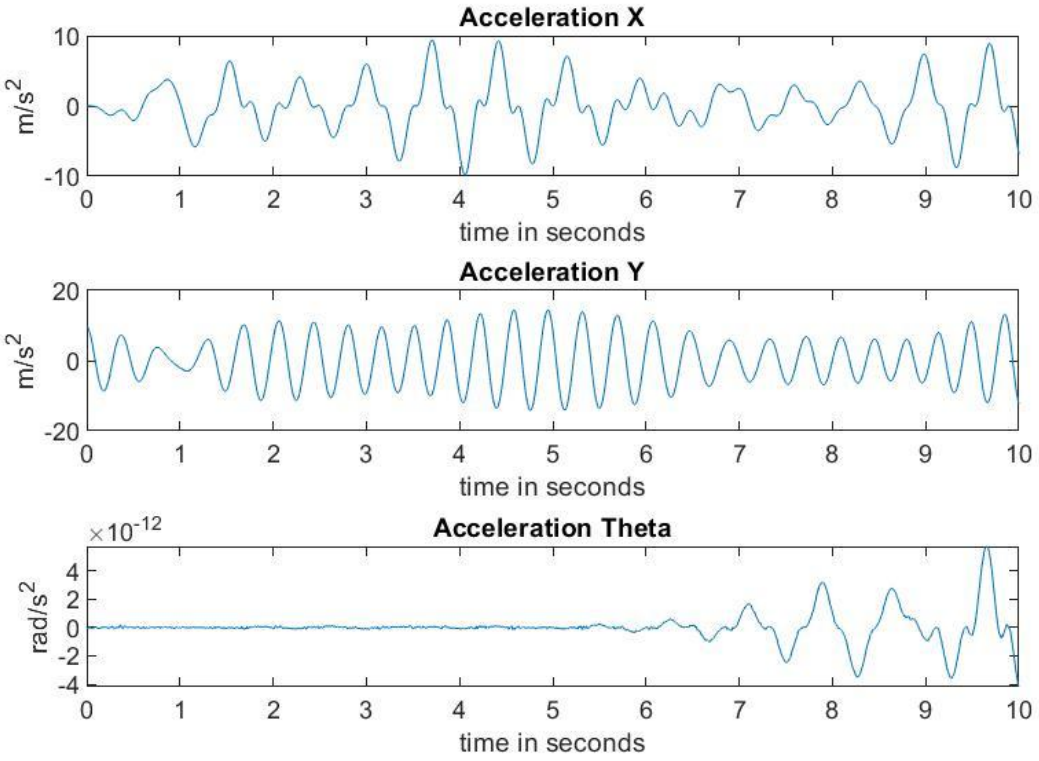
Acceleration X
m/s2
time in seconds
Acceleration Y
m/s2
time in seconds
Acceleration Theta
×10-12
rad/s2
time in seconds

N = 5

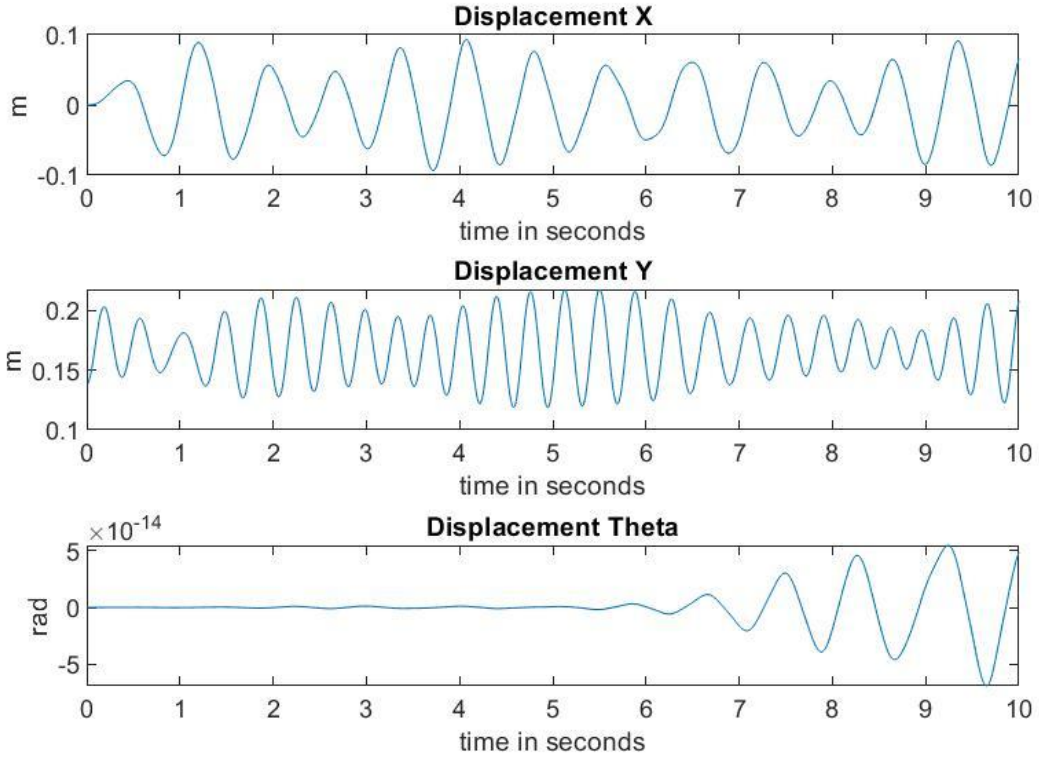
Displacement X
m
time in seconds
Displacement Y
m
time in seconds
Displacement Theta
×10-14
rad
time in seconds

N = 5

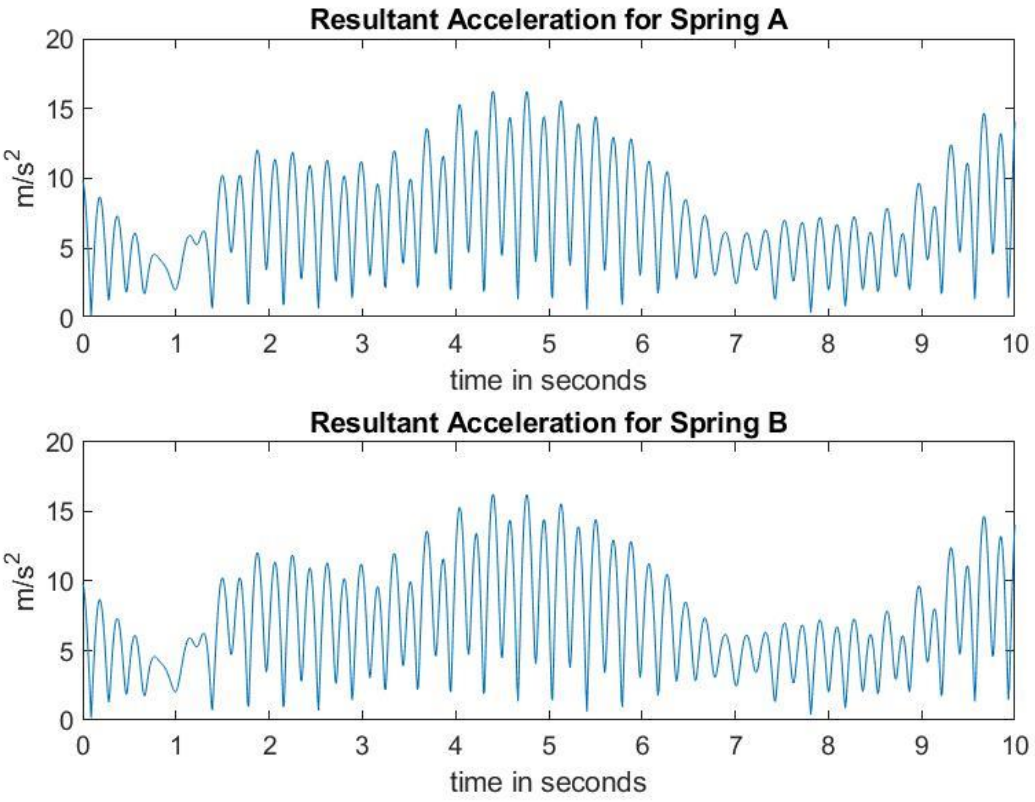
Resultant Acceleration for Spring A
m/s^2
time in seconds
Resultant Acceleration for Spring B
m/s^2
time in seconds

N = 6

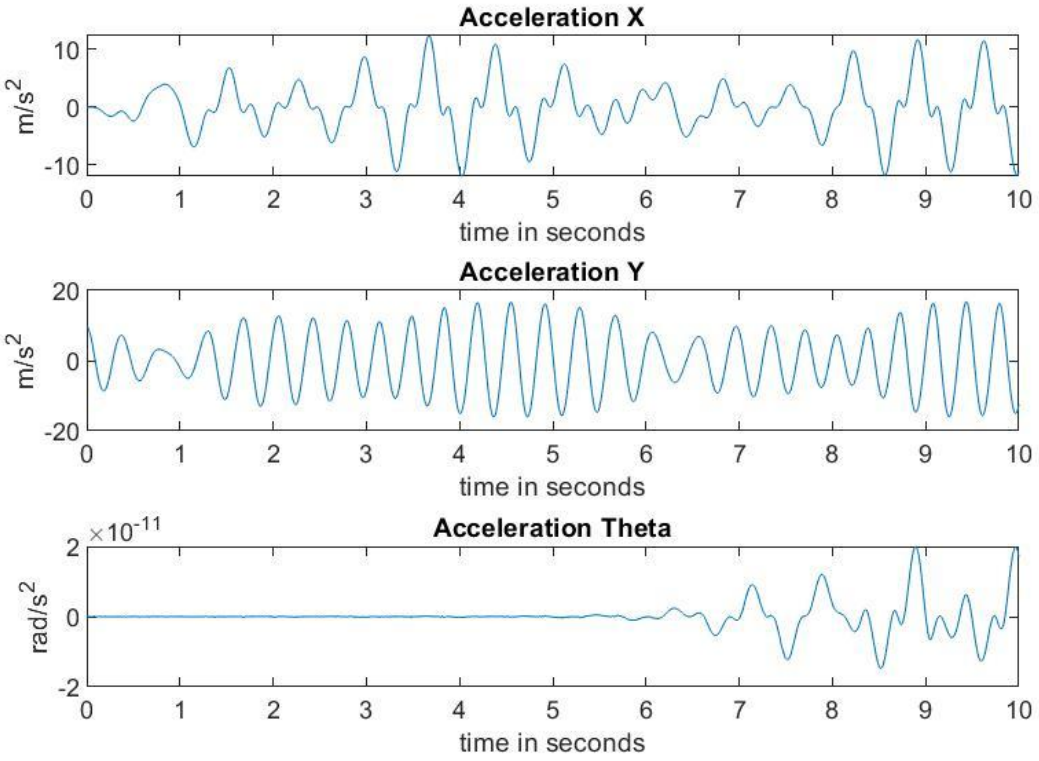
Acceleration X
m/s2
time in seconds
Acceleration Y
m/s2
time in seconds
Acceleration Theta
×10-11
rad/s2
time in seconds

N = 6

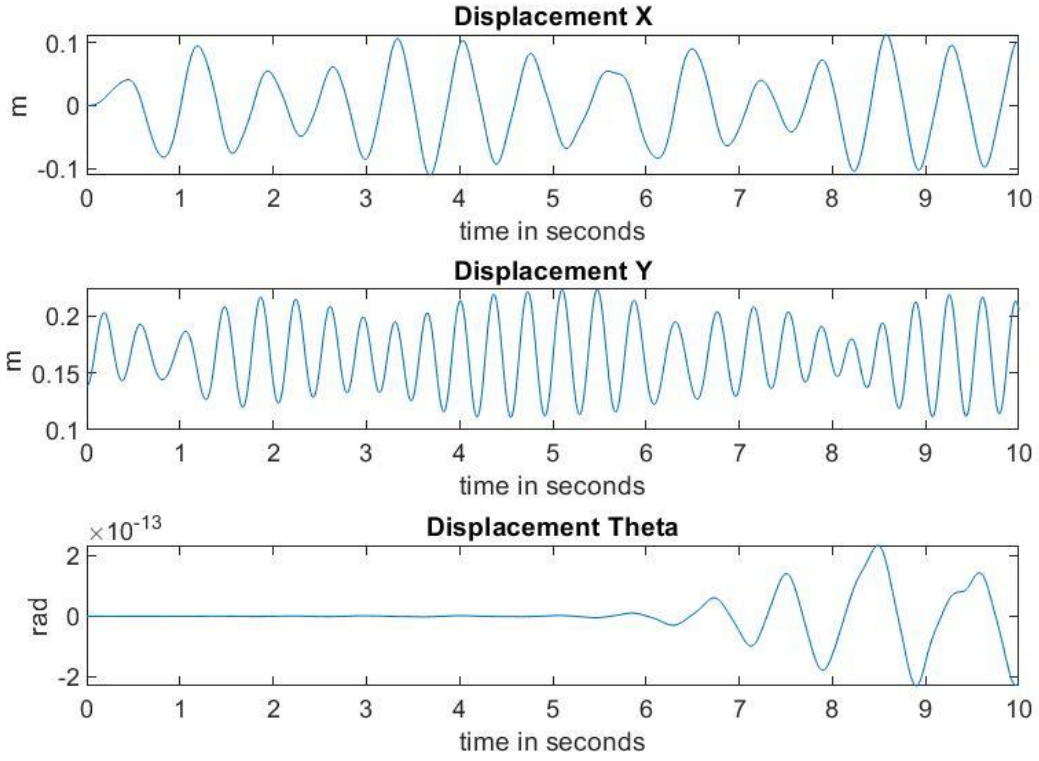
Displacement X
m
time in seconds
Displacement Y
m
time in seconds
Displacement Theta
×10-13
rad
time in seconds

N = 6

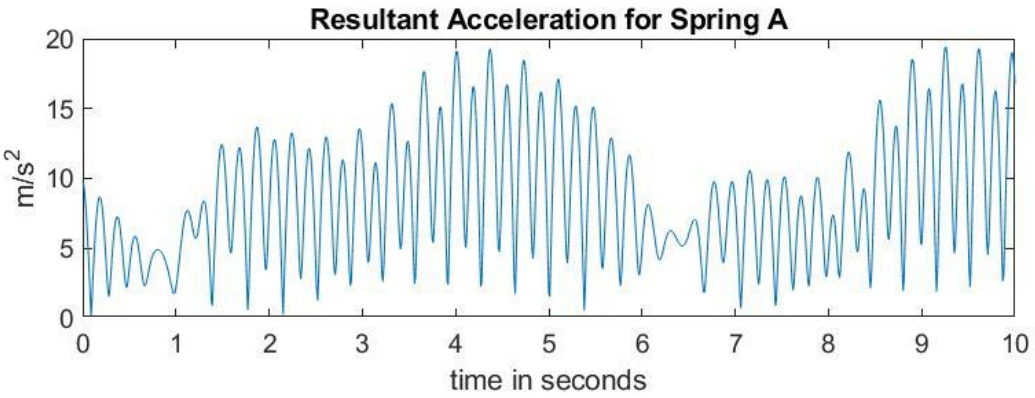
Resultant Acceleration for Spring A
m/s^2
time in seconds

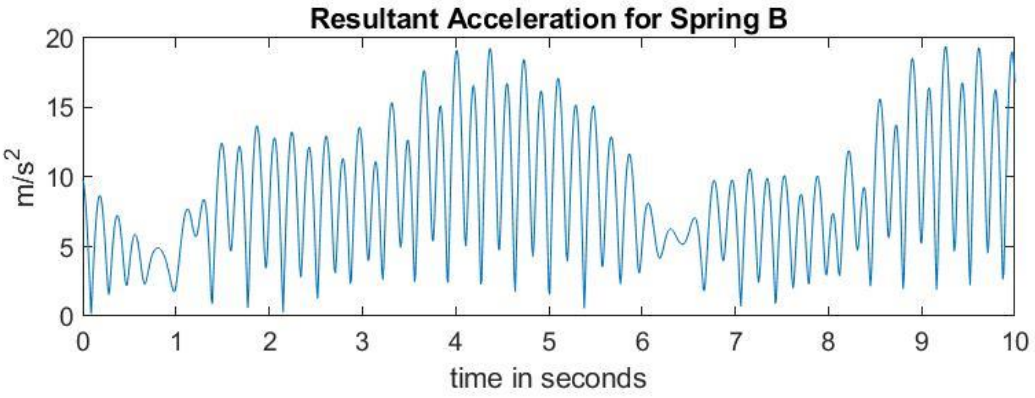
Resultant Acceleration for Spring B
m/s^2
time in seconds

N = 7

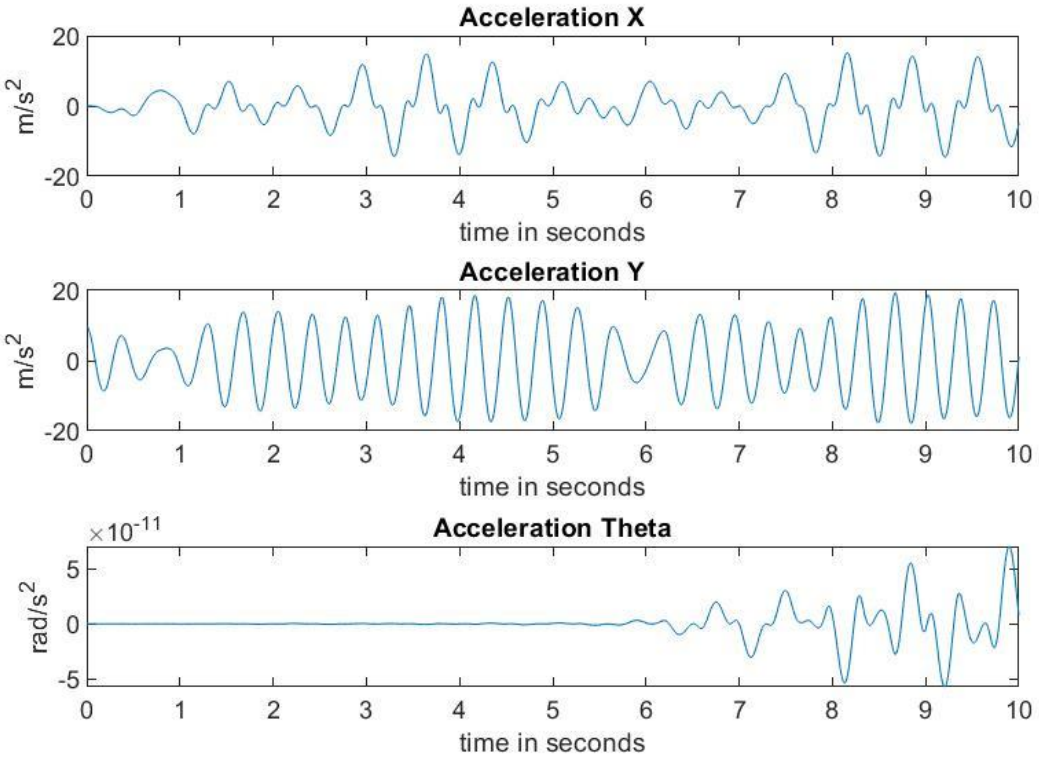
Acceleration X
m/s2
time in seconds
Acceleration Y
m/s2
time in seconds
Acceleration Theta
×10-11
rad/s2
time in seconds

N = 7

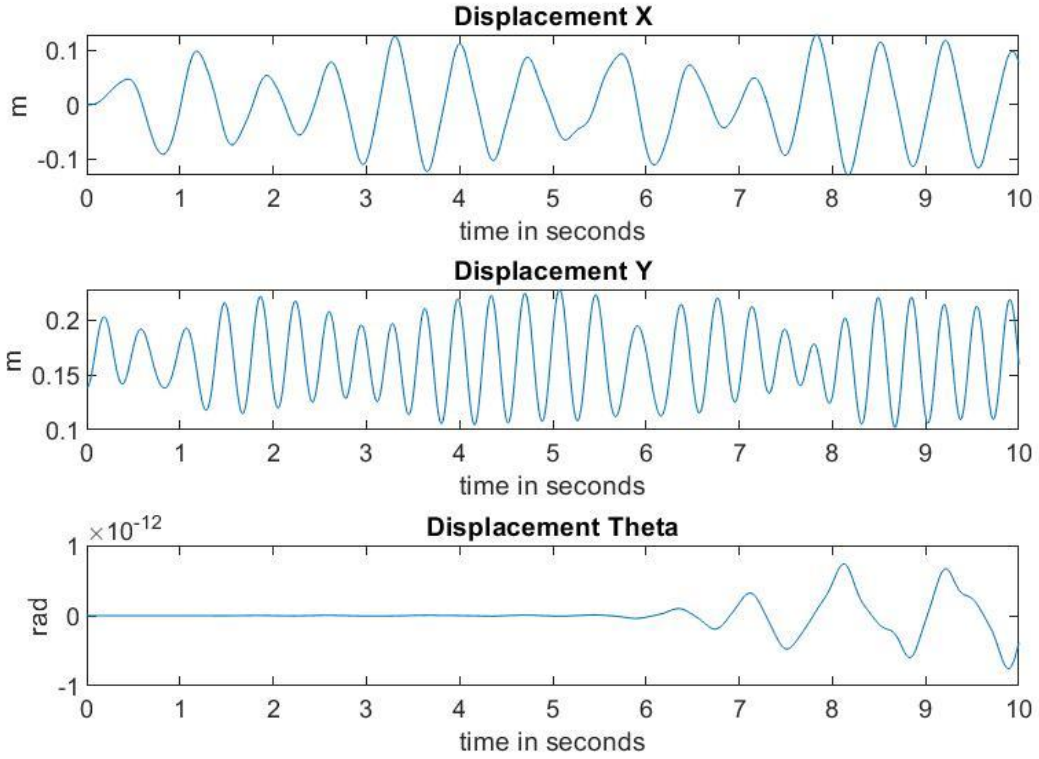
Displacement X
m
time in seconds
Displacement Y
m
time in seconds
Displacement Theta
×10-12
rad
time in seconds

N = 7

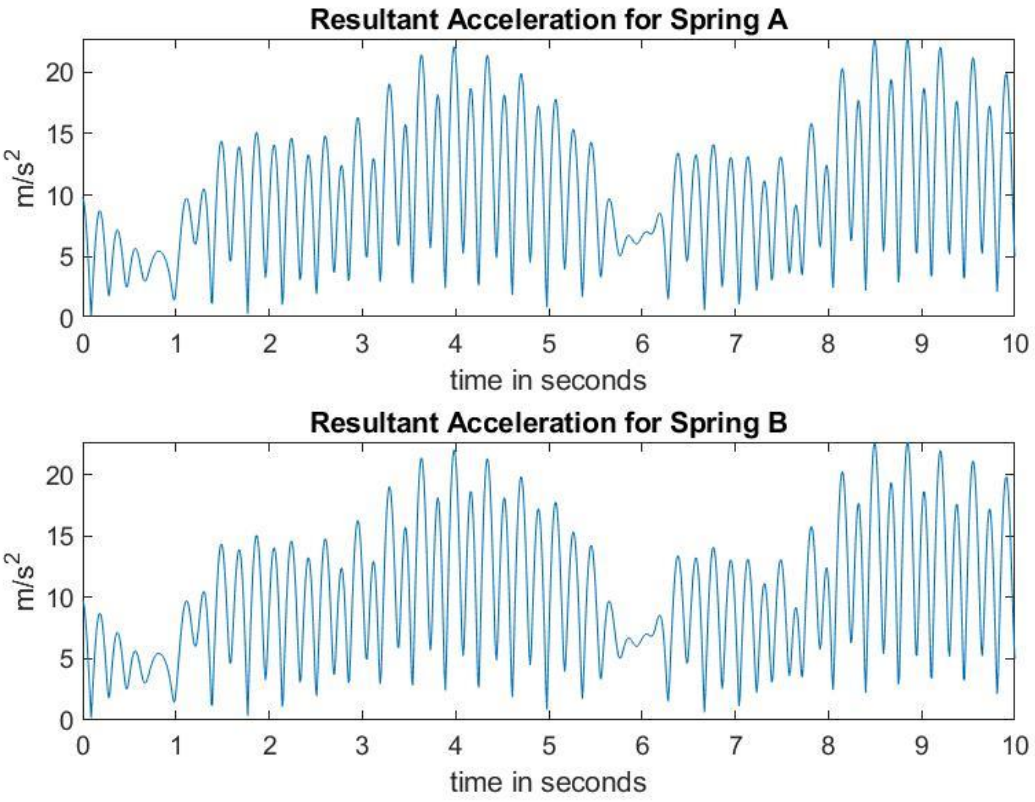
Resultant Acceleration for Spring A
m/s^2
time in seconds
Resultant Acceleration for Spring B
m/s^2
time in seconds

N = 8

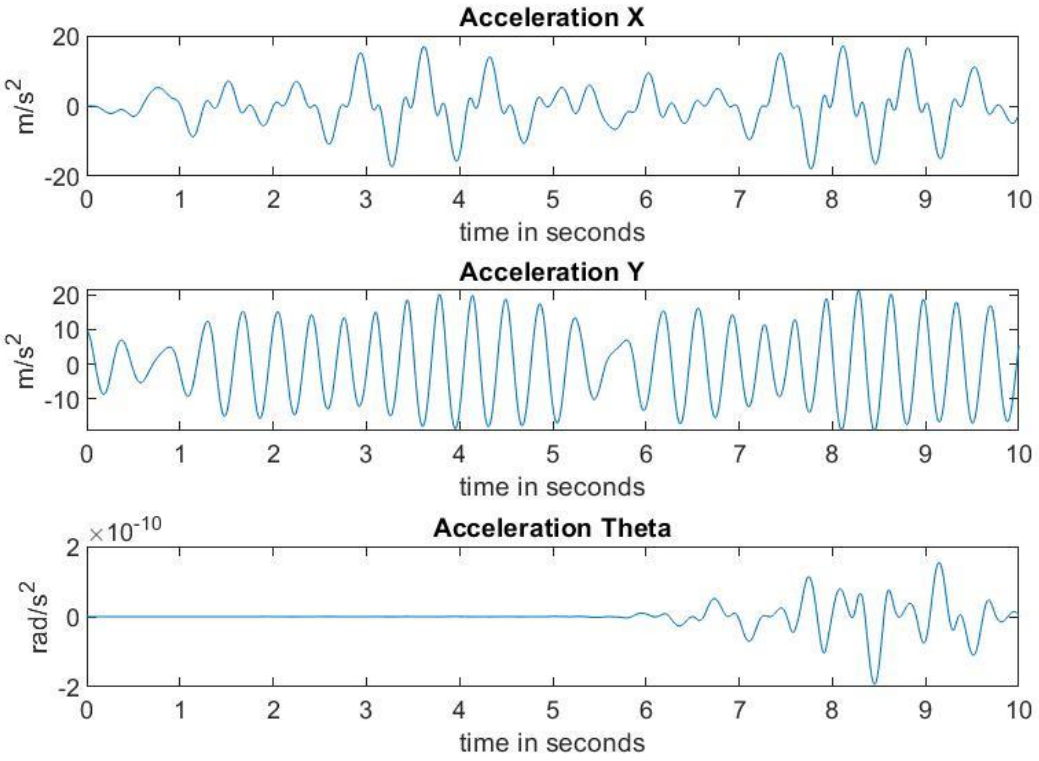
Acceleration X
m/s2
time in seconds
Acceleration Y
m/s2
time in seconds
Acceleration Theta
×10-10
rad/s2
time in seconds

N = 8

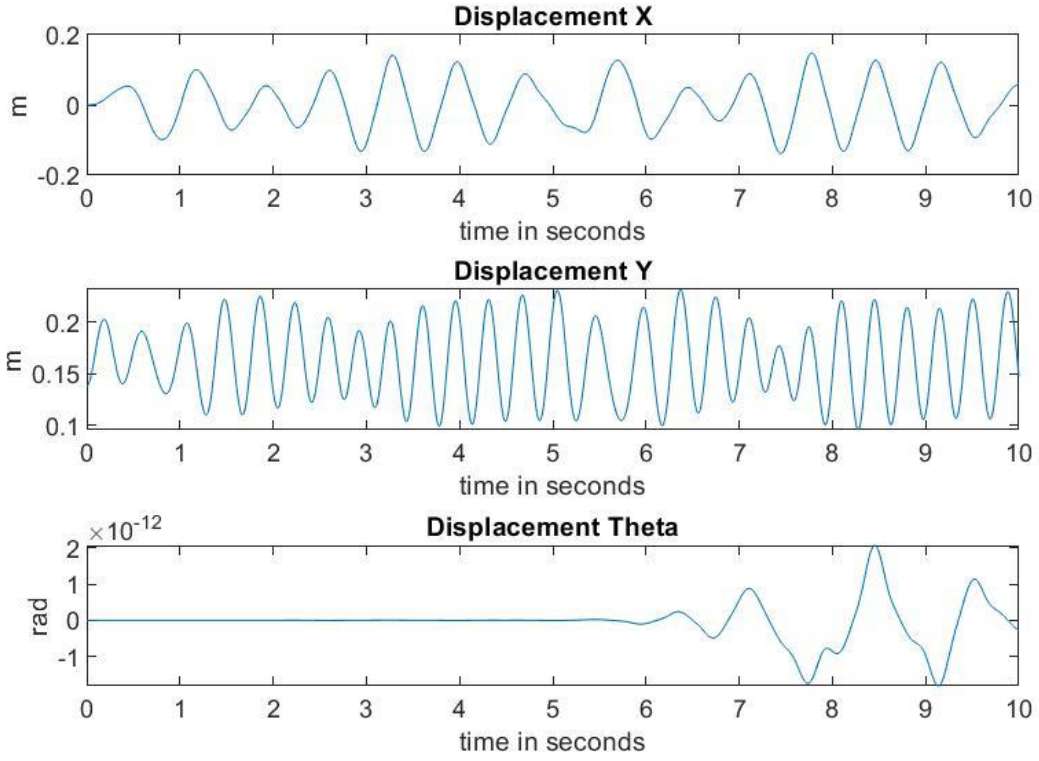
Displacement X
m
time in seconds
Displacement Y
m
time in seconds
Displacement Theta
×10-12
rad
time in seconds

N = 8

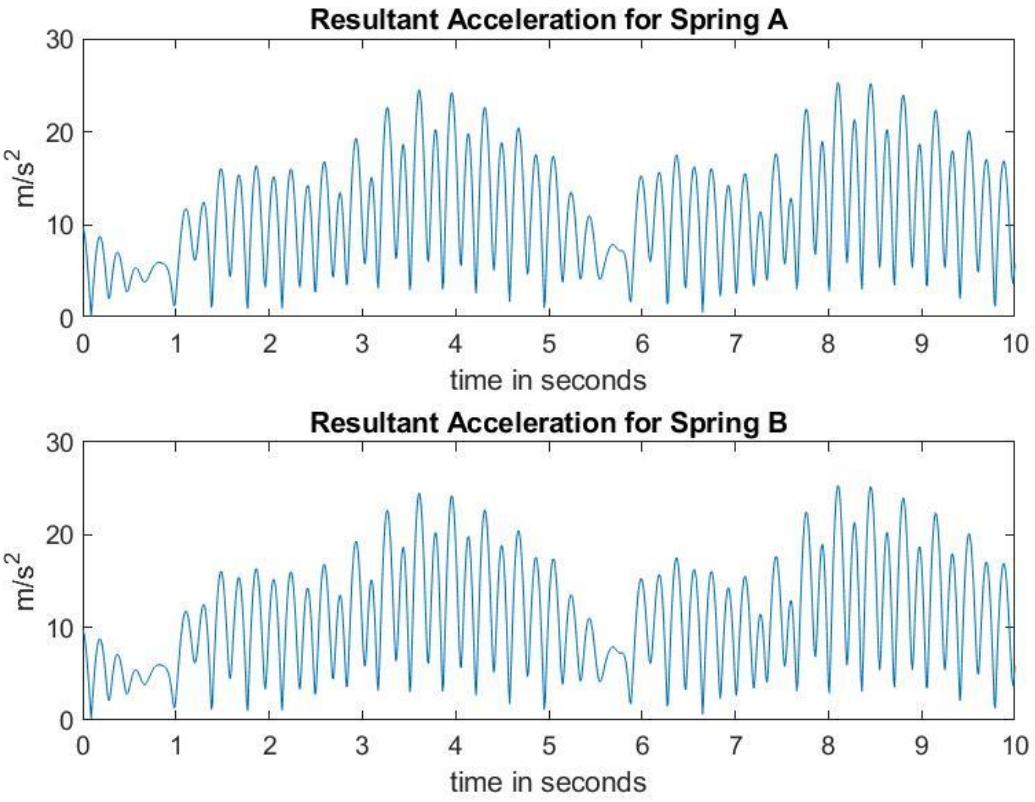
Resultant Acceleration for Spring A
m/s2
time in seconds
Resultant Acceleration for Spring B
m/s2
time in seconds

N = 9

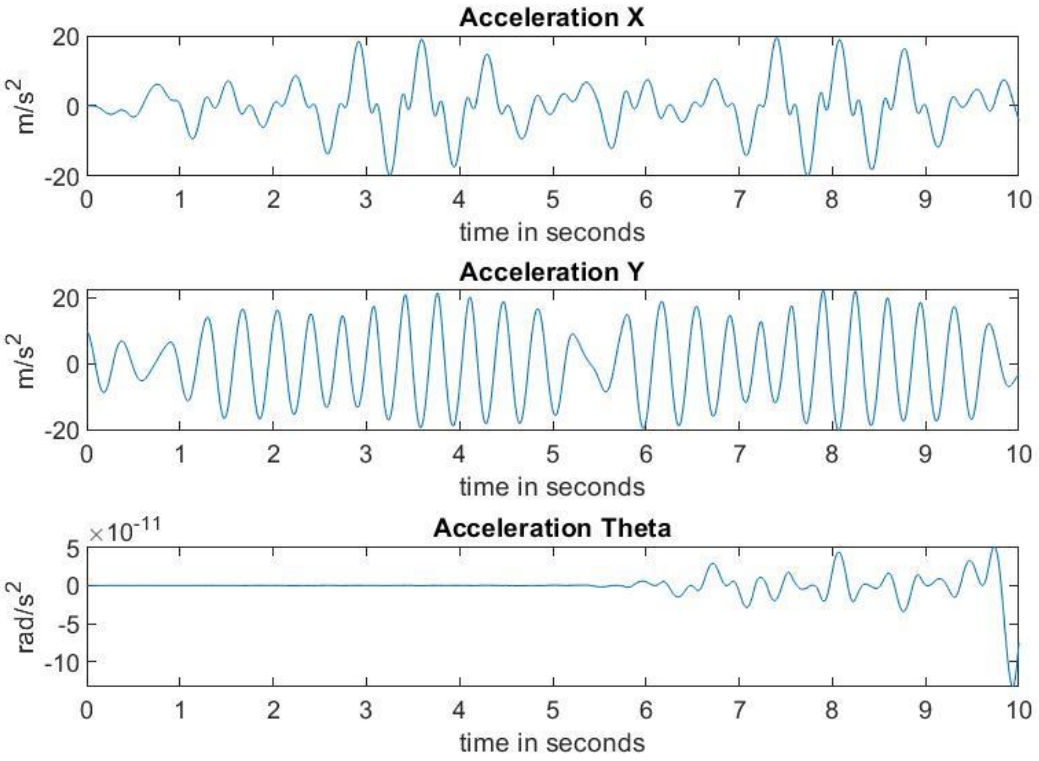
Acceleration X
m/s2
time in seconds
Acceleration Y
m/s2
time in seconds
Acceleration Theta
×10-11
rad/s2
time in seconds

N = 9

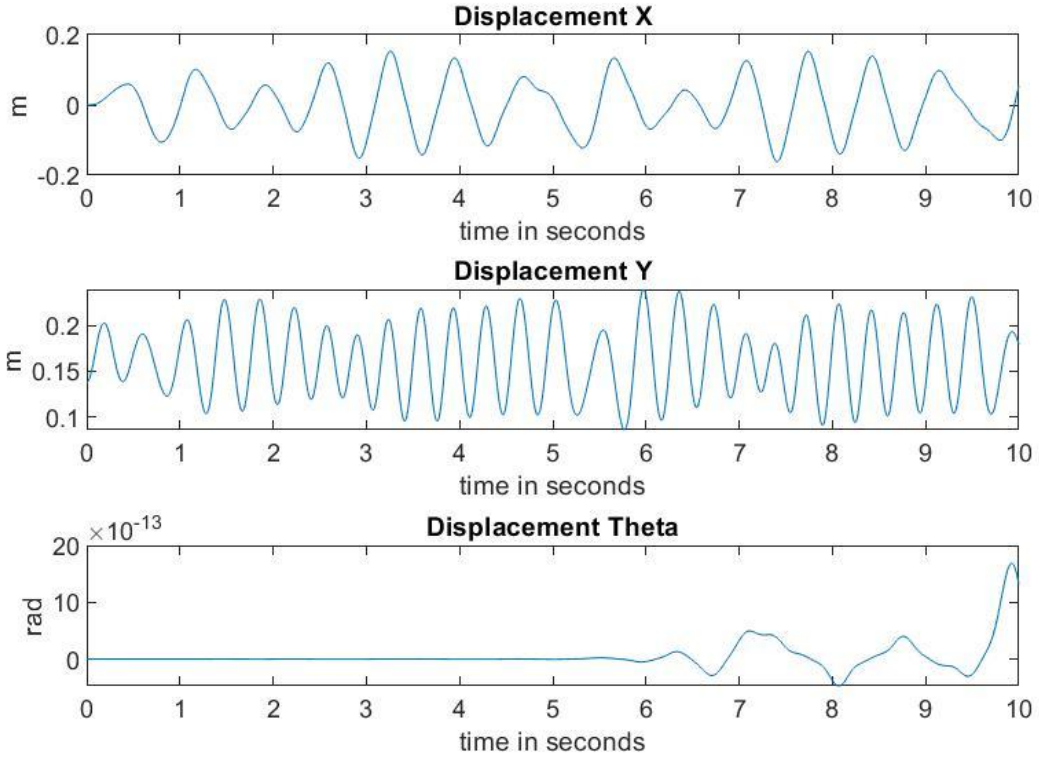
Displacement X
m
time in seconds
Displacement Y
m
time in seconds
Displacement Theta
×10-13
rad
time in seconds

N = 9

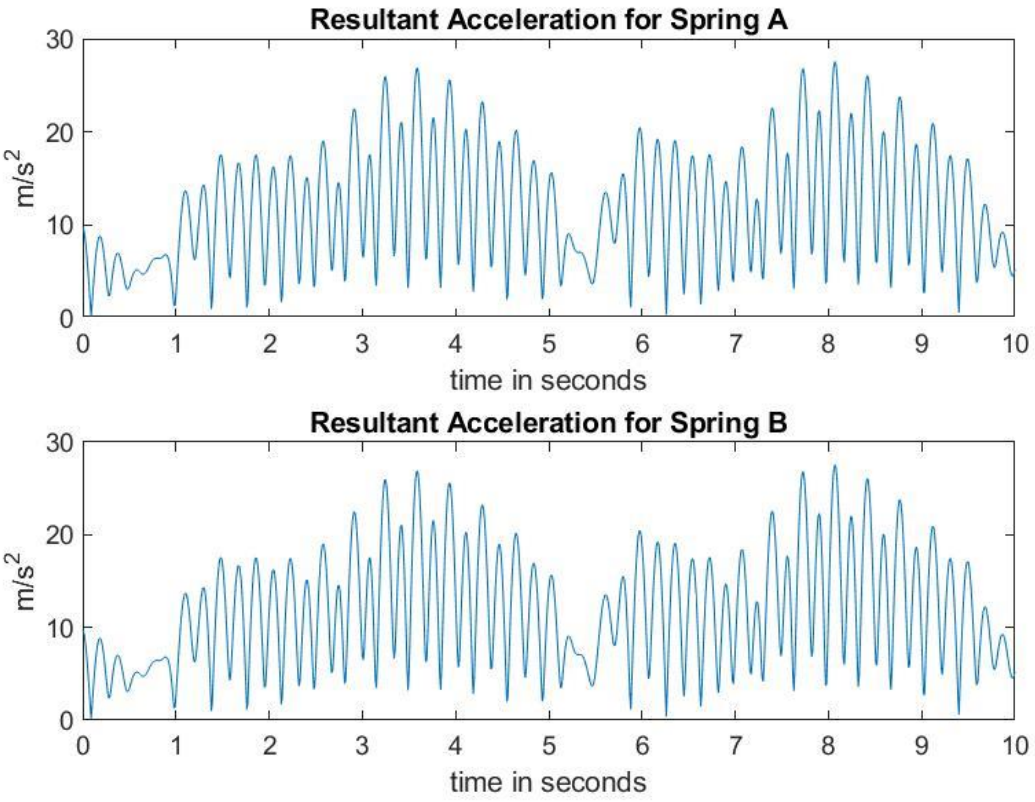
Resultant Acceleration for Spring A
m/s2
time in seconds
Resultant Acceleration for Spring B
m/s2
time in seconds

N = 10

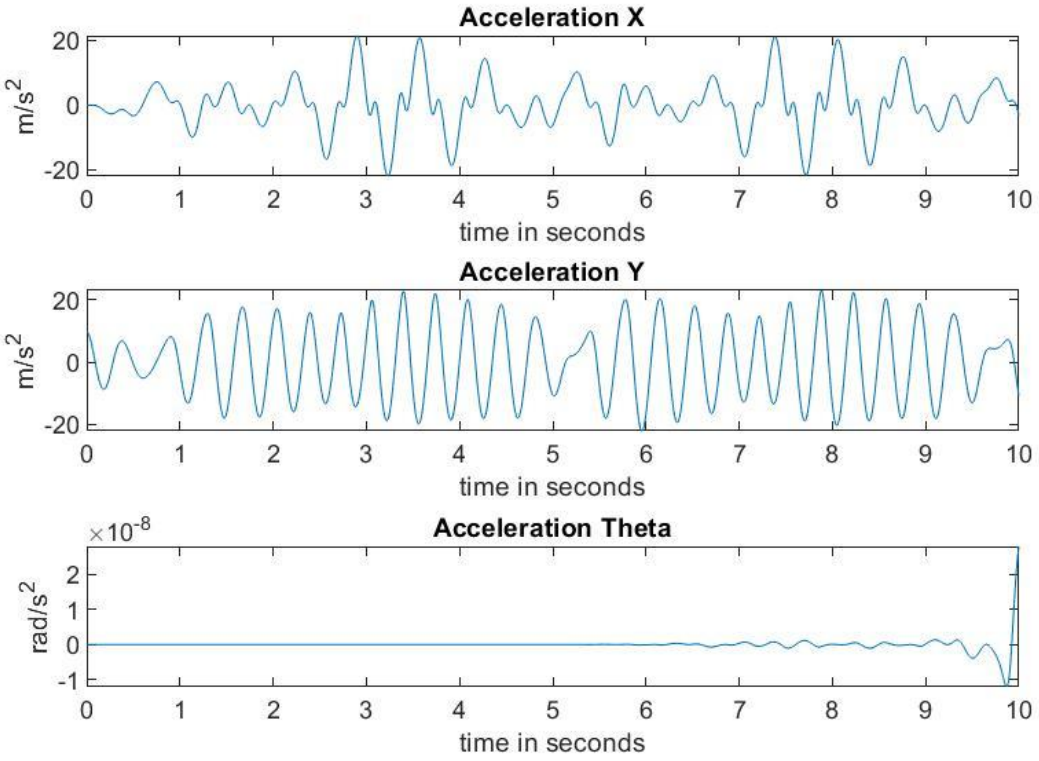
Acceleration X
m/s2
time in seconds
Acceleration Y
m/s2
time in seconds
×10-8
Acceleration Theta
rad/s2
time in seconds

N = 10

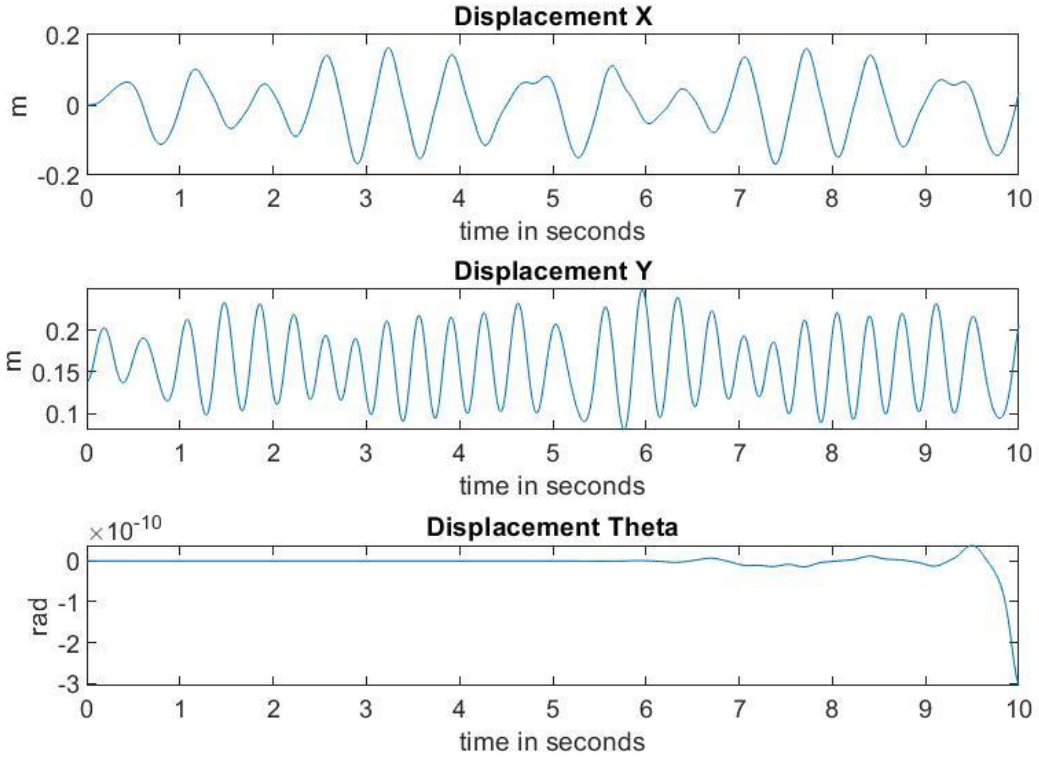
Displacement X
m
time in seconds
Displacement Y
m
time in seconds
×10-10
Displacement Theta
rad
time in seconds

N = 10

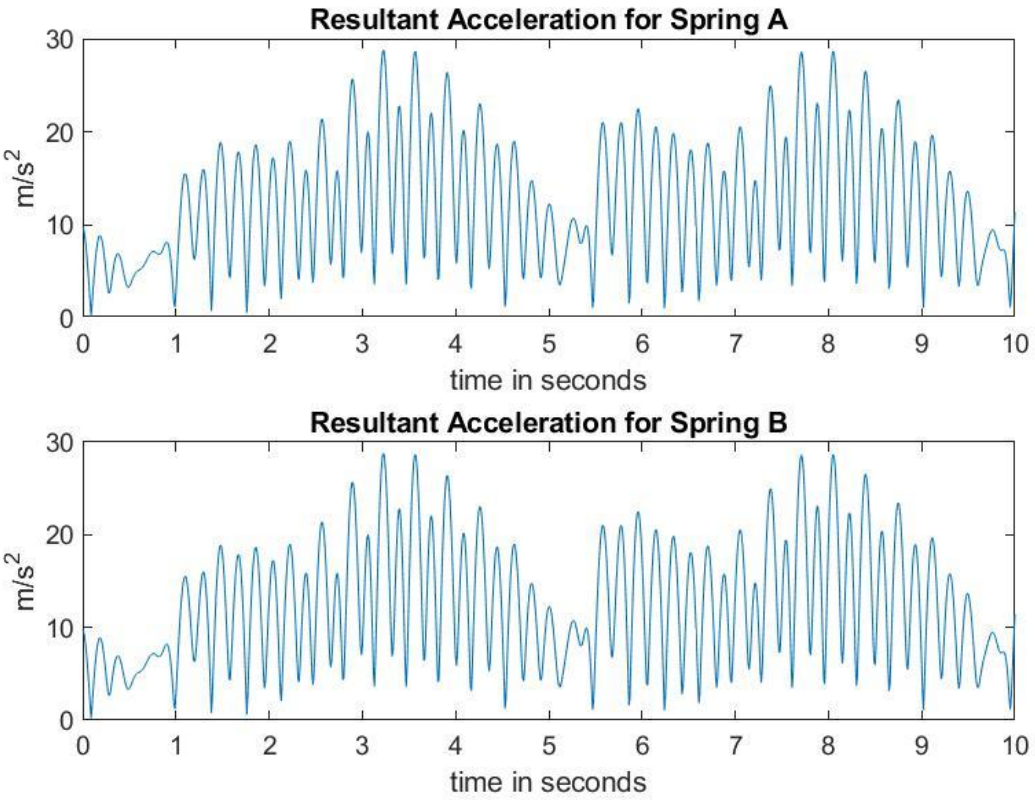
Resultant Acceleration for Spring A
m/s^2
time in seconds
Resultant Acceleration for Spring B
m/s^2
time in seconds

APPENDIX F – RESULTS FOR THE θN CASE

This section presents the acceleration and displacement plots for simulation discussed in for 6B, furthermore the resultant acceleration for simulation is plot.

N = 1

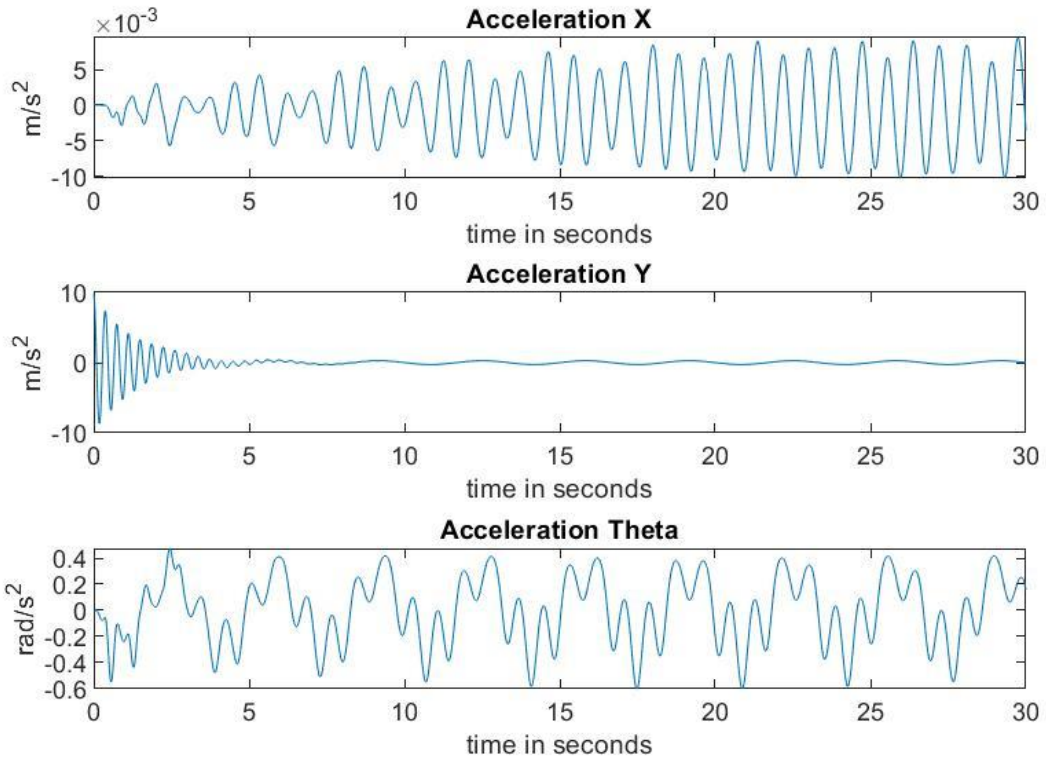
Acceleration X
×10^-3
m/s^2
time in seconds
Acceleration Y
m/s^2
time in seconds
Acceleration Theta
rad/s^2
time in seconds

N = 1

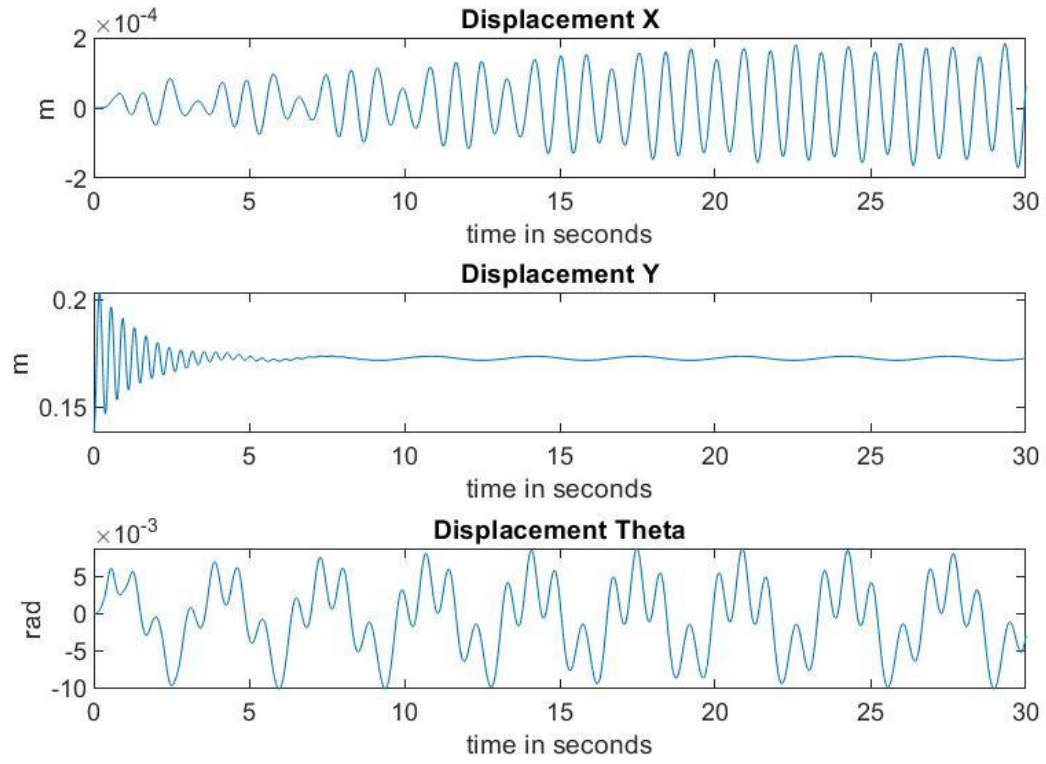
Displacement X
×10^-4
m
time in seconds
Displacement Y
m
time in seconds
Displacement Theta
×10^-3
rad
time in seconds

N = 1

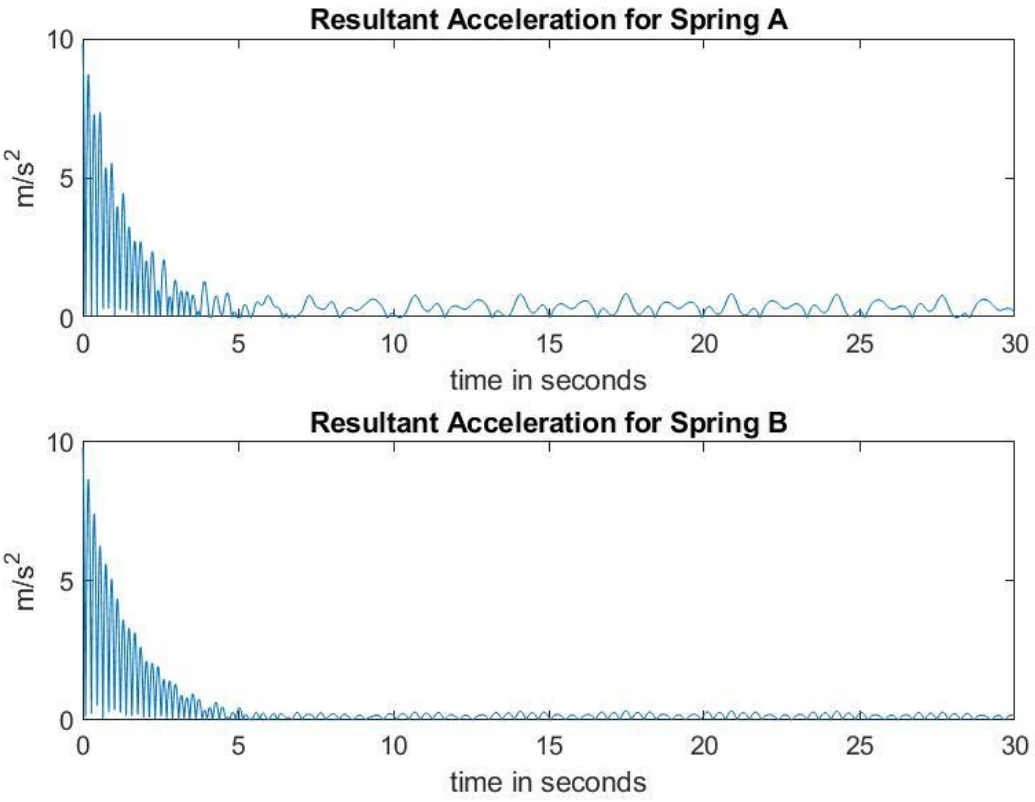
Resultant Acceleration for Spring A
m/s^2
time in seconds
Resultant Acceleration for Spring B
m/s^2
time in seconds

N = 2

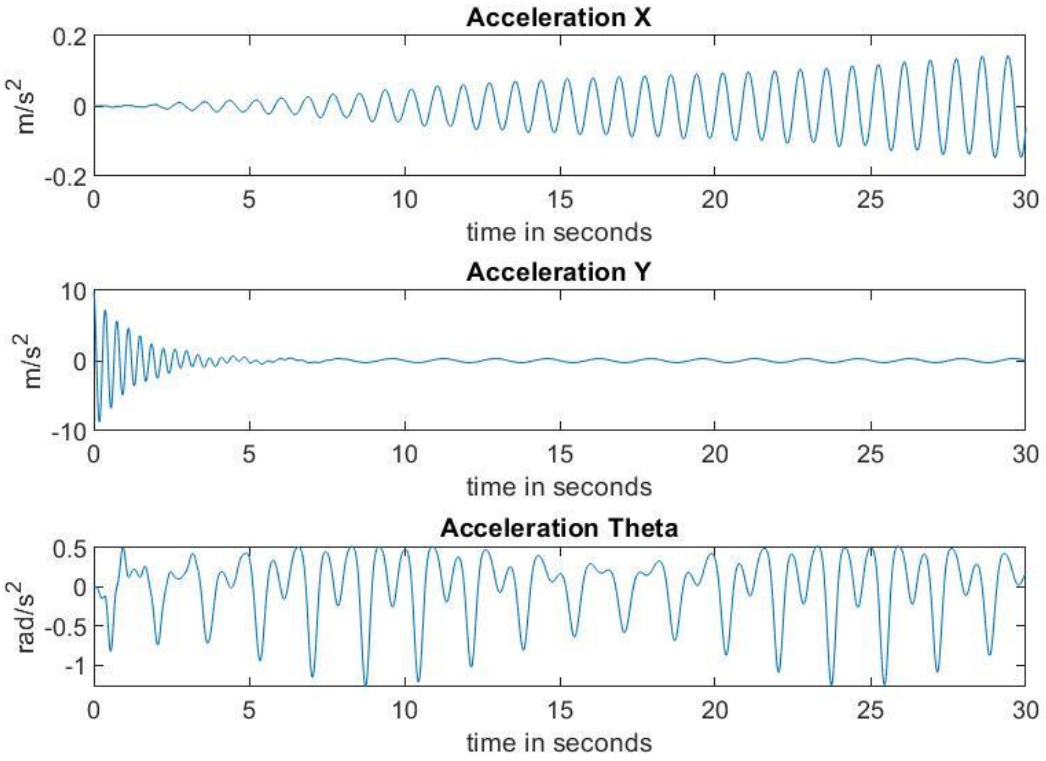
Acceleration X
m/s2
0.2
0
-0.2
0
5
10
15
20
25
30
time in seconds
Acceleration Y
m/s2
10
0
-10
0
5
10
15
20
25
30
time in seconds
Acceleration Theta
rad/s2
0.5
0
-0.5
-1
0
5
10
15
20
25
30
time in seconds

N = 2

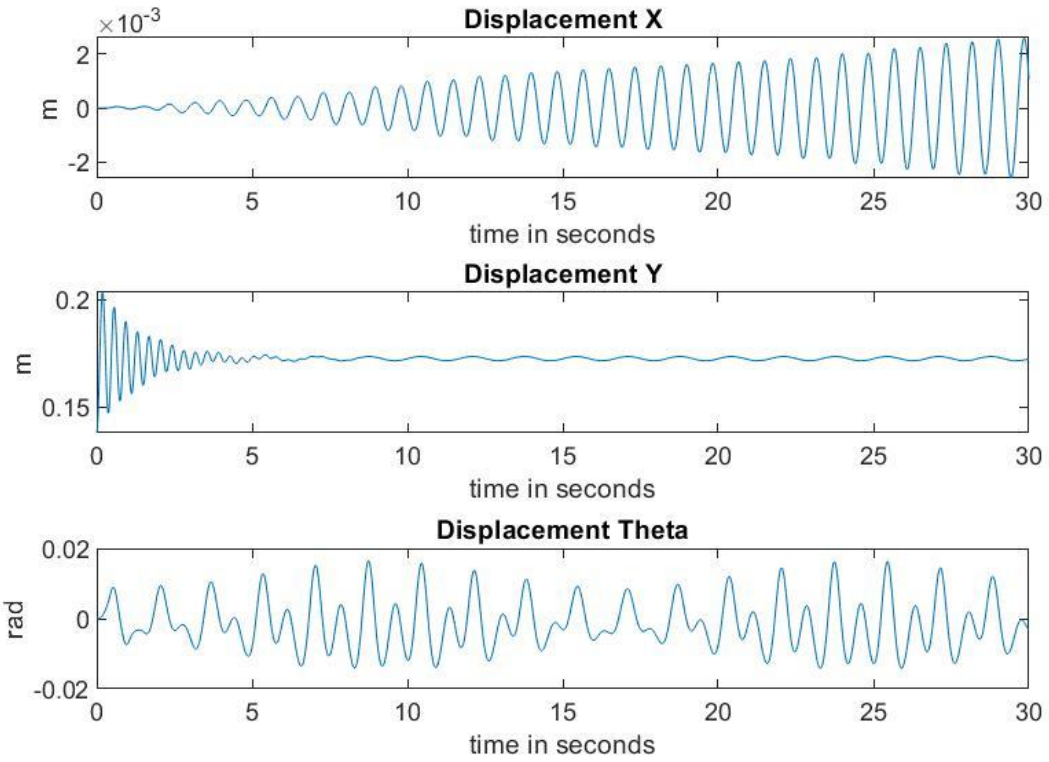
Displacement X
×10-3
m
2
0
-2
0
5
10
15
20
25
30
time in seconds
Displacement Y
m
0.2
0.15
0
5
10
15
20
25
30
time in seconds
Displacement Theta
rad
0.02
0
-0.02
0
5
10
15
20
25
30
time in seconds

N = 2

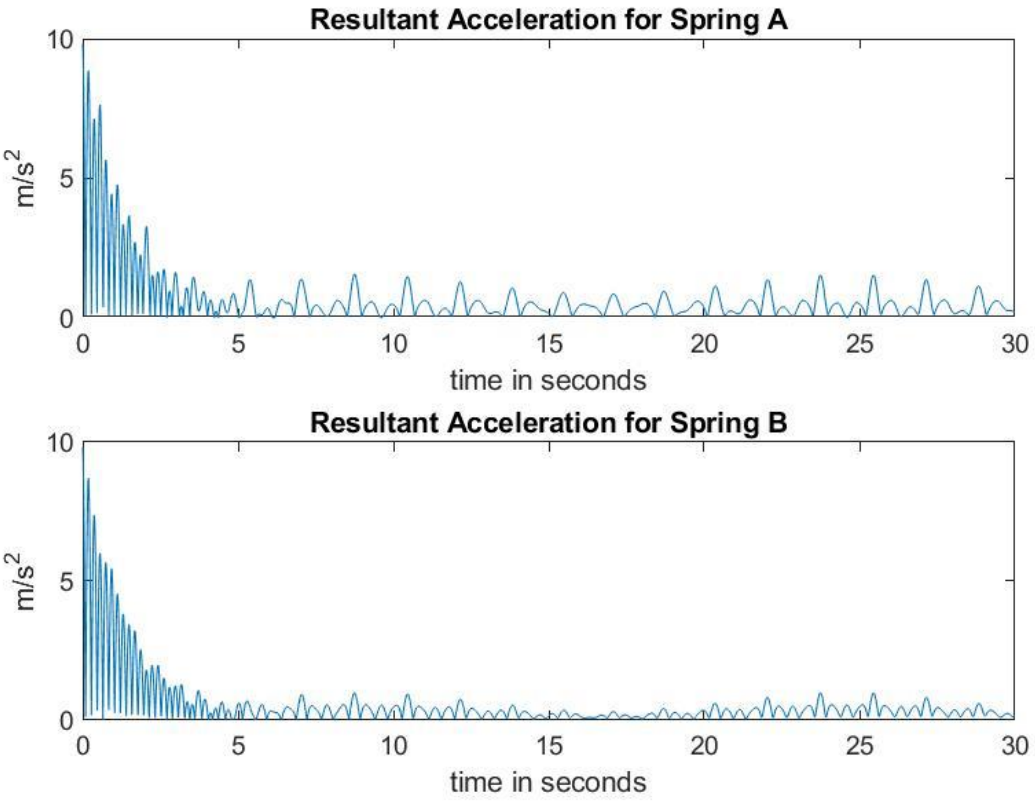
Resultant Acceleration for Spring A
m/s2
time in seconds
Resultant Acceleration for Spring B
m/s2
time in seconds

N = 3

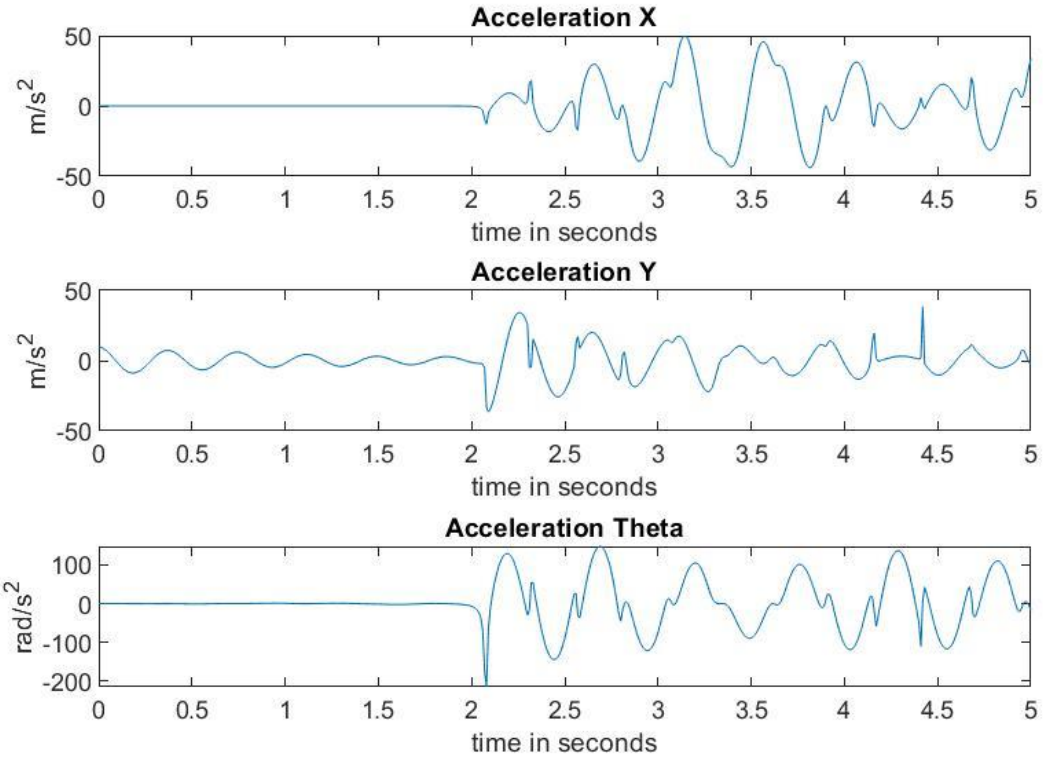
Acceleration X
m/s2
50
0
-50
0 0.5 1 1.5 2 2.5 3 3.5 4 4.5 5
time in seconds
Acceleration Y
m/s2
50
0
-50
0 0.5 1 1.5 2 2.5 3 3.5 4 4.5 5
time in seconds
Acceleration Theta
rad/s2
100
0
-100
-200
0 0.5 1 1.5 2 2.5 3 3.5 4 4.5 5
time in seconds

N = 3

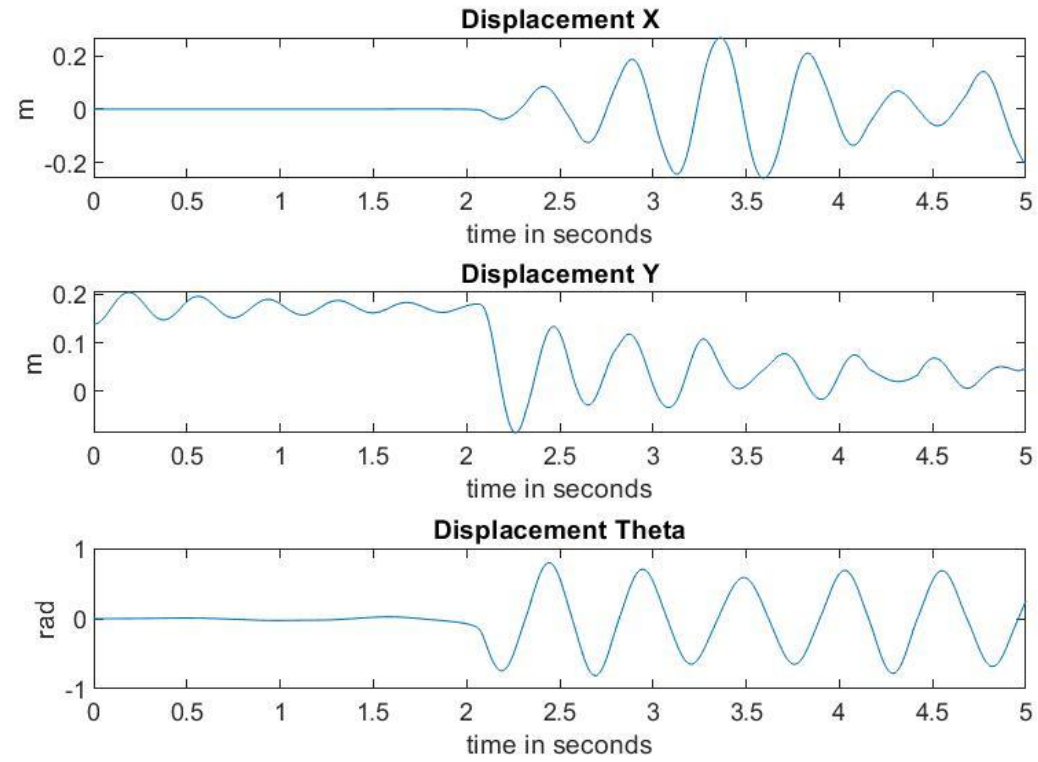
Displacement X
m
0.2
0
-0.2
0 0.5 1 1.5 2 2.5 3 3.5 4 4.5 5
time in seconds
Displacement Y
m
0.2
0.1
0
0 0.5 1 1.5 2 2.5 3 3.5 4 4.5 5
time in seconds
Displacement Theta
rad
1
0
-1
0 0.5 1 1.5 2 2.5 3 3.5 4 4.5 5
time in seconds

N = 3

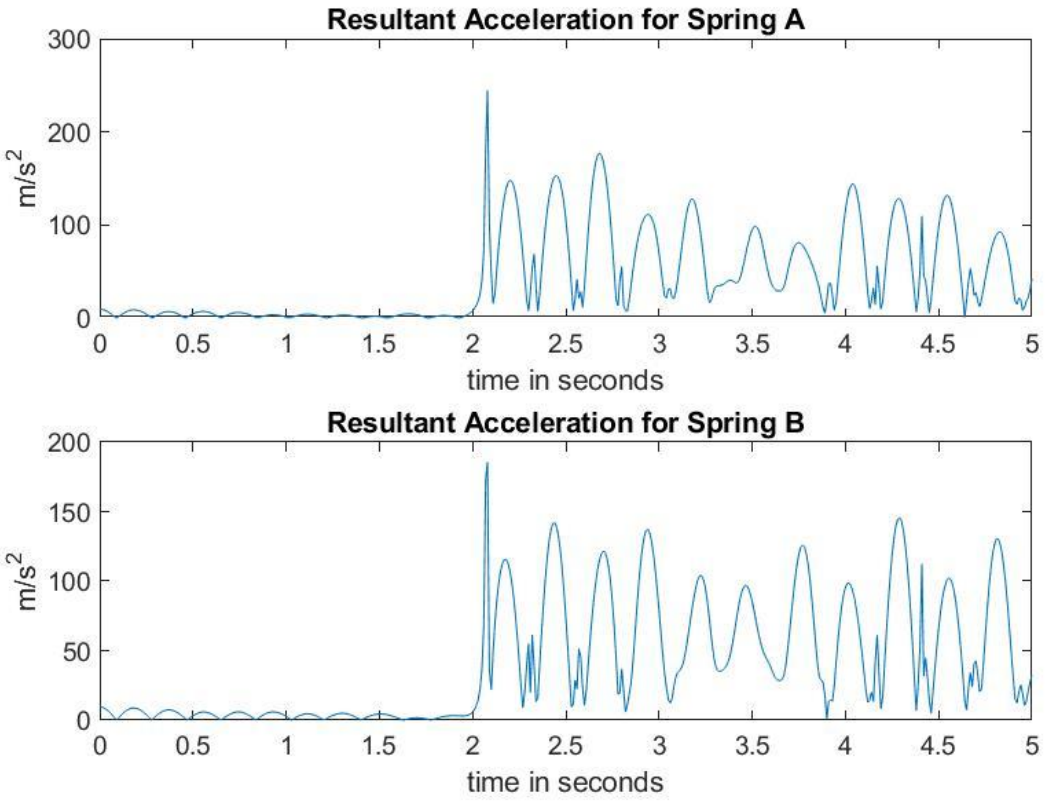
Resultant Acceleration for Spring A
m/s2
300
200
100
0
0
0.5
1
1.5
2
2.5
3
3.5
4
4.5
5
time in seconds
Resultant Acceleration for Spring B
m/s2
200
150
100
50
0
0
0.5
1
1.5
2
2.5
3
3.5
4
4.5
5
time in seconds

N = 4

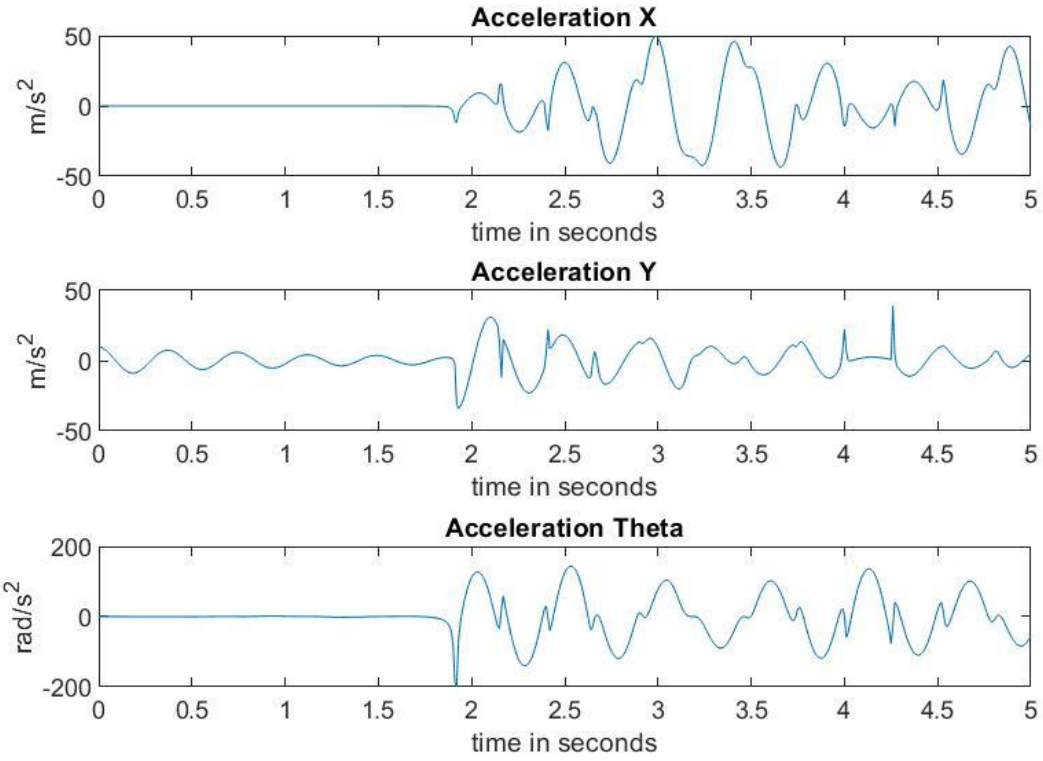
Acceleration X
m/s2
50
0
-50
0 0.5 1 1.5 2 2.5 3 3.5 4 4.5 5
time in seconds
Acceleration Y
m/s2
50
0
-50
0 0.5 1 1.5 2 2.5 3 3.5 4 4.5 5
time in seconds
Acceleration Theta
rad/s2
200
0
-200
0 0.5 1 1.5 2 2.5 3 3.5 4 4.5 5
time in seconds

N = 4

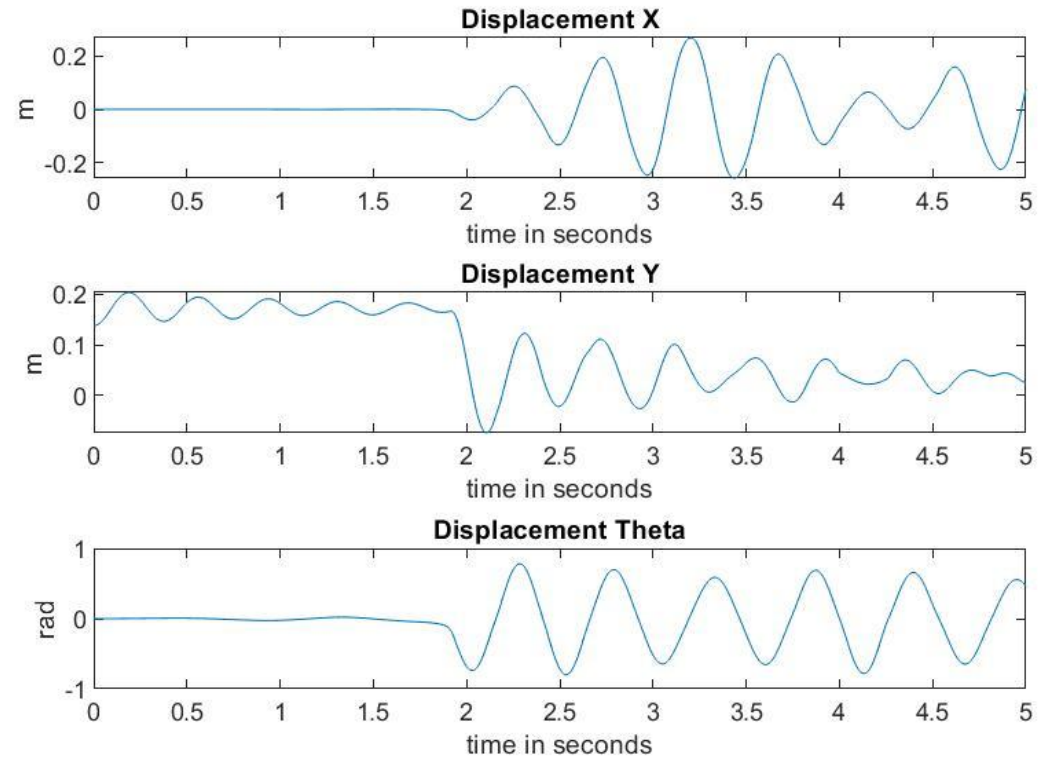
Displacement X
m
0.2
0
-0.2
0 0.5 1 1.5 2 2.5 3 3.5 4 4.5 5
time in seconds
Displacement Y
m
0.2
0.1
0
0 0.5 1 1.5 2 2.5 3 3.5 4 4.5 5
time in seconds
Displacement Theta
rad
1
0
-1
0 0.5 1 1.5 2 2.5 3 3.5 4 4.5 5
time in seconds

N = 4

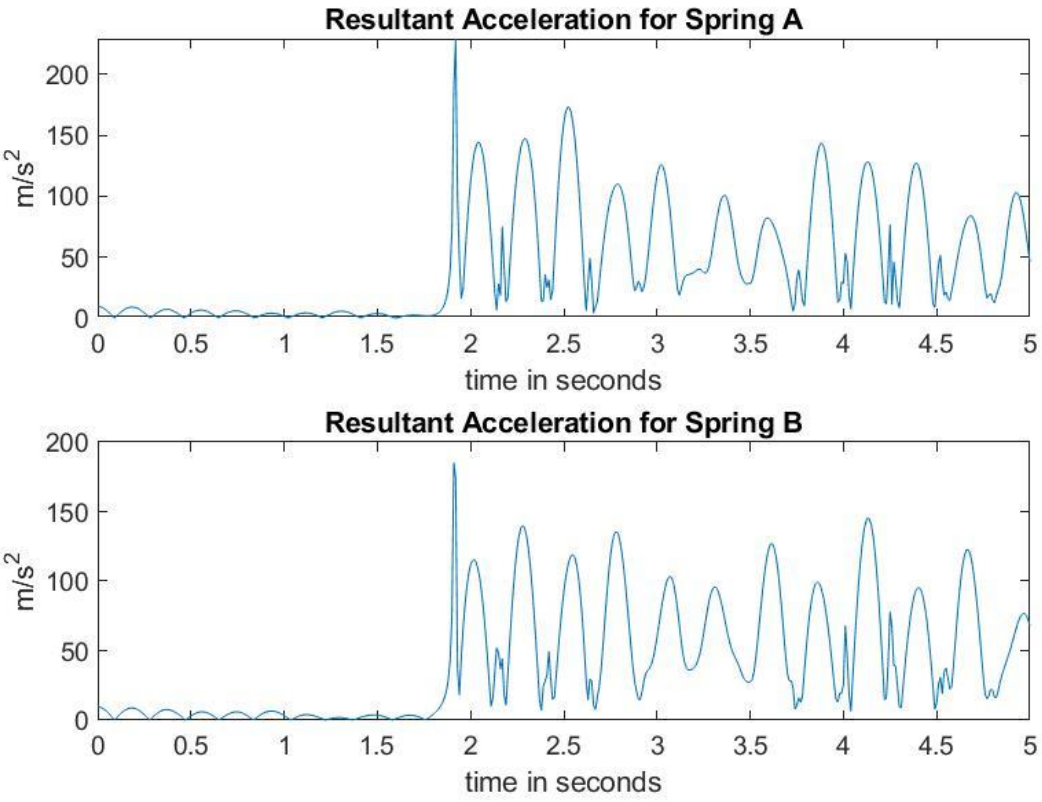
Resultant Acceleration for Spring A
m/s^2
200
150
100
50
0
0
0.5
1
1.5
2
2.5
3
3.5
4
4.5
5
time in seconds

Resultant Acceleration for Spring B
m/s^2
200
150
100
50
0
0
0.5
1
1.5
2
2.5
3
3.5
4
4.5
5
time in seconds

N = 5

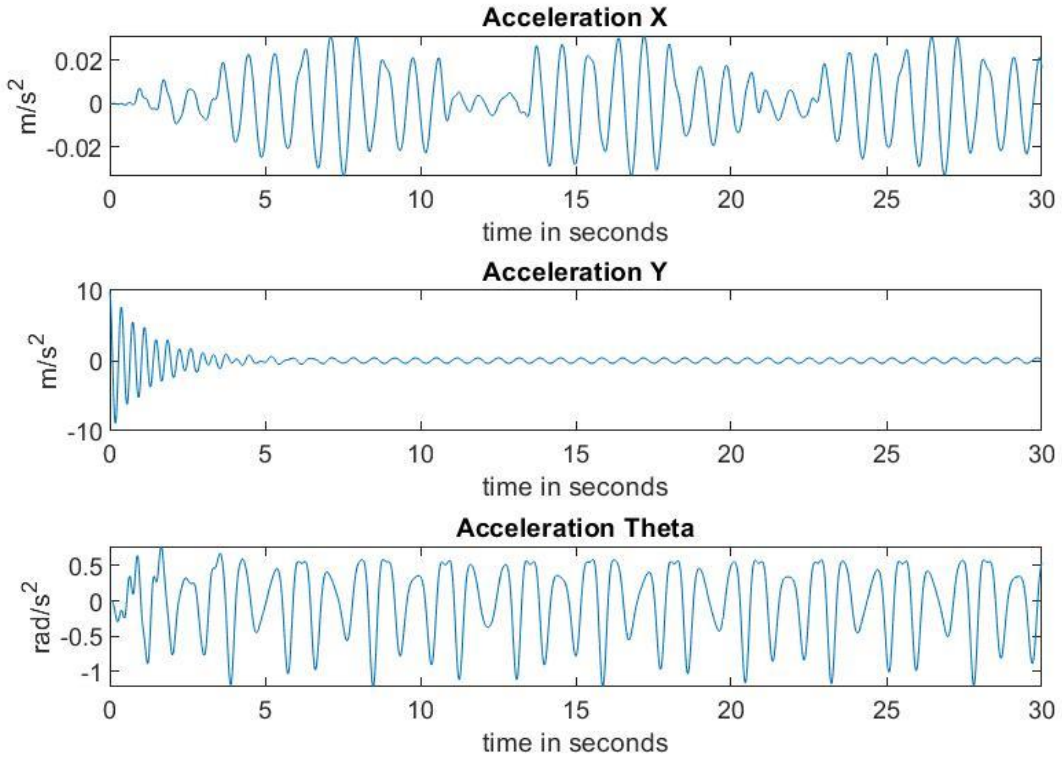
Acceleration X
m/s2
0.02
0
-0.02
0
5
10
15
20
25
30
time in seconds
Acceleration Y
m/s2
10
0
-10
0
5
10
15
20
25
30
time in seconds
Acceleration Theta
rad/s2
0.5
0
-0.5
-1
0
5
10
15
20
25
30
time in seconds

N = 5

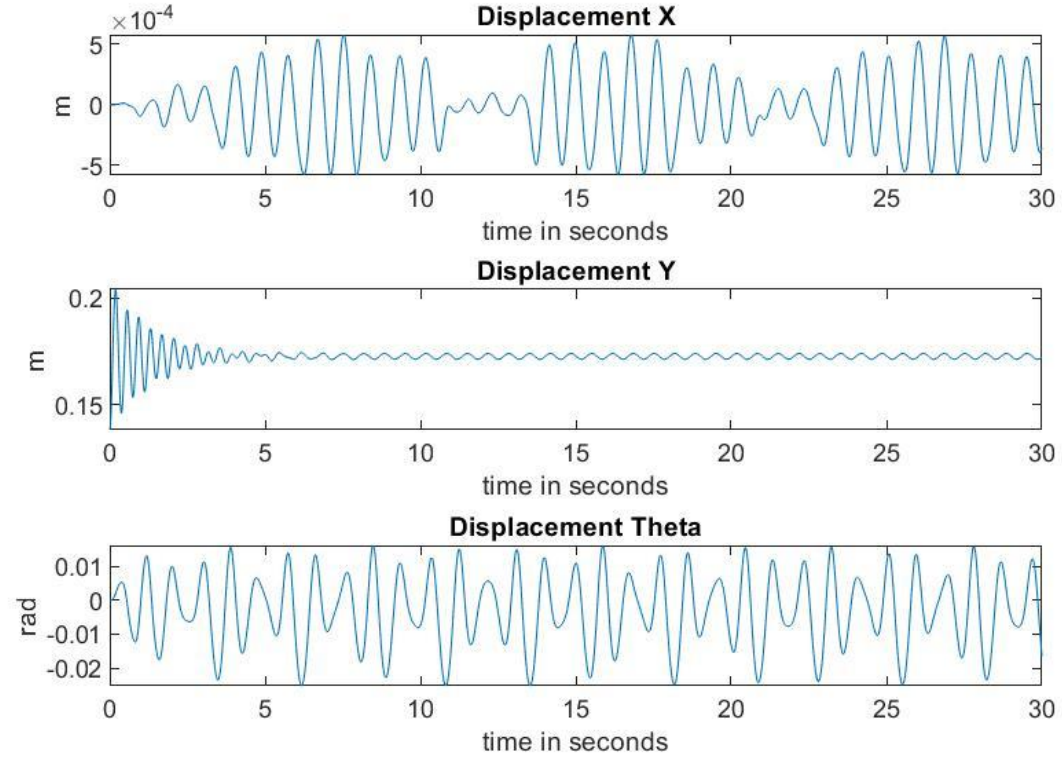
Displacement X
×10-4
m
5
0
-5
0
5
10
15
20
25
30
time in seconds
Displacement Y
m
0.2
0.15
0
5
10
15
20
25
30
time in seconds
Displacement Theta
rad
0.01
0
-0.01
-0.02
0
5
10
15
20
25
30
time in seconds

N = 5

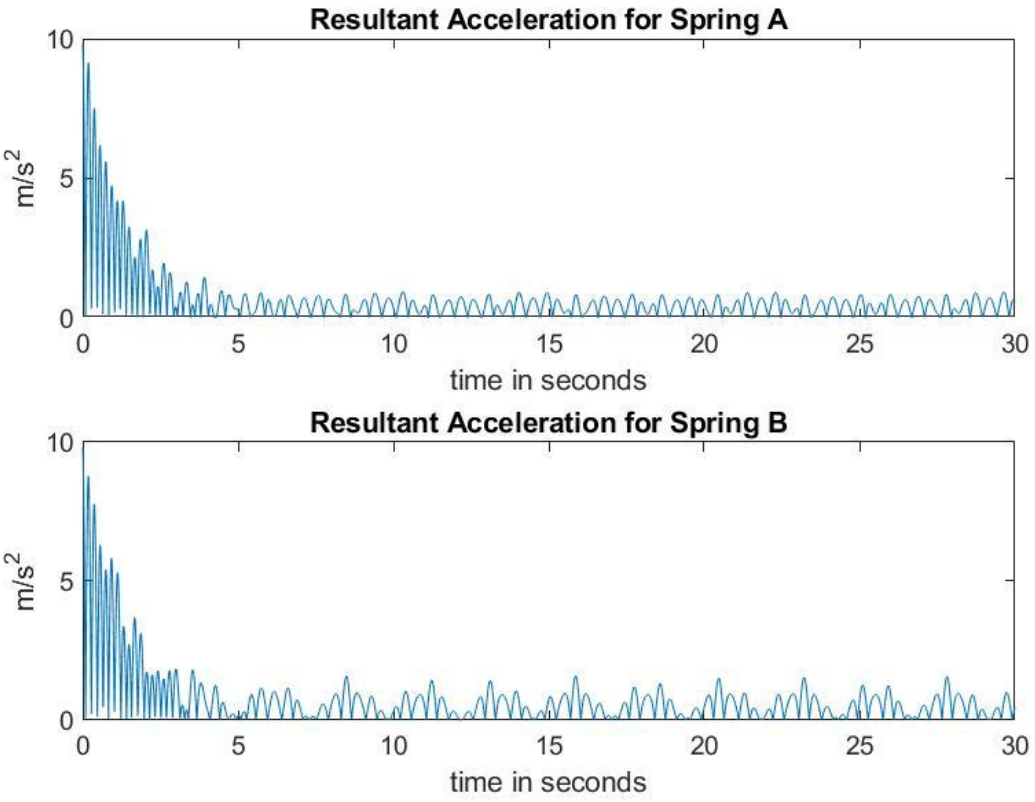
Resultant Acceleration for Spring A
m/s^2
time in seconds
Resultant Acceleration for Spring B
m/s^2
time in seconds

N = 6

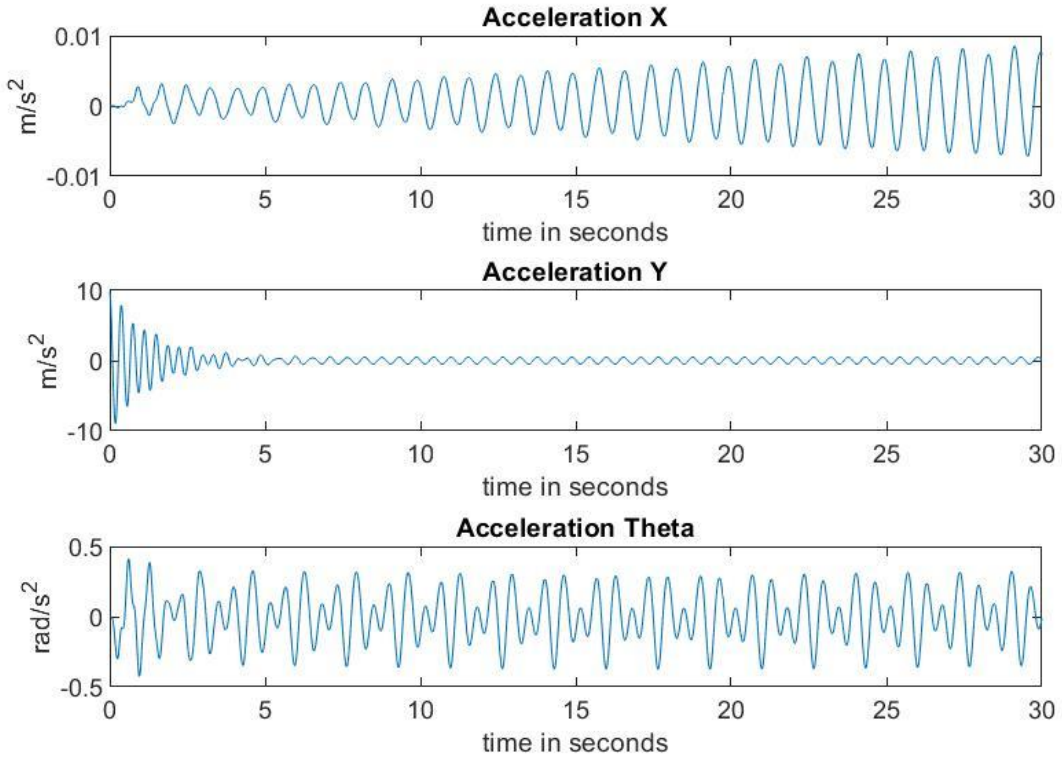
Acceleration X
m/s2
0.01
0
-0.01
0
5
10
15
20
25
30
time in seconds
Acceleration Y
m/s2
10
0
-10
0
5
10
15
20
25
30
time in seconds
Acceleration Theta
rad/s2
0.5
0
-0.5
0
5
10
15
20
25
30
time in seconds

N = 6

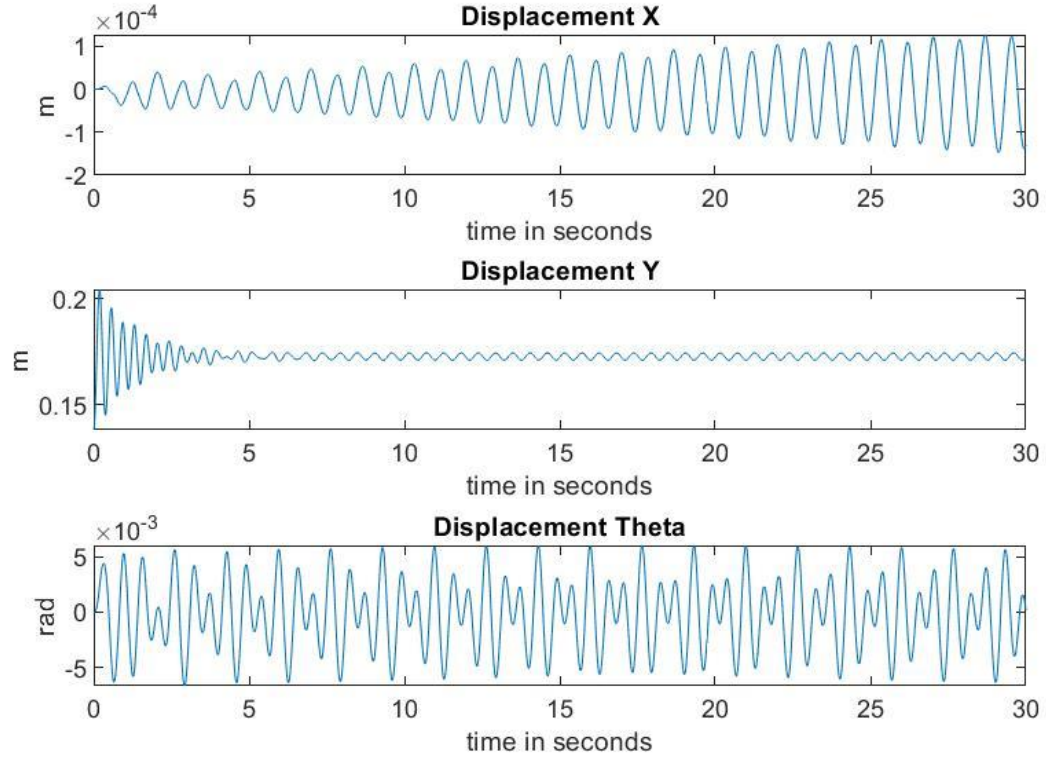
Displacement X
×10-4
m
1
0
-1
-2
0
5
10
15
20
25
30
time in seconds
Displacement Y
m
0.2
0.15
0
5
10
15
20
25
30
time in seconds
Displacement Theta
×10-3
rad
5
0
-5
0
5
10
15
20
25
30
time in seconds

N = 6

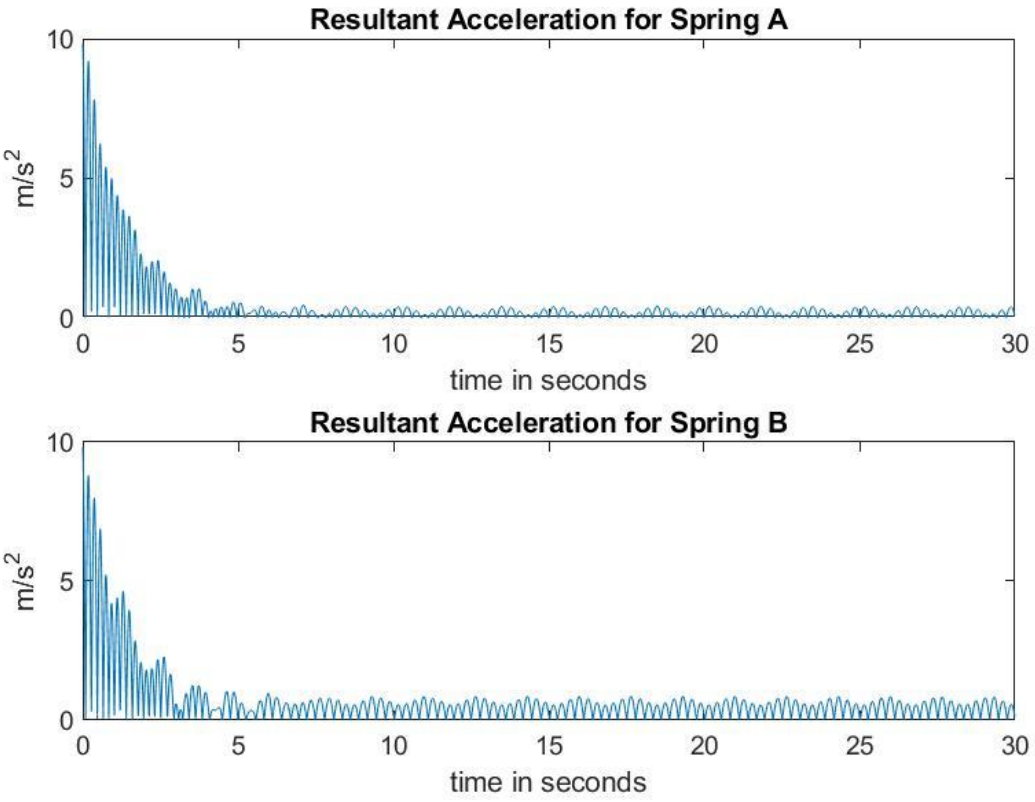
Resultant Acceleration for Spring A
m/s^2
time in seconds
Resultant Acceleration for Spring B
m/s^2
time in seconds

N = 7

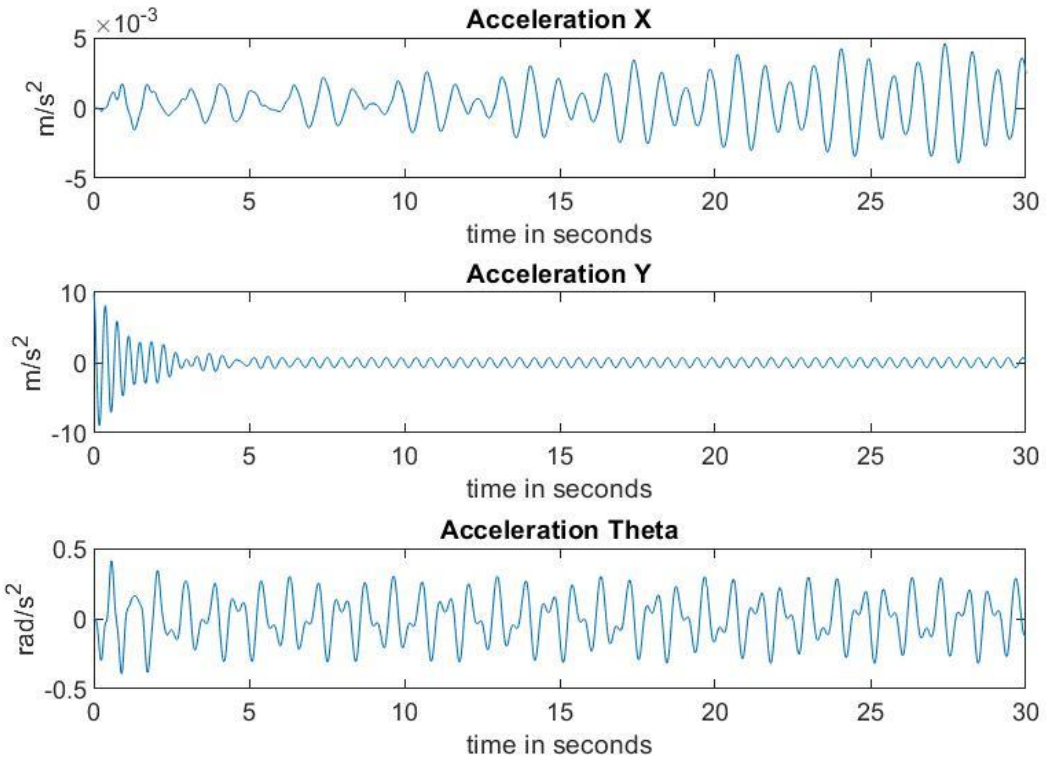
Acceleration X
×10^-3
5
0
-5
m/s^2
0
5
10
15
20
25
30
time in seconds
Acceleration Y
10
0
-10
m/s^2
time in seconds
Acceleration Theta
0.5
0
-0.5
rad/s^2
time in seconds

N = 7

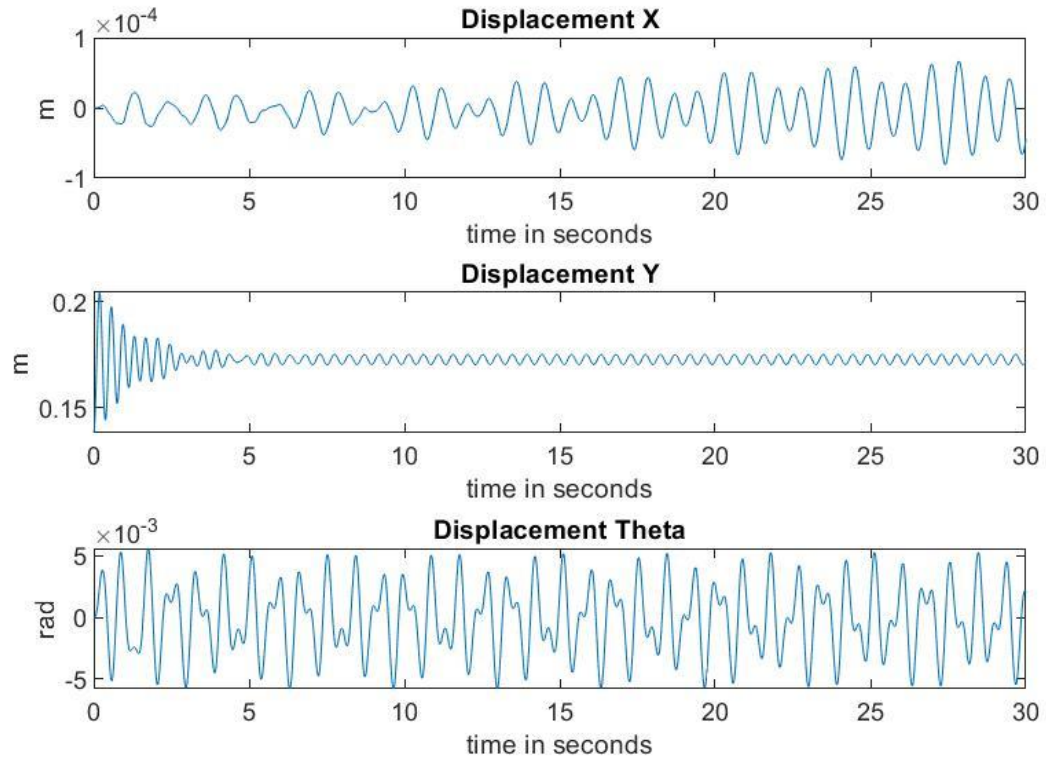
Displacement X
×10^-4
1
0
-1
m
time in seconds
Displacement Y
0.2
0.15
m
time in seconds
Displacement Theta
×10^-3
5
0
-5
rad
time in seconds

N = 7

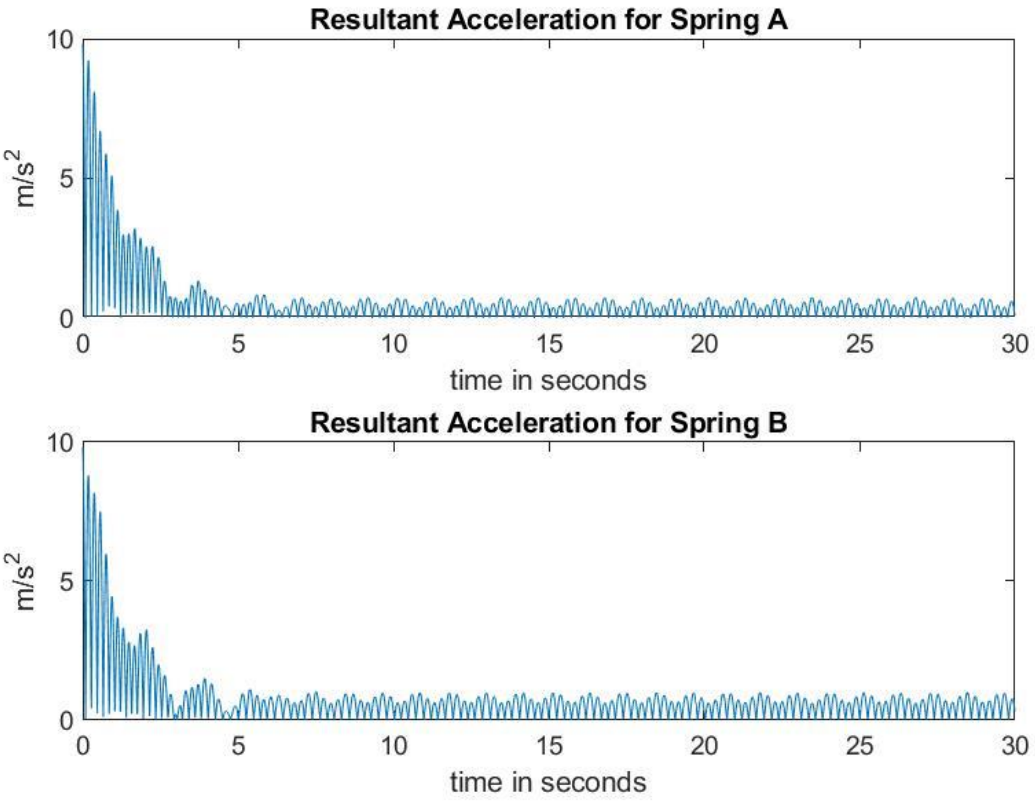
Resultant Acceleration for Spring A
m/s^2
time in seconds
Resultant Acceleration for Spring B
m/s^2
time in seconds

N = 8

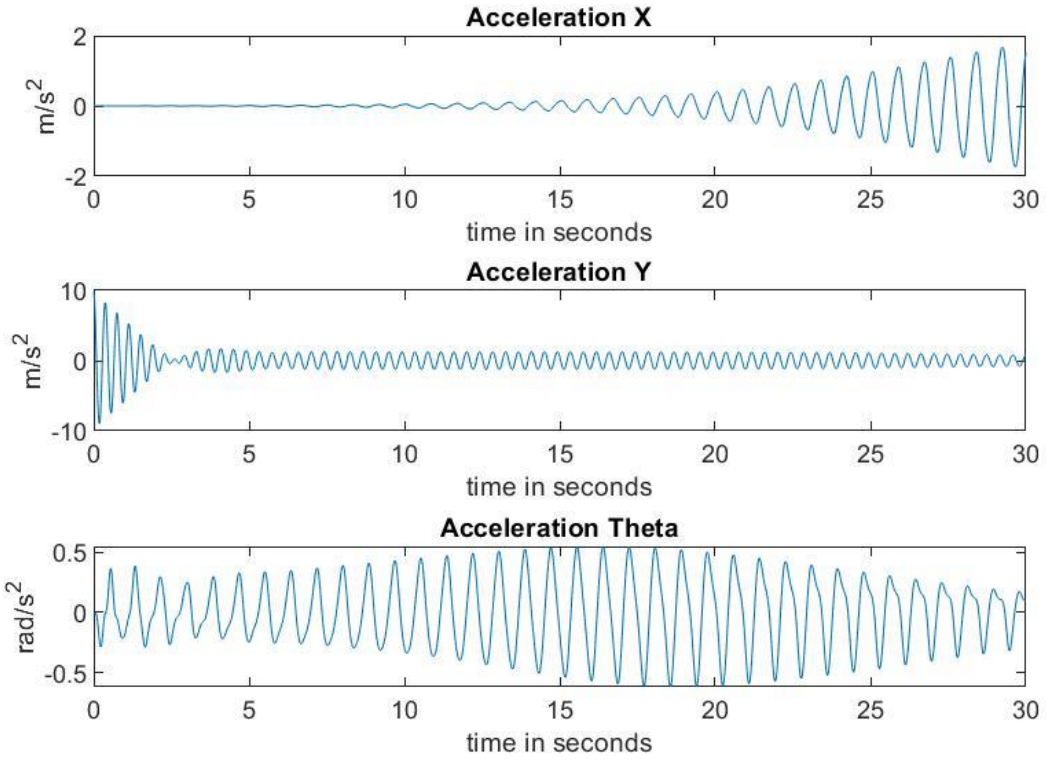
Acceleration X
m/s2
time in seconds
Acceleration Y
m/s2
time in seconds
Acceleration Theta
rad/s2
time in seconds

N = 8

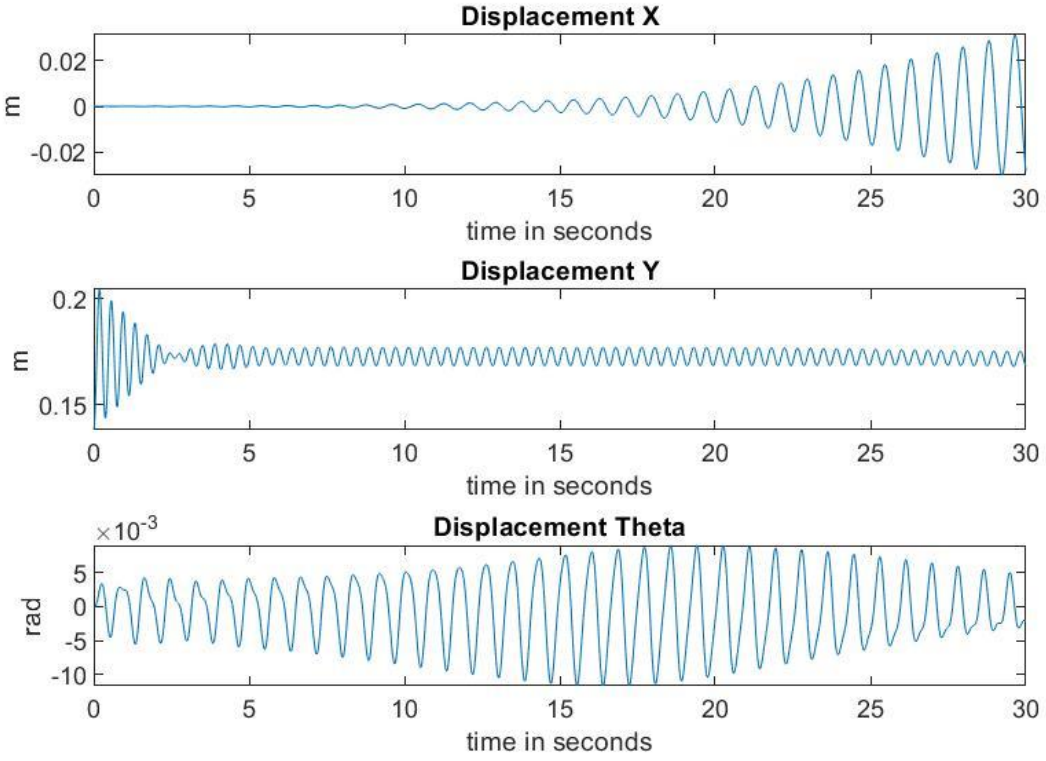
Displacement X
m
time in seconds
Displacement Y
m
time in seconds
Displacement Theta
×10-3
rad
time in seconds

N = 8

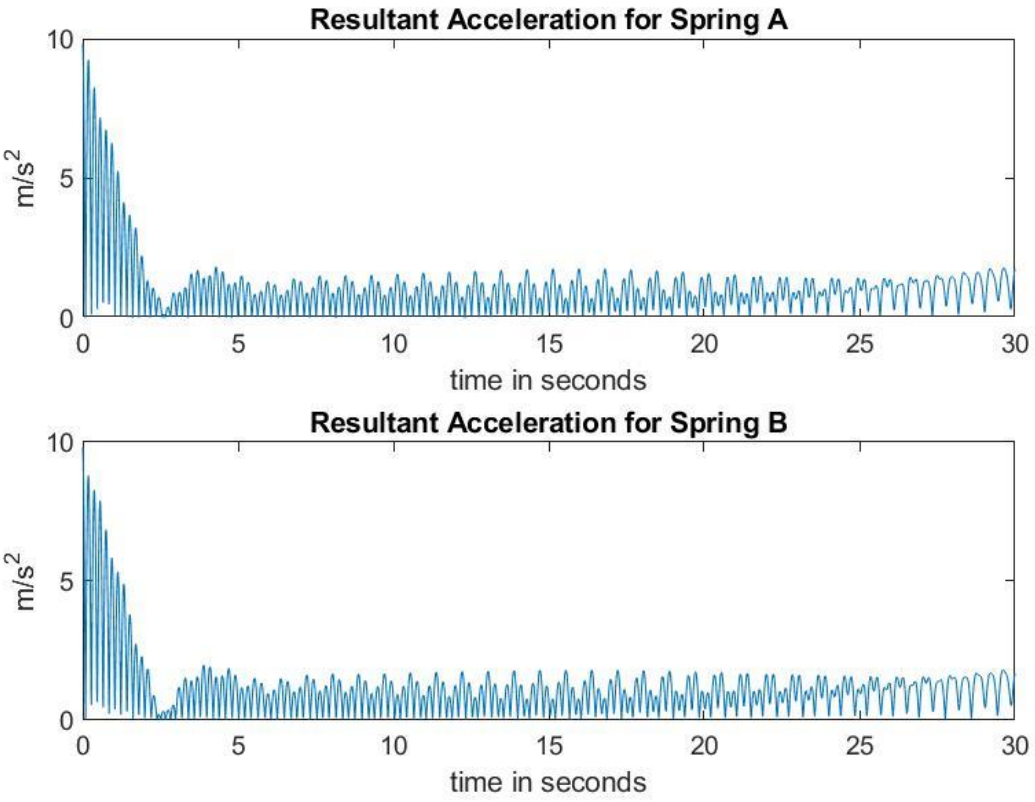
Resultant Acceleration for Spring A
m/s^2
time in seconds
Resultant Acceleration for Spring B
m/s^2
time in seconds

N = 9

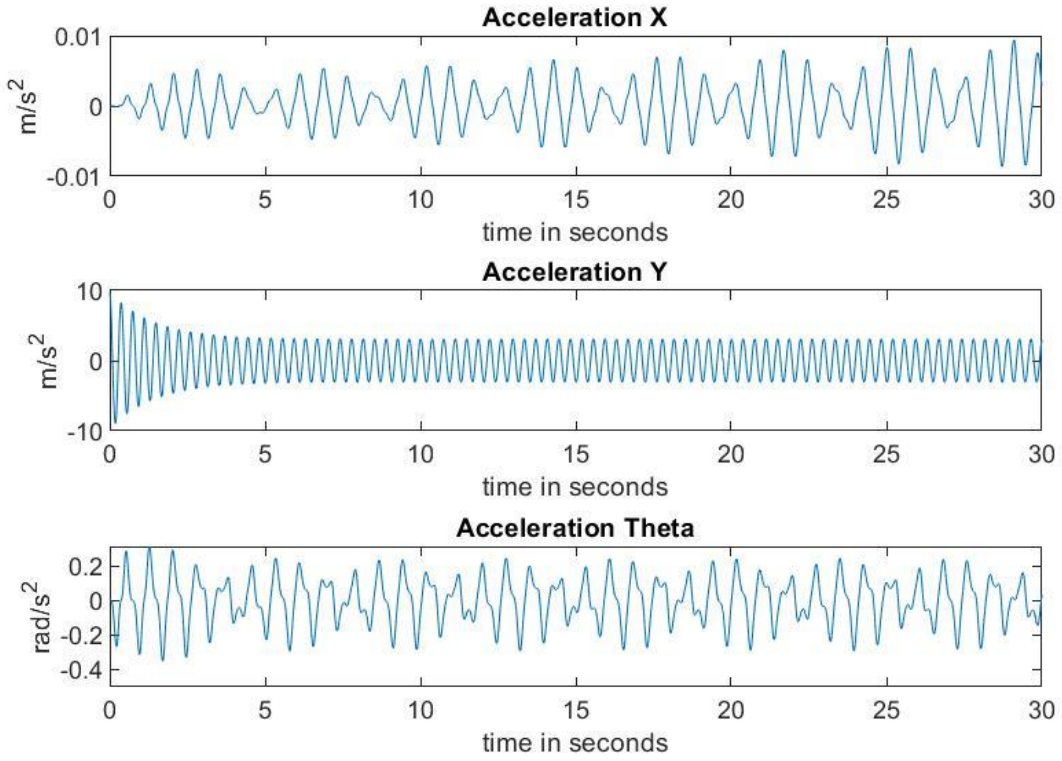
Acceleration X
m/s2
0.01
0
-0.01
0
5
10
15
20
25
30
time in seconds
Acceleration Y
m/s2
10
0
-10
0
5
10
15
20
25
30
time in seconds
Acceleration Theta
rad/s2
0.2
0
-0.2
-0.4
0
5
10
15
20
25
30
time in seconds

N = 9

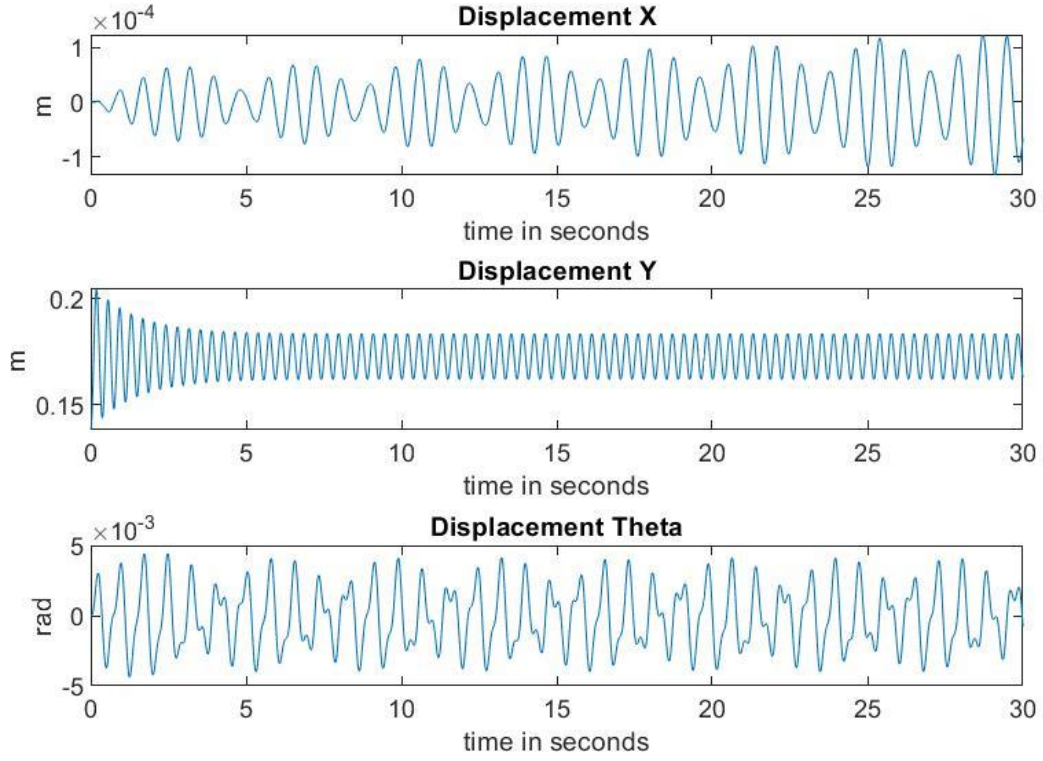
Displacement X
×10-4
m
1
0
-1
0
5
10
15
20
25
30
time in seconds
Displacement Y
m
0.2
0.15
0
5
10
15
20
25
30
time in seconds
Displacement Theta
×10-3
rad
5
0
-5
0
5
10
15
20
25
30
time in seconds

N = 9

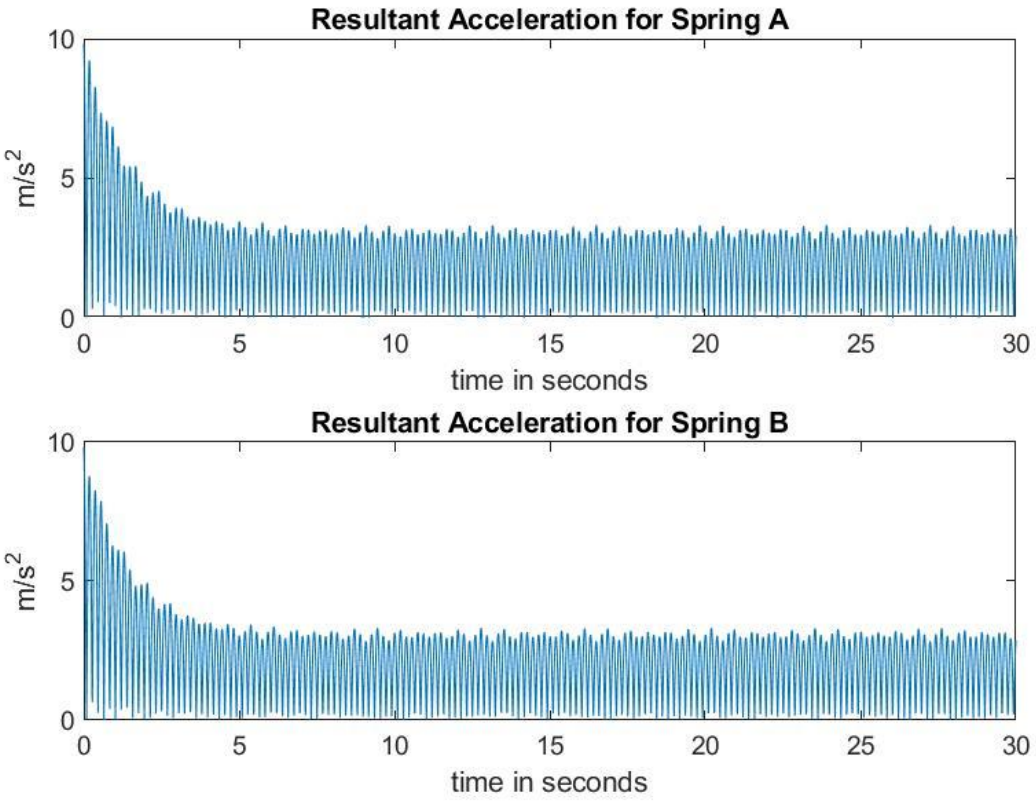
Resultant Acceleration for Spring A
m/s^2
time in seconds
Resultant Acceleration for Spring B
m/s^2
time in seconds

N = 10

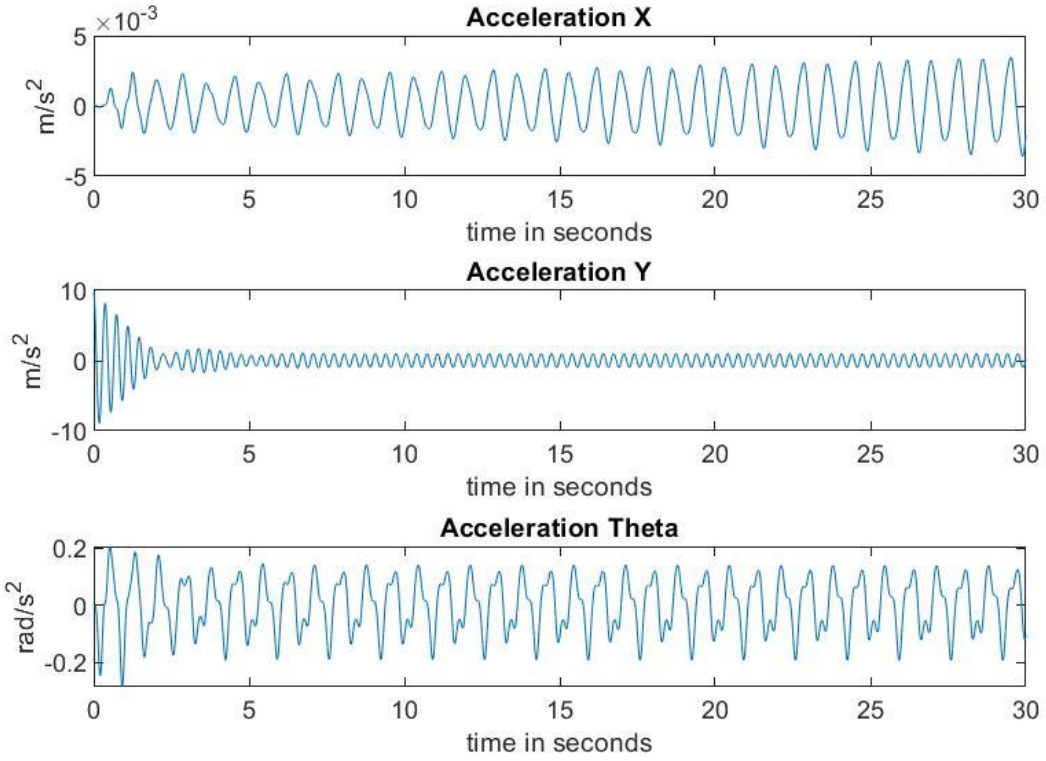
Acceleration X
×10^-3
m/s^2
time in seconds
Acceleration Y
m/s^2
time in seconds
Acceleration Theta
rad/s^2
time in seconds

N = 10

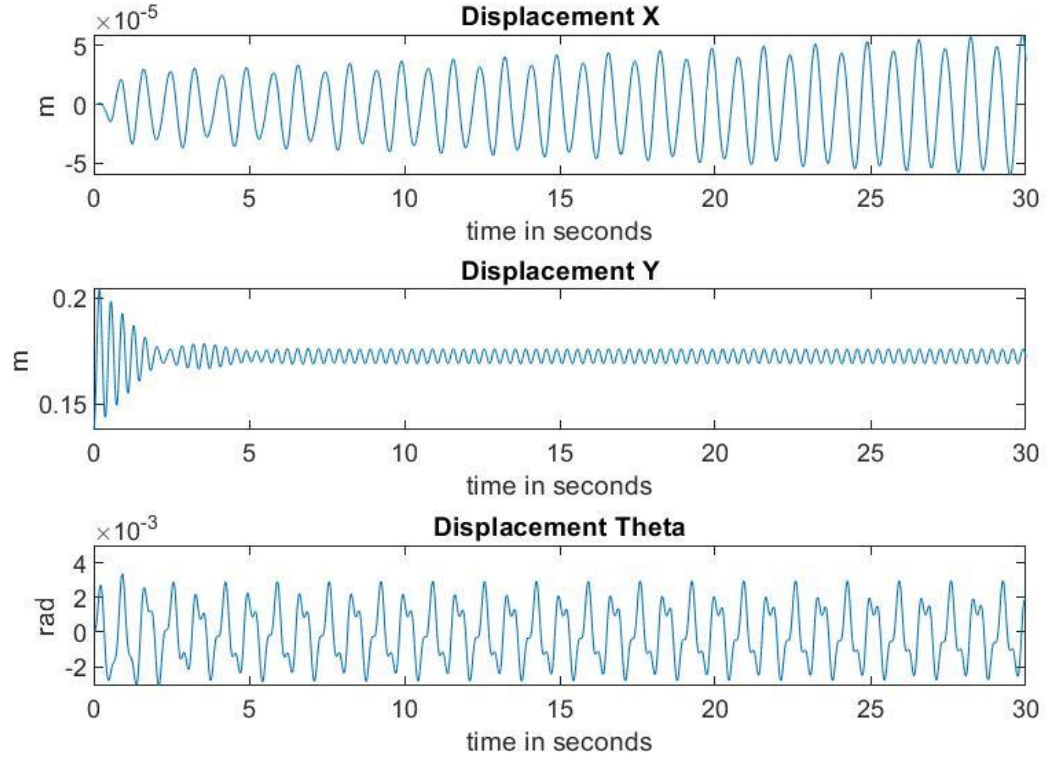
Displacement X
×10^-5
m
time in seconds
Displacement Y
m
time in seconds
Displacement Theta
×10^-3
rad
time in seconds

N = 10

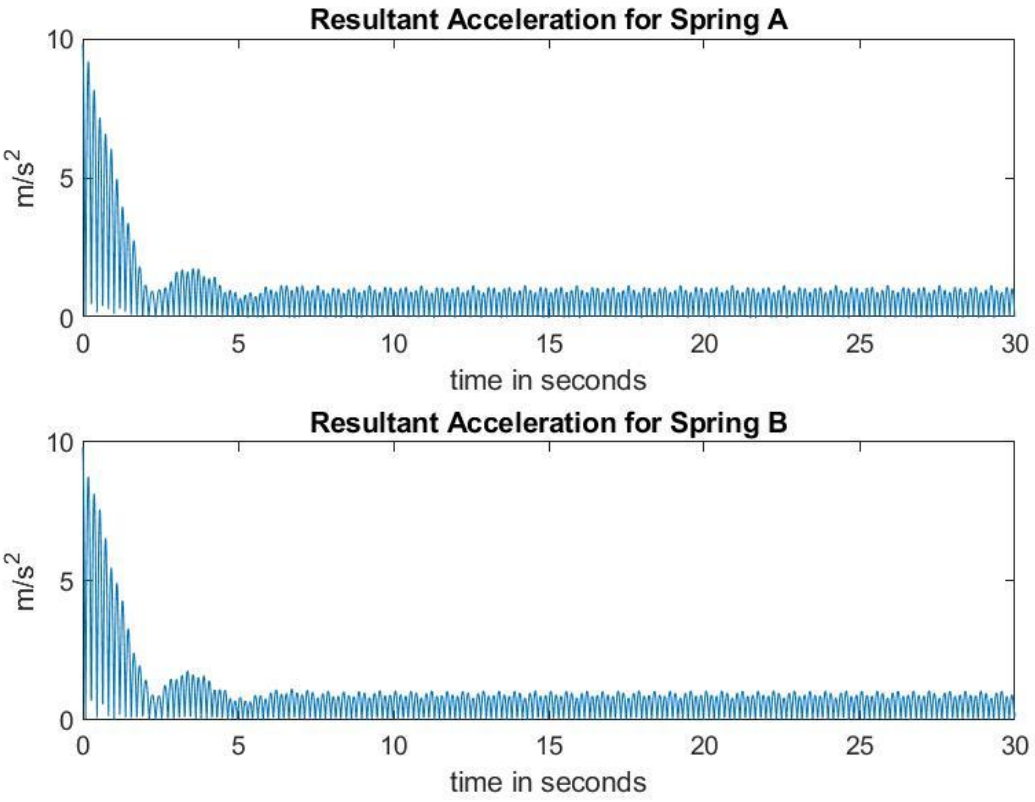
Resultant Acceleration for Spring A
m/s^2
time in seconds
Resultant Acceleration for Spring B
m/s^2
time in seconds

APPENDIX G – LIGGGHTS INSTALLTION

The following procedure can be used to install LIGGGHTS on Ubuntu 20.04. The following commands can be inputted into the terminal:

- sudo apt-get install ffmpeg
- sudo apt install openmpi-bin
- sudo apt install git
- git clone https://github.com/CFDEMproject/LIGGGHTS-PUBLIC.git
- sudo apt install cmake libavcodec-dev libavformat-dev libavutil-dev libboost-dev libdouble-conversion-dev libeigen3-dev libexpat1-dev libfontconfig-dev libfreetype6-dev libgdal-dev libglew-dev libhdf5-dev libjpeg-dev libjsoncpp-dev liblz4-dev liblzma-dev libnetcdf-dev libnetcdf-cxx-legacy-dev libogg-dev libpng-dev libpython3-dev libqt5opengl5-dev libqt5x11extras5-dev libsqlite3-dev libswscale-dev libtheora-dev libtiff-dev libxml2-dev libxt-dev qtbase5-dev qttools5-dev zlib1g-dev
- cd ~/LIGGGHTS-PUBLIC/src
- make auto
- gedit MAKE/Makefile.user

The last command opens the Makefile, where the following lines of code needs to be changed to “ON”:

- USE_VTK is set to “ON”
- AUTOINSTALL_VTK = "ON"

Once the above is completed, the terminal can be reopened and the following inputted:

- make auto
- sudo ln -s ~/LIGGGHTS-PUBLIC/src/lmp_auto /bin/lmp380
- lmp380

The above-mentioned procedure has been detailed by Engineerdo (Engineerdo, 2022)

APPENDIX H – AUTOMATION OF LIGGGHTS INPUT SCRIPT FOR MOTION

The below code is implemented on Excel using the VBA interface. The code allows the development of the LIGGGHTS script for the motion of the 3DOF vibrating screen. Figure 203 presents the layout of the excel data in order to allow the presented code to work. The following can be noted:

- Column A, presents the time
- Column B and C, present the displacement and velocity results for the x coordinate respectfully
- Column D and E, present the displacement and velocity results for the y coordinate respectfully
- Column F and G, present the displacement and velocity results for the θ coordinate respectfully

	A	B	C	D	E	F	G
1	0	0.000317	0.002315	-0.02631	0.0703	0.004025	0.018069
2	0.001	0.000318	0.002313	-0.02631	0.08005	0.004045	0.018097
3	0.002	0.000318	0.002311	-0.0263	0.089782	0.004065	0.018128
4	0.003	0.000318	0.002308	-0.02627	0.099495	0.004086	0.018161
5	0.004	0.000318	0.002306	-0.02624	0.109185	0.004106	0.018196
6	0.005	0.000318	0.002304	-0.0262	0.11885	0.004127	0.018234
7	0.006	0.000318	0.002302	-0.02615	0.128486	0.004148	0.018274
8	0.007	0.000319	0.0023	-0.02609	0.138092	0.004168	0.018316
9	0.008	0.000319	0.002297	-0.02602	0.147664	0.004189	0.01836
10	0.009	0.000319	0.002295	-0.02594	0.1572	0.004209	0.018406
11	0.01	0.000319	0.002293	-0.02586	0.166697	0.00423	0.018455
12	0.011	0.000319	0.002291	-0.02576	0.176153	0.004251	0.018506
13	0.012	0.00032	0.002288	-0.02565	0.185564	0.004272	0.018559
14	0.013	0.00032	0.002286	-0.02553	0.194929	0.004293	0.018614

Figure 203: Layout of excel data for automation

```
Sub textfile()
    Dim Path As String
    Dim FileNumber As Integer
    Dim counter As Single
    Dim check As Boolean
    Dim direction As Integer

    check = True
    counter = 0
    Path = "C:\Users\misha\Desktop\Masters reasearch component\Research
component\Excel data for LIGGGHTS\motion.txt"

    FileNumber = FreeFile

    Open Path For Output As FileNumber

    Do While check = True
        counter = counter + 1
        T = Cells(counter, 1)
        Vx = Cells(counter, 3)
        Vy = Cells(counter, 5)
        X = Cells(counter, 2)
        Y = Cells(counter, 4)

        X_revised = 1 + X
        Y_revised = Y - 0.5

        theta = Cells(counter, 6)
        theta_dot = Cells(counter, 7)
        direction = 1


        If Cells(counter + 1, 1) = "" Then check = False
        Print #FileNumber, "variable thetadot equal", theta_dot

       Print #FileNumber, "fix M1 all move/mesh mesh deck rotate/variable origin 0
", Y_revised, " ", X_revised, " axis ", direction, " 0. 0.", "omega v_thetadot"
       Print #FileNumber, "fix M2 all move/mesh mesh deck linear 0 ", Vy, " ", Vx

        Print #FileNumber, "run 10"
        Print #FileNumber, "group large type 1"
        Print #FileNumber, "group small type 2"
        Print #FileNumber, "unfix M2"
        Print #FileNumber, "unfix M1"
    Loop
    Close FileNumber

End Sub
```

Excel VBA 1: Code to develop a .txt. file with required arguments to perform DEM analysis

The results from a single iteration of running the above code is presented by LIGGGHTS script 1.

```
run 10
group large type 1
group small type 2
unfix M2
unfix M1
variable thetadot equal      1.80973059953909E-02
fix M1 all move/mesh mesh deck rotate/variable origin 0              -
0.526307048338017                         1.0003175230113            axis
1             0. 0.        omega v_thetadot
fix M2 all move/mesh mesh deck linear 0    8.00495294888815E-02
2.31276161881034E-03
```

LIGGGHTS script 1: Typical script for a single iteration of screen movement

APPENDIX I – LIGGGHTS INPUT SCRIPT

The below presents the input script used to develop the LIGGGHTS simulation. LIGGGHTS script 2 presents the general setup of the model which consists of the following:

- Defining particle parameters
- Declaring the analysis domain
- Time increment
- Importing of the screen box model and bounding box
- Setting up the required domains where the particle masses will be recorded
- Setting up the domain for the particle factory and the required flow rate

```
# Preliminaries

units si
atom_style granular
atom_modify map array
boundary f f f
communicate single vel yes
newton off #default, used for multicore systems

# Declare domain
variable xmin equal -10
variable xmax equal 10

variable ymin equal -10
variable ymax equal 10

variable zmin equal -10
variable zmax equal 10
region reg block ${xmin} ${xmax} ${ymin} ${ymax} ${zmin} ${zmax} units box
create_box 3 reg
neighbor 0.002 bin #default
neigh_modify delay 0 #default

 # Import Mesh
 fix deck all mesh/surface file Mesh/H2.stl type 3 scale 0.001
 fix undersize all mesh/surface file Mesh/uando2.stl type 3 scale 0.001
 fix walls all wall/gran model hertz tangential history mesh n_meshes 2 meshes
deck undersize

# Material properties

fix m1 all property/global youngsModulus peratomtype 2.e7 2.e7 3.e7
fix m2 all property/global poissonsRatio peratomtype 0.25 0.25 0.25
fix m3 all property/global coefficientRestitution peratomtypepair 3 0.2 0.2 0.2
0.2 0.2 0.2 0.2 0.2 0.2
fix m4 all property/global coefficientFriction peratomtypepair 3 0.5 0.5 0.3 0.5
0.5 0.3 0.3 0.3 0.3
fix m5 all property/global coefficientRollingFriction peratomtypepair 3 0.6 0.6
0.6 0.6 0.6 0.6 0.6 0.6 0.6

# Contact Physics

pair_style  gran model hertz tangential history #Hertzian without cohesion
pair_coeff  * *

# Integrator
```

```
fix integrate all nve/sphere

# Gravity
 fix grav all gravity 9.81 vector 0. 1. 0.


 # Particle insertion

 variable frac1 equal 0.03
 variable frac2 equal 0.06
 variable frac3 equal 0.1
 variable frac4 equal 0.16
 variable frac5 equal 0.09
 variable frac6 equal 0.16
 variable frac7 equal 0.1
 variable frac8 equal 0.3


fix pts1 all particletemplate/sphere 15485863 atom_type 1 density constant 2800
radius constant 0.03175
fix pts2 all particletemplate/sphere 15485867 atom_type 1 density constant 2800
radius constant 0.0254
fix pts3 all particletemplate/sphere 32452843 atom_type 1 density constant 2800
radius constant 0.019
fix pts4 all particletemplate/sphere 32452867 atom_type 1 density constant 2800
radius constant 0.0127
fix pts5 all particletemplate/sphere 49979687 atom_type 2 density constant 2800
radius constant 0.00953
fix pts6 all particletemplate/sphere 49979693 atom_type 2 density constant 2800
radius constant 0.00635
fix pts7 all particletemplate/sphere 67867967 atom_type 2 density constant 2800
radius constant 0.00478
fix pts8 all particletemplate/sphere 67867979 atom_type 2 density constant 2800
radius constant 0.00335
fix pts9 all particletemplate/sphere 86028121 atom_type 2 density constant 2800
radius constant 0.00239

fix pdd all particledistribution/discrete 86028157 8 pts1 ${frac1} pts2 ${frac2}
pts3 ${frac3} pts4 ${frac4} pts5 ${frac5} pts6 ${frac6} pts7 ${frac7} pts8
${frac8}

region factory block 1.8 1.95 -1 -0.5 0.5 1.5 units box


#fix ins all insert/rate/region seed 86028121 distributiontemplate pdd nparticles
50000 particlerate 10000 insert_every 1000 overlapcheck yes all_in yes vel
constant 0 0.45 0 region factory ntry_mc 10000

fix ins all insert/rate/region seed 86028121 distributiontemplate pdd mass 250
massrate 21.38 insert_every 1000 overlapcheck yes all_in yes vel constant 0 1 0
region factory ntry_mc 10000

group large type 1
group small type 2


dump   dmp all custom/vtk 1000 post/chute_*.vtk id type type x y z ix iy iz vx vy
vz fx fy fz omegax omegay omegaz radius
```

```
dump   dumpstress all mesh/gran/VTK 1000 post/mesh_*.vtk stress wear deck
undersize

  # Timestep
 timestep 0.0001

region undersizeblock block 0 3 3 5 -2 6 units box
variable undersmall equal mass(small,undersizeblock)
variable underlarge equal mass(large,undersizeblock)
variable underall equal mass(all,undersizeblock)

region oversizeblock block -5 0 -3 0 -2 6 units box
variable oversmall equal mass(small,oversizeblock)
variable overlarge equal mass(large,oversizeblock)
variable overall equal mass(all,oversizeblock)

fix output all print 1000
"${undersmall},${underlarge},${underall},${oversmall},${overlarge},${overall}"
screen no file regionmeaurements.csv title "under small,under large, under
all,over small,over large,over all"
```

LIGGGHTS script 2: DEM simulation setup excluding the modelling of screen motion

The motion of the SD vibrating screen is developed using LIGGGHTS script 3 which is just added at the end of the above main script. The "move/mesh" command is only used once at the beginning of the script while the rest of the script is repeated for the desired amount of time. Increments of 1000 are used which relates to increments of 0.1 seconds, which is also the time increment used to record the masses of the small and large material, noting that without the repeated script a single recording of masses will be created at the end, while the current script allows for a mass recording every 0.1 seconds.

```
fix move1 all move/mesh mesh deck wiggle amplitude 0.003 0.00424 0 period 0.0599

run 1000
group large type 1
group small type 2
```

Repeated part of the script

LIGGGHTS script 3: SD motion

The motion of the LM vibrating screen is developed using the script presented by LIGGGHTS script 4, noting the script only presents motion for 10 increments, the full script is not presented due to size constraints. The script uses a similar procedure as the script above, with the difference being that the numerical values of the motion will change after every 10 increments. The "unfix" commands are used to delete the motion developed in the previous set of 10 increments. The development of this script is automated by Excel VBA 1.

```
run 10
group large type 1
group small type 2
unfix M2
unfix M1
variable thetadot equal      1.80973059953909E-02
fix M1 all move/mesh mesh deck rotate/variable origin 0              -
0.526307048338017                         1.0003175230113            axis
1             0. 0.        omega v_thetadot
fix M2 all move/mesh mesh deck linear 0    8.00495294888815E-02
2.31276161881034E-03
```

LIGGGHTS script 4: LM motion

APPENDIX J – LM15 MATERIAL DISTRIBUTION ON THE DECK

The below images present LM15 screen from 0.5 seconds to 6 seconds in increments of 0.5 seconds. The images present the material movement as the LM15 screen is excited.

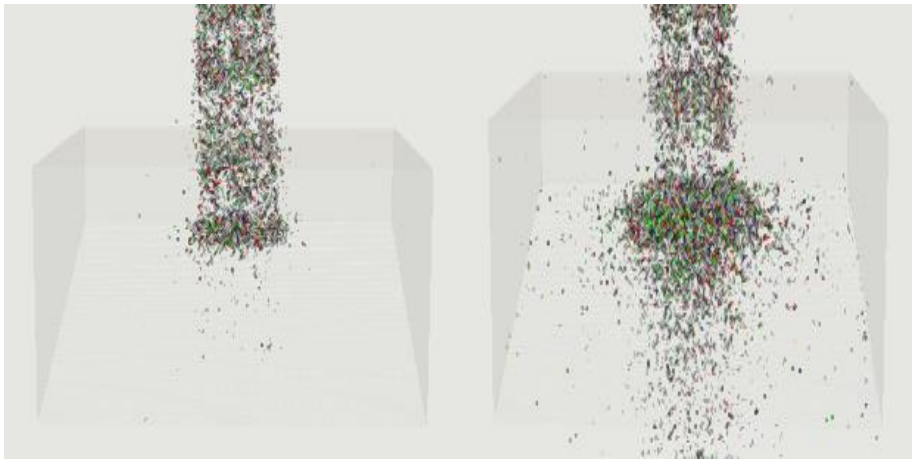

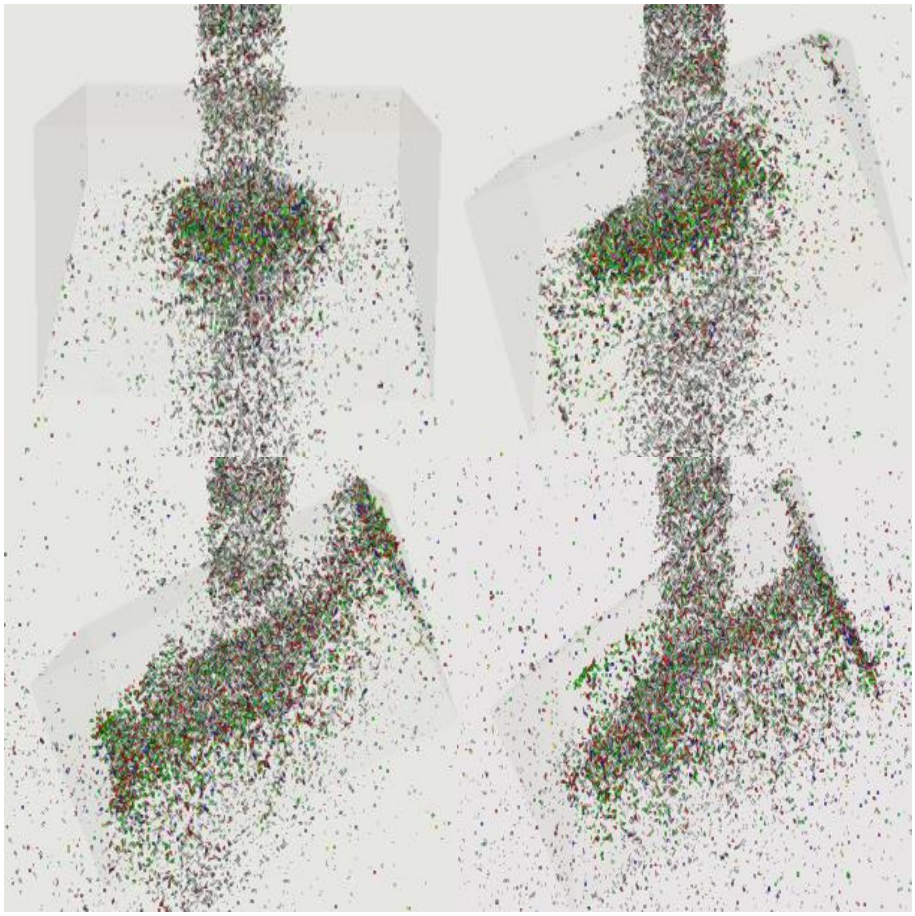



Figure 204: LM15 screen material profile

APPENDIX K – SPRING DATA SHEET

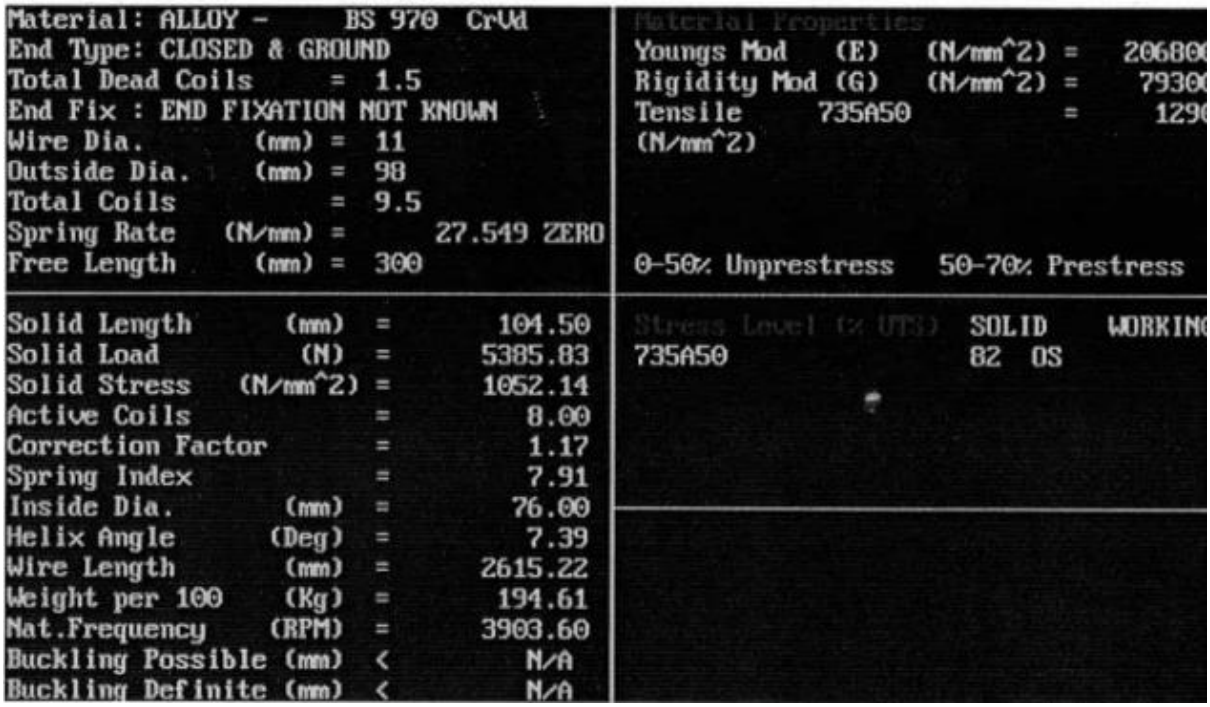

Material: ALLOY -	BS 970 CrVd	Material Properties	
End Type: CLOSED & GROUND		Youngs Mod (E) (N/mm^2) =	20680
Total Dead Coils =	1.5	Rigidity Mod (G) (N/mm^2) =	7930
End Fix : END FIXATION NOT KNOWN		Tensile 735A50 =	129
Wire Dia. (mm) =	11	(N/mm^2)	
Outside Dia. (mm) =	98		
Total Coils =	9.5		
Spring Rate (N/mm) =	27.549 ZERO		
Free Length (mm) =	300	0-50% Unprestress	50-70% Prestress
Solid Length (mm) =	104.50	Stress Level (% UTS)	SOLID WORKIN
Solid Load (N) =	5385.83	735A50	82 OS
Solid Stress (N/mm^2) =	1052.14		
Active Coils =	8.00		
Correction Factor =	1.17		
Spring Index =	7.91		
Inside Dia. (mm) =	76.00		
Helix Angle (Deg) =	7.39		
Wire Length (mm) =	2615.22		
Weight per 100 (Kg) =	194.61		
Nat.Frequency (RPM) =	3903.60		
Buckling Possible (mm) <	N/A		
Buckling Definite (mm) <	N/A		

Figure 205: Spring data sheet

APPENDIX L – DYTRAN 4401A2 6 AXIS ACCELEROMETER DRAWING

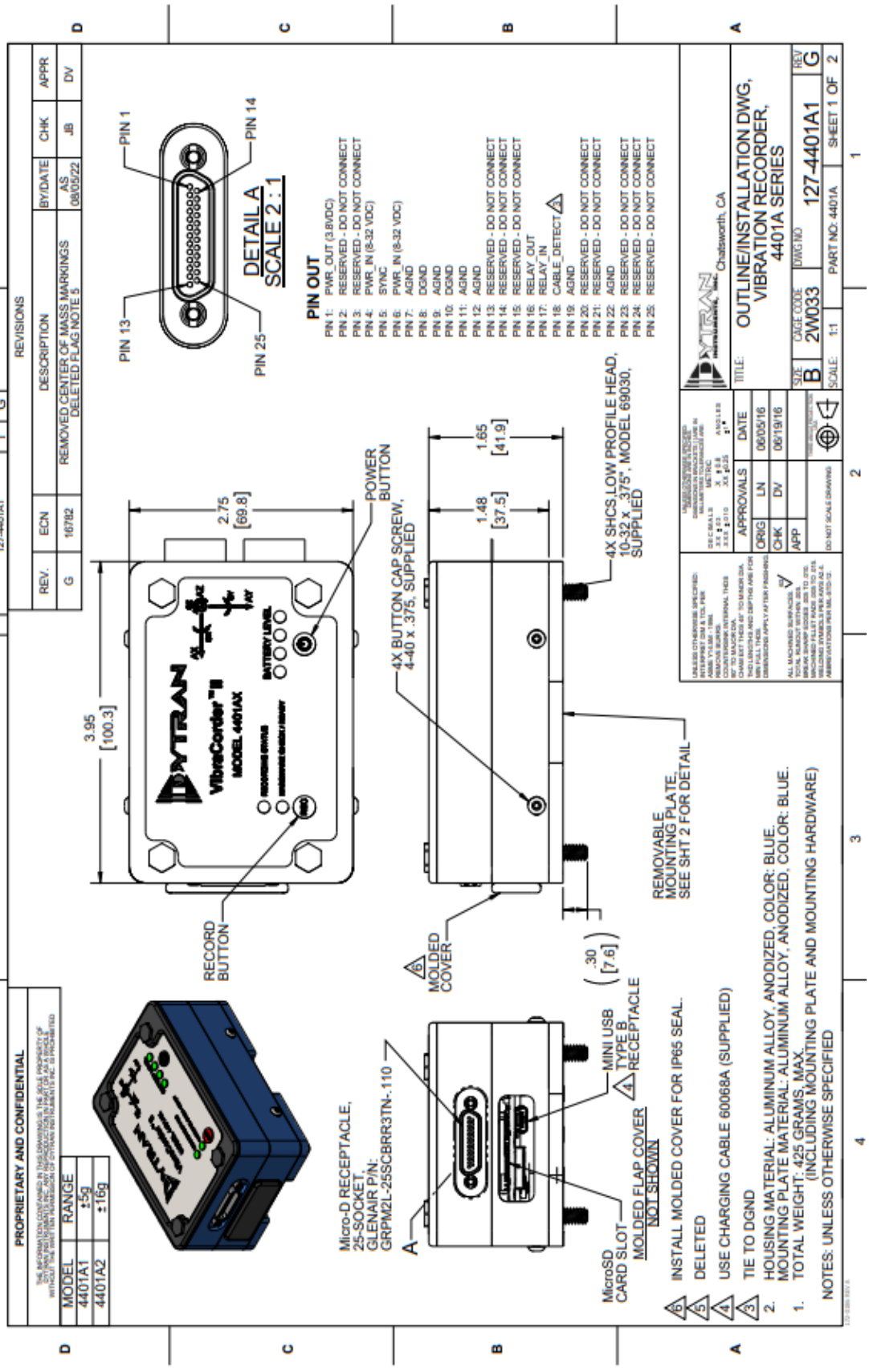

Figure 206: Dytran 4401A2 drawing

APPENDIX M – EXPERIMENTAL RESULTS

The below images present the acceleration results from the experimental setup with initial conditions imposed on the springs. The same setup is used for the numerical simulation where proportional damping is varied between 0.1-0.5%.

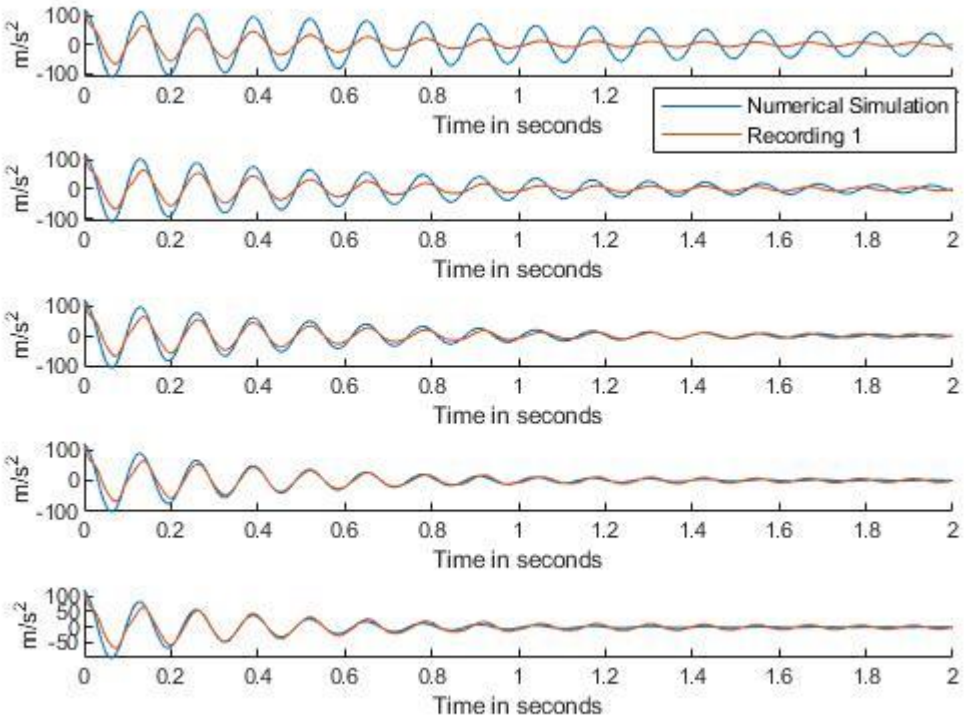

Figure 207: AZ and y coordinate acceleration results for recording 1 and numerical simulation (test case A)

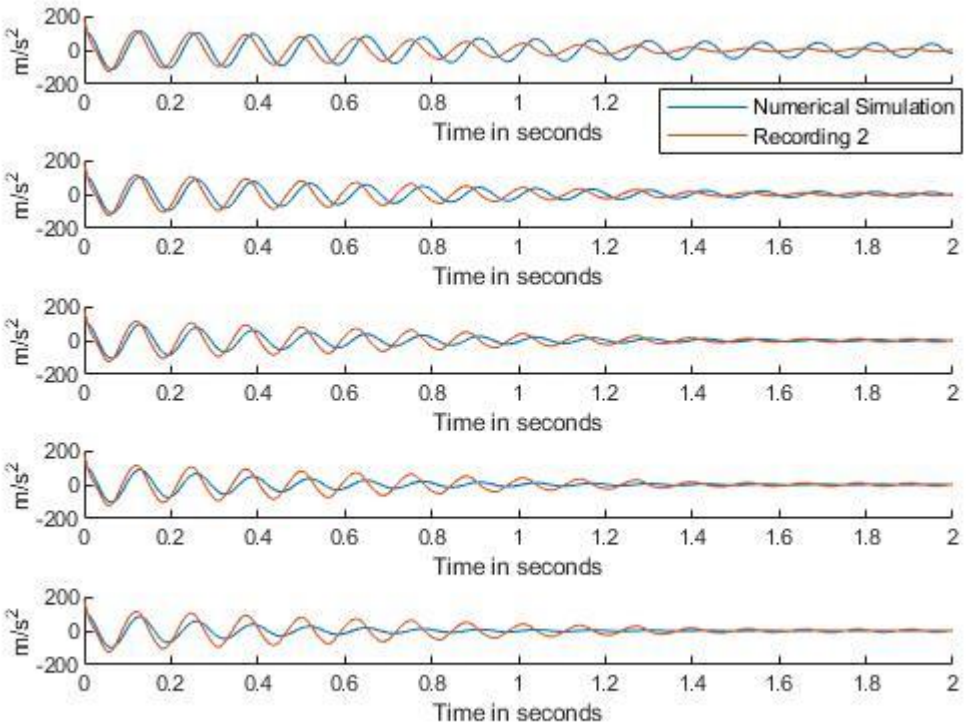

Figure 208: AZ and y coordinate acceleration results for recording 2 and numerical simulation (test case A)

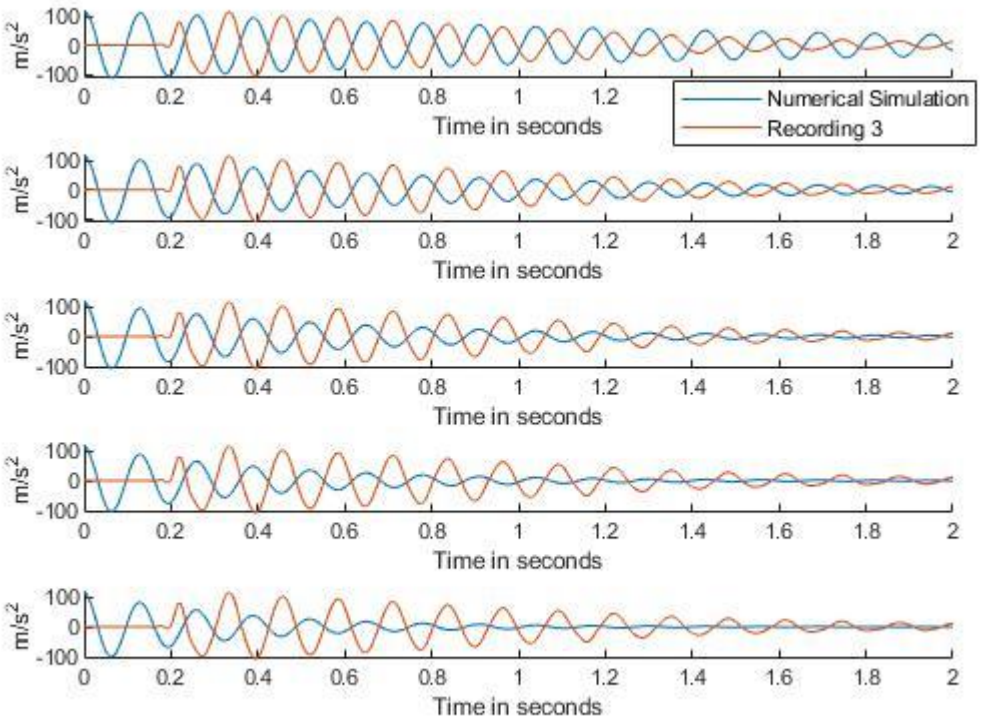

Figure 209: AZ and y coordinate acceleration results for recording 3 and numerical simulation (test case A)

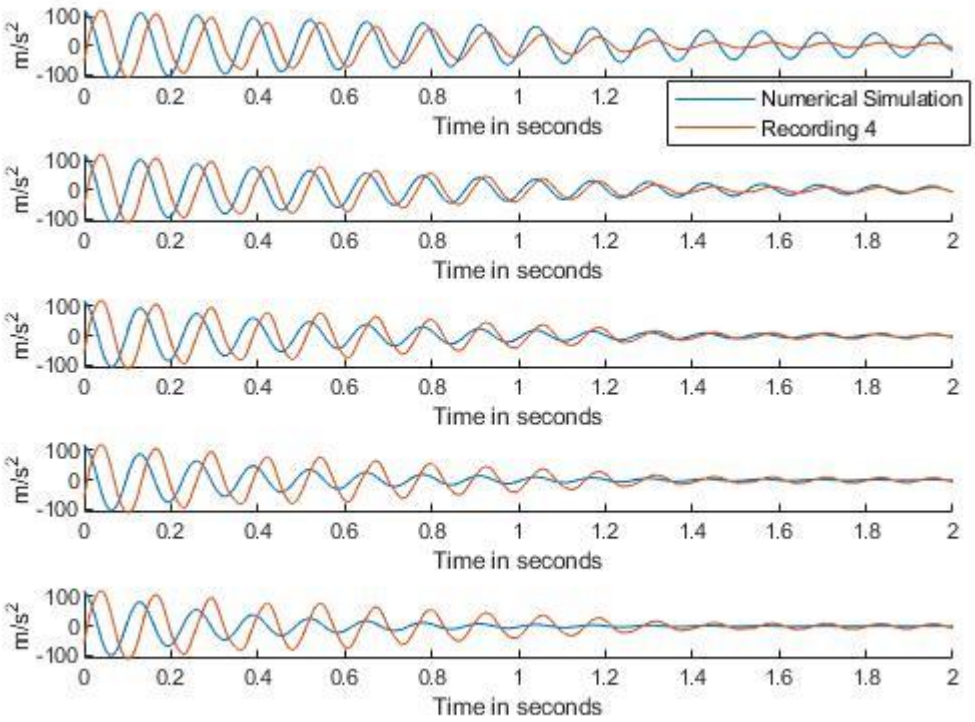

Figure 210: AZ and y coordinate acceleration results for recording 4 and numerical simulation (test case A)

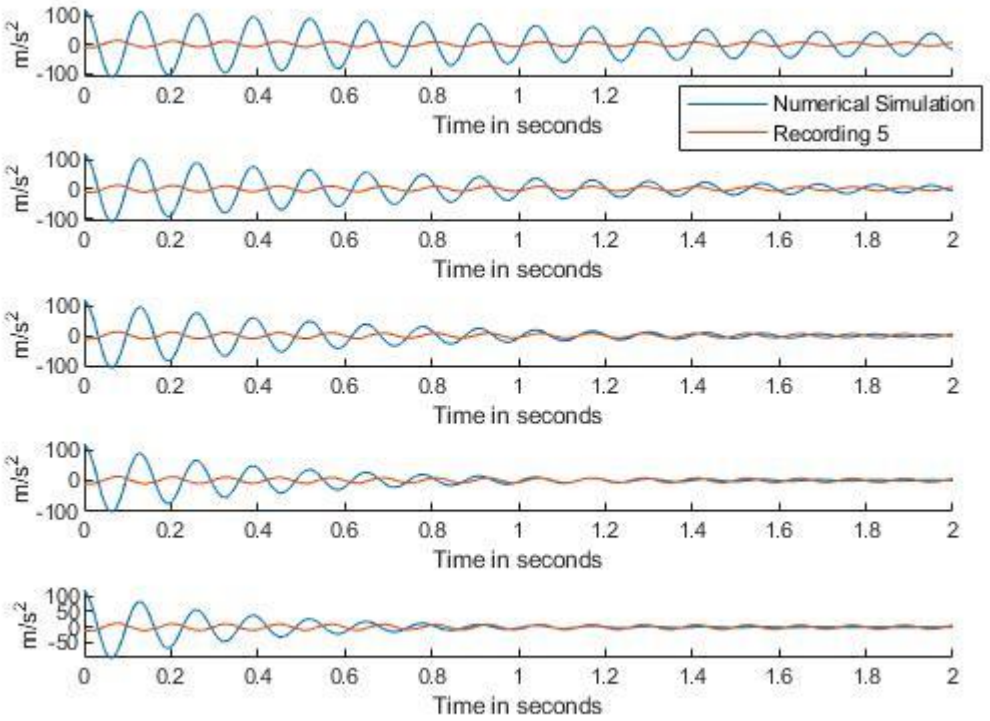

Figure 211: AZ and y coordinate acceleration results for recording 5 and numerical simulation (test case A)

The images below present the comparison between the experimental results and the numerical simulations where initial conditions are imposed on the x coordinate. Damping is varied as performed previously.

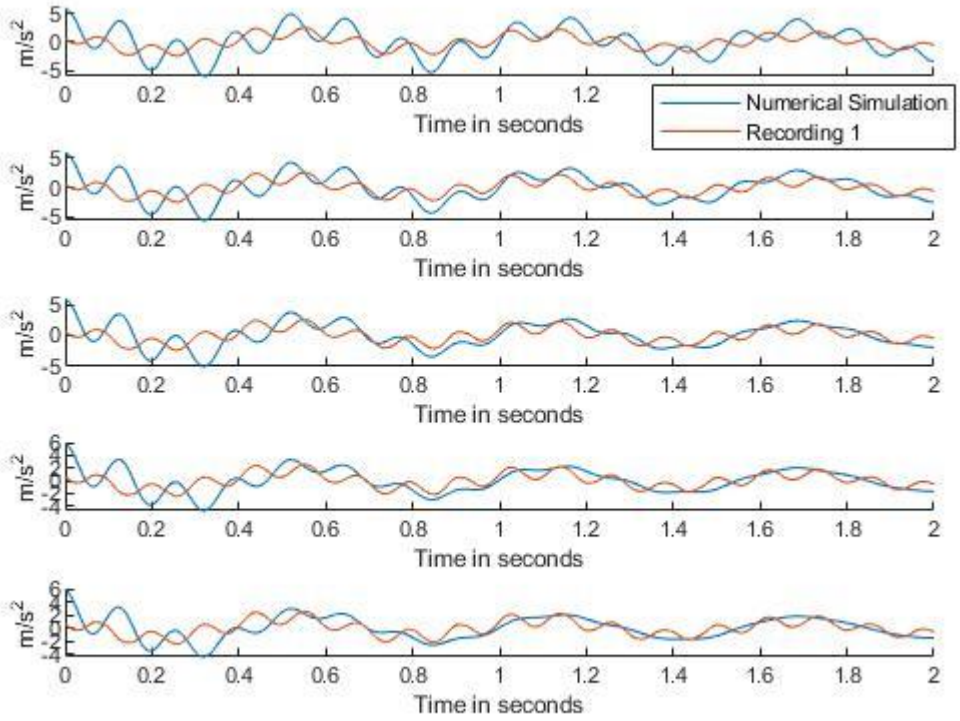

Figure 212: AZ and y coordinate acceleration results for recording 1 and numerical simulation (test case B)

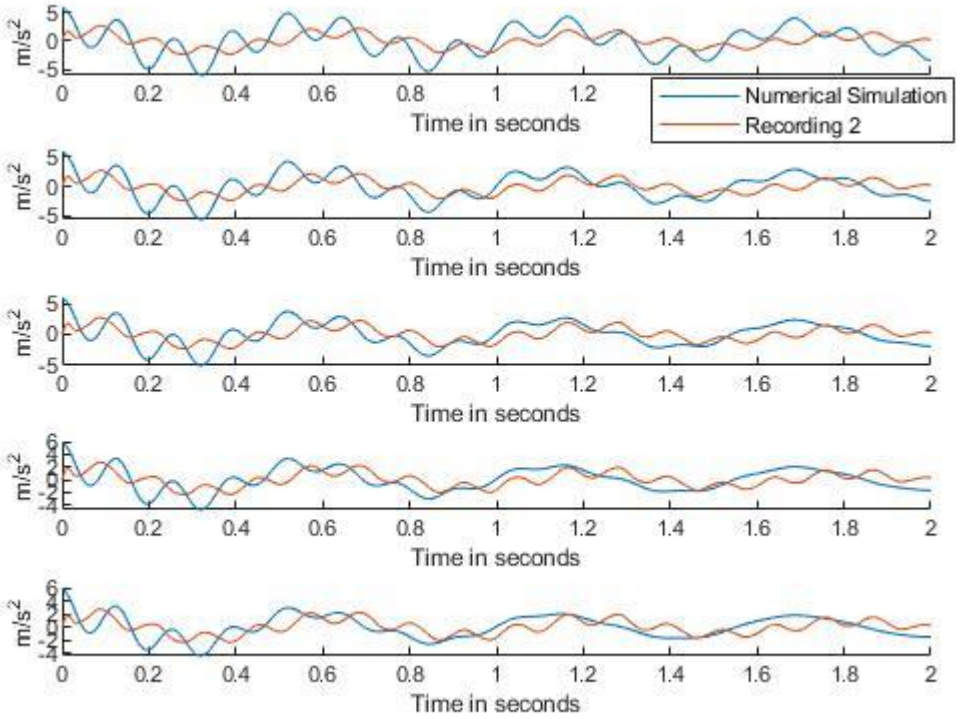

Figure 213: AZ and y coordinate acceleration results for recording 2 and numerical simulation (test case B)

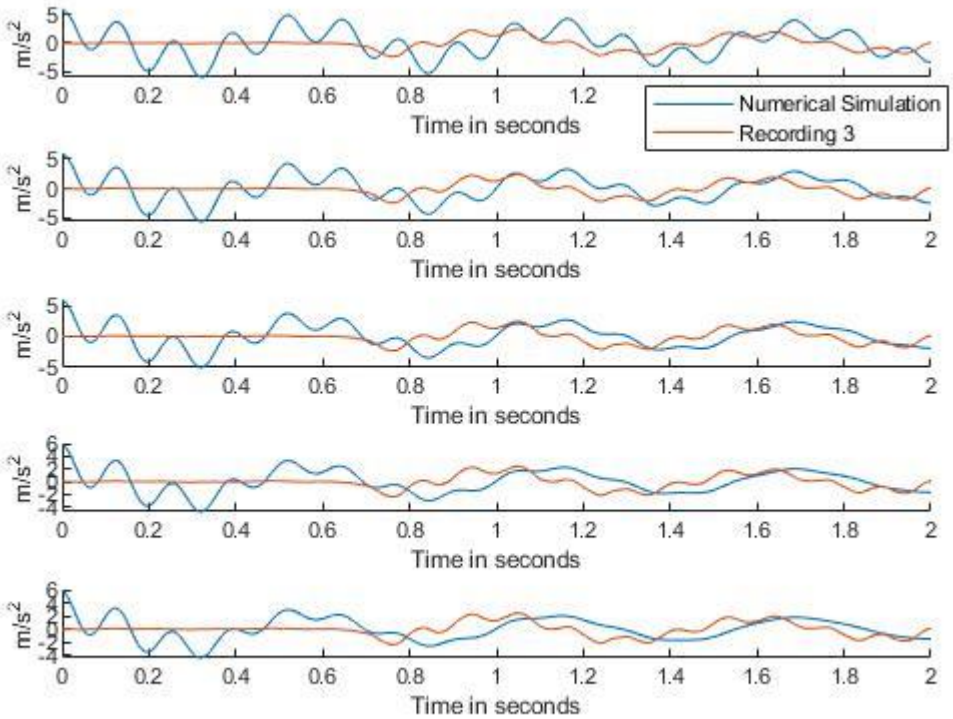

Figure 214: AZ and y coordinate acceleration results for recording 3 and numerical simulation (test case B)

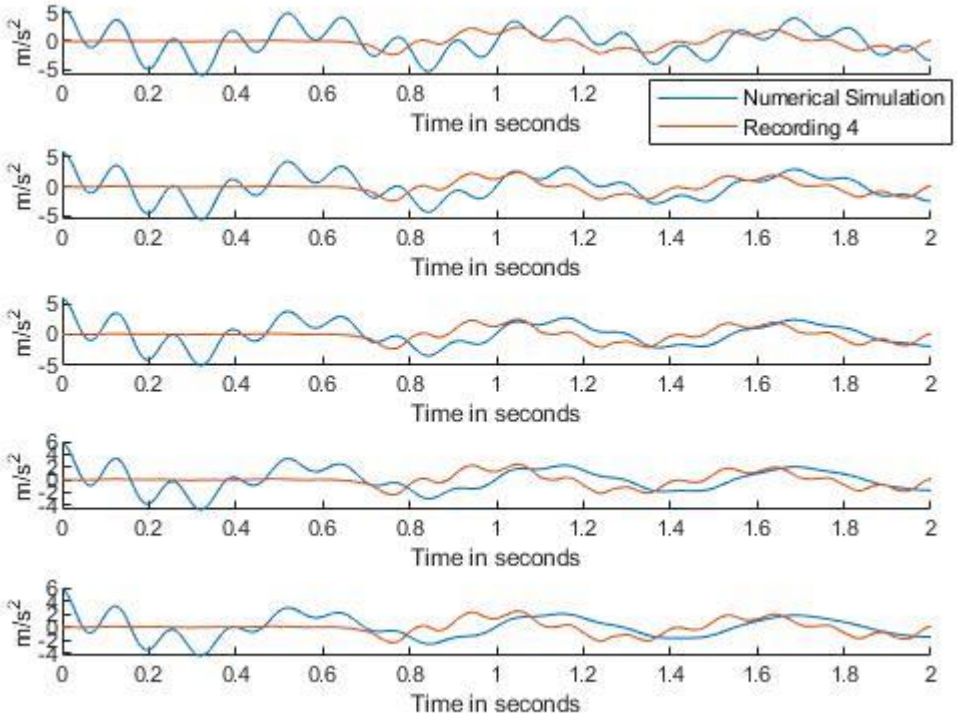

Figure 215: AZ and y coordinate acceleration results for recording 4 and numerical simulation (test case B)

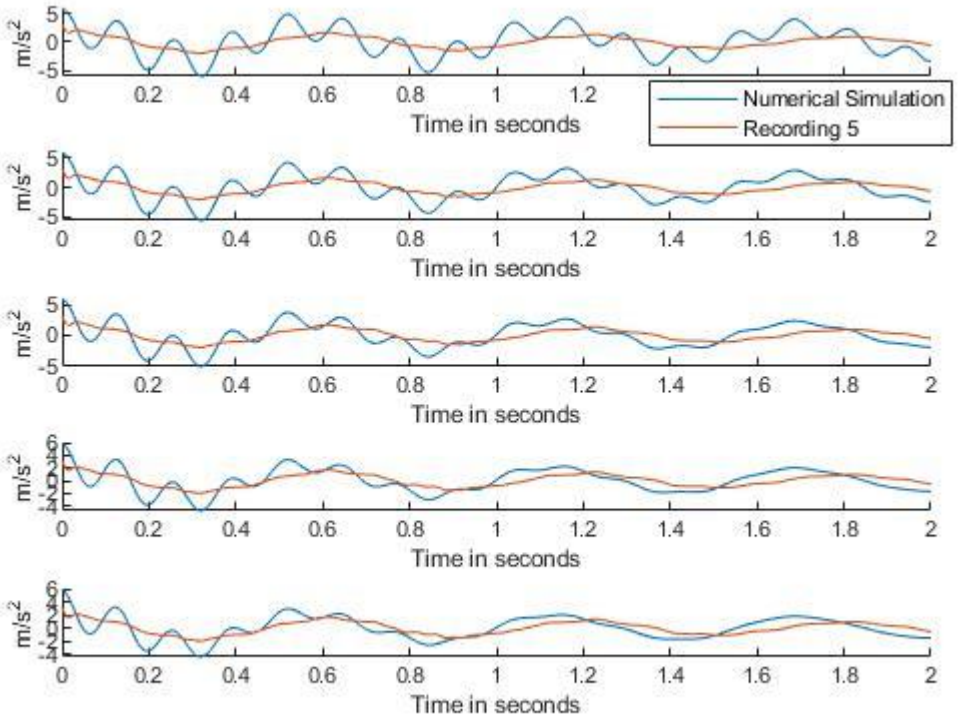

Figure 216: AZ and y coordinate acceleration results for recording 5 and numerical simulation (test case B)

The images below present the comparison between the experimental results and the numerical simulations where initial conditions are imposed on the x coordinate. The results pertain to the x coordinate (AY). Damping is varied as performed previously.

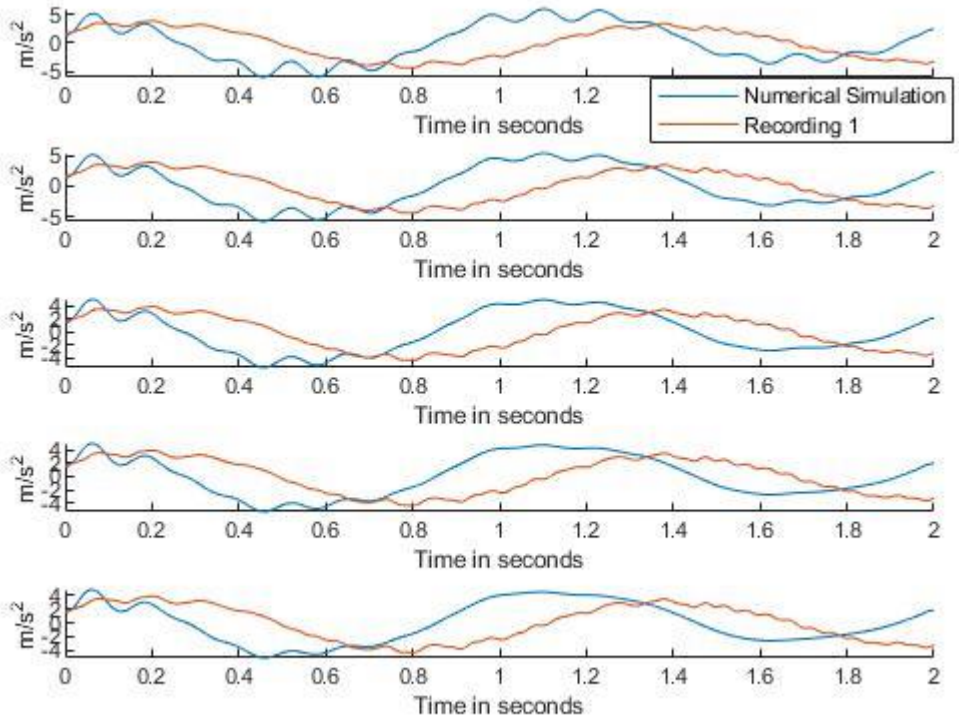

Figure 217: AY and x coordinate acceleration results for recording 1 and numerical simulation (test case B)

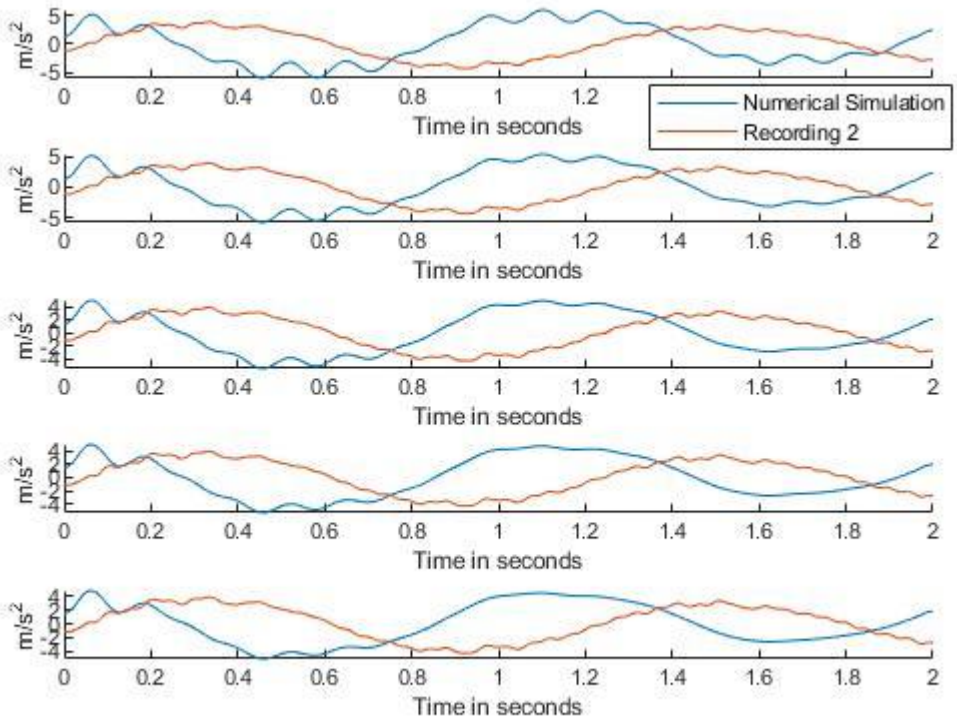

Figure 218: AY and x coordinate acceleration results for recording 2 and numerical simulation (test case B)

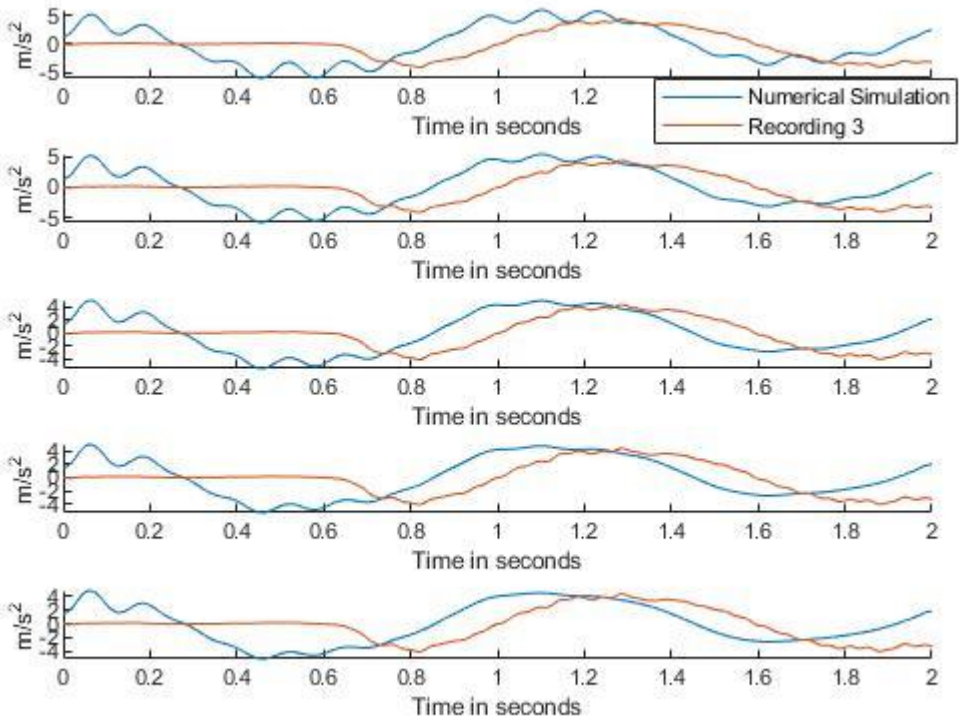

Figure 219: AY and x coordinate acceleration results for recording 3 and numerical simulation (test case B)

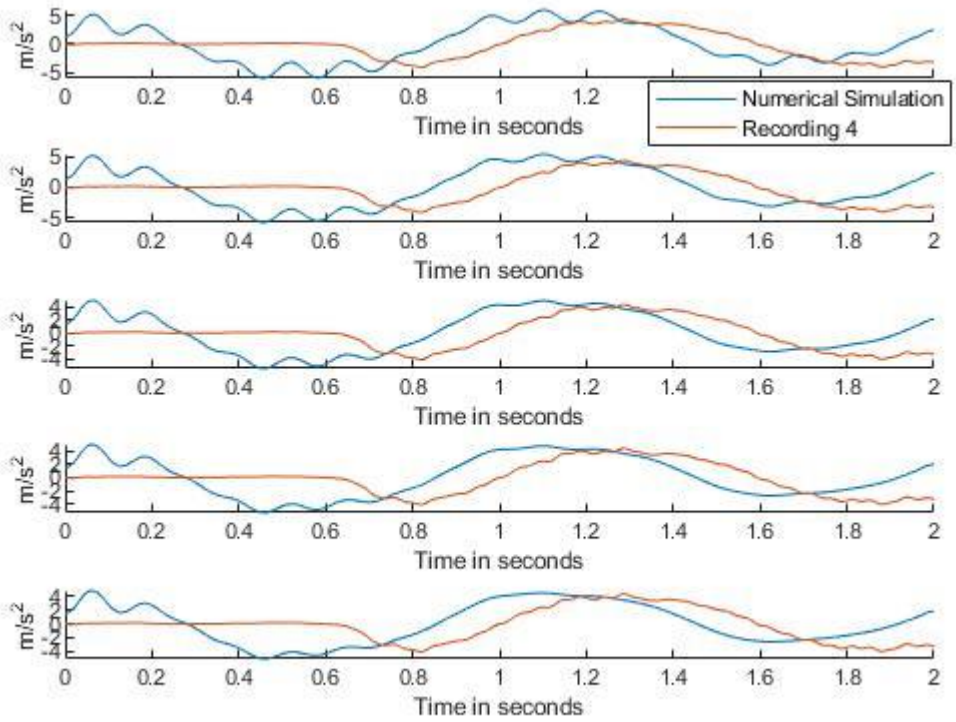

Figure 220: AY and x coordinate acceleration results for recording 4 and numerical simulation (test case B)

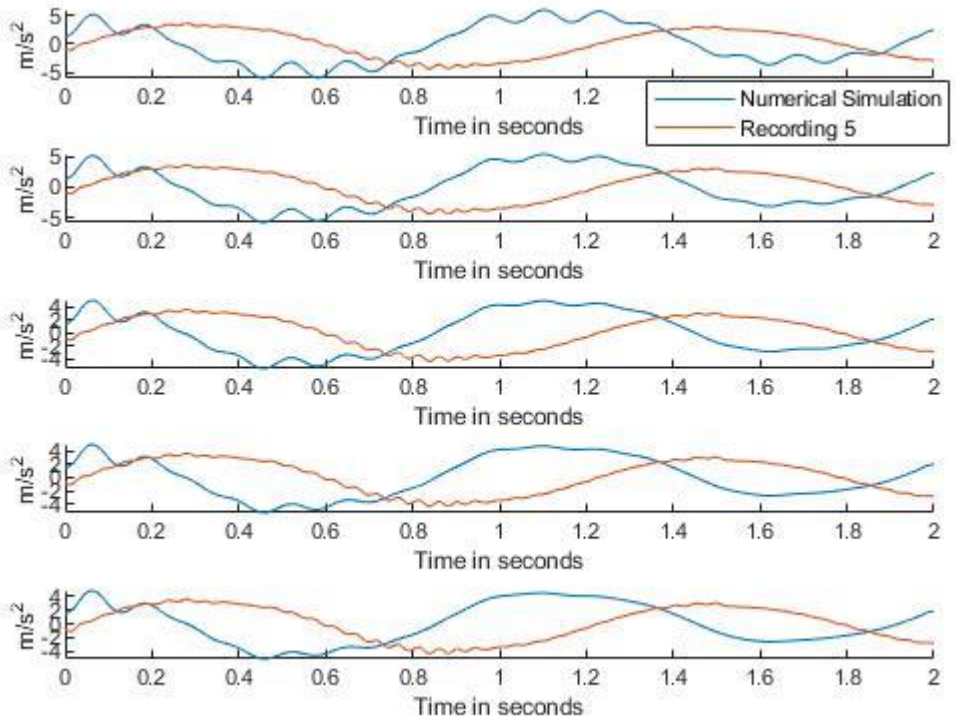

Figure 221: AY and x coordinate acceleration results for recording 5 and numerical simulation (test case B)

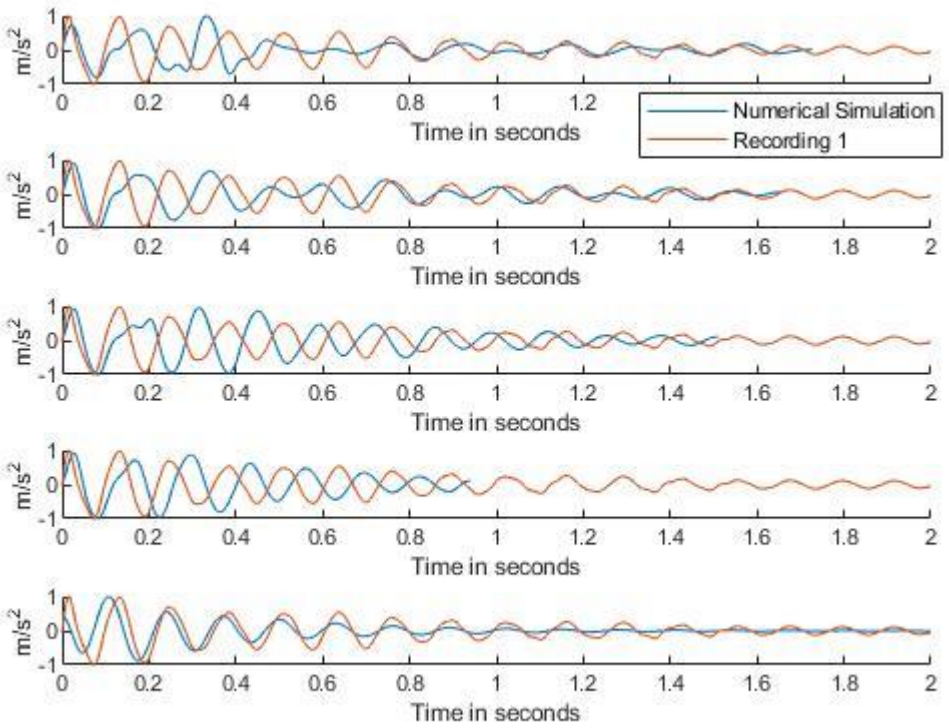

Figure 222: Normalised AZ and y coordinate acceleration results for recording 1 and numerical simulation (test case C)

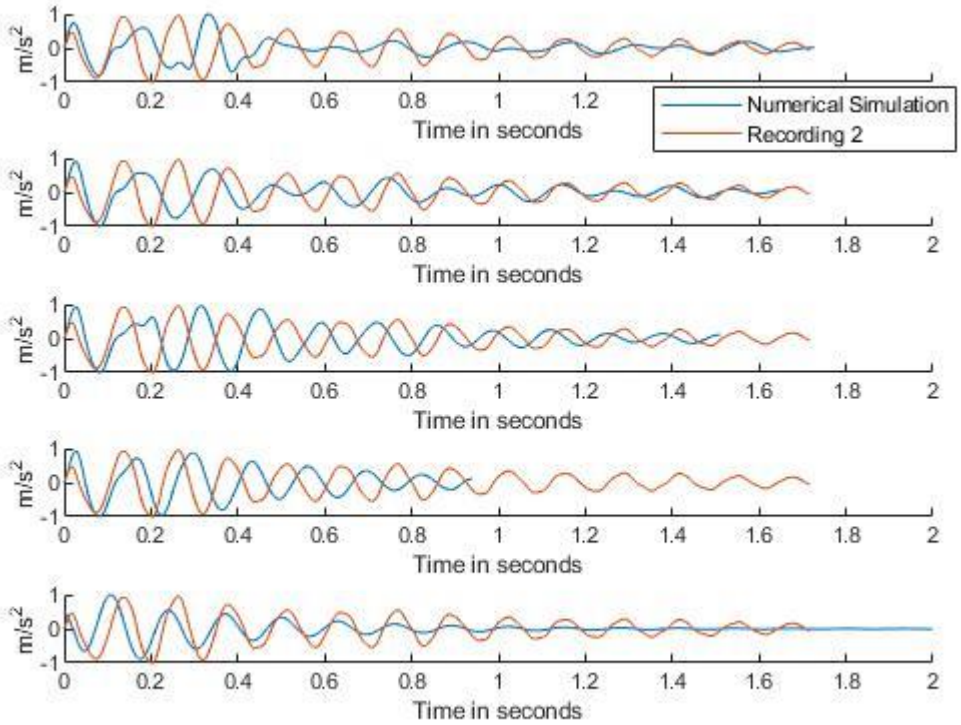

Figure 223: Normalised AZ and y coordinate acceleration results for recording 2 and numerical simulation (test case C)

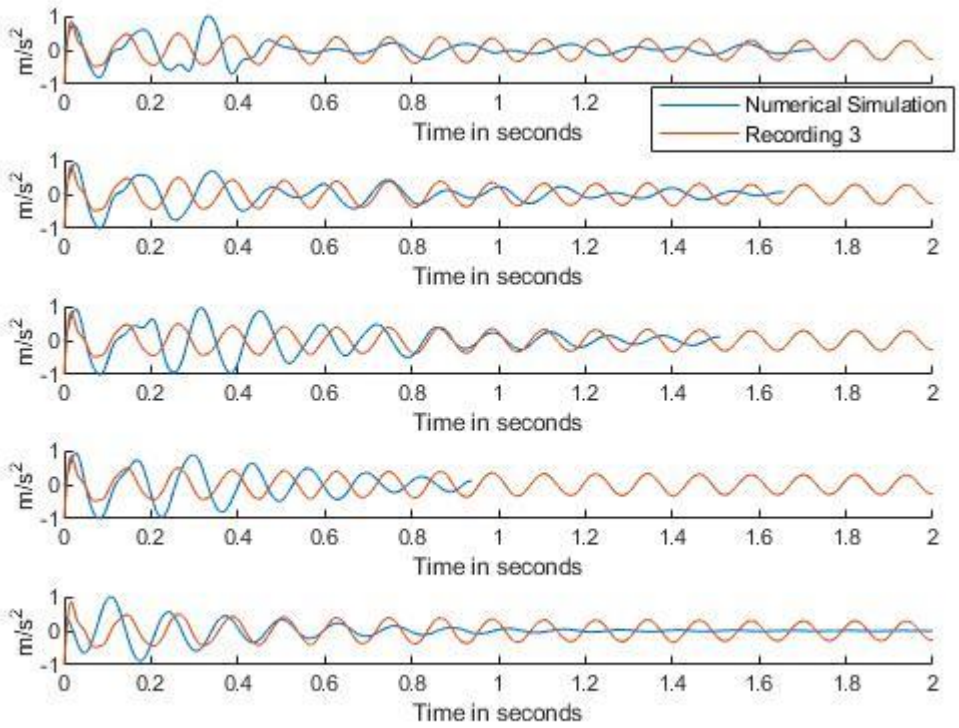

Figure 224: Normalised AZ and y coordinate acceleration results for recording 3 and numerical simulation (test case C)

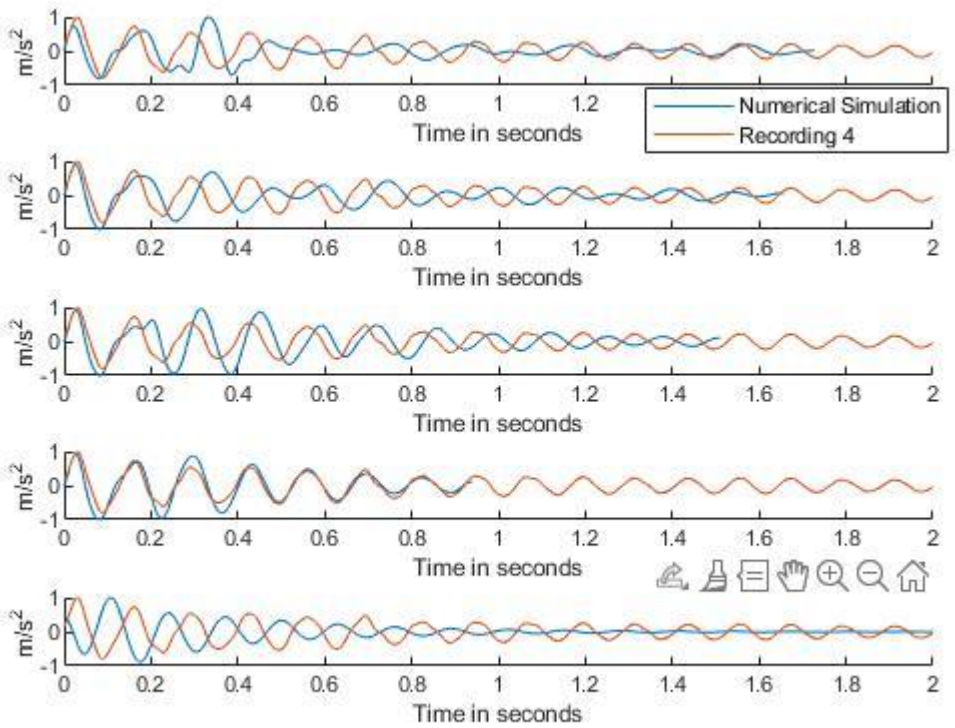

Figure 225: Normalised AZ and y coordinate acceleration results for recording 4 and numerical simulation (test case C)

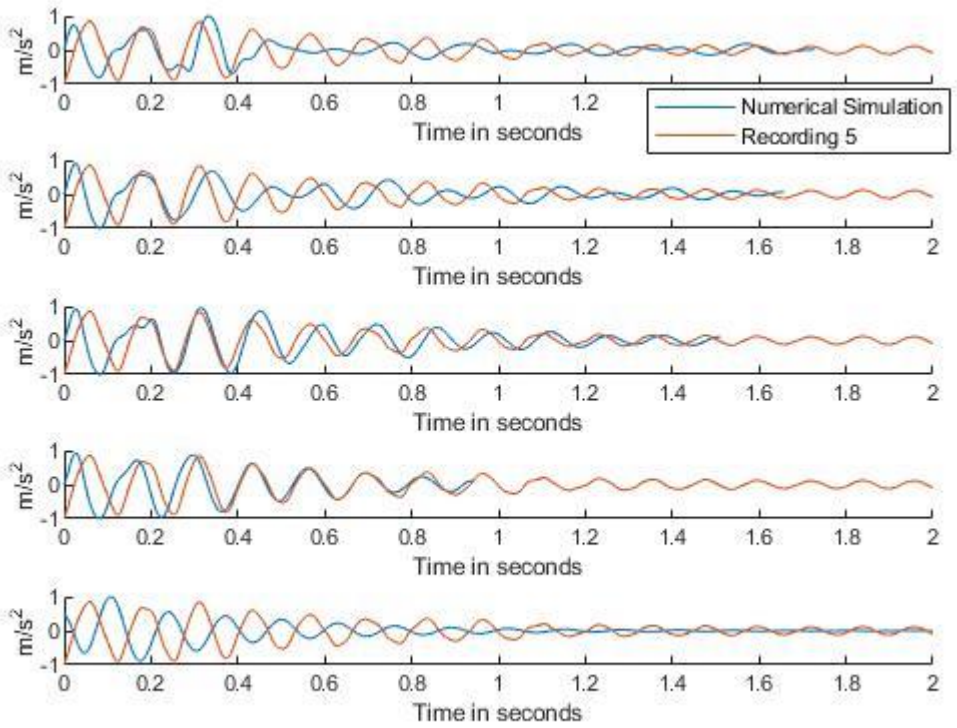

Figure 226: Normalised AZ and y coordinate acceleration results for recording 5 and numerical simulation (test case C)

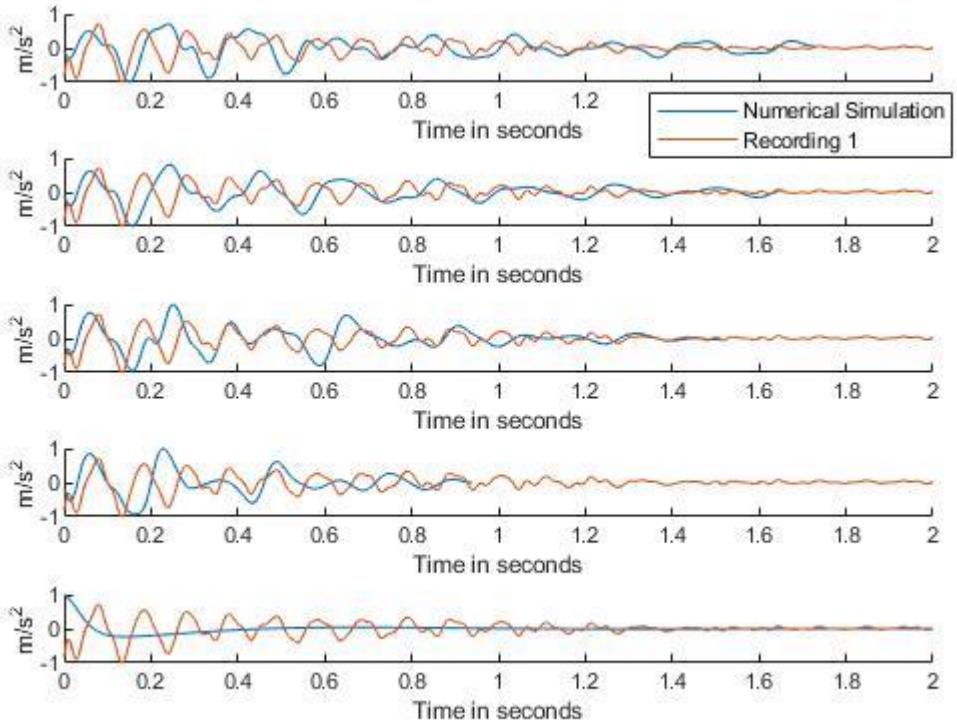

Figure 227:Normalised AY and x coordinate acceleration results for recording 1 and numerical simulation (test case C, no lag)

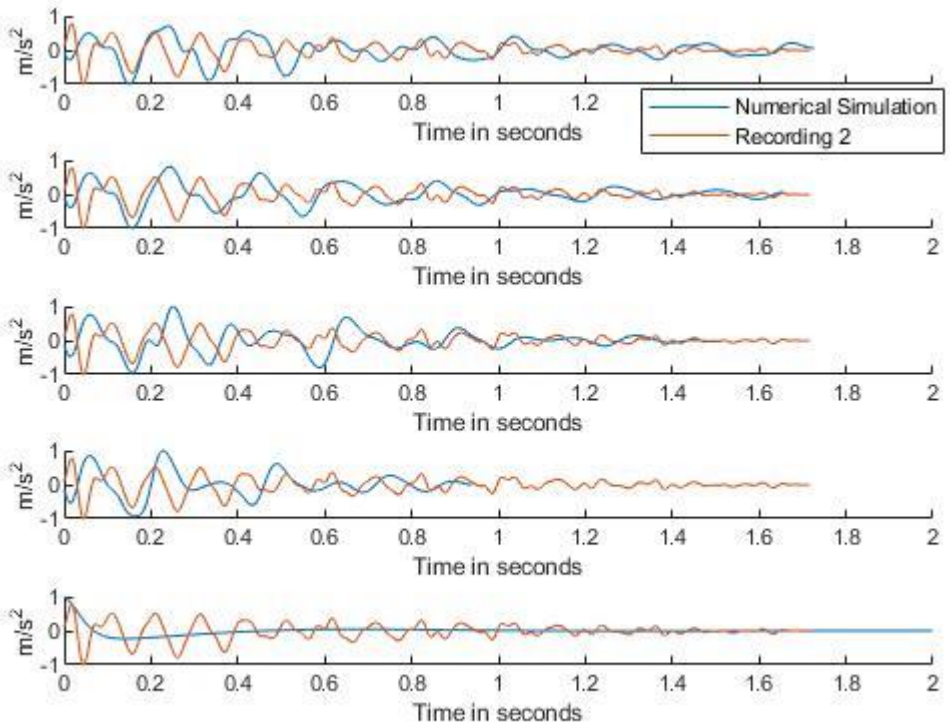

Figure 228: Normalised AY and x coordinate acceleration results for recording 2 and numerical simulation (test case C, no lag)

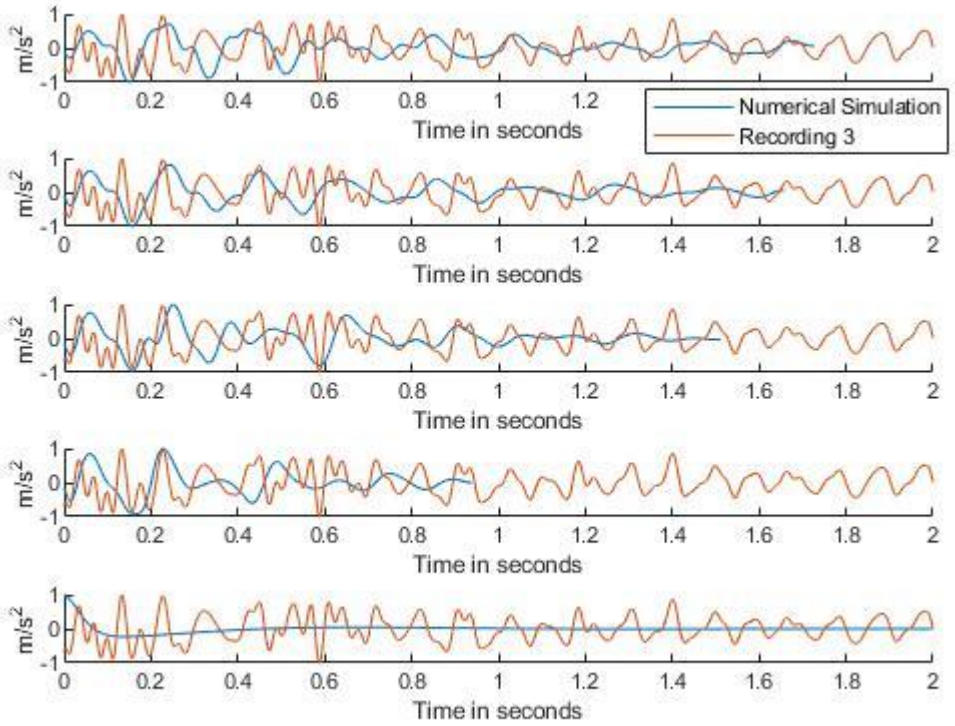

Figure 229:Normalised AY and x coordinate acceleration results for recording 3 and numerical simulation (test case C, no lag)

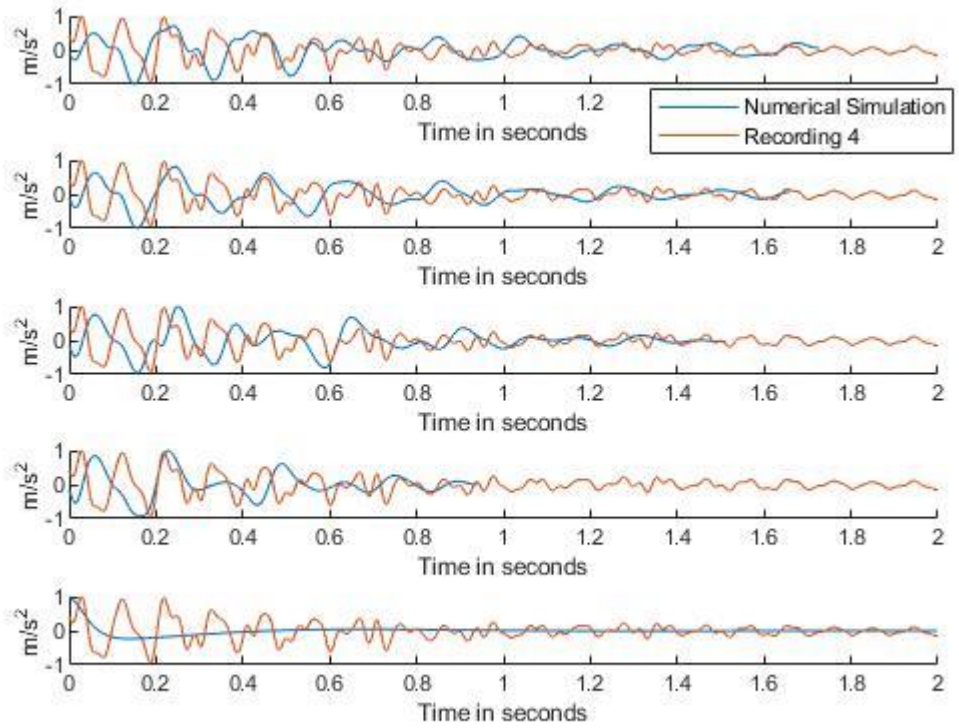

Figure 230: Normalised AY and x coordinate acceleration results for recording 4 and numerical simulation (test case C, no lag)

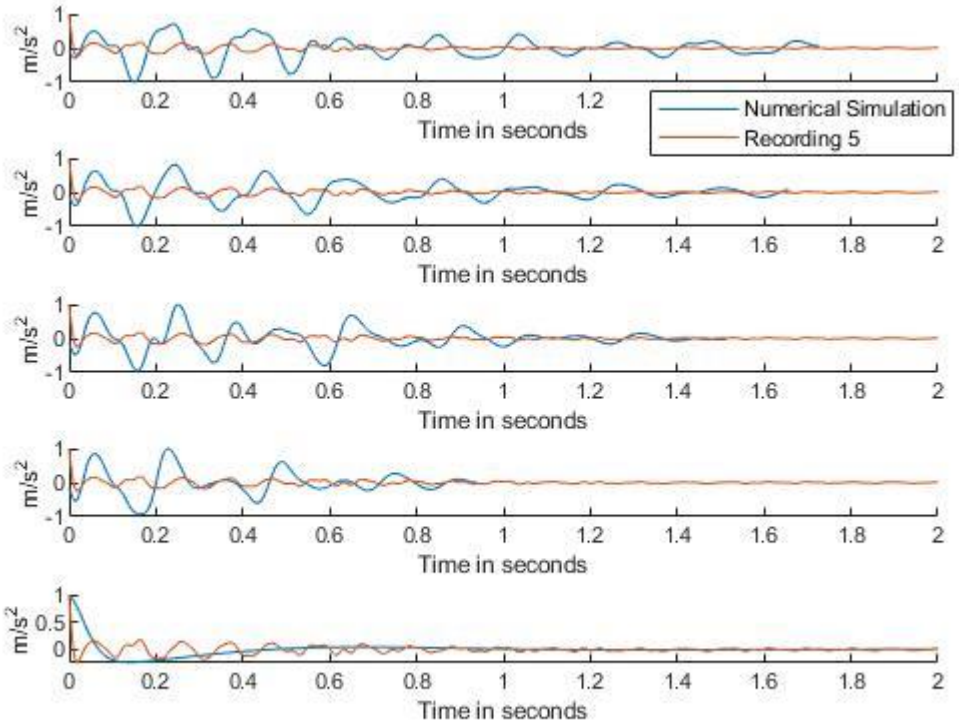

Figure 231:Normalised AY and x coordinate acceleration results for recording 5 and numerical simulation (test case C, no lag)

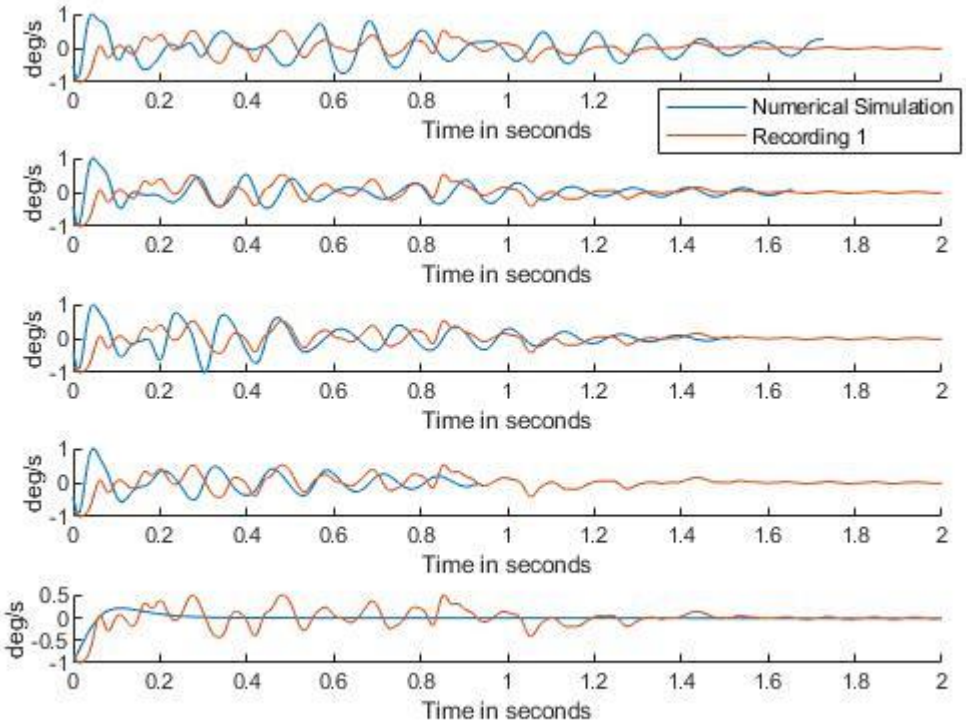

Figure 232: Normalised GX and ϑ coordinate acceleration results for recording 1 and numerical simulation (test case C, no lag)

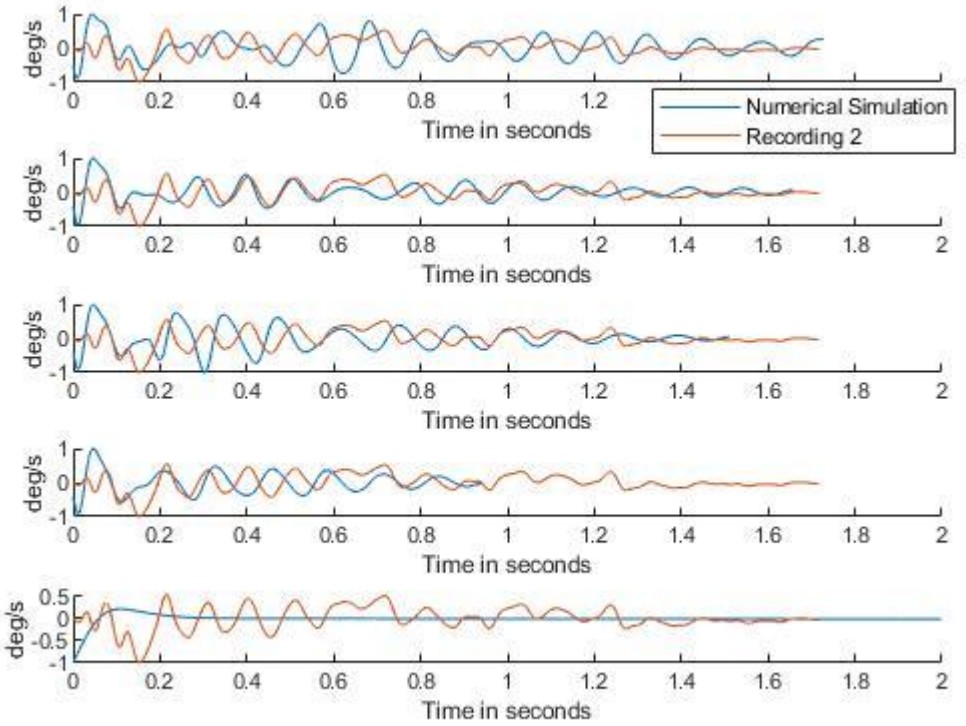

Figure 233: Normalised GX and ϑ coordinate acceleration results for recording 2 and numerical simulation (test case C, no lag)

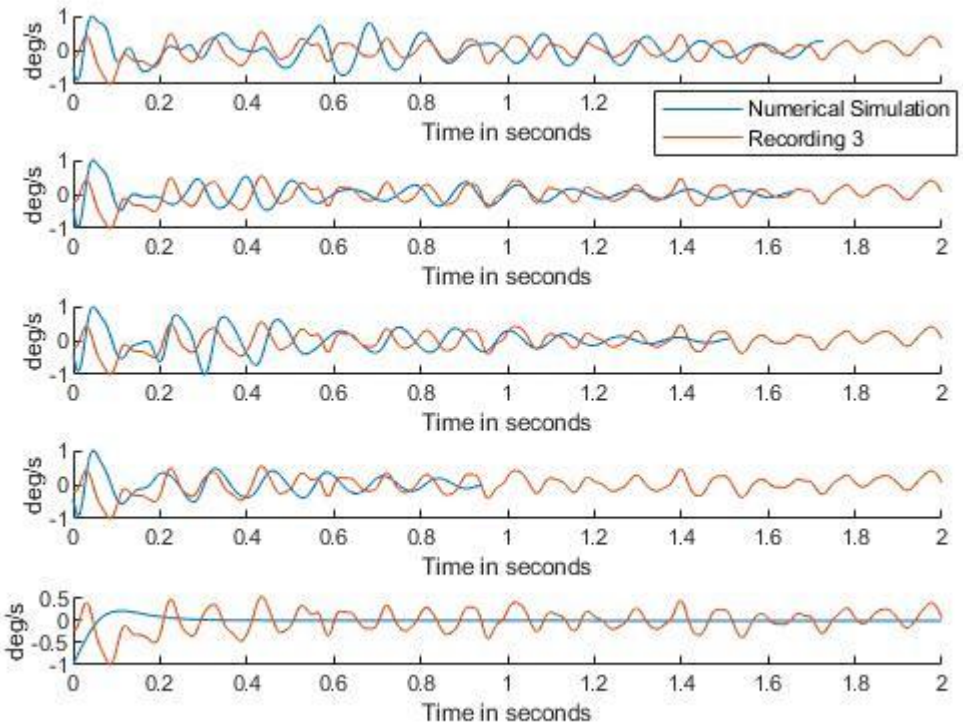

Figure 234: Normalised GX and ϑ coordinate acceleration results for recording 3 and numerical simulation (test case C, no lag)

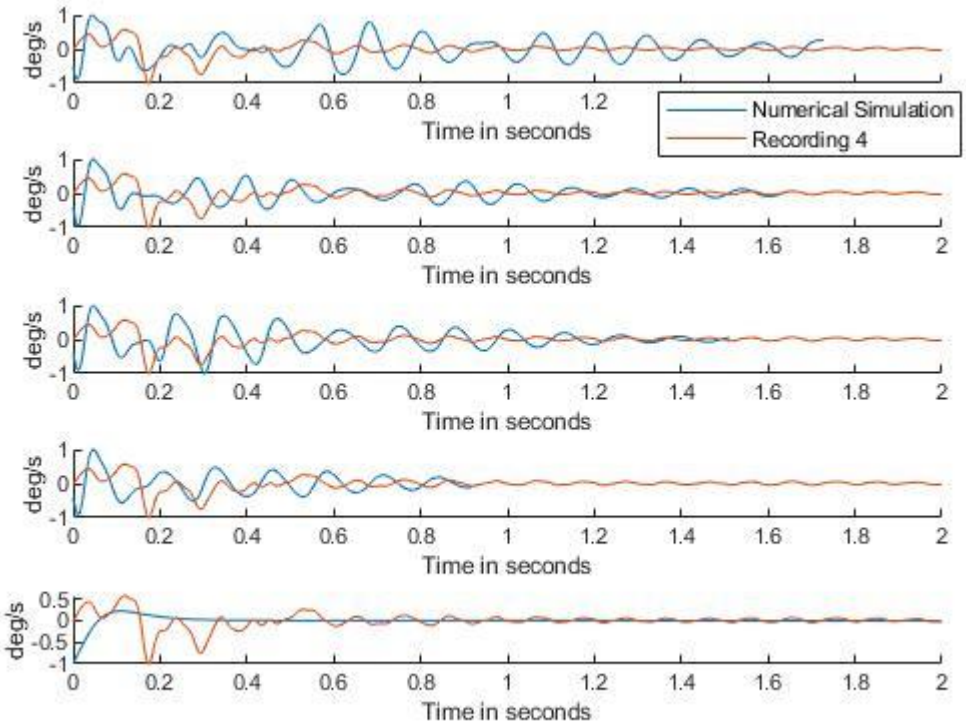

Figure 235: Normalised GX and ϑ coordinate acceleration results for recording 4 and numerical simulation (test case C, no lag)

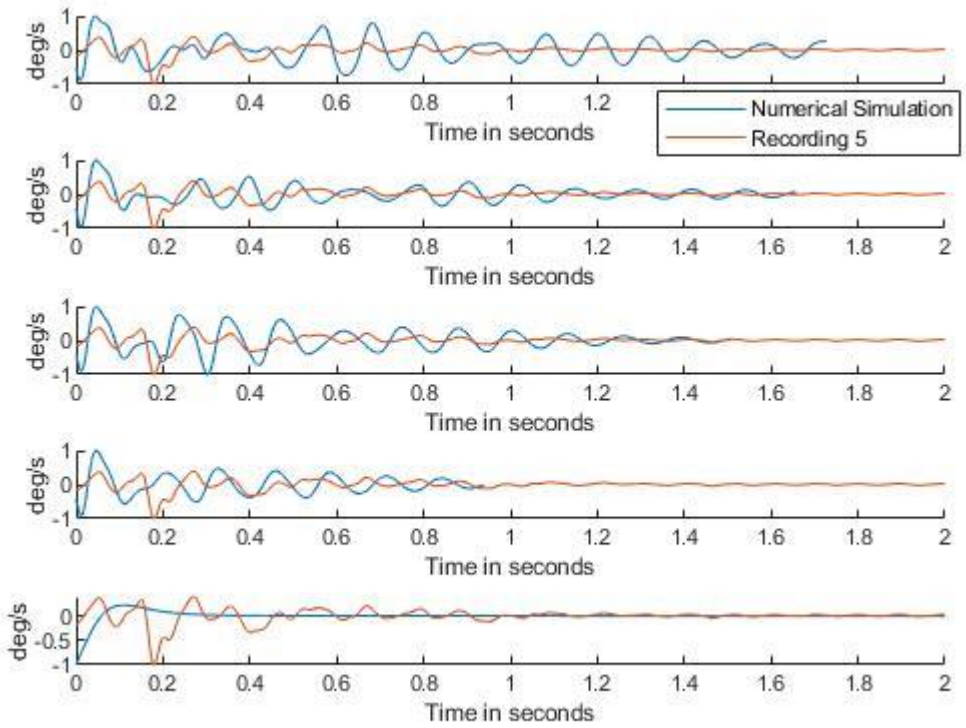

Figure 236: Normalised GX and ϑ coordinate acceleration results for recording 5 and numerical simulation (test case C, no lag)

.